INTERPRETATION OF FLOW AND PRESSURES IN FULL SCALE SILOS

by

Jian-Fei Chen

Thesis presented for the Degree of Doctor of Philosophy

Volume 1 of 2

Department of Civil and Environmental Engineering
The University of Edinburgh
August 1996

To my wife Hai-Ying and my parents

ABSTRACT

Silos are widely used for short and long term storage of bulk solids in many industries. However, silo failures are very common, and represent a source of major economic loss. The reasons for this high failure rate are believed to be strongly associated with the poor level of current understanding of solids flow patterns and pressures on the silo wall exerted by the stored solids.

This thesis is chiefly concerned with the interpretation of solids flow patterns and wall pressures in full scale silos. The data analysed are from a full scale silos research project at the University of Edinburgh. The technique of residence time measurement was adopted to measure solids flow patterns in the project because it probably provides the most information among all the feasible experimental methods when applied to full scale silos. However, interpretation of the results under funnel flow conditions is not at all straightforward, and numerical processing of the results to identify the changing flow channel boundary is still in its infancy.

Four techniques are used in this thesis to interpret the solids flow patterns from residence time measurements. These are: a) plotting contours of residence times; b) plotting contours of mean velocities; c) graphical flow visualisations and d) analysis of the emerged mass from each seeded level at a particular instant. All but the first method have been newly developed in this thesis.

The technique of graphical visualisation displays the flow pattern as a time-dependent phenomenon using residence time observations as raw data. The analytical formulation of the method is presented. A program suite has been developed to implement the technique. It is very flexible and is applicable to silos of different configurations and storing any material. The display of the solids flow pattern in a

graphical display format has immediate appeal to industrial engineers. It has great potential for industrial application.

The method of analysing mass emerged from each seeded level assumes that each marker represents the solid surrounding it at the given level. By integrating the mass emerged from a level over time, a normalised mass-time curve is obtained. By examining the characteristics of the normalised mass-time curve for typical mass and funnel flow modes, it is possible to identify the flow pattern from a single plot and to quantify the position of the flow channel boundary in funnel flow for the first time.

These techniques are used to interpret the solids flow pattern in two full scale silos. The 250 tonne gypsum silo was fitted with an inverted cone bin discharge aid and air pads on the hopper section. It contained ground gypsum powder. The tests revealed flow behaviour which was not expected and the commercial discharge aids were found to have a significant effect on the flow patterns.

Experiments in the new cylindrical steel silo at British Steel using iron ore pellets revealed that steep-sided funnel flow patterns occurred under both concentric and eccentric discharge conditions. The plan cross-section of the flow channel is close to, but not exactly, circular. Under eccentric (both fully eccentric and half eccentric) discharge, the flow channel inclines towards the nearest wall, but remains highly symmetrical relative to the vertical diametrical plane of symmetry through the outlets. Under fully eccentric discharge, the flow pattern develops as a narrow channel against the silo wall, similar to the pattern proposed by some earlier speculative writings on the subject. A two parameter model is proposed to describe the flow channel geometry.

A rigorous statistical method of inferring wall pressures from wall strain observations is developed for the first time in this thesis. The theory is presented in its fullest form, in which six strain observations at any point on the silo wall are used, and the loading parameters include normal pressure, vertical wall friction and circumferential

wall friction. The statistics of the method are comprehensively discussed using both theoretical and example analyses. A program suite is developed to implement the technique. This method is used in the thesis to infer the wall pressure distributions in a highly instrumented silo after filling and during discharge. It is believed that the outcome is the most comprehensive and detailed picture of pressure distributions on silo walls yet produced.

It is believed that this is the first time that the detailed changing form of the eccentric discharge pressure distribution at the start of discharge has been observed. The most critical instant under eccentric discharge is identified for the first time to be during the development of the flow channel, rather than after the flow channel has developed. The inferred pressures are compared with the solids flow patterns and it is found that the pressures occurring in each flow regime are highly correlated with the measured flow pattern.

The Appendices to the thesis include some additional studies of related problems: the local stiffening effect of a DD gauge, analysis of the effective section of a ring attached to a shell, and finite element predictions of wall pressures in a coal silo.

PREFACE

This thesis is submitted to the University of Edinburgh for the degree of Doctor of Philosophy. The work described in this thesis was carried out by the candidate during the years 1992-1996 under the supervision of Professor J. M. Rotter. All the work was carried out in the Department of Civil and Environmental Engineering at the University of Edinburgh.

In accordance with Regulation 3.4.7 of the University of Edinburgh governing the requirements for the degree of Doctor of Philosophy, the candidate submits that the thesis has been composed by himself and that the work described herein is his own unless otherwise stated in the text.

Twelve supporting papers which are based on the work presented in this thesis have been published in refereed international journals and conferences:

1. Chen, J.F., Ooi, J.Y. and Rotter, J.M. (1996) "A Rigorous Statistical Technique for Inferring Circular Silo Wall Pressures from Wall Strain Measurements", Engineering Structures, Vol. 18, No. 4, April, pp321-331.
2. Chen, J.F., Ooi, J.Y. and Rotter, J.M. (1996) "Local Stiffening Effect of 'Double Deck' Bending Strain Gauges: Part 1", Strain, Vol.32, No.1, February, pp13-22.
3. Chen, J.F., She, K.M., Rotter, J.M. and Ooi, J.Y. (1996) "Local Stiffening Effect of 'Double Deck' Bending Strain Gauges: Part 2", Strain, Vol.32, No. 2, May, pp43-48.
4. Ooi, J.Y., Chen, J.F., Lohnes, R.A. and Rotter, J.M. (1996) "Prediction of Wall Pressures in Coal Silos", Construction and Building Materials, Vol. 10, No. 2, April, pp109-116.
5. Chen, J.F., Rotter, J.M. and Ooi, J.Y. (1993) "A Technique for the Interpretation of Silo Wall Pressures from Strain Measurements", Proc., International

Symposium Reliable Flow of Particulate Solids II (RELPOWFLO II), Oslo, Norway, 23-25 Aug., pp255-267.

6. Rotter, J.M., Ooi, J.Y., Lauder, C., Coker, I., Chen, J.F. and Dale, B.G. (1993) "A Study of the Flow Patterns in an Industrial Silo", Proc., International Symposium Reliable Flow of Particulate Solids II (RELPOWFLO II), Oslo, Norway, 23-25 Aug., pp517-524.
7. Chen, J.F., Ooi, J.Y. and Rotter, J.M. (1994) "Local Stiffening Effect of 'Double Deck' Bending Strain Gauges and Its Correction", Proc., International Conference on Advances in Engineering Measurements, Edinburgh, 30 Aug. - 1 Sept., p32.
8. Ooi, J.Y., Chen, J.F. and Rotter, J.M. (1994) "Inferring Silo Wall Pressures from Strain Measurements on the Wall", Proc., International Conference on Advances in Engineering Measurements, Edinburgh, 30 Aug. - 1 Sept., pp33-40.
9. Chen, J.F., Ooi, J.Y., Rotter, J.M., Coker, I., Lauder, C., Zhang, K.F. and Dale, B.G. (1994) "Flow Pattern Measurements in a Full Scale Silo", Proc., International Conference on Advances in Engineering Measurements, Edinburgh, 30 Aug. - 1 Sept., pp58-63.
10. Chen, J.F., Zhang, K.F., Ooi, J.Y. and Rotter, J.M. (1995) "Numerical Predictions of Wall Pressures in Cylindrical Silos", Research in Structural Engineering-Current Status and Trends, Tongji University Press, pp425-445.
11. Chen, J.F., Zhang, K.F., Ooi, J.Y. and Rotter, J.M. (1995) "Visualisation of Solids Flow in a Full Scale Silo", Proc., Third European Symposium Storage and Flow of Particulate Solids (Janssen Centennial), Nuremberg, Germany, 21 to 23 Mar., pp427-436.
12. Chen, J.F., Tiley, P.J., Ooi, J.Y. and Rotter, J.M. (1996) "Flow Pattern and Pressures in an Iron Ore Silo", to be presented in the 12th International Congress of Chemical and Process Engineering, 25-30 Aug. 1996, Praha, Czech Republic.

Jian-Fei Chen

ACKNOWLEDGEMENTS

The author was financially supported by a scholarship awarded by the State Education Commission of the People's Republic of China under the Sino-British Friendship Scholarship Scheme which was funded by the Chinese Government, the British Government and the Sir Y. K. Pao Foundation (Hong Kong). The author is grateful for this support. The author is also thankful to Zhejiang University for nominating him to compete this scholarship.

A debt of thanks is due to the members of the steering committee and the members of the technical working party of the full scale silos research project at Edinburgh University. The data analysed in this thesis were from the project. Most of the work presented in this thesis, especially the development of the flow visualisation program, has been presented in various steering committee meetings and working party meetings. Their very valuable comments and suggestions and enthusiastic interests in the work are gratefully acknowledged. Special thanks go to the Chairman Dr Nick Rolfe of Brunner Mond, and the Secretary Mr Peter Middleton of the British Materials Handling Board.

The author is especially indebted to his supervisor, Professor J. Michael Rotter, and co-supervisor, Dr Jin Y. Ooi, for their continued encouragement, enlightening guidance and friendship.

Many thanks are due to my friends and colleges Peter J. Tiley, Iain Mackintosh, Colin Lauder and Ian Coker for their help and co-operation in the full scale silos research project in the Department of Civil and Environmental Engineering at the University of Edinburgh. Special thanks are due to Frances Bennett for her tremendous help.

Special thanks are due to Dr Jin-Guang Teng in the Department of Civil and Structural Engineering at Hong Kong Polytechnic University for his recommending the University of Edinburgh and for his many discussions during the candidature.

The author wishes to thank Professor M.C. Forde, Head of the Department, Dr R. Royles, Acting head of the Department, Dr J. Morgan, Dr R.B. Wardlaw and Dr M.S. Hardy, Directors of postgraduate students of the Department during different periods of this candidature, and Mr Chris Burnside, the computing officer of the Department of Civil and Environmental Engineering at the University of Edinburgh, who made available all the facilities of the department.

I would like to thank my friends and colleagues in the Department of Civil and Environmental Engineering at the University of Edinburgh. In particular, I wish to thank Ms Karen Melville, Mrs Betty McWilliam, Mrs Chris Corsie and Mr Niall McWilliam for their help. My thanks also go to Zhijun Zhong, Kefeng Zhang, Chee Liang Ng in the Department of Civil and Environmental Engineering at the University of Edinburgh and Mr Ronne McColl and Mrs Hazel McColl in Edinburgh who helped make my life in Edinburgh more enjoyable.

Last, special thanks go to my parents, brothers and sisters who made my education possible in the extremely difficult era, to my wife Hai Ying Luo for her love and her help during the candidature, and to my son Xuan Chen for his birth which brought me a totally different but very enjoyable life. To them I dedicate this thesis.

CONTENTS

VOLUME 1

VOLUME 2

VOLUME 1

Chapter 1

INTRODUCTION

1.1 General

Silos form a key part of the infrastructure of civilised life. They are widely used for short and long term storage of large quantities of bulk particulate solids in agriculture and many industries such as chemical engineering, mining, electric power generation and food processing. With the rise of the demands in these industries, the size and number of silos has been growing rapidly in recent years.

Silo structures are usually made of steel or reinforced concrete. The majority of silos are of circular planform because they are structurally more efficient than any other planform (e.g. rectangular). Silos may either be ground-supported or elevated. A typical elevated silo generally consists of a cylindrical shell and a conical hopper. The safe design of silo structures involves a sound understanding of such phenomena as granular solids behaviour, flow patterns, wall loadings, structural requirements and their relationships.

Silo failures are very common in all countries in the world, and represent a source of major economic loss. The rate of failure of silo structures is far higher than other engineering structures, estimated by some to be between 100 and 1000 times that of buildings (Weare, 1989). The reasons for this high failure rate are believed mainly to be the poor understanding of solids flow patterns and pressures on the silo wall exerted by the stored solids. Because of the economic importance of silos and their poor practice, many studies are needed to achieve an improved silo design and construction technology.

1.2 Problems in silos design

In silos flow, there are three key problems which regularly arise: first, the structural integrity of the silo may be jeopardised by pressures which are too high or too low; second, the stored solids may hang up in the container; and third, the flow pattern may cause segregation of the solids. All three are related to flow patterns in the silo, but the three phenomena have different characteristics.

High pressures are not in themselves necessarily a serious danger to the silo structure. High pressures must be seen in the context of the structural form and the way in which the structure carries loads. For this reason, local low pressures can be even more damaging than very high symmetrical pressures. This is a complex subject because the silo is a multi-segment shell structure, and is beyond the scope of this thesis, but is treated extensively elsewhere [Rotter, 1985a, 1990a, 1993]. If the silo collapses, the process which it feeds is arrested, and grave economic losses ensue.

Arching over the silo outlet, ratholing and incomplete cleanout are other means by which the solids flow is arrested. Arching over the outlet is generally attributed to the development of cohesion in the solid, though recent work suggests that the solids dilation requirement, which is often but not always related to the cohesion, must play a role too. Ratholing is the formation of a stable hole down the entire height of a silo, leading to major loss of effective storage capacity, and consequent serious economic losses. Both arching and ratholing are essentially static phenomena, so dynamic analyses are not necessary nor perhaps helpful in addressing these problems.

The third problem is that of segregation caused by flow. This has largely been addressed by the adoption of mass flow silo geometries and careful filling procedures whenever segregation must be avoided. The criteria for mass flow were developed by Jenike and others in the 1960s [Jenike, 1961, 1964a] and, whilst some improvements have been made more recently [Drescher, 1992], there does not appear to be great scope for further work on this topic. Funnel flow silos often lead to

segregation of the stored solid, so they are only useful for solids where this is not a serious problem.

The flow pattern in a funnel flow silo remains a major topic for serious research because asymmetries in the flow pattern can increase the unpredictability of the flow, and certainly endanger the silo's structural integrity. Reliable methods of predicting the details of the flow pattern, based on high quality experiments, are the first need. Prediction of the pressure distribution and magnitudes, including the details of its complex form with both low and high local pressures, must be achieved before further useful progress can be made in this field.

The relationship between material properties, filling process, flow patterns, wall pressures, structural stresses and structural failure is a complex one (Fig. 1.1). The mechanical characteristics of the stored solids and the process by which they are filled into the silo determine the distribution of densities and particle orientations in the silo, which strongly affect the flow pattern [Nielsen, 1983]. The filling process and flow pattern are largely responsible for segregation of the solids. The solids packing and material characteristics also determine whether arching or ratholing will occur across the outlet (Fig. 1.1). The flow pattern in turn strongly influences the pressures on the silo wall during discharge, so these cannot be predicted with certainty unless the flow pattern itself can be predicted. The pressures on the silo wall are, in general, unsymmetrical and non-uniform. The relationship between these pressures and the stresses which develop in the silo walls depend on shell bending phenomena, which can be very complex, and not easily understood, though they are predictable with finite element analyses. Finally, the silo wall stresses which will induce structural failure are only currently understood for simple cases, and much work remains to be done. These failure strengths can be very dependent on trivially small imperfections in the wall geometry, and the effect of bulk solids stiffness. They continue to be difficult to predict even with the best current non-linear finite element analyses.

1.3 Solids flow patterns in silos

Of the three principal interlinked aspects of silos design: flow, pressures and structural design, solids flow mechanics is the least-well comprehended, possibly because the flow of granular solids does not fit snugly into any one established analytical field.

Studies of flow patterns can be traced back to the earliest text of Ketchum [1907] which makes brief reference to differences in flow in different geometries. However, major progress in terminology and definition does not appear to have occurred until the work of Jenike and his colleagues (Jenike, 1961, 1964a). They made a huge number of observations of flow in silo models, and gave the definitions of mass and funnel flow which are widely used today. Indeed, it might be said that the difficulties we have in extending flow pattern definitions to other forms at present have their origins in the phenomena which were not observed by Jenike, and which he thus did not describe with clarity.

Jenike defined two principal flow pattern forms that can exist during the discharge of granular media from silos: mass flow and funnel flow (Fig. 1.2). Mass flow is the flow mode that prevails in a silo/hopper system where every grain of solid is moving from the instant the outlet opens and remains in motion until it passes through the outlet. In general, the velocity is very similar at all points in the cylindrical part of the silo. Mass flow is generally regarded as desirable to ensure a smooth even supply of solid with little danger of flow interruption, or loss of effective storage capacity. It has the advantage that the first material to enter the silo is the first to be discharged, so that ageing of stored material is not a problem. The disadvantage of mass flow is that a steep smooth hopper is needed to achieve it, and this means that the silo must be very tall, which brings a serious capital cost penalty. Wear of the silo walls may also be a problem when abrasive solids are stored and the tall silos required to

achieve a reasonable capacity may lead to particle degradation on impact during filling.

Funnel flow was effectively defined as any pattern which is not mass flow: later writers have sub-divided funnel flows into internal (or pipe) flow and semi-mass flow. A central zone of moving solid develops above the outlet, and usually expands outwards towards the silo walls. After much of the material is withdrawn, some of the solid which was originally stationary may begin to move, forming a wider flowing zone than before. In some silos, all the solid eventually discharges (these silos are known as self-cleaning): in others, not all the solid emerges, and the remainder is either left inside (producing a reduction in storage capacity with possible serious economic consequences) or must be removed by hand, vibratory devices or other ad hoc techniques (all of which tend to be costly). Funnel flow is thus generally regarded as undesirable, but its benefit in reduced headroom requirements, reduced capital expenditure and reduced wear make it attractive provided measures can be taken to ensure that the silo is self-cleaning.

Semi-mass flow is usually immediately preceded, at the start of discharge, by internal flow: after filling an empty silo and opening the orifice, a vertical pipe of flowing solid of the same diameter as the orifice rapidly extends upwards to the free surface and then swells laterally (*e.g.* Lenczner, 1963; Bransby *et al*, 1973; Arteaga and Tuzun, 1990).

The flow channel boundary is defined as the interface between flowing and stationary solid (Fig. 1.3). The point at which this boundary strikes the silo wall is termed the 'effective transition' (Fig. 1.3a). If the flow channel boundary stretches from the edge of the orifice right up to the free surface of the solid, the flow is termed pipe or internal flow and there is no effective transition (Fig. 1.3b). Semi-mass flow is typified by mass flow in the upper part of the silo whilst converging internal flow takes over nearer the orifice, forming an 'effective hopper' which is surrounded by stagnant zones of stationary solid (Fig. 1.3a). It is widely believed that the principal

overpressures during discharge occur either near the effective transition or where a sloping mass flow hopper meets the vertical bin wall (Jenike *et al*, 1973a, b).

In many industrial applications, mass flow is highly desirable because this has a 'first-in-first-out' operation and a more predictable discharge rate. However, where the solid is abrasive and non-degradable or where space restrictions constrain the geometry, funnel flow is often used. Funnel flow occurs in flat-bottomed or shallow-hoppered silos. The type of funnel flow depends upon the aspect ratio of the silo: in very squat silos internal flow will occur, whereas semi-mass flow is more likely in tall, slender silos. However, other factors such as the material properties, filling method and particle shape and size (Munch-Andersen and Nielsen, 1990; Carson *et al*, 1991) also affect the flow mode.

1.4 Loads on silos from bulk solids

The pressures in silos during emptying are very different from those after filling. This difference is often proposed as the cause of silo failures (Rotter, 1986a, b, 1990, 1991, 1993; Jenkyn and Goodwill, 1987; Ruckenbrod and Eibl, 1993; Savage, 1992), so it is important to distinguish between the two cases. Filling pressures usually follow the pattern of the Janssen distribution, though the magnitude of the lateral pressure ratio is often uncertain. Different theories and design codes can result in a huge difference in wall pressures (Bishara, 1985; Wilms *et al*, 1995). In addition, eccentric filling or segregation can lead to significant departures from the Janssen distribution after filling.

Munch-Andersen and Nielsen (1990) and Ooi *et al* (1990) also reported an unsymmetrical pressure distribution around the circumference at a given height for symmetrical filling. This suggests that either variations in wall roughness, geometric imperfections in the silo wall or anisotropic behaviour of the particulate solid may have important influences on either the flow pattern or the pressure distribution. The

incorporation of a statistical element may be useful in future particulate solids flow research (Ooi and Rotter, 1991c).

The pressure distributions during discharge or flow are generally more complex. The form of the flow channel is widely acknowledged to influence the pressures on the wall strongly. It has been observed by many (*e.g.* Walker, 1966; Walker and Blanchard, 1967; Deutsch and Schmidt, 1969; Pieper, 1969; Blair-Fish and Bransby, 1973; Richards, 1977; van Zanten and Mooij, 1977; Munch-Andersen and Nielsen, 1990) that overpressures occur during the discharge of dry bulk granular solids from silos. In extreme cases, these pressures have been reported to be up to five times the Janssen (1895) filling pressure at the same position. The overpressures are typically largest shortly after the start of discharge, when a flow channel has fully developed but the silo is still virtually full to capacity. For this reason, most research studies and design treatments are concerned with the condition of the silo when it is almost full. The difference between the predictions of different design codes for the wall pressures during discharge is even bigger than those for the filling pressures. A comparative study (Wilms *et al*, 1995) recently showed that a wide scatter (up to 60%) exists in the wall pressures calculated by engineers using the same design code DIN1055 (1987) (one of the best known), indicating that more precise definitions and guidelines are required.

The most damaging loading for the silo structure, however, the unsymmetrical pressures caused by eccentric discharge. A few theories have been advanced for the design of silos under eccentric discharge (Jenike, 1967; Wood, 1983; Rotter, 1986b). However, there have been many serious failures involving eccentric discharge, so most codes specifically exclude it. Existing experiments lead to a wide range of alternative descriptions and there is little consistency between the theoretical treatments. Codes which do include eccentric discharge treat it very differently (AS 3774, 1990; ACI 313, 1989). This has led to great confusion amongst silo designers.

1.5 Background and research approach

The principal difficulty in predicting patterns of solids flow during funnel flow is to establish the shape of the flow channel boundary (if this concept has validity for a time-dependent varying phenomenon). Many experimental observations (*e.g.* Lenczner, 1963; Brown and Richards, 1965; Gardner, 1966; Bransby *et al*, 1973; Nguyen *et al*, 1980; Tuzun and Nedderman, 1982; FitzHenry, 1986) have described the flow channel boundary as non-linear, usually becoming steeper away from the orifice. There is a considerable mis-match between most theoretical predictions and experimental observations. The observations recently made by Carson *et al* (1991) on eccentric discharge flow patterns suggest that the flow channel boundary may be close to linear in the vertical plane, especially in shallow silos with wide funnel flows. Other studies (Sugden, 1980; Munch-Andersen and Nielsen, 1990; Rotter and Zhong, 1995) also show that the locus of the flow channel boundary at the start of discharge depends strongly on the way in which the silo has been filled. Another factor that will affect the flow behaviour of a bulk solid is probably the height through which the grains free-fall before impacting in the silo.

Most of the above experiments were at model scale and the information from them has been inadequate to define the flowing channel geometry with certainty, though many proposals for flow channel shape prediction have been advanced (Jenike, 1961, 1964a; Giunta, 1969; Tuzun and Nedderman, 1979a, 1982; Kuznetsov, 1984; McLean and Bravin, 1985). Carson *et al* (1991) recently demonstrated convincingly that the traditional picture, which suggests that the flow channel geometry is governed by the effective angle of internal friction, is clearly wrong. The ACI Code (ACI-313, 1992), which needs a flow channel prediction method for its ADP design process (ACI-313, 1992), relies on the limited old model tests of Giunta (1969) for its advice.

Scientific measurements of flow patterns in full scale silos are almost unknown, and most observations rely on visual records of the top surface profile together with signs of abrasion, scouring and polishing of the walls. From these, the regions of flowing

solid are approximately deduced, though often it is not easy to ascertain whether the same flow pattern always occurs and whether it changes from time to time during a discharge. The extrapolation of observations made in laboratory models to full scale industrial silos is most uncertain.

A full scale silo experimental project, which was established in 1992 by the British Materials Handling Board with support from the British Department of Trade and Industry and many industrial organisations, has been carried out at the University of Edinburgh. Many experiments were conducted to measure solids flow patterns and wall pressures in full scale silos. The technique of residence time measurement was adopted to measure flow patterns. Many radio frequency tags were accurately placed in a systematic pattern in the solid at different levels, giving up to 300 measures of the movement of the solids during discharge. The chief difficulty associated with this technique is the interpretation of the results. The first part of this thesis is concerned with the interpretation of the data from these experiments. Several new techniques are developed to infer solids flow patterns from residence time measurements.

The commonest technique of wall pressure measurement in previous studies has been pressure cells mounted in the silo wall. Recent research has shown that the patterns of pressure are often very complex, and that the pressures can vary rapidly with position. Thus, a comprehensive picture can only be obtained at great expense, partly because many very expensive stiff pressure cells are needed. Several attempts have been made recently to infer wall pressures from wall strain measurements, but gross errors of interpretation have often been made by misunderstanding the complex structural behaviour of the circular silo as a thin shell structure.

In the new research silo at the University of Edinburgh, hundreds of strain gauges were used to measure strains in the wall with locations chosen in consultation with the author. The second part of this thesis is concerned with the interpretation of these wall strain measurements. A rigorous statistical procedure is developed to infer the wall pressures from the strain observations with reasonable accuracy. The procedure

involves back-figuring from a series of structural analyses of the silo using characteristic forms of pressure distributions, with a least-squares error minimisation. It is used to interpret the strain observations in the full scale silo experiments and to derive the most comprehensive pictures ever of both storing and eccentric discharge pressures. The first direct correlation in a full scale silo between the flow pattern and the wall pressures under eccentric discharge is thus established.

1.6 Review of topics covered in this thesis

The main body of this thesis is concerned with two topics in silos study: the inference of solids flow patterns from residence time measurements (Chapters 3 to 7) and the inference of wall pressures from wall strain measurements (Chapters 8 to 12). Other work done throughout the candidature to support the principal goals of the thesis, though not quite in its main stream, are presented in Appendices A to C. The subject matter in the following chapters may be briefly summarised as follows.

A literature review of the topics relevant to the contents of this thesis is presented in Chapter 2. It opens with a brief review of the analysis of solids flow, followed by short descriptions of the commonest and most successful flow pattern observation techniques. Attention is next turned to studies of silo wall pressures. A brief review of the classical theories and their limitations is presented first. Numerical predictions of silo wall pressures in the last thirty years are then discussed. Finally, a review of silo pressure observations is presented and some of the shortcomings of past practice in the interpretation of pressure observations are highlighted.

The first half of the thesis is concerned with the interpretation of solids flow patterns in full scale silos.

Computer graphics is used to represent the dynamic process of the solids flow in a silo from residence time measurements in this thesis. A program suite FLOWVIS is

developed to model the complete flow process, using as few assumptions as possible, and without invoking any assumptions concerning the properties or constitutive response of the solid. Chapter 3 presents a short description of the program suite and the analytical formulations used. The display of the solids flow pattern in a graphical format has immediate appeal to industrial engineers, and can be used to solve many industrial materials handling problems.

Chapter 4 presents a brief summary of a series of experiments carried out in a recently constructed 250 tonne steel silo at British Gypsum. The silo is of circular planform storing ground gypsum mineral powder. It was fitted with an inverted cone bin discharge aid and air pads on the hopper section. The data are analysed in Chapter 5. Four interpretation techniques, including contour plots of residence times and mean velocities, flow visualisation and the analysis of the emerged mass from each seeded level are used to interpret the flow patterns. The last method makes it possible for the first time to identify a classical flow pattern (mass or funnel flow) from a single plot and to define quantitatively the flow channel boundary from residence time measurements. The results show that a commercial discharge aid can have a major effect on the flow pattern, leading to a flow pattern which is different from any documented in the literature. Funnel flow occurred when no discharge aid was in operation.

Chapter 6 presents a brief summary of the experiments conducted in a specially designed cylindrical silo for research purposes at British Steel's Teesside Research Laboratories. The silo is 9.5m in height and 4.2m in diameter with three outlets. A series of experiments were conducted under concentric, half eccentric and fully eccentric discharge with iron ore pellets. The same techniques (as Chapter 5) are used to interpret the data in Chapter 7. The results show steep-sided funnel flow patterns under both concentric and eccentric discharges. The plan cross-section of the flow channel is close to but not exactly circular. The flow channel boundary is quantitatively defined through the analysis of the emerged mass from each seeded level and a two parameter model is proposed to describe its geometry.

The second half of the thesis is concerned with the inference of silo wall pressures.

Chapter 8 presents a new rigorous statistical procedure by which the complete pressure distribution may be inferred from strains measured on the silo wall, by back-figuring from a series of structural analyses of the silo using characteristic forms of pressure distributions. Errors are minimised by a least-squares adjustment. Because the pressure pattern is defined in advance, the assumptions about pressure patterns, normally made rather unwittingly by the choice of placement of pressure cells, are clearer to the user and also changeable in the light of the identified real patterns. A simple example is presented to illustrate the new procedure.

The statistics of this new procedure are discussed in Chapter 9, including the statistics of the inferred load coefficients, the estimation of the variance of strain observations, the analysis of strain residuals and the goodness-of-fit. A lower bound to the variance of load coefficients is discovered. A dependence index between two sensitivity vectors is proposed, which is useful in the selection of load functions when a large number of load functions are involved, and also in planning strain gauge locations. The influences of strain gauge locations and the use of load functions are further explored through the analysis of an example ring under harmonic pressures.

In Chapter 10, a program suite SIMA is developed to implement the new procedure of inferring wall pressures from wall strain measurements. The program suite is concerned with only axisymmetric thin elastic silos. It consists of a series of programs. Some techniques involved in developing the program suite are described, such as the calculation of strains in strain gauges under characterised loads, imposing linear constraints on load functions and the solution of the normal equations. A brief description is presented of the main features of the programs and their functions.

Chapter 11 briefly summarises the structure of the specially designed silo at British Steel and the strain measurement system used in the experiments. A total of 384 strain gauges were used to measure the strains in the silo wall and they were logged at 60 second intervals throughout the tests. The data are interpreted in Chapter 12 by using the new procedure developed in the previous chapters. Very complete pictures are obtained for the storing and incipient discharge pressure distributions. It is believed that this is the first time that the changing form of the eccentric discharge pressure distribution at the start of discharge has been observed, and indeed that the critical importance of the development of the flow channel to the silo's structural integrity has been identified. The pressures are highly correlated with the flow pattern in the solid.

Chapter 13 presents a review of the conclusions drawn in the previous chapters.

"Double deck" (DD) or sandwich strain gauges were used to measure both membrane and bending strains from the external wall surface in the silo at British Steel. In Appendix A, the local stiffening effect on the structure caused by the presence of a DD gauge is investigated. An approximate analytical solution based on classical elasticity theory is presented and verified using three dimensional finite element calculations. A parametric study and a correction method are also presented.

Appendix B presents an algebraic analysis for calculating deformations and stresses in a general asymmetric ring stiffener on a cylindrical shell. Under axisymmetric loadings, the deformations and stresses in the ring stiffener can be obtained from simple ring analysis using an effective cross-section.

Appendix C presents finite element predictions of static silo wall pressures using several constitutive models with parameters derived from material tests on coal samples. The predictions are compared with those of existing classical theories and design codes from different countries.

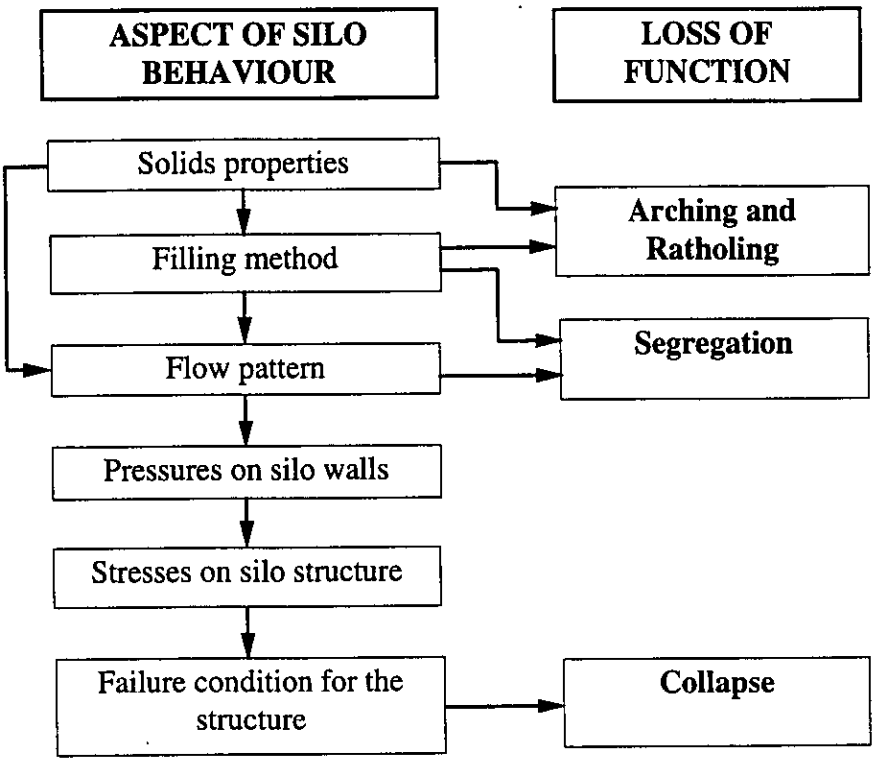

Fig. 1.1 Problems in silos

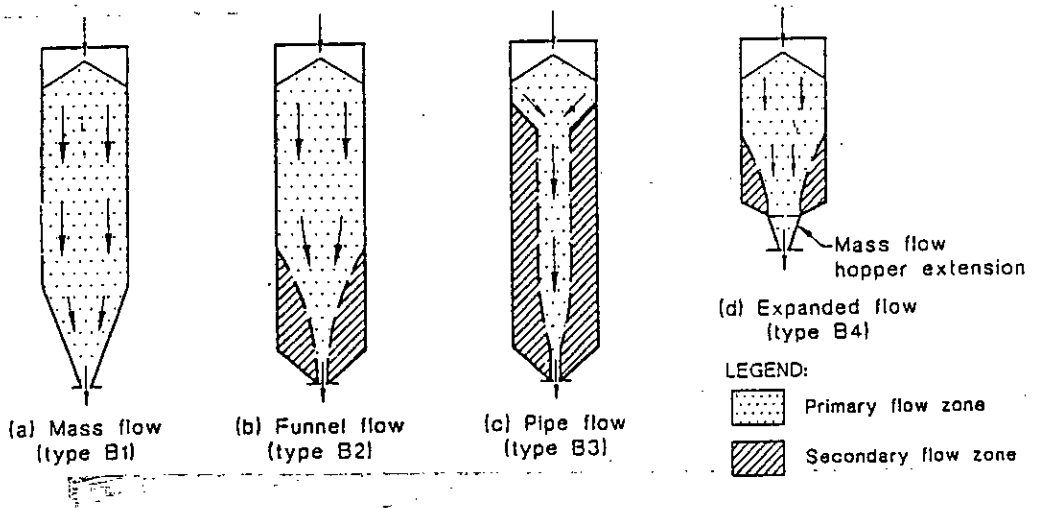

Fig. 1.2 Types of flow pattern (AS3774, 1990)

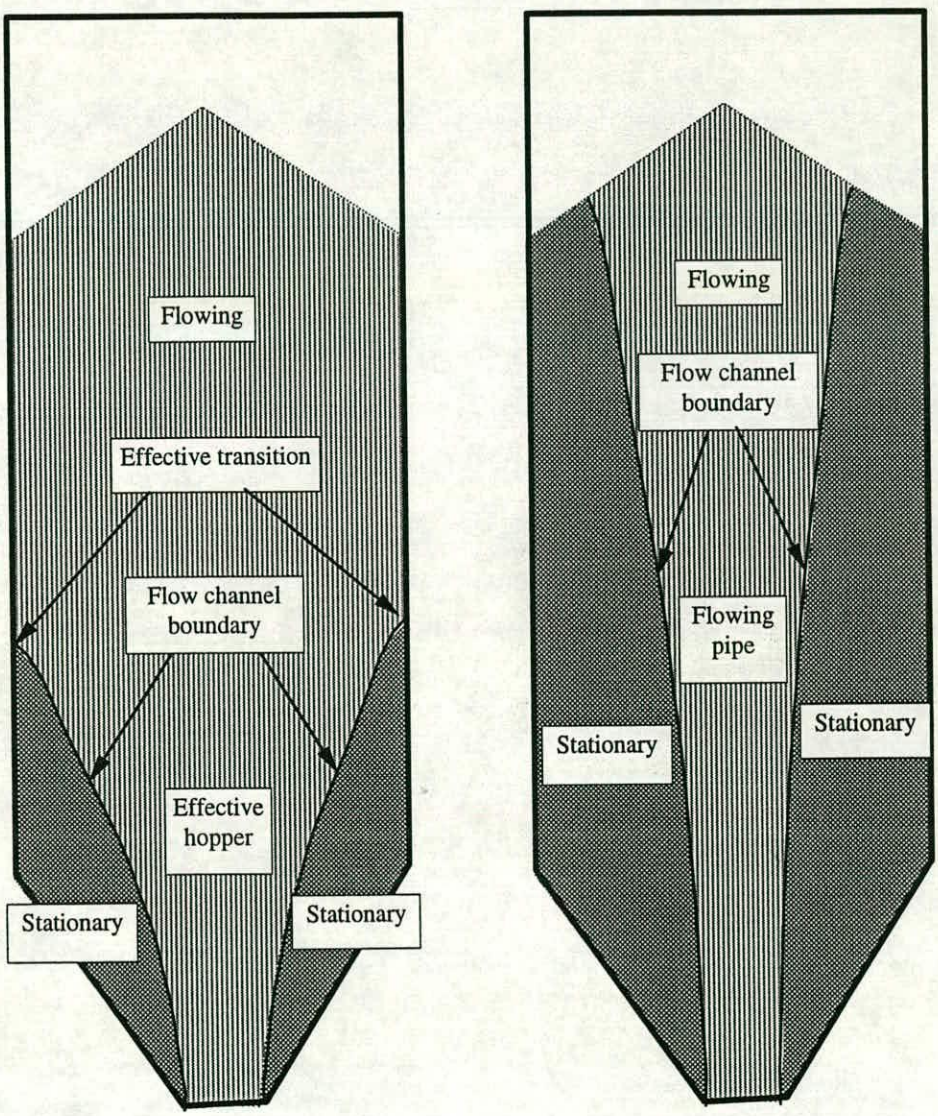

a) Semi-mass flow

b) Pipe flow (Internal flow)

Fig. 1.3 Flow channel boundary

Chapter 2

LITERATURE REVIEW

2.1 Outline

This chapter presents a review of the topics relevant to the contents in this thesis, including theoretical and experimental analyses in both solids flow patterns in silos and pressures exerted by the stored solids on silo walls.

The analysis of solids flow is not a part of this thesis, but the experimental data interpreted in this thesis define the phenomena which the analysis must model, and provide a good data set which analytical treatments may attempt to model. The topic is therefore briefly reviewed.

Short descriptions are presented of the commonest and most successful flow pattern observation techniques, including direct observation techniques, photographic techniques, radiographic techniques (X rays), tomographic techniques, the radio pill tracking technique, bed splitting techniques, indicator bars in penetrations in the silo wall and residence time measurement techniques. Advantages and disadvantages of each method, especially with respect to their feasibility in full scale silo tests, are highlighted.

Attention is next turned to classical, numerical and experimental studies of silo wall pressures. A brief review of the classical theories and their limitations is presented first. Numerical predictions of silo wall pressures in the last thirty years are then discussed. Finally, a review of silo pressure observations is presented and

shortcomings of past practices in the interpretation of pressure observations are highlighted.

2.2 Analyses of solids flow

Most analyses of flow assume a steady-state condition, corresponding to the silo being essentially full, but with a fully-initiated pattern of flow. A number of dynamic and steady-state analyses described by Drescher (1992) indicate that this steady-state assumption is a good engineering approximation for most practical purposes.

Steady-state flow analyses include those based on soil mechanics plasticity theory (*e.g.* Deutsch and Clyde, 1967; Giunta, 1969; Jenike *et al*, 1973b; McCabe, 1974; Van Zanten *et al*, 1977; Murfitt *et al*, 1981; Kuznetsov, 1984). These analyses were based on the assumption of a linear flow channel boundary (*i.e.* a wedge-shaped flow channel in planar silos and a conical channel in cylindrical silos). There is a considerable mis-match between most theoretical predictions and the experimental observations. The experiments made by Carson *et al* (1991) on eccentric discharge flow patterns also indicate that it is not clear which material parameters should be used in attempting to predict flow channel geometries, since a wide range of flow channel shapes can be found within free-flowing solids with the same internal frictional properties.

Of the simple approaches to the analysis of flowing granular solid, perhaps the two most promising are plasticity theory and kinematic modelling. Unfortunately, the plastic behaviour of dilated, free-flowing granular solids is not yet fully defined, yet the suitability of purely kinematic models for very frictional, consolidated, incipient flows is questionable. A universal description of all flow regimes is not yet available and it is certainly a considerable challenge to try to produce one. Different approaches for the various flow configurations may be required until a better understanding is achieved.

Finite elements and discrete elements have both been used in recent years in attempts to predict solids flow. Both have some serious shortcomings. Several major efforts have been made to develop time domain finite element analyses which can model the flow process as well as predicting the time-dependent pressure distribution. Most notable amongst these are Eibl *et al* (1982), Haussler and Eibl (1984), Runesson and Nilsson (1986), Eibl and Rombach (1987a, 1987b, 1988), Link and Elwi (1987), Schmidt and Wu (1989) and Wu (1990).

Others have attempted to model the flow process using discrete elements. Most of these models represent two-dimensional conditions with rigid or elastic discs (sometimes with uniform size) interacting dynamically with frictional contacts, and they produce qualitatively promising results. However, the calibration of the properties of the discs, their interpretation in three dimensions, and the relationship between the discs and real particles with non-circular shapes all present great challenges. In particular, it is very difficult to use an analysis of this kind to predict the effective transition in a silo filled with, for example, gypsum. Some of the best early work in this area is represented by Cundall and Strack (1979) and Thornton (1979). Much more has been undertaken in recent years, but a full description is beyond the scope of this thesis. It is generally agreed that the advantages of discrete elements lie principally in studying low density flows, such as occur in pneumatic conveying systems or very close to the outlet in a silo with free-fall gravitational unconfined discharge (Passman *et al*, 1994).

2.3 Flow pattern observation techniques

2.3.1 Introduction

The study of flow patterns in discharging silos presents several fundamental problems to the experimenter. Firstly, the majority of granular solids are opaque in nature, so the experimenter cannot look into the bed of solid. Very little information

can be gained from direct visual observation of the free surface. Even if the silo is made of a transparent material, only the flow adjacent to the walls can be studied. Visual observations are discussed in more detail below. Secondly, the method by which the silo has been filled affects the subsequent flow pattern. If it is necessary for the free surface to be levelled, for example, to position marker particles, it may affect the flow pattern. Thirdly, effects such as vibration and time of storage may also influence the flow pattern. The study of the internal flow fields in silos is seldom a simple affair. Many ingenious methods have been devised to chart the internal events in a discharging silo. These are discussed in turn below.

2.3.2 Direct visual observation technique 1: Observation of displacements of horizontal layers of dyed solid

In this technique, horizontal layers of visually-detectable solid are placed adjacent to a transparent front wall in a plane-strain apparatus during filling. The subsequent deformation of these layers is then observed. Unless the silo is filled in a distributed manner, some levelling of the free surface is necessary. Munch-Andersen and Nielsen (1990) have shown that the stacking arrangement affects the flow patterns and so this levelling may have an influence. The visually-detectable solid is usually either a sample of the granular solid that has been dyed or a similar granular solid of a different colour. In either case, the layers contain grains that have essentially the same properties as the bulk solid. In this experimental technique, the problems associated with the retarding effect of the front wall are pertinent. Litwiniszyn (1963), Gardner (1966) and Jenike and Johanson (1962) are amongst many who have used this technique. The results obtained are generally of a qualitative nature since it is not possible to determine the trajectory of any particles except those adjacent to the transparent front wall.

The technique is not applicable to full scale industrial installations.

2.3.3 Direct visual observation technique 2: Observation through transparent walls of the silo

Another visual observation technique was employed by Carson *et al* (1991). They carried out flow experiments on flat-bottomed, cylindrical model silos. The walls were made of transparent Plexiglas, so they could visually determine the boundary between flowing and stationary solid. By assuming a linear zone of stationary solid, they plotted the flow channel angle against the circumferential angle. Their experiments were carried out on silo models which were full, two-thirds full and one third full, and discharged either concentrically and eccentrically. They found that the flow channel closely followed a radial path from the outlet to the cylinder wall. The flow channel boundary, as observed through the wall, however, was neither distinct nor stable for most of the solids they tested. They also reported very little correlation between the flow channel angle and measured material properties such as the angle of internal friction.

Similar experiments on steeper flow channels in sand under eccentric discharge were conducted by FitzHenry (1986). The deduced flow channel form was found to have very non-linear vertical boundaries. This finding is at variance with the observations of Carson *et al* (1991). The flow channel boundary shape may be dependent on properties of the solid being stored which were not measured.

The technique is not applicable to full scale industrial installations, unless a large number of penetrations can be made in the silo wall.

2.3.4 Photographic techniques

Photographic techniques are one of the commonest methods used to study the behaviour of flowing granular solids and are often used in conjunction with observations of the movement of horizontal layers of dyed solid. Photographic techniques have been employed by many researchers (*e.g.* Pariseau, 1970; Bosley *et*

al, 1969; Tuzun and Nedderman, 1979a, b, 1982) using transparent plane-strain silos. Either high-speed photography (cine filming) or long exposures are often taken.

It is assumed that the flow behaviour observed adjacent to the front wall is representative of the behaviour throughout the bed. However, several researchers (*e.g.* Brown and Richards, 1965; Cleaver, 1991) have reported that the front wall exerts a retarding force on the flow. This must be taken into account somehow when velocities are calculated, as these velocities will almost certainly be less than those occurring at similar positions within the bed. However, it is not easy to devise a satisfactory technique to account for the retardation caused by the transparent wall (Watson, 1993).

Brown and Richards (1965) and Gardner (1966) took photographs of the flow through the transparent front walls of their plane-strain model silos. Careful scrutiny of these photographs reveals a surprising point of contraflexure in the flow channel boundary. It seems possible that the stationary zones start to curve into the flow field near the outlet. This phenomenon could, however, be caused by frictional effects against the front wall.

Laohakul (1978) and Tuzun and Nedderman (1979a) are amongst those to have used cine filming to determine particle trajectories. Polynomials describing the position of a tracer particle with time were then fitted to the tracer trajectories. On differentiation, these polynomials yielded the horizontal and vertical velocities at any point at any time on the trajectory.

Long time exposures were used by Gardner (1966) and Tuzun and Nedderman (1982) to determine the position of the flow channel boundary. Gardner laid horizontal layers of dyed solid in the silo during filling. Flow was allowed to proceed until steady-state conditions were achieved. The flow channel boundary was defined in this study as the edge of the stationary solid, and its location was assessed by measuring the extent of the remaining horizontal layers of dyed solid.

By using an exposure time of 0.5 secs whilst photographing their discharging planar silo, Tuzun and Nedderman (1982) observed that some particles appear blurred whilst others (those that moved at less than one particle diameter per exposure time) were in focus. In this way, they could determine a flow channel boundary based on a similar but slightly different definition. With a longer exposure time of 1 sec, the flow channel boundary altered giving the appearance of a larger flowing region. They reported that these boundaries were also velocity contours. They further suggested that no clear-cut interface could be experimentally observed between flowing and stagnant solid since the velocity appears to decrease asymptotically towards zero at points further and further from the orifice horizontally. They did not, however, increase the exposure time beyond 1 sec to investigate further shifts in the observed flow channel boundary.

Photographs are occasionally used by investigators of flow in full scale silo facilities. The concept is that photographs of the surface of the solid give an indication of the flow pattern. Whilst it is true that a developing depression in the surface of the solid must indicate that solid is flowing down a channel at this point, many anecdotal descriptions of this technique suggest that little can be learned about the pattern of flow lower down in the solid. As an example, observations of sugar flow in large silos in East Anglia (Gillingham, 1986), indicated that there was no determinable relationship between the outlet position and the location of solids movement on the surface. The silo had over 20 alternative outlets in concentric and eccentric positions.

The technique may be used in full scale industrial installations, but the information gathered is strictly limited in value.

2.3.5 Radiographic techniques (X rays)

In the radiographic technique, lead shot tracer particles, which are opaque to X rays, are seeded into a silo bed during filling. Because the X rays must be able to penetrate

the solid and be detected on the far side, this technique can only be used in thin non-metallic plane-strain models. It is therefore very susceptible to errors caused by friction on the 'side' walls, through which the observations must be made.

The flow is halted at frequent intervals during the discharge and the apparatus exposed to an X-ray source. The resulting X-ray photograph shows the positions of the tracer particles. By comparing successive X-rays, velocities can be calculated. This method is relatively rarely employed, presumably because of the expensive equipment required and the restricted size of the apparatus. Bransby *et al* (1973), Lee *et al* (1974), Cutress and Pulfer (1967) and Drescher *et al* (1978) are amongst those to have used this technique. Voidage changes, which often coincide with rupture surfaces, are more important phenomena which can be detected on the X-ray exposure.

The technique is not applicable to full scale industrial installations.

2.3.6 Tomographic techniques

Tomographic techniques form another class of radiation-based methods in which the tracer position is determined by its radiation emission rather than by radiation transmission, as in the case of X-rays (Bemrose *et al*, 1988; Beynon *et al*, 1993; Parker *et al*, 1993; Nikitidis *et al*, 1995; Seville *et al*, 1995). One of these techniques, termed Positron Emission Particle Tracking (PEPT) uses a radio-labelled particle which emits a positron, which in turns gives rise to matched γ-ray pairs. The detection of a few such γ-ray pairs using positron-sensitive detectors serves to locate the tracer position by triangulation. PEPT has been used in the investigation of flow characteristics in a multiphase granular medium (Seville *et al*, 1995). Whilst the technique is useful in some ways, it is very restricted in that up to now, only one particle can be traced at a time, and the cost involved is very high. This technique is naturally not suitable for measuring the solids flow pattern in full scale silos.

2.3.7 Radio pill tracking technique

The radio pill tracking technique involves following the fate of a miniature radio-transmitter (a radio pill) as it passes through a model silo. Handley and Perry (1965, 1967), Perry *et al* (1975, 1976) and Rao and Venkateswarlu (1973) are amongst those to have employed this technique. Perry and his co-workers carried out the most comprehensive study using cylindrical radio pills of length 25 mm and diameter 8.8 mm. In an attempt to measure the stresses in the granular solid, some pills were fitted with a pressure sensitive diaphragm. The pills were placed within axisymmetric model silos filled with fine sand. The signals from the radio pills were received by an aerial adjacent to the wall.

Since the radio pills were much larger than the mean particle diameter, the problem of segregation must be addressed when analysing the results. Later work by Arteaga and Tuzun (1990) can be used to demonstrate that segregation was not a problem in the observations of Perry *et al* (1975, 1976). However, the major drawback in the work of Perry *et al* is the short range over which the radio pills can be detected. For reliable detection, the radio pills must never be more than about 50 mm from the wall, so the technique is restricted to very small models. The unfortunate death of Dr Perry in the early 1970s has meant that this method has been used little since.

The technique is not applicable to full scale industrial installations.

2.3.8 Bed splitting techniques

In the bed-splitting technique, horizontal layers of dyed granular solid are included into the silo during filling. After an appropriate period of flow, the discharge is halted. The bed of granular solid is then immobilised. The commonest immobilisation technique is to pour in a fixing medium which fills the interstices between the granular particles and then solidifies, rendering the particulate solid rigid. Brown and Richards (1965) and Novosad and Surapati (1968) used molten

paraffin wax and Chatlynne and Resnick (1973) used a polyester resin as the fixing medium. The solidified granular solid can then be sliced up to reveal the internal deformation of the coloured layers.

In their experiments with sand in a plane-strain mass-flow hopper, Brown and Richards (1965) reported that the velocity profiles were unsymmetrical about the vertical centreline and that the flow rate generally increased with distance from the end face. However, the maximum flow rate did not occur in the central section of the hopper.

Brown and Richards also made measurements of the 'angle of approach'. This angle, β, was defined as the angle the flow channel boundary, near the exit, made with the vertical. In plane-strain silos, the angle of approach was measured from direct observation through the transparent end face. In axisymmetric silos, large numbers of tracer particles were initially seeded in layers into the silo at known positions. From a study of the particles that were left in the silo after a few seconds of discharge, an estimate of the angle of approach could be made. The angles of approach were measured for different solids in three flat-bottomed silos of different geometries:

(a) discharge through an edge slot adjacent to a side wall in a planar silo (this angle of approach was designated β_e).

(b) discharge through a central slot, parallel to the side walls, in a planar silo (β_c).

(c) discharge through a central circular orifice in the base of a cylindrical silo (β_3).

They found that all these angles fluctuated but in general $\beta_e > \beta_c > \beta_3$. They thus showed that the geometry of the silo has an influence on the angle of approach.

Giunta (1969) investigated the position of the flow channel boundary in an axisymmetric model silo. By continuously replenishing the top surface, steady-state conditions were allowed to develop. A different method to the fixing technique

described above was then used to split the flow field. After fitting a semi-circular lid, the silo was rotated through 90° about the horizontal axis. A vacuum shovel was then used to remove the uppermost half-cylindrical section, thus exposing the longitudinal plane of symmetry. Although it was Giunta's intention to study the flow channel boundary in only flat-bottomed silos, his apparatus included a conical hopper of a smaller diameter than the cylindrical silo and so perhaps a reliable comparison with other results from flat-bottomed silos perhaps cannot be made.

Takahashi and Yanai (1973) used a technique similar to Giunta's to measure the flow pattern and void fraction of 4 mm diameter glass, silica and alumina spheres during flow through a vertical pipe. They reported a central constant-velocity region and a peripheral shear region where the velocities fell abruptly.

Although bed splitting techniques allow the flow patterns in true three-dimensional silos to be investigated, the results are generally only of a qualitative nature since trajectories are unknown. A further disadvantage of the fixing technique is that it is both time-consuming and labour-intensive.

The technique is not applicable to full scale industrial installations.

2.3.9 Indicator bars passing through penetrations in the silo wall

The commonest current method used by practising engineers to investigate solids movement in a full scale industrial installation is to drill a series of holes in the silo wall at different heights, and to insert a bar through each hole into the solid (Levison and Munch-Andersen, 1993). During discharge, the bar is seen to move if the solid inside is moving, and in careful studies, the rotational velocity of the bar about the hole can be used to estimate the local velocity of the moving solid. By placing such bars at many heights, the boundary between the moving and stationary material in a semi-mass flow silo can be detected.

However, the technique has many disadvantages. The movement does not measure a real velocity since the bar's rotation means slow translation near the wall, but more rapid translation further inside. Second, the bar must be repeatedly installed as flow progresses, involving much human interaction with no potential for automation. Thirdly, the movement of the bar only indicates the flow of solids against the wall, so events deeper in the silo are undetectable. Fourthly, many penetrations must be made into the wall to achieve the goal. These penetrations may be permitted by silo owners with serious flow problems, but those who are undertaking the study with prevention of problems rather than cure of known difficulties in mind are rarely enthusiastic about the drilling of holes in their silos.

Although the method is applicable to full scale industrial installations, most silo owners are reluctant to drill holes in their silo walls.

2.3.10 Residence time measurements

In this technique, the time taken for a tracer particle to travel through the bulk from an initial known starting position to the outlet (*i.e.* its residence time) is measured. This technique lends itself very conveniently to the analysis of flow in truly three-dimensional systems. The resources needed to implement this technique are few and inexpensive and the method is simple, if time-consuming.

In circumstances where mass flow occurs and small asymmetries are not a concern, streamlines and velocity fields can be assessed from residence times. A stream function analysis can be used. Velocity distributions can only be calculated if either the trajectory of the particle or a constant bulk density is assumed. With the latter assumption, contours of equal time (isochrones) may be fitted to the residence time data and stream function values may then be evaluated. Streamlines are calculated by numerically differentiating these stream functions (Cleaver, 1991). Smallwood and Thorpe (1980) continued the analysis to calculate velocity fields. This technique works well in mass flow regimes, but is much more difficult to apply to funnel flows.

Cleaver (1991) reported that the stream function analysis was very sensitive to errors in the experimental results from his mass-flow silo. In the funnel flow experiments described by Watson (1993), many tracer particles remained stationary for a considerable period until the flow front reached them. Therefore, the measured residence times of these tracers do not represent the time that the tracer was in motion. This phenomenon renders such residence time data unsuitable for stream function analysis.

Different methods of placing the tracer particles into the silo have been employed. Smallwood and Thorpe (1980), Murfitt (1980), Graham *et al* (1987), Nedderman (1988) and Cleaver (1991) used permanent positioning tubes to introduce tracer particles into discharging silos. Cleaver (1991) showed that the presence of a positioning tube in the flow field causes the subsequent movement of the tracer particle to be impeded. For the most accurate results, therefore, the tubes must be retracted after positioning a tracer particle. Tracer particles were dropped from marked positions at the top of the silo onto a pre-flattened free surface by van Zanten *et al* (1977). The accuracy of this method of positioning the tracer particles is in doubt because the degree of burrowing of the tracers is unknown.

From the literature, it can be seen that the residence time technique is a commonly adopted approach. A drawback of the technique is that the positioning of tubes and the recovery of tracer particles in full scale silos may be hampered by problems of access. The question of segregation of the markers must also be addressed.

In addition, interpretation of the observations made using residence time measurements under funnel flow conditions is not at all straightforward, and numerical processing of the results to identify the changing flow channel boundary is still in its infancy.

The residence time technique can be used in full scale industrial installations, and is the adopted method in a full scale silo research project in the University of Edinburgh

(Rotter *et al* 1995). One of the main tasks of this thesis is to develop new techniques to interpret the solids flow patterns from residence time measurements gathered in these experiments.

2.4 Classical theories for the pressure distribution in silos

2.4.1 Filling

Many classical theories exist for predicting the static pressures in silos after initial filling (Janssen, 1895; Koenen, 1895; Pieper and Wenzel, 1963; Walker, 1966; Homes, 1972; Walters, 1973; Jenike *et al,* 1973; Reimbert and Reimbert, 1976; Rankine, 1857; Coulomb, 1773; Abdel-Sayed *et al,* 1985). Most of these theories were derived from plastic equilibrium considerations on the basis of different simplifying assumptions. Discussions of these theories and fuller descriptions may be found elsewhere (Arnold *et al,* 1980; Gaylord and Gaylord, 1984; Abdel-Sayed *et al,* 1985; Bishara, 1985; Ooi and Rotter, 1990b; Roberts, 1995).

Janssen (1895) assumed that the ratio of horizontal pressure against the wall to the mean vertical stress in the stored solid (the lateral pressure ratio k) is invariant with depth in the silo, but he did not define it. Koenen (1895) proposed that the Rankine active pressure ratio should be used for this quantity, and most of the other theories for silo pressure attempted to find better means of predicting this single quantity (Jaky, 1948; Pieper and Wenzel, 1963; Walker, 1966; Homes, 1972; Walters, 1973; Jenike *et al,* 1973). Thus all these authors adopted the Janssen pressure distribution as a basis. Jaky (1948) proposed that k should be given by $k = 1 - \sin\phi$, a relationship originally suggested for silos, but which is still widely used in the field of soil mechanics. The parameter ϕ in this expression is the solid's internal friction angle. Pieper and Wenzel (1963) adopted this too. Walker (1966) deduced k by assuming that the material adjacent to the wall is sliding down the wall and is at active failure. Walters (1973) extended Walker's analysis to include non-uniformity of the vertical stresses and assumed that all the solid is at active failure. Jenike *et al*

(1973) empirically proposed k=0.40 and Homes (1972) similarly suggested k=0.45 for most common solids. Ooi and Rotter (1990b) showed that under storing conditions, much of the solid is not at failure, so the lateral pressure ratio k can be approximated by the elastic value for a solid confined within an elastic shell, $k=\nu/(1-\nu+\alpha)$, in which ν is the Poisson's ratio and α is the relative stiffness parameter and is given by $\alpha=E_S R/E_W t$ (Ooi, 1990).

Reimbert and Reimbert (1976) produced an alternative solution to the Janssen differential equation by curve fitting experimental results within the confines of the equation, thus effectively allows k to vary between zero at the surface and the value of Rankine active pressure ratio at great depth. Some comparisons of this solution with Janssen have been made (Briassoulis 1986, 1987, 1991; Reimbert and Reimbert 1987). Much simpler design proposals for squat silos were made by Lambert (1968) who proposed Rankine theory (1857) and Stewart (1972) who recommended Coulomb theory (1773). Abdel-Sayed *et al* (1985) attempted to modify Coulomb theory to a cylindrical wall.

Most design codes use Janssen theory, but different codes have adopted different values for the lateral pressure ratio k. A few examples are given here: ACI 313 (1992) adopted $k=1-\sin\phi$ (Jaky, 1948); ISO (1991) and EC1 Part4 (1992) adopted $k=1.1(1-\sin\phi)$ from a proposal by Nielsen; and AS3774 (1990) adopted Walker's (1966) expression.

Finite element calculation (Ooi and Rotter, 1990b) indicates that the pressure variation near the bottom in flat-bottomed silos is much influenced by the silo base boundary condition: the restraint of the base naturally influences the pressures, but this is completely ignored in all classical theories, which are also used as the basis of code descriptions. The conical surcharge at the solid surface is traditionally accommodated by adjusting the origin of the depth coordinate to one third of the conical pile height when Janssen's (1895) theory or its modifications are used (e.g. Pieper and Wenzel, 1963; Walker, 1966; Homes, 1972; Walters, 1973; Jenike *et al.*,

1973). This results in finite pressures above the first wall contact, which are clearly wrong: the wall pressure at the highest wall contact must be zero (therefore k must be zero). This phenomenon is important in squat silos.

Many other factors cannot be dealt with by the classical theories: wall imperfections, inhomogeneities in the solids, which are known to be important, realistic constitutive laws for the solid and the stress history of the solid. Numerical methods represent a powerful tool for studying these effects.

2.4.2 Discharge

The pressure distributions in silos when the bulk solid is being symmetrically discharged are more unpredictable than those after filling. Attempts to describe them and to produce satisfactory codified rules have included such phenomena as switch pressures and local patch pressures (Rotter, 1988, 1990a, 1991). Nanninga (1956) attempted to explain the higher pressures during flow in terms of a "switch" from an active plastic stress field after filling to a passive field during discharge. This idea was extended by Jenike and Johanson (1968), Jenike *et al* (1973), Walker (1966) and Walters (1973), but is by now largely discredited. Walters' theory (1973) predicts much higher pressures than are observed experimentally. Jenike's minimum strain energy theory (Jenike *et al*, 1973; McLean and Arnold, 1976; Arnold *et al*, 1980) gained some acceptance, but the theory is still poorly understood (Rotter 1990b). McLean (1984) made a simple but unsubstantiated proposal when he suggested that cylindrical wall pressures under funnel flow should not exceed static filling values, whilst a flow multiplier of two should cover mass flow discharge pressures.

Almost all design codes are restricted to essentially symmetric discharge. Design pressures are obtained by multiplying the static filling pressure by an over-pressure factor or flow multiplier. But very different values for this over-pressure factor are found in different codes (e.g. ISO, 1991: 1.0-1.35; ACI 313, 1992: 1.5; AS 3774, 1990: 1.2-2.6; EC1 Part4, 1992: 1.0-1.5). This wide variation is currently the subject

of a major international study by the European Federation of Chemical Engineers (Wilms *et al*, 1995).

If the discharge is eccentric to the silo axis, the problem is much more complicated. A few theories have been advanced for the design of silos under eccentric discharge (Jenike, 1967; Wood, 1983; Rotter, 1986b). However, there have been many serious failures involving eccentric discharge, so most codes specifically exclude it. Existing experiments lead to a wide range of alternative descriptions and there is little consistency between the theoretical treatments. Codes which do include eccentric discharge treat it very differently (AS 3774, 1990; ACI 313, 1989). This has led to great confusion amongst silo designers. Full-scale experiments at the University of Edinburgh are beginning to establish a sound scientific basis for codified rules for eccentric discharge.

2.5 Numerical predictions of pressure distributions in silos

2.5.1 Introduction

Due to the limitations of classical theories, numerical methods were gradually introduced in the early 1960s and many advances have been made since then. The method of characteristics was first applied to the flow of material in a hopper by Jenike (1961) to validate his radial stress theory: further studies of both filling and discharge continued until the 1980s. Pitman (1986) used the finite difference method to solve the partial differential equations for the stress and velocity fields in hoppers. However, with rapid increases in computing power, the finite element method has dominated the field through its versatility and ability to model complex geometries and material properties. While the use of finite elements to model the solids as a continuum is still increasing, the behaviour of individual particles is also being studied using the discrete element method. However, this last method requires enormous computer power, and reproducing elementary results such as a silo filling pressure distribution remains a considerable challenge. A few attempts have also

been made to apply the boundary element method for the stress calculation in silos. The four principal numerical methods are described briefly in the following sections.

2.5.2 The Method of Characteristics

The method of characteristics is a mathematical tool for solving partial differential equations by transforming them along the characteristics into ordinary differential equations. Starting with the differential equations governing equilibrium and introducing a yield locus for the material, it is possible to derive a system of two hyperbolic differential equations that describe the stress field in the material (Sokolovskii, 1965).

Horne and Nedderman (1976) used this method to calculate limiting stress distributions in two-dimensional vertical-sided bins. Wilms (1984, 1985) performed extensive calculations with this method. The results agreed well with Janssen's theory for the vertical section of the silo, though the assumption of horizontally uniform vertical stress is incorrect. It has been useful in understanding stress fields near singularities in hoppers. Some researchers (Gardner, 1966; Bransby and Blair-Fish, 1974) used this method to study the stress field at the transition between the vertical walls and the sloping hopper walls. The method of characteristics predicts discontinuities in the stress field in many practical situations (Horne and Nedderman, 1976, 1978a and b; Wilms, 1985; Wilms and Schwedes, 1985). This method has been extensively used to find both filling and flowing stress fields in hoppers (Jenike, 1961; Johanson, 1962; Gardner, 1966; Bransby, 1974; Horne and Nedderman, 1978a and b; Wilms, 1985; Wilms and Schwedes, 1985). The method depends on the solids being in a plastic state: a condition which is rarely true of solids after filling, and sometimes of doubtful value for parts of the solid during discharge. It is therefore seriously limited.

2.5.3 The Boundary Element Method

The boundary element method was proposed as early as the FEM (Brebbia, 1978). It involves numerical solution of a set of integral equations that connect the boundary, or surface, tractions to boundary displacements. Unlike FEM, the BEM is based on solution of integral rather than differential equations and consists of discretization of only the boundary or the surface of the body into a number of elements. Thus the number of dimensions in the problem is reduced by one (e.g. from 3 to 2 and 2 to 1), and the computational effort is greatly reduced. Wu and Schmidt (1992a) applied the boundary element method to silo stress calculations and compared the results with observed filling and flow pressures in silos and hoppers (1992b).

2.5.4 The Finite Element Method

In the last quarter century, the finite element method has experienced enormous growth in both theoretical development and applications (e.g. Zienkiewicz, 1977; Zienkiewicz and Taylor, 1989, 1991). Having been used since the early 1960s, it is certainly the most popular, flexible and powerful tool for silo pressures research.

2.5.4.1 Filling pressures and silo-structure interaction

Many attempts have been made to calculate silo filling pressures using finite elements (e.g. Bishara and Mahmoud, 1976a, b; Chandrangsu and Bishara, 1978; Jofriet *et al*, 1977; Mahmoud and Abdel-Sayed, 1981; Bishara *et al*, 1981; Eibl *et al*, 1982; Smith and Lohnes, 1982; Bishara *et al*, 1983; Bishara, 1983). Jofriet *et al* (1977) showed that there was a good agreement between Janssen's theory and finite element predictions. Mahmoud and Abdel-Sayed (1981) modelled the interaction between solids and a flexible wall in shallow grain bins. They adopted the hyperbolic stress-strain model for the stored sand, and found some agreement with experiment measurements. Bishara and his co-workers studied many problems, beginning with silage, to determine the effect of solids behaviour in cylindrical silos. They devised non-linear bulk modulus and shear modulus responses from materials tests on coarse and fine materials and modelled a concrete silo wall with elastic hoop

elements. The predicted wall pressures were similar to those of the Janssen and Reimbert theories. Aribert and Ragneau (1990) used a perfectly plastic (Drucker-Prager) and a more complicated Wilde (1979) model for their constitutive laws. Zhang and his co-workers (Zhang *et al*, 1986, 1987, 1989a and b) also carried out many finite element studies to predict static and thermal pressures in grain bins.

Although all of these studies used complex material characterisation, the correlation between their experimentally observed pressures and theoretical predictions was generally not close and only a limited range of relevant parameters was studied. Ooi and Rotter (1990b, 1991b) used a comparatively simple elastic finite element model with wall friction characteristics. The results show that the key non-linearity in filling pressures is the wall friction, not the material constitutive model. A wide range of parametric studies for wall flexibility was also presented.

The effect of silo wall flexibility was first studied by Mahmoud and Abdel-Sayed (1981). Ooi and Rotter's (1990b) thorough studies for a squat silo show that the wall flexibility can be best represented by the parameter $E_S R/E_W t$ and that, in practice, only very light designs for squat silos lie in the range where wall flexibility influences the wall pressures if the system is entirely symmetrical.

Other studies explored different aspects of solid-wall interactions using finite elements. Rahim (1989) analysed a cylindrical concrete silo and concluded that imperfections in the silo wall have very little effect on the internal forces in the silo wall if the wall pressures are independent of the wall geometry. However, the effect of the wall imperfections on the wall pressures was not investigated. Askegaard *et al* (1990) used finite elements to estimate the measuring error caused by the stiffness of a pressure cell mounted in a thin silo wall and concluded that serious measuring errors will occur if the cell thickness is slightly different from that of the wall. A recent finite element study of wall-solid interaction (Ooi and She, 1996) shows that geometric imperfections in the wall may have a very significant effect on the wall pressures in thin-walled metal squat silos.

2.5.4.2 Solids flow and discharge

The stress and velocity fields during flow of granular materials has also been a field of much finite element activity (Haussler and Eibl 1984; Runesson and Nilsson, 1986; Askari and Elwi, 1988; Schmit and Wu, 1989, Rombach and Eibl, 1989; Ruckenbrod and Eibl, 1993).

Haussler and Eibl (1984) developed an elegant Eulerian formulation to simulate the silo discharge process. The granular bulk material was considered to satisfy a complex elastic-plastic-viscous law, and the velocity and stress fields in mass-flow silos were calculated using finite differences in time. They obtained the transient velocity and stress fields within the bulk material for the beginning of discharge and noted the strong stress redistributions causing increased wall pressures. Progressively improved models have been developed, until a complete simulation of the filling and discharge processes is now possible with realistic material behaviour, density variations, and varied boundary conditions (Ruckenbrod and Eibl, 1993).

While many researchers adopted complicated stress-strain relationships to analyse the wall pressure distributions, Askari and Elwi (1988) adopted a simple technique using a double iterative scheme over the friction and the perfect elastic-plastic bulk material model. The material was assumed to be no-tension Drucker-Prager elastic-perfectly plastic. By simulating incipient flow conditions in strong materials, a switch load was claimed to be simulated at an open outlet. The effect of load history was included by applying gravity in stages to the bulk material during filling (Link and Elwi, 1990).

A few studies have explored the effect of a switch stress at the transition on the silo structure. These have generally shown that symmetrical switch stresses are not very serious in steel structures (Rotter, 1986a; Teng and Rotter, 1991), provided the loading remains axisymmetric. Unsymmetrical loading conditions lead to much

more serious conditions for a cylindrical wall (Rotter, 1983a; Ansourian, 1983; Rotter, 1986a, 1987).

The most serious unsymmetrical load distribution is that arising from eccentric discharge of the solids, which has caused many failures. Some attempts have been made to predict the very different structural effects of these loads in concrete (Mahmoud, 1977; Ibrahim and Dickerson, 1983; Emanuel *et al*, 1983a and b) and steel silos (Rotter, 1986a). Ibrahim and Dickerson (1983) performed a two dimensional finite element analysis of a horizontal slice of a concrete silo for powdered coal with eccentric discharge. Core flow was assumed, with the horizontal pressure in non-flowing material taken as Janssen values. Mahmoud (1977) conducted a similar 2D analysis for eccentric discharge. This work was later carried further by later papers (Emanuel *et al*, 1983a and b). The bending moments in a concrete silo wall can be predicted, but they are very sensitive to the assumed stiffness of the stationary solids, which makes them difficult to apply in practice.

The existence of the stiffness of solids also increases the buckling strength of a metal silo very significantly (Rotter *et al*, 1980; Rotter and Zhang, 1990; Zhang and Ansourian, 1990; Knoedel and Schulz, 1992). The analysis of shell buckling with the effects of granular solids restraint added to those of geometrical imperfections and internal pressurisation is a very complicated problem, and requires much further work.

2.5.5 The Discrete Element Method

The Discrete Element Method, proposed by Cundall (1971, 1979), is a relatively new technique for simulating moving granular particles. Different terms such as "Discrete Element Method" (Cundall, 1971), "Molecular Dynamics" (Ristow and Hermann, 1993), "Distinct Element Method" (Thornton, 1989) and "Granular Dynamics" (Poschl, 1992) have been used for this method. It is based on the use of an explicit

numerical scheme in which the interactions between a finite number of particles is monitored contact by contact and the motion of the particles is modelled particle by particle. Newton's equations of motion for each particle effectively replace the equilibrium equations used in continuum mechanics, and the model of inter-particle contacts replaces the constitutive model.

The discrete element method has been extended by many authors in recent years (Cundall, 1971, 1978, 1979; Shahinpoor, 1983a, b; Muhlenbein *et al*, 1988; Goldberg, 1989; Thornton, 1989, 1991; Broug, 1990; Bardet, 1993; Schwedes and Feise, 1993). While most researchers are concerned with spherical particles, a few studies (Hogue, 1991; Poschl, 1992) on non-spherical particles have been undertaken. The normal and shear stiffnesses between two particles are generally represented by a contact model which consists of a spring and a friction slider (Bardet, 1993). Nevertheless, the huge computational effort required to monitor a useful number of particles makes the method very difficult to use practically. The number of particles which can be considered is still very small, e.g. 20,000, which is tiny compared with the huge number of particles in a real situation (e.g. 10^8).

2.6 Silo pressure observations

2.6.1 Introduction

Experimental investigations into the pressures on silo walls have been undertaken at least since the tests of Roberts (1882, 1884), which precede Janssen's (1895) theory by eleven years. A huge number of tests have been conducted by a great variety of researchers, so that a full review is well beyond the scope of this thesis. The literature is much larger than that for solids flow, so a limited review is given here.

The early experiments on silos were reported in detail by Ketchum (1907). From his review, it could already be seen that the Janssen (1895) theory provides good predictions of the pressures which occur on filling, that larger pressures were

sometimes encountered during discharge, and that eccentric discharge could cause high unexpected pressures. In some respects, the progress of knowledge has been rather difficult since that time: considering the huge efforts put into both experimental and theoretical silos research, it is perhaps an indication of the difficulty of the field that not a lot more can be said today!

Ketchum's (1907) book was very influential, and dominated silo design, at least in the English speaking world, for many decades. A number of major studies influenced the development of thought in the field of silo pressures since Ketchum. These may be chosen as the studies of Pieper's large experimental group in Braunschweig (Pieper and Wenzel, 1963; Pieper, 1969; Pieper *et al*, 1981), the experimental and theoretical investigations of Jenike and his co-workers (Jenike, 1961, 1964a, 1967; Jenike and Johanson, 1968, 1969; Jenike, Johanson and Carson, 1973a, b, c), the experiments of Deutsch and Clyde (1967) and the full scale, model scale and centrifuge studies of the Danish group under Askegaard and Nielsen (Askegaard *et al*, 1971; Nielsen and Askegaard, 1977; Nielsen and Kristiansen, 1979, 1980; Nielsen, 1979, 1983a, b; Nielsen and Andersen, 1982; Hartlen *et al*, 1984; Askegaard and Munch-Andersen, 1984; Munch-Andersen and Nielsen, 1986, 1990). Many other important studies have been made, as described below, but the above have probably been more influential than any others.

The conclusions which arise from these studies may be summarised as follows:

(a) when a silo is filled, the pressures are close to those defined by Janssen's theory, provided the lateral pressure ratio can be appropriately chosen;

(b) the pressures during discharge do not increase significantly if the silo is shallow so that the flow is entirely internal;

(c) the pressures during discharge in a mass flow silo increase markedly at the transition between the hopper and the vertical barrel, but they may or may not increase in the barrel;

(d) the pressures during discharge in a funnel flow silo can be very high in the area around the effective transition, where the flow channel reaches the wall. If this is close to the surface, the pressures will be significantly higher than those nearby, but in absolute terms they will be small. By contrast, if this point is in a region where the filling pressure was reasonably high, these increased pressures may be very large and damage the structural integrity of the silo;

(e) eccentric flow may occur due to many reasons, and leads to strongly unsymmetrical pressures. The pressures may be small close to the outlet, with high pressures at the same level but further around the circumference, or they may be high on the opposite wall from the outlet: no systematic pattern or logic for these pressures has been advanced yet, and eccentric discharge remains one of the most serious events which can occur in a silo.

2.6.2 Other studies in the last thirty years

Sundaram and Cowin (1979) reviewed much of the early work on static bin pressure experiments. They referred to experimental work by Roberts, Janssen, Prante, Toltz, Ketchum, Jamieson, Bovey, Lufft, Pleissner, Amur and Caugney being done in the period 1882-1951.

Rowe (1959) measured wall stresses using a strain gauge pressure cell in a 10m diameter, 30m high reinforced concrete silo containing cement. Air slides were used to extract the material. Rowe concluded that the pressures measured in the silo were not predicted well by Janssen's theory.

Turitzin (1963) summarised much of the early work in Russia and France on the measurement of stresses that arise during the discharge from silos. He reported the work of Takhtamishev, Reimbert, Kim and Kovtun and Platonov. He concluded that lateral pressures during filling are generally less than those during emptying.

Walker and Blanchard (1967) measured wall pressures in pilot scale hoppers with up to 5 tonne capacity. Conical hoppers with 3, 15, 30 and 45 degree half angles and pyramid shaped hoppers with 15, 30 and 45 degree half angles were used. Experiments were performed using coal as the test material. A water filled football bladder connected to a pressure transducer was also used to measure internal pressures within the material. The stress fields during discharge were found to be very different from those set up after filling. For the steeper smoother hoppers, the resulting pressures showed good agreement with Walker's theory. The bladder is, however, an extremely unreliable method of measuring pressures in a stiff solid such as coal.

Aoki and Tsunakawa (1969) measured wall pressures in small mass flow hoppers and found that Walker's theoretical approach predicted experimental results well. Aoki and Tsunakawa (1972) later summarised much other Japanese work on silo loads. Tsunakawa and Aoki (1974) found that Janssen's theory produced good estimates of the pressures in a 530mm diameter model bin.

Wenzel (1973) investigated the pressures in double cylindrical silos in which a narrow tube is used to store material within a wider cylindrical silo. He used in inner silo diameter of 0.2 m and an outer silo diameter of 0.75 m.

Sugita (1972) measured the wall pressures in a 7 m diameter, 28 m high reinforced concrete bin containing wheat using diaphragm type pressure gauges. Flow in the bin was described as funnel flow, though no measurements were made. Static pressures were nearly equal to the values computed using Janssen's theory. Pressures during discharge were very much higher and showed a maximum part way up the cylindrical silo. Sugita related his full scale pressure measurements to the flow patterns he observed in a small model bin.

Smid (1975) used the model cylindrical silo (300mm diameter), previously used for flow experiments by Novosad and Surapati (1968), to investigate wall pressures in

silica sand. Experimental results for the pressures after filling were in good agreement with predictions based on Janssen's or Reimbert's theories. Novosad and Surapati (1968) had found internal or core flow during discharge. Smid noticed that the measured stresses oscillated during discharge.

Mukhopadnyay and Sristava (1980) also measured pressures during filling and discharge on model bins.

Wright (1980) reported an investigation carried out in 1961 of the pressures in a 3000 tonnes capacity reinforced concrete coal bunker. The bunker was approximately 21 m high with two rectangular compartments each 8.09 m wide and 14.5 m long. The flow regime in the hoppers was mass flow. Pressures recorded using strain gauge diaphragm pressure cells were significantly higher than expected particularly during discharge near to the hopper/bin transition.

Stoffers (1983) measured wall pressures using diaphragm pressure cells in a 6m reinforced concrete silo for soya meal. It was 32 m high. Pressures measured appeared to vary strongly from one place to another and were generally higher than given in existing standards. Pressures were particularly high in the hopper area during emptying.

Blight (1983) measured pressures in a 20m diameter steel maize storage bin using mercury-filled strain-gauged diaphragm pressure cells. The profile of the maize surface in the bin was determined by dropping a tape from the top of the bin. The height of the material in the bin fluctuated during the measurement period as a result of normal transfers of grain in and out of the bin. Rusting of the bin walls at the bottom identified the extent of the dead material in the base of the bin. Blight reported an increase in lateral pressure at the "effective transition" where the flow changes from parallel to convergent flow.

Blight *et al* (Blight *et al*, 1982; Schaffner and Blight, 1983) measured the strains in the hoop reinforcing of a concrete silo during rapid filling with cement raw meal. The silo was 43m high with a diameter of 15m. When a fine powder is rapidly loaded into a silo it entrains a large proportion of air. The pressure exerted on the silo walls at any depth is made up of the pressure in the entrained air and that exerted by solid particles. As the air escapes from the powder (the soil mechanics consolidation process) the pressure distribution changes. These authors suggested that the maximum pressure could be predicted reasonably accurately by solving Janssen's differential equation with special allowance for consolidation of the stored solids.

In pilot scale hoppers approximately 2m diameter, Murfitt and Bransby (1982) found that the total stresses (pore air plus material stress) during discharge approached the hydrostatic distribution.

Nielsen (1983b) measured stresses in a 16 m diameter, 23 m high concrete walled aerated silo for fly ash. Both funnel flow and mass flow was found to be possible in the silo and a shift was observed several times between mass flow and funnel flow.

Suzuki, Akashi and Matsumoto (1985) measured the stress distribution at the wall and the fractional loss at the transition in small (0.3m diameter) and medium sized (1.4m diameter) silos. They found that the lateral and vertical stress distributions at the bin wall were predicted by the Janssen theory and that the stress distribution during discharge in the hopper could be predicted by Walters' (1973) modification of the method of differential slices.

Blight (1987a, 1988a) measured the strains in the walls of a free-standing cylindrical steel sugar silo. The silo diameter was 20m and it was 40m high. Discharge was through 24 extractor cones situated around a central deflector cone. Although the flow pattern during discharge was concentric, wall loads were radially non-uniform during discharge. The authors suggested that variations in wall friction caused the

non-uniformity. Horizontal pressures increased during discharge resulting in a reduction in the wall load. They noted that temperature has a significant effect on wall loads during further investigations with this silo (Blight, 1987b, 1988b).

Blight made pressure measurements on a number of large silos. He believed that much of the early work on pressure measurement in silos was seriously flawed (Blight, 1988b), as was noted above. He used strain gauge diaphragm pressure cells to measure the pressure in a 20m diameter, 54 m high concrete walled coal silo (Blight, 1986a, b). The coal in the bottom of the silo formed a conical hopper with walls 60 to 70 degrees to the horizontal. His interpretation of the experiments indicated that the horizontal pressure in the silo increase linearly with depth. He asserted that maximum design pressures in the silo could be estimated by assuming that the vertical pressure is unaffected by the wall and the solid stress state is a Ko condition.

In situ strain measurements were also made on the reinforcement of a reinforced concrete coal storage silo by Blight and Dreyre (1989). The results indicated that the reinforced concrete was still carrying load as an uncracked shell after eleven years of service.

2.6.3 Eccentric discharge

Murfitt and Bransby (1982) measured the pressure during discharge of fine chalk from a hopper 2.44 m in diameter with four outlets. When discharging through one outlet the total stresses (pore air pressure plus material pressure) approached "hydrostatic" values with fluctuating stresses superimposed on them particularly in the flowing regions near the outlet.

Blight and Midgley (1980) measured wall pressures in a 20 m diameter, 30m high reinforced concrete coal load-cut bin with a double pyramid hopper bottom with twin outlets. When emptying from the eccentrically placed outlets a zone of reduced

pressure developed on the walls adjacent to the outlet in use, while pressures increased elsewhere.

Nielsen and Kristiansen (1980) measured pressures in a 46 m high, 7 m diameter concrete barley silo with an eccentric outlet. During discharge the pressure distribution was asymmetrical with maximum pressures up to 3.1 times the pressures predicted by the Janssen theory.

Jumikis, Rotter, *et al* (1986) investigated the buckling strength of thin-walled flat-bottomed silos for eccentric discharge conditions using small-scale model silos made of thin Mylar plastic sheeting. This study showed that the unsymmetrical pressures associated with a flowing channel could cause buckling failures in thin-walled silos. The conditions for buckling were identified.

Mahmoud and Abdel-Sayed (1981) used finite element techniques to model the material wall interaction in shallow flexible grain bins. The material was assumed to have a hyperbolic stress-strain relationship. The rigidity of the wall was found to affect the predicted stresses. They attempted to validate their model using tests with sand but it can be argued that Janssen's theory gives better agreement with the tests.

Ibrahim and Dickenson (1983) carried out a two-dimensional finite element study of a horizontal slice of a thick walled silo for powered coal with eccentric discharge. It was assumed that the flow pattern was core flow and the horizontal pressure in the flowing core was estimated using Walker's theory. The coal was assumed to deform elastically. They concluded that it is important to consider relative motion between the material and the silo wall. Mahmoud (1977) also carried out a two dimensional analysis of a silo with eccentric discharge. Later papers (Emanuel *et al*, 1983a, b) carried this work further.

Rotter (1985b) applied the linear bending theory of shells to the stress analysis of bins and silos. He showed that unsymmetrical loading conditions can be either

unimportant to the structure or seriously affect its load carrying capacity, depending on the location and form of the asymmetry.

Rotter (1986a) analysed the structural consequences of eccentric discharge on steel silos. He demonstrated the mechanisms of buckling failure in thin walled silos. He noted that most existing descriptions of the structural consequences of eccentric discharge pressures are concerned only with the silo wall acting as a ring at any given level: as a result they assume that circumferentially non-uniform pressures simply give rise to circumferential tensions and bending moments. Rotter commented that this may be acceptable for reinforced concrete silos which have little vertical bending strength, but it is dangerous for thin-walled steel silos.

2.7 Interpretation of pressure observations

2.7.1 Common past practice

Most of the above experimental studies were undertaken with little thought for the interpretation which should be put on pressure cell observations. The general philosophy adopted was often that the largest pressure observed must always be the most damaging to the structure, irrespective of its location, spatial extent or duration. The habit of most researchers has been to observe pressures at several levels in a silo during the discharge, to find the highest peak occurring at each height, irrespective of whether the events were simultaneous, and to plot the envelope of the highest pressures with respect to height in the silo. All information concerning the variation of pressure with height at any instant was lost, and very little attention was paid to the variation of the pressures around the silo at any instant. Finally, groups of experimental results were overlaid, and envelopes drawn around the largest of the largest pressures at each level, producing a set of pressures which had little relationship to any direct observations. These unsatisfactory features of experimental philosophy were described in detail by Rotter *et al* (1986).

This is a poor philosophy of experimental interpretation for many reasons.

2.7.2 Shortcomings of the above practices

The common simple philosophy used for interpreting experiments in the past has been outlined above. The reasons why it is poor are outlined here.

First, since the structure generally responds to the complete pressure pattern and has a weaker response to uneven or unsymmetrical pressures than to symmetrical or even pressures, the envelopes of maximum pressure described above often produced a pressure distribution which was less critical to the structure's integrity than the real pressures measured at a single instant.

Second, an observed pressure is part of a statistical distribution, which may generally be regarded as normally distributed. The maximum pressure observed depends on how many observations are made, and the peak observation will tend to increase progressively as more and more observations are made, in the same manner as the highest wind velocity ever observed steadily increases as records are kept for longer periods. The only remedy for this apparently increasing maximum pressure is to use a statistical method of assessment to deduce the pressure which has a defined probability of occurrence.

Third, the spatial extent of a pressure observation is very important. A high pressure which acts on a very small area (perhaps because that point is a protrusion into the flow), has little significance for the integrity of the structure. The structural implications of measured pressures were rarely considered in most studies of silo pressures.

Fourth, the duration of the pressure peak is also important. A high pressure which lasts for only a fraction of a second may not have time to produce a failure of the structure, but instead produces dynamic effects.

These issues began to be addressed in writings during the 1980s. Rotter *et al* (1986) produced one of the first critiques of existing interpretation of silo pressure observations. Ideas relating to the statistical treatment of silo loads were advanced by Pham, Rotter and Gorenc (1986a, b). The line of reasoning has been followed by Ooi *et al* (1989, 1990), Ooi and Rotter (1990, 1991a), Maj (1993), da Silva and Calil (1993), Munch-Andersen and Ditlevsen (1995), Munch-Andersen *et al* (1995), Ditlevsen *et al* (1995). The work undertaken in this thesis to infer solids pressures from wall strain measurements represents a continuation of this research.

It is now becoming widely recognised that the traditional simplistic process described above is flawed. Instead, rigorous statistical interpretations are being established which defines the pressure levels with a defined probability of being exceeded. The observed distributions are also now being used without the masking effect of the envelope of peaks at different times in the discharge.

This thesis develops a much more rigorous method of interpreting the observations, which represents a very valuable tool for industry and researchers alike.

2.8 Conclusions

This chapter has reviewed the existing knowledge relevant to the analysis and interpretation of experiments on solids flow patterns and wall pressures in silos. It is evident that the residence time measurement technique probably provides the most information for flow patterns among the feasible experimental methods when applied to full scale silos. However, interpretation of the observations made using residence time measurements under funnel flow conditions is not at all straightforward, and numerical processing of the results to identify the changing flow channel boundary is still in its infancy. One of the main tasks of this thesis is to develop new techniques to interpret the solids flow patterns from residence time measurements.

Many classical theories are available for the wall pressure distributions in silos but their predictions are often a very poor match with experimental observations, especially during discharge. Large differences may be found in the codified design pressures from different countries. Numerical methods, and especially the finite element method, provide an ideal tool for researchers to simulate the interactions between bulk materials and the silo structure. Nevertheless, these methods are not yet adequate to describe many phenomena observed in experiments, such as the random fluctuation of pressures with time and silo quaking.

A huge number of tests have been conducted by a great variety of researchers since the last century. The general philosophy in the interpretation of pressure observations was often that the largest pressure observed must always be the most damaging to the structure, irrespective of its location, spatial extent or duration. It is now becoming widely recognised that this assumption is poor. Instead, rigorous statistical interpretations, defining the pressure levels with a defined probability of being exceeded, are being established. A much more rigorous method of inferring wall pressures from wall strain observations is developed in this thesis.

Chapter 3

INTERPRETATION AND GRAPHICAL DISPLAY OF SOLIDS FLOW PATTERNS

3.1 Introduction

Many techniques have been used to investigate the flow of granular solids in model silos. These include visual observations through transparent silo walls or through transparent 'windows' in a silo wall (Johanson, 1964; Rotter *et al*, 1989; Munch-Andersen, 1990), insertion of markers to measure residence times (e.g. Graham *et al*, 1987; Watson, 1993), freezing of the flow with paraffin and dissection (e.g. Chatlynne and Resnick, 1973), photographic techniques (e.g. Bosley *et al*, 1969), X rays (e.g. Bransby and Blair-Fish, 1974), and radio pills (e.g. Perry *et al.*, 1976). Among these methods, residence time measurement has probably been used most frequently and appears to be the only practicable one applicable to full scale silo tests without damaging the silo itself (Rotter *et al.*, 1995). A fuller review was given in Chapter 2.

Several methods have been used to present the results of residence time measurements. These include raw data plotting (Watson, 1993) and simple maps of residence time plotted in the initial positions of markers (Ebert and Dau, 1993). The use of contours of residence time and contours of mean velocity in this thesis (see Chapters 5 and 7) significantly improves the presentation technique. They present a clear picture of how the residence time and the mean velocity are distributed. However, the information contained in these plots is not easily assimilated, and the variation of the flow pattern with time is not addressed at all. Even a static image of

a flow channel is only discoverable with considerable effort, and much is left to the imagination to understand how the particles flow in a silo. Although the new analysis of mass emerged from a level which will be described in Chapter 5 identifies the flow patterns with clarity and further defines the flow channel boundary in the case of funnel flow, the dynamic process of particle flow is still not represented. Visualisation of the flow process is not only helpful in interpreting the flow patterns, but is also in demand by industrial engineers.

As one of the interpretation methods developed in this thesis, computer graphics are used to represent the dynamic process of the solids flow in a silo during discharge. A program has been developed and several algorithms have been implemented. It was developed to model the complete flow process, using as few assumptions as possible, and without invoking any assumptions concerning the properties or constitutive response of the solid. This is necessary if the observations are to be used later to verify theoretical predictive methods, as the same assumptions cannot be used in both experimental interpretation and theoretical prediction.

Some strong visual images have been created which make it much easier to see how the particles move in a silo. The test data in both the new 250 tonne steel silo at British Gypsum's East Leake plant and the experimental silo at British Steel have been run on this program and some of the results are presented in Chapters 5 and 7 respectively.

3.2 The silo geometry and stored solids

The silo geometries used here are a cylinder with a conical hopper and a flat-bottomed cylinder. The height and the radius of the cylinder are H and R respectively, while the hopper half angle is β. A Cartesian coordinate system with its origin at any point on the axis of the cylinder may be used. The outlet is of radius R_o with its centre at (x_o, y_o, z_o).

The British Gypsum silo was fitted with an inverted cone discharge aid in the hopper, so this was included in the simulation (Fig. 3.1a). The discharge aid is treated here as a cone of radius r_a with a height h_a. It may be either concentrically or eccentrically placed in the hopper. The centre of the base of the discharge aid is placed at (x_a, y_a, z_a) and its top at (x_a, y_a, z_a+h_a). The geometry of the hopper adjacent to the discharge aid is shown in Fig. 3.1b. If r_a is specified as 0 and put at the centre of the outlet, the discharge aid is removed. Furthermore, a flat-bottom silo is obtained by setting β to 90°.

No assumption is made about the properties of the stored solids. The visualisation technique is therefore applicable to any bulk solids.

3.3 Residence time measurement

The principle of residence time measurement is to place markers at defined positions during filling of a silo and to measure the time that each marker takes to reach the outlet during discharge. Once the original position and residence time of each marker has been determined, the solids flow pattern may be interpreted using several alternative methods.

In past experiments many different particles have been used as the tracing markers. Some examples are marbles (e.g. Watson, 1993), hollow steel particles, and headless screws (e.g. Ebert and Dau, 1993). In the tests described in this thesis, radio tags were used; these tags emit radio signals which can be detected electronically.

A primitive method of residence time measurement is to record the instant when a marker passes through the outlet. The residence time is then the difference between this time and the time when discharge began. Electronic time measurement systems have been applied in some tests (Rotter *et al,* 1995; Ebert and Dau, 1993). A key

problem is to identify a marker uniquely and reliably when it passes the outlet. A clear coding system is needed. In the experiments on which the data analysed in this thesis are based, each marker was uniquely coded electronically and also physically by colour, letter and number.

3.4 Trajectories of markers

To simulate the motion of a marker in a silo, its trajectory and velocity at any instant should be known. Before a more rigorous interpretation procedure was implemented, a few simple assumptions were made to define the trajectory and velocity of a particle, and appropriate algorithms were implemented. The trajectory is here used to mean the locus of successive positions from the point at which the marker was placed to the centre of the outlet. The current available trajectories include: a) shortest path; b) converging flow path and c) streamline paths which are defined by varying horizontal and vertical velocities. With different horizontal and vertical velocities, many different shapes of streamline path can be generated. The analytical formulations of the first two trajectories are described as follows whilst the last one is described in Section 3.5 on velocities of markers.

3.4.1 Shortest path

The simplest assumption for the trajectory is to assume each marker moves along the shortest path towards the outlet. For many markers in mass flow, this may be not far from the reality. As shown in Fig. 3.2a, the distance from the original position (x_i, y_i, z_i) to the centre of the outlet (x_o, y_o, z_o) for a marker consists of two parts: the distance S_a from its initial position to the discharge aid level and S_o from the discharge aid level to the outlet

$$S = S_a + S_o \tag{3.1}$$

where

$$S_a = \sqrt{(x_i - x_u)^2 + (y_i - y_u)^2 + (z_i - z_a)^2} \tag{3.2a}$$

$$S_o = \sqrt{(x_u - x_o)^2 + (y_u - y_o)^2 + (z_a - z_o)^2} = \sqrt{r_u^2 + (z_a - z_o)^2} \tag{3.2b}$$

$$x_u = r_u(\theta)\cos(\theta) \tag{3.2c}$$

$$y_u = r_u(\theta)\sin(\theta) \tag{3.2d}$$

$$\theta = \tan^{-1}\left(\frac{y_i}{x_i}\right) \tag{3.2e}$$

in which $r_u(\theta)$ is the mean radius of the gap around the discharge aid (Fig. 3.1b). If the discharge aid is axisymmetrically placed in the silo, $r_u(\theta)$ is constant. Otherwise it may vary with the circumferential coordinate θ.

3.4.2 Converging flow path

An alternative assumption may be that each marker moves down vertically until it reaches the conical surface whose apex lies at the top of the discharge aid and whose perimeter is at the cylinder/hopper transition. It is then assumed to move towards to the outlet along its shortest path (Fig. 3.2b). If the solids in the silo move in mass flow and the velocity distribution is uniform across the cross section of the silo, the path of a marker may approximately follow this trajectory as demanded by volumetric continuity. The distance from the initial position to the outlet for a marker also consists of two parts as Eq. 3.1 but where

$$S_a = z_i - z_c + \sqrt{(x_i - x_u)^2 + (y_i - y_u)^2 + (z_c - z_a)^2} \tag{3.3}$$

in which the vertical coordinate z_c of the intersection point between the vertical path and the conical surface through the top of the discharge aid and the cylinder/hopper transition is given by

$$z_c = z_a + h_a + \frac{(z_t - z_a - h_a)\sqrt{(x_i - x_a)^2 + (y_i - y_a)^2}}{\sqrt{(R\cos\alpha - x_a)^2 + (R\sin\alpha - y_a)^2}} \tag{3.4}$$

3.5 Flow velocities of markers

Real markers have velocities which vary with time. However, the velocity variation cannot be known, so assumptions must be made which produce global images which seem credible to the engineers. The simplest assumption for the velocity variation with time is that each particle moves at constant speed at its mean velocity. However, it is clear that few particles really travel in such a way. Instead, the velocity of a particle most possibly varies with time when it is moving from its initial position to the outlet. A simple improvement would be to assume that the velocity of a marker changes continuously from the beginning of the discharge. Whilst it is true in the case of mass flow that that all the particles start to move as soon as the discharge starts, in other flow modes the solids outside the initial flow channel are initially stationary for an extended period. They only start to move when the flow channel expands or the top surface lowers down so that they are within the flow zone. An alternative proposition might therefore be that a marker remains stationary until a certain time T_s and then starts to move at a variable velocity to the outlet.

In the above algorithms, a marker may be assumed to follow either the shortest path or the converging path, both of which consist of straight lines. An alternative method is to assume vertical and horizontal projections of the velocity of a marker. Its advantage is that the resulting trajectory is a smooth curve, termed a streamline trajectory here. With different variations of horizontal and vertical velocities, many

different trajectories can be produced (Fig. 3.2c). Two algorithms of this kind were implemented in the program here.

3.5.1 Mean velocity

Under the "mean velocity" assumption, it is assumed that all the markers move at a constant velocity v_o between the discharge aid and the outlet to reflect the effect of the discharge aid. Above the discharge aid, a marker moves at its mean velocity. The value of v_o may be assumed to be the fastest mean velocity of all the markers, i.e.

$$v_o = \max\left(\frac{S}{T}, \text{for all markers}\right) \tag{3.5}$$

in which S is the length of the trajectory for a marker as defined in Eqs 3.1 to 3.3. The mean velocity of a marker above the discharge aid is therefore

$$\bar{v} = \frac{S_a}{T - \frac{S_o}{v_o}} \tag{3.6}$$

At a given time t, the distance travelled by the marker from the beginning of the discharge is given by

$$s(t) = \bar{v}t, \qquad \text{for } t \le T - \frac{S_o}{v_o} \tag{3.7a}$$

$$s(t) = S_a + \bar{v}t, \quad \text{for } t > T - \frac{S_o}{v_o} \tag{3.7b}$$

Having known the trajectory and the distance travelled, it is straightforward to determine the coordinates of the marker position at time t.

3.5.2 Exponential decay velocity variation

In this algorithm, the velocity of a marker is assumed to vary as

$$v(t) = \xi\left(1 - e^{-\alpha\frac{t}{T}}\right) \tag{3.8}$$

in which the coefficient ξ may be determined by the condition that the marker must reach the outlet at time t=T. If the distance from the initial position of the marker to the outlet along a given trajectory is S, this leads to

$$s(T) = S = \int_0^T v(t)dt = \xi T\left(1 + \frac{e^{-\alpha} - 1}{\alpha}\right) \tag{3.9}$$

Thus

$$\xi = \frac{S}{T}\frac{\alpha}{\alpha + e^{-\alpha} - 1} \tag{3.10}$$

and

$$v(t) = \frac{S}{T}\frac{\alpha}{\alpha + e^{-\alpha} - 1}\left(1 - e^{-\alpha\frac{t}{T}}\right) \tag{3.11}$$

v(t) may be normalised by dividing by S/T which is the mean velocity of the marker. Figure 3.3 shows the variation of the normalised velocity of a marker with time. It is seen that different values of α result in different shapes of velocity variation. For a small value of α (e.g. 0.1), the velocity of a marker increases almost linearly and is

close to twice the value of its mean velocity when it reaches the outlet. For a large value of α (e.g. 20), a marker accelerates very fast and then moves at a constant velocity with a value close to its mean velocity. The results may be very similar to that by assuming that a marker moves at its mean velocity. This assumed velocity distribution is thus very flexible. In practice, the initial acceleration of a marker cannot be infinite, so movement at constant velocity is impossible. Therefore, the value of this initial acceleration may be restricted to below a given value. For discharges under gravity alone, the upper limit value of acceleration may reasonably be assumed to be the gravitational acceleration. This leads to

$$a(t=0) = \left.\frac{dv}{dt}\right|_{t=0} = \frac{S}{T^2}\frac{\alpha^2}{\alpha + e^{-\alpha} - 1} \le g \qquad (3.12)$$

The distance s(t) travelled by the marker at a time t<T is obtained by integrating Eq. 3.11 from 0 to t

$$s(t) = \int_0^t v(\tau)d\tau = \frac{S}{T}\frac{\alpha}{\alpha + e^{-\alpha} - 1}\left[t + \frac{T}{\alpha}(e^{-\alpha\frac{t}{T}} - 1)\right] \qquad (3.13)$$

3.5.3 Stationary followed by exponential decay velocity variation

In this option, particles are assumed to be stationary for a period T_s and then start to move with a variable velocity. The value of T_s may vary for different particles depending on their initial positions and residence times. Further, it may also be assumed that all particles pass through the outlet at a constant velocity v_o and the gap between the discharge aid and the hopper walls at v_a. If the discharge rate ρ is uniform throughout the whole discharge process, v_o and v_a may be estimated as

$$v_o = \frac{\rho}{A_o \gamma_f} \qquad (3.14a)$$

$$v_a = \frac{\rho}{A_u \gamma_f} \tag{3.14b}$$

in which A_o and A_u are the opening areas of the outlet and gap between the discharge aid and the hopper walls respectively and γ_f is the density of the stored solids during flow.

Due to the presence of the discharge aid, the trajectory of a marker is conveniently divided into two parts: one above the discharge aid and one below it (Eqs 3.1–3.3). The distance for a marker to move from the discharge aid at the velocity $v=v_a$ to the outlet at $v=v_o$ is S_o (Eq. 3.2b). During this part of the trajectory of the marker, its velocity may be assumed to vary linearly from v_a to v_o. The time for the marker to flow from the discharge aid to the outlet is then given by

$$T_o = \frac{2S_o}{v_o + v_a} \tag{3.15}$$

Similar to Eq. 3.8, it is also assumed that the velocity of the marker increases exponentially when it starts to move above the discharge aid:

$$v(t) = \begin{cases} 0 & \text{for } t \le T_s \\ \xi \left[1 - e^{-\alpha(t - T_s)/(T - T_s - T_o)} \right] & \text{for } T_s < t \le T - T_o \end{cases} \tag{3.16}$$

Integrating Eq. 3.16 from T_s to t gives the distance the marker has travelled at time t

$$s(t) = \xi \left[t - T_s + \frac{T - T_s - T_o}{\alpha} \left(e^{-\alpha(t - T_s)/(T - T_s - T_o)} - 1 \right) \right] \tag{3.17}$$

The coefficient ξ and the stationary time T_s for the marker in Eqs 3.16 and 3.17 may be determined by applying the following conditions:

$$v(t) = v_a \text{ and } s(t) = S_a, \qquad \text{for } t = T - T_o \tag{3.18}$$

Substituting Eqs 3.16 and 3.17 into Eq 3.18 leads to

$$\xi[1 - e^{-\alpha}]) = v_a \tag{3.19a}$$

$$\xi(T - T_o - T_s)\left(1 + \frac{e^{-\alpha} - 1}{\alpha}\right) = S_a \tag{3.19b}$$

Solving Eqs 3.19 gives

$$\xi = \frac{v_a}{1 - e^{-\alpha}} \tag{3.20a}$$

$$T_s = T - T_o - \frac{S_a}{v_a}\frac{\alpha(1 - e^{-\alpha})}{\alpha + e^{-\alpha} - 1} \tag{3.20b}$$

Substituting Eqs 3.20 into Eqs 3.16 and 3.17 leads to the velocity and the distance travelled by the marker at time t

$$v(t) = \begin{cases} 0 & \text{for } t \le T_s \\ \dfrac{v_a}{1 - e^{-\alpha}}[1 - e^{-\alpha(t - T_s)/(T - T_s - T_o)}] & \text{for } T_s < t \le T - T_o \end{cases} \tag{3.21a}$$

$$s(t) = \frac{v_a}{1 - e^{-\alpha}}\left[t - T_s + \frac{T - T_s - T_o}{\alpha}(e^{-\alpha(t - T_s)/(T - T_s - T_o)} - 1)\right] \tag{3.21b}$$

The value of α in this algorithm affects not only the variation of velocity with time (Fig. 3.4) but also the value of time T_s when a marker starts to move (Fig. 3.5). The velocity of a marker increases linearly from 0 to the v_a when α is small (e.g., 0.1). If

α is large (e.g. 20), the marker accelerates very fast when it starts to move and then flows at the constant velocity v_a.

The duration of the stationary period T_s is dependent on the values of S_a/v_a, T, T_o and α. For given values of S_a/v_a, T and T_o, a small α results in a small value of T_s (large $T-T_s-T_o$) and vice versa. However, the relationship is not linear as shown in Fig. 3.5.

It may also be necessary to constrain α so that the acceleration of a marker does not exceed a given value (e.g. the gravitational acceleration). This requires

$$a(t=T_s) = \left.\frac{dv}{dt}\right|_{t=T_s} = \frac{\alpha v_a}{(T - T_s - T_o)(1 - e^{-\alpha})} \leq g \tag{3.22}$$

3.5.4 Exponentially decaying horizontal and vertical velocities

In this algorithm, the trajectory of a marker is not explicitly defined. Instead, it is determined by independently defined vertical and horizontal velocities of a marker. Both vertical and horizontal velocities of the marker are assumed to vary as

$$v_v(t) = \frac{\Delta Z}{T}\frac{\alpha_v}{\alpha_v + e^{-\alpha_v} - 1}\left(1 - e^{-\alpha_v \frac{t}{T}}\right) \tag{3.23a}$$

$$v_h(t) = \frac{\Delta H}{T}\frac{\alpha_h}{\alpha_h + e^{-\alpha_h} - 1}\left(1 - e^{-\alpha_h \frac{t}{T}}\right) \tag{3.23b}$$

in which the ΔZ and ΔH are the vertical and horizontal distances from the initial position of the marker to the outlet respectively. If a discharge aid is present, they should be the vertical and horizontal distances from the initial position of a marker to a point (e.g. the nearest point) at the gap between the discharge aid and the hopper

walls and the time from the gap to the outlet T_o should be subtracted from the residence time T. α_h may be obtained by solving

$$\Delta Z \frac{\alpha_v^2}{\alpha_v + e^{-\alpha_v} - 1} = \tan\phi_a \Delta H \frac{\alpha_h^2}{\alpha_h + e^{-\alpha_h} - 1} \tag{3.24}$$

Equation 3.24 constrains the ratio of the initial vertical acceleration to the initial horizontal acceleration of the marker to be $\tan\phi_a$ (with $0° \le \phi_a < 90°$), i.e.

$$\left.\frac{a_v}{a_h}\right|_{t=0} = \tan\phi_a \tag{3.25}$$

in which ϕ_a constrains the initial slope of the trajectory of a marker, i.e. the initial slope is of the angle ϕ_a to the horizontal. A small ϕ_a (<45°) results in a slower initial horizontal acceleration than the vertical acceleration. By contrast, a large ϕ_a (>45°) results in a faster initial horizontal acceleration than the vertical acceleration (Fig. 3.6). In practice, ϕ_a is expected to relate closely to the angle of repose of the solid for particles near the surface.

Coefficients α_v and ϕ_a in Eqs 3.23 to 3.25 may be defined by the user. However, the value of α_v may be automatically adjusted to satisfy

$$a_v(t=0) = \left.\frac{dv_v}{dt}\right|_{t=0} = \frac{\Delta Z}{T^2} \frac{\alpha_v^2}{\alpha_v + e^{-\alpha_v} - 1} \le g \tag{3.26}$$

The effects of α_v and α_h on the variation of v_v and v_h with time are similar to those defined in Eq. 3.11 and Fig. 3.3.

The vertical and horizontal distances travelled by the marker at time t may be found by integrating Eqs 3.23

$$s_v(t) = \frac{\Delta Z}{T}\frac{\alpha_v}{\alpha_v + e^{-\alpha_v} - 1}\left[t + \frac{T}{\alpha_v}(e^{-\alpha_v\frac{t}{T}} - 1)\right] \tag{3.27a}$$

$$s_h(t) = \frac{\Delta H}{T}\frac{\alpha_h}{\alpha_h + e^{-\alpha_h} - 1}\left[t + \frac{T}{\alpha_h}(e^{-\alpha_h\frac{t}{T}} - 1)\right] \tag{3.27b}$$

An example of the resulting trajectory is shown in Fig. 3.8.

3.5.5 Exponentially decaying vertical velocity with triangular horizontal velocity

In the algorithm in section 3.5.4, both horizontal and vertical velocities are assumed to vary exponentially. Whilst it could be close to reality for many cases, it does imply that any particle which must move horizontally to reach the outlet will have a significant horizontal velocity as it reaches the outlet. An alternative was therefore devised in which the horizontal velocity may increase and then decrease again. It is assumed that the horizontal velocity of a marker increases linearly to a maximum value and then decreases linearly to zero when it reaches the outlet, i.e. the marker flows throughout the outlet vertically (Fig. 3.7). The vertical velocity is assumed to be the same as Eq. 3.23a. The horizontal velocity is expressed as:

$$v_h(t) = \begin{cases} \frac{2\Delta H}{T}\frac{t}{T_t} & \text{for } t \le T_t \\ \frac{2\Delta H}{T}\frac{T - t}{T - T_t} & \text{for } t > T_t \end{cases} \tag{3.28}$$

Similar to the previous algorithm, the time T_t when the horizontal reaches the maximum value is also defined by the angle ϕ_d so that the initial vertical and horizontal accelerations satisfy Eq. 3.25. This gives

$$T_t = \frac{2\Delta H}{\Delta Z}\frac{\alpha_v + e^{-\alpha_v} - 1}{\alpha_v^2}\tan\phi_a T \tag{3.29}$$

An example of the resulting trajectory is shown in Fig. 3.8.

3.6 Graphical Transformation

Having known the residence time of a marker and defined its velocity variation with time and trajectory, its position at any time t can be obtained. The positions of all the markers at time t form a set of data. To graphically present the dynamic movement of markers or particles, it is needed to a) calculate a great number of data set at various time; b) transform each set of data into an image and c) continuously present the images in time sequence.

Coordinate transformation and projection are two essential steps for 3D graphical presentation. To represent the transformation in matrix form, homogeneous coordinates are used (Maxwell, 1946, 1952). The coordinate transformation equations used here follow the procedures described by Newman and Sprouli (1973), Foley and van Dam (1984) and Harrington (1983).

The purpose of the projection is to display a 3D object on a 2D projection plane (e.g., the screen). It is defined by straight projection rays emanating from a chosen centre of projection, passing through each point on the object, and intersecting a projection plane to form the projection view (Foley and van Dam, 1984).

The two basic classes of projection are perspective and parallel. Perspective projection has the effect of perspective foreshortening (the size of the perspective projection of an object varies inversely with the distance of the object from the centre of the projection). This effect is similar to that of photographic systems and the human visual system. However, it is not very useful for recording the precise shape and dimensions of objects as, in general, measurements cannot be taken from the projection, angles are not preserved and parallel lines do not remain parallel on

projection. On the other hand, parallel projection lacks the perspective foreshortening effect but records exact measurement to within a scale factor and parallel lines remain parallel. Parallel projection is adopted here.

3.6.1 3D coordinate transformation

A point at the coordinate x, y, z is expressed as P(x, y, z, 1) in homogeneous coordinates. If the coordinate system is translated by (D_x, D_y, D_z), the point becomes P'(x', y', z', 1) in the new coordinate system. The translation equations can be represented as:

$$P'[x' \; y' \; z' \; 1] = P[x \; y \; z \; 1] \; T_3(D_x, D_y, D_z) \tag{3.30}$$

Similarly, rotation about one of the axes through a positive angle θ is achieved using matrix:

$$P' = PR_i(\theta) \tag{3.31}$$

in which i=x, y or z. The translation matrix T_3 and rotation matrices R_i, i=x, y, z are given in Appendix 3A.1.1.

3.6.2 2D coordinate transformation and scaling

A point P(x, y) in 2D coordinates is similarly represented as P(x, y, 1) in homogeneous coordinates. The translation equations are represented as:

$$P' = P \cdot T_2 \tag{3.32a}$$

$$P' = P \cdot R_2 \tag{3.32b}$$

in which the translation and rotation matrices T_2 and R_2 in 2D are given in Appendix 3A.1.2.

An object can be scaled (stretched) by S_x along the x-axis and by S_y along the y-axis into a new size to display on output devices. The proportions of the object are changed if a different scaling ($S_x \neq S_y$) is used. They are unaffected with a uniform scaling ($S_x = S_y$). The scaling equations for a point P are represented as:

$$P' = P \cdot S(S_x, S_y) \tag{3.33}$$

in which the scaling matrix $S(S_x, S_y)$ is given in Appendix 3A.1.2.

3.6.3 Parallel projections

Parallel projection is defined by a projection plane and the direction of projection. The projection plane is conveniently defined by a point on the plane and the normal to the projection plane. If the direction of projection is same as the normal to the projection plane, the projection is called orthographic parallel projection. If these directions are not same, the projection is called oblique parallel projection.

The matrix for parallel projection can be written in terms of α and l in Fig. 3.9. If the direction of projection is a line $\overline{QQ'}$ passing through Q(0, 0, 1) and Q'($l\cos\alpha$, $l\sin\alpha$, 0) and the projection plane is the xy-plane, the point Q projects onto Q'. The direction for the projection is Q' – Q = ($l\cos\alpha$, $l\sin\alpha$, –1). For a general point P(x, y, z) which projects onto P'(x', y' ,0) on the xy-plane, the projection equations are represented as:

$$P' = SH_z P \tag{3.34}$$

where

$$SH_z = \begin{bmatrix} 1 & 0 & 0 & 0 \\ 0 & 1 & 0 & 0 \\ a_l & b_l & 1 & 0 \\ 0 & 0 & 0 & 1 \end{bmatrix} \tag{3.35}$$

in which

$$a_l = l\cos\alpha,\ b_l = l\sin\alpha \tag{3.36}$$

The effect of this operation is to shear and then project the object. Planes of constant $z = z_l$ are translated in x by $z_l l\cos\alpha$ and in y by $z_l l\sin\alpha$, and are then orthographically projected to z=0.

When l = 1 and 1/2, the projections are cavalier projection and cabinet projection respectively which are two important oblique projections. For an orthographic projection, l =0.

To follow the conventions of computer graphics (Newman and Sprouli, 1973; Harrington, 1983; Foley and van Dam, 1984), Eq. 3.35 and Fig. 3.9 are presented in a left-handed coordinate system. (For perspective projection, a left-handed coordinate system has the convenient effect that the larger z projects onto a small value, i.e., the further the separation, the smaller the image.) This requires conversion of the normal right-handed coordinate system into left-handed coordinates. The transformation equations are represented as

$$P' = PT_{rl} \tag{3.37}$$

As people are more familiar with objects presented in right-handed coordinates, the results should be transformed back from the left-handed to the right-handed coordinates after appropriate operations.

$$P' = PT_{lr} \tag{3.38}$$

The transformation matrices T_{rl} and T_{lr} in Eqs 3.37 and 3.38 are given in Appendix 3A.1.

3.7 Implementing on a micro-computer

To display the dynamic motion of markers in a silo, the following procedure was programmed:

1) Data preparation

The positions of all the markers at each time step are calculated at first in the global coordinates using the appropriate algorithms. Graphics data preparation of this kind increases the drawing speed.

2) Forming the geometrical transformation matrix N_T

The flow may need to be seen from different directions. This may be achieved by projection from different directions. An alternative way is to translate the silo by D_x, D_y and D_z and rotate it by ϕ_x, ϕ_y and ϕ_z about the x, y and z axes respectively. The matrix for doing this is

$$N_T = T(D_x,D_y,D_z)R_x(\phi_x)R_y(\phi_y)R_z(\phi_z) \tag{3.39}$$

3) Defining the projection plane and projection direction

The projection plane (view plane) is defined by a view reference point (VRP) $P_1(x_1, y_1, z_1)$ and the view plane normal (VPN) $\overline{P_1P_2}(x_1-x_2,\ y_1-y_2,\ z_1-z_2)$ where $P_2(x_2,\ y_2,\ z_2)$ is a point at the view plane normal. The projection direction (also called view up, VUP) is defined by $\overline{P_1P_3}(x_1-x_3,\ y_1-y_3, z_1-z_3)$ where $P_3(x_3,\ y_3,\ z_3)$ is a point at the line of the projection direction. VRP, VPN and VUP consist the projection system.

4) Forming the projection matrix N_p

a) Translate P_1 to the origin using the translation matrix $T(-x_1, -y_1, -z_1)$

b) Rotate so that VPN lies in the yz-plane

The rotation is about the y-axis and the rotation matrix is $R_y(\theta_y)$ where

$$\theta_y = \cos^{-1}\left(\frac{-(z_2 - z_1)}{\sqrt{(z_2 - z_1)^2 + (x_2 - x_1)^2}}\right) \tag{3.40}$$

c) Rotate so that VPN becomes the negative z-axis

The rotation is about the x-axis and the rotation matrix is $R_x(-\theta_x)$ where

$$\theta_x = \cos^{-1}\left(\frac{-z_2''}{\sqrt{(x_2 - x_1)^2 + (y_2 - y_1)^2 + (z_2 - z_1)^2}}\right) \tag{3.41}$$

in which z_2'' is the z-coordinate of P_2 after steps a and b.

d) Rotate so that the projection of VUP on the view plane becomes the y-axis

The rotation matrix is $R_z(\theta_z)$ and the rotation is about the z-axis where

$$\theta_z = \cos^{-1}\left[\frac{y_3'''}{\sqrt{(x_3''')^2 + (y_3''')^2}}\right] \tag{3.42}$$

in which x_3''' and y_3''' are the coordinates of P_3 after steps a to c.

e) Change from right-handed to left-handed coordinates (Eq. 3.37)

f) Shear so that VUP is normal to the projection plane

The matrix for doing this is defined by Eqs 3.34 and 35 where

$$a_1 = -\frac{x_1'''' - x_3''''}{z_1'''' - z_3''''}, \quad b_1 = -\frac{y_1'''' - y_3''''}{z_1'''' - z_3''''} \tag{3.43}$$

in which $(x_1'''', y_1'''', z_1'''')$ and $(x_3'''', y_3'''', z_3'''')$ are coordinates of P_1 and P_3 after steps a to e;

g) Change from left-handed back to right-handed coordinates (Eq. 3.38)

To summarise, N_p is found as

$$N_p = T(-x_1,-y_1,-z_1)R_y(\theta_y)R_x(-\theta_x)R_z(\theta_z)T_{rl}SH_z(a_1,b_1) \quad (3.44)$$

A point P(x, y, z, 1) in global coordinates is then transformed to P'(x', y', 0, 1) in viewing coordinates. The third coordinate of P'(x', y', 0, 1) can be ignored and P' is expressed as P'(x',y',1) in 2D (i.e. the viewing plane) coordinates and is transformed further into output coordinates (e.g. screen coordinate).

5) Forming the transformation matrix from the viewing coordinates into the output device coordinates N_o

a) Scale so that the silo can be displayed on the output device (Eq. 3.33)

b) Rotate so that the silo has the right orientation (Eq. 3.32b)

c) Translate the silo so it is at the right position on the output device (Eq. 3.32a)

Summarising, N_o is found as

$$N_o = S_2(S_x,S_y)R_2(\theta)T_2(D_x,D_y) \quad (3.45)$$

6) Drawing markers at time t (start from t=0)

The position of each marker in the global coordinates is transformed into the output device coordinates by multiplying N_p and N_o. The marks together with some supporting effects (e.g. lines) are then drawn on the output device (i.e. the screen).

7) Erase the markers

8) set $t=t+\Delta t$ and repeat step 6) to 8) until the discharge of the silo is complete.

3.8 Description of the program suite FLOWVIS

On the basis of above descriptions, a user friendly interactive program suite FLOWVIS has been developed. It was designed to run on a micro-computer. It consists of two main programs and a few supporting programs. The first, program TAG, processes the raw data to produce transformations of the recorded times, allowing for non-uniform flow, into remaining volume and mean velocity measures, to develop data for different flow algorithms and to define appropriate boundary conditions. The second, program MOVE, simulates the dynamic flow process of particulate solids and displays the progressive discharge in sectional, 3D and bar chart images.

The experiments described in Chapters 6 and 7 produced a data set relating the time of exit of a marker to its original coordinates when placed in the silo during filling. The discharge was conducted at a non-uniform rate (controlled by the feeder) so that good quality data on wall pressures could be obtained by slow flow in the early stages, but a faster discharge rate could be used to expedite the test later on. As all the algorithms described above implicitly assume a uniform discharge rate, the observed residence times were therefore required to be converted as if the discharge rate was uniform. This was performed by the program TAG. The principle of this transformation is described in Chapter 7.

The visualisation program MOVE permits the progressive stages of the silo discharge to be shown, displaying the possible paths of tags from their original seeding position to the outlet. Two images are displayed simultaneously: one being a 3D view of the silo, and the other a chosen 2D section through the silo. The 3D image naturally gives the fullest information, but it is very complicated and difficult to assimilate, especially because most engineers are accustomed to viewing 2D sections. The 2D sections can be chosen on any diametral plane through the silo. Progressive changes in the flow pattern during the discharge process can be easily assimilated, and the

concept of a fixed 'flow pattern' for the discharge is seen to be only valuable in tall silos where the lower part can have a long term stable flow configuration.

Macro commands were used to permit the user to interact with the display. The user may improve the quality of the result by modifying the assumptions used in the interpretation. By using simple macro commands, the user may customise the display, including

a) The colour and thickness of lines for the silo outline, marker trajectories and the colour and size of fonts of position labels and title;
b) Time stepping in flow;
c) Number of levels to be plotted in the 3D picture;
d) Rotation of 3D picture;
e) Appearance and size of the contour bars; and
f) Switch for display of either discharge time or percentage of remaining mass.

Details on the use of each of the programs are given in Chen (1995a). The experimental test results described in Chapters 4-7 have been displayed using this program and many clear images have been produced, some of which are presented in Chapters 5 and 7.

3.9 Conclusions

A program suite FLOWVIS has been developed as one of the new methods in the interpretation of solids flow patterns from residence time measurements. The analytical formulation used in the program suite has been presented. The program suite is used to process data obtained from residence time measurements using radio tags and to simulate the dynamic discharge process. The dynamic discharge process is visualised using two and three dimensional graphics and counter bars.

The display of the solids flow pattern in a graphics display format has immediate appeal to industrial engineers, and can be used to gain a better understanding of many industrial materials handling problems. The display has proved very effective in demonstrating flow modes using only minimal assumptions. The program is very flexible and is applicable to silos of different configurations and storing any material. It has great potential for industrial application.

3.10 Notation

A_a cross sectional area of gap between the discharge aid and the hopper

A_o cross sectional area of the outlet

D_x, D_y , D_z translation value of a coordinate along x, y and z axes

H height of the cylinder

R radius of the cylinder

R_2 rotation matrix in 2D

R_o radius of the outlet

R_x, R_y, R_z rotation matrix about x, y and z axes respectively

S distance of a marker travelled from its original position to the outlet

S_2 scaling matrix in 2D

S_a distance of a marker travelled from its original position to the discharge aid

S_o distance of a marker travelled from the discharge aid to the outlet

T residence time of a marker

T_2, T_3 translation matrix in 2D and 3D coordinate

T_{lr} transformation matrix from left-handed to right-handed coordinates

T_{rl} transformation matrix from right-handed to left-handed coordinates

T_o time for a marker to travel from the discharge aid to the outlet

T_s the part of residence time when the marker is stationary

T_t time when the horizontal velocity of a marker reaches the maximum value

a acceleration

g gravitational acceleration

h_a height of the discharge aid

r_a radius of the discharge aid

r_u mean radius of the gap between the discharge aid and the hopper

v velocity of a marker

v_a velocity of a marker at the discharge aid

v_o velocity of a marker at the outlet

x_i, y_i, z_i initial coordinates of a marker

z_o, y_o, z_o coordinates of the centre of the outlet

α coefficient for defining the shape of velocity variation with time/projection angle

β half angle of the hopper

ΔH Horizontal distance from the initial position of a marker to the centre of the outlet

ΔZ vertical distance from the initial position of a marker to the outlet

ϕ_a angle related to the initial vertical to horizontal accelerations of a marker

γ density of solids during flow

θ circumference angle of the initial position of a marker/rotation angle in coordinate transformation

$\theta_x, \theta_y, \theta_z$ rotation angles about x, y and z axes in projection

ρ discharge rate

ξ velocity coefficient

Subscripts

2 in two dimensional coordinates

3 in three dimensional coordinates

a discharge aid/acceleration

h horizontal

i initial position of a marker

o outlet

s stationary

t cylinder/hopper transition

u gap between the discharge aid and the hopper walls

v vertical

Appendix 3A Coordinate transformation matrices

3A.1 Coordinate transformation matrices for 3D

3A.1.1 Translation matrix T_3

$$T_3(D_x, D_y, D_z) = \begin{bmatrix} 1 & 0 & 0 & 0 \\ 0 & 1 & 0 & 0 \\ 0 & 0 & 1 & 0 \\ D_x & D_y & D_z & 1 \end{bmatrix} \quad (3A.1)$$

3A.1.2 Rotation matrices R_x, R_y and R_z

$$R_x(\theta) = \begin{bmatrix} 1 & 0 & 0 & 0 \\ 0 & \cos(\theta) & \sin(\theta) & 0 \\ 0 & -\sin(\theta) & \cos(\theta) & 0 \\ 0 & 0 & 0 & 1 \end{bmatrix} \quad (3A.2a)$$

$$R_y(\theta) = \begin{bmatrix} \cos(\theta) & 0 & -\sin(\theta) & 0 \\ 0 & 1 & 0 & 0 \\ \sin(\theta) & 0 & \cos(\theta) & 0 \\ 0 & 0 & 0 & 1 \end{bmatrix} \quad (3A.2b)$$

$$R_z(\theta) = \begin{bmatrix} \cos(\theta) & \sin(\theta) & 0 & 0 \\ -\sin(\theta) & \cos(\theta) & 0 & 0 \\ 0 & 0 & 1 & 0 \\ 0 & 0 & 0 & 1 \end{bmatrix} \quad \text{(3A.2c)}$$

3A.1.3 Transformation matrix from right-handed to left-handed coordinates T_{rl}

$$T_{rl} = \begin{bmatrix} 1 & 0 & 0 & 0 \\ 0 & 1 & 0 & 0 \\ 0 & 0 & -1 & 0 \\ 0 & 0 & 0 & 1 \end{bmatrix} \quad \text{(3A.3)}$$

3A.1.3 Transformation matrix from right-handed to left-handed coordinates T_{lr}

$$T_{lr} = \begin{bmatrix} -1 & 0 & 0 & 0 \\ 0 & 1 & 0 & 0 \\ 0 & 0 & 1 & 0 \\ 0 & 0 & 0 & 1 \end{bmatrix} \quad \text{(3A.4)}$$

3A.2 Coordinate transformation and scaling matrices for 2D

Translation matrix

$$T_2(D_x, D_y) = \begin{bmatrix} 1 & 0 & 0 \\ 0 & 1 & 0 \\ D_x & D_y & 1 \end{bmatrix} \quad \text{(3A.5)}$$

The rotation matrix about the origin through an angle θ

$$R_2(\theta) = \begin{bmatrix} \cos(\theta) & \sin(\theta) & 0 \\ -\sin(\theta) & \cos(\theta) & 0 \\ 0 & 0 & 1 \end{bmatrix} \quad (3A.6)$$

Scaling matrix in 2D

$$S_2(S_x,S_y) = \begin{bmatrix} S_x & 0 & 0 \\ 0 & S_y & 0 \\ 0 & 0 & 1 \end{bmatrix} \quad (3A.7)$$

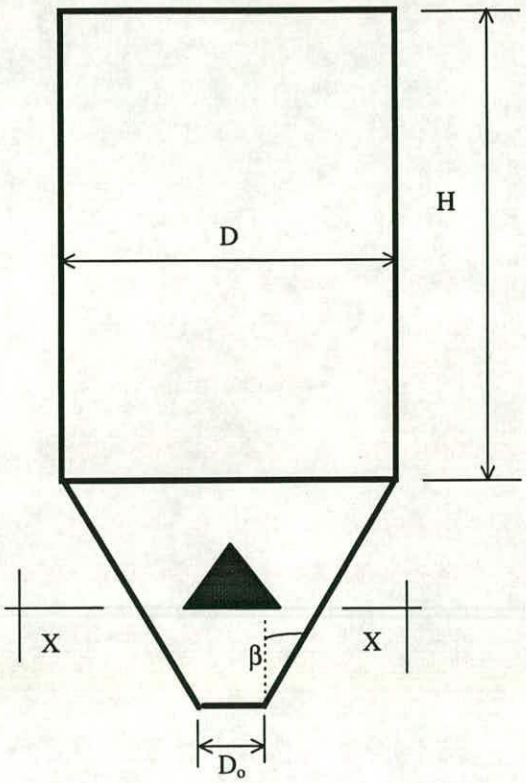

Fig. 3.1a Elevation

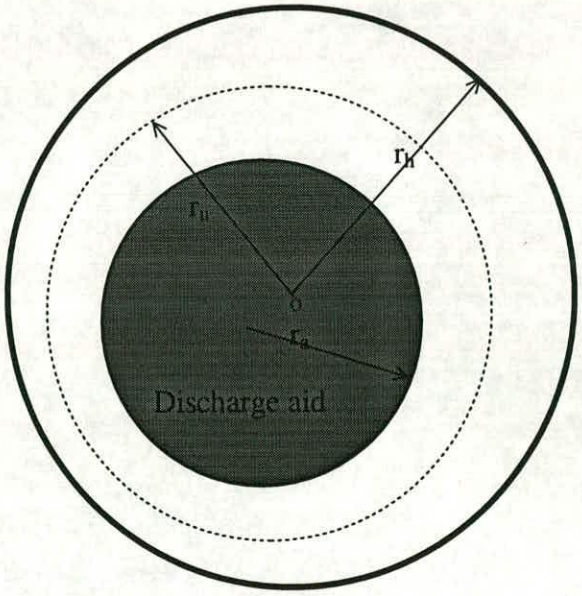

Fig. 3.1b Cross section X-X

Fig. 3.1 An example silo

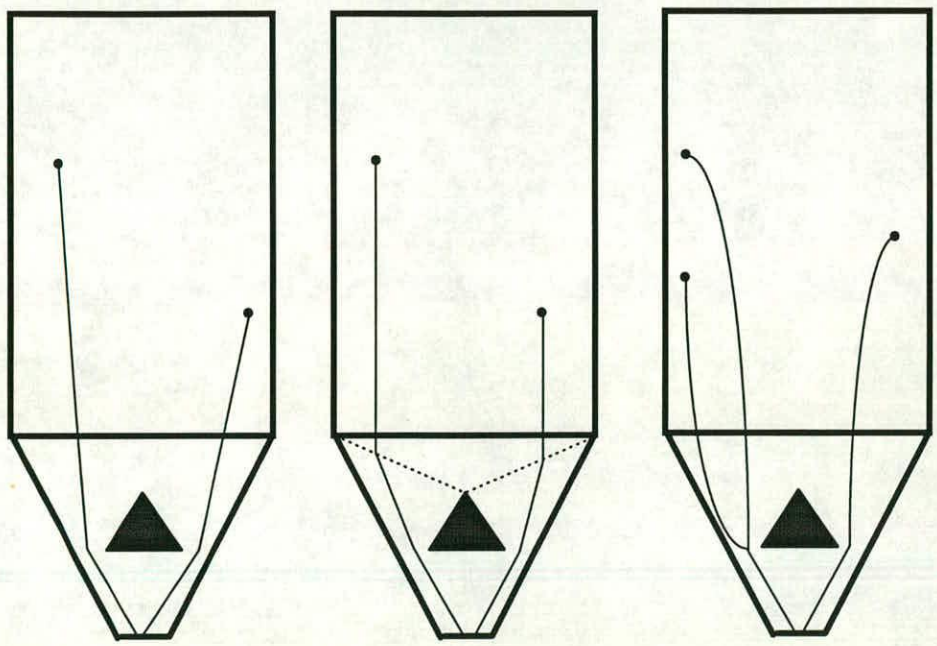

a) Shortest path b) Converging flow path c) Streamline path

Fig. 3.2 Markers trajectories

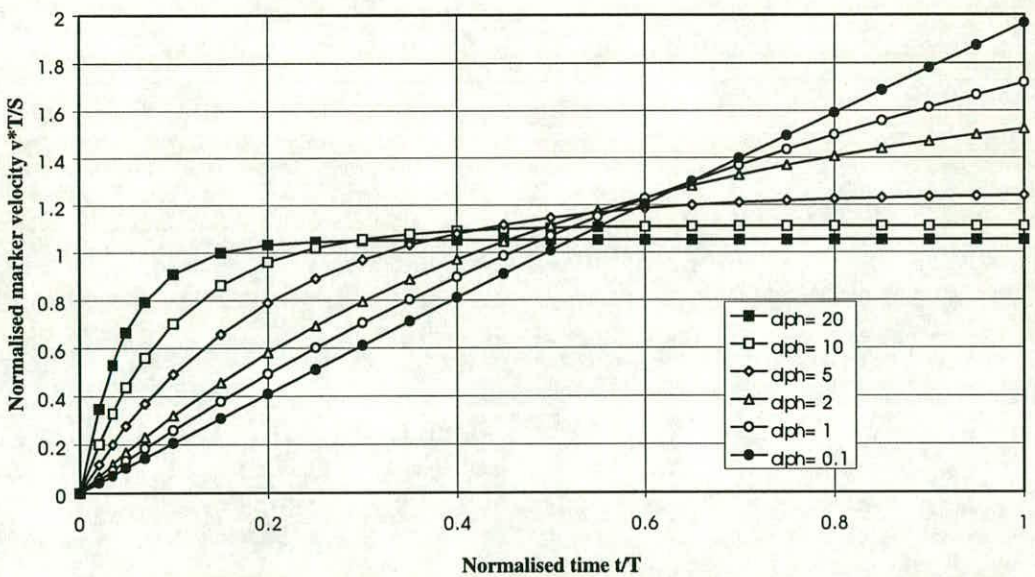

Fig. 3.3 Velocities of markers: Exponential decay velocity variation

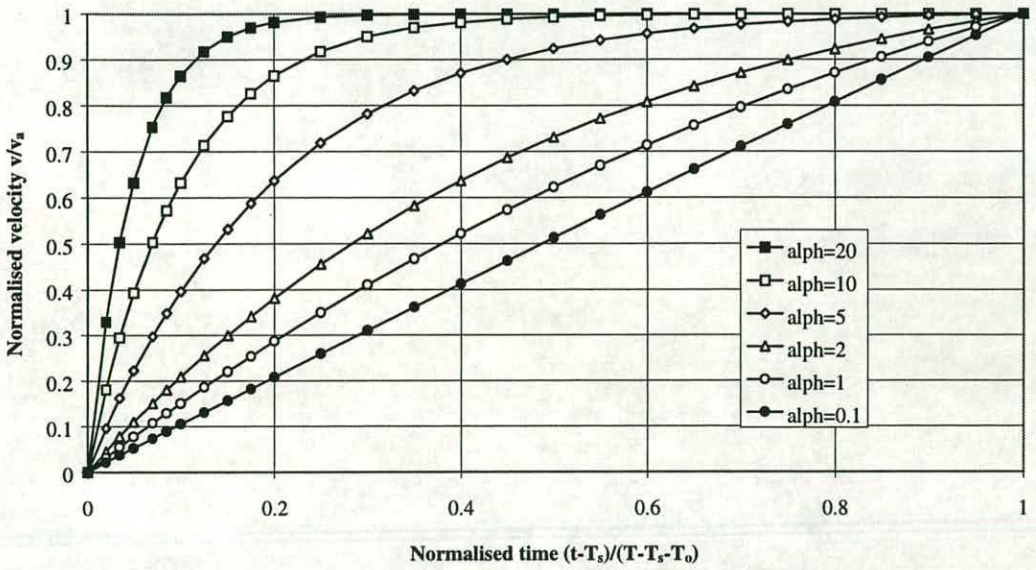

Fig. 3.4 Velocities of markers: Stationary followed by exponential decay velocity

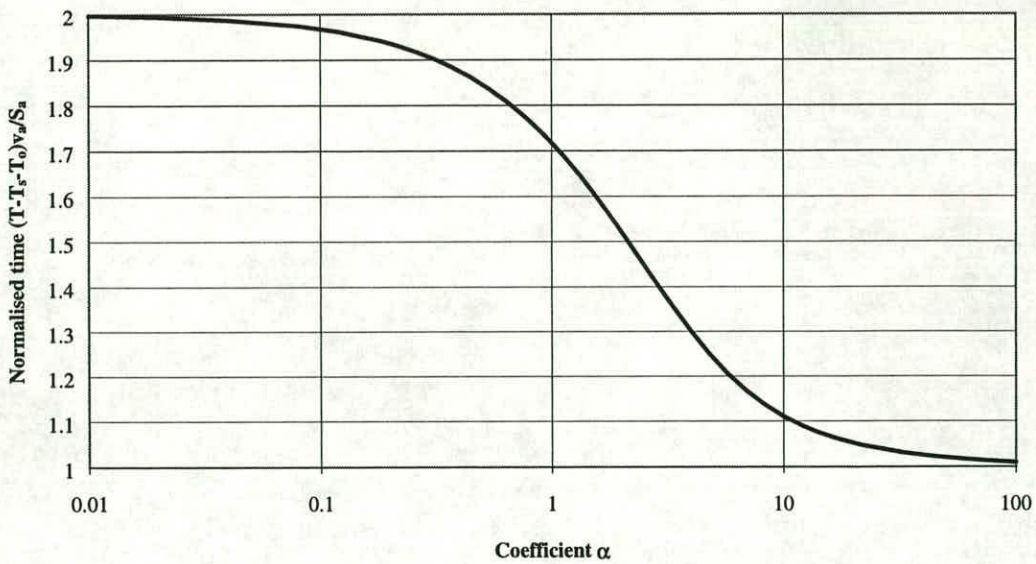

Fig. 3.5 Effect of coefficient α on stationary time T_s of a marker

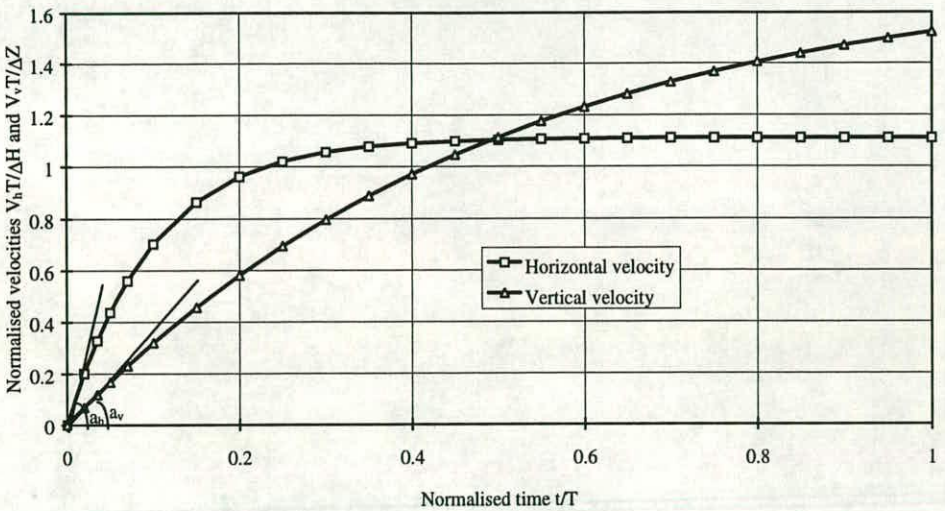

Fig. 3.6 Exponential decay horizontal and vertical velocities

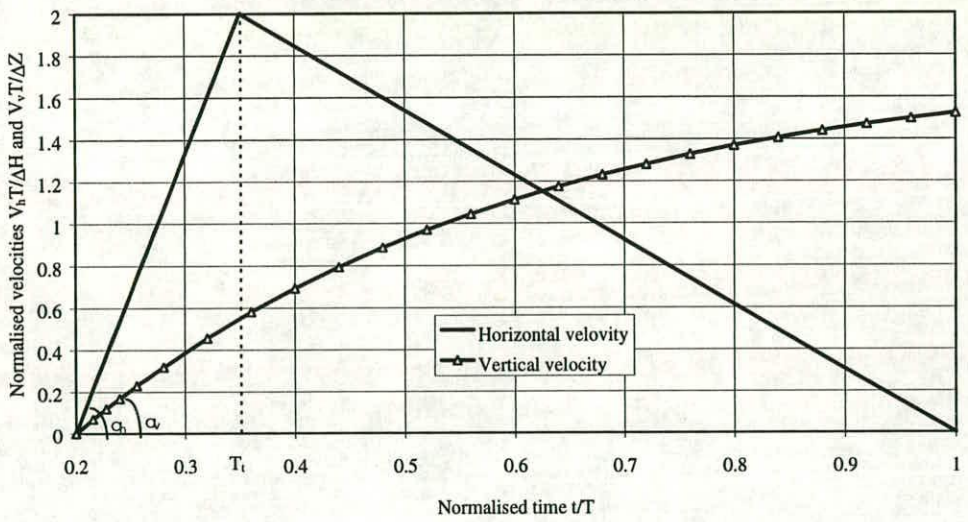

Fig. 3.7 Exponential decay vertical velocity and triangular horizontal velocity

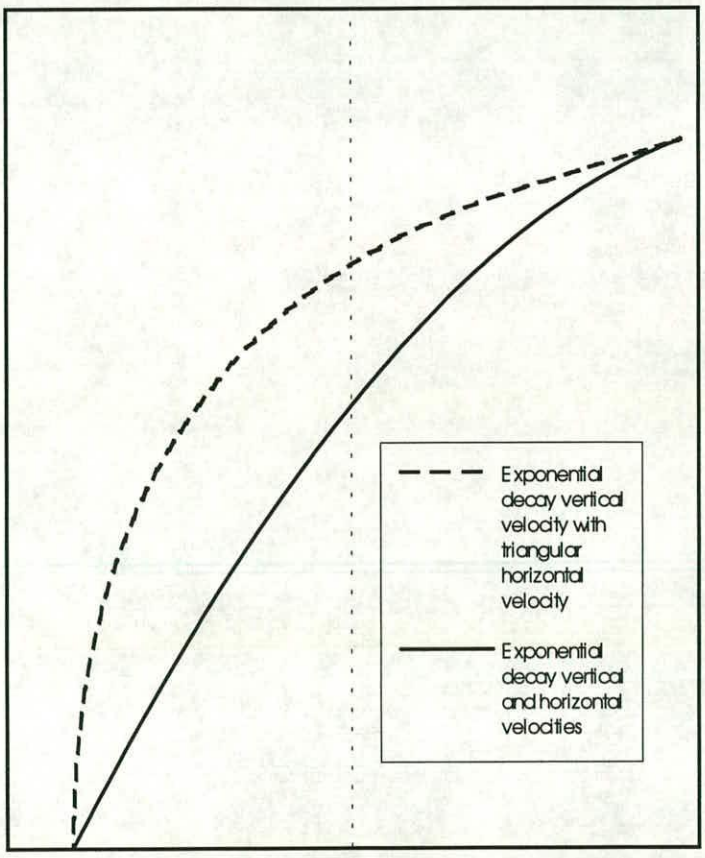

Fig. 3.8 Trajectory of a marker

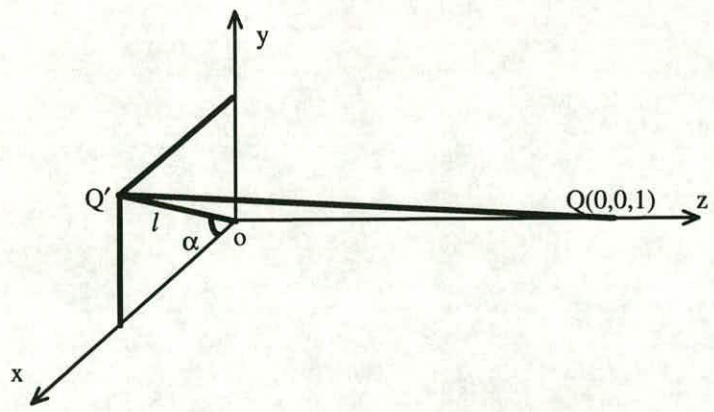

Fig. 3.9 Parallel projection of Q(0,0,1) into Q'($l\cos\alpha$, $l\sin\alpha$,0)

Chapter 4

FLOW PATTERN MEASUREMENT IN A FULL SCALE SILO AT BRITISH GYPSUM

4.1 Introduction

The experiments carried out in a silo at British Gypsum in early 1993 may represent the first ever scientific measurement of flow patterns at full scale in a fine powder. These tests were conducted by the project team as part of a collaborative venture between the British Materials Handling Board, British Gypsum and the University of Edinburgh which was sponsored by the UK Department of Trade and Industry.

The first task of this thesis is to interpret the flow patterns from these test data. Before the results of interpretations are presented in the next chapter, it is necessary to give a brief description of the development of the flow pattern measurement system used, the verification of its reliability and the conduct of the experiments to form a background in this chapter. Full details of these are presented by Rotter *et al* (1995).

The circumstances of the installation at British Gypsum had a strong influence on the methods adopted. The recently constructed steel silo is used to store gypsum. The discharge is concentric and either mass or funnel flow is expected to occur in practice. Further, the flow mode may be affected by the aeration.

Special equipment was developed to carry out tests under these circumstances. A variety of different control tests were conducted to ensure that the equipment and the procedure would be effective when in operation.

One of the key features of these tests is that the study was constrained to the window of opportunity presented by a quieter period in the operating plant. The requirements for this part of the study were therefore

(a) to undertake the tests in the minimum time;
(b) to make a minimal impact on the operation of the plant;
(c) to undertake the tests without entering the silo at all;
(d) to undertake tests which were very reliable, since there might not be an opportunity to repeat any test.

4.2 The silo

The silo used in the investigation was a new cylindrical steel structure with a conical hopper (half angle 30°), as shown in Fig. 4.1. It was filled with gypsum mineral by a pneumatic conveying system operating in a dense phase (Fig. 4.2), and discharged through a blow pot which operates in a 65-second conveying cycle (~15 seconds to fill).

The silo was fitted with an inverted cone bin discharge aid (Fig. 4.1), though this was not fully functional during the tests (as described later), due to malfunction since the installation. The silo was also fitted with air pads on the hopper section, through which compressed air was supplied in the early tests of the series reported here.

The silo was thought to be an interesting vessel for flow pattern measurement studies for two reasons:

(a) fine powders display different phenomena in flow from coarse granular solids. Few tests had ever been undertaken on full scale powder silos (Nielsen, 1983b is one exception) and no scientific measurements of flow patterns at full scale in a fine powder are known. It was thought that the flow patterns could differ qualitatively from current predictions based on small model tests; and

(b) this silo presented an opportunity to investigate the effects of a commercial aeration and discharge aid system on flow patterns in a powder.

4.3 The stored solids

The material stored in the silo was ground gypsum mineral with 65% passing a 100 mesh sieve (150μm) and a maximum size of about 1.5mm. The poured bulk density after settling was quoted as between 1.1 t/m^3 and 1.4 t/m^3, with a settling time to achieve this of between 4 and 5 minutes. Its average bulk density is 1174 kg/m^3 and moisture content is very low. It was placed into the silo at temperatures between ambient and 70°C (typically between 60°C and 70°C), though this variation in temperature is thought to have very little influence on its flow properties.

Jenike shear cell tests were performed in Edinburgh on samples of the solid taken at the time of the tests. A typical shear test result is shown in Fig. 4.3 and the Mohr circles fitted to the yield functions in Fig. 4.4. The resulting Jenike flow function is shown in Fig. 4.5. The effective angle of internal friction of the gypsum is 40°, and the slope of the yield locus corresponds to a tangent internal friction angle of 36°. Further details including density variation with consolidating stress and other gypsum properties are given in Rotter *et al* (1995).

The material was highly aerated on entry into the silo, leading to an almost horizontal top surface in the stored solid. Slight depressions occurred in some places, but the variations from the horizontal were not in a simple pattern which could be easily

related to the inlet system and the large quantity of dust in the air made visual observations difficult. It is possible that the surface was initially far from flat and that the settling dust filled the hollows producing a surface which appeared flat but was actually composed of very different particle sizes from the uneven surface beneath. The flat surface has a considerable advantage for the placement of markers in the solid, as there is no need to level the surface and relatively simple checks can be undertaken to ensure that the markers have not moved after placement.

The experimental procedure was designed to minimise the effect of aeration during filling on the bulk density by allowing a period of about 10 minutes after termination of the filling process before seeding with radio tags was begun. This was deemed adequate to allow de-aeration of the gypsum to occur.

4.4 Requirements of the flow pattern measuring system

The chief challenges of full scale silo flow pattern measurement lie in the difficulty of making direct observations, the expense of conducting full scale studies, the constraints of the operational needs of the plant, and the critical importance of making reliable observations. The need for reliable observations was the over-riding consideration in this study.

The system chosen for measuring the patterns of flow in this full scale silo was the logging of the residence time of markers. The alternatives and their relative merits were discussed in Chapter 2.

To ensure that high quality information was obtained, a large number of markers were used in a regular axisymmetric grid pattern. If a large number of markers is used, the data cannot be collected by hand, and the industrial application also called for an automated arrangement. This was achieved by using radio tag markers which are individually identifiable.

The critical data required for this technique are the location of each marker when the silo is filled and the time it takes to reach the outlet during solids flow. Since the time taken to reach the outlet depends on the rate at which solids are withdrawn, which may vary during the discharge, it is desirable to transform the data of time into a measure which is not sensitive to the rate of discharge or the arresting of the discharge process. This was achieved in these experiments by using the remaining mass of solid in the silo as an unbiased measure of the instant when the marker emerged.

The technique of residence time measurements using radio tag markers was chosen as the only technique which could be implemented in a large silo with the following constraints: steel walls which were not to be penetrated, a large number of markers, a fine bulk solid, and safety conditions which prevented entry by those conducting the experiment. Photography of the top surface was not a possible technique for this silo because of the large quantities of dust suspended in the air above the surface, which obscured the surface when viewed from the silo roof.

In a silo which mass flows, a relatively small number of markers can be used to characterise the entire flow regime, because the variations in velocity are smooth and discontinuities in flow (flow channel boundaries) do not occur. However, such flow pattern measurements are of lesser interest since mass flow is by now well understood. By contrast, where funnel flows and narrow channel pipe flows occur, a very large number of observations are required, since the flowing channel may be missed entirely by a wide placement of markers. In addition, the techniques of residence time interpretation developed during the course of this project depend on a large body of data being available so that a scientifically rigorous description of the flow can be made from the observations.

One of the problems with the residence time technique is that the movement of a marker may not be representative of the movement of the solid particles adjacent to its starting position. This question was investigated by Arteaga and Tuzun (1990)

who undertook a study to explore the flow of binary mixtures out of silos. They defined a coarse-continuous bed as one in which the particle lattice is made up of coarse particles, with fines filling the interstitial spaces and a fines-continuous bed as one in which the microstructure is dominated by fines in which coarse particles are retained in relatively few numbers. They reported that segregation of fine particles occurs in a coarse-continuous bed whereas no segregation of coarse particles occurs in a fines-continuous bed. Advice was sought from Dr Tuzun on the interpretation of this work for the present study, and the conclusion was drawn that the markers would be representative provided they have approximately the same density as the bulk solid, and provided the size of a marker is no smaller than that of a typical large particle.

The location of each marker is very important, since there is no independent means of verifying where the marker was placed once it has been covered by additional bulk solid. Thus the chosen technique had to give certainty that (a) the marker was correctly identified at the time of placement, and (b) it was placed in exactly the intended location. Both of these features become uncertain if the markers are placed by a 'hockey stick' or placing by tube into what is judged to be the right place. Anomalies which are later discovered in the observations can then never be resolved. In this study, the markers were carefully identified by colour coding, alphabetic and numerical markings, and were precisely placed by using a placement template within the silo.

The pattern of markers was chosen to reflect the shape of the silo. The circular planform was divided using a simple axisymmetric coordinate system (r, θ, z), so that markers were placed in concentric rings (fixed r coordinate), on fixed radial lines (fixed θ coordinate), and at defined single heights (fixed z coordinate). The use of a regular grid makes consistent interpretation of the data much simpler.

The layout of the holes in the template, and thus the pattern of the markers, was an axisymmetric pattern of concentric rings. This was chosen because it was initially

assumed that the gypsum would flow in either mass flow or concentric funnel flow. If either pattern occurred, the markers would give a very clear picture of the irregularities in the flow pattern and the differences between the simple descriptions and the real behaviour. However, as will be seen later, these simple flow patterns did not occur, and the marker pattern provided a very satisfactory means of showing two-dimensional sections through the three-dimensional flow pattern. In addition, situations in which flow appeared to involve horizontal movements out of the plane of a vertical section through the diameter of the silo were also identified.

4.5 Design of a flow pattern measurement system

4.5.1 Seeding template

To satisfy the above requirements, the template should rest on the surface of the solid with the holes in the template close to the solid's surface so that the position of each marker could be checked immediately after placement. A template on the solid surface meant that the filling process had to be arrested to place the markers, the template laid on the surface, markers placed, and the template then removed so that further solid could be filled into the silo. This procedure meant that a deployable template was needed which could be manoeuvred from the top of the silo.

The template took the form of an inflated toroidal ring within which lay a membrane punctuated with holes for the placement of the markers (Fig. 4.6). This design minimises the potential for mechanical problems in a dusty environment and permits the maximum flexibility for insertion of the template through a small hole and its removal after completing the experiments. The template was made of rubber which could be pushed through the access to the silo and lowered to the surface of the solid where it would resume its shape. The membrane was carefully marked out so that each hole could be easily identified even after a considerable exposure to gypsum dust. The colloquially termed "paddling pool" proved very effective in service.

4.5.2 Seeding device

Once the template was deployed in the silo, the markers needed to be positioned at each level of seeding. Placement of the tags was made difficult by the poor lighting conditions inside the silo and by the presence of dust following pneumatic filling of the silo. A further potential problem arose because the low density of the newly filled surface could be penetrated by the placed tags. The unchecked fall of the markers from the top of the silo to the template would result in their vertical position being impossible to establish.

In response to these concerns a telescopic tube was developed with a trapdoor at its lower end. This design enabled the kinetic energy of the marker falling down the placement tube to be removed before it was permitted to fall onto the surface from a small height (approx. 80mm). The tag was placed into the tube and allowed to slide into contact with the trapdoor. When the peashooter was correctly aligned at the point of placement, a trigger was used to open the trapdoor, and the tag was released.

Both the template and markers were colour coded in order to minimise the concern that the wrong marker would be placed in a particular hole in the template. The placement was then verified by logging the tag, providing a final check that the correct tag had been placed into the peashooter.

4.5.3 Radio tagging system

Radio tags were chosen as markers in the experiments. A radio tag consists of a miniature radio receiver and transmitter with a unique code in each tag so that the detection system can uniquely identify each one. Cotag markers were used because they were both cost-effective and robust. These markers had a plastic outer box which protected the radio circuit from solids, and which could be painted and marked for unique identification (Fig. 4.7). The aerial is relatively small, and can be conveniently placed at the outlet to the silo.

The final feature of the radio tag marker arrangement was the levels in the silo at which they were to be placed. The template determined the pattern in which markers would occur at any level at which they were placed, but the choice of vertical coordinates at which to place the markers could be varied from one experiment to another. In these first experiments, the tags were placed at approximately even spacings to provide a complete and unbiased sample throughout the solid. A typical marker layout (Test BG0302) is shown in Fig. 4.8.

4.5.4 Tag retrieval system

On discharging the silo the tags passed down through the silo outlet, past a dome valve into a blow pot. From there they were conveyed pneumatically to the top of the adjacent silo. A trap was installed at this point which permitted the tags to be retrieved by hand. The chief difficulties associated with the radio tag system were the accuracy and certainty of placement and the detection of tags as they passed through the aerial detector at the silo outlet (either through high speed or through multiple tags passing simultaneously). Some tags were lost in the experiments, and may have been crushed by the dome valve, or by lodging at some point inside the silo.

The issue of the reliability of the outlet radio tag detection system was addressed by control tests in which the aerial was modified until a good detection rate was achieved and by documenting the probability of detection.

4.6 Control tests of the flow pattern measuring system

4.6.1 Penetration tests on markers falling into gypsum

The possibility that markers would penetrate the surface of the solid on placement, leading to vertical errors in the starting point was explored in control experiments. A bed of fresh loosely-placed gypsum was placed at a fixed level, and sample markers

dropped from different heights into it. On each occasion, the depth of penetration of the marker was found by excavation, and the process repeated many times.

There is considerable scatter in the results, as might be expected from the thin rectangular shape of the marker, but the approximate bounds are given by 8 and 40mm per metre of fall. This suggests that, in the British Gypsum silo, where falls of up to 9 metres might be expected, the penetration could be as high as 360mm, which was regarded as unacceptable.

4.6.2 Tag detection experiments

If a tag passes too quickly through the aerial, it may not be detected at all. If two tags pass through the aerial at precisely the same time, only one can be detected, so the other is not recorded. Thus it is desirable that each tag should be reliably detected, by appropriate matching of the aerial size and detection time delay to the velocity of the tags passing through.

Many control experiments were conducted to explore the effects of field strength and loop shape of the aerial, the speed of the tag, the distance between two consecutive tags and a tag between two tags on the detection of tags. An optimum aerial was devised on the basis of these tests, and used in the tests at British Gypsum.

In relation to the tests at British Gypsum, these tests proved that the detection system would be able to cope with the expected speed of the gypsum and tags passing the aerial. Further, with 400 tags placed in 250 tonnes of material with a bulk density of approximately 1.0 tonne/m^3, the spacing of the tags should generally be adequate when the solid is forced through a 300 mm diameter outlet.

More generally, the chief conclusion of these tests is that care is needed with these silo flow experiments to ensure that a high proportion of the tags are observed. Little can be done about two tags which pass through the aerial simultaneously, but where this does not occur, the detection rate can be enhanced by

(a) minimisation of the number of tags being used;

(b) slower discharge rates from the silo; or

(c) use of detection equipment with a shorter response time.

4.7 Experiments in the British Gypsum Silo

A total of four tests were conducted at British Gypsum in late January and early February 1993. The number of experiments was restricted by the operational needs of the plant, and the duration of the period when the plant could be run at less than full capacity. These are summarised in Table 4.1.

Table 4.1 Summary of Tests at British Gypsum

Test	BG2901	BG0302	BG0902	BG1202
Date of test	29 Jan. 93	3 Feb. 93	9 Feb. 93	12 Feb. 93
No. of markers read	90	239	208	263
No. of marker levels	5	9	7	8
Height of fill at each marker level (above hopper transition)	0.45, 1.85, 3.22, 4.59, 5.26	0.33, 0.91, 1.49, 2.21, 2.80, 3.53, 4.10, 5.01, 5.68	0.48, 1.20, 1.92, 2.59, 4.22, 5.14, 5.73	0.52, 1.23, 1.90, 2.54, 3.29, 4.03, 4.69, 5.29
Mass of solids at each marker level (tonnes)	58.7, 100.0, 138.4, 184.2, 204.8	55.0, 71.7, 89.7, 108.8, 127.5, 148.6, 167.4, 194.6, 214.8	58.8, 80.0, 100.3, 121.5, 172.9, 199.3, 217.9	61.2, 79.0, 99.7, 118.5, 140.5, 162.9, 180.0, 200.3
Mass of solids before discharge (tonnes)	204.8	214.8	217.9	200.3
Mean discharge rate (tonnes/hour)	392	410	390	220
Height of fill before discharge (metres)	5.26	5.68	5.73	5.29
Other details	discharger and air both on	discharger and air both on	discharger and air both on	discharger and air both off

Different numbers of radio tags were used in the different experiments, but three of the tests were intended to be comparable with each other, and were thus used to explore the repeatability of the flow pattern. The fourth test was conducted without air feed to the gypsum, and with the flow aid device out of service.

The number of levels which could be seeded was governed by the total number of tags available, the time taken to seed a layer (approx. 1 hour) with the delay in the total experiment time this involved, and the problem that if two or more tags emerge simultaneously only one would be detected: thus a silo filled with tags would not provide a quality experiment!

The possibility of using photographic or ultrasonic measurements on the top surface was explored, but visual observations indicated that these would probably reveal little. Observations of the surface profile during filling were made using a plumb-bob.

4.8 Summary

This chapter has set out the background, design and establishment of the tests at British Gypsum. The interpretation of flow patterns for these tests conducted in the gypsum silo is presented in Chapter 5.

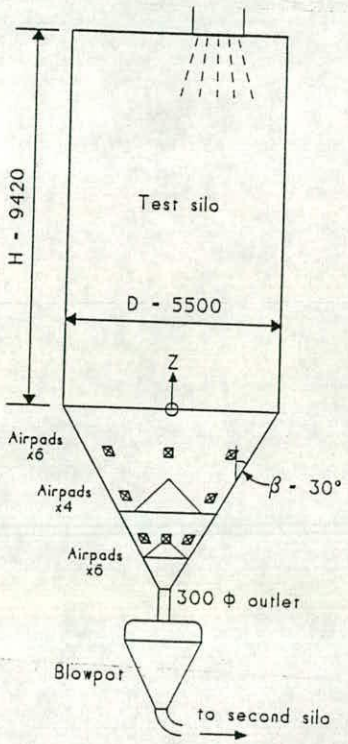

Fig. 4.1 The gypsum silo

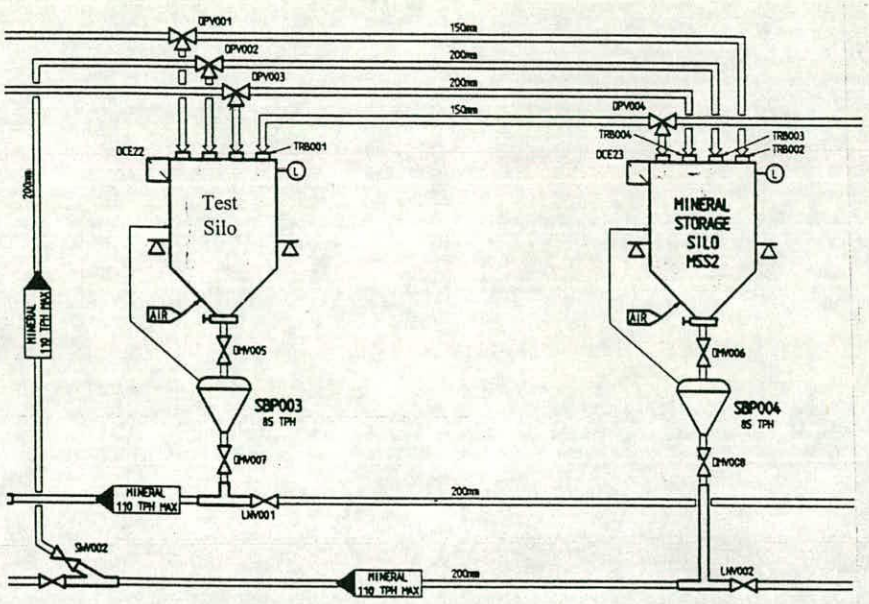

Fig. 4.2 Gypsum silo layout

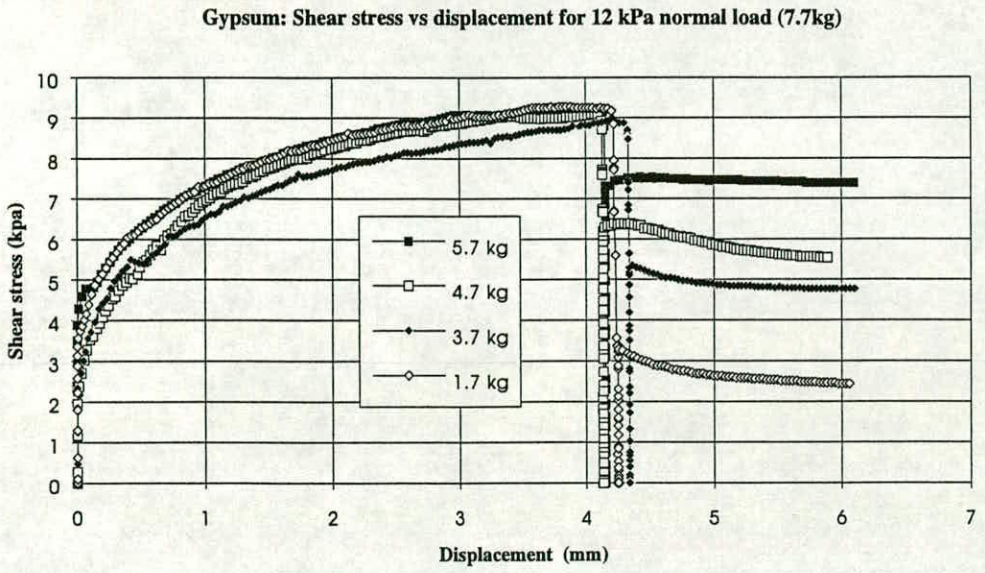

Fig. 4.3 Jenike shear test results

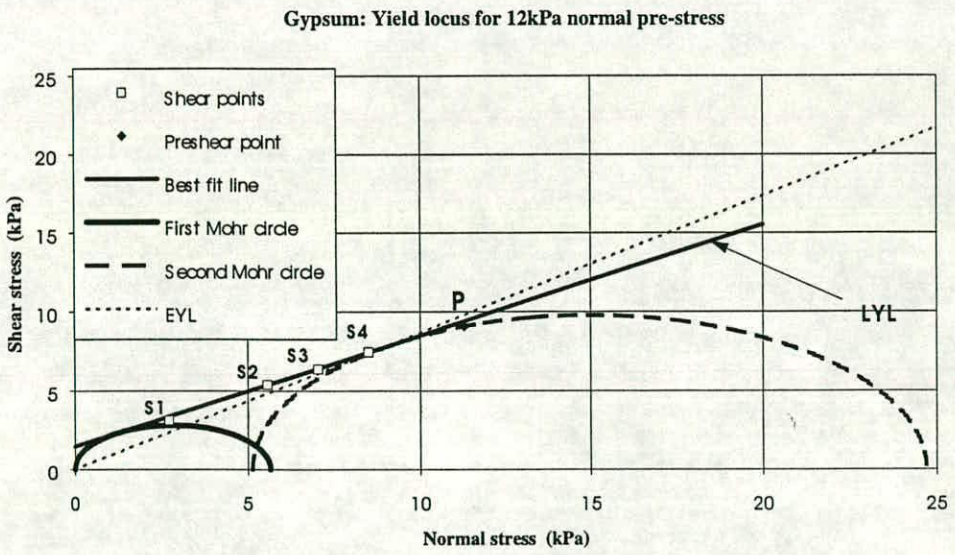

Fig. 4.4 Mohr circles fitted to the yield function

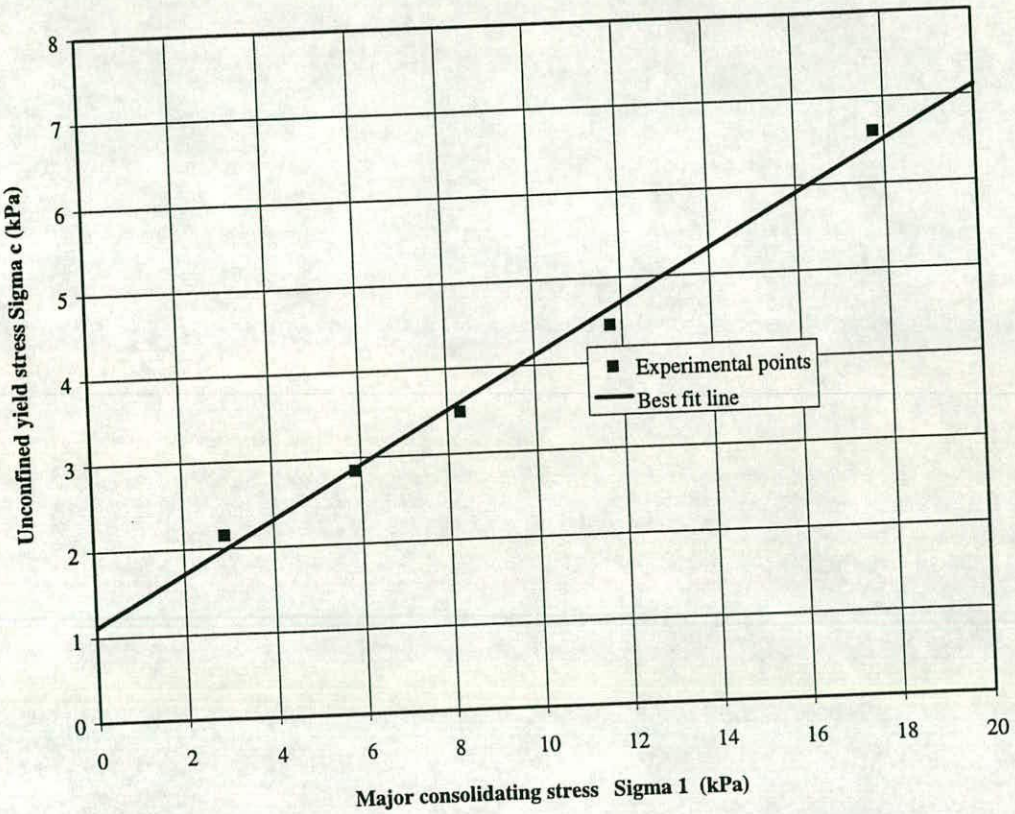

Fig. 4.5 Jenike flow function

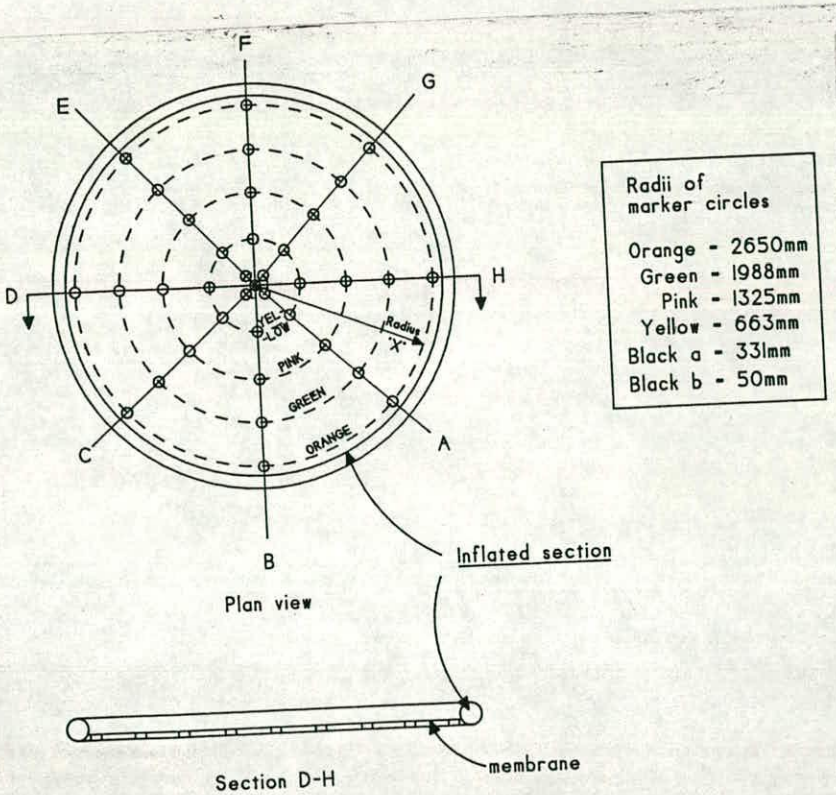

Fig. 4.6 Toroidal inflated ring template (paddling pool)

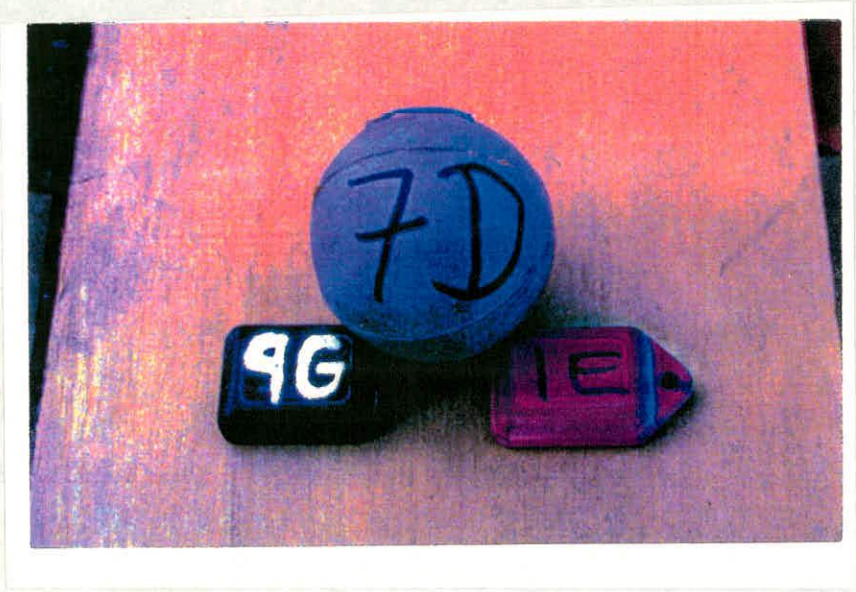

Fig. 4.7 Radio tag markers

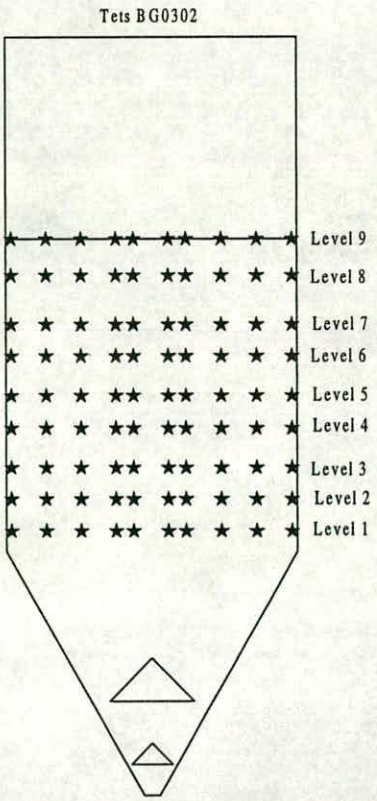

Fig. 4.8 A typical marker vertical layout

Chapter 5

FLOW PATTERNS IN THE GYPSUM SILO

5.1 Introduction

As summarised in the last chapter, a total of four tests were conducted at British Gypsum (Table 4.1). The first three experiments were notionally identical and were conducted to study the flow patterns under normal plant operating conditions. Under these conditions, the bin discharger, which was partly operational (horizontal vibration when the valve was open), and a supply of air to the hopper were used to promote flow. These tests were intended to be comparable with each other, and were used to explore the repeatability of the flow pattern. The fourth test (BG1202) was conducted without air injection to the gypsum, and with the flow aid device out of service.

As the radio tags emerged from the silo outlet, the time of their emergence was recorded. In addition, the total mass of gypsum in the silo at any time was constantly recorded. The rotary valve opened intermittently, so the mass of solids changed whilst it was open and tags were recorded passing the aerial during this period. The valve then closed, the total mass remained fixed and no tags were detected until it opened again. The time when the valve opened and when it closed was also constantly recorded. The total time taken for a tag to emerge can be divided into two parts: when the valve was open, and when it was closed. The residence time used in the following analyses is the actual time taken for the tag to emerge less time during which the valve was closed. Simple interpretation of the results in terms of the actual time taken for each tag to emerge is meaningless.

A more appropriate measure than the residence time is the mass of solid remaining in the silo at the time when the marker emerges, though the technique being used here is commonly referred to as 'residence time measurement'. The remaining mass also has the advantage that it is independent of changes in the flow rate, temporary arresting of the flow and similar disturbances to time observations. The remaining mass in the silo at any instant is therefore taken as a direct equivalent of the residence time, but a high value represents an early part of the discharge and low value a late part.

Four different methods are used to interpret the test data in this chapter: plotting contours of remaining mass, drawing contours of mean velocity, computer visualisation and analysing emerged mass from seeded levels. All but the first methods are techniques newly developed in this thesis. In particular, the last method may be used to identify from a single plot whether the flow is one of the classical types (mass flow and funnel flow) when there is only one layer of markers. For funnel flow, it can also be used to define the size of the flow channel. With the help of residence time contours, the 3D flow channel boundary may then be interpreted. The plot may also contain information on how the flow channel expands with time. This represents a significant advance in the interpretation of flow patterns from residence time measurements.

The results interpreted by using all four methods are presented. They are compared with the expected flow patterns and the reasons leading to the unexpected flow patterns are discussed.

5.2 Expected flow patterns

The difference between mass and funnel flow has long been noted, and many texts and standards define simple flow patterns (e.g. Fig. 1.2). A short description of them was presented in Chapter 1.

The flow patterns which may be expected to occur in a silo of this geometry are indicated in Fig. 5.1. If this silo were to discharge gypsum under conditions of mass flow, the tags at any level would emerge at substantially the same time. Because the solid does not move with a completely uniform velocity (the centre tends to move slightly faster), there would be small differences in the instants at which different tags at a given level reach the outlet. Nevertheless, these would be minor compared with the total time taken by each tag. The residence time of each marker would thus be highly correlated with the level at which it was seeded, and contours of residence time at a given level would not be closely spaced (Fig. 5.2).

By contrast, if the silo were to exhibit funnel flow, the material immediately above the outlet can be expected to emerge first, followed by solid from higher up the flow channel, then material from higher zones near the wall and finally solid from lower regions which has remained stationary throughout most of the discharge process. The residence times of the markers would then depend strongly on their initial horizontal and vertical coordinates. Researchers who have used residence times in the past have relied on sectional contours of residence time to indicate the area of the flowing channel by low residence times for the fast moving material. Where the flow is three-dimensional, sections are more difficult to interpret and contour plots must be used at each given level in the silo. Here, a wide range of times is seen, and the area of the flowing channel is indicated by low residence times for the fast moving material (Fig. 5.3).

However, it is not easy to translate the residence time observations into a flow pattern such as that shown in Fig. 1.2. At a low level in a narrow funnel, the boundary of the flow channel may be detectable from the close spacing of contours, but this does not define the flow channel well, nor does it define the flow channel at higher levels in the silo. The chief problem is that flow channel diagrams, such as that shown in Fig. 1.2, are drawn to indicate the flowing state shortly, but not immediately, after the outlet is opened. This pattern of flow changes progressively as more material is discharged, and often changes significantly by the time perhaps 30% of the stored solid has

emerged. The residence times, by contrast, show how long materials from all parts of the silo take to emerge, so only 30% of them have typically been recorded by the time 30% of the solid has emerged.

As a result, residence times have usually been left as a qualitative indicator of the flow pattern, and attempts have not been made in previous studies to translate them into more certain knowledge. The one limitation on this statement is the use of residence times to distinguish mass flow from funnel flow, which is more straightforward, as noted above.

In this thesis, a major effort has been put into interpreting the flow regime in a funnel flow silo from the residence time data. The principal reason for this is that differences between funnel flow patterns are important in themselves, partly because they influence silo wall pressures strongly, and partly because the probability of arrested flow is well related to the shape of the flow channel and the solids properties.

5.3 Methods of interpretation used on these tests

5.3.1 Introduction

The data used in determining the flow pattern were obtained by placing tags in the silos in a well-defined pattern. The plan of the marker layout is shown in Fig. 5.4. It consists of an axisymmetric pattern of radial spokes, giving a high resolution of differences between the residence times of tags which were placed in theoretically identical positions, and thus of the discrepancies between the idealised axisymmetric pattern and the real pattern.

If the flow pattern is symmetrical with respect to the central axis (a condition assumed in most theories of silo pressure and flow and predicted by all known flow prediction computer programs), the differences between behaviour on different radial spokes of

the template of Fig. 5.4 are insignificant. The circumferential coordinate of the spoke is then immaterial.

However, where unsymmetrical flows develop, the circumferential coordinate can be described in a variety of ways: two are used here. The first is the spoke name A to H. When the template is placed at different levels in the silo, with these spokes always in the same orientation, each spoke produces a generator of the silo cylinder. These positions are then referred to as "Generator F", etc. Sometimes the circumferential position must be defined with greater clarity, or is needed for plotting purposes. The circumferential coordinate θ is then defined. This is chosen in a natural manner relative to Fig. 5.4 with an anticlockwise coordinate in degrees beginning at Generator H. The generators are then situated respectively at A:315°; B:270°; C:215°; D:180°; E:135°; F:90°; G:45°; and H:0°.

The marker seeding was undertaken at a series of defined levels in the silo, which varied from test to test. The levels at which seeding was undertaken in each test are shown in Fig. 5.5.

Four types of analysis were applied to all the measured observations. They are briefly described in the following sections.

5.3.2 Plotting contours of residence time

Plotting contours of remaining mass in vertical and horizontal sections through the silo (the traditional method of presenting this information) is the first method used here to interpret the flow patterns which occurred in the silo. If the flow pattern is simple, it should be able to be recognised from these contours as mentioned in Section 5.2.

Many techniques are available to plot contours in a plan. Some examples are the inverse distance method (Franke, 1982; Davis, 1986), Kriging interpolation (Journel and Huijbregts, 1978; Ripley, 1981; Isaaks and Srivastava, 1989; Journel, 1989; Cressie, 1990, 1991; Deutsh and Journel, 1992; Isaaks and Journel, 1992), the

minimum curvature method (Smith and Wessel, 1990; Briggs, 1974), polynomial regression (Draper and Smith, 1981), radial basis function (Calson and Foley, 1991a, b; Franke, 1982), Shepard's method (Shepard, 1968; Franke and Nielson, 1980; Renka, 1988) and triangulation with linear interpolation (Lawson, 1977; Watson, 1982; Lee and Schachter, 1989; Watson and Philip 1986). Most of these are weighted average interpolation algorithms, but the weighting factor used is different from one to another.

All of these methods have their advantages and disadvantages. Among them, the Kriging technique is one of the more flexible methods and generates the best overall interpretation of most data sets (Keckler, 1994), though it may be slower. The choice of method is also very dependent on the size of the data set. However, if speed is not a concern, Kriging interpolation probably produces the best maps regardless of the size of the data set (small <200, or large >1000).

It may be noted that triangulation with linear interpolation has an advantage over all the other methods in that it can preserve break lines defined in a data file with enough data. This would be the preferred method to retain a discontinuity of residence time across the flow channel boundary in the case of funnel flow, provided that it can be defined in the gathered data. However, the position of the flow channel boundary is unpredictable so that it is very difficult to gather this data effectively. Furthermore, the triangulation algorithm creates triangles by drawing lines between data points. The original data points are connected in such a way that no triangle edges are intersected by other triangles. Data sets that contain sparse data result in distinct triangular facets on a contour plot. Triangulation only works well for a moderate sized data set (from 250 to 1000), evenly distributed over the griding area. In the present data, the number of points is less than 40 for horizontal sections and less than 70 for vertical sections. Data points are also not available on the border and some large holes exist due to failure to detect some of the tags. Triangulation is therefore not an effective method here.

The test data were examined by using many of the different methods and Kriging interpolation was found to produce the best overall results. It is therefore used for plotting all the contours.

5.3.3 Plotting mean velocity contours

The residence time makes no allowance for the fact that a very slow-moving marker that is initially close to the outlet may emerge at the same time as a very fast moving marker initially situated at the top surface. The latter is certainly involved in the flow channel, but the former may have remained stationary for an extended period and only begun to move as the flow channel shape changed later. The simplest improvement to the residence time measures to overcome this problem is to use contour diagrams of the mean velocity of the marker in moving from its initial position to the outlet. The length of the shortest path from the initial position to the centre of the outlet is divided by the residence time to give the mean velocity.

Contours of mean velocity represent a considerable improvement on residence time readings, as indicated in Figs 5.6 and 7. Here the flow patterns of Figs 5.2 and 3 are redrawn, giving a picture which is much better related to Fig. 1.2 and thus easier to interpret. The boundaries of the flow channel are better defined, particularly in vertical sections through the silo.

The same technique used for plotting remaining mass contours (Kriging interpolation) is used to plot the mean velocity contours.

5.3.4 Flow visualisation

Unfortunately, the mean velocity contour has significant disadvantages when attempts are made to use it as a more precise tool. First, the path of the marker is often very different from the shortest path to the outlet, so that the mean velocity underestimates the real mean speed. Secondly, many markers remain stationary for a period before

beginning to move rapidly, so the mean speed is also a poor indication of the real flow condition.

The first of these problems can be addressed by making assumptions about the path taken by markers, but these tend to be ad-hoc, silo specific and can only be guessed by first examining mean velocity contours or theoretical predictions of the expected flow pattern. The technique therefore lacks rigour.

The second problem can be addressed by assuming that the speed of the marker towards the outlet is non-uniform, and that the non-uniformity is governed by its initial location. Inspection of the results of these predictions and modification of the assumptions leads to progressively more convincing results, but the human interpretation element is too large for the technique to be acceptable in a quality scientific endeavour.

The lack of rigour in these possible assumptions is closely related to the problem that the flow pattern does not have a stable pattern during flow. It begins with small movements near the outlet, grows upwards and perhaps outwards, and eventually reaches the free top surface. Thereafter the top surface level begins to fall and any picture of the 'flow pattern' is only of transitory value. Thus although the flow channel boundary near the outlet may be well defined for an extended period, it is not so well defined towards the top of the silo. These difficulties are really only overcome by interpreting the flow as a time-dependent phenomenon, using the residence times as data, together with a minimum number of assumptions about the nature of the flow.

However, it is important to retain the character of the experimental data. If assumptions about the constitutive properties of the material are used to assist in the interpretation, it really ceases to be a direct interpretation of the experiment and becomes inextricably mixed with a flow prediction. This is particularly dangerous if the experimental data are later to be used to assess the quality of predictions derived from purely theoretical calculations. The above data transformations are therefore only

adopted as part of a rigorous time-dependent flow visualisation, which has been described in detail in Chapter 3.

5.3.5 Analysing emerged mass at a horizontal level versus discharge time

The chief difficulty with the visualisation process is that the results cannot easily be transformed back to an image in the form of Fig. 1.2. This is a considerable drawback because the silos literature and descriptions of silo flow are dominated by images in the form of Fig. 1.2. Furthermore, all of the above techniques lack a method of drawing the flow channel boundary (FCB), even though it changes with time. Finding a method which would not only identify the flow type as shown in Fig. 1.2 but would also define the FCB in the case of funnel flow remained a considerable challenge until a late stage of this thesis. This is achieved by analysing the characteristics of emerged mass data from horizontal levels at different heights.

The strategy adopted here is to seek an alternative way of presenting the data, that permits the key features of the transitory 'flow pattern' to be identified, despite the lack of precise placement of markers in potentially critical locations which cannot be known before the experiment. More importantly, the technique should permit the approximate size of the flow channel at different heights to be derived for funnel flow, providing that enough data have been gathered.

5.3.5.1 Characteristics of normalised mass-time curves: Mass flow

Consider a thin horizontal layer of unit thickness in a silo. If the stored solid in the layer is discharged under conditions of mass flow, the mass in the layer will emerge at substantially the same time. Because the solid may not move with a completely uniform velocity, there may be some differences in the instants at which different masses in the layer reach the outlet. Furthermore, because all the solid in the layer is moving and no discontinuity occurs in the velocity profile, the solid must emerge continuously. Therefore, when the emerged mass is plotted against residence time, a smooth curve is obtained. Its shape is dependent on the velocity profile. In the

extreme case, where all the solids move with a completely uniform velocity, this plot reduces to a vertical step, i.e. all the solid in the layer reaches the outlet at the same time. The time when the solid in the chosen level first reaches the outlet depends on its vertical coordinate. If it is close to the top surface, this time is a considerable portion of the total discharge time. Figure 5.8a shows an example in which mass flow occurs, but differences between the centre and wall velocities exist. The residence time T has been normalised by dividing by the total discharge time T_0

$$\tau = \frac{T}{T_0} \tag{5.1}$$

and the emerged mass M_l of the given layer has been normalised as

$$\mu = \frac{M_l}{M_{l0}} \tag{5.2}$$

in which M_{l0} is the total mass of the layer.

For the layer is of unit thickness, M_{l0} can be expressed as

$$M_{l0} = \gamma A_0 \tag{5.3}$$

in which γ is the density of the solids and A_0 is the cross-sectional area of the silo at the chosen height. Similarly, M_l can be expressed as

$$M_l = \gamma A \tag{5.4}$$

in which A represents that part of the cross-sectional area from which solids have reached the outlet at the instant being considered.

Substituting Eqs 5.3 and 5.4 into 5.2 leads to

$$\mu = \frac{A}{A_0} \tag{5.5}$$

Thus, the normalised emerged mass of the layer also represents the relative size of the cross-sectional area from which solids have emerged through the outlet at the given time.

Residence times may alternatively be expressed in terms of discharged mass M_d, which is the total mass that has been discharged from the silo from the beginning of discharge until the instant being considered. This measure is similar to the residence time in that a low value of discharged mass represents an early part of the discharge and high value a late part. The discharged mass is also the difference between the total mass in the silo at the end of filling and the remaining mass at the instant being considered:

$$M_d = M_0 - M \tag{5.6}$$

M_d may also be normalised by dividing by M_0:

$$m = \frac{M_d}{M_0} = 1 - \frac{M}{M_0} \tag{5.7}$$

The measurement of discharged mass similarly has the advantage that it is independent of the rate of discharge. If the discharge rate is uniform throughout the whole discharge process, the normalised discharged mass is equal to the normalised residence time (Fig. 5.8a). The curves plotted in Figs 5.8 and 5.9 are critically important to the interpretation technique described in the following sections. They are therefore given the name "normalised mass-time curves" for brevity.

Under conditions of mass flow, the rule of first-in-first-out is preserved. This means that, for solids at the same initial horizontal coordinate, material at a lower level always reaches the outlet before that at a higher level. The plots of emerged mass

against time for the two levels will never intersect, but remain closely parallel to each other (Fig. 5.8a).

In summary, under conditions of mass flow, the relationship between the emerged mass and time (normalised mass-time curve) has the following characteristics:

a) For a given horizontal level at a given height, this relationship may be represented by a smooth curve. The starting point of the curve on the normalised time axis (the time when some part of the mass from the layer first reaches the outlet) is not small compared with unity (the maximum residence time or mass after filling), but depends on the relationship between its vertical coordinate and the initial top surface in the silo.

b) Given two or more horizontal layers at different heights, the curves representing this relationship do not intersect, but remain close to parallel to each other. Their separation depends on the separation of their initial vertical coordinates.

5.3.5.2 Characteristics of normalised mass-time curves: Internal funnel flow

If the stored solids are discharged under conditions of funnel flow, the solid within the flow funnel at the chosen horizontal layer emerges shortly after the outlet is opened. The remainder of the layer is outside the flow channel and remains stationary until the top surface moves down to this level and intersects it. Thus, there is a period in which no solid from this layer reaches the outlet. When the emerged mass is plotted against time, this absence of emerging solid appears as a horizontal "plateau" (Fig. 5.8b). The curve rises steeply at a low time because the solids in the flow funnel come out shortly after discharge starts. It reaches the plateau and remains on it until the first part of the solid outside the flow channel reaches the outlet.

The length of the plateau is related to the period between the formation of the flow channel and the top surface intersecting the rest of the solid in the layer. Because the

velocity distribution is not uniform in the flow channel, the difference between the time when the solid from within the flow channel first reaches the outlet and that when the last solid reaches the outlet also depends on the vertical position of the layer. If the layer is relatively low in the silo, the two events are very widely separated and the difference between the flow channel and stationary surrounding solid is very marked. However, if the layer is at a relatively high position, some solid outside the flow channel may slide into the faster part of the flow zone and begin to catch up solid from the slower parts of the flow zone. Thus the plateau length also depends on the vertical coordinate of the layer. If the layer is close to the top surface, the material at the top near the wall may even roll into the faster part of the flow zone and overtake the solid in slower parts of the flow zone. This then eliminates the plateau on the curve. Therefore, the plateau only occurs in lower levels where the flow channel is stable. Nevertheless, the idea of a flow channel is meaningless if the level is very close to the top surface because this region changes very rapidly.

The solid inside the flow channel may display characteristics similar to those of mass flow. For two levels at different heights, the solid from the lower level always reaches the outlet first. In most cases, the size of the flow channel is only a small portion of the cross-sectional area of the silo. Therefore, the time for the material in this channel to travel from its original position to the outlet is small compared with the total discharge time. This is reflected in the normalised mass-time curve, which begins to rise at very low dimensionless times (Fig. 5.8b).

By contrast, the solid outside the flow channel at higher levels soon rolls into the flow channel and emerges at a relatively early time, whilst that near the bottom is the last to emerge. The result is that the normalised mass-time curve for a higher level crosses that for the lower level at some point and reaches 100% before a lower level (Fig. 5.8b).

In summary, under conditions of funnel flow, the normalised mass-time curve has the following characteristics which are different from those under mass flow:

a) For a horizontal level at a given height, there is a plateau in the normalised mass-time curve for the layer. The length of the plateau is related to the duration of the stable channel at the vertical coordinate of the level. However, this plateau may disappear if the level is close to the top surface. The starting point for the curve (the dimensionless time when some solid from the layer first reaches the outlet) is small compared with unity (the total mass after filling /total discharge time).

b) For two or more horizontal layers at different heights, their normalised mass-time curves intersect each other: some of the mass at a lower level reaches the outlet early but other parts are discharged much later or not at all.

5.3.5.3 Identification of classical flow patterns

The normalised mass-time curves from different levels can be used to distinguish mass and funnel flow. The flow type can be identified by characteristic (a) above of mass flow and internal funnel flow if a plot of emerged mass against discharge time is available at a low level in the silo: a plateau should appear on the curve for the case of funnel flow and the curve should rise close to the origin. The layer should be chosen to be in the lower parts of the silo so that the funnel is stable for an extended period in the case of funnel flow. If two or more levels are available, the flow type can be identified with less uncertainty using both characteristics of mass flow and internal funnel flow ((a) and (b) above).

In practice, however, the flow channel may not be stable, but may expand outwards slowly. This is represented by a slightly inclined plateau instead of a flat plateau. The slight differences between the idealised model and the practical case do not invalidate the interpretation of test results.

The above description concerns only mass flow and internal funnel flow. If the flow funnel expands toward the wall at higher levels in the silo (semi-mass flow) (Fig. 1.2),

the normalised mass-time curve from a lower level exhibits the characteristics of funnel flow, but that from a higher level exhibits those of mass flow. This situation is not difficult to identify but more levels are required to interpret the results correctly. It is essential that there are at least two levels in the mass flow upper part and at least one level in the internal flow lower part (Fig. 1.2). To identify the position of the effective transition accurately (where the flow channel reaches the wall), more levels in this critical zone are required.

It may be noted that no assumptions about the silo geometry or the symmetry of the flow have been made. Therefore, this analysis may also be applied to non-circular silos and to unsymmetrical flow conditions.

5.3.5.4 Determination of flow channel boundary

The plateau on the normalised mass-time curve represents one of the characteristics for funnel flow. The part of the curve below the plateau represents the proportion of the layer which lies inside the flow channel while that above it represents the proportion in the static zone (Fig. 5.9). Because the layer is chosen to have unit thickness, the corresponding coordinate μ_f of the plateau on the vertical axis represents the relative size of the flow channel at this level. From Eq. 5.5, the cross-sectional area of the flow channel A_f can be calculated from

$$A_f = \mu_f A_0 \tag{5.8}$$

The position of the flow channel at this level may be determined by analysing the position of the plateau on the normalised discharged mass axis. If the start of the plateau is m_{f1} and the end is m_{f2} on this axis, those data points which lie at a discharged mass less than $m_{f1}M_0$ are in the flow channel and the others are outside it. This may alternatively be expressed by using remaining mass (Eq. 5.7). Those data points with remaining mass M such that

$$M > (1 - m_{f1})M_0 \tag{5.9}$$

lie inside the flow channel.

If the flow channel has a regular geometric form (e.g. circular in plan section), the horizontal dimension of the channel may be calculated from its cross-sectional area (Eq. 5.8) and the location may then be determined by identifying those data points within the channel (Eq. 5.9). Alternatively, the flow channel boundary may be determined from the remaining mass contours. Where a flat plateau exists in the normalised mass-time curve, no mass from the level reaches the outlet at times corresponding to remaining masses between $(1-m_{f1})M_0$ and $(1-m_{f2})M_0$. The values m_{f1} and m_{f2} are then effectively the same measure. However, the flow channel geometry may change slightly with time so that a small difference exists between m_{f1} and m_{f2} in practice. Further, the flow boundary cannot be known before the experiment begins so often the boundary may be poorly defined by the data. In addition, contouring softwares may undertake smoothing and not strictly observe the measured data. A rule of thumb might be to adopt a contour at the mean value of the two remaining masses

$$M_f = \left(1 - \frac{m_{f1} + m_{f2}}{2}\right) M_0 \qquad (5.10)$$

to define the approximate boundary of flow channel.

If there are many levels which are relatively evenly distributed down the height of the silo, the total volume of the flow channel may be integrated from the channel size at each level. This integration is, however, inaccurate because the flow channel is widest near the top where its boundary are less clearly defined.

5.3.5.5 Calculating emerged mass at a level from residence time measurement

The application of the above technique to interpret the tests at British Gypsum is not straightforward because the emerged mass from a given layer was not directly recorded. Where markers are evenly distributed over the area of the silo cross section,

it may be assumed that each marker represents an equal proportion of the mass at that level so that the percentage of emerged markers accurately reflects the percentage of the mass which has emerged.

To apply the technique successfully in the interpretation of the British Gypsum tests, two obstacles must be overcome:

a) The tags were seeded in a well-defined grid, but were not evenly distributed over the area of the cross section. The separations between some tags are much larger than between others. Therefore, it cannot be assumed that the percentage of tags which have emerged represents the percentage of mass which has emerged.

b) Some tags were not detected as they passed the outlet. The consequence is that there are some holes in the data, where the residence time measurement is sparse.

The first problem may be addressed by assigning different weightings to different tags so that each tag represents an appropriate proportion of the mass in the level. For a given grid, a simple rule is to assume that each tag represents the surrounding area as far as half way to its nearest neighbour in all directions (Fig. 5.10). Using this assumption, tags in the same ring have the same weight and tags in different rings have different weights. Because only four tags were used for the innermost ring, the weight for these tags is a quarter of the inner circle area. Other tags have a weight of one eighth of the appropriate ring area. Table 5.1 shows the weightings for tags in different rings. The sum of all the weightings for all the tags is 23.76m^2 which is the cross sectional area of the cylinder of 5.5m diameter.

The second problem may be solved by interpolating the missed data points. From the experience of drawing contours of remaining mass, an interpolation based on the data available from the same level is often not adequate, especially when extrapolation is

needed (for the holes close to the boundary). To overcome these difficulties, a computer program was written to perform spatial interpolation using all the available residence time/remaining mass observations. The results are satisfactory and much better than those obtained by using data from each individual level alone.

The emerged mass from a seeded level can then be integrated with respect to the residence time (or discharged mass) by using the weightings of the individual tags. The emerged mass is then plotted against the discharged mass for each level to give the normalised mass-time curve.

Table 5.1 Weightings for tags at different rings: British Gypsum tests

Ring No.	1	2	3	4	5
Colour	Black	Yellow	Pink	Green	Orange
Weighting (m^2)	0.194	0.291	0.690	1.034	0.858

5.4 Test BG2901, BG0302 and BG0902: First three experiments

Interpretations of the flow pattern found in the first three experiments (BG2901, BG0302 and BG0902) are presented in this section. They are grouped together here because the test conditions were identical (normal plant operating) for them and they were designed to explore the repeatability of the flow pattern. To keep the total volume of information within reason, only residence times are presented in full for all the tests. For other interpretations, only one typical experiment is presented in detail.

5.4.1 Residence time observations: remaining mass

5.4.1.1 Test BG2901

Only five levels were seeded with markers in the first experiment (BG2901) because it was effectively a trial of the experimental system.

The simplest clear interpretation of the observations involves plotting contours of remaining mass on horizontal planes through the silo. The remaining mass M of gypsum within the silo at the time that each marker emerged through the outlet is shown in Figs 5.11a-e for each of the seeded Levels 1 to 5. In each sectional plot, two pictures are shown: on the right, the individual measured values at each marker position, and on the left, contours of the remaining mass. In the experiments the levels were numbered from bottom upward (Fig. 5.5a). The plots are presented here in reverse order so that the highest level appears first at a higher position on a page. The purpose of this arrangement is for the ease of comprehension. The same presentation order is used for all other experiments in this thesis.

The same information is presented in a series of vertical sections through the silo on the four possible diameters in Figs 5.12. The contouring for vertical sections was performed including the boundary conditions that the solid near the outlet discharges immediately at time t=0. This condition was prescribed both at the outlet and at positions adjacent to the bin discharge aid. The value of M at the outlet was assumed to be equal to M_0 (total mass of the solids before discharge: see Table 4.1) and those adjacent to the discharge aid were taken as values slightly less than M_0. These boundary conditions were required to constrain the residence time field. The region above the highest level in the vertical sections has been blanked in the plots because extrapolation beyond the real data area is of very doubtful validity.

It should be noted that the precise values at the data points are sometimes not exactly honoured by the contouring process. Contours have been plotted based on a griding data file which consists of data on a rectangular grid. The data at the grid nodes were calculated by weighted interpolation using the measured data points, though different contouring methods which were tried use different weighting factors. A data point can only be precisely honoured if it coincides with a grid node and the interpolation method does not involve smoothing (e.g. "Kriging without nugget effect" which is used here). The data values are more accurately represented when the number of grid lines is large. However, when the number of grid lines is large, the size of the grid

data file is dramatically increased, so that the time taken to perform both the griding and contouring tasks is greatly increased. The "Spline smoothing" technique was also used here to reduce the angular appearance of the contours and to reduce noise in the contour maps.

Because a small proportion of the tags were not detected in the experiments, some "holes" exist where the data points are sparse in both the horizontal and vertical sectional plots. The contours in these areas should be interpreted with caution because the wide spacing makes the result very uncertain. This is particularly true if the "hole" is adjacent to a boarder (e.g. the hole adjacent to the wall between θ=0° and 135° in Level 4 (Fig. 5.11b)). Doubtful extrapolation is required to produce contours in this case.

The above discussion is applicable to all the contour plots in this thesis but is not repeated elsewhere.

It is clear from these residence time plots that the flow behaviour is not simple. In Figs 5.11, the contour patterns change from one level to another in a quite alarming manner. The remaining mass is very scattered both at high levels and lower levels. Some of the markers at the highest level (Level 5, Fig. 5.11a) emerged as early as when there was 175t (comparing with M_0 = 204.8t) of solids still in the silo, but other parts did not emerge until almost all the solids had been discharged (M = 6t). The upper and lower bounds on the remaining mass at the lower levels are also very close to these values (Level 1-4, Figs 5.11b-e). This feature is shown more clearly in the vertical sections (Fig. 5.12). The observed flow pattern is certainly not a simple mass, funnel or semi-mass flow regime.

From all the horizontal sections (Fig. 5.11) and vertical sections (Fig. 5.12), the flow pattern is very far from axisymmetric. Unfortunately, this means that it is difficult to display the results in a manner which allows them to be quickly assimilated, since 3D plots of a fourth variable are not easily represented on a 2D page. By contrast, if

symmetry exists in a flow pattern, it is possible to reduce the geometric variation to 2D, and to use contours in a vertical planar section to indicate the third variable (remaining mass). This simplification has been used in previous studies (e.g. Lee-Wilson, 1989; Watson, 1993). This problem of presentation does not disappear as the data are analysed further.

If the results at all the different levels (Fig. 5.11) and all four vertical sections (Fig. 5.12) are carefully examined, it is possible to identify narrow funnel flows occurring, though the flow is certainly not a classical funnel flow. In particular, the highest value of remaining mass at Level 3 (M = 145t, Fig. 5.11c) is less than all the values at the higher levels (Levels 4 and 5, Figs 5.11 a and b), indicating that either the flow evaded all markers on Level 3 and removed a marker from a higher level, or one high speed marker at Level 3 has not been recorded.

These funnel flows appear in slightly different places at different layers. The fastest flow zone (with a high value of remaining mass in the plot) at Level 5 (Fig. 5.11a) appears at around r = 1m and θ=160°. It rotates anticlockwise to about r = 1.2m and θ=180° one level down (Level 4, Fig. 5.11b). The fastest flow zone rotates in the same direction for the lower levels and reaches about r = 1.1m and θ=270°. The vertical sections (Fig. 5.12) also show that the funnel is not vertical. Figure 5.12a shows that the funnel tilts toward Generator E (θ=135°) in Section AE. Figures 5.12b-d show that it inclines towards Generator B (θ=270°), C (θ=215°) and D (θ=180°) in Sections BF, CG and DH respectively.

5.4.1.2 Test BG0302

Nine levels were seeded with markers for the second experiment (BG0302). It was the first complete test and provided a much fuller body of information than was available in the first experiment.

Figures 5.13a-i present computer-generated contour maps of horizontal sections showing the remaining mass at the instant the marker reached the outlet. The same information is also shown for vertical sections in Figs 5.14a-d. These again show patterns which vary from level to level in a manner that defies simple description. Some of the markers in the highest level (Level 9, Fig. 5.13a) emerged as early as when there was 208t (comparing with M_0 = 214.8t) of solid still in the silo, but other parts did not emerge until almost all the solids had been discharged (M = 7t). The same phenomena were seen at all levels. There are more layers of markers here, and the data capture is better, but the behaviour is qualitatively similar: the flow cannot be given a simple description.

In the contour maps of horizontal sections (Fig. 13), there are many "bull's eyes" surrounding data observations. As a typical example, consider the contours at about r =1.2m and θ=45° on the top level (Level 9, Fig. 5.13a). Having carefully examined the spot values on the right side, it may be seen that many of these densely packed contours around data points are not a result of the contouring process but caused by the very radically different values at neighbouring points, which make it difficult to avoid such phenomena in the contouring process. The cited example is caused by the very late emergence of one marker (M=7t) between two markers which emerged very early (M=196 and 210t). A few "bull's eyes" also occur on the contour maps for the vertical sections. They may be caused either by stochastic variations in the flow or circumferential movement of the solids, which would mean that fast moving material can overtake other solids below it by moving out of the plane being shown.

The contours at the highest level (Fig. 5.13a) are seen to be rather complicated and very unsymmetrical. These become simpler at lower levels and the fast flowing zone tends to move slightly inwards. At the lowest level (Fig. 5.13i), the contours become more symmetric than at the top level and the fast flow zone moves to positions over the gap between the discharge aid and the hopper wall, instead of against the silo wall as at the top level. Again, the fastest flow zone is different from one level to another.

The vertical section AE (Fig 5.14a) shows that the flow funnel tilts towards Generator A. Similar sections show that the funnel inclines to Generators F, G and H in Sections BF, CG and DH respectively. The image shown in Fig. 5.14b is particularly noteworthy, with a contour for 200 tonnes swooping upwards towards the right hand wall at the Generator F (θ=90°) and indicating the formation of a flow channel in this location. Figures 5.13a and b both show that the central part of the silo discharges at remaining masses of the order of 150 tonnes, but it is notable that solid adjacent to the full height of the right wall in Fig. 5.13a remains in the silo until only 40 tonnes remain. The flow is very non-uniform.

In summary, this experiment shows the similar flow behaviour to the first experiment (BG2901). The flow is not simple and the contours vary from one level to another. However, it is very noticeable that the fast flowing zone does not occur in the same place as in the first experiment. The contours are also different in shape. Therefore, the experiment cannot be described as reproducible in detail.

5.4.1.3 Test BG0902

Seven levels were seeded with markers in the third experiment (BG0902). The number of tags seeded in this experiment (208) is close to the second experiment (BG0302, 239 tags).

Contours of remaining mass are shown in Fig. 5.15 for horizontal sections and Fig. 5.16 for vertical sections. The remaining mass observations show the same essential character as found in the previous tests but some different effects are seen. At the bottom Level 1 (Fig. 5.15g), the remaining mass figure shows two adjacent zones with high values (rapid flow) which are also found in the higher Levels 2, 3 and 4 (Figs 5.15d-f), and again with slight modifications in Levels 5, 6 and 7 (Figs 5.15a-c). Similar to the previous test (BG0302), the "bull's eyes" surrounding the data points also occur at the contour maps of high levels and vertical sections.

The zones of fast flow are seen to be close to the centre in the horizontal sections, though the positions again vary slightly from one level to another. In the vertical sections (Fig. 5.16a-d), a more uniform flow was found than in the earlier experiments, with much of the centre of the silo moving. The slowest flow zone appears to be near the wall between 45° and 150° at all the lower levels (Levels 1-5).

The contours are again in very different places from the two earlier experiments, they are different in shape, and no two experiments can be described as quantitative reproductions of each other in detail. It is therefore clear that this silo discharges in a different flow pattern on each discharge. The general form of the flow pattern is, however, retained from discharge to discharge.

5.4.1.4 Effect of discharge aid on residence time

In the third experiment (BG0902), some markers were placed down in the conical hopper near the opening into the discharge aid to explore the effect of the discharge aid on the residence time. These markers gave a clear indication of the time taken for material situated right at the discharge aid opening to reach the dome valve and radio aerial. This time was found to vary between 28 and 642 seconds (and 10½ minutes!). This fact appeared rather astonishing on first discovery, but clearly the discharge aid does not function axisymmetrically. Instead, some zones have strongly promoted flow whilst others can remain stationary for an extended period. The circumferential distribution of the residence times of these markers is shown in Fig. 5.17, where evidently the zone between $\theta = 70°$ and 150° was effectively stationary for the first part of the discharge. This is a close match to the position of the slow flow zone for Test BG0902.

5.4.2 Mean velocity contours

A clearer picture of the flow pattern may be obtained by determining the mean velocity of discharge of each marker. The mean velocity was evaluated by dividing the shortest distance from the marker position to a point on the circle of the bin discharger by the

residence time. The residence time used was slightly reduced to allow for the time a marker should take to move from the bin discharger level to the outlet, as determined from Test BG0902.

Interpretations of the mean velocity are only presented in full for one typical experiment to limit the volume of figures. The results for other tests are very briefly covered at the end of this section. Figures 5.18a-i show the mean velocity contours and values for horizontal sections for BG0302. The results in vertical sections are presented in Figs 5.19a-d. To produce neat pictures, the area below the lowest level in the vertical sections has been blanked off. These figures may be compared with the corresponding remaining mass diagrams shown in Figs 5.13 and 5.14 respectively.

The mean velocity is not quite the same as the flow velocity at any instant, since it assumes that each marker has moved at constant speed towards the outlet and followed the shortest path. Nevertheless, it does provide a much better picture of the pattern of flow in the solid. Because the fast flow in the initially flowing regions is so distinct from the slower movement in zones which are initially stationary, the image is clear. The snaking pipe flows suggested in Section 5.4.1.2 can be seen more clearly in these mean velocity plots.

Figure 5.18a shows that the fastest flow is around Generator F (90°) against the wall in the topmost level. It moves clockwise to around 45° (Generator G) one level down (Fig. 5.18b) and comes back to around 90° at two levels down (Fig. 5.18c). The same position is seen on all the lower levels, except for Levels 6 and 1 (Figs 5.18d-i). It is noticeable that the strong contours associated with very fast flow are mainly caused by one marker at each level emerging very early. However, the markers at the key position in Levels 1, 3, and 6 have been missed. From Figs 5.13a-i, the remaining mass at marker exit on different levels is very close to the same value on that vertical line. Thus, some markers in this fast flow pipe must have gone undetected due to the very short time interval between them as they passed through the outlet. The flow

channel can then be seen to be almost vertical at the lower levels (Levels 1 to 7) but circumferential moment is involved near the top surface (Levels 8 and 9).

At lower mean velocities (e.g. 10 mm/sec), the contour encompasses a larger area at high levels than low levels. The large area at Level 9 (Fig. 5.18a) indicates surface sloughing of material into the flow channel, giving a large region of high speed solid at the top. There are two zones for the contour of 10 mm/sec at all levels. The positions of these zones are typically at θ=90° and θ=270°, though they change slightly from one level to another. This indicates that there are two flowing zones, unsymmetrically located relative to the silo axis.

The fast pipe flow is seen more clearly in the vertical section BF (Fig. 5.19b). It shows the formation of a strong flow channel against the wall at θ = 90° (Generator F). However, the very slow markers against the wall at Generator F indicate that the funnel does not touch the wall. This flow channel draws material from the top surface, and produces a strange-looking contour in Fig. 5.19c (Section CG), where material near the surface shows a remarkable isolated high mean velocity. This shows one of the difficulties of plotting truly 3D phenomena in 2D sections. Sections AE (Fig. 5.19a) and DH (Fig. 5.19d) seem not to intersect with the fast flowing pipe so the mean velocities are all small compared with those in the pipe. However, the asymmetry of the mean velocity distribution is clearly seen.

Both very high and very low mean velocities are found at all heights in the silo. The very low mean velocities for low level markers close to Generators E, B, C and D (Figs 5.19a-d, θ= 135° to 270°) may indicate that part of the silo is operating in the internal flow mode. They may also suggest that the gap beside the discharge aid in these places may have been blocked for an extended period.

Horizontal (Fig. 5.18) and vertical (Fig. 5.19) section plots show that many of the fast moving markers lie between θ=-45° to θ=90° (Generators A, H, G and F) and above the opening in the discharge aid through which all markers must pass. This indicates

that the funnel flows occur above this opening. It can also be seen that one marker from the ring immediately inward from this opening also comes out fast, but thereafter tags at inner and outer radii come out next, indicating that the sloughing behaviour is strongly radial.

In summary, the phenomena observed in the remaining mass observations have been confirmed and more information has been found by analysing mean velocity contours. The automatic plotting of mean velocity contours provides the first measure of the flow pattern. However, the program used for this purpose is not able to interpolate between levels, so no cognisance could be taken of the data at adjacent levels. Moreover, since there are relatively few markers at each level (typically 36 in a fully seeded level), there is plenty of scope for the automatic contouring program to be rather inventive about the shape of the contours. Contours across large holes in the data should be treated with scepticism.

The same conclusion may be drawn for Tests BG2901 and BG0902. The contours of mean velocity confirm that a fast flowing pipe occurs in Test BG2901 between θ=135° and θ=270° and that in Test BG0902 a similar fast flowing pipe lies between θ=-90° and θ=90°. Many of the phenomena seen in Test BG0302 are also seen in these tests. The three tests all show the same behaviour, so the tests may be described as reproducible. However, the position of the fast flowing pipe does vary from test to test.

5.4.3 Computer flow visualisation

The computer program written to represent the progressive discharge of solids was described in Chapter 3. It is intended for use as a visual aid in its own right. The descriptions of the flow behaviour given above in relation to these experiments are borne out by this computer visualisation of the experimental data. Because dynamic images are often more effective than static ones which can be shown on paper, only a small sample of stills from those computer images at different stages of the discharge

is shown here for a typical experiment (BG0302). Again, a brief outline of other experiments is given at the end of this section.

Figures 5.20a and b show two examples of the colour images produced on the computer screen. Due to the high cost involved in presenting colour pictures, the remainder will be presented in black and white, though this further reduces the quality of the dynamic images.

Each screen image shows a 3D display of the silo on the right, with Levels 1, 4, 7 and 9 shown. The number of displayed levels has been restricted because the screen image becomes extremely congested if all levels are shown. The number of levels displayed and the choice of these levels can be easily adjusted by the program user. In the right hand image, all markers in these levels are defined by a number to indicate the level to which they belong, with lines drawn between them to indicate the inferred position of solid at that level lying between the known marker positions.

On the left of Fig. 5.20a, one diametral section through the 3D image is drawn. This allows a more precise study of one section to be made during the discharge process. If the behaviour were axisymmetric, corresponding to the simple images drawn in the literature (Jenike, 1961, 1964a; Gaylord and Gaylord, 1984; Safarian and Harris, 1985; Hampe, 1991), then one diametral section would be adequate and would contain all the required information. However, the serious lack of symmetry in these experiments makes the presentation of the data very difficult. The 2D plot indicates that some markers are missing from each level. These are markers which were not detected on discharge, generally because they passed through the radio aerial at the same time as another marker (only one can be detected at a time). However, it should be noted that these experiments were the first to use this flow detection system, and that the proportion of markers detected improved later. Both images include the two inverted cones of the flow promotion device.

In the right hand bottom corner of the computer screen image, a small bar chart shows the proportion of the markers which has emerged from each level at this instant. As a marker emerges from the outlet, it is recorded here. The changing patterns of these bar charts provide very valuable information. In particular, the chief reason why flow patterns need to be studied in industry is to obtain information about the location in the silo from which solid is being drawn off at a particular instant, and to assess the degree of mixing, ageing or dead zones in the silo. This small bar chart serves this purpose extremely well.

The time at which this set of marker positions occurs is displayed at the middle of the bottom of the computer screen image, measured relative to the start of discharge in hours, minutes and seconds. This is the effective duration of discharge (i.e. the periods when the valve was closed have been subtracted from the total elapsed time). The value may be switched to display instead the percentage of discharged mass (ratio of discharged mass to the total mass in the silo before discharge) by the program user.

The four levels shown in their initial condition in Fig. 5.20a are followed through the discharge process in Figs 5.20b-e. At 2 minutes 30 seconds after the start (Fig. 5.20b), the 3D plot shows that a significant zone of material is rushing towards the outlet around Generators F and G, but Section AE captures only one point of this, so that a single marker in Level 9 on the 2D plot looks very anomalous. Slower movement is occurring on the opposite side, and is more evenly distributed through the levels. The bar chart shows that more markers have emerged through the outlet from the top Level 9 than from any other, so the evidence for a pipe flow in incontrovertible.

In Fig. 5.20c (5 mins 30 secs), the fast flow described above has emptied out of the silo and the second flow zone is developing nicely. This is captured more effectively by the chosen 2D plot and occurs around the vertical Generators A and H. Again, the bar chart indicates that the top Level 9 has produced more markers leaving the silo than any other.

At 9 minutes (Fig. 5.20d), the second flow zone has fully developed. It is a broad-based funnel flow which has some similarities with mass flow: all the solid except that right against the wall near Generator E is now inside the flow zone. This description is further supported by the bar chart, which shows that more markers have emerged through the outlet from lower Levels 1-4. However, the flow is very unsymmetrical. The solid around Generators A and H moves much faster toward the outlet than that around Generator E. This situation is not expected in either classic mass flow or funnel flow, and can only be attributed to the action of the discharge aid which appears to change the flow pattern from conventional expectations.

In the last still image chosen from this continuous series of screen images (Fig. 5.20e) at 14 minutes, the 2D plot indicates that the middle part of the silo has mostly emptied, but material from all levels remains at other positions. Again, the bar chart indicates that the lower levels are leading in the quantity passing through the outlet.

As noted above, the 2D image in Figs 5.20a-e shows only the diametral cross-section AE. One image from the discharge for each of the other diametral sections BF, DH and CG is shown in Fig. 5.20f-h. All three are chosen from early in the discharge (1 minutes 30 seconds after the start). Section BF (Fig. 5.20f) shows that the right hand side of the silo is almost devoid of markers because all have emerged through the outlet in the fast flow pipe. Section CG, shown in Fig. 5.20g, indicates that higher levels are drawn into the funnel flow channel seen in BF, but that lower levels are not in significant motion. The last section, DH (Fig. 5.20h), indicates little movement at this early stage, but the proximity of H to the flow pipe (Fig. 5.20g) means that some small movements are seen here.

To make the full use of the bar chart, a computer program was written to plot only bar charts at different stages. The result is shown in Fig. 5.21 for Test BG0302. The percentage of the mass which has been discharged is indicated at the bottom of the chart. At early stages of discharge (when less than 10% of the mass has emerged), the bar charts show that a small number of tags have emerged through the outlet from all

levels, but more came from the top Level 9, indicating the formation of a narrow pipe flow. When 20% of the mass has been discharged, the bars for high Levels 5-9 show that there are still more tags from the upper levels, as expected in classical funnel flow. While the number of markers emerging through the outlet increases steadily from all levels, more markers emerge from the lower levels and eventually exceed those from higher levels before half (50%) of the solid has been discharged. However, tags from the top level catch up and overtake those from the low levels again at late stages (60% - 80%) of the discharge. This suggests that solids emerged from about 20% to about 80% mass discharged are mainly from the above proposed broad-based flow funnel which has some similarities with mass flow. Furthermore, the identity numbers of the markers which emerge at late stages (>60%) are scattered and cannot be described in simple terms. This fact may indicate that the flow is even more complicated than a simple combination of mass flow and pipe flow.

Figure 5.22 shows the bar charts for Test BG2901. It may be described in a similar manner to Test BG0302 (Fig. 5.21), though it is different in detail. When 20% of the solid has been discharged, the bar charts show that nearly 50% of markers from the bottom level have emerged through the outlet. This may indicate that the broad-based flow funnel is even wider than that for Test BG0302. The mixed flow is best illustrated by the chart when 30% of the mass has been discharged, where the bars for Levels 4 and 5 indicate pipe flow and that of Levels 1-4 indicate wide funnel flow which is like mass flow.

The bar charts for Test BG0902 are shown in Fig. 5.23. Again, they are very similar to those for the other two tests (Figs 5.21 and 5.22). The formation of a narrow channel pipe flow is clearly seen in the first few charts (<20%) and a mixed flow is seen in the next two charts (30% and 40%).

In summary, the flow appears to be a rapid pipe flow, with a superimposed wide funnel flow for all the three experiments. This flow pattern may well be characteristic for silos using this kind of vibratory discharge aid and injected air.

5.4.4 Analysis of mass emerged from seeded levels

Following the procedure described in Section 5.3.5, each marker was assigned a tributary mass and the resulting discharged mass was integrated over time. The total mass from each level was then plotted against discharged mass (or residence time) to produce a normalised mass-time curve. The result is presented in Fig. 5.24 for Test BG2901. Because relatively few markers were used, the emergence of one marker may represent a substantial portion of the mass at the layer, especially where the marker is close to the walls (coloured green and orange). The curves are therefore not as smooth as would be found if more markers are used.

It is clear that Fig. 5.24 cannot be described as revealing a simple flow pattern when it is compared with Figs 5.8a (mass flow) and b (funnel flow). All the curves in Fig. 5.24 are close to the diagonal, indicating that the solid being discharged come from all heights in the silo. The silo is very good at mixing the stored solids on discharge. Further, all the curves rise from points quite close to the origin, which may suggest the formation of a flow funnel. The very low plateau on the curves (about 3% of the cross-sectional area, Fig. 5.24b) further indicates that the funnel is very narrow (pipe flow).

The overall picture from Levels 3-5 (Fig. 5.24b) also looks like a funnel flow (see Fig. 5.8b). However, the picture from Levels 1-3 (Fig. 5.24a) looks something more like mass flow (see Fig. 5.8a) or wide funnel flow. This is particularly true for Levels 1 and 2. These information indicate that there is a wide funnel flow.

However, the curves seem to be more complicated than just a simple combination of a stable pipe flow and a wide funnel flow, which should lead to clear plateaux in the curves and much simpler remaining mass contours than those observed (Figs 5.11 and 12). The best interpretation may be that the flow consists of a pipe flow with a superimposed wide funnel flow, but the location of the flow pipe may vary with time (Fig. 5.25), which results in the complicated picture and extracts solids from all

heights of the silo. If the flow pipe is stable, it may extract solids only from the higher levels.

Figure 5.24a shows that there is a plateau exists on the curve for Level 1 after 60% of the mass has been discharged. This indicates that about 16% mass at this level remained stationary for an extended time (from 60% to 90% of the total discharged mass) and started to emerge through the outlet only when there was less than 10% of the mass remaining in the silo. Level 2 shows a similar phenomenon though not as clearly as Level 1. Figure 5.24b shows that between 15 and 20% of the solid in Levels 4 and 5 was blocked for an extended time.

The results for Test BG0302 are presented in Figs 5.26a and b. This experiment is qualitatively similar to but more complicated than Test BG2901 (Fig. 5.24). This is not surprising because its remaining mass contours (Figs 5.13 and 5.14) are more complicated than those of Test BG2901 (Figs 5.11 and 5.12). Again, the flow consists of a wide funnel flow and a pipe flow. Some solid at most levels was stationary for a period and the flow funnel appears to have been unstable. The same conclusions can be drawn for Test BG0902 (Figs 5.26c and d).

5.5 Test BG1202: Fourth experiment

5.5.1 Residence time observations: remaining mass

For the fourth experiment (BG1202), eight levels were seeded with 36 markers in each level, making a total of 288, of which 92% (266 markers) were detected on discharge. It was different from the preceding three experiments only in that the discharge aid and air injection were turned off. The silo was discharged under gravity alone. This test is significant in that it shows the differences in behaviour which these flow aids cause.

The contour plots of remaining mass at different levels are shown in Figs 5.27. The lower Levels 1-3 (Figs 5.27e-h) show a fairly axisymmetric pattern, with the central

core moving in a fairly uniform flow, surrounded by much slower material. In Fig. 5.27h, the lowest Level 1 shows the central core emerging when the silo contains between 180 and 200 tonnes. The walls show a very different picture, with remaining masses of the order of 30 to 60 tonnes, which includes the lowest remaining masses in the test (Fig. 5.27h). The same form is repeated at higher levels (Figs 5.27e-g). Towards the top, the large difference between the central zone and the edges is lost, as is expected in classic internal funnel flow, and by the top Level 8 the remaining mass is relatively uniform throughout the silo (Fig. 5.27a).

Having stated that the remaining mass contours are fairly axisymmetric at lower levels, the flow is not exactly axisymmetric. The fastest zone at the top level (Fig. 5.27a) is seen to be slightly biased towards the bottom of the picture (around Generators A and B ($250°<\theta<350°$)). It moves toward the centre of the silo at lower levels and is well centred at the lowest Level 1 (Fig. 5.27h). Slow movement occurs at the opposite side (in the range of $45°<\theta<135°$). It is interesting, and possibly significant, that the region of $70°<\theta<150°$ was identified in the third experiment (BG0902) as having no flow through the gap between the discharge aid and the hopper during the early part of the test (Fig. 5.17).

The same data are presented in vertical diametral sections in Fig. 5.28. All sections show the same pattern and the central large funnel flow zone is very clearly defined. Sections AE (Fig. 5.28a) and BF (Fig. 5.28b) also show that the flow channel tilts slightly toward the Generators A and B in the respective sections. However, it is fairly symmetrical in Sections CG (Fig. 5.28c) and DH (Fig. 5.28d).

These images demonstrate very clearly that the strange results found in the first three experiments were not a consequence of an experimental procedure, but of a silo whose flow pattern does not conform very well to accepted images of silo flow patterns.

5.5.2 Mean velocity contours

The mean velocity contours at different levels for the flow in experiment BG1202 are shown in Figs 5.29a-h. These images conform quite well to the pictures drawn in Fig. 5.7. The peak value of mean velocity at a level falls with height in the silo, as the flowing zone spreads out. It falls from values around 190mm/sec at Level 1 (Fig. 5.29h) to about 13mm/sec at Level 8 (Fig. 5.29a). The smallest value of mean velocity increases with height in the silo, indicating that the materials at lower levels outside the flow channel emerged through the outlet later. This smallest value increases from about 1mm/sec at Level 1 (Fig. 5.29h) to about 4mm/sec at the highest level (Fig. 5.29a). This is entirely consistent with a funnel flow discharge with solids sloughing of the surface into a central channel.

However, the flow pattern is not exactly axisymmetric (Fig. 5.27). It is also not as neat as might be expected in a classical funnel flow. For instance, one marker in the top Level 8 has a mean velocity of 9mm/sec and lies between two markers with mean velocities of 4 and 5mm/sec (Generator F in Fig. 5.29a). This would not be expected in classical funnel flow. At the lowest level (Fig. 5.29h), a marker with a high mean velocity of 39mm/sec near the wall on Generator A is surrounded by markers with the lowest values of mean velocity in the level. However, these are small aberrations. The occurrence of funnel flow is inconvertible.

The same information is presented in vertical diametral sections in Fig. 5.30a-d. The central flowing zone is very clearly displayed in all images, and demonstrates the simplicity of this flow pattern compared with those found in the earlier experiments.

5.5.3 Computer flow visualisation

A small sample of computer images from the visualisation program is again shown here. In Fig. 5.31a, the starting positions of the markers in Section CG are shown. Only Levels 1, 5, and 8 are shown in the 3D picture to avoid congestion. This is followed in Fig. 5.31b by the beginning of flow (2 min) where a much simple behaviour is seen than was found for the earlier tests. The bottom Level 1 has moved

fastest and the levels above it have all descended sympathetically. A later stage is shown in Fig. 5.31c (4 mins), where the flow pattern can be seen to be chiefly internal funnel flow. It is approximately symmetrical in the 2D section shown but a faster flow zone around Generator A can be seen in the 3D picture. The small asymmetrical details are exaggerated somewhat in Fig. 5.31d (6 mins), but there is no doubt about the flow pattern, with all levels showing stationary material against the wall.

Other diametral cross-sections are shown in Fig. 5.32a-c. The symmetry achieved in the velocity field in Figs 5.31 is visible in Section DH (Fig. 5.32c) but not in Sections AE (Fig. 5.32a) or BF (Fig. 5.32b). However, the same interpretation of the flow pattern is sustained.

Figure 5.33 shows the bar charts for this experiment. The first three charts (with less than 15% mass is discharged) show that markers reached the outlet first from the lowest level, after which markers from higher levels gradually catch up. There are always more markers from the lower levels than from higher levels at this stage. However, once markers start to emerge from the top level, their number quickly exceeds that from the one level below (discharged mass = 20%) and then exceeds those from all the lower levels (discharged mass = 30%). Almost all the tags from the top level have passed through the outlet by the time 50% of the contents has been discharged. This is the pattern which is expected in classical funnel flow.

It should be noted that the black area of each bar chart does not represent the proportion of the stored solid at a level which has discharged. For example, the bar charts indicate that far more than 50% of the tags have emerged through the outlet when only 50% of the total stored solid has been discharged. When 80% of the contents has been discharged, almost all the tags have passed through the outlet from all levels. The reason for this is that the tags were not evenly seeded throughout the volume of the solid. They were seeded close together near the axis of the silo (Fig. 5.4) in which the solid discharges first. Further, the levels were not evenly distributed through the height of the silo. Finally, no tags were placed in the hopper at all.

5.5.4 Analysis of mass emerged from seeded levels

Having interpolated the remaining mass for the undetected markers and integrated the emerged mass for each level, the results are shown in Figs 5.34a and b as normalised mass-time curves. These curves contrast with the strange results from the previous three tests, being much simpler and agreeing well with the characteristic form for funnel flow as described in Section 5.3.5.2 (see Fig. 5.8b). The four lowest levels (Fig. 5.34a) have almost all the key features: markers from higher levels initially emerge through the outlet later than those below them but the curves soon cross over and the plateaux in the curves for lower levels are clear. At higher levels (Fig. 5.34b), the curves are initially in the expected sequence (discharged mass < 20%), but the proportion from the top Level 8 rapidly overtakes all the others. By the time 65% of the total mass has been discharged, the expected inverted sequence has been properly established, corresponding to classic internal funnel flow. However, no plateaux can be seen in them, possibly because they are so close to the top surface that the flow channel boundary is poorly defined. It may also be possible that several flow boundaries form at different stages so no single plateau can be seen on a normalised mass-time curve.

The flow is not as neat as expected in classical funnel flow in which a higher level would always be expected to be fully discharged before lower levels. The last part of the curve for Level 8 (after a discharged mass of 50%) indicates that there is a very small portion (about 3%) of the mass from this level which did not discharge for an extended period. Otherwise all the material from this level would have passed through the outlet before 50% of the mass in the silo had been discharged. This phenomenon also occurs at some lower levels (e.g. Level 6). The position of the solid which was delayed in this manner may be identified in the region of $45°<\theta<135°$ and against the silo wall from the remaining mass and mean velocity contours (Figs 5.27-30). If the last parts of each curve is removed, a clearer picture is produced. This has been done for the first five levels (Fig. 5.34a) and re-plotted in Fig. 5.34c as an example.

As noted above, when the data are presented in the form of a bar chart indicating the proportion of tags at a particular level which have emerged from the silo at a given time (Fig. 5.33), the result is misleading because different tags correspond to different volumes of solid. If instead, the volumes are attributed to individual tags, the data of Fig. 5.34 can be transformed into a set of bar charts representing different instants during the discharge, as shown in Fig. 5.35. Although the patterns of these two pictures are similar, the differences are clear. When 50% of the solid has been discharged, Figure 5.33 shows that far more than 50% of the tags have emerged through the outlet from all the levels, but Figure 5.35 shows that less than 50% of the mass has passed through the outlet from the lower levels. This difference exists at most stages of discharge.

It may be concluded that the flow is predominately funnel flow, with a small portion of solid adjacent to part of the wall being blocked for an extended time.

5.5.5 Position and size of flow channel

In sharp contrast to the first three experiments, funnel flow clearly occurs in this test. The size of the flow channel was determined from the normalised mass-time curves for different levels using the procedure described in Section 5.3.5.4. Figure 5.36 shows the deduced cross-sectional area of the flow channel at each level, which is obtained by multiplying the height of the plateau (Fig. 5.34) by the cross-sectional area of the cylinder. Because the plateaux are not very clear for the higher levels of seeded markers, subjective interpretation is inevitably involved (e.g. the slow increasing part between 33% and 47% of discharged mass was taken as the plateau for Level 8). The deduced size of the flow channel can only be an approximate measurement because

a) a relatively small number of tags was used in the experiment. As each tag is assumed to represent a portion of the cross-sectional area at that level in the silo, using more tags implies that each represents a smaller portion of the area, leading to a more precise result; and

b) errors may have been introduced during the process of interpolating the remaining mass for the tags which were not detected. Although all the data

were used to interpolate between the measurements in 3D and great care was paid to the programming, the mathematical interpolation has considerably less reliability than experimental observations.

Nevertheless, Figure 5.36 does provide a quantitative measurement of the flow channel area for the first time. It was initially thought to be strange that the channel is slightly bigger at the bottom level than at two of the higher levels (Fig. 5.36). The reason for this was subsequently discovered to be caused by the early emergence of a marker outside the main flow channel (Level 1, Ring 5, Generator H).

The starting and finishing points on the plateau may be found as m_{f1}=16% and m_{f2}=59% on the discharged mass axis for Level 1 (Fig. 5.34a). The value of remaining mass for determining the flow channel boundary at this level was obtained by substituting these numbers into Eq. 5.10. This leads to

$$M_f = \left(1 - \frac{m_{f1} + m_{f2}}{2}\right) M_0 = 125 \text{ tonnes} \qquad (5.11)$$

in which M_0 = 200.3 tonnes (Table 4.1). Therefore, any points with remaining mass greater than 125 tonnes at this level are inside the flow channel.

This procedure was applied for all the levels and the values of M_f were identified as 125, 129, 132, 131, 111, 103, 110 and 131 tonnes for Levels 1 to 8 respectively.

Contours of remaining mass with the above values at the appropriate levels may then be used to define the approximate flow channel boundary at each level. The result is shown in Fig. 5.37a where all the boundaries have been superimposed onto one figure. Each contour is labelled by its remaining mass value with a symbol to indicate its level number (e.g. L5 for Level 5). The flow channel boundary is fairly axisymmetric at lower levels with a radius of r=1.6m. However, an axisymmetric flow channel does not necessarily mean that the flow is axisymmetric. It is possible that the velocity distribution is not concentric within the flow channel, and this is clearly the case here,

as seen from the remaining mass (Fig. 5.27) and mean velocity (Fig. 5.28) contours. The flow channel expands upward and tilts toward Generators A and B and the shape is no longer circular. There is a second flow zone at Level 1 near the wall at Generator H (0°) due to one marker emerging early. There are also two smaller flow zones apart from the main one at Level 8. They are not expected in classical funnel flow and may be the cause of the less neat results in the remaining mass contours, mean velocity contours and normalised mass-time curves.

It is possible that the flow was not stable initially and some pipe flows occurred which extracted some material from places other than within the main flow channel. The flow may then have stabilised shortly after the discharge started. This is discussed further in the next section.

Some differences may exist between the size of the flow channel shown in Fig. 5.36 and that shown in Fig. 5.37a because different mathematical processes were used. Figure 5.36 was deduced by integrating the volumes attributed to markers and 3D interpolation was used to define the remaining mass for each undetected marker. By contrast, Fig. 5.37a was obtained by interpolation of data at one section only. If the former process had been used earlier in the analysis processing, the interpolated data in 3D could have been incorporated into the 2D sectional data used to draw the plots of Figs 5.27 and 28 leading to better contouring definitions.

While Fig 5.37a presents the flow channel boundaries in 2D form, giving a better definition of the position within each section, the third (vertical) dimension is totally missing. To provide a 3D image, these sections are re-plotted in Fig. 5.37b. Although the seeded levels are exactly equally spaced on the vertical coordinate in this figure (they should not be equally spaced really, see Table 4.1), it does provide a clearer picture of the complete flow channel geometry. The flow channel is almost vertical for the lower three levels but tilts a little towards Generators A and B at Level 4. It expands and inclines further one level up and touches about one third of the wall. It expands further upwards and most of the top level is within the flow funnel.

5.6 Discussion

The above results have shown that a commercial discharge aid can have a major effect on the flow pattern, leading to flows which are different from any documented in the literature.

When no air injection or discharge aid vibration was used (Test BG1202), most of the gypsum flowed out of the silo in funnel flow, with a wide flow channel that is almost as wide as the cross section of the cylinder at the top surface. The slight difference between this and classical funnel flow suggests that unstable pipe flows may have occurred at the early stages. The inverted cone of the discharge aid gives the effective response of a very large outlet. Inverted cones have been used in designs of very large silos for cement and similar products in recent years (e.g. Peter, 1983), but little information on the flow behaviour is available in the open research literature.

When the discharge aid is activated and the air injection system started, the flow changes significantly. Commercial publicity for this type of flow promotion device suggests that mass flow will result. The findings of these tests are a little different. Very high speed narrow flow channels develop through the solid, extracting a limited amount of material from near the top surface early in the discharge, whilst the remainder of the solid exhibits a broad based funnel flow which is close to mass flow. The narrow channel funnel flows can occur in many different locations in the silo, and certainly vary from one experiment to another. It is also possible that the narrow flow channels are not stable even in one experiment. The location may change from time to time.

The unpredictable aspects of the influence of the discharge aid and of air injection on the flow mode may be chiefly due to the variable effect on the stress field in the solids. The vibration of the inverted cone may continually disturb the stress field around it. The resulting stress wave may propagate through the stored solid and be reflected

when it encounters boundaries and discontinuities. As a consequence, the whole stress field may be affected. These changes in the stress field may also affect the stress wave propagation. Further, the decrease in the solids density in the flowing zone and the changes in the top surface geometry as the discharge process progresses will all affect the stress wave propagation. A combination of these effects may affect the flow from time to time, and changes of flow may affect the stress field in return.

A further complication arises because the discharge promoters are operated only at irregular intervals, like the rotary valve of the outlet. When the discharge aid stops, it may take up a position which is slightly off-centre because the gap between it and the hopper wall is filled with gypsum. Any unsymmetrical position for the cone will inevitably produce an uneven stress field in the surrounding mass. Because the arrested position may be different from time to time with random variability, the stress field may also be random, further influencing the flow pattern in a random manner.

Undoubtedly, the effect of the air injection could be even more variable. However, no test was conducted to identify the individual effect of each of these two discharge promoters due to limitation on the time available for the experiments.

It has been suggested in the previous sections that the flow may be not stable at the early stages even if the discharge is under gravity alone. Something like a narrow pipe flow may occur before the flow channel is well developed, which may not only extract a small portion of gypsum outside the flow channel but also may mix some solids from different levels. This concept could explain why some of the solids at the top level did not pass through the outlet as expected in typical funnel flow.

All the experiments showed unsymmetrical features, though it is not very pronounced when the discharge promoters are not in use. Many factors may lead to such a result. One possibility is that the opening past the upper cone of the discharge aid may have been non-uniform around the circumference: a small difference in the opening at different points can lead to a considerable difference in flow rate (mass flow rate varies

approximately as the opening size raised to the power 2.5) (Beverloo *et al*, 1961). If this is the case, it should affect all the tests, but the operation of the discharge aids may exaggerate the effect. This may be found in all the experiments if the remaining mass contours are carefully re-examined. Table 5.2 presents the estimated fast flow and slow flow zones at the bottom level for all the experiments (Figs 5.11e, 5.13i, 5.15g and 5.27h). The results from the tags placed at the discharge aid gap level in Test BG0902 (Fig. 5.17) are also presented. It is seen that a systematic pattern does exist, though the position of the fastest flowing material is different from test to test in the first three experiments. It is very possible that the gap is slightly wider on the 270° side than that on the 90° side.

Table 5.2 Fast and slow flow zones at bottom level

Test	BG2901	BG0302	BG0902	BG1202	Aid level (BG0902)
Fast flow	180°–315°	135°–280°	180°–360°	180°–360°	-180°–45°
Slow flow	20°–160°	-80°–120°	30°–160°	30°–170°	70°–150°

However, the non-symmetry of the flow could also be attributed to inhomogeneities in the solid due to the slight segregation of the solid on filling, uneven wall surfaces which result in different wall friction factors at different positions and the sensitivity of the stress condition at the bottom of a converging hopper after filling to any flow which may occur through the opening (Walker, 1966).

There is clearly scope for many additional experiments to be usefully made on this same British Gypsum silo to investigate the effect of the flow aids and the repeatability of tests without flow aids. It is evident from these tests that a complicated flow pattern results from the silo geometry and the discharge aid. The flow pattern contains very narrow unpredictable funnel flows, and these can only be explored properly by using a very dense pattern of markers within the solid. Any new experiment should be undertaken with many additional markers in carefully determined positions. In addition, the extent of segregation during filling, the variability of the gap between the flow aid and the hopper wall and the local in-situ wall friction between the gypsum

and the hopper surface near the outlet should all be investigated. However, if the flow channels do change from time to time in a random manner in one experiment as suggested here, difficulties may still exist in interpreting the results even if a very large number of markers is used.

5.7 Conclusions

Many different interpretation techniques have been developed and used to interpret the observations carried out on the British Gypsum silo. All of them have led to similar conclusions, but only the analyses of mass emerged from seeded levels can quantitatively determine the size of the flow channel.

When the discharge aid is not being vibrated and no injected air is used, the flow pattern in the silo has been found to be a broad-based funnel flow, occupying a zone as wide as if the inverted cone and its surrounding gap were virtually all one large outlet. The flow channel is fairly concentric in the lower part of the silo but becomes unsymmetrical at higher levels. It touches one side of the silo wall half way up the cylinder and contains almost all the cross section of the cylinder at the top surface, so that the surface appearance is of mass flow. In addition, unstable pipe flows may have occurred at the early stages before the wide stable flow channel was formed.

By contrast, when discharge aids are in operation, a complex flow pattern results. Narrow pipe funnel flows with 3D features rise to the surface and result in rapid movement of a limited amount of material from the top surface to the outlet. This pattern is superimposed on a broad funnel flow which is similar to mass flow. The location of the narrow pipe funnel flows is unpredictable and varies rather randomly from one experiment to another. It is also possible that the narrow pipe flow is not stable but changes from time to time in a random manner even in a single experiment. The flow cannot be described as reproducible in a quantitative sense.

The tests revealed behaviour which was not expected in the silo. The test results, and some imponderable questions associated with their interpretation, suggest that a further series of tests on the same silo would be most useful.

5.8 Notation

A	that part of the cross-sectional area from which solids have reached the outlet
A_0	cross-sectional area of the silo at a chosen height
A_f	cross-sectional area of the flow channel at a chosen height
M	remaining mass
M_0	total mass in the silo before discharge
M_d	mass discharged
M_f	reaming mass for defining the flow channel boundary
M_l	mass emerged from a layer
M_{l0}	total mass of a layer
T	residence time of a marker
T_0	total discharge time
m	normalised mass discharged
m_{f1}	start coordinate of a plateau on the normalised discharged mass axis
m_{f2}	end coordinate of a plateau on the normalised discharged mass axis
γ	density of solid
μ	normalised mass emerged from a layer
μ_f	normalised size of flow channel at a layer
τ	normalised residence time

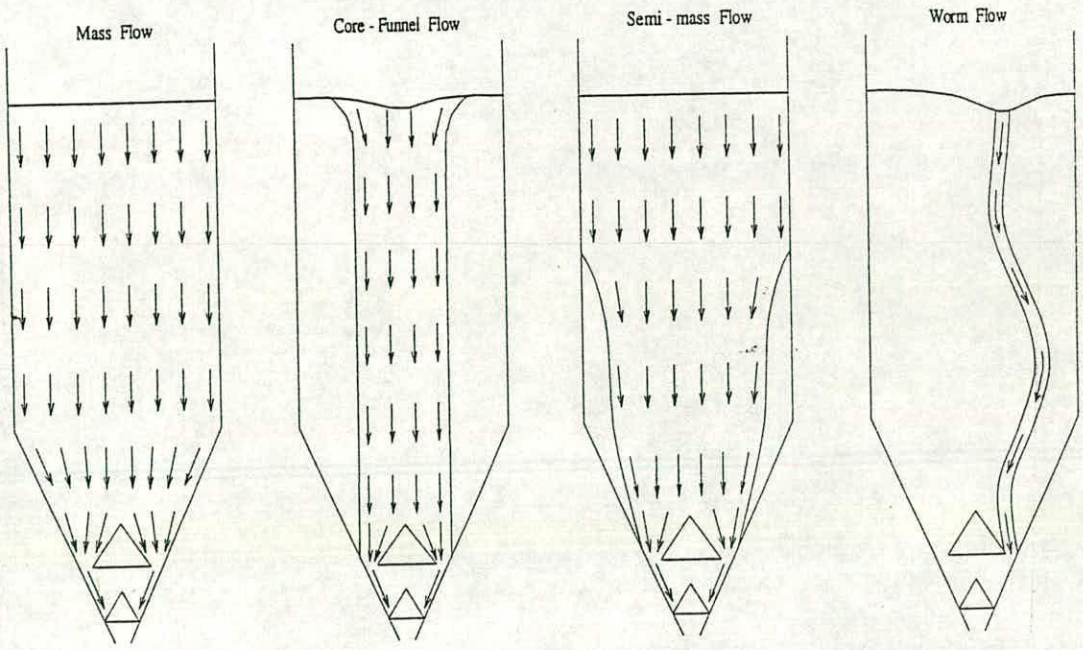

Fig. 5.1 Flow patterns expected in this silo in axisymmetric flow

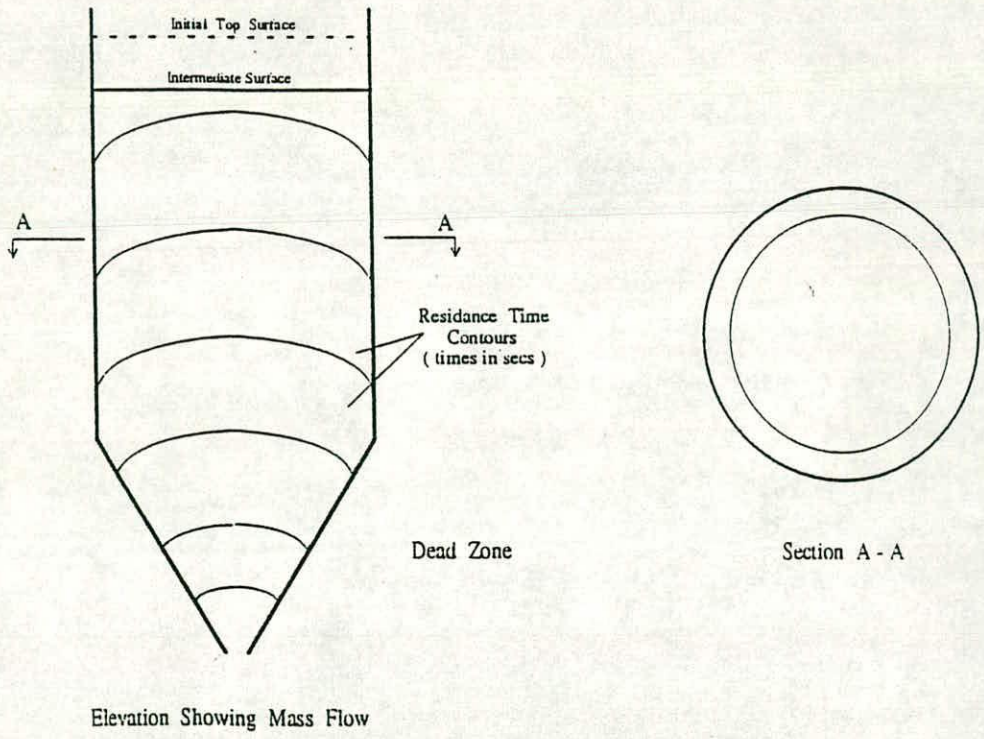

Fig. 5.2 Residence time contours for markers in mass flow

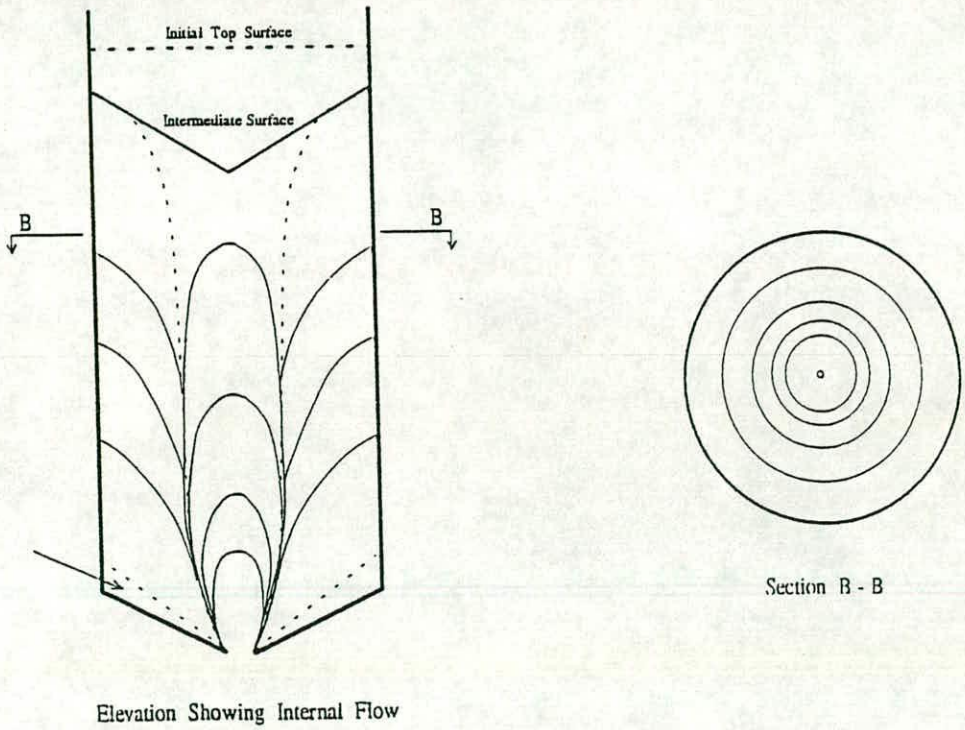

Fig. 5.3 Residence time contours for markers in funnel flow

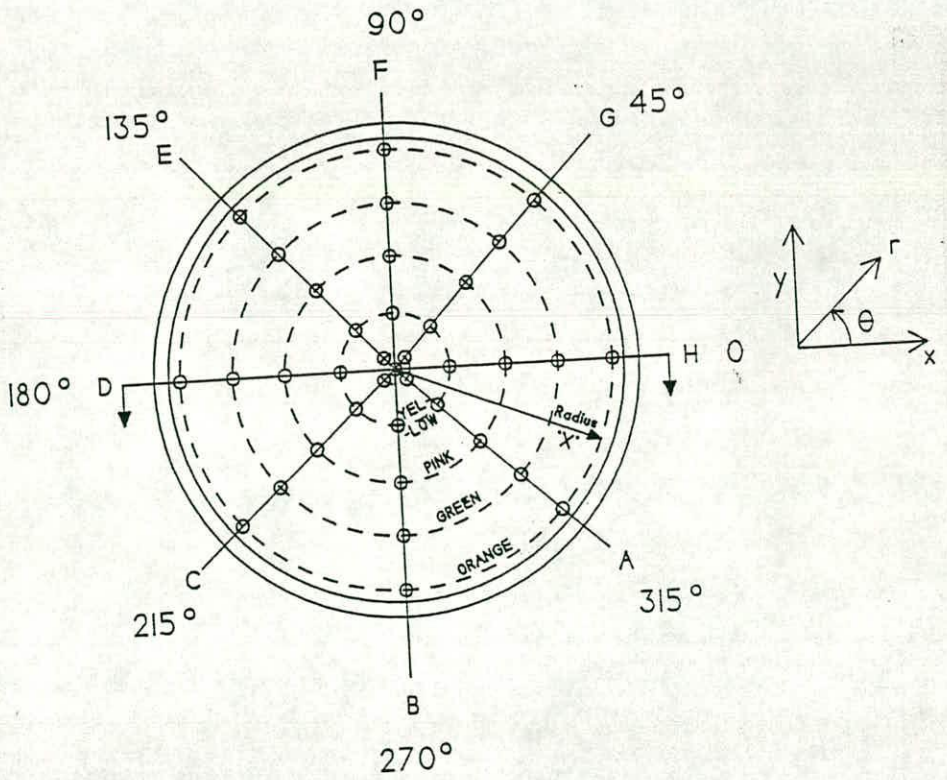

Fig. 5.4 Plan of marker layout

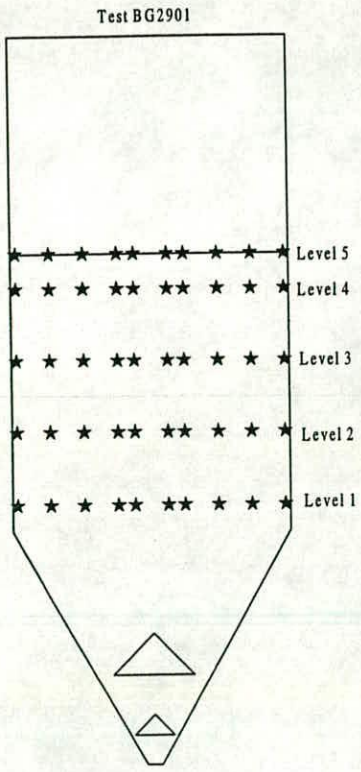

a) Test BG2901

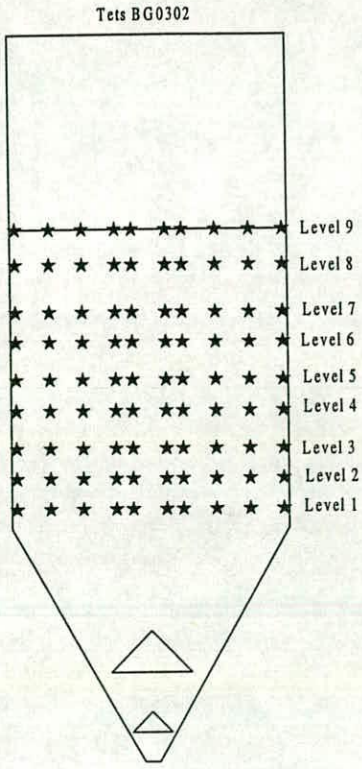

b) Test BG0302

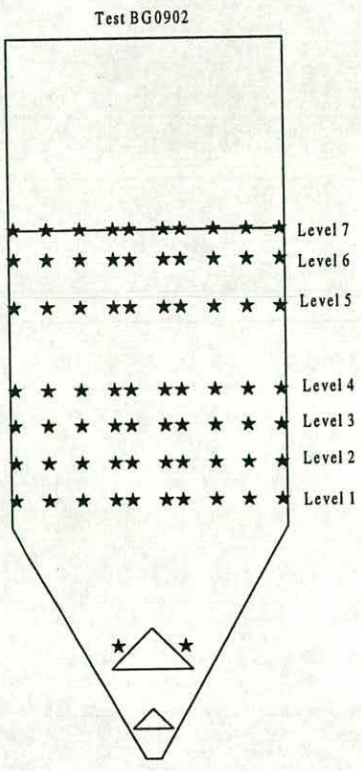

c) Test BG0902

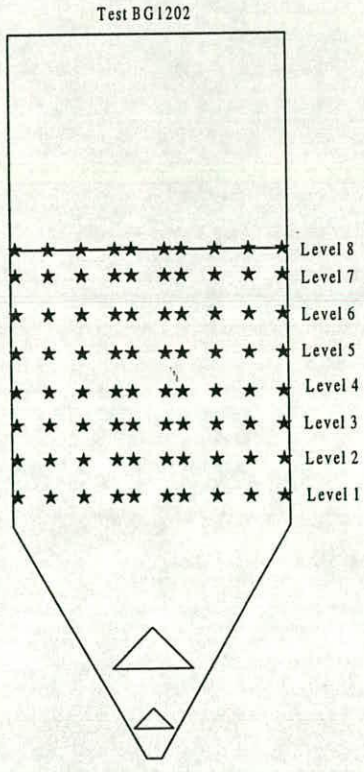

d) Test BG1202

Fig. 5.5 Seeding levels in the tests at British Gypsum

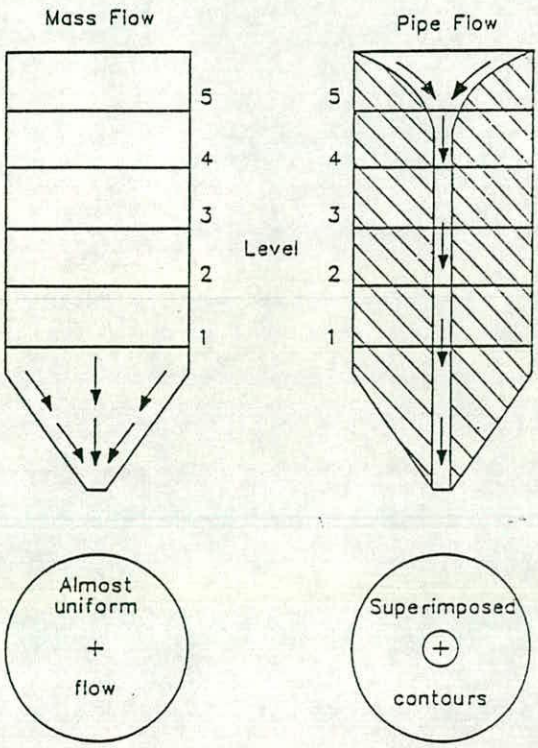

Fig. 5.6 Recognising flow patterns from mean velocity contours (mass and pipe flow)

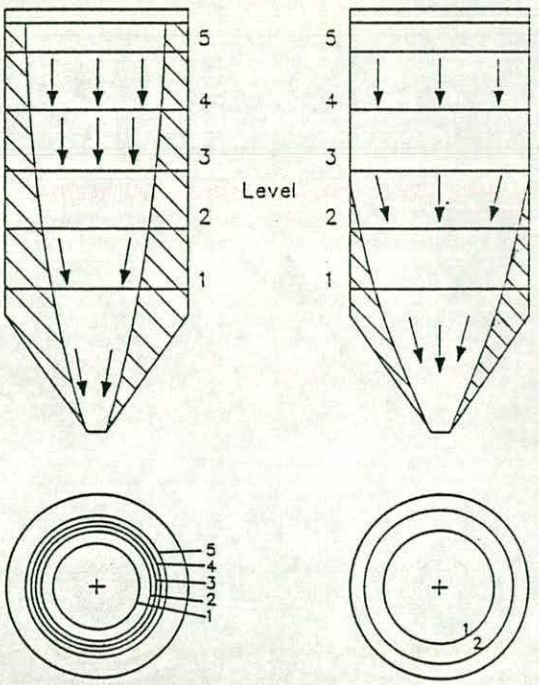

Fig. 5.7 Recognising flow patterns from mean velocity contours (funnel and semi-mass flow)

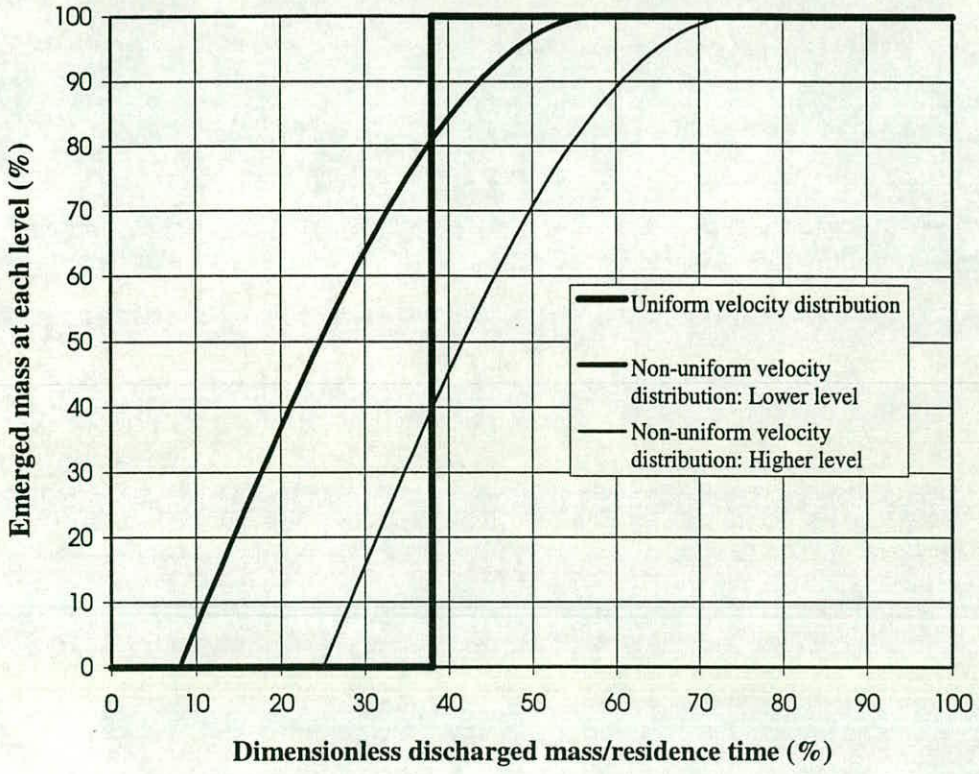

Fig. 5.8a Characteristics of emerged mass at a horizontal level: mass flow

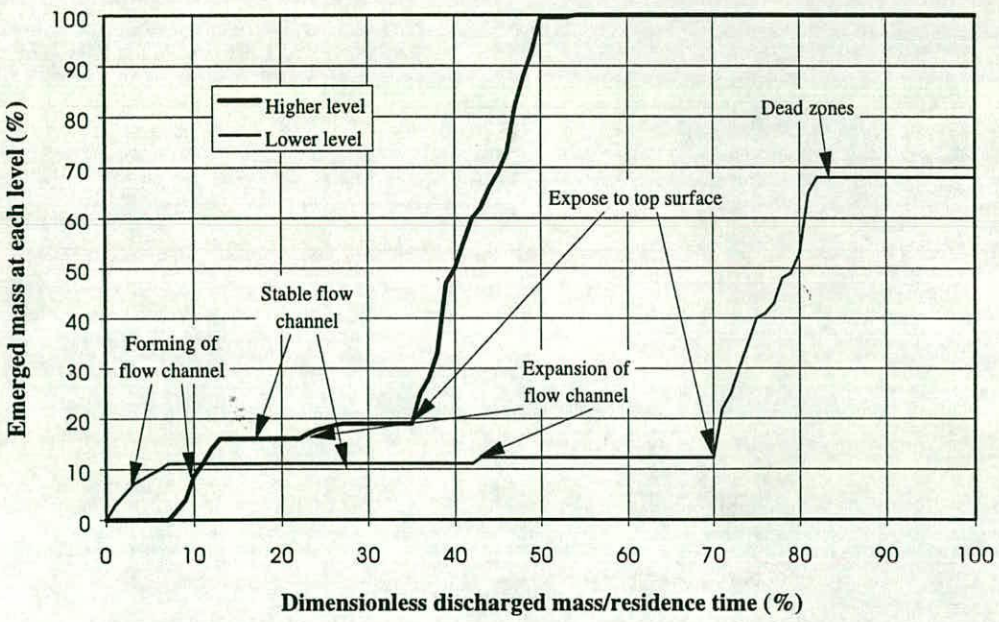

Fig. 5.8b Characteristics of emerged mass at a horizontal level: funnel flow

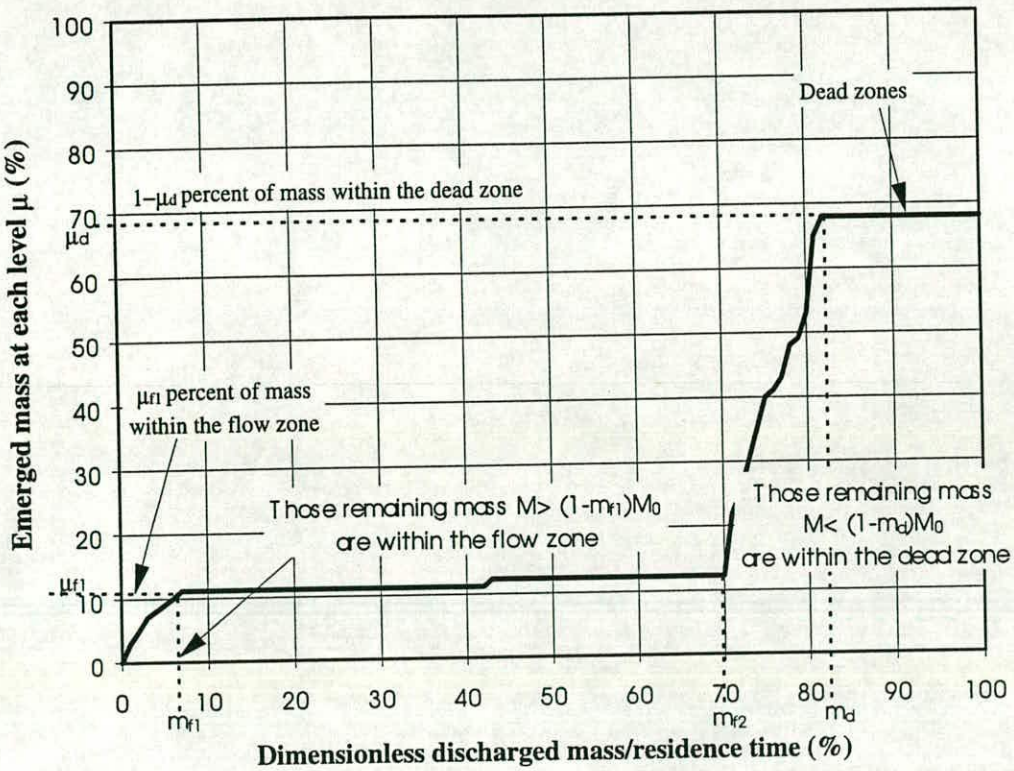

Fig. 5.9 Determination of the flow channel size

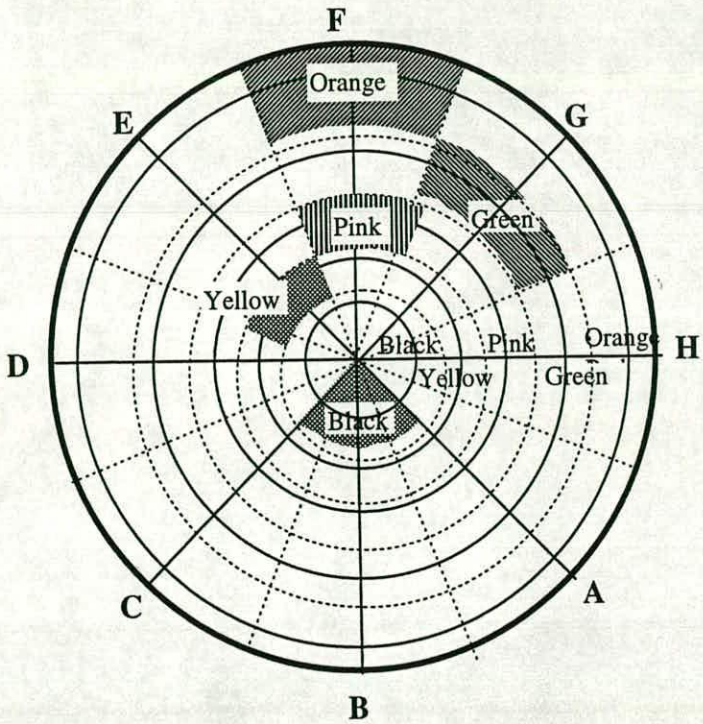

Fig. 5.10 Areas represented by markers at different rings

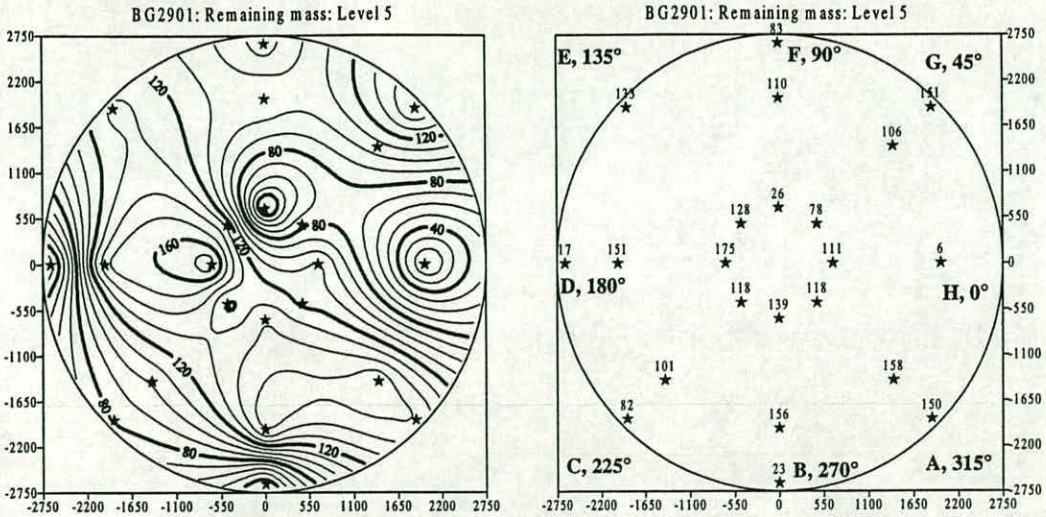

Fig. 5.11a BG2901: Remaining mass: Level 5: Contours and spot values

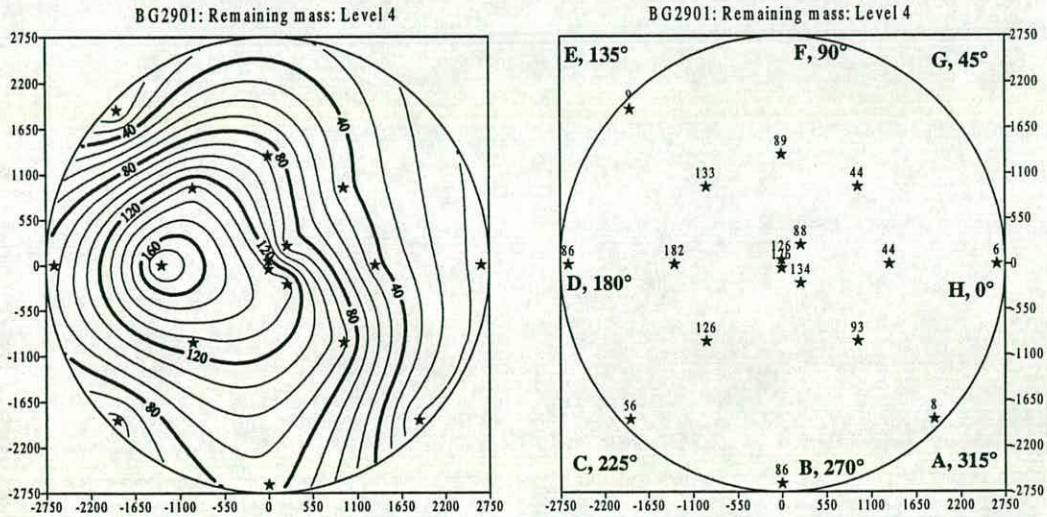

Fig. 5.11b BG2901: Remaining mass: Level 4: Contours and spot values

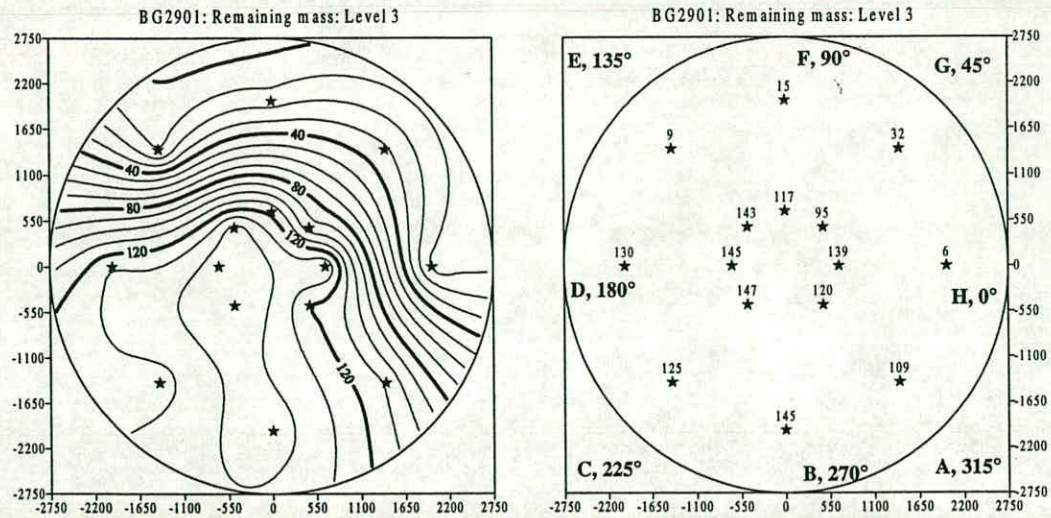

Fig. 5.11c BG2901: Remaining mass: Level 3: Contours and spot values

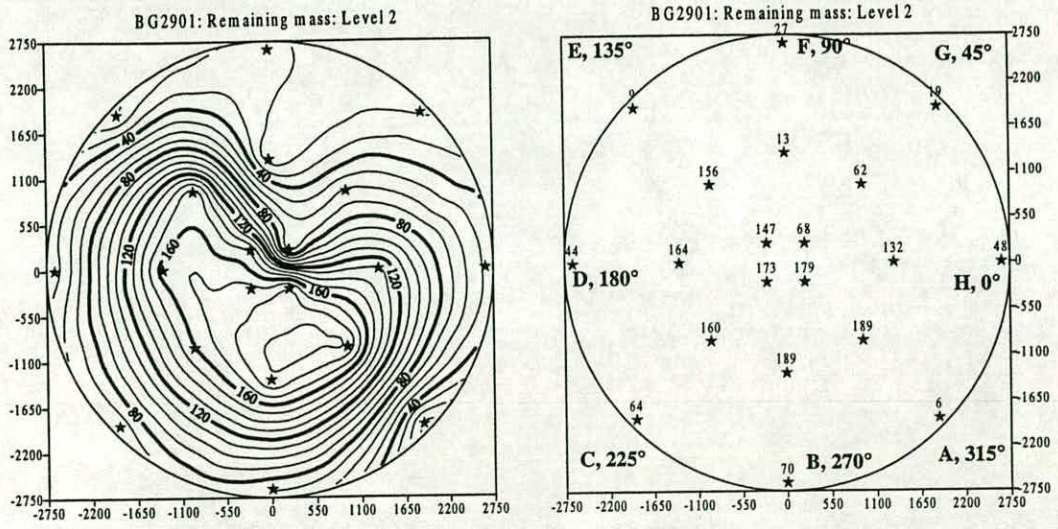

Fig. 5.11d BG2901: Remaining mass: Level 2: Contours and spot values

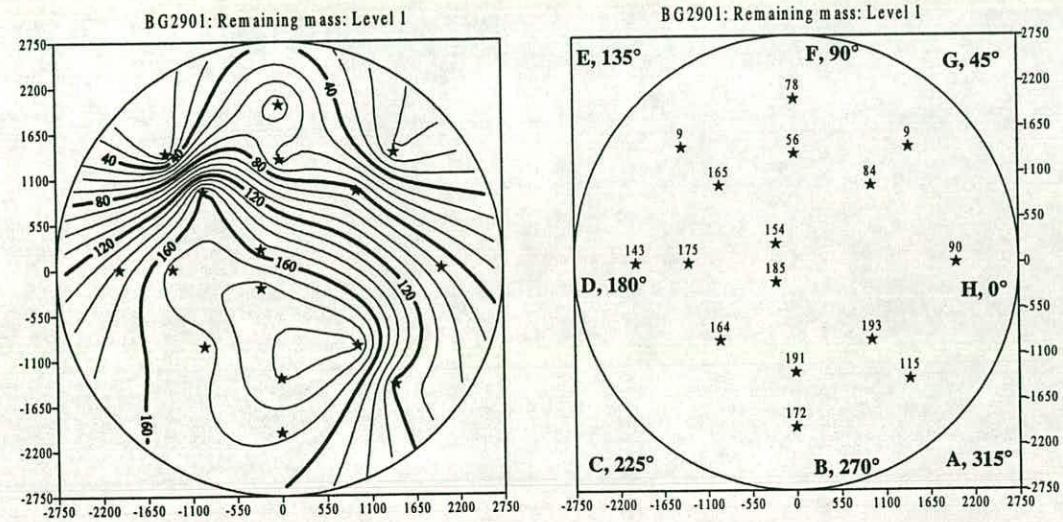

Fig. 5.11e BG2901: Remaining mass: Level 1: Contours and spot values

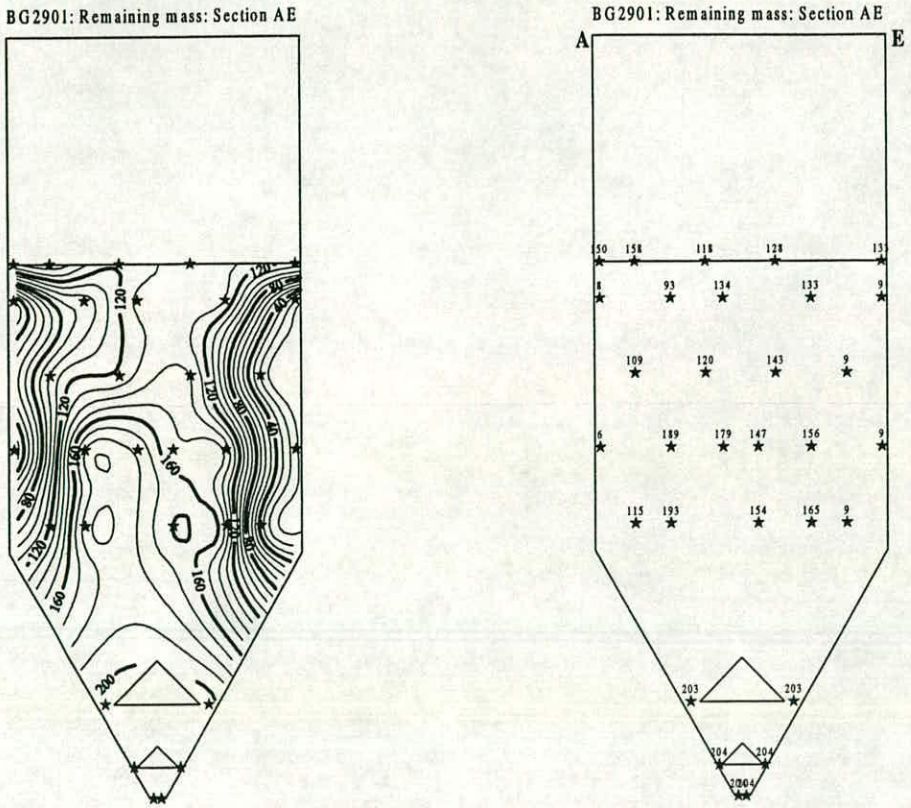

Fig. 5.12a BG2901: Remaining mass: Vertical diametral section A-E: Contours and spot values

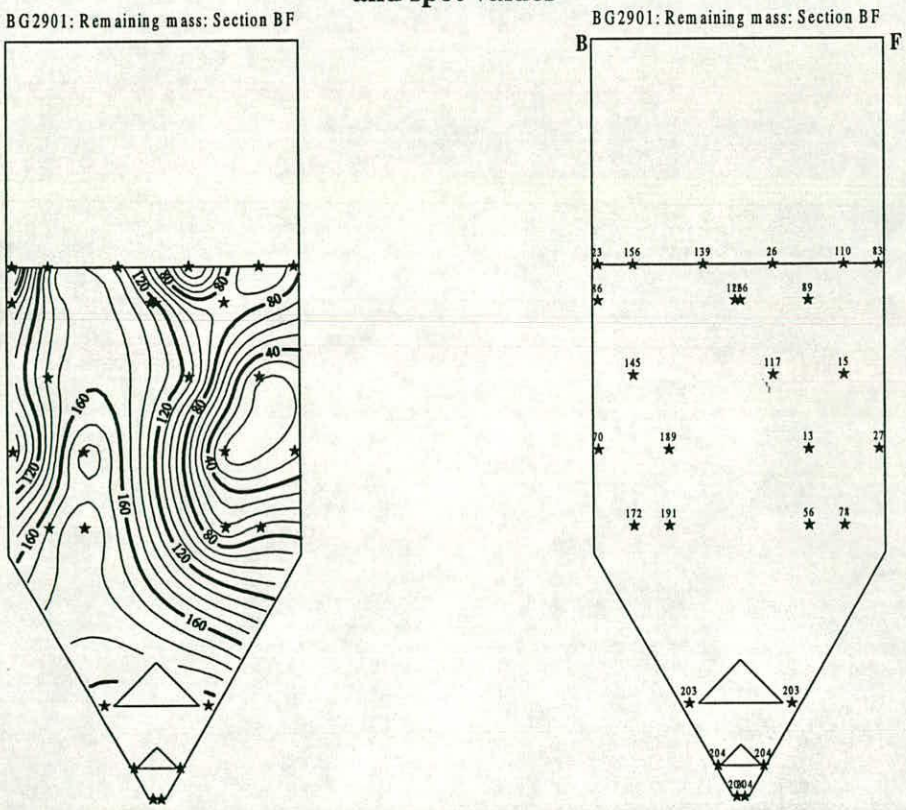

Fig. 5.12b BG2901: Remaining mass: Vertical diametral section B-F: Contours and spot values

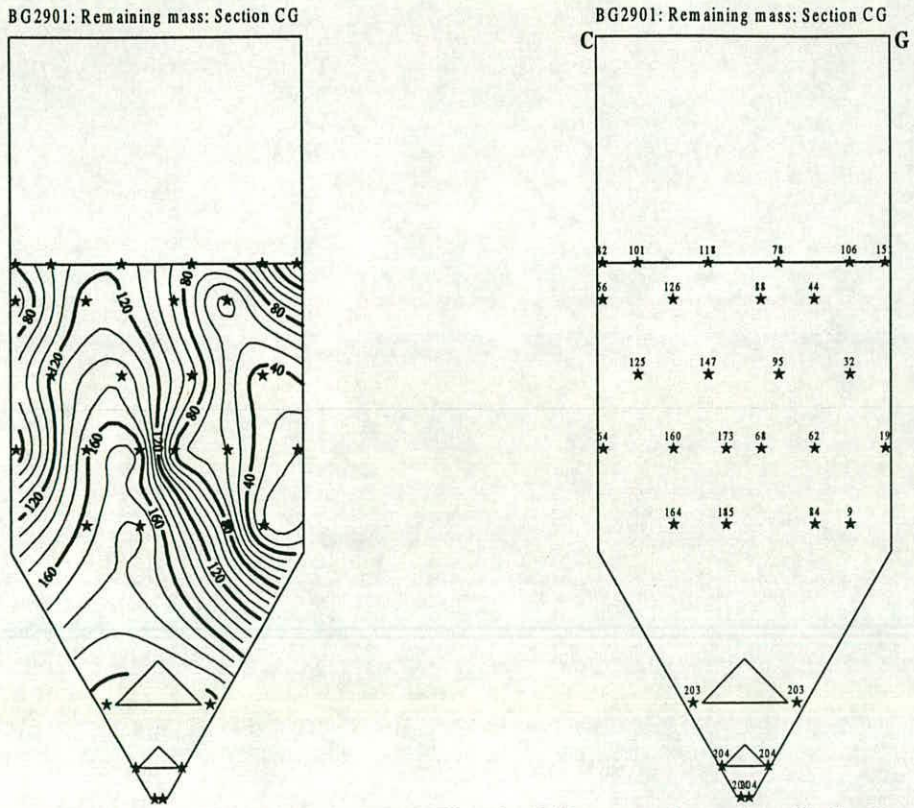

Fig. 5.12c BG2901: Remaining mass: Vertical diametral section C-G: Contours and spot values

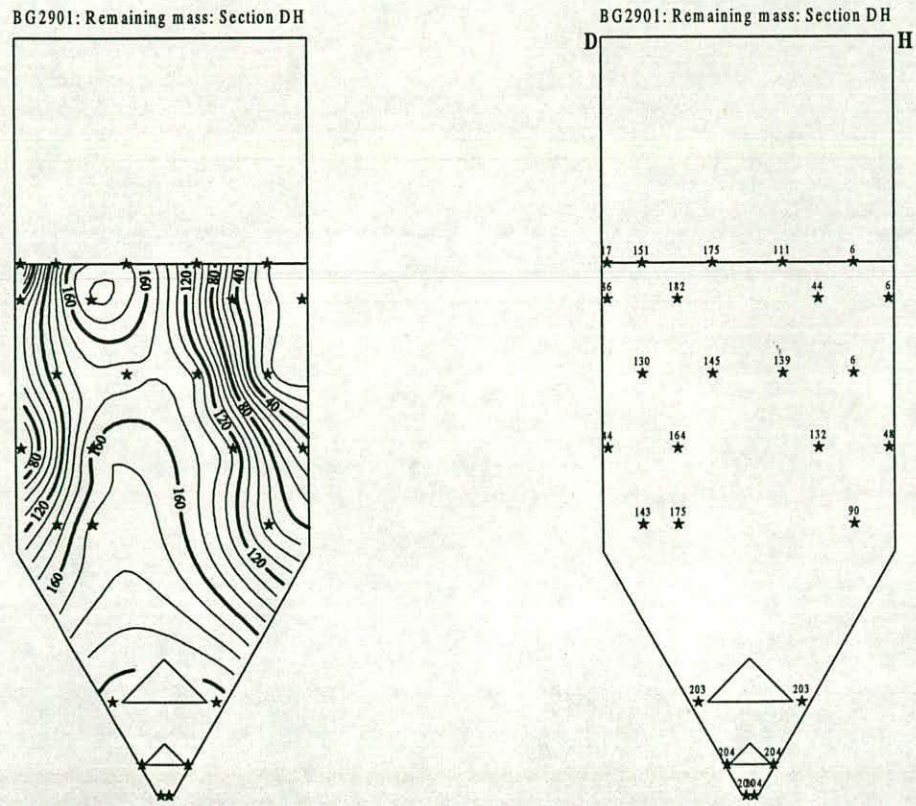

Fig. 5.12d BG2901: Remaining mass: Vertical diametral section D-H: Contours and spot values

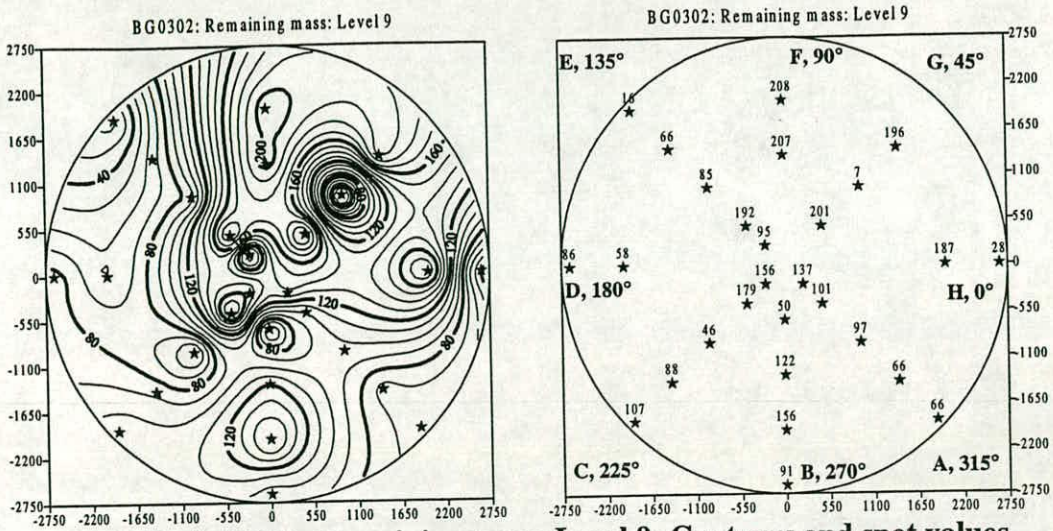

Fig. 5.13a BG0302: Remaining mass: Level 9: Contours and spot values

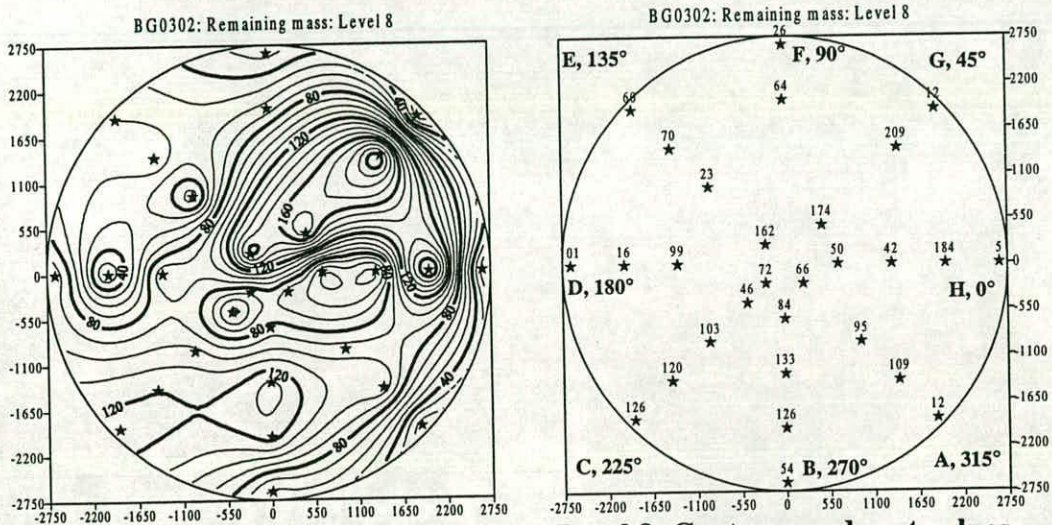

Fig. 5.13b BG0302: Remaining mass: Level 8: Contours and spot values

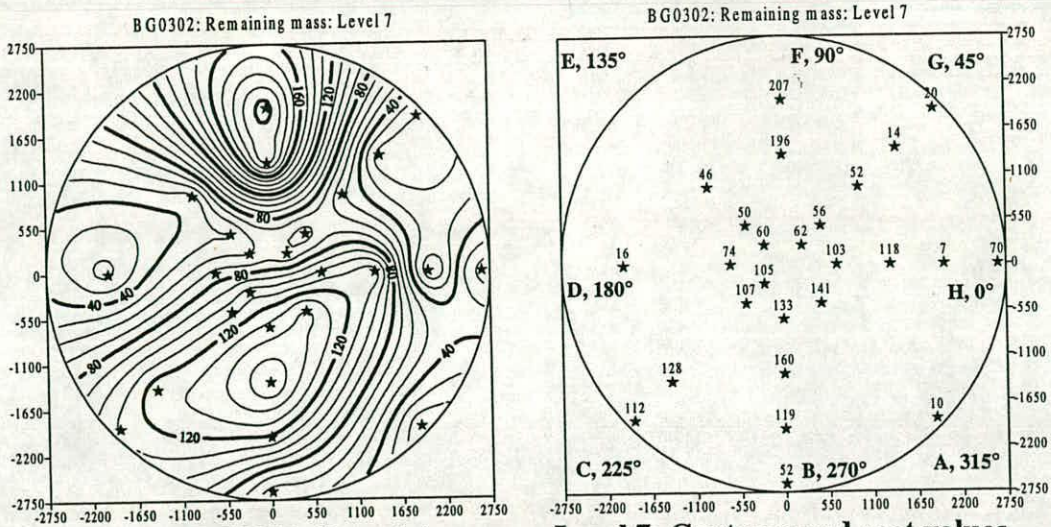

Fig. 5.13c BG0302: Remaining mass: Level 7: Contours and spot values

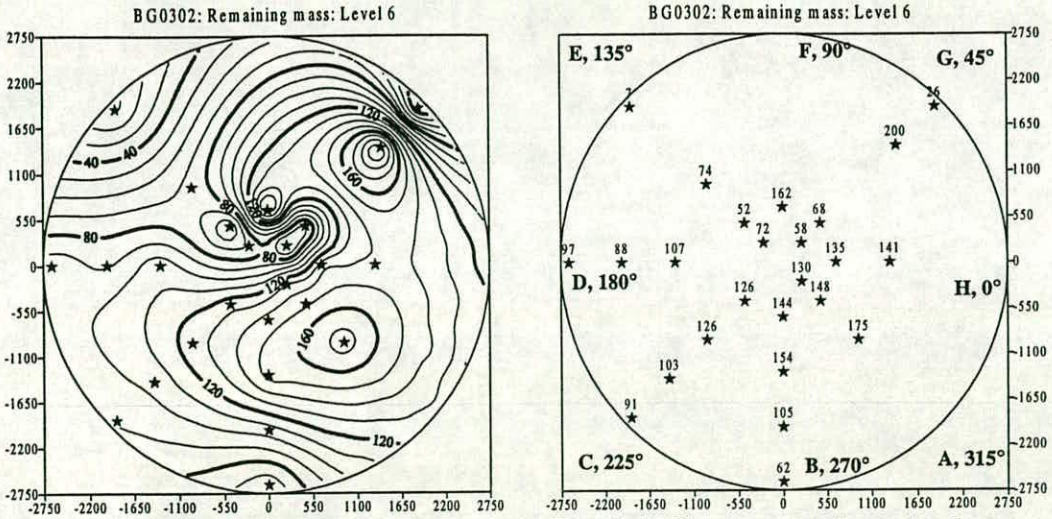

Fig. 5.13d BG0302: Remaining mass: Level 6: Contours and spot values

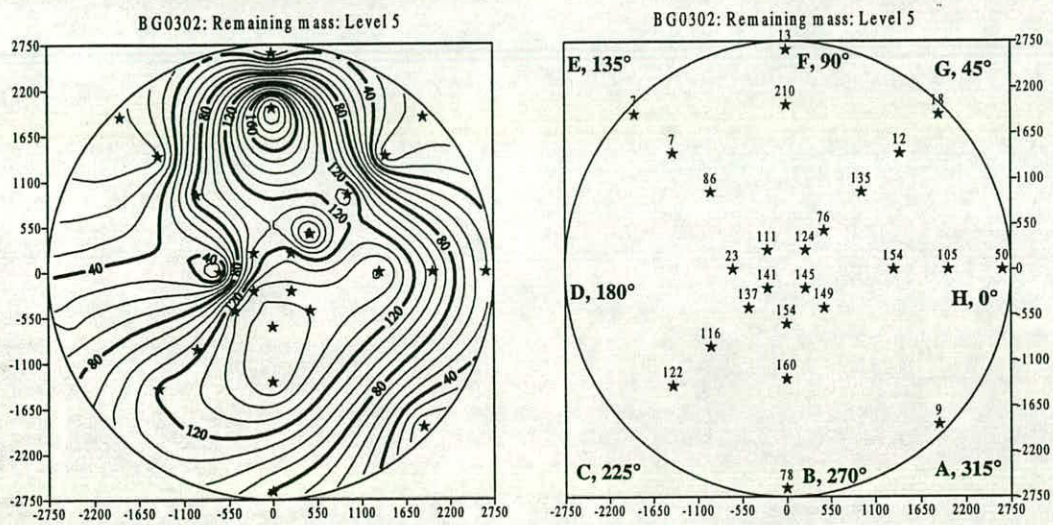

Fig. 5.13e BG0302: Remaining mass: Level 5: Contours and spot values

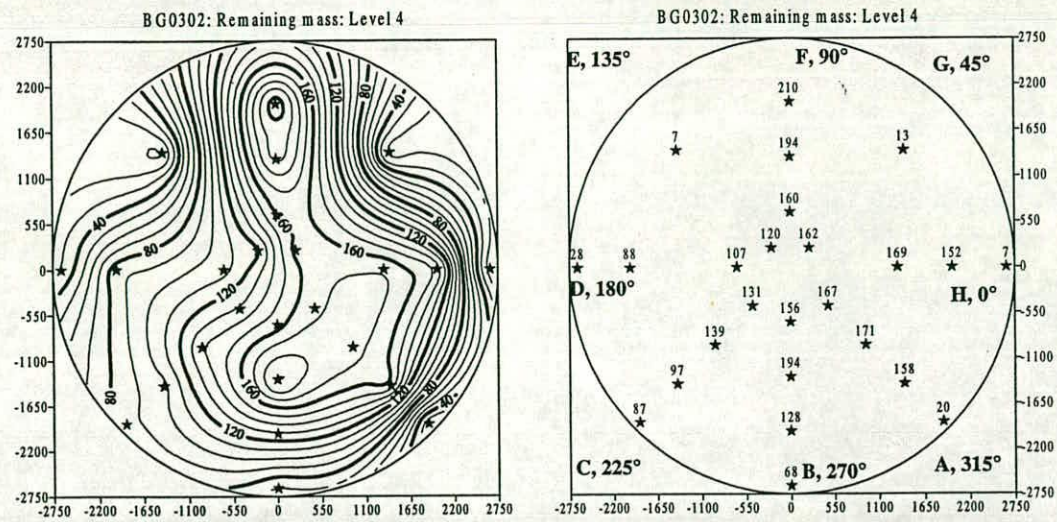

Fig. 5.13f BG0302: Remaining mass: Level 4: Contours and spot values

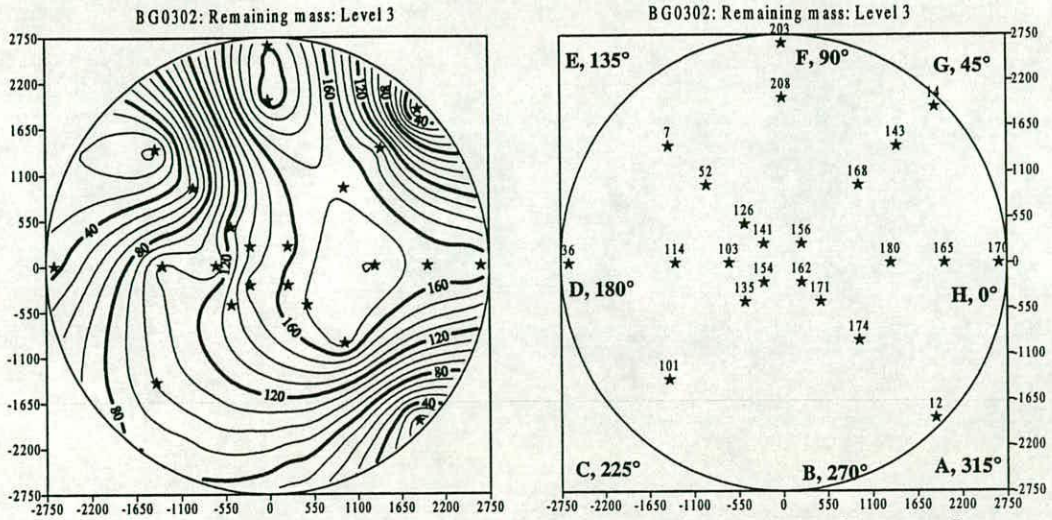

Fig. 5.13g BG0302: Remaining mass: Level 3: Contours and spot values

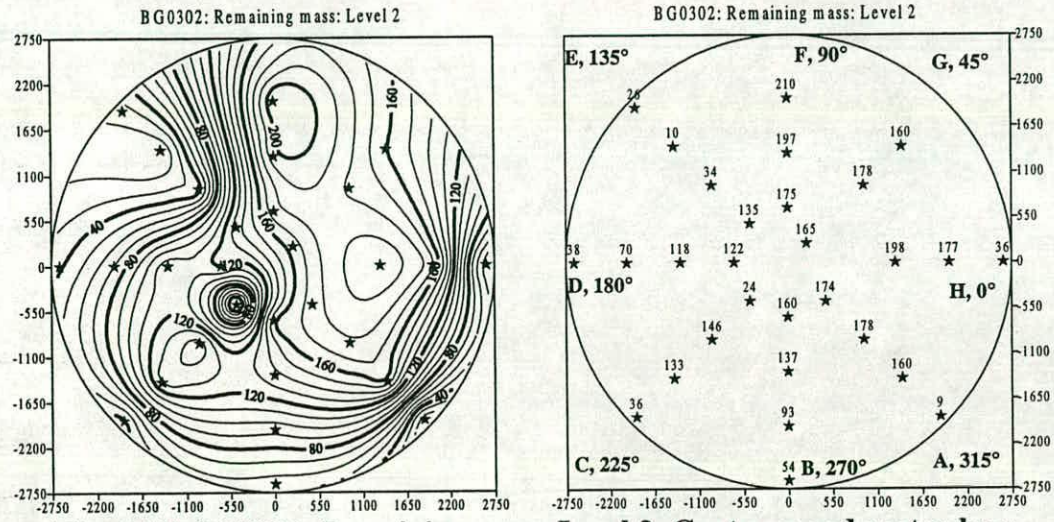

Fig. 5.13h BG0302: Remaining mass: Level 2: Contours and spot values

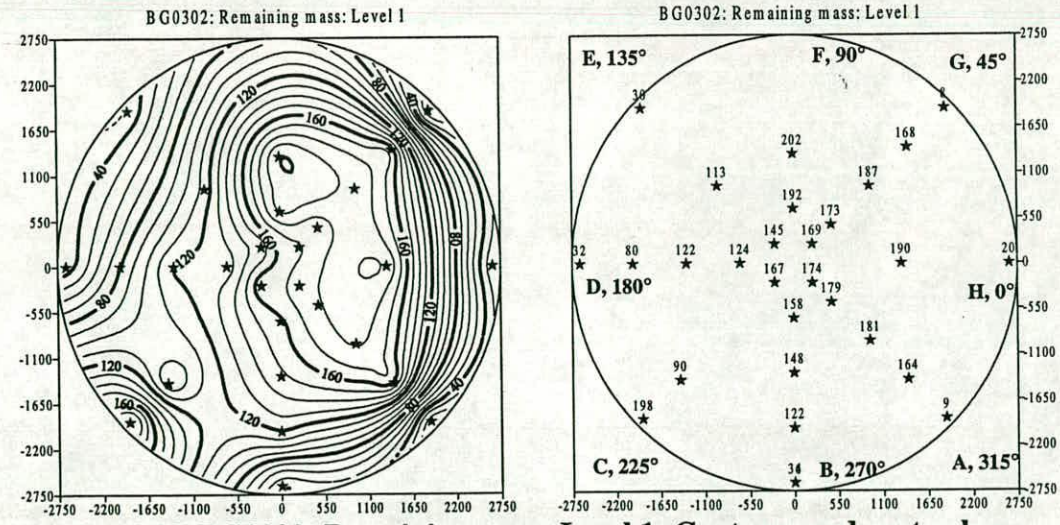

Fig. 5.13i BG0302: Remaining mass: Level 1: Contours and spot values

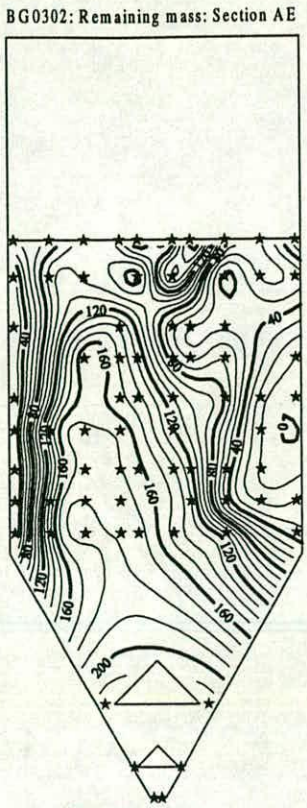

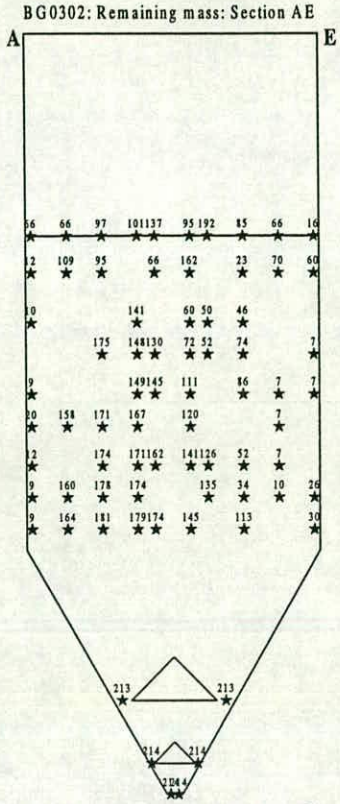

Fig. 5.14a BG0302: Remaining mass: Vertical diametral section A-E: Contours and spot values

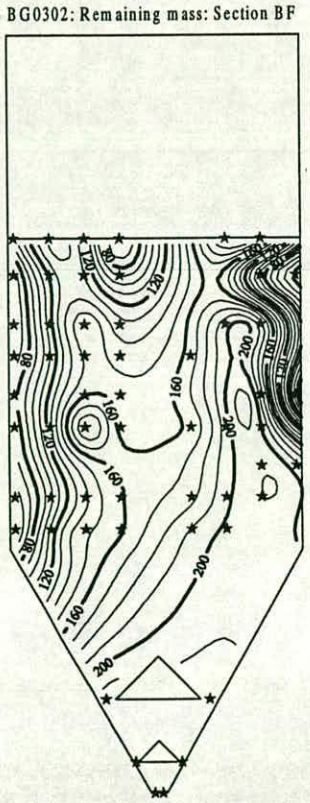

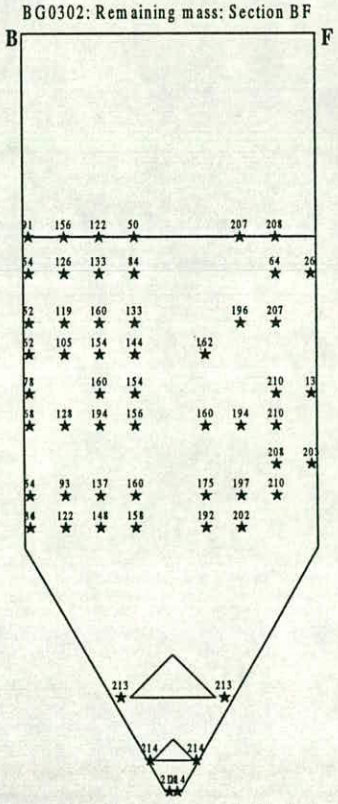

Fig. 5.14b BG0302: Remaining mass: Vertical diametral section B-F: Contours and spot values

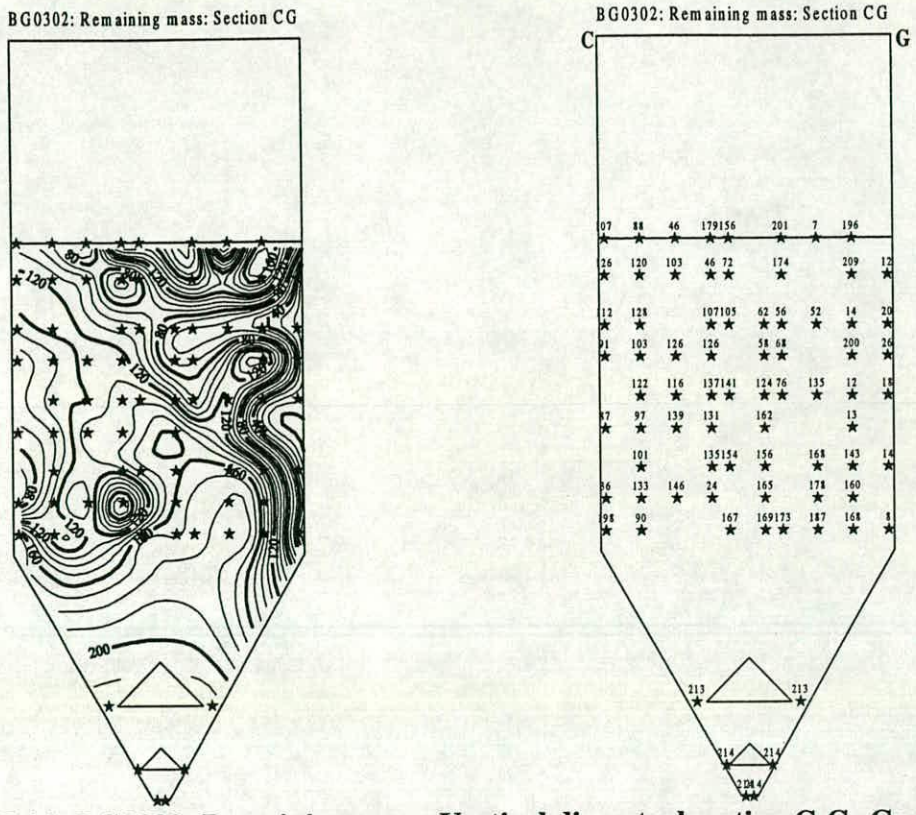

Fig. 5.14c BG0302: Remaining mass: Vertical diametral section C-G: Contours and spot values

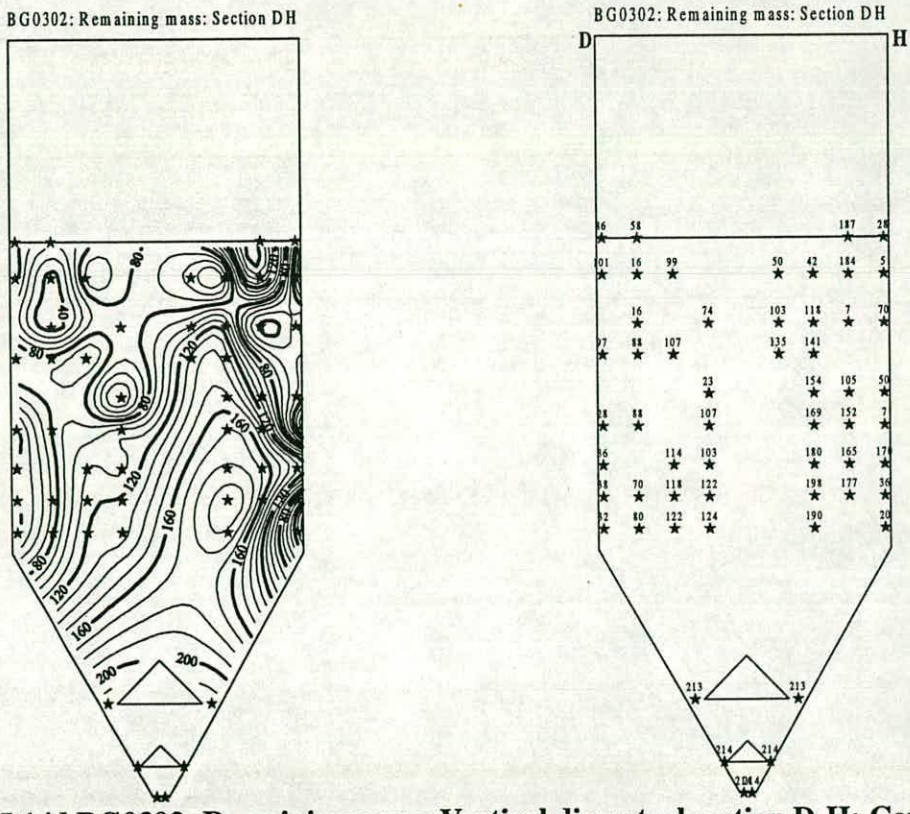

Fig. 5.14d BG0302: Remaining mass: Vertical diametral section D-H: Contours and spot values

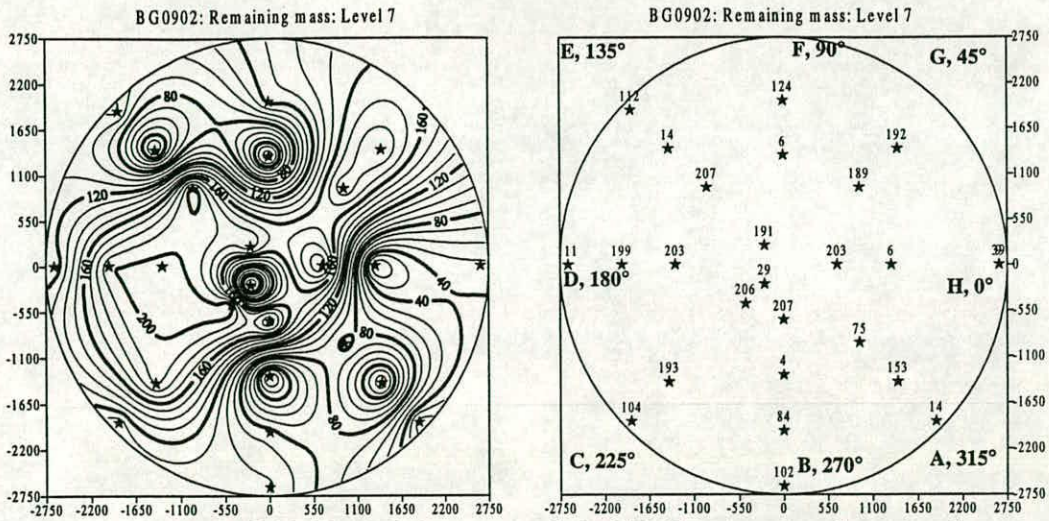

Fig. 5.15a BG0902: Remaining mass: Level 7: Contours and spot values

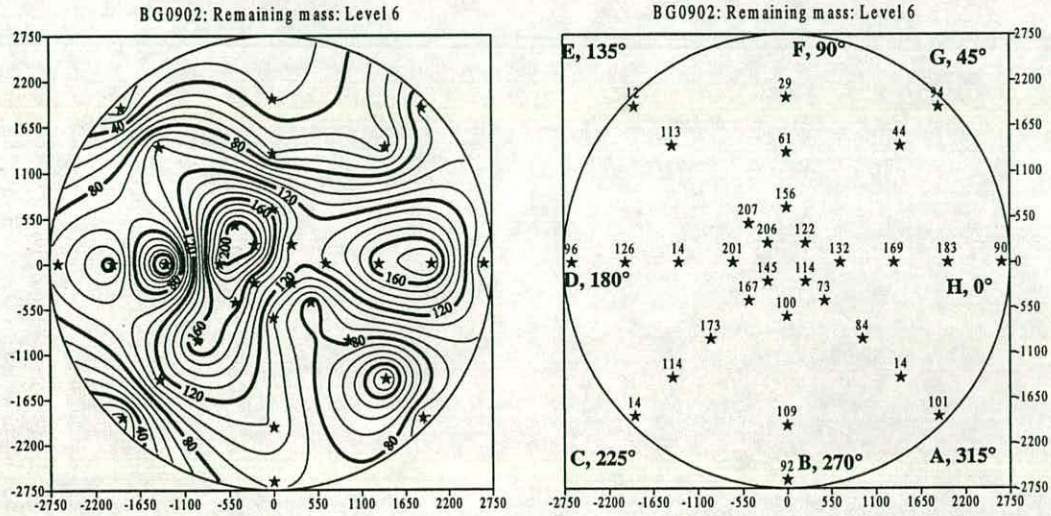

Fig. 5.15b BG0902: Remaining mass: Level 6: Contours and spot values

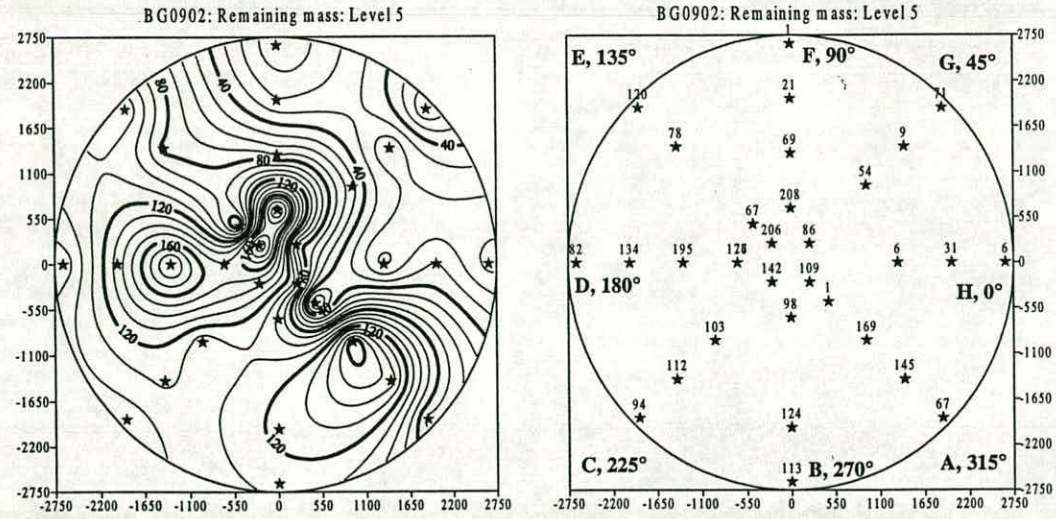

Fig. 5.15c BG0902: Remaining mass: Level 5: Contours and spot values

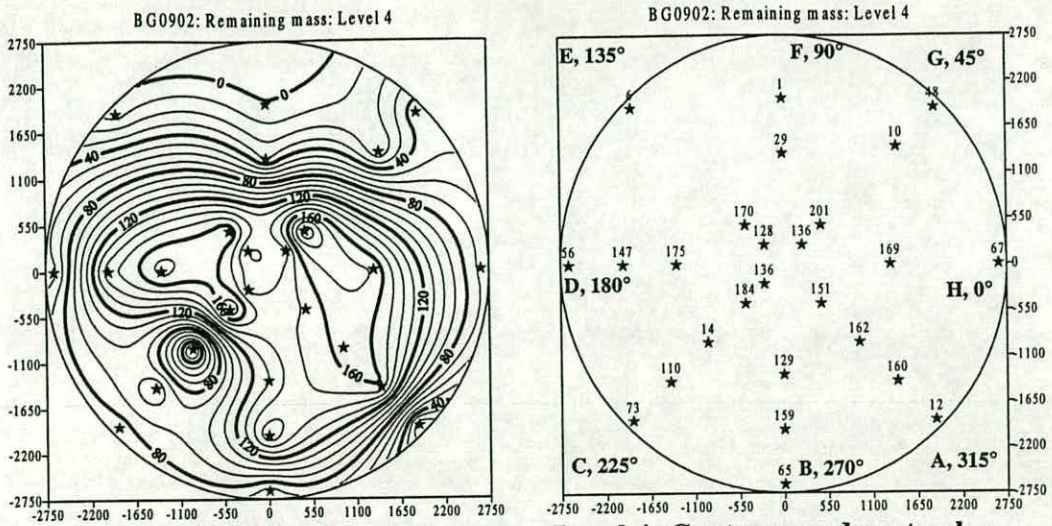

Fig. 5.15d BG0902: Remaining mass: Level 4: Contours and spot values

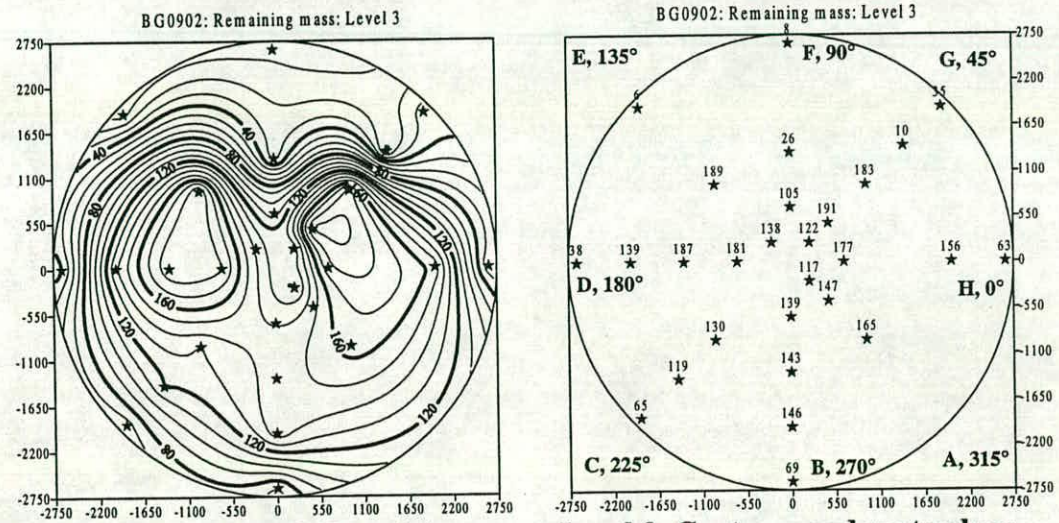

Fig. 5.15e BG0902: Remaining mass: Level 3: Contours and spot values

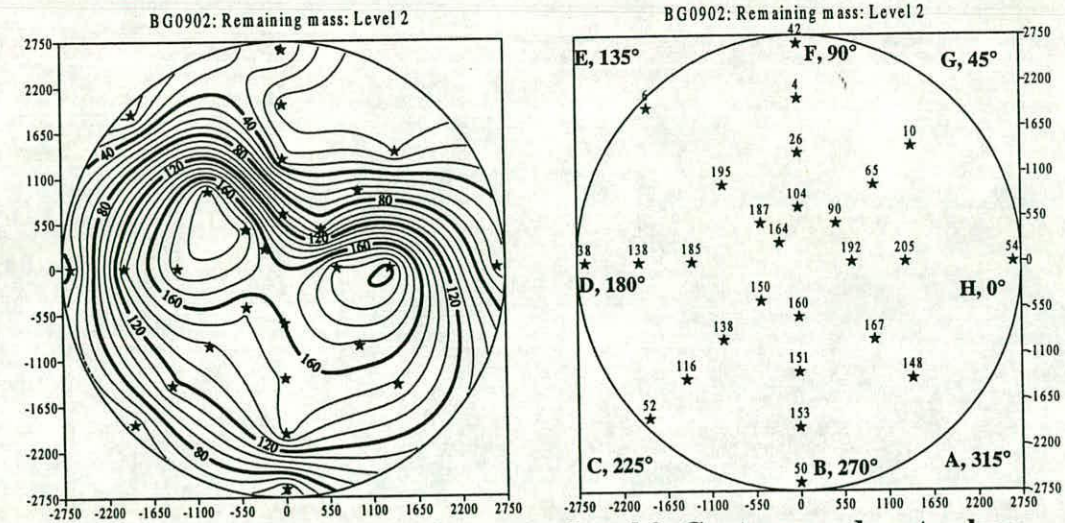

Fig. 5.15f BG0902: Remaining mass: Level 2: Contours and spot values

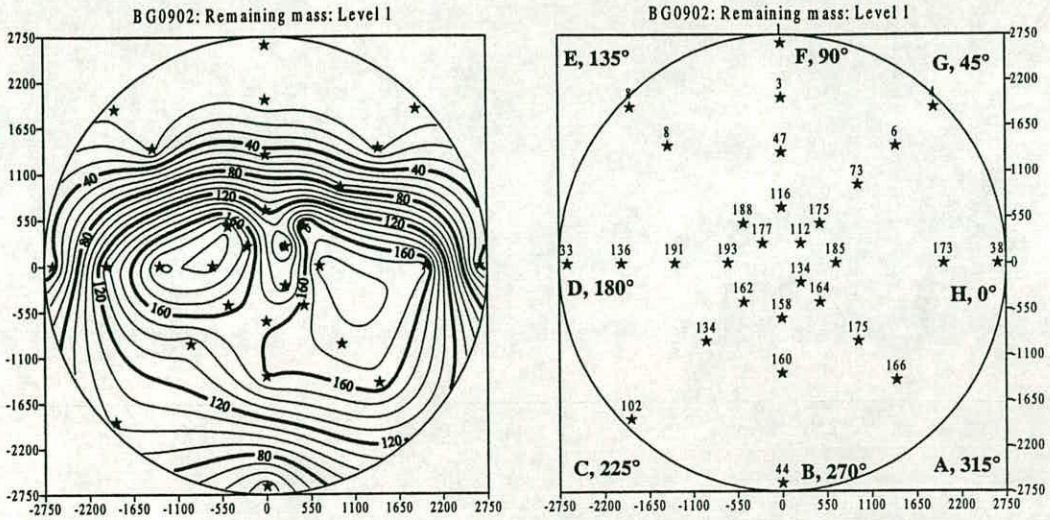

Fig. 5.15g BG0902: Remaining mass: Level 1: Contours and spot values

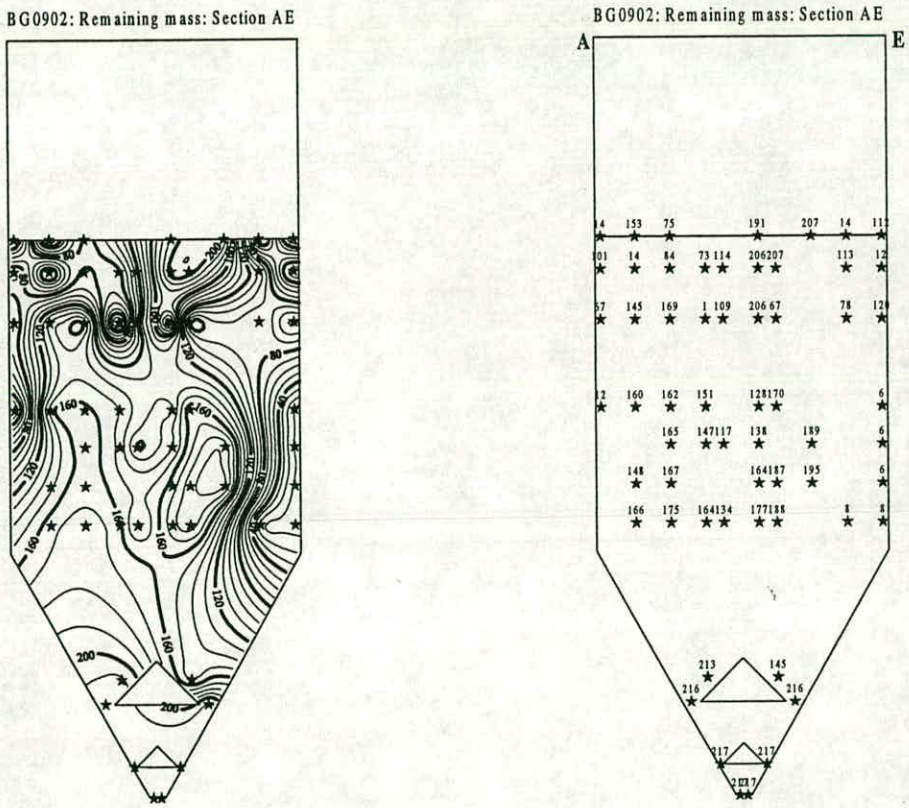

Fig. 5.16a BG0902: Remaining mass: Vertical diametral section A-E: Contours and spot values

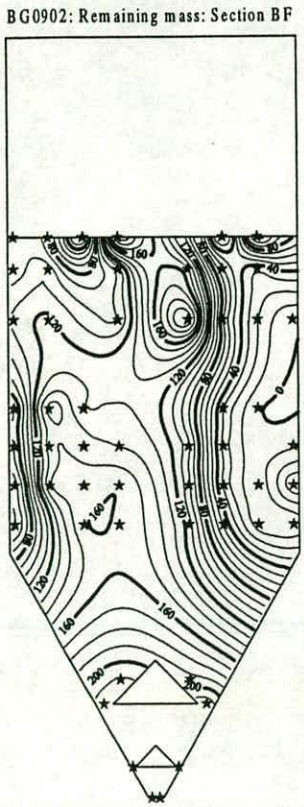

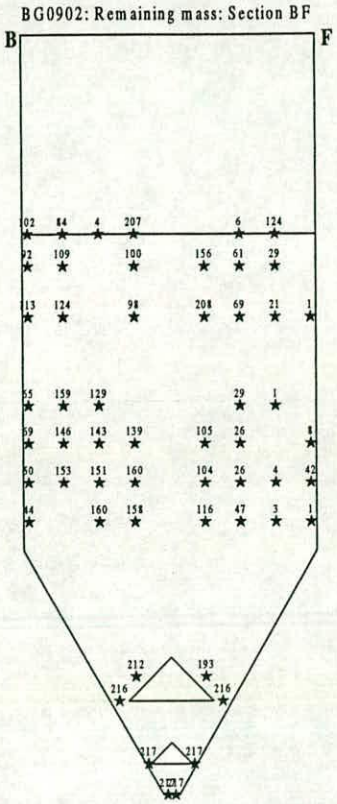

Fig. 5.16b BG0902: Remaining mass: Vertical diametral section B-F: Contours and spot values

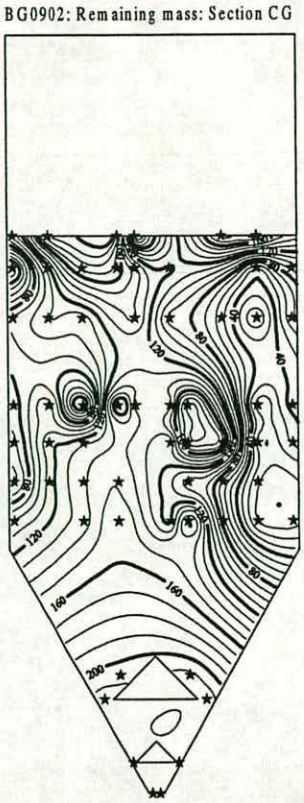

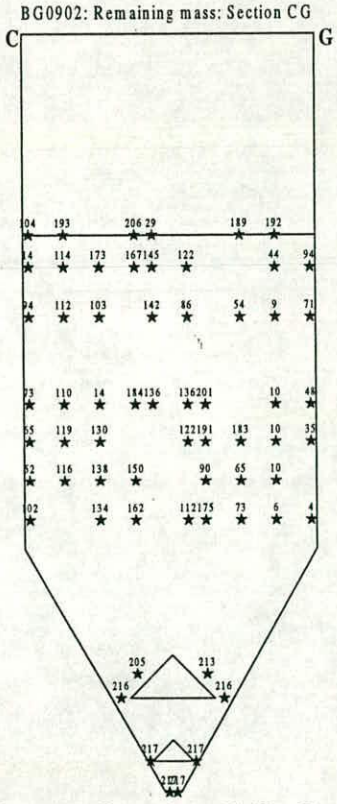

Fig. 5.16c BG0902: Remaining mass: Vertical diametral section C-G: Contours and spot values

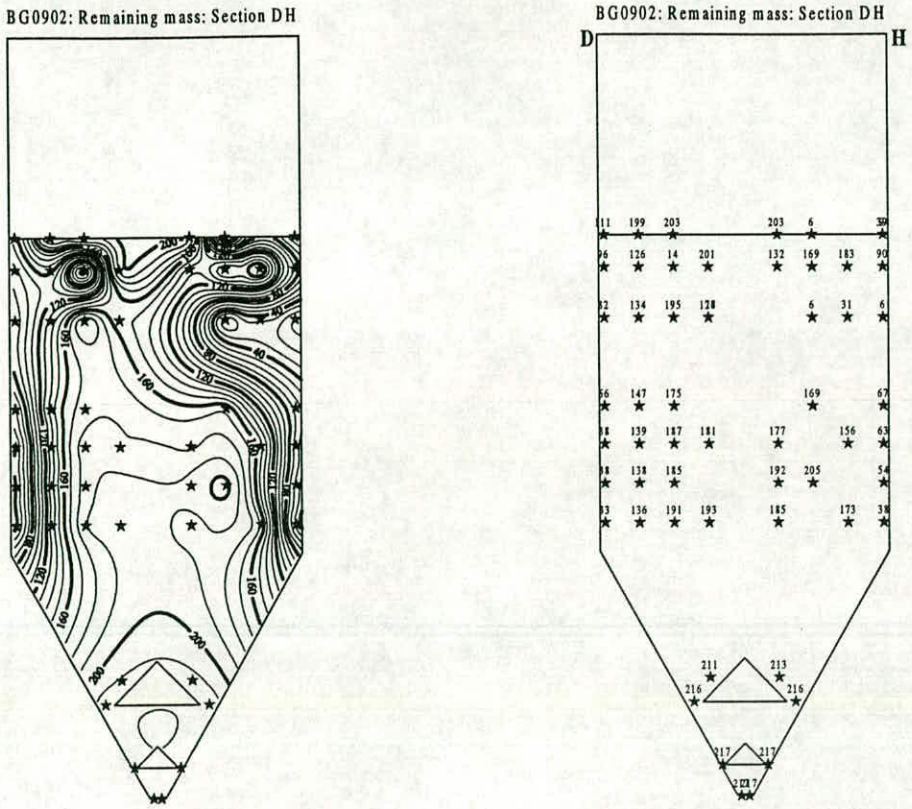

Fig. 5.16d BG0902: Remaining mass: Vertical diametral section D-H: Contours and spot values

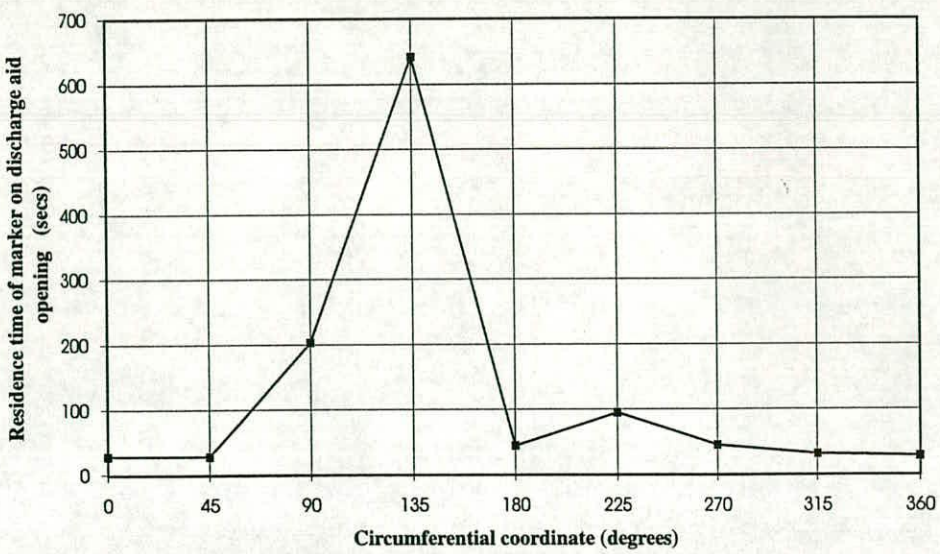

Fig. 5.17 Variation of discharge aid effectiveness with circumferential position

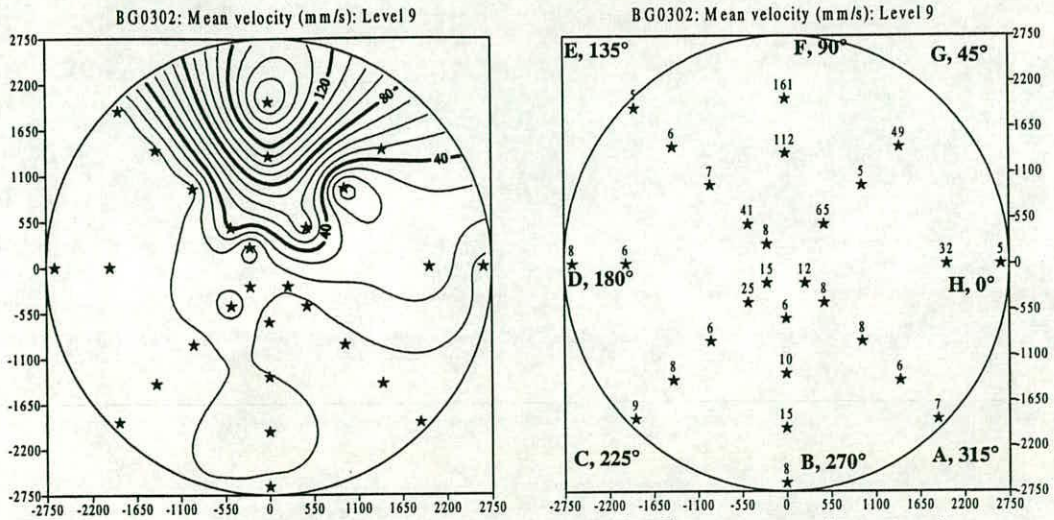

Fig. 5.18a BG0302: Mean velocity: Level 9: Contours and spot values

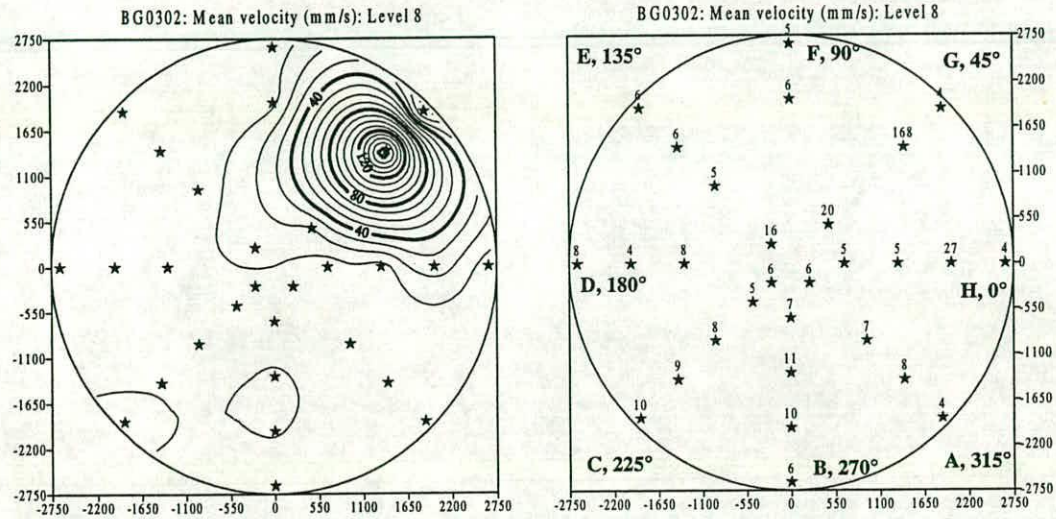

Fig. 5.18b BG0302: Mean velocity: Level 8: Contours and spot values

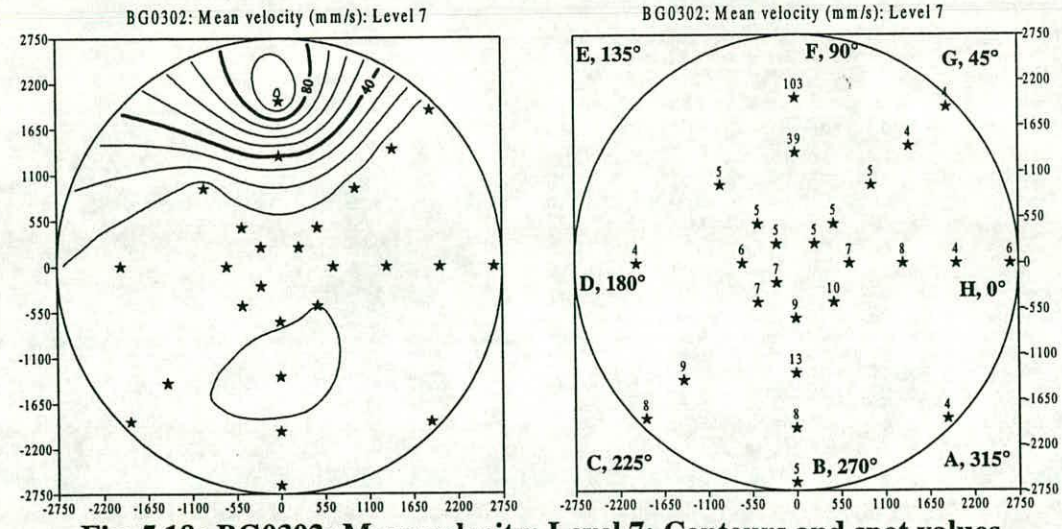

Fig. 5.18c BG0302: Mean velocity: Level 7: Contours and spot values

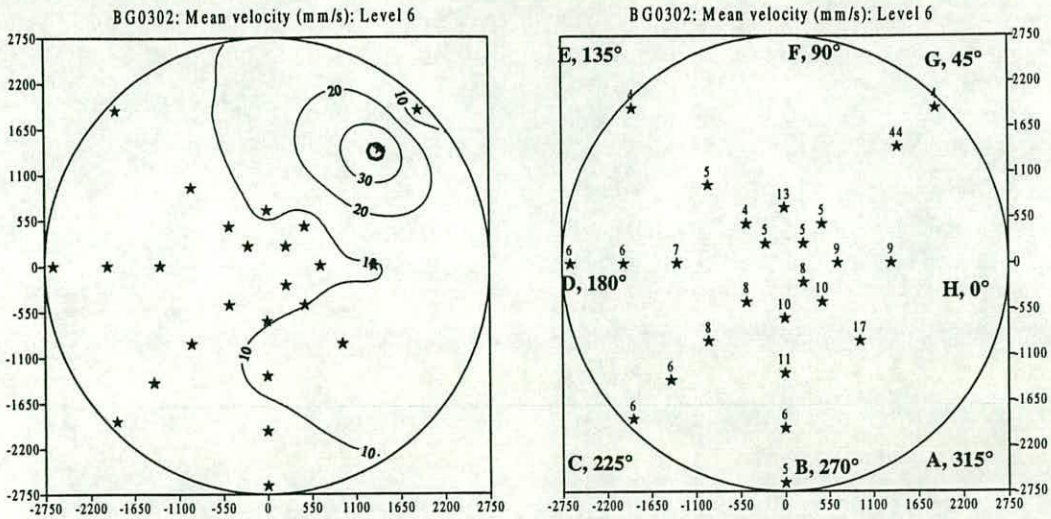

Fig. 5.18d BG0302: Mean velocity: Level 6: Contours and spot values

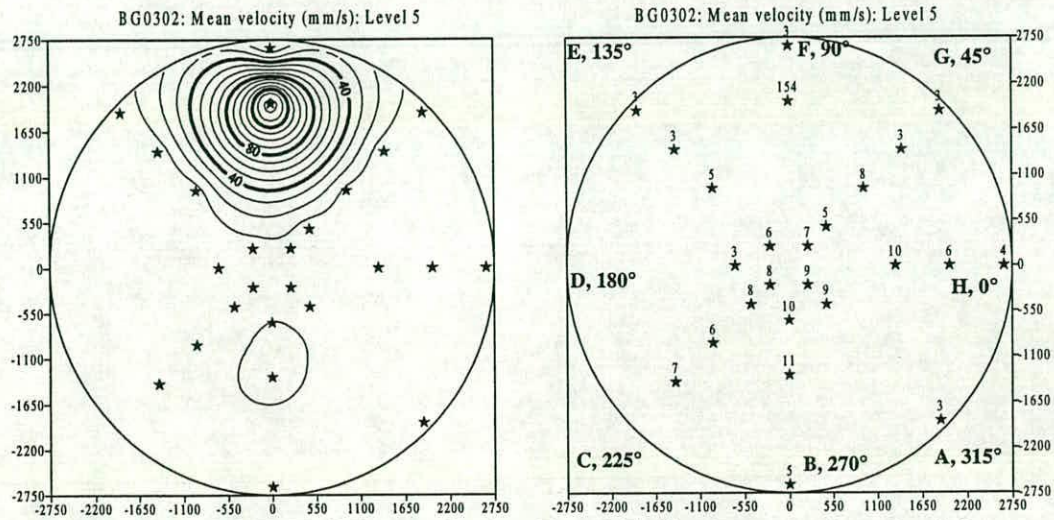

Fig. 5.18e BG0302: Mean velocity: Level 5: Contours and spot values

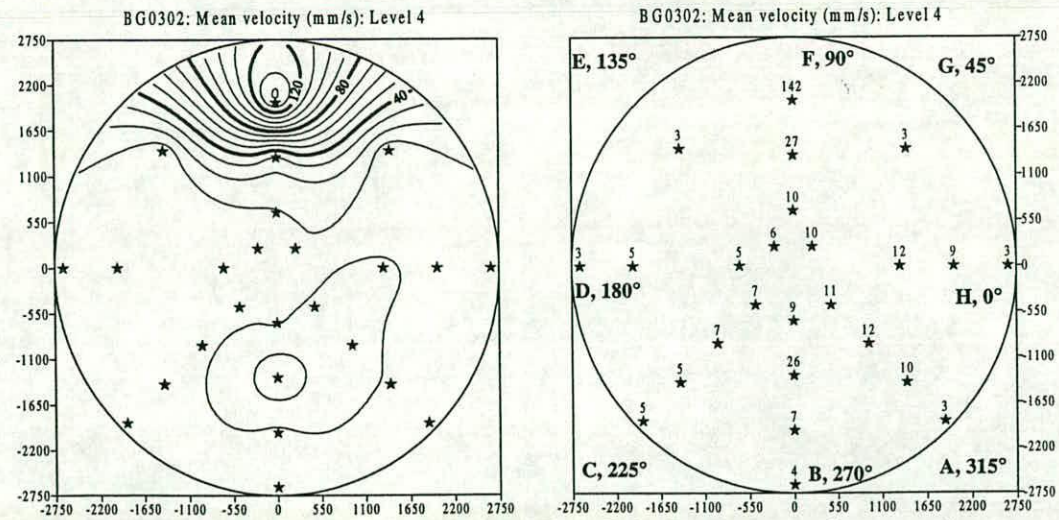

Fig. 5.18f BG0302: Mean velocity: Level 4: Contours and spot values

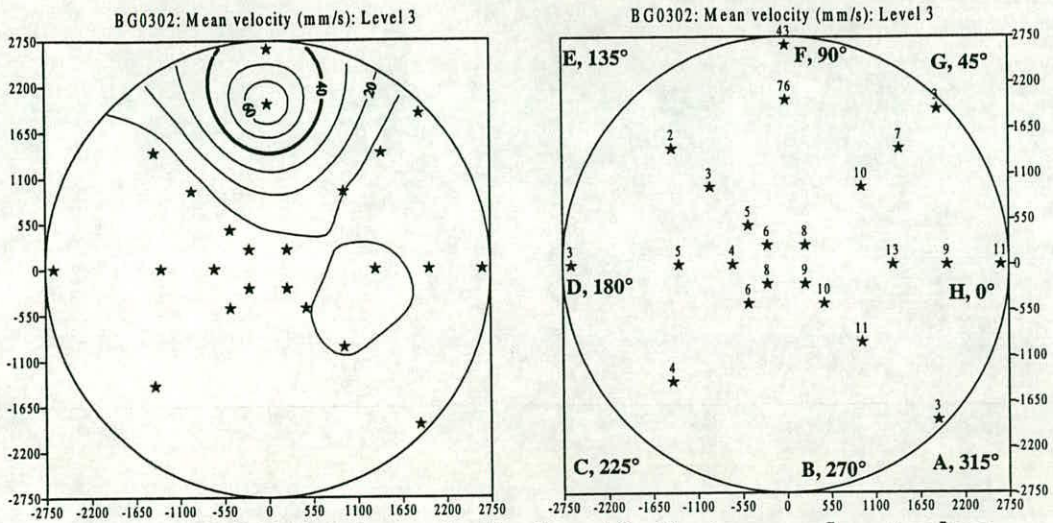

Fig. 5.18g BG0302: Mean velocity: Level 3: Contours and spot values

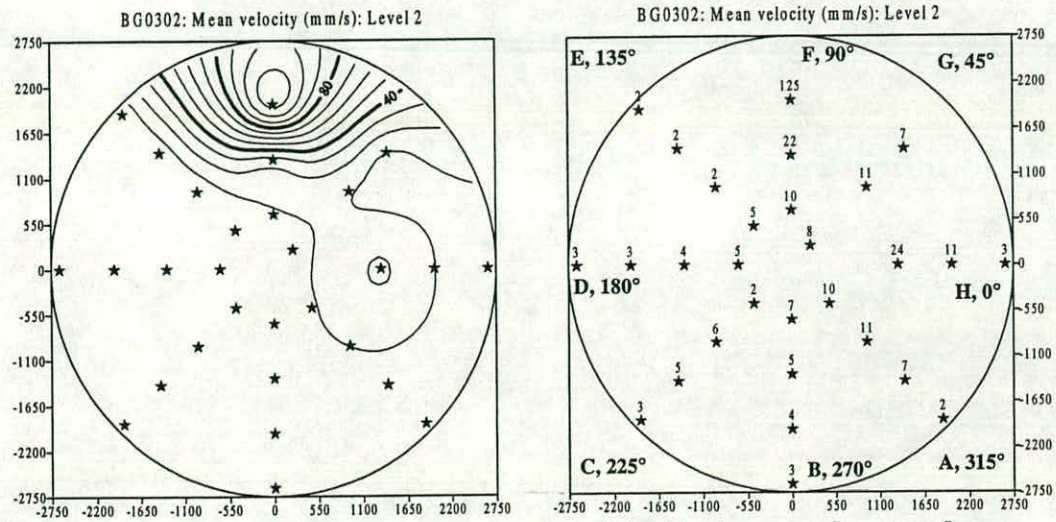

Fig. 5.18h BG0302: Mean velocity: Level 2: Contours and spot values

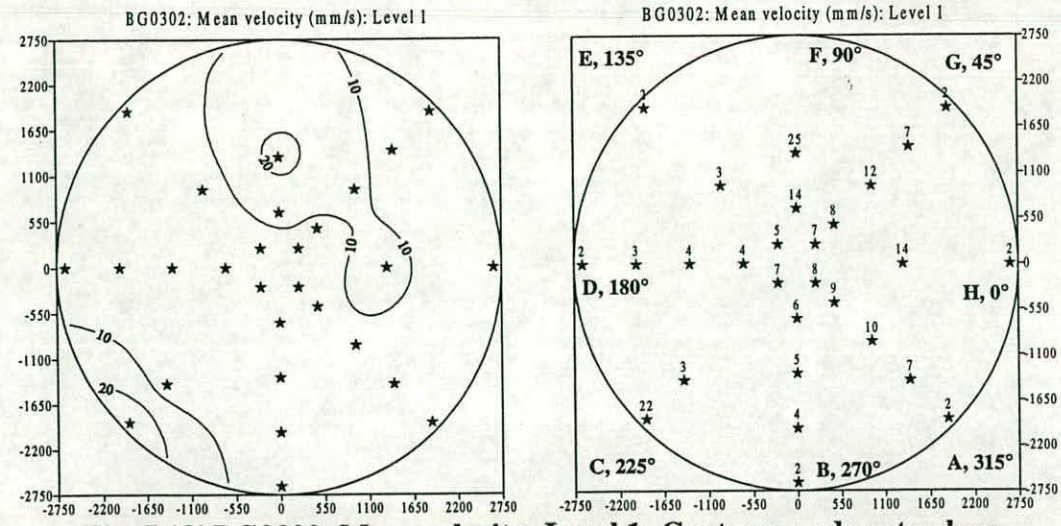

Fig. 5.18i BG0302: Mean velocity: Level 1: Contours and spot values

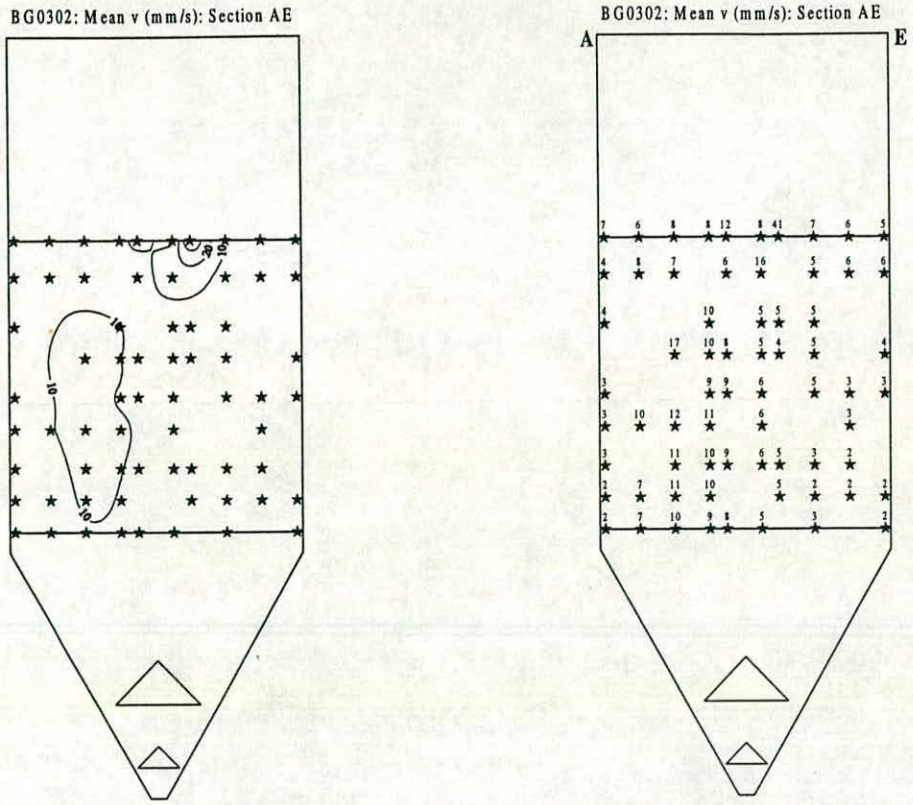

Fig. 5.19a BG0302: Mean velocity: Vertical diametral section A-E: Contours and spot values

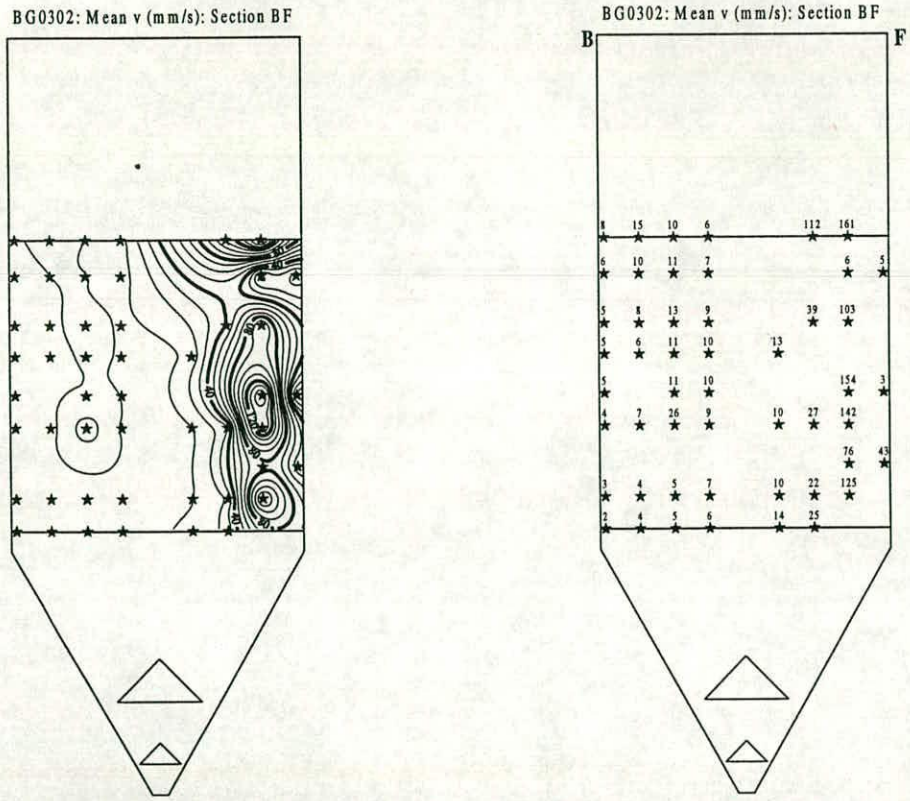

Fig. 5.19b BG0302: Mean velocity: Vertical diametral section B-F: Contours and spot values

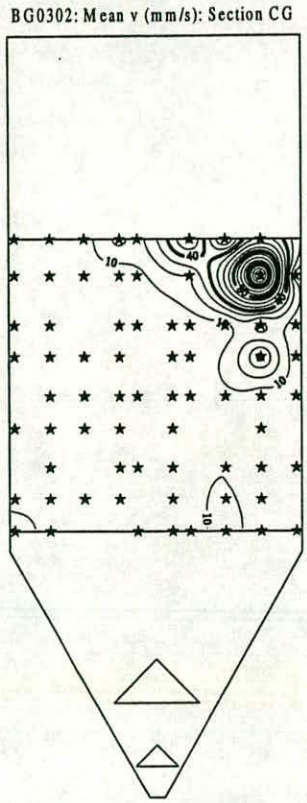

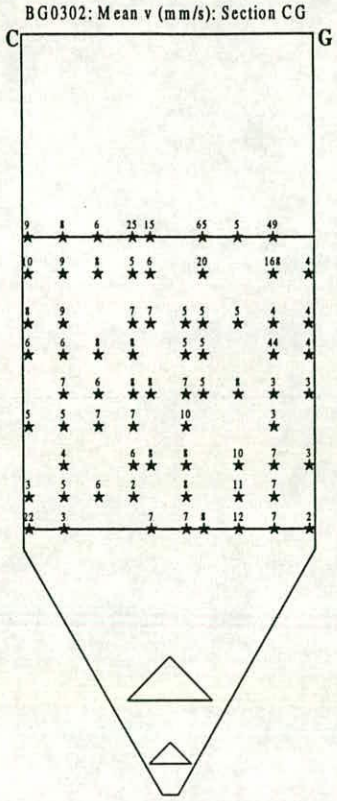

Fig. 5.19c BG0302: Mean velocity: Vertical diametral section C-G: Contours and spot values

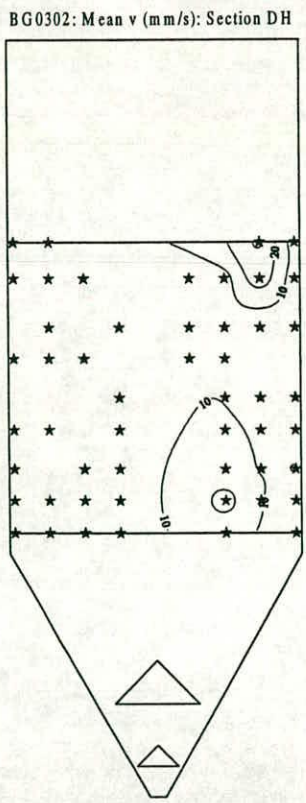

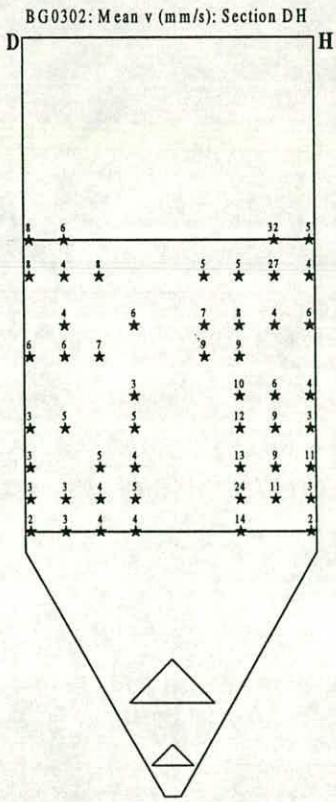

Fig. 5.19d BG0302: Mean velocity: Vertical diametral section D-H: Contours and spot values

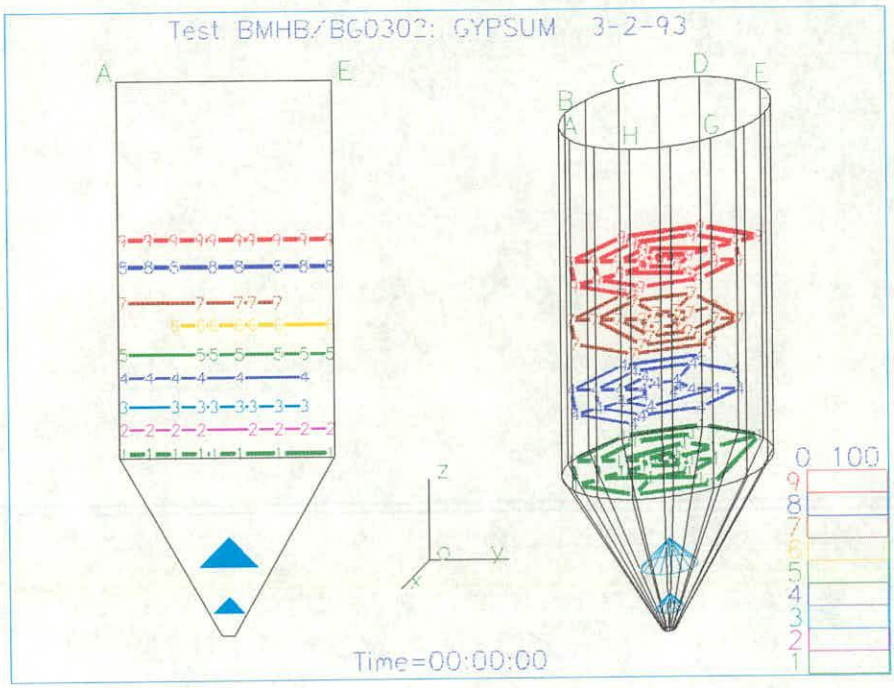

Fig. 5.20a Test BG0302: Simple visualisation: Diametral section AE

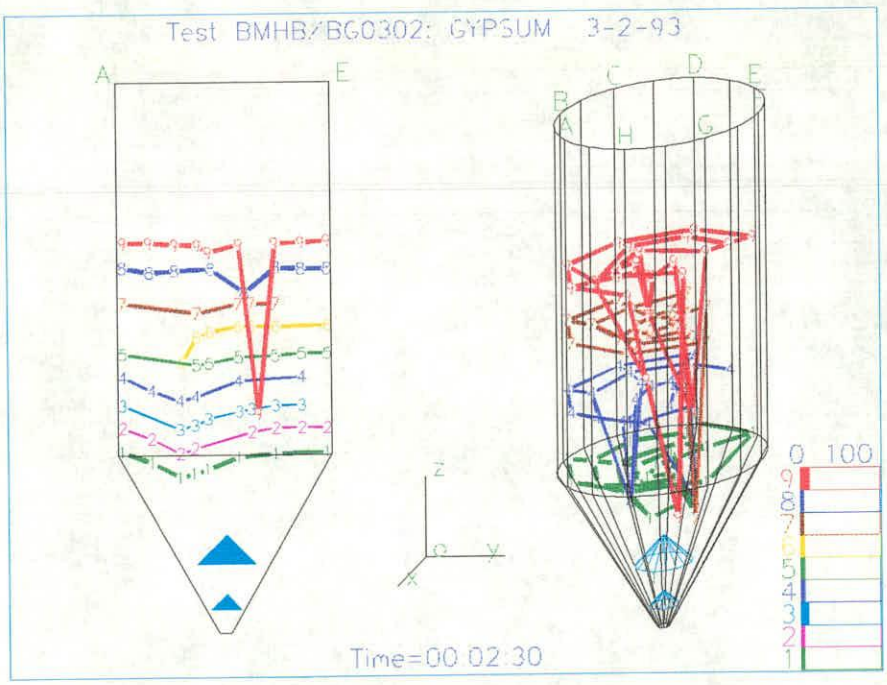

Fig. 5.20b Test BG0302: Simple visualisation: Diametral section AE

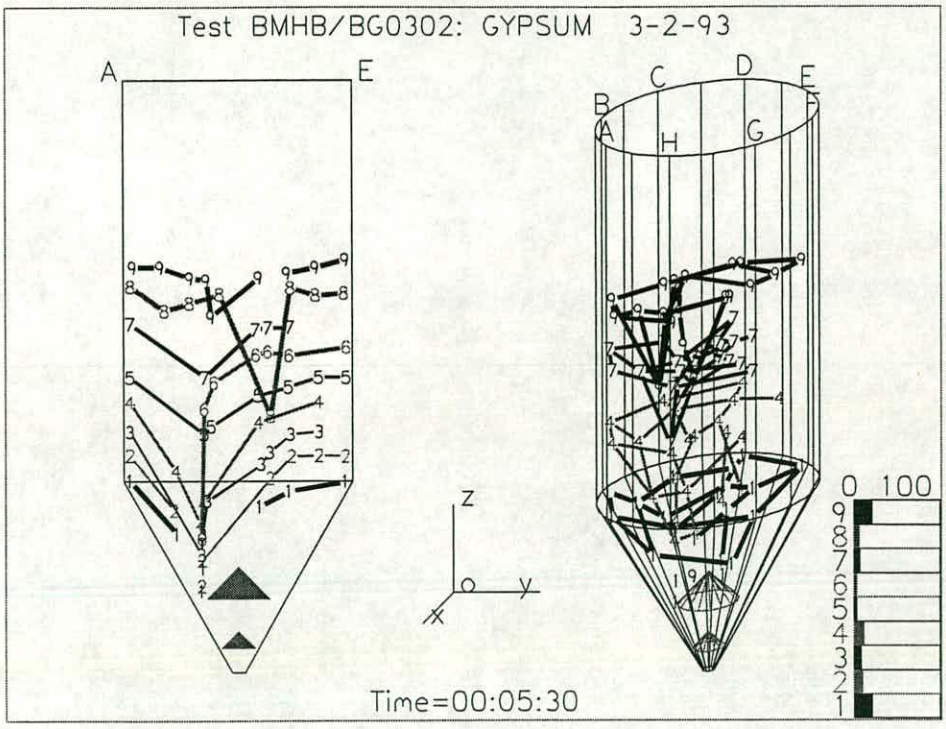

Fig. 5.20c Test BG0302: Simple visualization: Diametral section AE

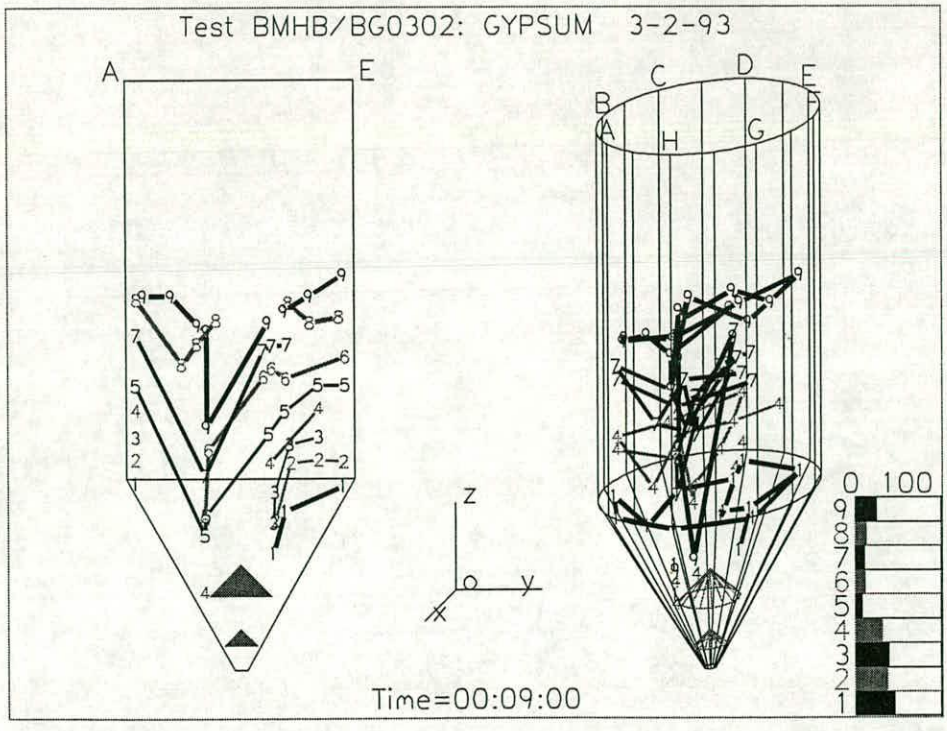

Fig. 5.20d Test BG0302: Simple visualization: Diametral section AE

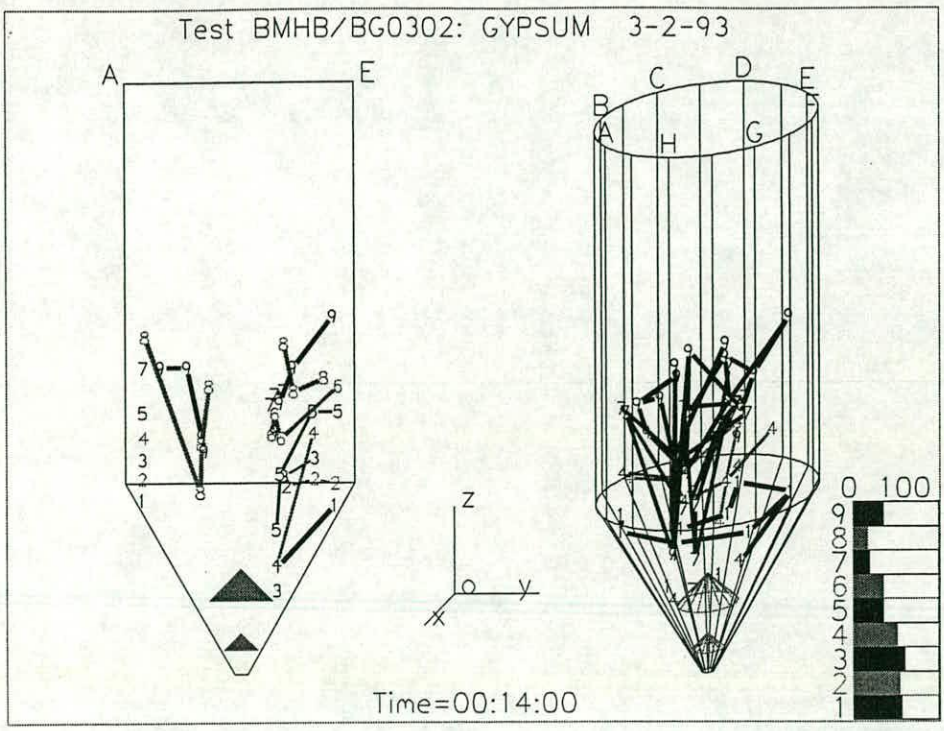

Fig. 5.20e Test BG0302: Simple visualization: Diametral section AE

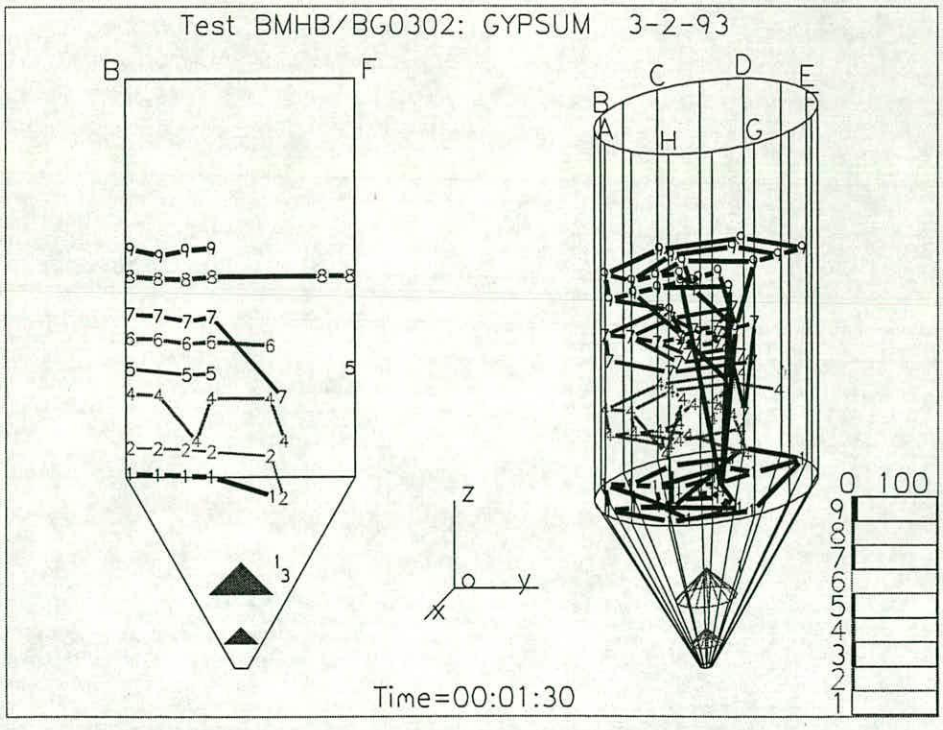

Fig. 5.20f Test BG0302: Simple visualization: Diametral section BF

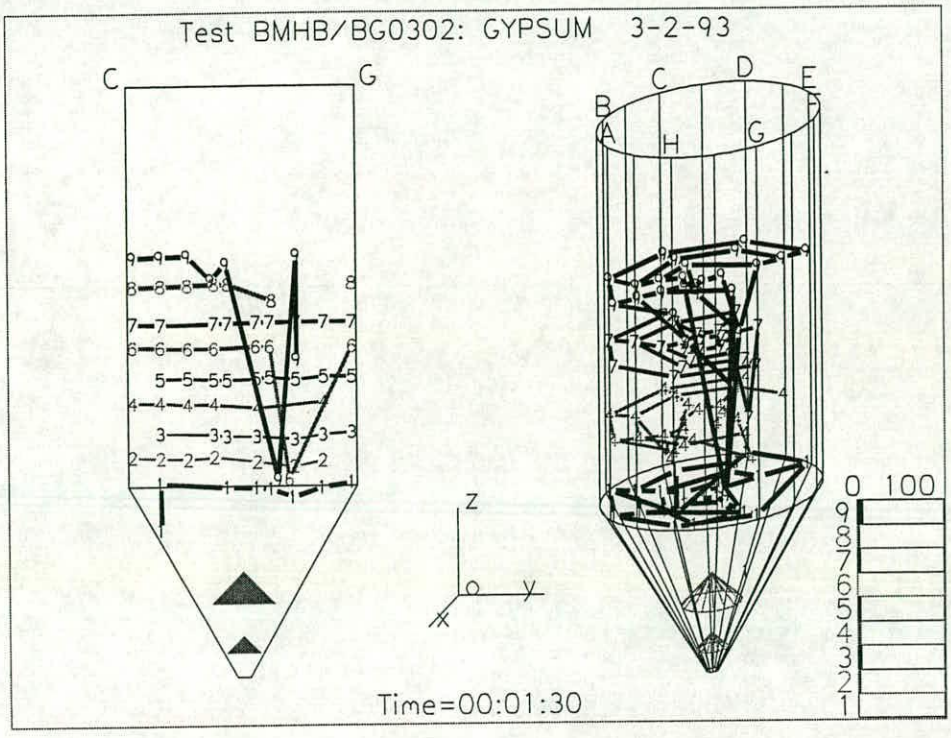

Fig. 5.20g Test BG0302: Simple visualization: Diametral section CG

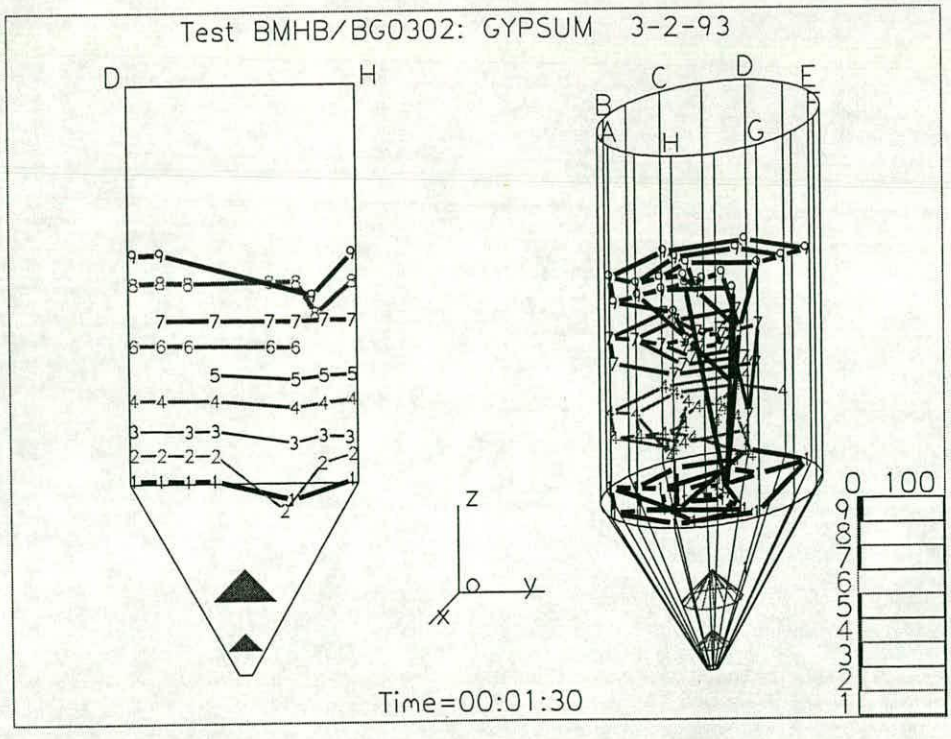

Fig. 5.20h Test BG0302: Simple visualization: Diametral section DH

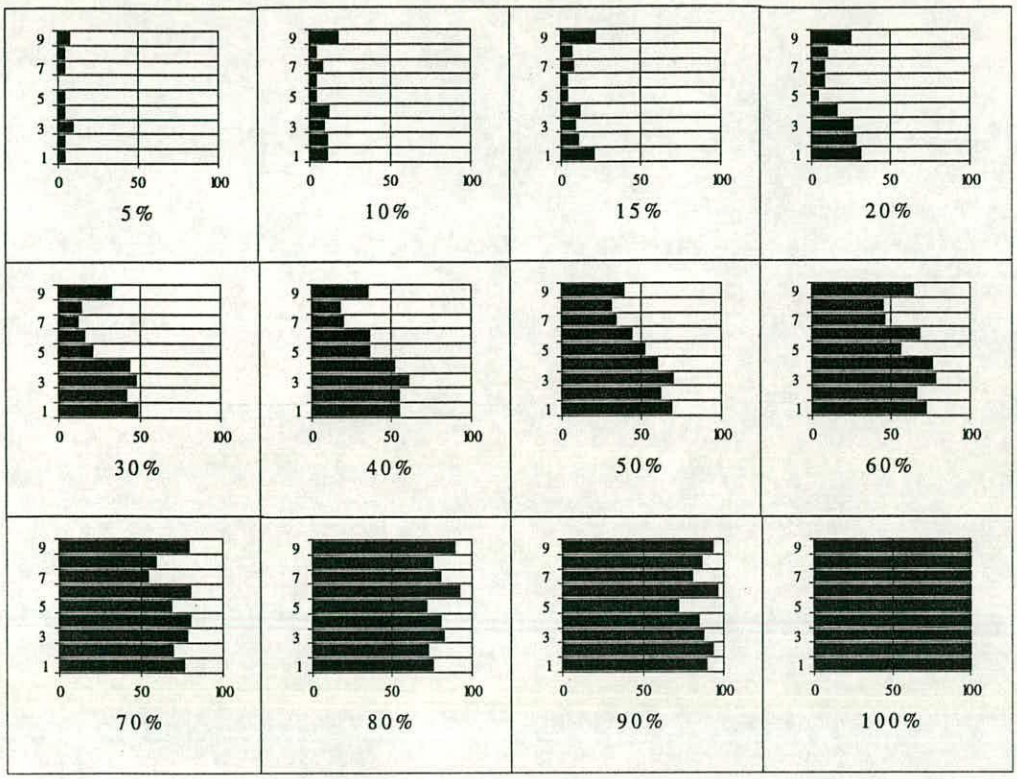

Fig. 5.21 Test BG0302: Bars of tags exited from the outlet at different stages

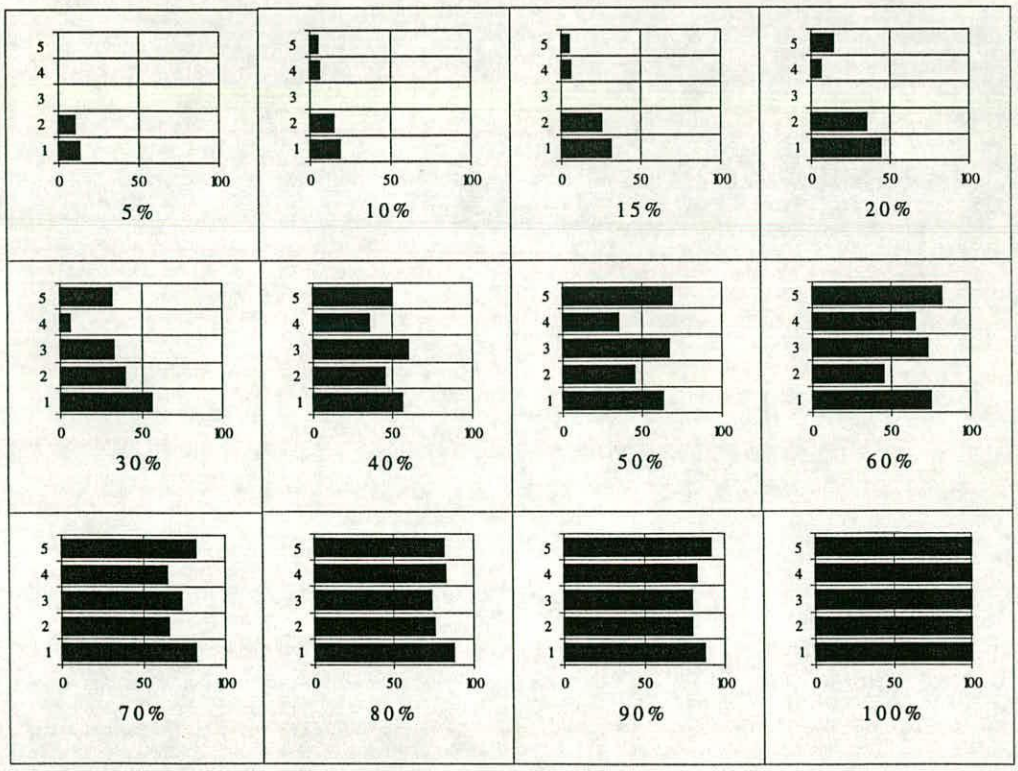

Fig. 5.22 Test BG2901: Bars of tags exited from the outlet at different stages

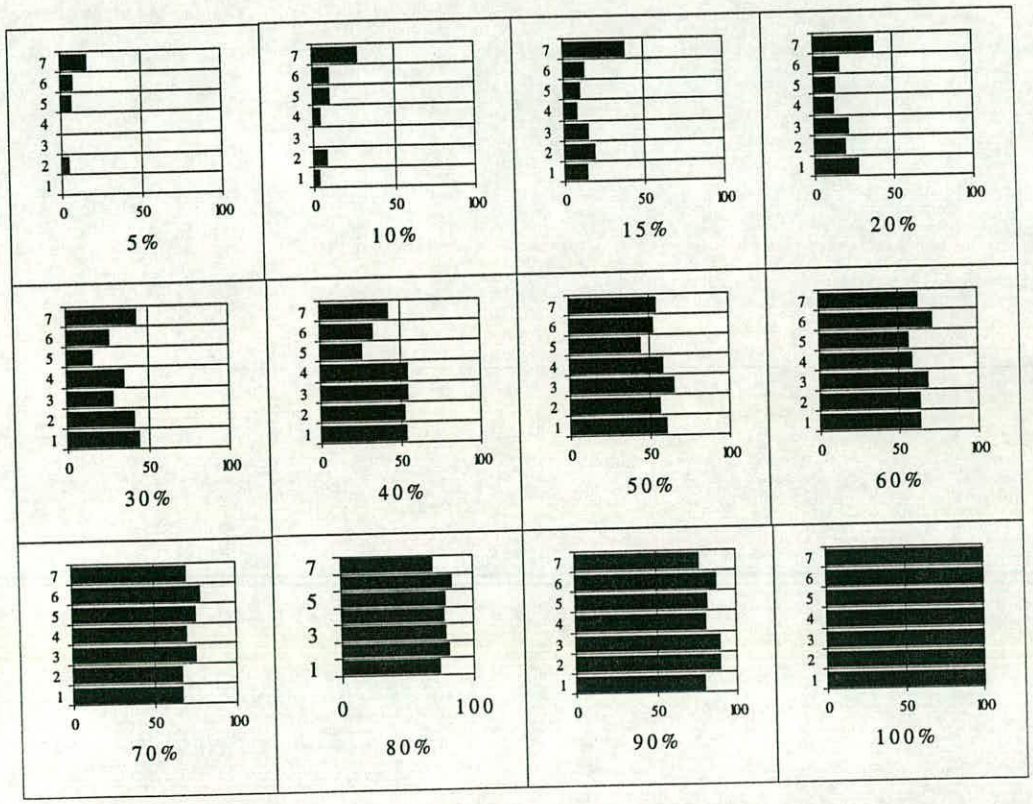

Fig. 5.23 Test BG0902: Bars of tags exited from the outlet at different stages

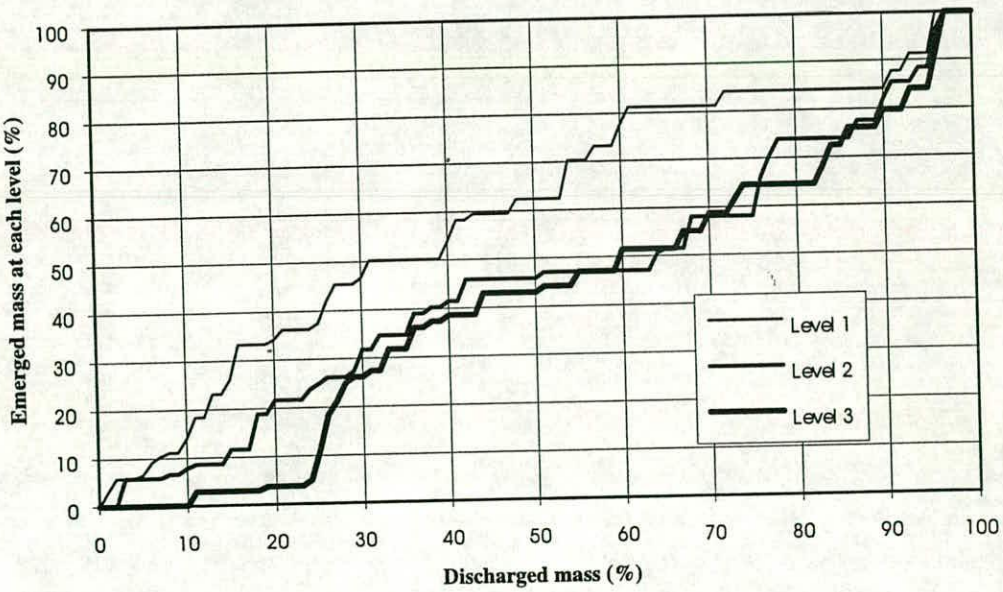

Fig. 5.24a Test BG2901: Emerged mass from seeded levels vs. discharged mass

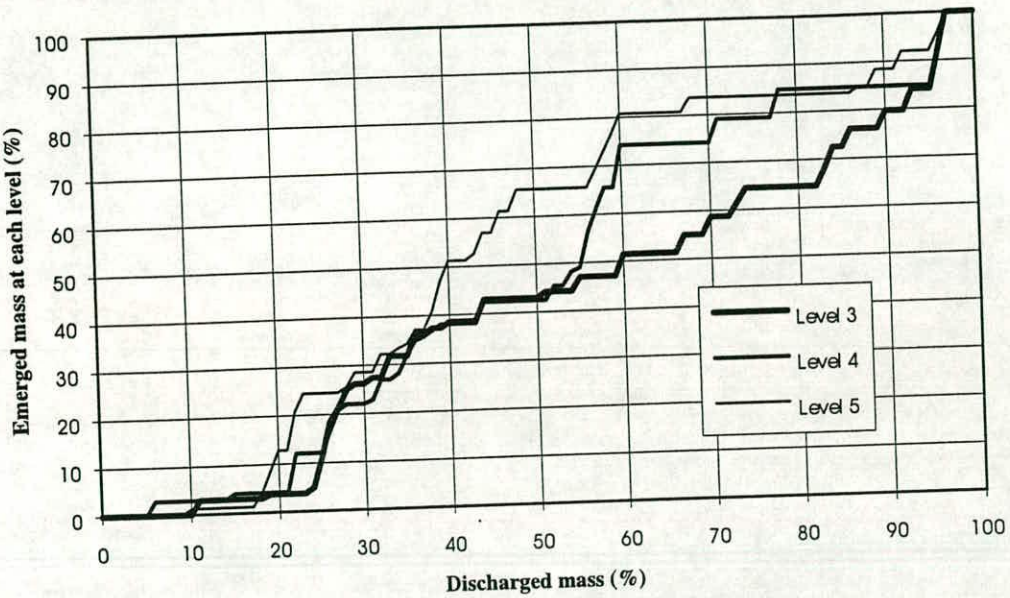

Fig. 5.24b Test BG2901: Emerged mass from seeded levels vs. discharged mass

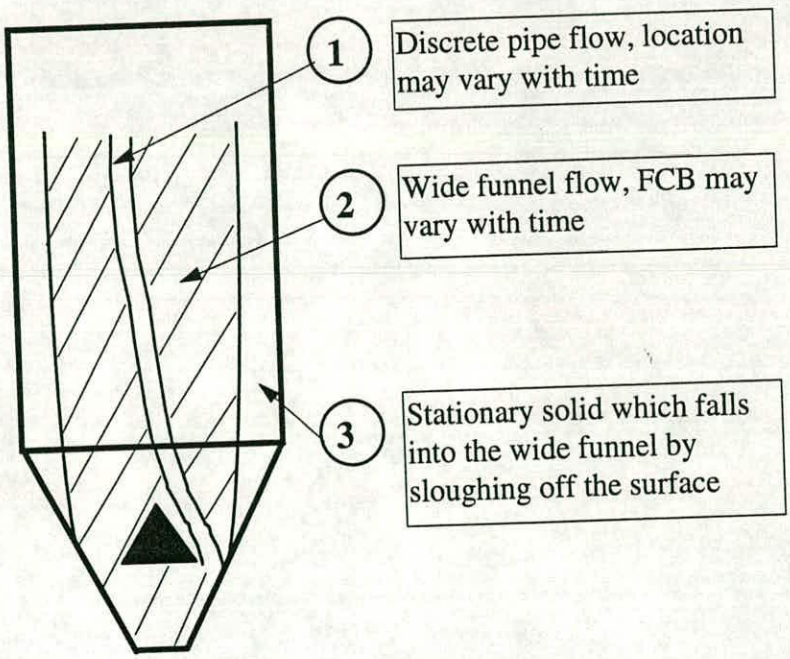

Fig. 5.25 Flow pattern in the British Gypsum silo: discharge aids on

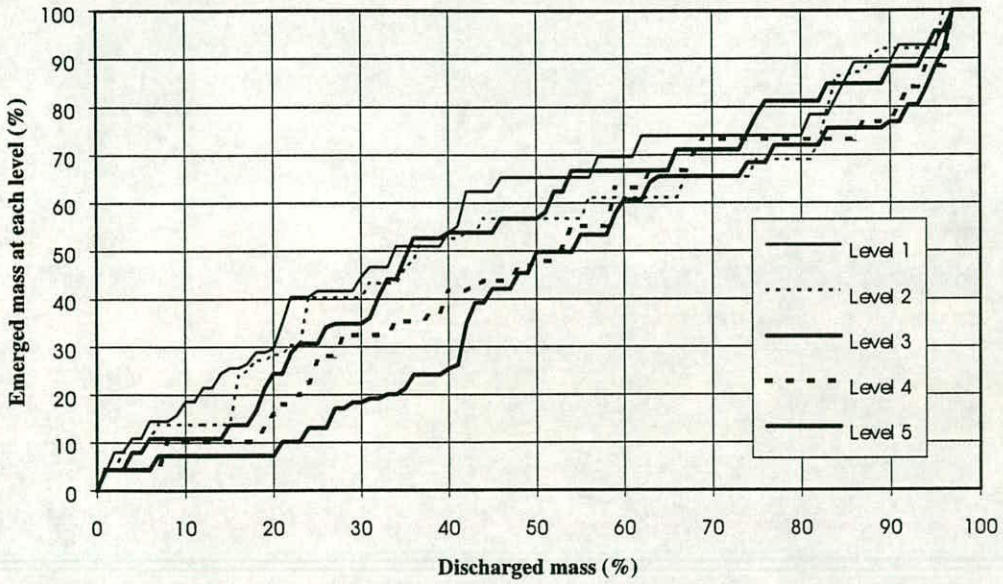

Fig. 5.26a Test BG0302: Emerged mass from seeded levels vs. discharged mass

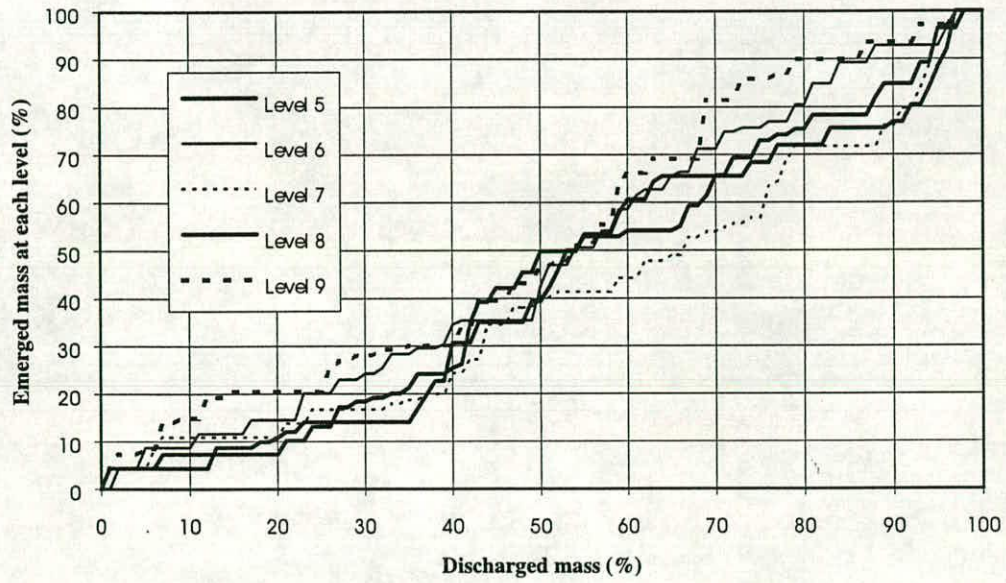

Fig. 5.26b Test BG0302: Emerged mass from seeded levels vs. discharged mass

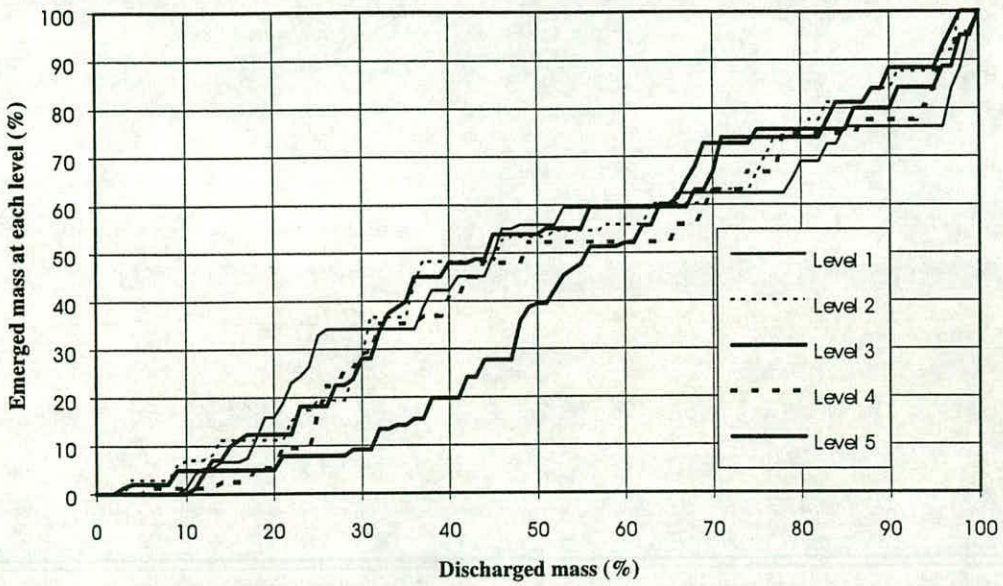

Fig. 5.26c Test BG0902: Emerged mass from seeded levels vs. discharged mass

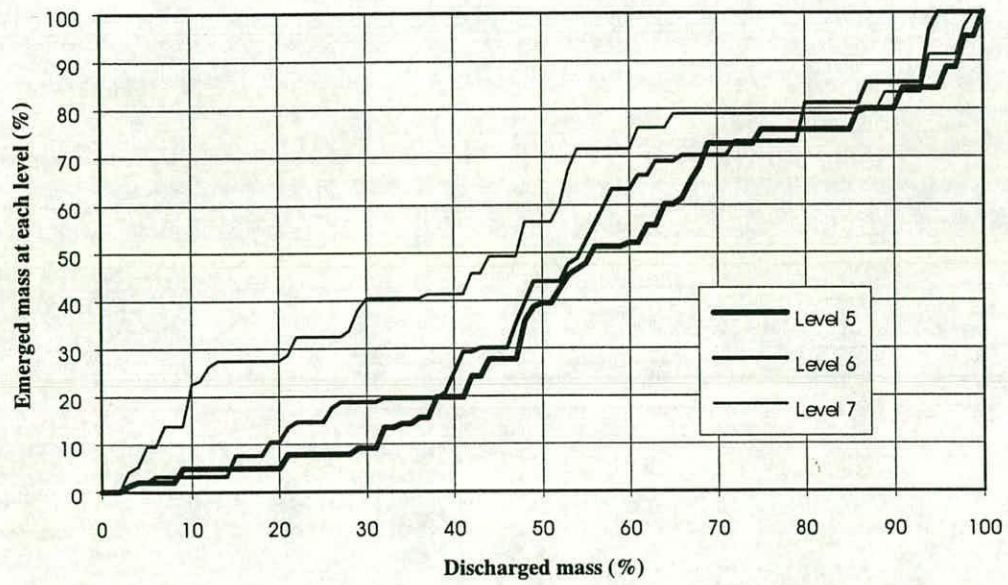

Fig. 5.26d Test BG0902: Emerged mass from seeded levels vs. discharged mass

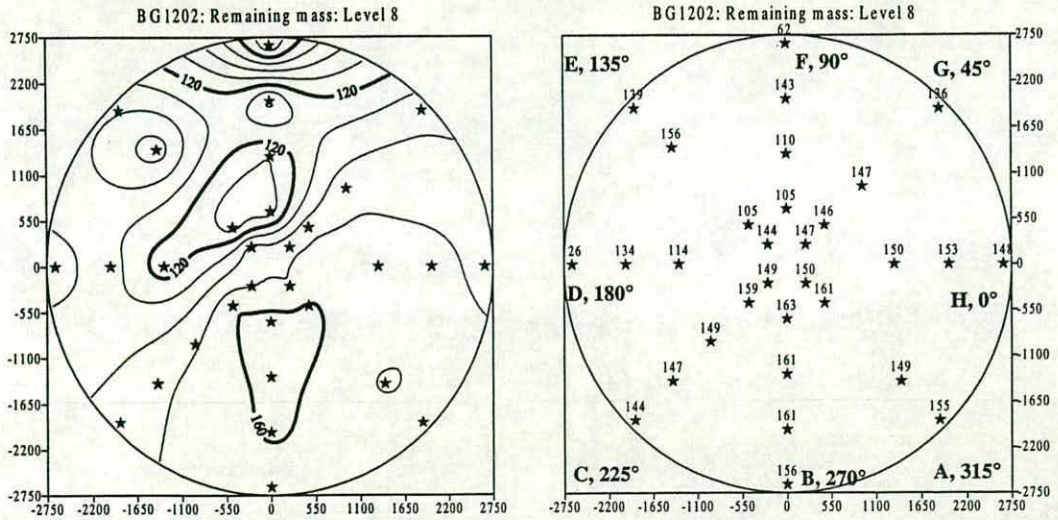

Fig. 5.27a BG1202: Remaining mass: Level 8: Contours and spot values

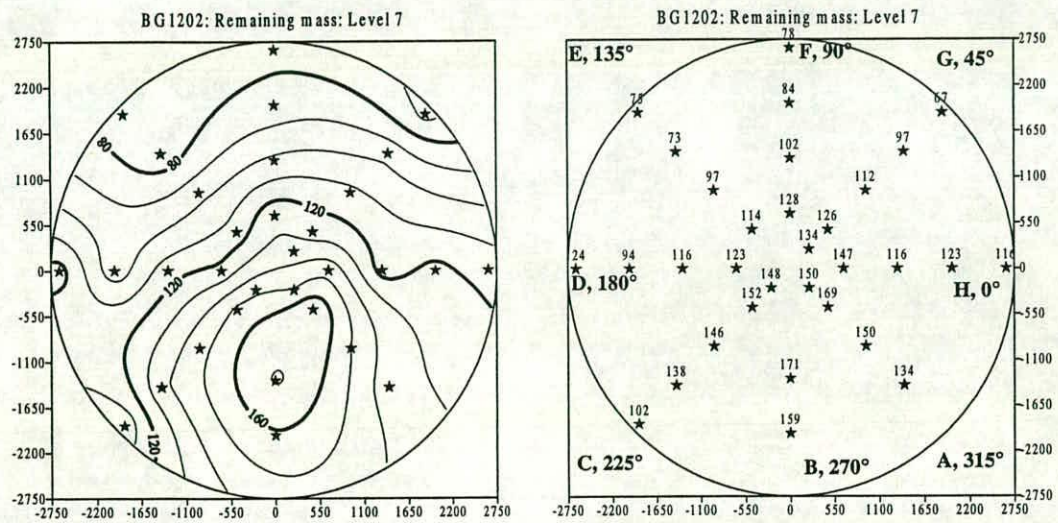

Fig. 5.27b BG1202: Remaining mass: Level 7: Contours and spot values

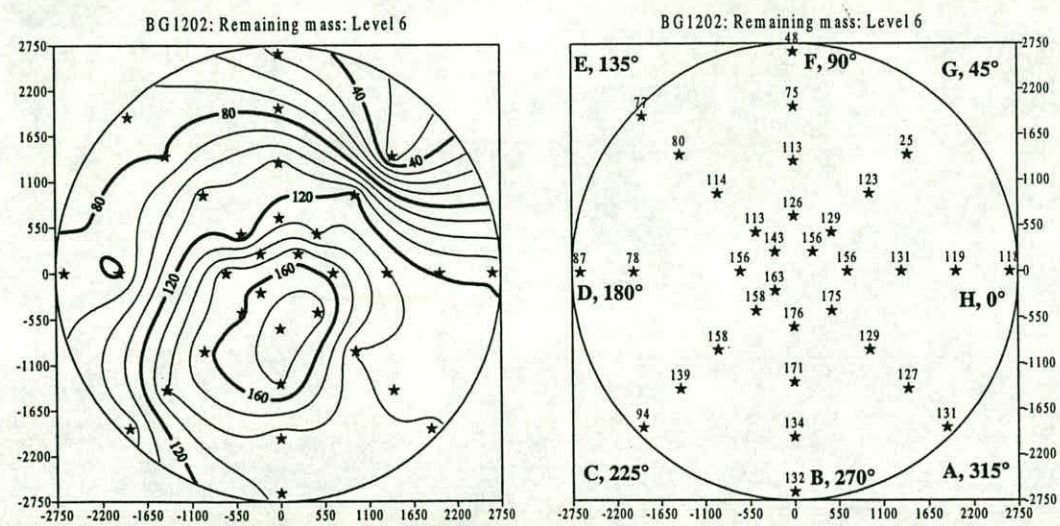

Fig. 5.27c BG1202: Remaining mass: Level 6: Contours and spot values

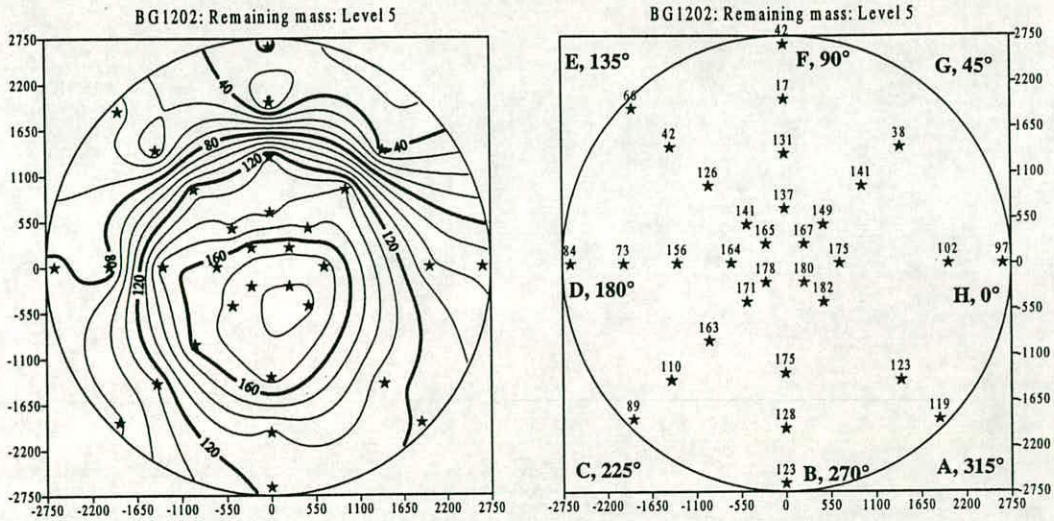

Fig. 5.27d BG1202: Remaining mass: Level 5: Contours and spot values

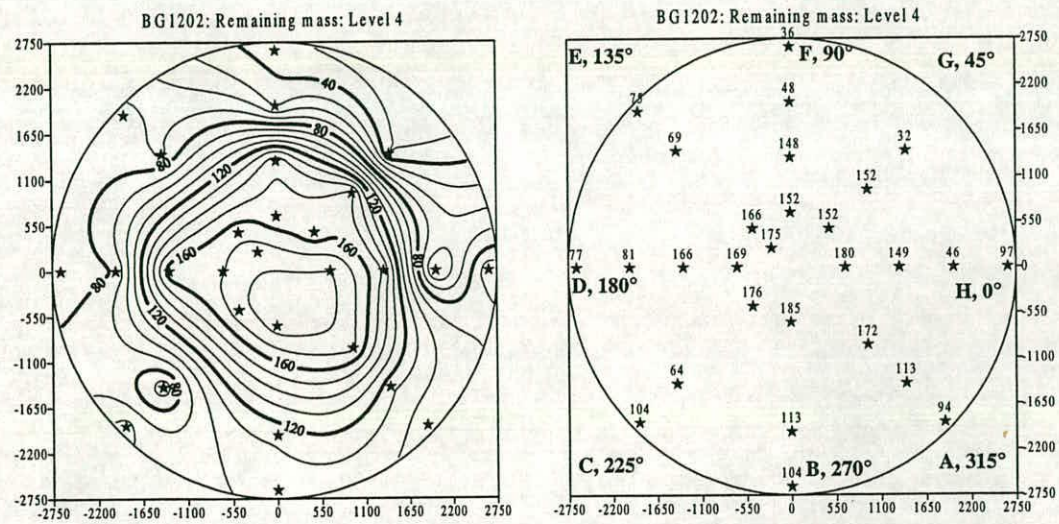

Fig. 5.27e BG1202: Remaining mass: Level 4: Contours and spot values

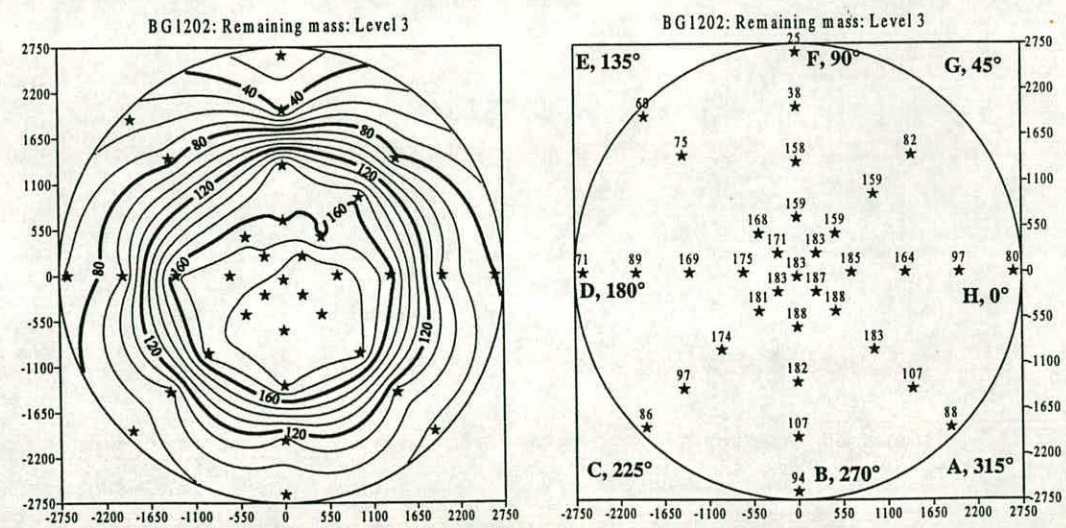

Fig. 5.27f BG1202: Remaining mass: Level 3: Contours and spot values

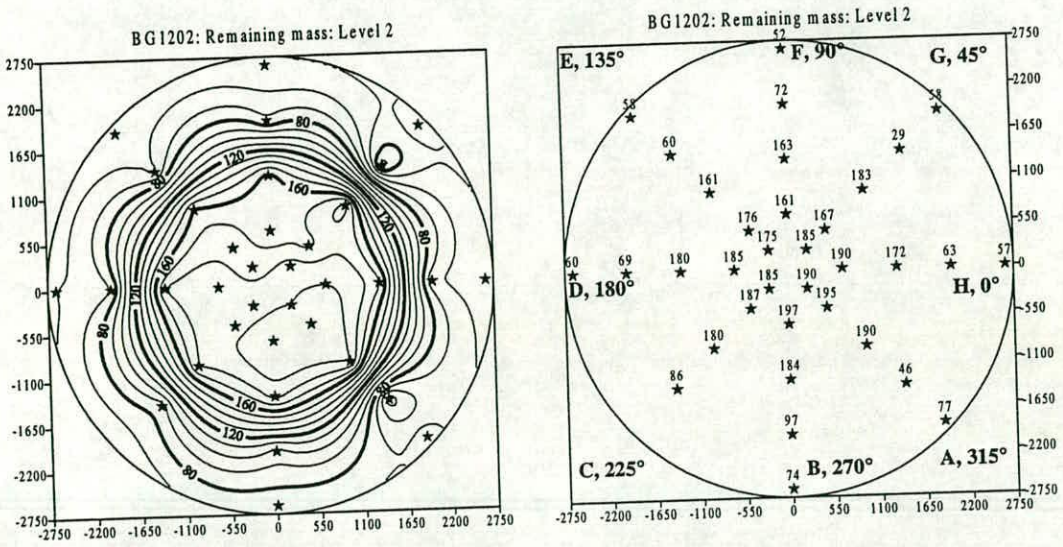

Fig. 5.27g BG1202: Remaining mass: Level 2: Contours and spot values

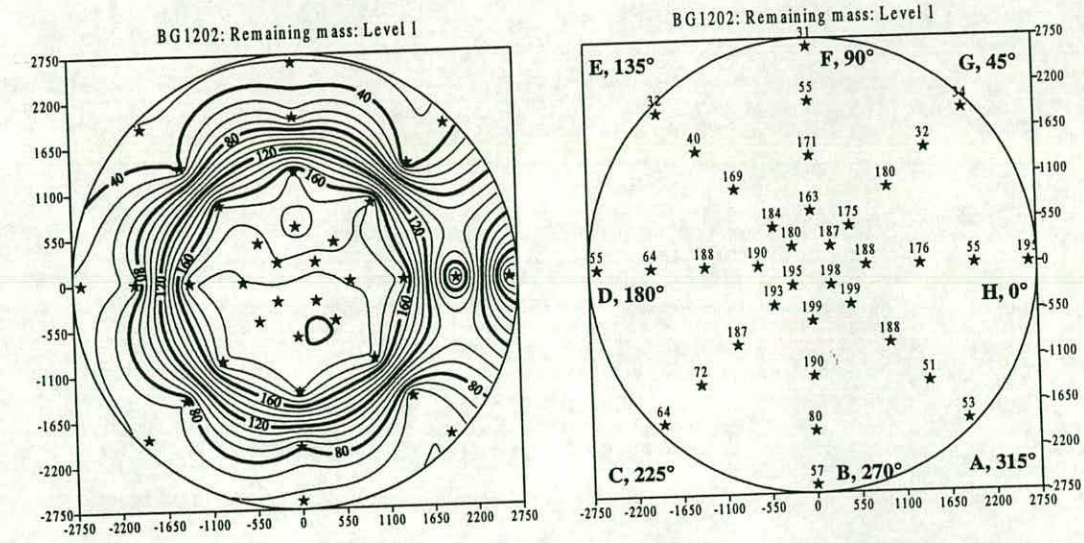

Fig. 5.27h BG1202: Remaining mass: Level 1: Contours and spot values

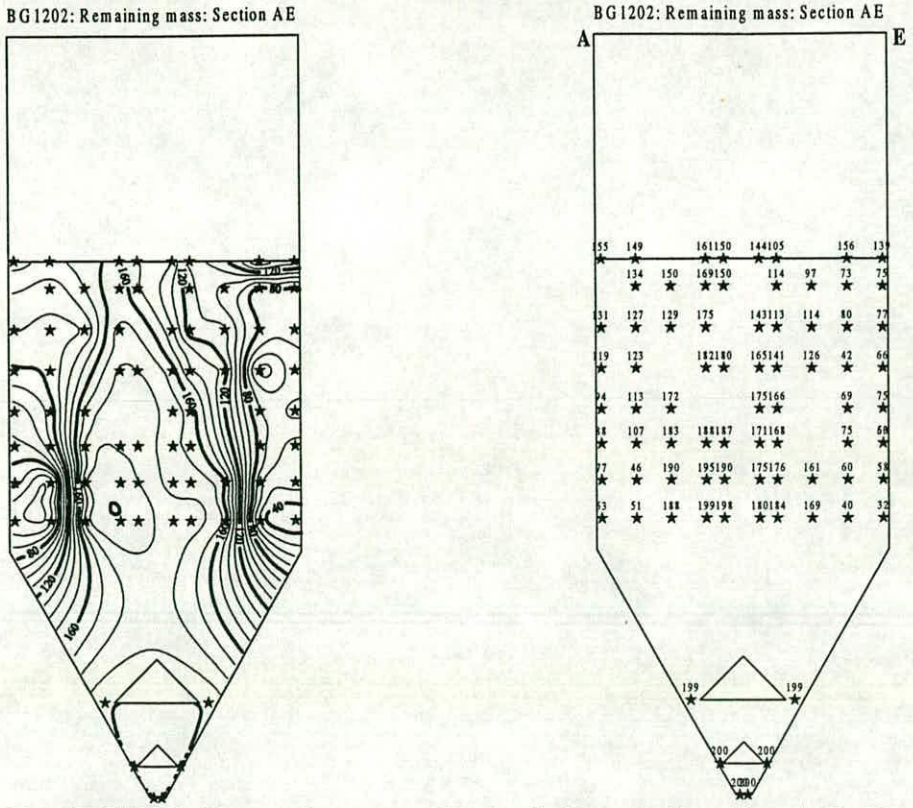

Fig. 5.28a BG1202: Remaining mass: Vertical diametral section A-E: Contours and spot values

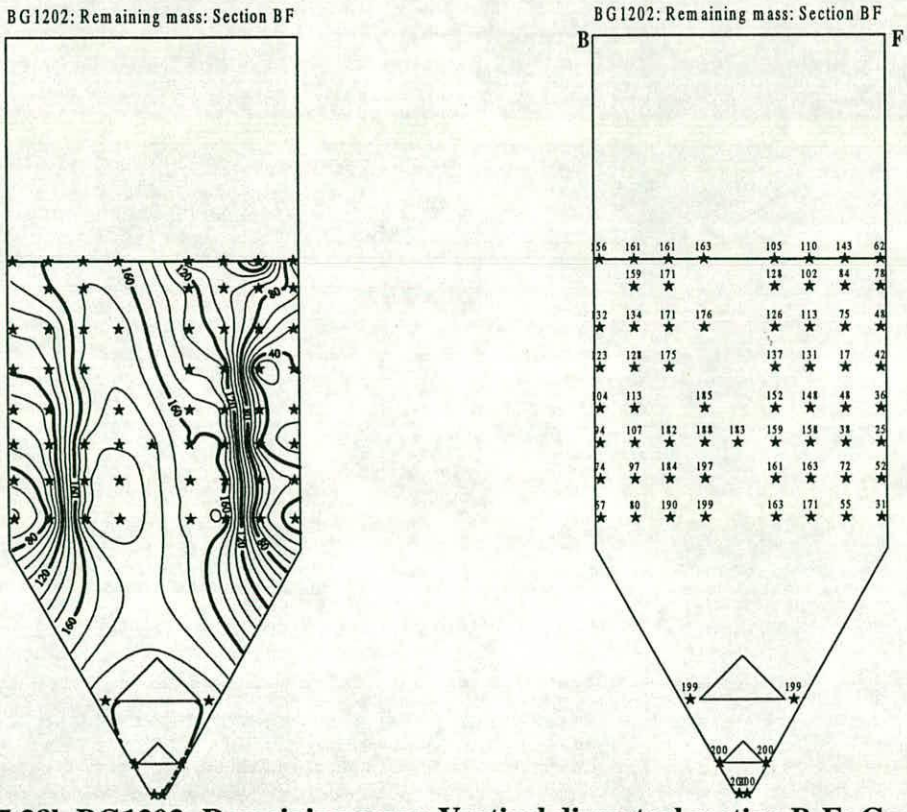

Fig. 5.28b BG1202: Remaining mass: Vertical diametral section B-F: Contours and spot values

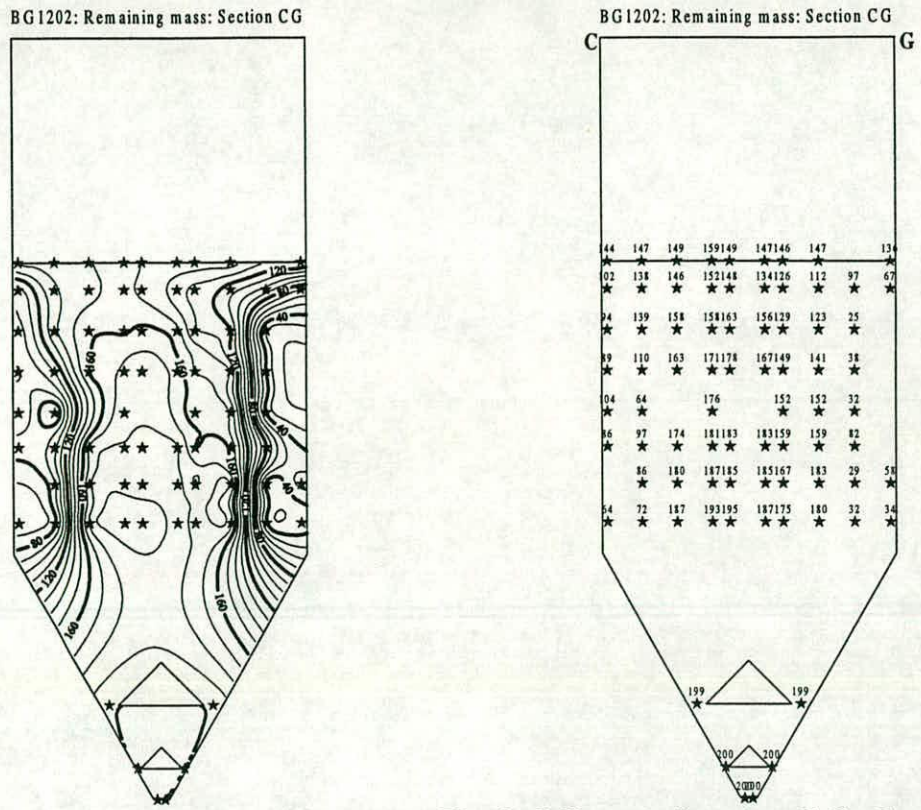

Fig. 5.28c BG1202: Remaining mass: Vertical diametral section C-G: Contours and spot values

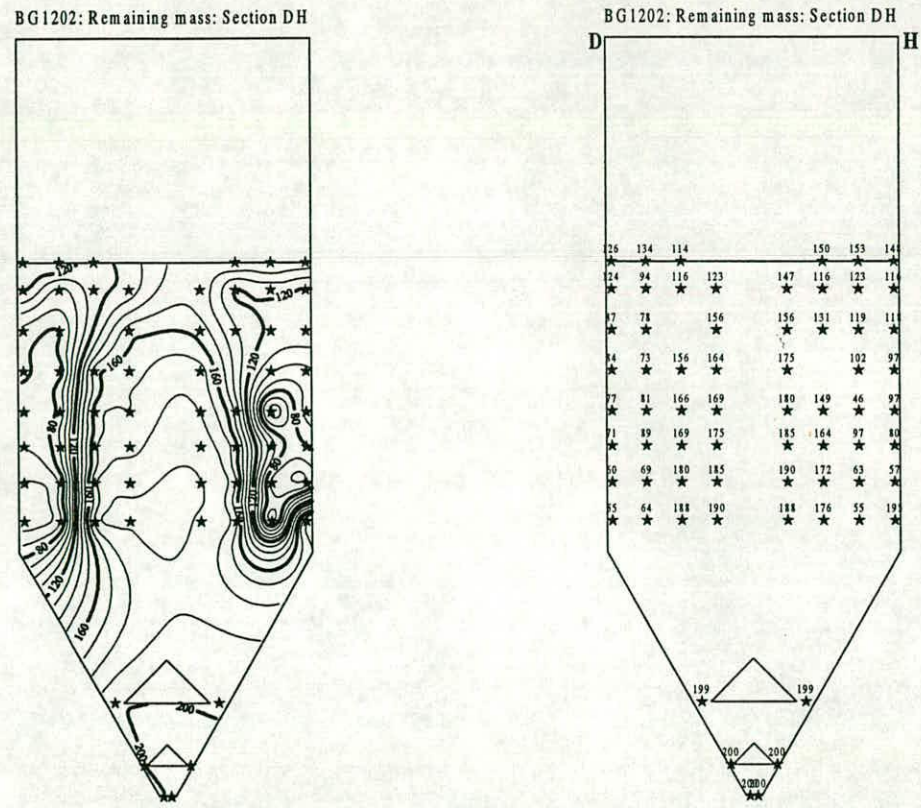

Fig. 5.28d BG1202: Remaining mass: Vertical diametral section D-H: Contours and spot values

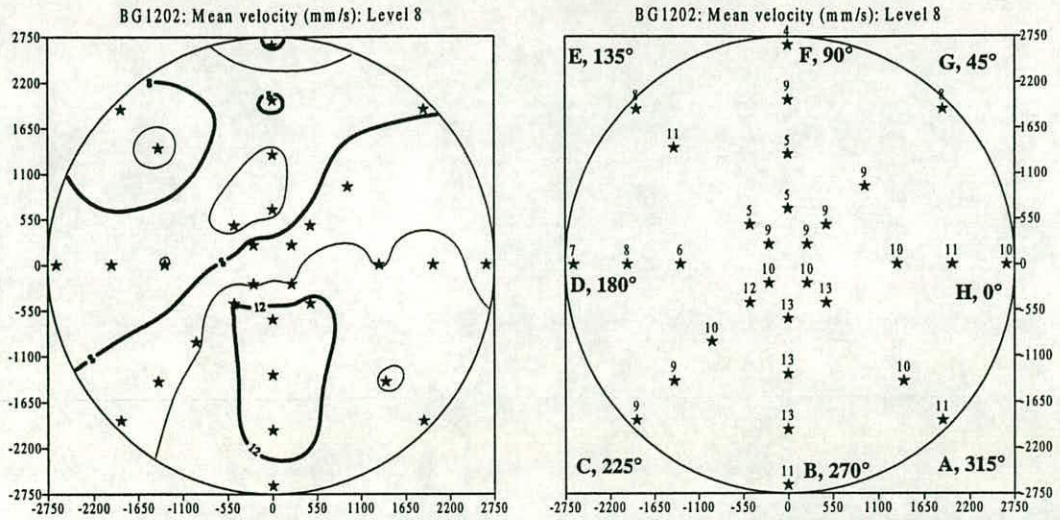

Fig. 5.29a BG1202: Mean velocity: Level 8: Contours and spot values

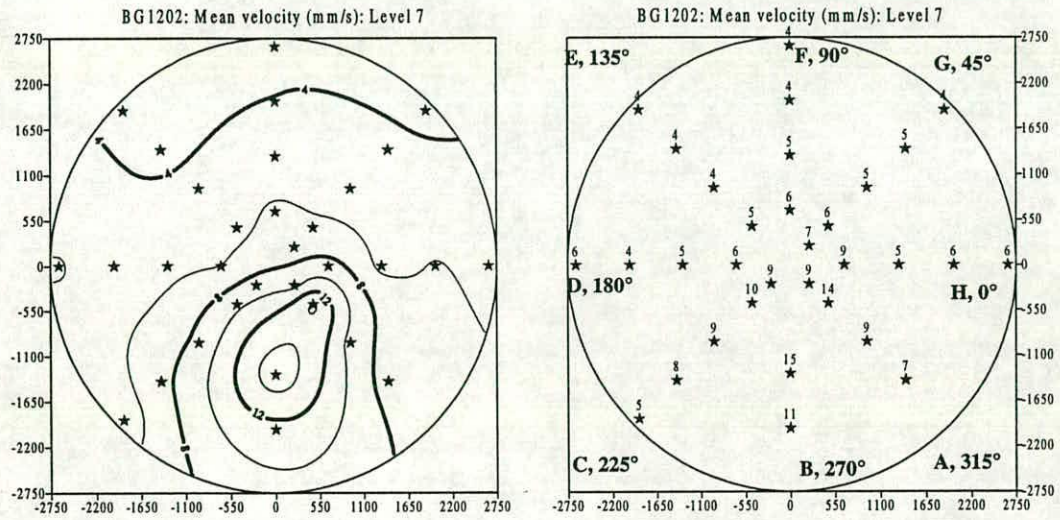

Fig. 5.29b BG1202: Mean velocity: Level 7: Contours and spot values

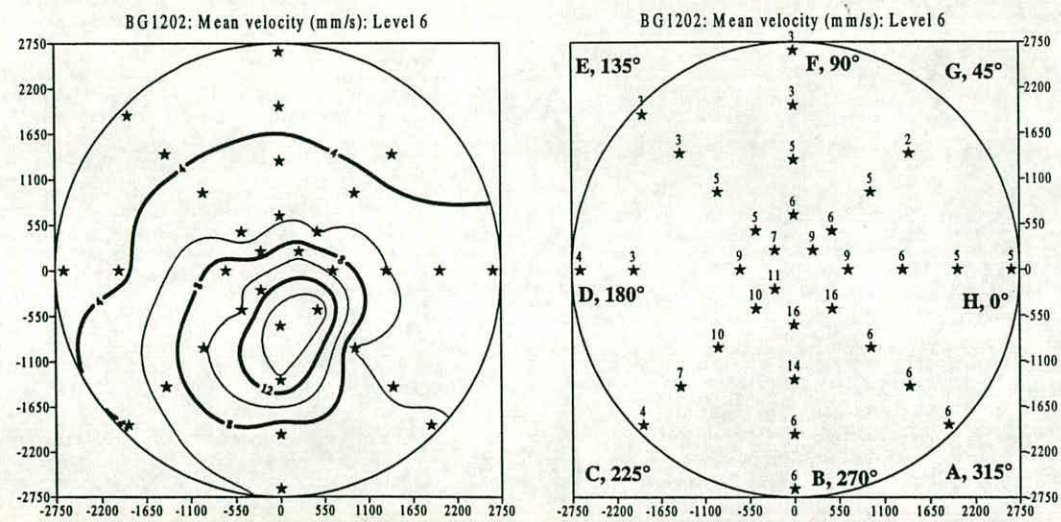

Fig. 5.29c BG1202: Mean velocity: Level 6: Contours and spot values

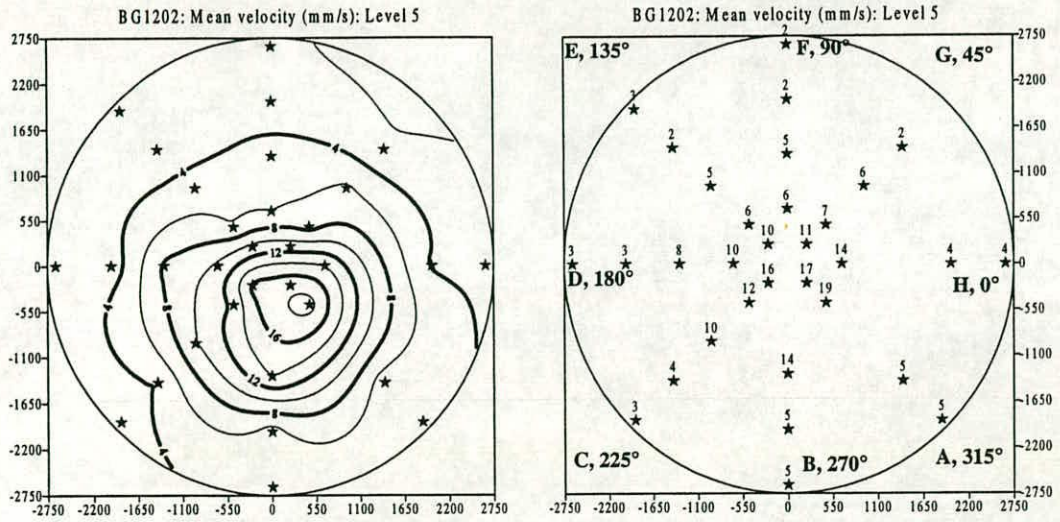

Fig. 5.29d BG1202: Mean velocity: Level 5: Contours and spot values

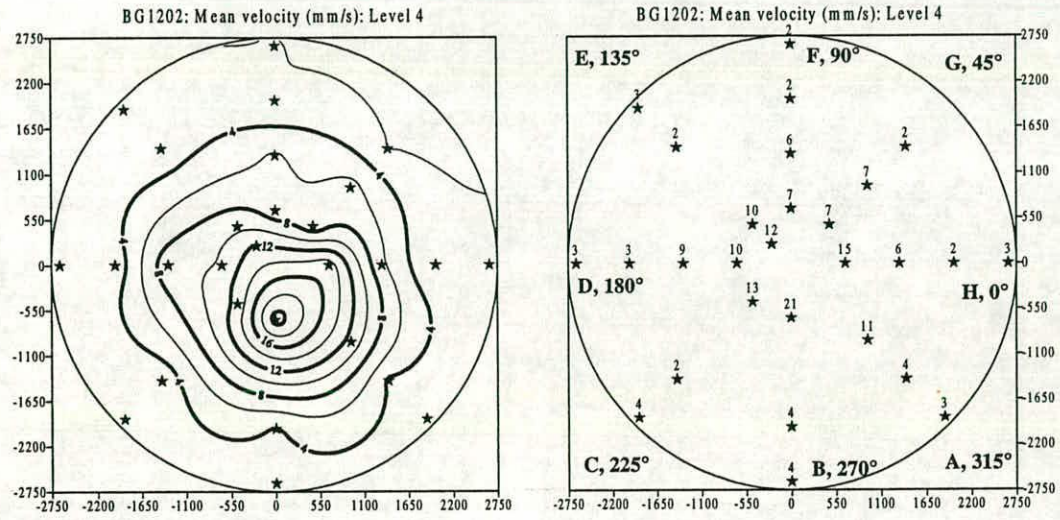

Fig. 5.29e BG1202: Mean velocity: Level 4: Contours and spot values

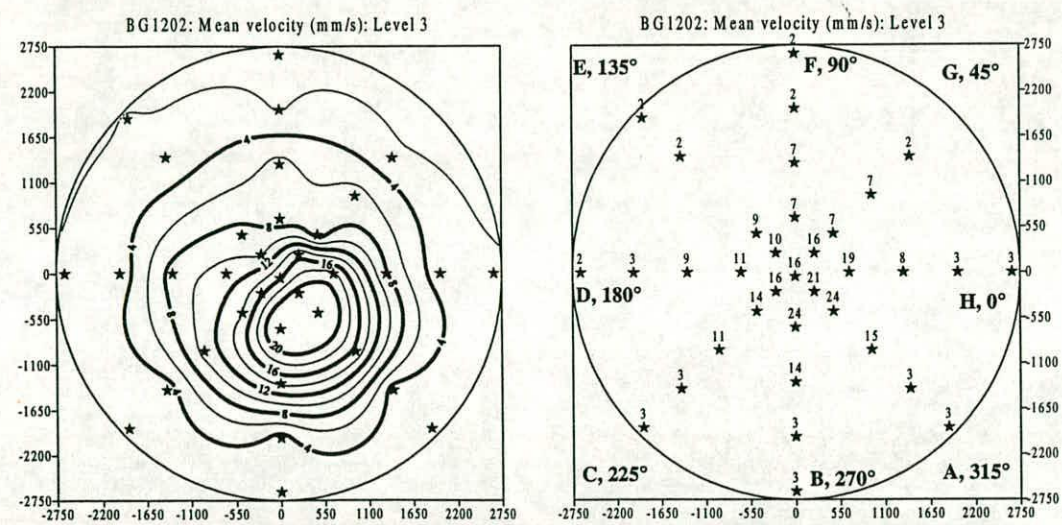

Fig. 5.29f BG1202: Mean velocity: Level 3: Contours and spot values

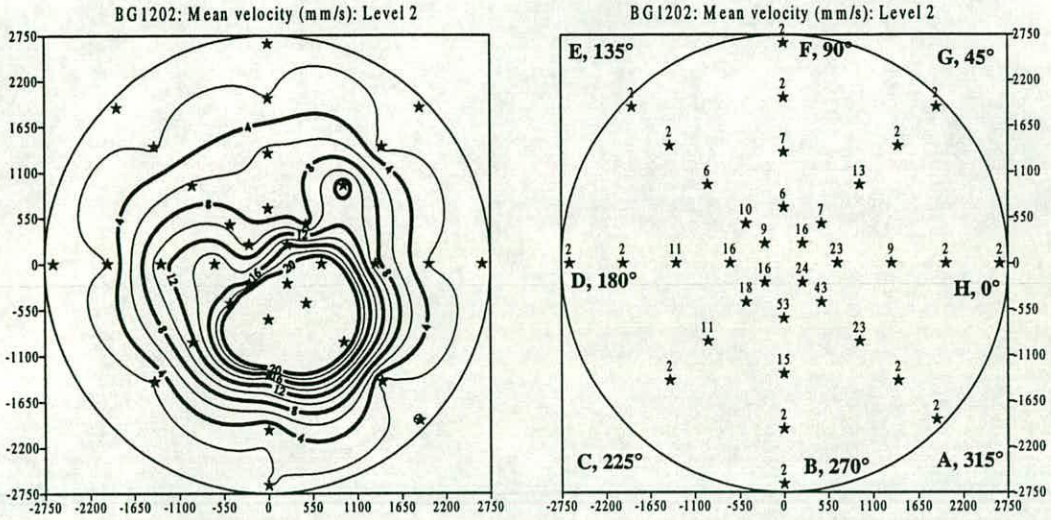

Fig. 5.29g BG1202: Mean velocity: Level 2: Contours and spot values

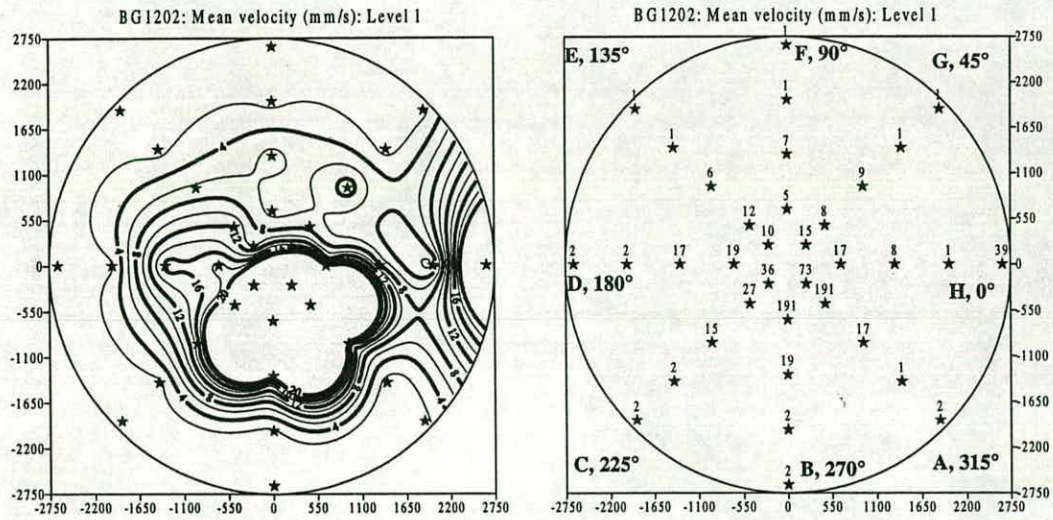

Fig. 5.29h BG1202: Mean velocity: Level 1: Contours and spot values

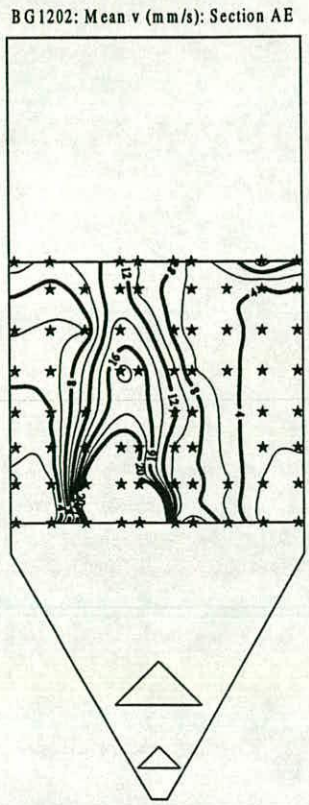

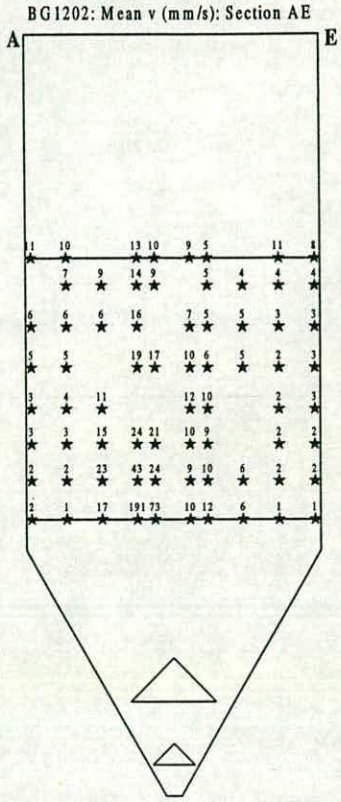

Fig. 5.30a BG1202: Mean velocity: Vertical diametral section A-E: Contours and spot values

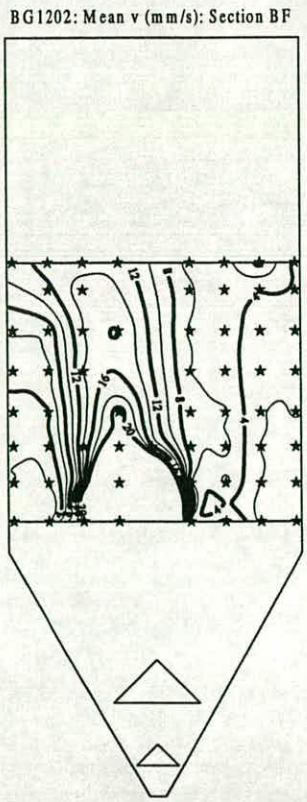

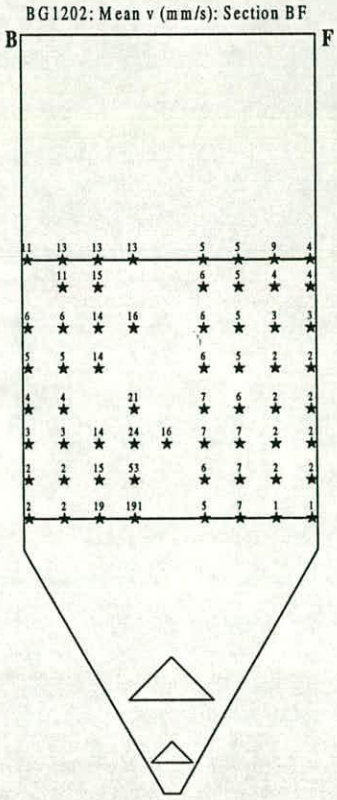

Fig. 5.30b BG1202: Mean velocity: Vertical diametral section B-F: Contours and spot values

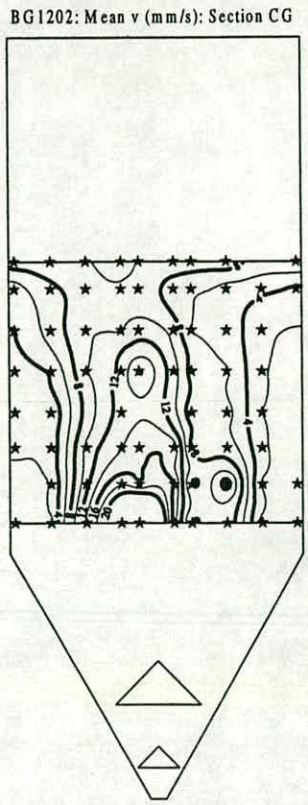

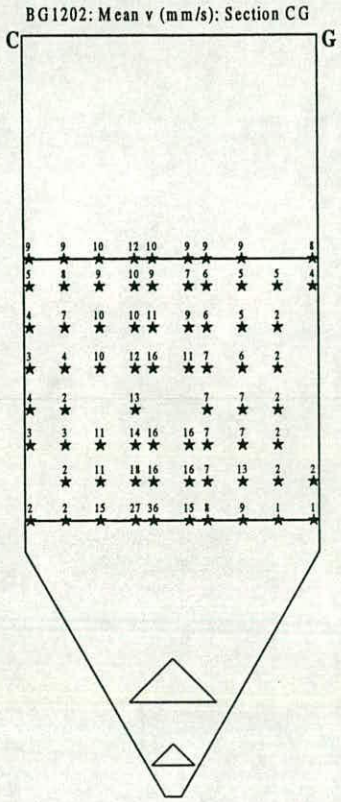

Fig. 5.30c BG1202: Mean velocity: Vertical diametral section C-G: Contours and spot values

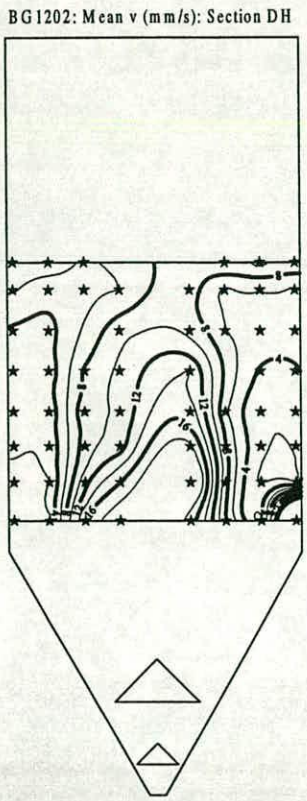

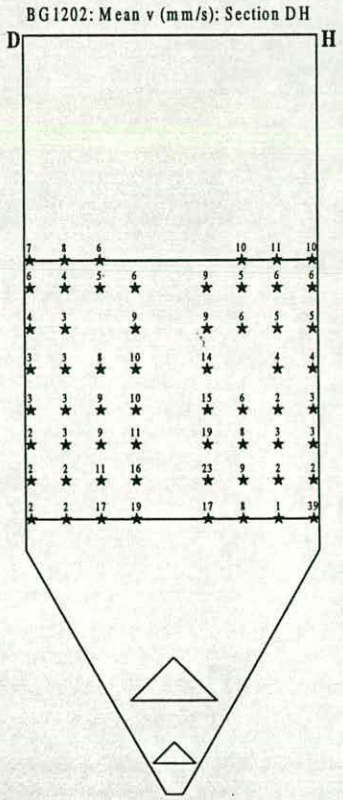

Fig. 5.30d BG1202: Mean velocity: Vertical diametral section D-H: Contours and spot values

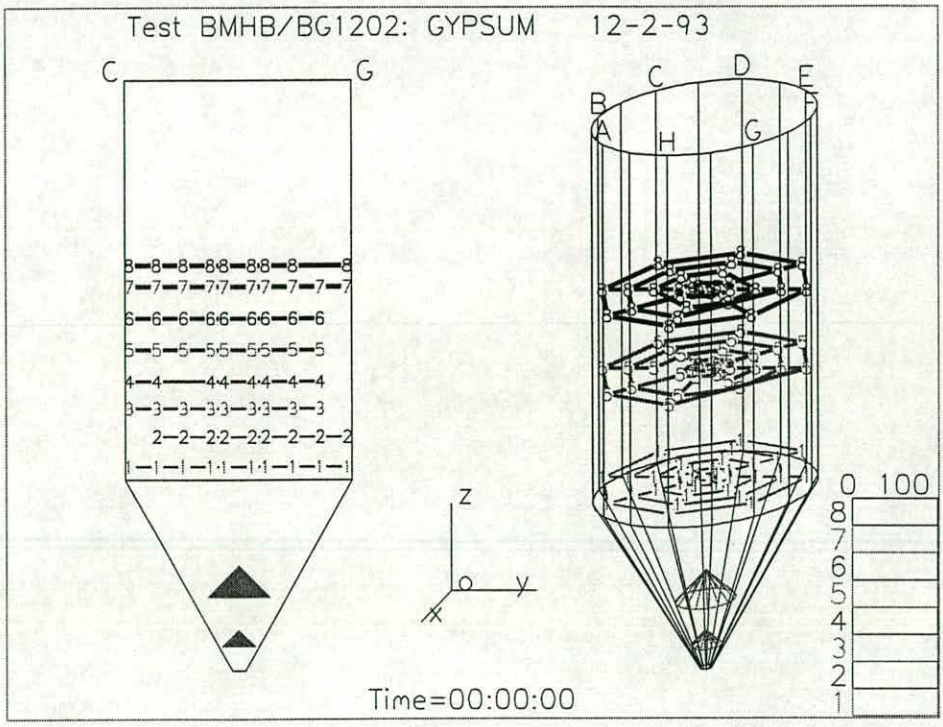

Fig. 5.31a Test BG1202: Simple visualisation: Diametral section CG

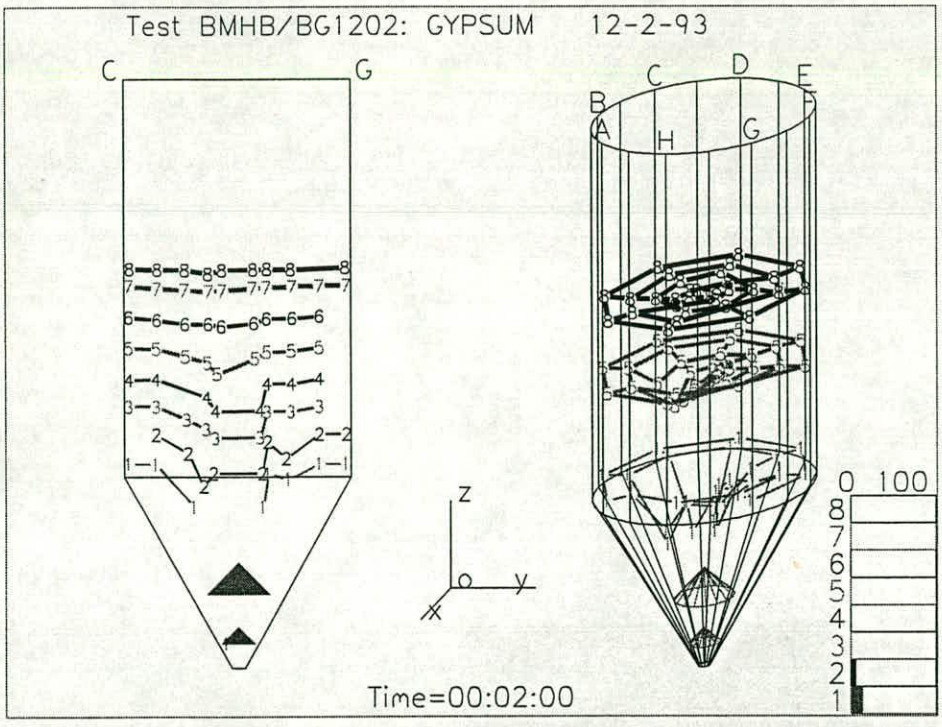

Fig. 5.31b Test BG1202: Simple visualisation: Diametral section CG

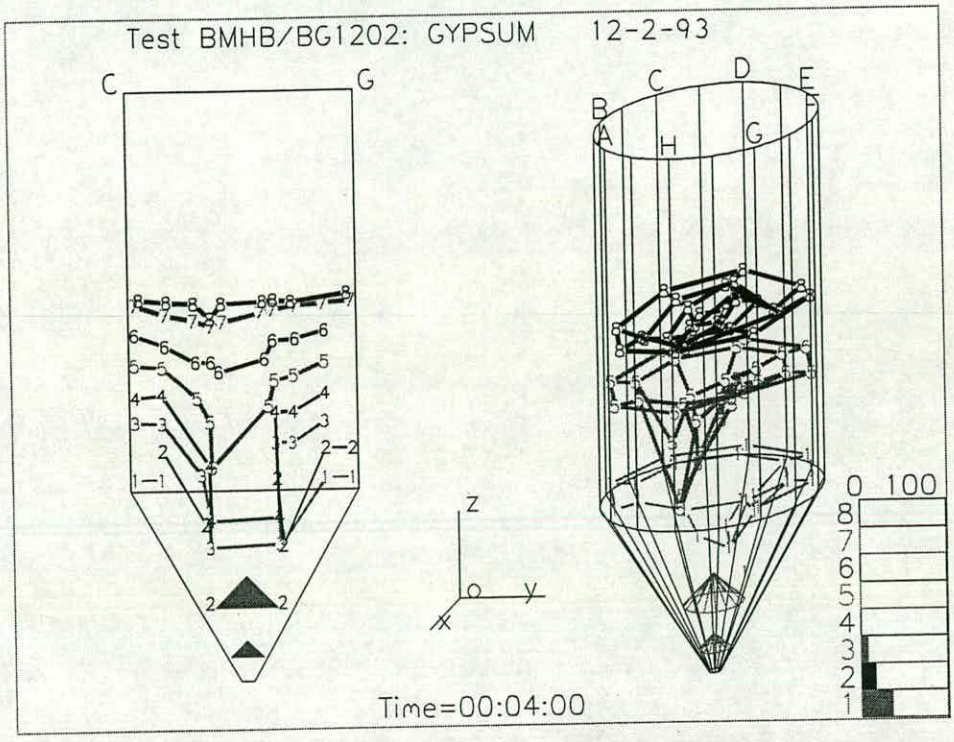

Fig. 5.31c Test BG1202: Simple visualisation: Diametral section CG

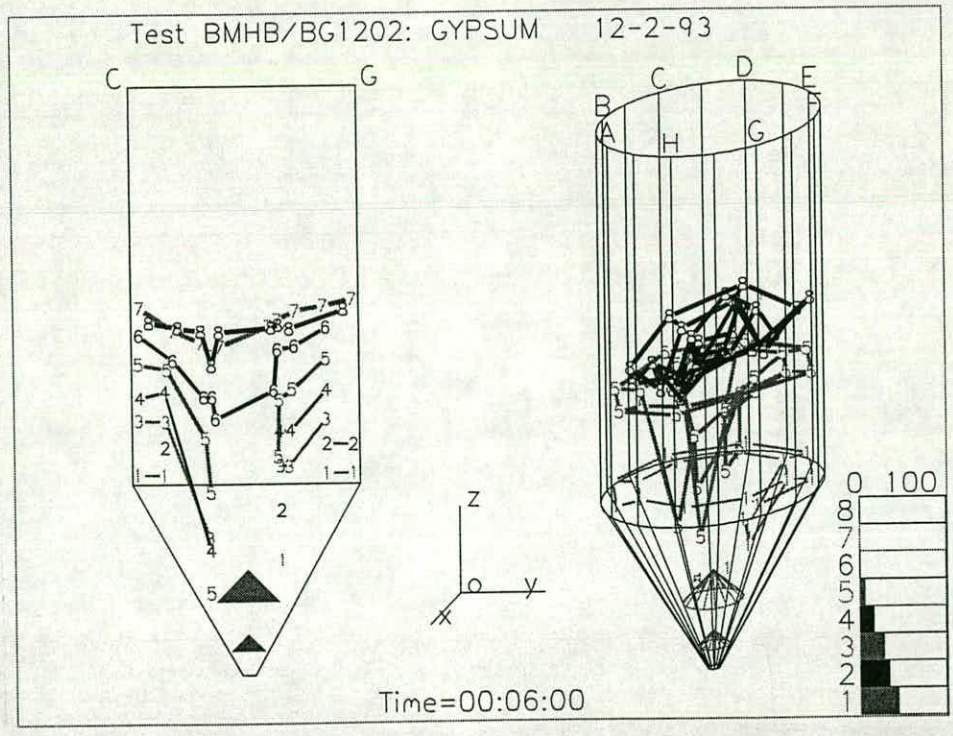

Fig. 5.31d Test BG1202: Simple visualisation: Diametral section CG

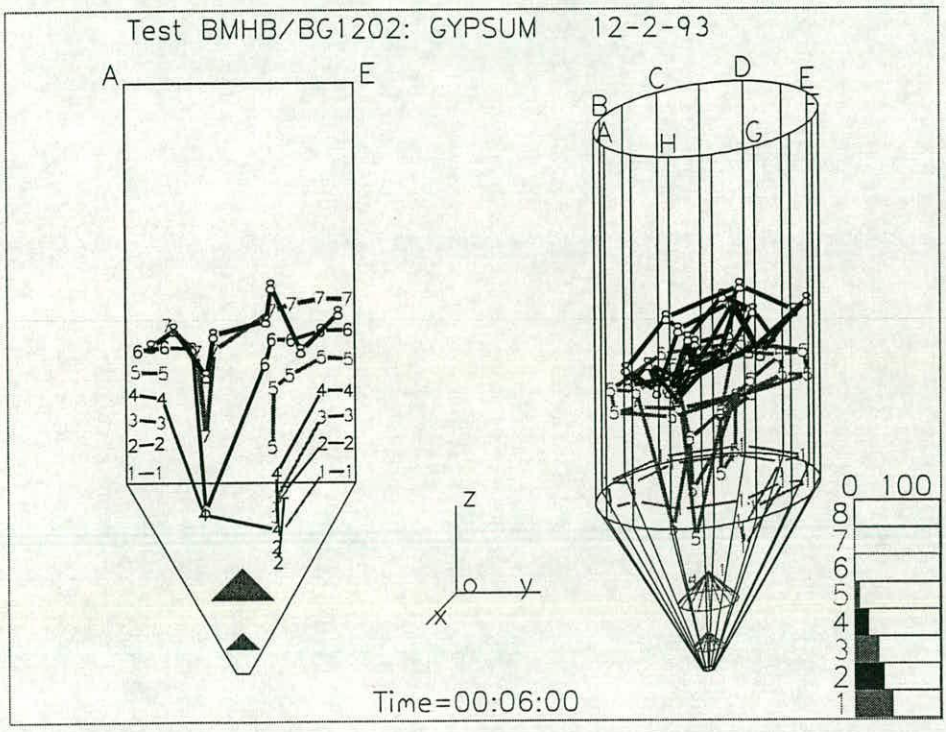

Fig. 5.32a Test BG1202: Simple visualisation: Diametral section AE

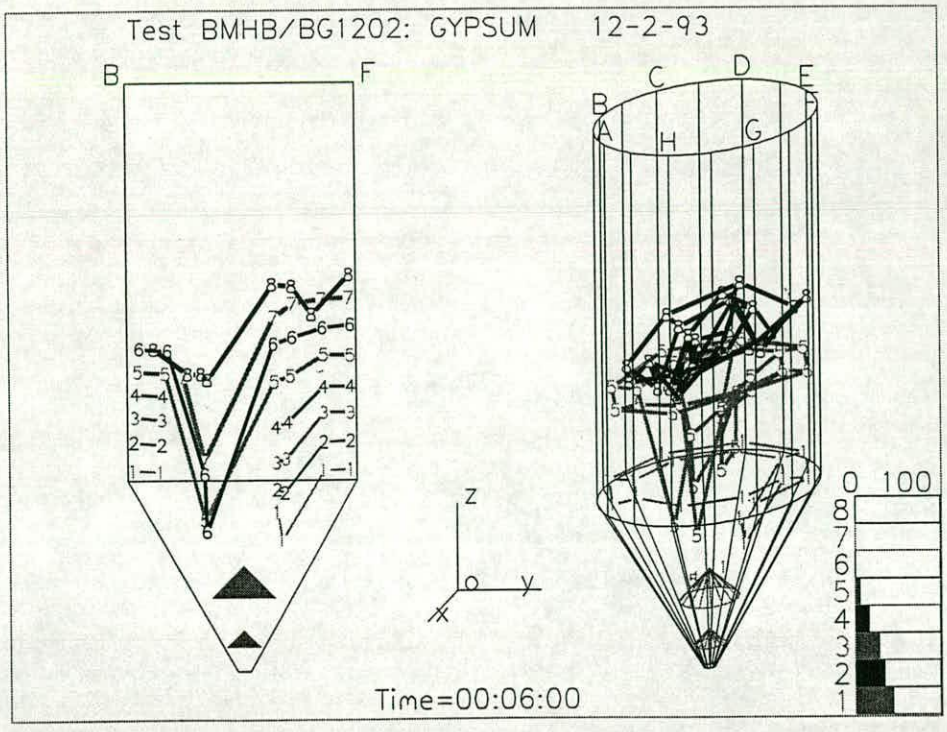

Fig. 5.32b Test BG1202: Simple visualisation: Diametral section BF

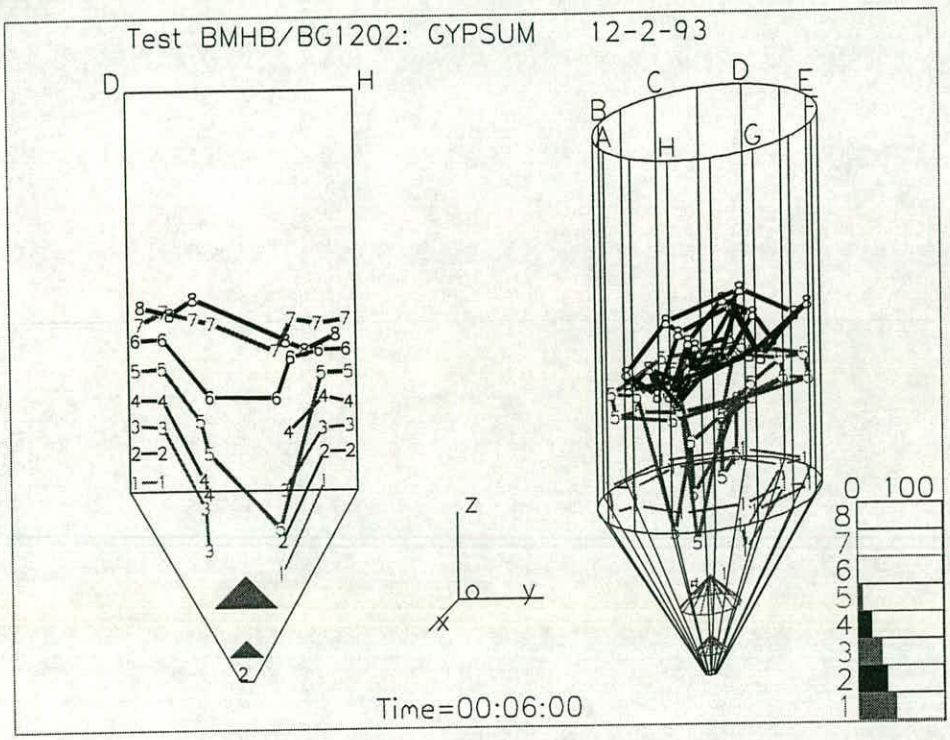

Fig. 5.32c Test BG1202: Simple visualisation: Dilametral section DH

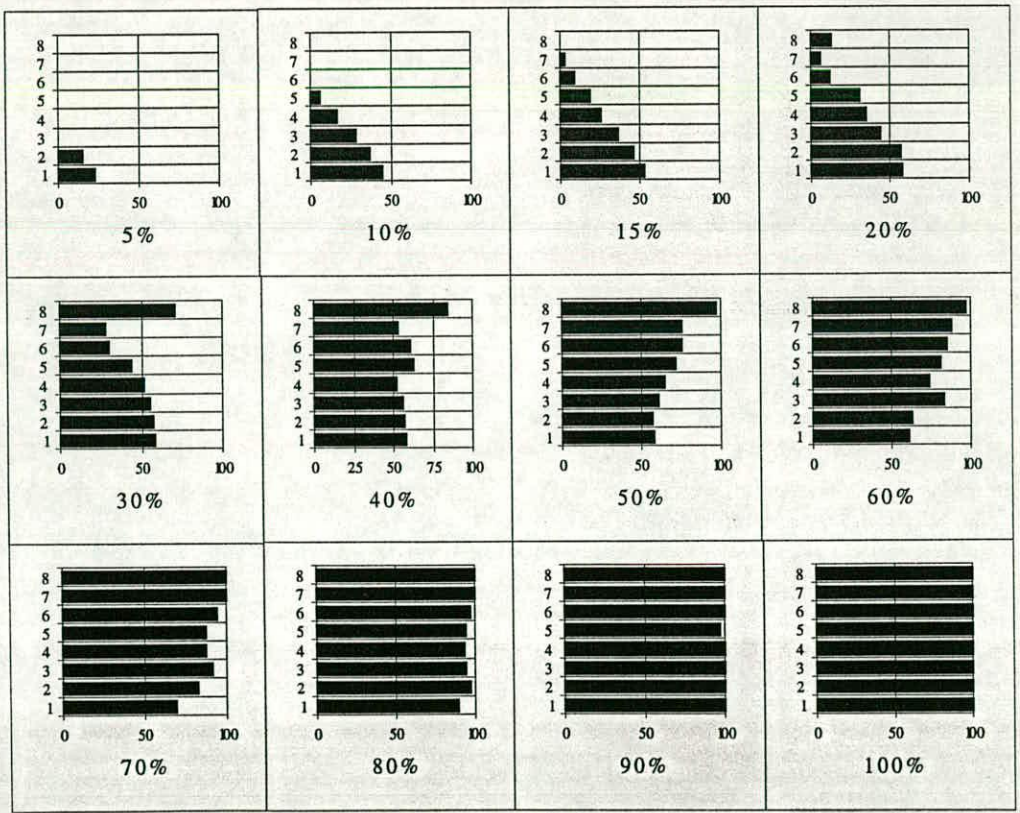

Fig. 5.33 Test BG1202: Bars of tags exited from the outlet at different stages

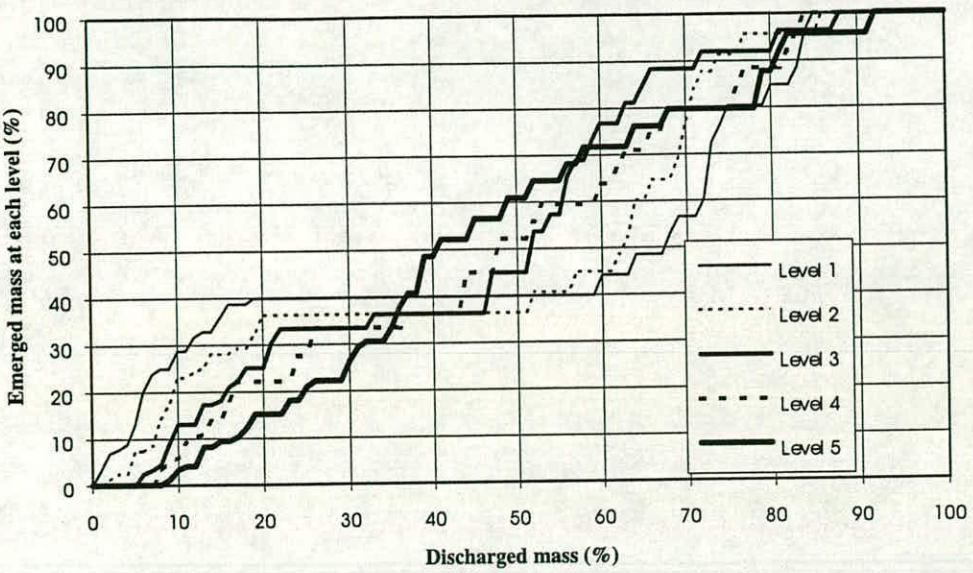

Fig. 5.34a Test BG1202: Emerged mass from different levels vs discharged mass

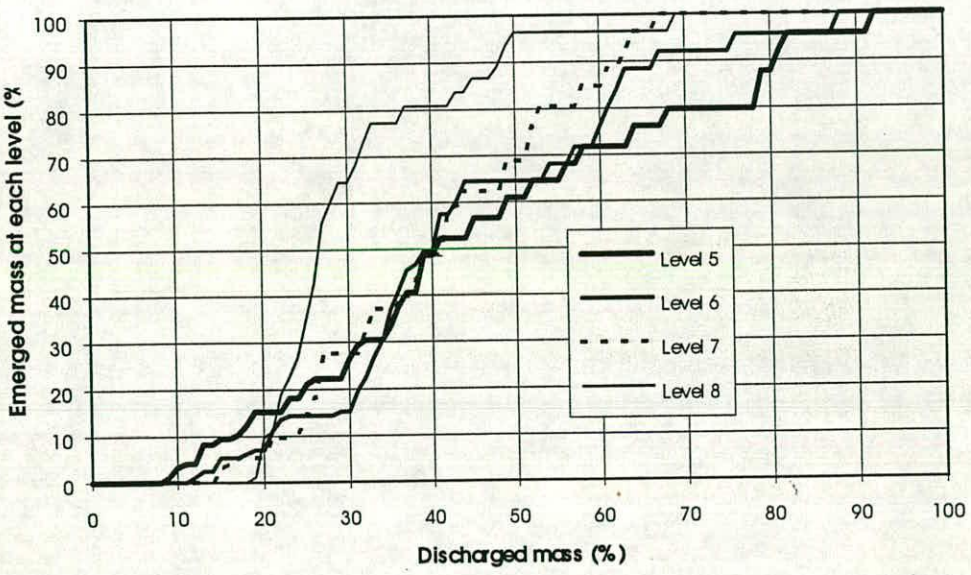

Fig. 5.34b Test BG1202: Emerged mass from different levels vs discharged mass

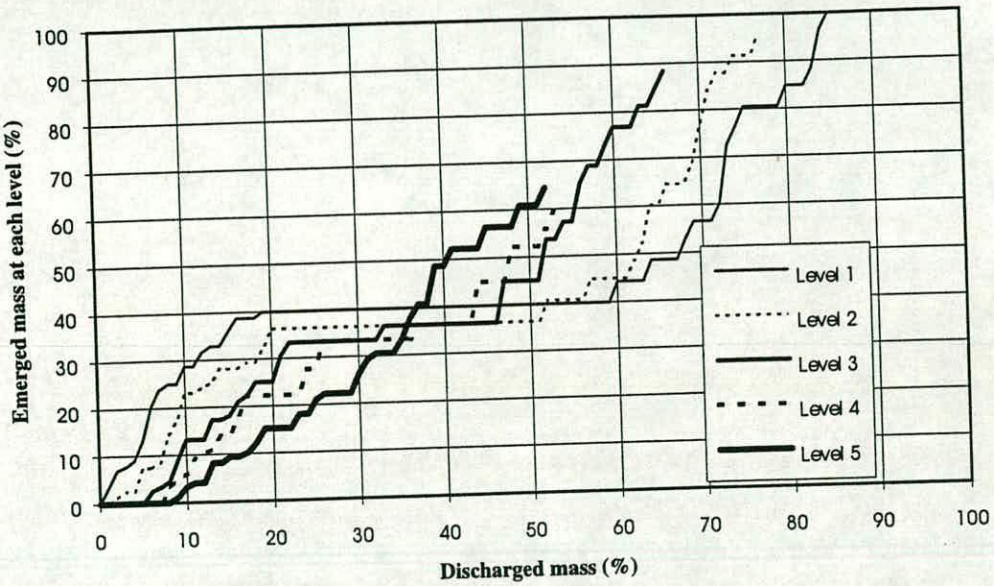

Fig. 5.34c Test BG1202: Emerged mass from different levels vs. discharged mass

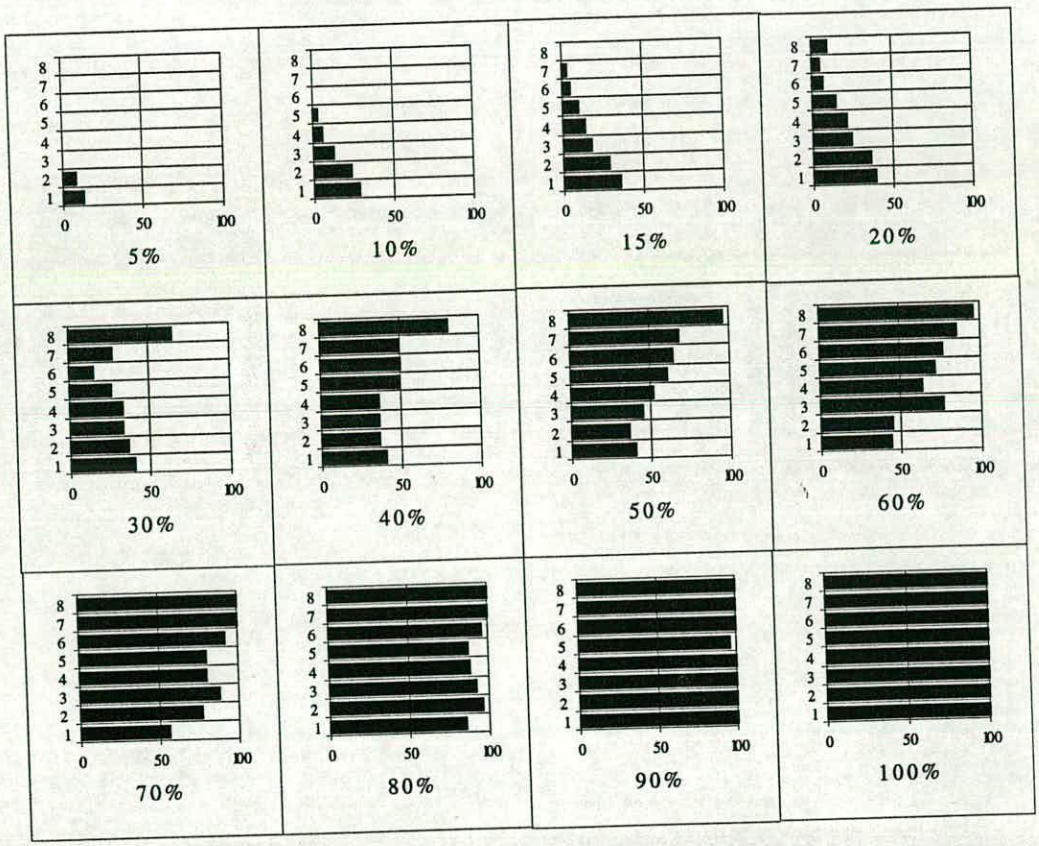

Fig. 5.35 Test BG1202: Bars of materials emerged through the outlet at different stages

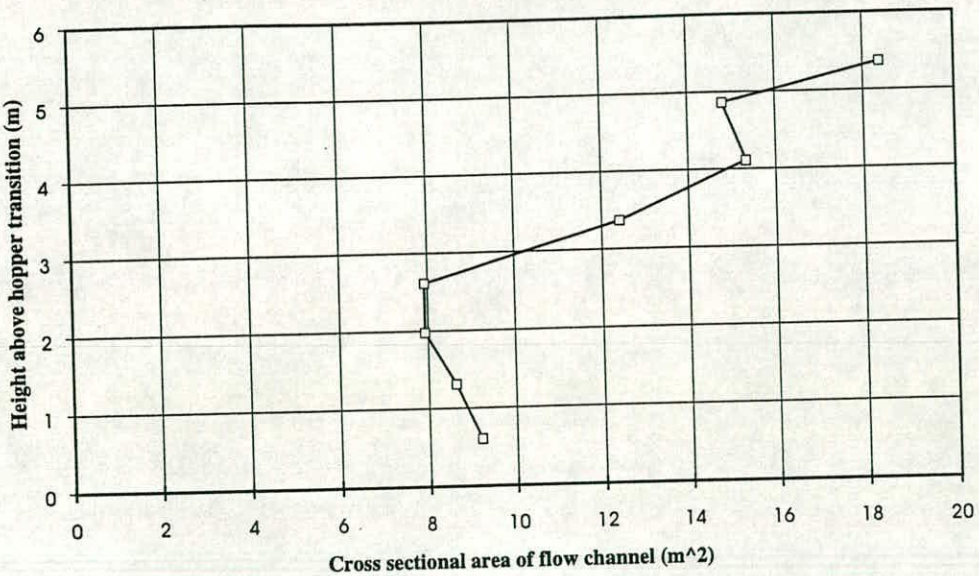

Fig. 5.36 Test BG1202: Approximate size of flow channel

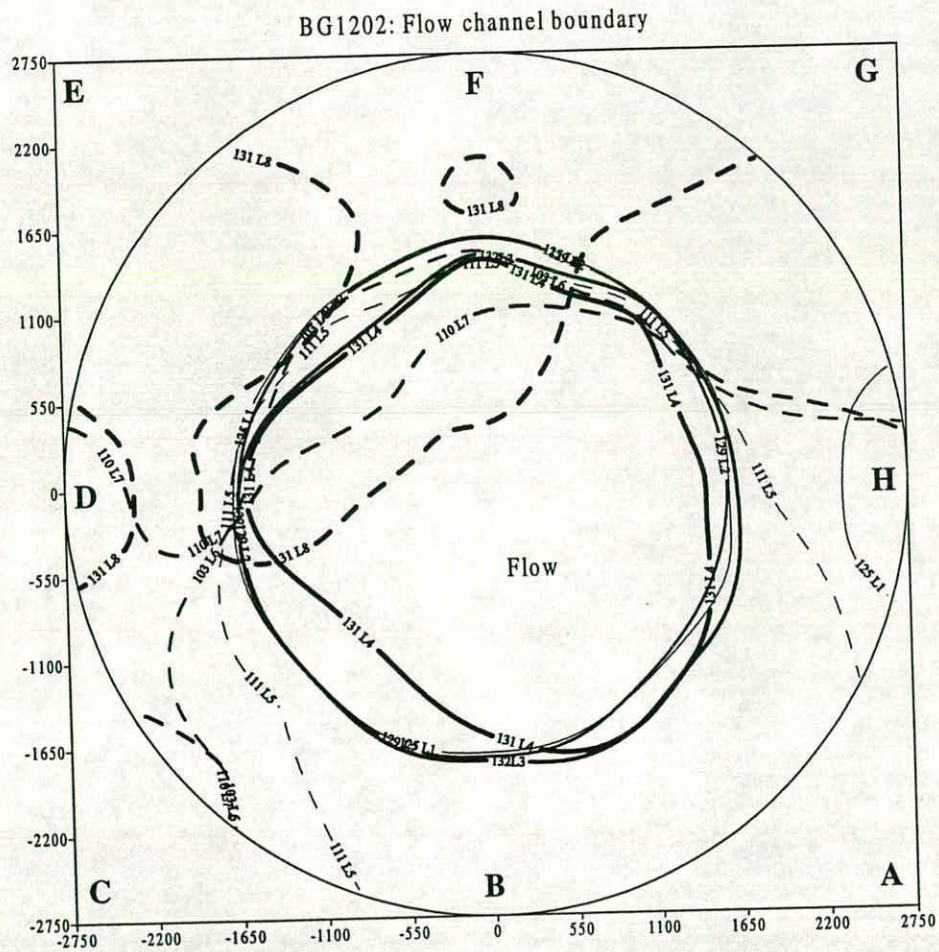

Fig. 5.37a Test BG1202: Approximate flow channel boundary

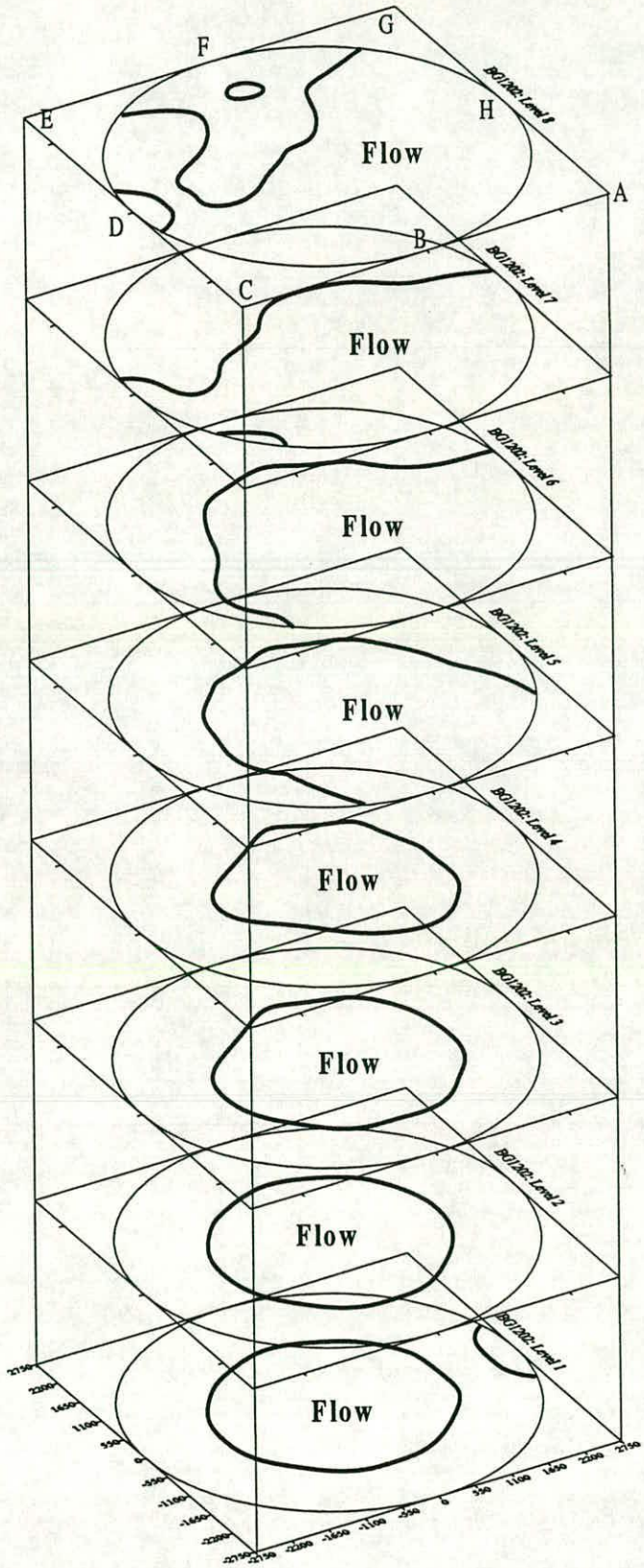

Fig. 5.37b Test BG1202: Approximate flow channel boundary

Chapter 6

FLOW PATTERN MEASUREMENT IN A FULL SCALE SILO AT BRITISH STEEL

6.1 Introduction

The same research team mentioned in Chapter 4 carried out their second series of experiments on solids flow patterns in a full scale experimental silo at British Steel's Teesside Research Laboratories. These were conducted during the summer and autumn of 1993. Unlike the experiments conducted in the British Gypsum silo which were under the constraint of normal industrial operations, these experiments were carried out in a silo specially designed for research purpose (Fig. 6.1).

The second task of this thesis is to interpret the solids flow from these test data. Because the flow pattern measurement system is very similar to that used in the experiments at British Gypsum (see Chapter 4), only the differences and a brief summary of the experiments are presented in this Chapter. Although the candidate did not participate in the experimental work, information on these tests is needed as background before the interpretation work can be understood. Full details of the design, organisation, construction, checking and operation of the test facility are given by Rotter *et al* (1995).

6.2 The silo

The silo used in the studies was a cylindrical steel structure with a diameter of 4.2m (Fig. 6.2). It was specially designed for these experiments by Professor J. M. Rotter in the Department of Civil and Environmental Engineering at the University of Edinburgh. Its working section is 9.5m high and is supported on a 2.4m high skirt wall. The aspect ratio (H/D) of the storage section of the silo is 2.26 and its capacity is 131.6m^3.

The silo was designed for experiments under both concentric and eccentric discharge and to relate the measurements of the flow pattern to pressures on or stresses in the silo walls. A flat bottom was used to ensure that it is possible to have several outlets at the bottom with the solids flowing in a funnel flow mode. There are three outlets at the bottom, two of which are eccentrically positioned with the third outlet being concentric. Each outlet is 480mm in diameter and they are positioned at 850mm centres with the fully eccentric outlet centred at 400mm from the silo wall. The outlet arrangement in the silo floor is shown in Fig. 6.3.

An inlet was placed concentrically above the centreline of the silo. This arrangement ensured that the filling mode was perfectly concentric.

The brief description given here is intended to provide enough information for the solids flow in the silo to be properly understood. Structural details of the silo and strain measurement on the walls are described in Chapter 11 before the strain measurements on the walls are processed to infer the wall pressures.

6.3 Properties of the stored solids

Several materials were used in the experiments (dolomite chips, iron ore pellets and slag fines), but the most successful tests were carried out using iron ore pellets and

only these test data will be analysed in the next chapter. A summary of the material properties of iron ore pellets is presented in this section.

The particle diameter was measured at between 5mm and 21.5mm with a mean value of 12.9mm using a sample of 50 virgin iron ore pellets which had not been subjected to testing. However, a brief search for larger particles produced one of diameter 33.2mm. The particles had a mean aspect ratio of 1.3, which shows that they were typically ellipsoidal rather than spherical.

The virgin samples had a mean loose bulk density of 2320 kg/m^3 and a mean maximum vibrated bulk density of 2510 kg/m^3. Samples with higher proportions of fine particles as a consequence of handling and segregation were found to spread this range from 2270 kg/m^3 to 2830 kg/m^3. A useful mean figure for initial filling was proposed as 2300 kg/m^3 (Rotter *et al*, 1995).

The moisture content changed from one experiment to another but always lay within the range 2% to 5.6%. These differences are thought to be relatively small and did not have a major influence on the solids behaviour.

Figure 6.4 shows a typical Jenike shear cell test result on a sample of fines of iron ore pellets. The deduced Jenike flow function is shown in Fig. 6.5a. The effective angle of internal friction was 52°. Wall friction shear tests on clean mild steel plate, representative of the silo wall interior, showed that the wall friction angle is 26.2° for iron ore pellets (Fig. 6.5b).

6.4 Surface level and remaining solids volume measurement

A manual approach was adopted to measure the top surface level and profile. These measurements are used here to calculate the top surface contours and to deduce the volume of solids in the silo during both filling and discharge. Depth measurements

were taken at eight positions from the roof of the silo (Fig. 6.6). The measurements were taken with a tape measure carrying a weight on its end that was unreeled at each of the positions until it reached the solid. The value was read from the tape where the tape coincided with the top surface of the roof. The values were also taken for each position when the silo was empty. The difference between the two yielded the depth of solid above the floor of the silo at each of the eight positions. This process was carried out each time after the surface was levelled during filling. The results were used to determine the height at which markers were placed in the solid. During discharge, this surface measurement process was carried out continuously and the time of each reading was also recorded. It generally took about ten minutes to record all eight readings.

6.5 Residence time measurement system

The system for residence time measurement in the tests at British Steel was the same as that used in the British Gypsum experiments (see Chapter 4). The key differences were as follows:

a) The solids entering the silo formed a concentric cone. It was raked flat before placing the markers on the surface by hand;
b) The markers were again placed through a colour-coded template, but this time the template was made of wood. It was suspended on ropes from the roof, and could be raised and lowered easily. It remained inside the silo at all times, and could easily be moved out of the line of the entering solids when not in use. The geometry of the seeding pattern is illustrated in Fig. 6.7;
c) Each radio tag was enclosed in a tennis ball to eliminate the possibility that markers could be damaged by the hard and heavy iron ore pellets. To ensure that the marker trajectory during discharge represented the trajectory of neighbouring bulk solid, each ball was filled with iron ore fines to produce a mean density close to that of the bulk solid; and

d) The logging system was identical to that used at British Gypsum, but a larger radio aerial was needed to detect the tags. In addition, some uncertainty was initially expressed about the ability of the tag detection system to identify radio markers when they are immersed in iron ore. This was investigated with control tests, and found not to be a problem.

6.6 Test procedure

Each test began with an empty silo. Each experiment was conducted as follows:

a) Filling: A given amount of solid was filled into the silo before seeding markers. Central filling was adopted in all experiments. A controlled inflow from the inlet was achieved by placing a tun-dish insert at the inlet into the silo. Several inserts with different diameters were available (Fig. 6.8). By changing the insert, the flow could be controlled so that the tun-dish was completely flooded during filling;
b) Sampling: Samples were taken at different points (near the centre, near the wall and in between) for later testing;
c) Levelling: the conical pile of solid at the top was levelled by shovelling from the pile and throwing the material outwards;
d) Depth measurement: When the solid appeared to be level and horizontal, depth readings were taken from the roof of the silo at the eight locations mentioned in Section 6.4 to check for significant variations. If there were found to be major discrepancies, the solid was shovelled further until a satisfactory surface level was achieved;
e) Placing template: Once the solid surface was level, the seeding template was lowered down to rest on the surface. It was carefully oriented so that Spokes A and E lay on the diameter along which the outlets are located, with Spoke A above the eccentric outlet. This process was assisted by the markings which had

been painted on the internal surface in the factory, which permitted both the orientation and the level in the silo to be quickly identified;

f) Seeding markers: The tags, previously labelled with the level of the seeding layer, a spoke letter and a colour, were placed through their appropriate holes, being very careful to ensure that the code on the tag matched the code of the hole. During the placement of the tags, they were half buried in the solid so that they could not be displaced by the impact of later incoming solids during the filling of the next layer.

Steps a) to f) were repeated until all the levels of tags were seeded. A final conical pile of material was sometimes used to fill up the silo;

g) First discharge (slow discharge): The discharge of solids from the silo was initiated by starting the feeder beneath the outlet. The solids flowed out of the silo in a fully controlled manner, with no free fall involved. To obtain the maximum number of strain observations during the early stages of discharge, the solid was very slowly discharged. Any tags which emerged through the outlet were detected by the aerial and recorded by the data logging system. The tags were recovered on a metal grillage. Discharged materials were transported back to the stock pile. This first period is termed First discharge here;

h) Second discharge (fast discharge): To limit the discharge process within a certain length of time, the slow discharge process was changed to a fast discharge after about one hour to reduce the duration of the experiment. This is termed Second discharge here;

i) Removal of dead solids: The flat silo bottom naturally caused some materials to remain in the silo as dead solid and some markers remained in this dead solid at the end of the discharge. After the experiment was complete, the dead solid was removed from the silo. The remaining markers were recovered before the beginning of the next test.

6.7 Experiments in the silo at British Steel

The full set of tests conducted in the new silo test facility are summarised in Table 6.1 at the end of this chapter.

The first two tests were calibration tests, performed using water and designed to check the strain gauge system. These tests showed that thermal effects are very marked when cold water is filled into a warm silo in the summer, and led to increased thermal instrumentation for the bulk solids tests. Some interference from electrical machinery nearby was also found to affect the strain gauge readings, as both the gauges and the logging equipment are very sensitive.

The tests on bulk solids were performed at night to ensure a stable thermal and electrical environment.

The first tests on bulk solids were planned to use crushed dolomite. This material was one of those specified in the materials handling equipment specification. However, although many attempts to fill the silo with this dolomite were made, no successful test could be achieved because of the failure in the solids handling system.

The first successful tests on bulk solids were performed on iron ore pellets. A total of seven tests were performed. These covered the three eccentricities and several repetitions to investigate the repeatability.

In the First discharge of each test, the slide valve at the outlet was not always fully opened. The extent of opening certainly had a minor effect on the flow pattern. It is shown in Table 6.2. The opening direction is shown in Fig. 6.9.

Observations were made of the surface profiles after filling. These were later used to deduce the angle of repose achieved in each test and the symmetry of the filling arrangement. The measurements were made on three radial lines or spokes at 120° to

each other, one of which was through the axis of the discharge outlets. The deduced repose angles from these surface profiles after filling are shown in Table 6.1.

Table 6.2 Opening of slide valve in the First discharge in each test

Test	Opening	Comments
PCA	110mm	
PCB	110mm	
PHA	76mm	
PFA	250mm	Outlet opened before filling
PFB	250mm	Outlet opened before filling
PFC	250mm	Outlet opened before filling
PCC	250mm	Outlet opened before filling

6.8 Segregation on filling

As noted above, samples of the solids were taken from several points on the solid surface at different periods during the filling process. These were later sieved to explore the particle size distribution.

The sieving showed that the sample taken from the centre of the silo generally had a markedly higher proportion of fines than those further out, and the solids near the wall were almost free of fines. It was also found that the percentage of fine particles increased significantly through the tests, and may have had a marked influence in the later experiments. These iron ore pellets, which looked very much like dirty ball bearings, were subject to serious wear. For samples taken from the centre of the silo in an early test PHA (begun 2 Nov. 1993), the proportion of fines (<1mm) is less than 10%. This proportion increased dramatically to about 24% for a later test PFB (begun 18 Nov. 93).

The fine particles, coupled with a high moisture content, produced a cohesive solid when the concentration of fines was high in the late test PCC (begun 6 Dec. 93). Since the fines were relatively free to percolate down through iron ore pellets, the

proportion of fines which accumulated at the centre of the silo towards the bottom was very high. This high fines content led to bonding of the pellets into a solid mass of significant strength. The solid mass became visible to the naked eye towards the end of discharge, and was typically described as looking like a termite's nest.

This may be a most important observation for silo design. A material which can become bonded like this when handled and in the presence of quite small moisture contents can lead to significantly asymmetric flow patterns under apparently symmetrical conditions, leading to unsymmetrical wall pressures.

6.9 Summary

This chapter has summarized the background, design and establishment of the experiments in a new silo at British Steel. Significant observations made during the tests have also been noted. The interpretation of flow patterns for the tests conducted with iron ore pellets (see Table 6.1) will be presented in the next chapter.

Table 6.1 Summary of Tests at British Steel

Test	WFA	WFB	PCA	PCB	PHA	PFA	PFB	PFC	PCC
Start of test	29/7/93	5/10/93	7/10/93	19/10/93	2/11/93	13/11/93	18/11/93	30/11/93	6/12/93
End of test	30/7/93	6/10/93	15/10/93	28/10/93	13/11/93	18/11/93	27/11/93	2/12/93	11/12/93
Material	Water	Water	Iron-ore pellets	Iron-ore pellets	Iron-ore pellets	Iron-ore pellets	Iron-ore pellets	Iron-ore pellets	Iron-ore pellets
Discharge	Concentric	Fully eccentric	Concentric	Concentric	Half eccentric	Fully eccentric	Fully eccentric	Fully eccentric	Concentric
Early discharge rate (m^3/h)				11.2	8.71	8.35	9.27		9.27
Late discharge rate (m^3/h)				36.6	14.3	18.0	18.2		18.5
Height of fill [near wall] mm	9500	9500	4399	6398	8200	8056	7905	7997	7942
Height of fill [at centre] mm	9500	9500	4548	6506	9569	9490	9173	9135	9271
Height of fill [mean] mm	9500	9500	4449	6434	8475	8534	8328	8376	8385
Initial repose angle (degrees)	0	0	Almost flat	Almost flat	40.0	34.3	31.1	28.5	32.3
Number of tag levels	N.A.	N.A.	3	7	8	8	8	N.A.	8
Tags:									
seeded	N.A.	N.A.	108	252	288	288	288	N.A.	288
detected			84	163	221	228	231		259
retrieved			107	236	263	239	243		271
% detected			78.1%	69.1%	84.0%	95.4%	95.1%		95.6%

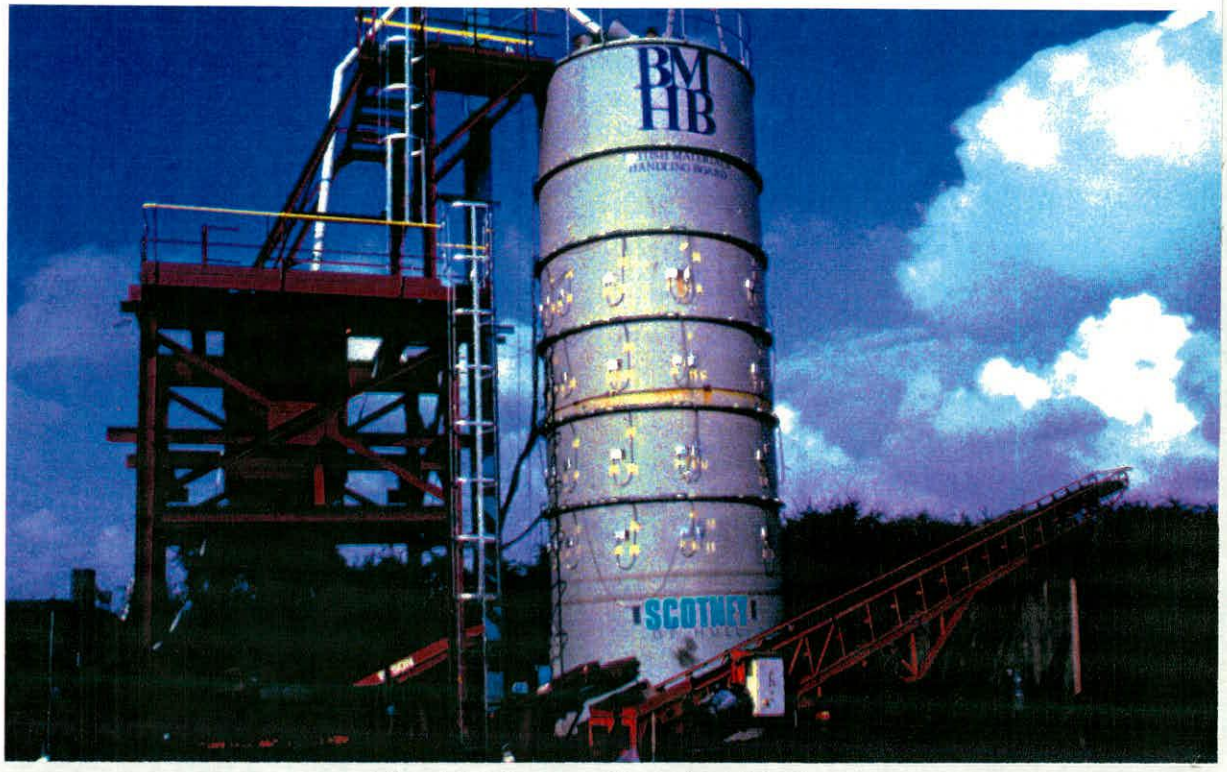

Fig. 6.1 The test silo at British Steel

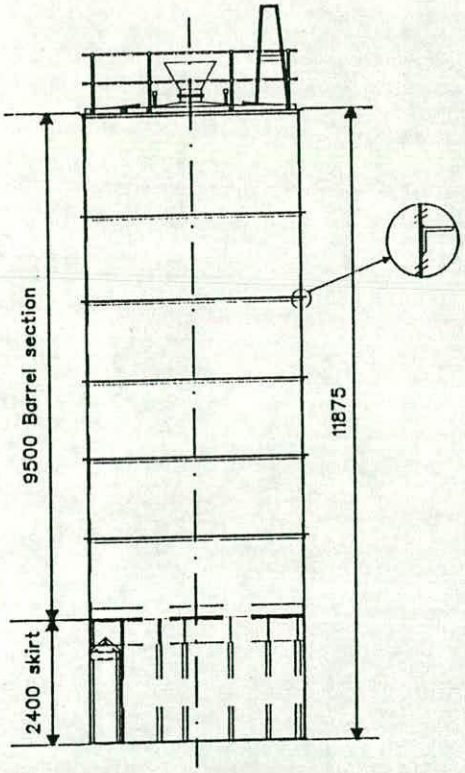

Fig. 6.2 Silo structure

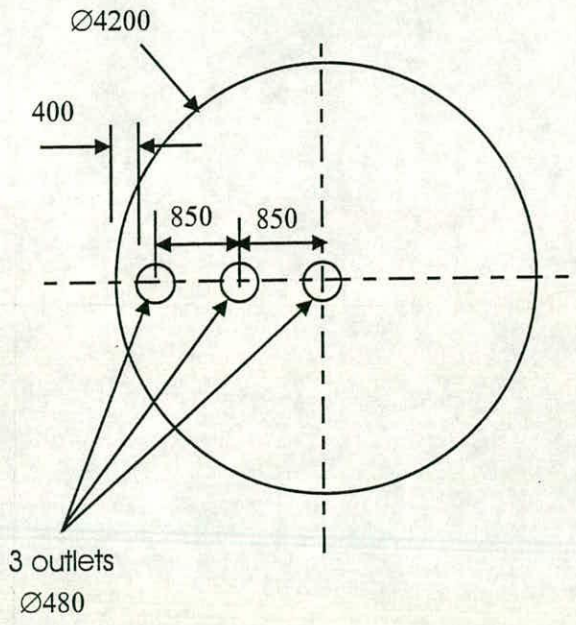

Fig. 6.3 Silo outlets in floor

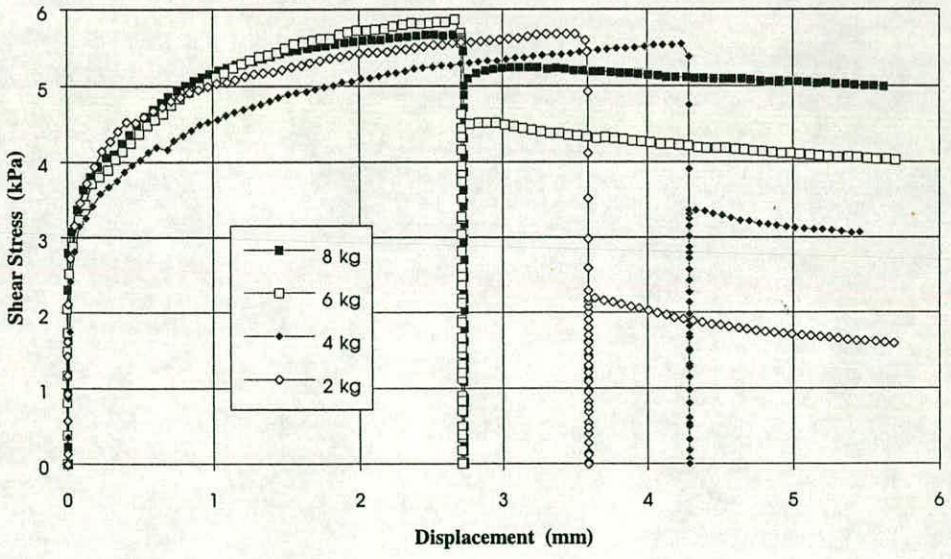

Fig. 6.4 Jenike shear cell shearing test results: 8 kg normal load

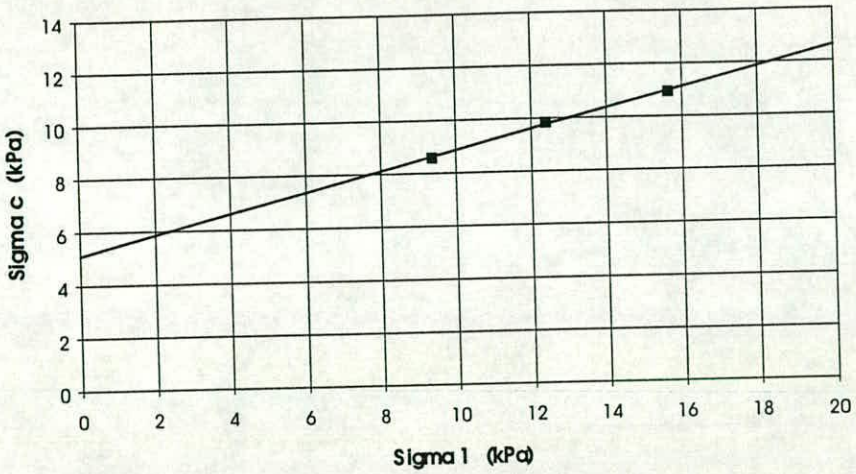

Fig. 6.5a Jenike shear cell flow function for iron ore fines

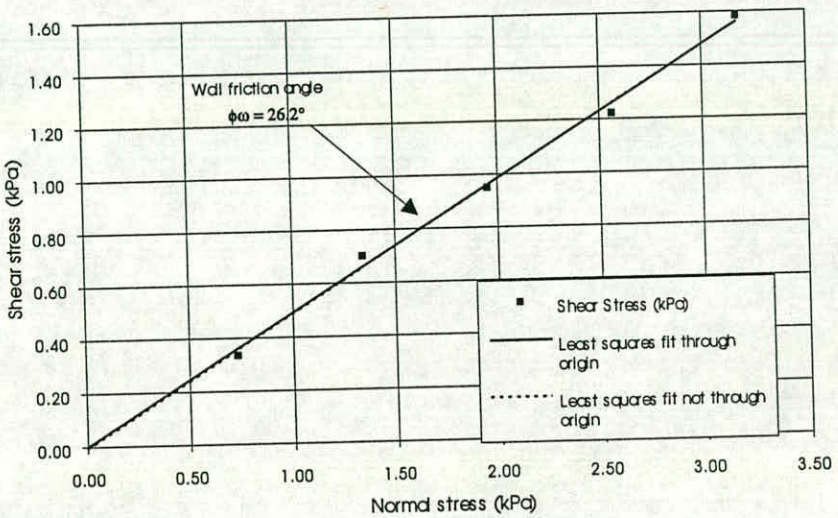

Fig. 6.5b Wall friction angle for iron ore pellets

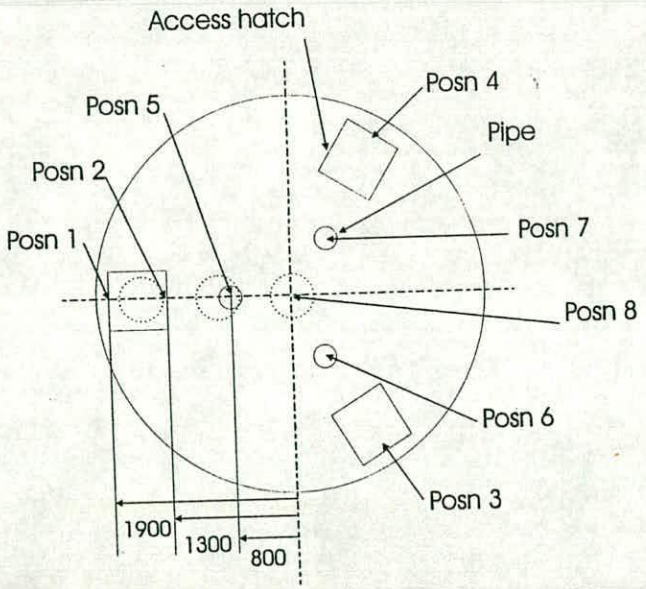

Fig. 6.6 Positions of depth measurement on the solid surface

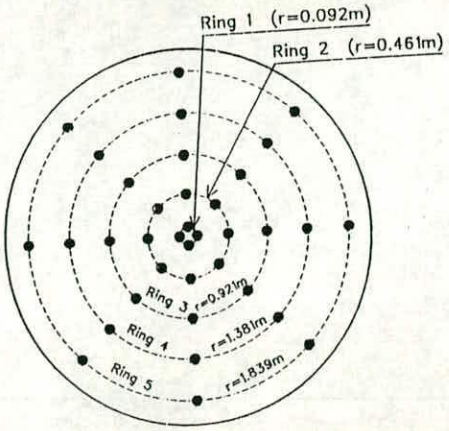

Fig. 6.7 Geometry of marker seeding pattern

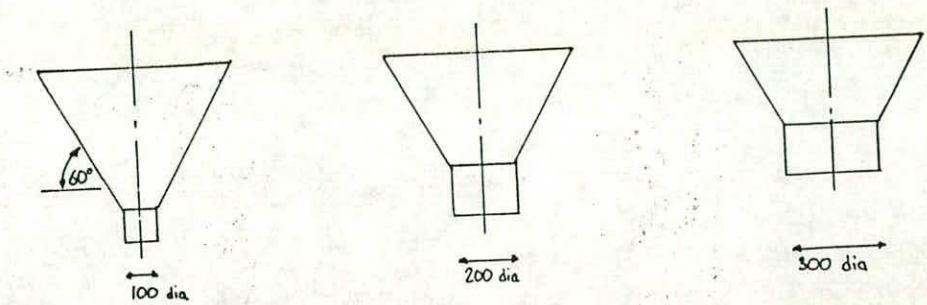

Fig. 6.8 Geometry of the inlet tun-dishes

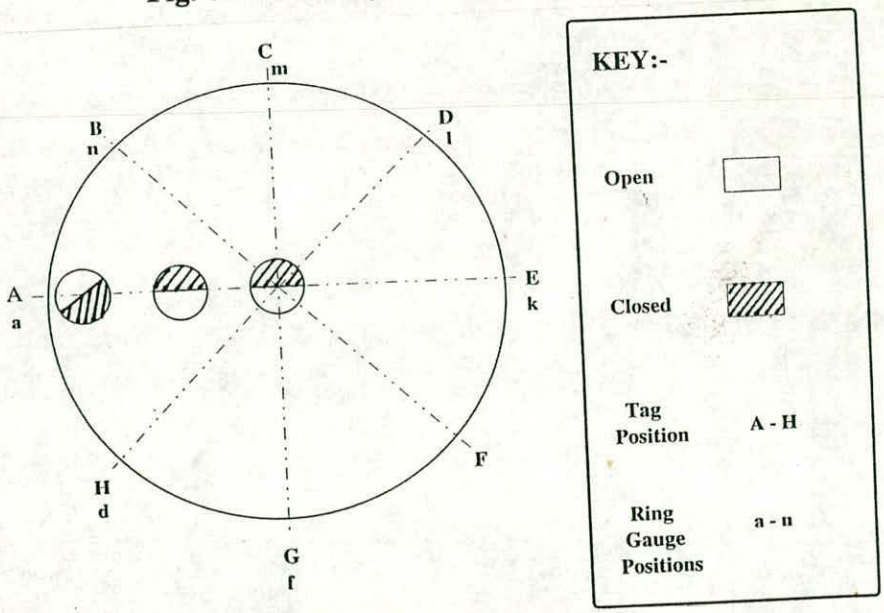

Fig. 6.9 Plan view of outlets and slide valve opening directions

Chapter 7

INTERPRETATION OF FLOW PATTERNS IN THE SILO AT BRITISH STEEL

7.1 Introduction

As summarised in the last chapter (Table 6.1), a total of seven tests were conducted in the newly established test facility at British Steel using iron ore pellets. Six of them involved both the seeding of markers and the measurement of strains in the walls of the silo, whilst the last test (PFC) only used strain measurement. A comprehensive data set was obtained, from which it is possible to deduce matches between flow patterns and wall pressures.

The number of marker layers and the filling height of the solids varied from one test to another. Details are shown in Table 6.1 in Chapter 6.

The chief aims of these tests were to investigate:

a) the repeatability of the observations;
b) the form of the flow pattern in concentric funnel flow;
c) the form of the flow pattern in fully eccentric funnel flow;
d) the relationship between half eccentric flow and these simpler flow patterns;
e) the pressures arising on the silo wall, especially for eccentric flow; and
f) the relationship between flow patterns and silo wall pressures.

This chapter presents the interpretation of solids flow patterns in the six experiments conducted with iron ore pellets (Tests PCA, PCB, PCC, PFA, PFB and PHA, see Table 6.1). The interpretation of wall pressures and their correlation with the corresponding flow patterns will be presented in later chapters.

7.2 Expected flow patterns

The flow patterns which may be expected to occur in a concentrically filled and discharged silo are shown in Fig. 7.1a. However, this silo has a flat bottom which restricts the flow mode to those with internal flow, at least in the lower part. Flow patterns which may be expected with either fully eccentric or half eccentric discharge in this silo are indicated in Fig. 7.1b. Mass flow cannot occur, since by definition it requires all the solids to be moving towards the outlet simultaneously, and clearly a flat bottom will guarantee that some solids never flow out under gravity alone.

The flow channel may widen as it rises up the silo. It may or may not impinge on the wall, depending on the extent of widening. Thus, with different solids, behaviours from narrow channel flow or ratholing through to semi-mass flow with an effective transition part way up the silo wall may be expected (Fig. 7.1b).

The meaning of the term 'flow pattern' is not straightforward. Since the flow develops progressively, the shape of the zone of flowing solid varies through the discharge, and the drawings shown in Figs 7.1 relate to the condition when the silo is still virtually full, but a little while after discharge has begun, so that some material is moving at the top surface.

The sketches shown in Figs 7.1 are drawn according to conventional wisdom about flow patterns, as expressed in international standards (e.g. ISO, 1990; DIN1055, 1987; BMHB, 1987; AS3774, 1990, etc.).

A review of the literature on flow channel shape prediction was presented in Chapter 2. However, it is worth noting here that most authors who have no personal allegiance to a particular method have difficulty in identifying any method of prediction as reliable. Part of this difficulty is undoubtedly the dependence on model

tests for the data. Thus, it is not straightforward to predict the precise shape which the flow channel is expected to take in the experiments described here. A funnel flow, with sides whose slope depends on the solids used, may be expected.

7.3 Methods of interpretation

The plan of the marker layout used in these experiments and the coordinate system to be used in the following interpretations are shown in Fig. 7.2. The concentric rings are at the radii of 92, 466, 921, 1381 and 1839 mm for the Black, Yellow, Purple, Green and Red rings respectively. The spacing of the rings divides the silo into approximately equal zones radially. The marker pattern, in concentric rings above the discharge outlet, was designed to detect any subtle asymmetries in the flow pattern in a concentric discharge test.

The number of levels at which each experiment was seeded with markers is shown in Table 6.1 in Chapter 6. The marker seeding layers are always numbered from the bottom (Fig. 7.2). The height above the silo floor for all the levels in each experiment is listed in Table 7.1. The filling height for each experiment which is shown in Table 6.1 is shown here again for completeness.

For a typical funnel flow, the raw remaining volume readings show higher values near the outlet, decreasing with height in the silo within the flow channel. By contrast, the residence time readings show lower values near the bottom and increase with height in the silo outside the flow channel. Some of the difficulties of interpreting this data were discussed in Chapter 5, in relation to the British Gypsum tests. Here, the flow pattern is simpler and much closer to accepted wisdom, so that the interpretation is easier. However, the different geometry of the silo at British Steel led to different flow pattern forms.

The same types of analysis are applied to the measured observations as were used for the British Gypsum tests, but more efforts are devoted to quantitatively defining the flow channel boundary. The computer animation also requires some small modifications to allow for the multiple outlets and the flat floor in the British Steel test facility. In addition, some direct measurements of the top surface profile were made during the discharge process. They are used to calculate the remaining volume at the instant that each marker emerged through the outlet and as an aid to interpret the flow patterns.

In analysing the emerged mass from a given level as a function of the total mass discharged, it is also assumed that each marker represents the area surrounding it up to half way to the neighbouring markers (Fig. 7.3). These areas are assigned as weightings to markers in different rings. The values are listed in Table 7.2.

Because the discharge rate was not uniform during whole discharge process, the measured residence times need to be transformed before they can be used to calculate the mean velocities of markers or in computer visualisation.

Table 7.1 Tests at British Steel: Filling heights above silo floor

Test		PCA	PCB	PHA	PFA	PFB	PFC	PCC
Start of test		7/10/93	19/10/93	2/11/93	13/11/93	18/11/93	30/11/93	6/12/93
End of test		15/10/93	28/10/93	13/11/93	18/11/93	27/11/93	2/12/93	11/12/93
Discharge		Con-centric	Con-centric	Half eccentric	Fully eccentric	Fully eccentric	Fully eccentric	Con-centric
Height of fill [near wall] m		4.399	6.398	8.200	8.056	7.905	7.997	7.942
Height of fill [at centre] m		4.548	6.506	9.569	9.490	9.173	9.135	9.271
Height of fill [mean] m		4.449	6.434	8.475	8.534	8.328	8.376	8.385
No. of tag levels		3	7	8	8	8	N.A.	8
Height above silo floor for each level, m	Level 1	2.485	0.9	0.839	0.748	0.709	N.A.	0.728
	Level 2	3.315	1.736	2.094	2.024	1.849		1.999
	Level 3	4.079	2.603	2.888	2.707	2.891		3.136
	Level 4		3.687	3.947	3.832	3.766		4.222
	Level 5		4.836	4.906	4.914	4.819		5.157
	Level 6		5.893	6.074	6.037	5.850		6.063
	Level 7		6.310	6.967	6.958	7.136		7.044
	Level 8			8.200	8.007	7.900		7.882

Table 7.2 Weightings for tags in different rings: Tests at British Steel

Ring No.	1	2	3	4	5
Colour	Black	Yellow	Purple	Green	Red
Weighting (m^2)	0.061	0.158	0.331	0.498	0.714

7.4 Calculation of remaining volume of solids at maker exit

In the experiments at British Steel, the actual residence time of each marker was directly measured. However, this is not the most useful parameter as noted in Chapter 5. At British Gypsum, the industrial instrumentation of the silo allowed the total stored mass to be easily automatically measured. Here, the volume of solids remaining in the silo is deduced instead from measurements of the solid surface position and profile. These measurements have the advantage of giving additional information on change in the surface profile which may be related to the flow pattern measurements.

For each seeded level in the seeded experiments, eight depth measurements were taken to measure the height of material in the silo for that level. The positions of these eight points are shown in Fig. 6.6 in Chapter 6. During discharge, observations were continuously made of the surface profiles at the same positions.

At the end of the filling process, the top surface was approximately a cone. The value of the mean height was easily obtained by simple integration of the individual observations. The value in each test is listed in Table 7.1.

During discharge, the process is a little more complicated for two reasons. First, the top surface was not as simple as a cone and its shape changed with time. Secondly, the measurements were continuously made so that no two measurements were made at the same time.

To find the remaining volume at any instant during the discharge process, two steps were involved:

a) To interpolate the depth reading at the given instant from a series of readings made at different times at a point. This should be done for all the eight points at the given instant; and
b) To integrate up the remaining volume of solids in the silo at the given instant.

A computer program was written to fulfil these tasks. There was no difficulty in accomplishing the first task. However, no simple integration rule could be used to achieve satisfactory results because the top surface profile changed with time and could not be described by a simple equation. After investigation of many alternatives, it was found that the best results were given by interpolating the depth values in a regular grid and integrating up the values over these grid nodes. This method is also robust because there is no restriction on the number of depth readings.

In this way the remaining volume of solids in the silo was found at each instant when a marker emerged through the outlet. These values were used for all later data processing.

However, it may need to be noted that the deduced remaining volumes are not as precise as the residence times because the depth readings were made manually and the number of observations was limited. By contrast, the residence times were automatically recorded with an accuracy of 1.0 second. Nevertheless, remaining volume is still used because it is independent of the discharge rate.

7.5 Transformation of residence time

Although remaining volume is independent of the discharge rate and used in many of the following interpretations, the residence time is inevitably required to calculate the

mean velocity of each marker and to perform computer visualisations. As mentioned in Chapter 6, the discharge rate was low during the first discharge and was then increased to a higher value in the second discharge. Direct use of the measured residence times is therefore rather meaningless. This problem was solved by transforming the residence times of markers into the values which would have been obtained with a fixed discharge rate.

A simple way of doing this is to divide the remaining volume at the time a marker reaches the outlet by a fixed discharge rate (volume/time) to obtain the transformed residence time of the marker. However, the higher precision of the residence time observations is totally lost in this way. It is particularly serious for the markers which emerged early (with small residence times). The resulting mean velocity contours in the fast flowing zone above the outlet became rather distorted. It is therefore desirable that the residence times are transformed in a manner which preserves their precision.

Because the discharge rate was constant in the first discharge and again in the second discharge, plotting the remaining volume against residence time is bilinear, as shown in Fig. 7.4. The two lines may be expressed as

$$V = -\rho_1 T + V_1 \qquad (7.1a)$$

$$V = -\rho_2 T + V_2 \qquad (7.1b)$$

in which V is the remaining volume and T is the residence time and ρ_1 and ρ_2 are the discharge rates in the first and the second discharge respectively. The values of ρ_1, ρ_2, V_1 and V_2 can be found from best fits to the relationship between remaining volume and residence time for all the markers in an experiment. The results for Test PFA are shown in Fig. 7.5a. The fitted discharge rates for all the tests are listed in Table 6.1 in Chapter 6.

Since remaining mass M may be calculated by multiplying the remaining volume V by the solid density γ and γ may be treated as a constant, the remaining volume here is essentially the same measurement as remaining mass used in Chapter 5.

To transform the residence times so that the discharge rate is as if it were uniform during the whole discharge process, while the precision of the measured residence times is preserved, the discharge rate in the first discharge was used as the fixed discharge rate and the residence time T for a marker emerging in the second discharge was transformed to T′ as follows

$$T' = \frac{\rho_2}{\rho_1} T + \left(1 - \frac{\rho_2}{\rho_1}\right) \frac{V_1 - V_2}{\rho_1 - \rho_2} \qquad (7.2)$$

Figure 7.5b shows the remaining volume versus residence time for Test PFA after the transformation.

7.6 Flow patterns under concentric discharge

7.6.1 Introduction

The observations of flow in the three concentric discharge tests (Tests PCA, PCB and PCC) on iron ore pellets are discussed here. The three tests are grouped together because they are repeats of each other.

Test PCA was an initial trial test, seeded with only three layers. The silo was filled only to a depth of 4.4 metres. Test PCB was thoroughly seeded. Test PCC was even more completely seeded, and a very high proportion of the tags was observed on discharge, so this test is particularly complete. The full results of the interpretation of Test PCC are presented, together with more limited results from PCA and PCB.

7.6.2 Residence time observations: remaining volume at marker exit

7.6.2.1 Test PCA

There were only three seeded levels in this test. Horizontal profiles of the volume of remaining solids at the time that each marker emerged from the silo outlet are shown in Figs 7.6a-c. In each of the figures, the actual observed values are shown on the right side and the contour plot is shown on the left. These contour plots show a flow pattern which is almost but not exactly axisymmetric. An internal flow channel is clearly seen from these contours: the markers in the central zone emerged early but all the markers around the wall emerged later from the lower levels.

These horizontal contours present the complete raw information. Vertical sections through the data are not shown for the sake of brevity.

7.6.2.2 Test PCB

Seven levels were seeded in Test PCB. The volume of remaining solids at Levels 7, 5, and 2 are presented in Figs 7.7a-c as representative of typical high levels, intermediate levels and lower levels respectively. They show the similarity between Tests PCA and PCB and that the test was quite reproducible. Again, the contour plots show a flow pattern which is fairly symmetrical about the outlet, but not exactly so.

At the highest Level 7 (Fig. 7.7a), the remaining volume is virtually constant ($77m^3$) which might suggest semi-mass flow (Fig. 7.1b). However, examination of data from the level immediately below, it is clear that this is not the case. Therefore, the flow is also internal as in Test PCA. However, it is significant that the sloughing flow of the top layer inwards is very rapid, and permits the outer material there to reach the outlet very soon after the material which was in the centre at the top.

At the intermediate Level 5 (Fig. 7.7b), the value of the remaining volume ($82m^3$) at the centre of the channel has increased slightly above that for Level 7, indicating that the lower material has taken a shorter time to reach the outlet.

At Level 2 (Fig. 7.7c), the raw data show that the centre of the flow channel is fast moving, with remaining volumes of 87-88 m^3, but the outer part of the flow channel is much slower at 77-80 m^3. Points at larger radii are not part of the flow channel, and the solid only emerges near the end of the discharge as the last zones above the dead area slide out.

7.6.2.3 Test PCC

Test PCC is comprehensively described here, because it is the most complete test among the three and because it has some unexpected features. Horizontal profiles of the volume of remaining solids at the time that each marker emerged from the silo outlet are shown in Figs 7.8a-h. A quick review of the contour plots indicates a flow pattern which is quite unsymmetrical about the outlet. More comments can be made as follows.

At the higher Levels 5 to 8 (Figs 7.8a-d), the flow is very unsymmetrical about the outlet and the solids near Generator A (0°) flow faster. It tends to be less unsymmetrical at the lower Levels 3 and 4 (Figs 7.8e and f) and is quite concentric at Level 2 (Fig. 7.8g).

At the lowest Level 1 (Fig. 7.8h), it appears from the contours that there is a bulb of the flow channel towards Generator H (45°). However, it should be noticed that this is a figment of the computer's computational strategy: there are no real observations to suggest the existence of this bulb. The raw data give a much more helpful picture. To make the interpretation easier, the raw data in this figure are presented with one decimal place by contrast with those without a decimal place in other figures. The inner markers all emerged at times between the remaining volumes of

115.5m^3 and 117.7m^3, and none of the surrounding ones emerged until there was only 15.5m^3 left. The final residue in the silo at the end of this test was 13.5m^3, so these were the last to appear. These data points thus represent the first and last tags to emerge, and it is clear that the funnel flow channel is wider than the widest of the points marked between 115.5m^3 and 117.7m^3 for most of its life, and that the outer markers just emerge as the final runoff before the dead material beneath them is left behind. Markers at the outer radii at Level 1 did not emerge at all and are omitted. The raw data suggest that there is a slight asymmetry: the solids in the $x>0$ half plane emerged slightly earlier than those in the $x<0$ half plane. The bulb towards Generator H is due to a missing data point in the second inner ring at this Generator. Because no data is available, the contours can only be produced by extrapolating the data around the area. The asymmetry is well overstated so that the result is very misleading and indeed wrong.

The value of the remaining volume at the highest Level 8 varies between 60 and 100 m^3 (Fig. 7.8a). This large scatter suggests that the flow is a pipe flow, or at least a pipe flow below this highest seeded level (there are some solids above the highest seeded level). The difficulty here is to determine whether the unsymmetrical flow channel touches the walls around Generator A. It may be suggested that the flow is internal at the highest seeded Level 8 because the markers around Generator A near the wall at the level immediately below (Level 7 in Fig. 7.8b) almost all have higher residence times (lower remaining volumes), indicating that they emerged later. However, this proposition is not easy to defend if the values of remaining volume on Generator A at Level 7 are compared with those one level below (Level 6 in Fig. 7.8c). There are some markers on Generator A at Level 6 which emerged earlier than those at Level 7, which is to be expected of makers inside the initial flowing zone. A possible explanation may be that the flow channel touches the wall around Level 6. Because the velocity is not uniform within the flow channel, the solids in the higher parts (around Level 8) enter the fast flowing zone earlier than those in the lower parts (around Level 6) so that they reached the outlet early. This will be further discussed in later sections. At the lower Levels 1 to 6, it is clearer that within

the flow channel, markers emerged early from lower levels, but outside the initial flowing zone, it is markers at higher levels which emerged early.

The same data on remaining volume can be presented in vertical sections through the silo. In Figs 7.9a-d, diametral sections are drawn showing the volume remaining in the silo as raw data on the right and as computer contouring on the left. The contours clearly show a steep sided funnel flow regime. The flow channel can be seen to be very unsymmetrical in Section AE (Fig. 7.9a) but rather symmetrical in Section CG (Fig. 7.9c) with Sections BF (Fig. 7.9b) and DH (Fig. 7.9d) in between. The wavey contours between different levels in the lower parts of the silo are due to wider vertical spacing of the data points than the horizontal spacing and fewer data points available at Level 1. Better contours could possibly be achieved by exploring different methods and constraining the missing data points at Level 1.

The asymmetry seen in these contours is difficult to relate to the direction of the outlet opening during the first discharge, shown in Fig. 6.9 and Table 6.2 in Chapter 6. Figure 6.9 indicates that the opening of the outlet was symmetrical in Section AE but slightly unsymmetrical in Section CG with the outlet at Generator G side opened. This clearly contrasts with the contours presented in Figs 7.8 and 7.9. Therefore, the asymmetry of the opening must not be the cause of the asymmetry of the flow channel. A reasonable alternative hypothesis is that the asymmetry of the flow channel was due to the increased level of fines in the iron ore, described in Chapter 6.

Further information is not easily deduced from the contours presented here, though it is evident that the flow channel formed unsymmetrically up the height of the silo and is very different from Tests PCA and PCB.

7.6.3 Mean velocity contours

The fast flowing zone can be better defined by examining contours of mean velocity. Because the contours of remaining volume have demonstrated that the solids flow

patterns are rather axisymmetric and simple in Tests PCA and PCB, only the results for Test PCC are presented. The horizontal profiles are shown in Figs 7.10a-h.

The value of mean velocity at the top Level 8 (Fig. 7.10a) is small and varies between 0.4mm/s and 1.0mm/s. The flow is unsymmetrical and a fast flowing zone lies around Generator A (0°) as observed in the remaining volume contours. The range of mean velocities becomes larger and larger at the lower Levels 7, 6 and 5 (Figs 7.10b-d), but the location of the fast flowing zone does not change very much. The difference between the highest and lowest values of mean velocity at each level continues to grow at lower Levels 4, 3 and 2 (Figs 7.10e-g), whilst the fast flowing zone tends to move inwards to a position above the outlet. At the lowest Level 1, the fast flowing zone is right above the outlet. It has the highest mean velocity of 5.6mm/s and the lowest one of 0.03mm/s, which represent the largest and smallest values for all the markers in the silo. They also represent the first and last emerged markers. It may be noted that the lowest mean velocity is so small that two decimal places are required to meaningfully display the mean velocity spot values in this figure. Only one decimal place is displayed at all the other levels.

These contours of mean velocity also show that the fast flowing zone is smallest at the lowest level and expands outwards as it goes up the height of the silo. As the flow channel expands outwards, continuity considerations demand that the material in the flowing zone must flow slower at higher levels. This is clearly seen in these contours (Fig. 7.10). The highest mean velocity gradually decreases from 5.6mm/s at the lowest Level 1 to 4.9, 3.7, 2.6, 2.0, 1.7, 1.3 and 1.0mm/s at Levels 2 to 8 respectively.

The same data on mean velocities can also be displayed in diametral sections through the silo as shown in Figs 7.11a-d. These figures are similar to the remaining volume contours shown in Figs 7.9a-d, but they also show that the flow channel is very unsymmetrical in Section AE (Fig. 7.11a) and quite symmetrical in Section CG (Fig. 7.11c) with Sections BF (Fig. 7.11b) and DH (Fig. 7.11d) in between.

However, these images of mean velocity are far superior to the residence time observations, as can be judged by comparing any of the matching figures in Figs 7.9 and 7.11.

The difficulty which arose in analysing the remaining volume contours (uncertainty about whether the flow channel touches the wall in the region of 0° on Generator A) does not disappear here. Although the mean velocity contours give a clearer image of the location of the flow channel, the flow channel boundary is still poorly defined. The contours in Fig. 7.11a show that it is possible that the flow channel expands outwards and touches the wall around this region at the highest few levels. However, the value of mean velocity right against the wall is larger at higher levels than that at the lower levels. This is what would be expected in internal funnel flow.

7.6.4 Surface profile measurements during discharge

One of the techniques of 'flow pattern identification' described in Chapter 2 and commonly quoted by persons unfamiliar with the difficulties of this work is the use of observations of the surface profile. It is stated that this can be done quickly and easily using photography. A more rigorous approach was taken in these experiments, with the surface shape measured manually at eight locations. The results from the concentric discharge Test PCC are described here.

In Figs 7.12a-f the top surface profiles in Test PCC are shown, these are more illuminating. Because the measurements were made on eight points which form three radial lines at θ=0°, 120° and 240° (see Fig. 6.6 in Chapter 6), no two lines are on a same vertical plane. However, for ease of reading and presentation, all of them are presented in the same 2D plots with some modifications. Figures 7.12 present the results on the x-z plane (0°). The results measured at 0° are correctly presented in the right half plane of these plots. Those measured at 120° and 240° are presented on the left half plane, though they are actually not on this plane. The radial coordinate of

these two lines is presented as the minus x-coordinate. To avoid congestion, fewer of the measured results are shown on these two lines.

In Fig. 7.12a, the initial profile is seen at the angle of repose. Filling was performed in Test PCC after the last level of markers had been placed. The surface after the final filling was not raked flat. The second and third profiles (20:17 and 20:22pm) indicate that a depression is beginning to form at the crown of the top pile. However, the fourth profile sees the start of an unsymmetrical depression forming at a radius of about 800 mm. The last profile shows that the depression continues but the solids against the walls at θ=120° and 240° are still stationary. The close spacing of the profiles at θ=120° and 240° indicates that the flow is almost symmetrical about θ=0°.

In Fig. 7.12b, the above depression grows further and moves closer to the wall, possibly actually reaching the wall by 22:03pm. The last profile in this figure shows that the material against the wall at θ=240° has just started to move while that at θ=120° has moved a little bit further. There is a slight asymmetry about θ=0°. By now, the depression zone is as large as the whole silo cross section.

As the discharge develops further (Fig. 7.12c), the depression moves back towards the middle, to have its centre at a coordinate of around 800mm at 23:17pm and perhaps 600mm at 23:45pm. The discharge has now become rather symmetrical about θ=0° again. In Fig. 7.12d, the profile steadily resumes the axisymmetric shape which might have been anticipated at the start, and this is substantially retained throughout the remainder of the test (Fig. 7.12e-f).

Another possible cause of the difficulty which arose in the previous sections in determining whether the flow channel touches the wall may be due to changes in the flow channel position as seen in the surface profiles here.

The top surface profiles for Test PCC are probably the most interesting of all in these experiments. Whilst Figs 7.12 do show interesting phenomena and show that the

flow is unsymmetrical, little else can be deduced from them. It is not possible to draw conclusions about how narrow the funnel flow channel might be, nor whether semi-mass flow eventually develops late in the discharge. As the top surface profiles are much simpler and symmetrical about the outlet in all the other tests, they are not shown for brevity.

7.6.5 Computer flow simulations

A small sample of still images from the computer simulation of flow at different stages of the discharge are shown in Figs 7.13a-g for Test PCC. Only Levels 2, 4, 6 and 8 are displayed in the 3D image on the right side of each figure to avoid congestion. Figure 7.12a presents the starting point of the markers in the planar Section AE. The asymmetry of the flow, noted from the top surface profiles, is very clear in the following images in Figs 7.13b-d in Section AE. The cohesive body of fine material low down in the silo, which probably caused the asymmetry, was almost centrally placed, but slightly biased towards Generator E, restricting the flow velocities from that side considerably.

Figures 7.13e-f show one image for each of the other sections early in the discharge (48 mins). The asymmetry of the flow in Section AE inevitably leads to unsymmetrical flow in Sections BF (Fig. 7.13e) and DH (Fig. 7.13g) because they are not perpendicular to Section AE. The flow is rather symmetrical in Section CG (Fig. 7.13f) which is perpendicular to Section AE.

Figure 7.14 shows bar charts which represent the percentage of tags which have emerged through the outlet from each levels at different stages of the discharge. The percentage indicated at the bottom of each bar chart represents the percentage of the total mass discharged at the time for which the chart was plotted. It is seen that more tags emerge from the lower levels than from the higher levels at early stages of the discharge (≤25%). As the discharge progresses, the number of tags from the top Level 8 soon catches up that from the level immediately below and exceeds it (30%). When 40% of the total solids have been discharged, there are more tags from the top

Level 8 than from any lower levels. Tags from the top Level 8 start to pass through the outlet only after 20% of the total mass has been discharged, but this level has been completely discharged by the time 50% of the total mass is discharged. The number of tags from Level 1 which have exited is very stable between 5% and 80% of the total mass discharged, and the number from Level 2 is very similar between 20% and 70% of the total mass discharged, indicating that the flow channel boundary is very stable for quite a long time in the lower parts of the silo.

The bar charts showing the proportion of tags which have exited at several stages through the discharge in Tests PCA and PCB are shown in Figs 7.15 and 7.16. Although the flow pattern in these tests is somewhat different from that in Test PCC, the bar charts are very similar to each other. They show the standard form for funnel flow.

7.6.6 Analysis of emerged mass from seeded levels

As noted in Chapter 5, all the above methods of interpretation lack the capability to define the flow channel boundary very well. The method of analysing the emerged mass from each level as a function of the total discharged mass was developed in Chapter 5. It is used again here to identify the flow patterns and to define the flow channel boundary. Four steps are involved in doing this:

a) Ensure that the data set is complete by evaluating the remaining volume at the missing tag positions. This is done by interpolation using all the adjacent measured data in the 3D plot;
b) Integrate the emerged mass from each level from the beginning of discharge to the instant being considered and plot the results;
c) Identify the flow pattern from the plots; and
d) Draw the flow channel boundary if a boundary has been identified.

More details are given in Chapter 5.

The results of this process applied to Test PCC are shown in Figs 7.17a and b. All the characteristics of funnel flow as described in Chapter 5 (see Fig. 5.8b) are seen at the lower levels. The emerged mass from Level 1 is very stable from about 2% to about 87% of the total mass being discharged, indicating that the flow channel boundary is very stable for a long time at this level. There is a very small expansion seen on the curve when 40% of the total mass has been discharged. The final expansion began at 87% of the total mass discharged, and represents the last bit which sloughs off the dead solids (the final 10%). The emerged mass from Level 1 does not reach 100%, but stops at about 30%, indicating that only 30% of the mass from Level 1 is discharged and 70% is left in the dead zone. The final level of this curve therefore represents the area of the dead zone.

The flow channel boundary is very stable at Level 2 from about 17% of the total mass being discharged until 78% of the total mass, though the period of this stability is significantly shorter than that for Level 1. This change from level to level continues as the flow channel goes up the height of the silo. At Level 6, the plateau representing the presence of a flow channel boundary is barely identifiable. However, an obvious plateau is seen at the top Level 8. This may suggest that the flow channel is still stable for a short time until this level. Because the velocity is non-uniform in the flowing zone, the slower materials at intermediate levels (e.g. Level 6) take a long time to reach the outlet. Thus they can easily be overtaken by material from the secondary flowing zone when the top surface level is reduced (Fig. 7.1b). By contrast, the solids in the slower parts from the top Level 8 may slide across into the faster zone shortly after the discharge starts so that they reach the outlet earlier than solids from lower levels.

About 13% of the mass from Level 2 is left in the silo when the discharge finishes, as indicated by the final height of the curve. At the higher levels, all the curves go up to 100%, so no solid is left in the dead zone. The size of the dead zone at each of the lower levels (the height of the corresponding curve) is used later to determine the average repose angle of the dead solids as a check on the methods described here.

Some tiny portions of the solid in Levels 5 and 6 seem to have been blocked for a short time, as indicated by the last part of the relevant curves in Fig. 7.17. Apart from this, the flow is as expected in classical funnel flow (see Chapter 5). However, this does not mean that the flow is symmetrical. One of the better features of this method of interpreting the flow pattern from residence time measurements is that it is not restricted by the assumption of symmetrical flow.

The results for Test PCA are shown in Fig. 7.18. The plateaux are barely detectable on these curves. This is because the silo was only filled to a height of 4.4m and the seeded levels are close to the top surface (see Table 7.1). Because all the seeded levels lie above the final dead zone (as indicated by the fact that all the curves reach 100%), it is not possible to deduce anything about the dead zone here.

Figures 7.19 show the normalised mass-time curves for Test PCB. The picture is similar to that for Test PCC. The flow channel is very stable in the lower part of the silo. The flow is neater than that in Test PCC. These normalised mass-time curves are used in the next section to determine the size of the flow channel.

As noted in Chapter 5, the proportion of seeded tags at a level does not correspond to the proportion of mass at that level. Some tags represent relatively large amount of solid. The bar charts of Fig. 7.14 are transformed to represent emerged mass in Fig. 7.20 for Test PCC. The patterns of these two pictures are the same, but differences are also clear. For instance, when 20% of the total mass has been discharged, Figure 7.14 shows that about 50% of the tags have emerged through the outlet from Levels 3, 4 and 5, while Fig. 7.20 shows that only about 25% of the mass from these levels has passed through the outlet. This is because the initial flowing zone (near the centre) was seeded with a relatively high density of tags. This difference cannot be eliminated unless tags are uniformly seeded over the area of the level.

7.6.7 Size of flow channel

As described in Chapter 5, the height of the plateau on the normalised mass-time curve indicates the cross-sectional area of the flow channel at this level (Eq. 5.5). It may need to be restated here that the deduced area is only an approximate measure of the actual flow channel because errors can arise from any of the following factors:

a) the interpolation of the remaining volume values for the missed tags;
b) the relatively small number of tags used;
c) the method of weighting used; and
d) the subjective factor in determining the height of the plateau at high levels.

The accurate flow channel can only be determined by using a great number of markers so that they are very closely spaced across the flow channel boundary.

For Test PCC, there is no difficulty in determining the heights of the plateaux for every level (Fig. 7.17). This may be attributed to the fact that filling was continued after the highest level had been seeded, so the flow channel right up to the highest level is stable for an extended period, though the duration of the stable flow channel is much shorter for high levels than for lower levels.

The plateaux are most difficult to assess in Test PCA (Fig. 7.18) because all the seeded levels are close to the initial top surface so that the duration of the stable funnel is very short at every level. There appear to have been a few "steps" on these curves. The lowest step on each curve represents less than 5% of the mass for each level. Comparing with the remaining volume data (Fig. 7.6), these steps correspond to the few early tags which emerged when the remaining volume was $58m^3$. These few tags (3 at Level 1, 2 at Level 2 and 1 at Level 3) emerged distinctively earlier than any others in the silo. It may be suggested that a very narrow tall pipe flow formed immediately after the outlet was opened and that these few tags are within this pipe flow. The flow channel may then have expanded outwards to form a stable flow channel. However, it is also possible that these few early tags indicate that they

are in a fast flowing central zone in the flow channel. This explanation is particularly convincing when it is noted that there are more tags from the lower levels than from the higher levels as the fast flowing zone is generally expected to be elliptical as shown in Fig. 7.21 (e.g. Krapil, 1965; Tuzun and Nedderman, 1982; Hampe, 1991). Because Level 1 is so high (Table 7.1) that all the three levels may be in the upper half of the elliptical fast flowing zone. Whatever the correct explanation, these lower plateaux do not represent a stable flow channel.

The second plateau has a height of 25% at Level 1 in Test PCA (Fig. 7.18). This should represent the stable flow channel as the next plateau with a height of 58% is too large for the flow channel at this lowest level. The third plateau may represent the expansion of the flow channel at a later stage. The plateau chosen to represent the stable flow channel at Level 2 should be the one with a height of 41%, because the flow channel could not realistically be smaller than its size at Level 1. The flow channel for a higher level should only be smaller than that for a lower level when arching occurs. The flow channel at Level 2 should not be smaller than that at Level 1 because arching did not occur in the experiment. There seems to be no sign of the plateau at Level 3 at all. The flow channel boundary is indeed meaningless at this level as it is almost at the top surface so that the flow channel boundary is not stable at all. However, the slight change of slope at a height of 58% may possibly indicate the initial position of the flow channel.

In Test PCB (Fig. 7.19), it is not difficult to determine the plateaux representing the flow channel boundary for all but the highest Level 7. Again, the difficulty arises because this level is almost at the top surface (Table 7.1). The small change of slope at a height of 64% was used for plotting the flow channel boundary at Level 7.

The cross-sectional area of the flow channel at each level was calculated by multiplying the above determined height of the plateau by the cross-sectional area of the silo ($=\pi\times2.1^2=13.85m^2$). The results are shown in Fig. 7.22. The cross-sectional area of the flow channel in Test PCC expands upwards almost linearly with height at

the lower two levels. It then changes little through Levels 3 to 7, but significantly expands outwards again near the top surface. The flow channel is almost vertical between Levels 4 and 5. The flow channel may be typically divided into three sections: an expanding channel, as seen in the lower part of the silo; a steep-sided channel, representing the middle part; and a highly expansive channel which is close to the top surface.

The shape of the curve for Test PCB is remarkably similar to that for Test PCC. However, in Test PCB the steep-sided section is very short and slightly smaller in area. This may be because the filling height for Test PCB (6.4m) is smaller than that for Test PCC (8.4m, see Table 7.1).

In Test PCA, the steep-sided section is not seen at all from the test data, but it is otherwise very similar to the results of other two tests. Again, the omission of the second section may be attributed to the very small filling height (4.4m) for this test. Although there is no significant difference between the size of the flow channel in the three tests in the lower part of the silo, it is interesting and may be important that at the height around 2m, Test PCA has the largest flow channel cross-sectional area, whilst Test PCC has the smallest one. This will be further discussed later.

7.6.8 Flow channel boundary

7.6.8.1 Methods used to draw flow channel boundary

Two methods are used here to draw the flow channel boundary (FCB) at each level. The first assumes the plan cross-sectional form and the centre of the flow channel. The cross-sectional area of the flow channel is determined at each level as above, and the FCB at each level can be deduced directly. Typically, the flow channel may be assumed to be circular, but different shapes and locations may be assumed at different levels by inspection, using for example the remaining volume contours. This approach is easy to apply and the cross-sectional area at each level determined in the above section is precisely honoured. The chief advantage of this method is that

the parameters describing the flow channel can be derived easily from the result. However, the requirement that the shape and location of the flow channel must be assumed a priori is sometimes unacceptable.

The second method adopts the procedure of remaining volume contour which was described in Chapter 5. This method has the advantage that there is no need to assume the shape or location of the flow channel. The results may be much closer to the actual flow channel boundary if the contours can be properly plotted. However, it is implicitly assumed that a remaining volume contour is coincident with the flow channel boundary at each level. Although this is certainly true if the flow is axisymmetric, it should be noted that it may not always be the case if the flow is non-axisymmetric. Nevertheless, this assumption is probably adequate until some theoretical or experimental evidence is available to test the hypothesis. Therefore, the means of drawing a good contour for remaining volume remains the biggest technical challenge in this method.

Following the procedure described in Chapter 5, the remaining volume value V_f of the contour drawn as the flow channel boundary at each level is determined from the appropriate normalised mass-time curve. The value of V_f for all levels in all the three concentric discharge tests are listed in Table 7.3.

Table 7.3 Value of remaining volume at the flow channel boundary V_f (m^3) (Concentric discharge tests)

Test	Level 1	Level 2	Level 3	Level 4	Level 5	Level 6	Level 7	Level 8
PCA	50	46	50					
PCB	69	63	63	60	57	69	73	
PCC	93	62	71	71	64	62	68	74

7.6.8.2 Test PCA

Figures 7.23a-c show the flow channel boundary for Test PCA. The flow is clearly internal. By assuming that the flow is axisymmetric, the radius of the flow channel may be calculated from the cross-sectional area (Fig. 7.22) at each level. The FCB is drawn here for one of the diametral cross-sections (Fig. 23a). It is interesting to see that the flow channel is approximately in the form of a conical hopper with an average half angle of 18.5° (18.2° at the bottom and 19.4° close to the top surface). Because the lowest seeded level is very high that all the markers emerged through the outlet during the discharge, the boundary of the dead zone cannot be drawn here.

Figure 7.23b shows the flow channel boundary for Test PCA drawn from the remaining volume contours. The flow channel boundaries at all levels are superimposed onto the same plot, but each is labelled with the value of the remaining volume followed by a number indicating the level number (e.g. L2 for Level 2). Figure 7.23c shows the same flow channel boundary in a 3D view. The relative heights of the levels are retained in this 3D picture. The flow channel boundaries are hatched inwards to the flow channel. It is clear that the FCB is rather unsymmetrical and moves towards Generator A as it rises from the outlet, though this was less obvious in the remaining volume contours (Figs 7.6). However, both figures are drawn from the same gridding data files and a careful inspection does show that they match each other. The slightly misleading impression of a very symmetrical flow in this test, drawn from the remaining volume contours, may be attributed to the fact that the values of remaining volume at each level are not very scattered and the contours are almost equally spaced. Since the filling height was low and the seeded levels were close to the initial top surface, the small difference between the remaining volume values inside and outside the flow channel is rather to be expected.

The cross-sectional areas determined for Test PCA in Fig. 7.22 are clearly not honoured at the two higher levels in Fig. 7.23b. This may be partly due to small errors in determining the contour values for drawing FCBs (Table 7.3). Because the remaining volume is relatively uniform, small differences in the chosen value for a

contour may result in a big difference in the area deemed to lie within the FCB. The difference may also partly be attributed to the fact that the contours were drawn using only the observed data at that level, while the values of remaining volume for the missed markers were interpolated in 3D when the normalised mass-time curve was plotted.

7.6.8.3 Test PCB

The flow channel boundary for Test PCB is shown in Fig. 7.24a-c using different methods. Figure 7.24a shows the assumed axisymmetric FCB at one of the diametral cross-sections. The flow channel boundary shape is very much like an inverted bell. The slope of the flow channel boundary close to the outlet is found to be 23.9° from the vertical. The middle section of the flow channel is almost vertical with a radius of 1.19m. It expands again as it approaches the surface. The half angle of the FCB close the top surface is found to be 28.8°, which is slightly greater than the value near the bottom. The last solids remained in the silo (dead zone in Fig. 7.24a) formed a slope angle of 43.9° to the horizontal (46.1° to the vertical).

The FCB drawn from the remaining volume contours for Test PCB (Figs 7.24b and c) shows that it is fairly axisymmetric at Levels 2-4 with the channel at Level 4 slightly larger than the other two. This boundary agrees well with that drawn by assuming a circular flow funnel (Fig. 7.24a). The flow channel then expands rather unsymmetrically and tilts towards Generator F (θ=135°). The very unsymmetrical FCB at Level 1 is a result of poor computer automatic contouring, because there are only a few data points available. This is similar to the phenomenon seen in the remaining volume contours at the first level in Test PCC (see Section 7.6.2.3) but the contour here is even worse.

All the results in Figs 7.24 show that the flow is internal.

7.6.8.4 Test PCC

The flow channel boundaries drawn using both methods are shown in Figs 7.25a-c for Test PCC. By assuming that the flow is axisymmetric (Fig. 7.25a), the flow channel is deemed to be very similar to that in Test PCB. The flow channel angle close to the outlet is found to be 31.9° from the vertical. The central section of the flow channel is again very steep with a radius of approximately 1.38m. The flow channel is quite steep close to the top surface with an angle of 14.6° to the vertical. This may be attributed to the fact that additional material was added above the highest seeded level. The dead zone is found to have a repose angle of 47° (to the horizontal), which is considerably larger than that in other tests. This is attributed to the increase in the proportion of fines and moisture.

Because the flow appears to have been unsymmetrical as noted earlier in this chapter, Fig. 7.25a also shows the flow channel with its centre inclining towards to Generator A (0°). As a first order approximation, it was assumed that the locus of the centre of the flow funnel is a single inclined straight line. The assumption that the flow channel was circular remains unchanged. The angle of inclination of the centre of the flow channel was assumed to be 3°. It is assumed here that the sides of the flow channel always form an expanding cone, whose sides are always inclined at some angle to the vertical (no overhanging permitted). For this reason, the chosen angle of 3° for the slope of the flow channel centre cannot realistically be made further from the vertical as the inside edge would overhang. Even though this silo is not very tall, the 3° slope results in a considerable displacement of the flow channel towards the wall near the surface.

The flow channel drawn from remaining volume contours (Fig. 7.25b and c) is better defined than those in Tests PCA (Figs 7.23) and PCB (Figs 7.24) because more measured data points are available in this test. The FCB is fairly axisymmetric at Levels 1 and 2, but inclines to Generator A as it rises (Levels 3-8). The FCB is

almost vertical on the left side (Generator E) and fairly symmetrical about the diametral section AE.

Figures 7.25b and c show that the flow channel first touches the wall between Levels 5 and 6. The FCB intersects the walls at circumferential coordinates of about +15° and -15° at Level 6, but widens at higher levels to intersect the walls at circumferential coordinates of about +75° and -75° at Level 8. The contour at Level 7 shows that the FCB does not touch the wall at all, but this may well be caused by an error. Many sources of error as noted earlier in this section (Section 7.6.8) could lead to small errors in the locus of the FCB. One of them is that the position of the flow channel changes slightly from time to time, as observed from the surface profile. Another is that the computer automatic contouring program may infer more than is justifiable. It may be noted that there is no data point really near the wall, so the contours there depend heavily on extrapolation. It should not be a surprise if an extrapolation technique sometimes produces inaccurate results. If human intelligence is used instead, the FCB probably touches the walls at circumferential coordinates of about +45° and -45° at Level 7.

The shape of the flow channel at the higher Levels 6-8 in Fig. 7.25b is apparently not circular. This may be the main reason why the FCB only touches the wall at the highest level if a circular flow channel is assumed (Fig. 7.25a). Nevertheless, the flow channel at the higher levels is short lived and not very important.

7.6.8.5 Comparison and discussion

The easiest way to compare the flow channels in these experiments may be to compare the pictures drawn by assuming that the flow is axisymmetric. They are shown in Figure 7.26 for all three concentric discharge tests. The initial top surface profiles before discharge are also shown for reference. By ignoring the asymmetries in these tests, it may be seen that the flow channels are very similar to each other. The flow channel is largest in Test PCC and smallest in Test PCA in the lower parts

of the silo. These dimensions may be correlated with the filling heights in the tests, which will be explored later in this chapter. If the filling heights had been the same in all three experiments, it might have been concluded that the tests were precisely reproducible except for the asymmetry which deserves further discussion as follows.

It was demonstrated in the previous section that the asymmetry of the flow in Test PCC was possibly because the centre of the flow channel was slightly inclined. As a first order approximation, the locus of the centre of the flow channel may be assumed to be a straight line. The angle of deviation of this line from the vertical may be a simple measure of the asymmetry. Because asymmetry was also seen in Tests PCA and PCB, it is interesting to compare the degree of asymmetry in the three tests.

By assuming that the flow channel is circular and that the centre of the flow funnel is inclined in some directions at an angle of 3° from vertical in all three tests, the FCBs at different levels were redrawn (Figs 7.27a-c). It was found that the results match Figs 23b, 24b and 25b best if the channel was assumed to be inclined towards Generator A (0°) in Tests PCA (Fig. 7.27a) and PCC (Fig. 7.27c) and towards Generator F (135°) in Test PCB.

Although the sizes and shapes of the flow channel do not exactly match each other in these two sets of figures (the reasons have been discussed earlier), the chosen degree of asymmetry seems to produce convincing results when it is taken to be similar. It is not claimed that the asymmetries of flow in all three experiments are solely due to the centre of the flow channel being inclined at a single angle. Instead, it may be stated that the asymmetries evident in all three tests appear to be explicable in terms of a small deviation of the centre of the flow channel from vertical. The value and direction of the deviation angle of the flow centre may vary in a random manner. It is evident that the flow channel in Tests PCA and PCC inclined towards Generator A (0°) while that in Test PCB inclined towards Generator F (135°). The value of the deviation angle from vertical may be of the order of 3°.

Thus, the asymmetry of the flow channel position is strongly related to its height above the silo floor. The higher the level, the more unsymmetrical the flow may become. Given that the angle of deviation of the flow channel may well be similar in all three tests, the appearance of a grater asymmetry in Test PCC may simply be because the filling height of Test PCC was largest. Similarly, the asymmetry at higher levels in Test PCA is smallest while that in Test PCB is in between.

Thus, the conclusion drawn in early sections of this chapter analysing the remaining volume and mean velocity contours that the flow was fairly axisymmetric in Tests PCA and PCB but very different in Test PCC may well be wrong. The key point missed in drawing this conclusion in the early sections is that the asymmetries at higher levels were compared with each other without considering their heights above the silo floor.

The asymmetry of the flow might normally be attributed to many factors, such as segregation and asymmetry during filling. However, the great care taken to ensure symmetry in the filling process in these experiments indicates that a certain level of asymmetry is almost inescapable in silos. One probable cause in this case is the slight drying of solids on the "sunny" side of the silo relative to those on the "shadow" side, leading to minor changes in bulk solids flow properties. The experiments certainly show that very minor effects can produce asymmetries of significant proportions. It is therefore important in design that a small random asymmetry is always considered, especially in the design of silos of high aspect ratio, which may lead to very unsymmetrical flow in the higher parts.

7.7 Flow patterns under fully eccentric discharge

7.7.1 Introduction

In many senses, the fully eccentric discharge tests are the most important of this experimental series. Eccentric discharge has often led to catastrophic collapse of silos, and the form of the flow channel has been the subject of extensive discussion.

The observations of flow in two of the three fully eccentric discharge tests on iron ore pellets are discussed here. Test PFB was a repeat of Test PFA, but Test PFC is not discussed here as it was not seeded with radio tags.

7.7.2 Residence time observations: remaining volume at marker exit

Test PFA is described here first. Horizontal profiles of the volume of remaining solids at the time that each marker emerged from the silo outlet are shown in Figs 7.28a-h. Again, both contours (left) and actual observed values (right) of remaining volume are shown in each figure. A quick review of the contour plots shows a symmetrical flow channel propagating up the wall of the silo.

At the highest Level 8 (Fig. 7.28a), all the markers emerge at a similar time, and the entire cross-sectional area of the silo falls between the 105 and the 80m^3 contours. This indicates that the discharge was being fed by material from the top levels, as would be expected in a narrow pipe funnel flow, such as were seen in the concentric tests. The materials which emerged earlier (V=103m^3) at this level are from the region directly above the outlet. With the development of a depression of the top surface above the outlet, the materials outside the flowing channel gradually slide down into the funnel. The materials at the opposite side of the outlet (Generator E) are the last to emerge at this level.

The picture becomes clearer at the level immediately below (Level 7 in Fig. 7.28b). The solids above the outlet emerged earlier (V=107m^3) than those at Level 8, as is expected in a flow channel. All the tags in the right half plane emerged before the

time when $75m^3$ of solid were left in the silo. The solid on the opposite side of the outlet emerged later ($V=70m^3$) than those at Level 8, as is expected outside the flow channel (in the secondary flowing zone).

Whilst the scatter in the remaining volume increases at lower levels (Figs 7.28c-h), the pattern of the remaining volume contours remains unchanged. At Levels 1 and 2 (Figs 7.28g and h), the points shown with a remaining volume value of 0 are tags which were left in the silo after the discharge was complete. They are used here to constrain the contours around the outlet, for which no meaningful contour could be produced otherwise.

It is unfortunate that the "cartwheel" pattern of the marker layout was not arranged to be symmetrical with respect to the outlet. Very few tags were in the region above the outlet. The flow at Level 1 (Fig. 7.28h) was very localised and it remained so throughout the discharge with only three of the tags being recorded because of the sparsely placed tags in that area. Of the three emerged tags, two were within the flow channel and emerged immediately after the outlet was opened ($V=119$ - $120m^3$) while the third represents some of the last solid to emerge ($V= 25m^3$).

By examining the raw data at all seeded levels, it can be seen that a column of material above the outlet was discharged initially and that the flow channel grew into a steep-sided funnel flow configuration, as assumed in the design (Fig. 7.1b). Because the tags were sparsely placed in the region above the outlet, the flow channel boundary cannot be precisely identified. By definition, the distribution of residence time (remaining volume) is discontinuous across the FCB. The interpolation technique looses its power in this case. Furthermore, the contours near the wall can only be produced by extrapolation, which may easily produce poor results. For these reasons, the computer contours above the outlet are often misleading. The most obvious example of this can be seen in Fig. 7.5.1c (Level 3) where a very convoluted flow channel geometry was produced by automated contouring. The remaining

volume contours are therefore not a good method of identifying the flow channel boundary in this case.

Figures 7.29a-b show two perpendicular diametral sections through the silo. Section AE (Fig. 7.29a) shows a steep-sided funnel flow pattern. The flow channel widens relatively rapidly for the first three levels and then becomes very steep in the next five. Section CG (Fig. 7.29b) illustrates the symmetry of the measured flow. Sections BF and DH are less interesting and not shown here.

Test PFB was very similar indeed to Test PFA. The computer contour plots of remaining volume at Levels 8, 5 and 2 are shown in Figs 7.30a-c as representative samples from higher, intermediate and lower levels. The vertical Sections AE and CG are shown in Figs 7.31a and b. Whilst the contour plots themselves are slightly different, the actual recorded values of remaining volume in Test PFB are generally only 1 or 2 m^3 smaller than those in Test PFA throughout the silo. Considering the $3m^3$ difference of filling volume ($120m^3$ for PFA and $117m^3$ for PFB), this shows a remarkable degree of repeatability and demonstrates beyond any doubt that these tests are scientifically reproducible, given the same initial conditions.

7.7.3 Mean velocity contours

The mean velocity of each marker in Test PFA is shown in Figs 7.32a-c. It has been demonstrated in the previous sections that although mean velocity contours show a clearer picture of the flow pattern than remaining volume contours, the FCB is still poorly defined and further analyses presented here are all based on remaining volumes. For this reason, only Levels 8, 5 and 2 are shown in Figs 7.32a-c as representative of higher, immediate and lower levels. The markers in a column directly above the discharge outlet have the highest mean velocities but these velocities decrease slightly with height as do the mean velocities of the markers in the surrounding flow channel. This indicates that the flow channel is expanding slightly.

At each level, the mean velocities of all the markers which are not in the initial flowing zone are remarkably similar. However, the real variations here are obscured by the fact that only one significant figure is presented in the diagram for these velocities.

The mean velocity contours on the vertical Sections AE and CG are presented in Figs 7.33a and b. The channel shape identified in Fig. 7.33a is very characteristic of eccentric pipe flow. It may be noted that a recent extensive set of model tests on eccentric discharge (Carson *et al*, 1991) did not find such steep-sided funnel flows, and that model tests may contain serious scale errors for this phenomenon. Section CG again shows the symmetry of the flow.

The comparable results for Test PFB are not shown as they are virtually identical to those of Test PFA and the similarity has already been demonstrated.

7.7.4 Computer flow simulations

A small sample of still images from the computer simulation of the flow regime at different stages of the discharge is shown for Test PFA in Figs 7.34a-d. Only Levels 2, 4, 6 and 8 are displayed in the 3D picture to avoid congestion. Figure 7.34a shows the initial position of the tags. In Fig. 7.34b, a narrow well-defined channel is clearly forming with apparently vertical walls. As the discharge progresses (Figs 7.34c and d), the channel seems to widen slightly and the top Level 8 material sloughs off. The results for Test PFB are remarkably similar so they are not shown.

Figures 7.35a and b show bar charts of the proportion of tags which have emerged through the outlet from different levels for Tests PFA and PFB respectively. A small number of tags emerge from all the levels at an early stage (15% of the total mass discharged), indicating that the flow channel is a narrow pipe. Tags at Level 8 appear at the outlet last (15% of the total mass discharged) but are completely discharged first (35% of the total mass discharged) in Test PFA (Fig. 7.35a). While the proportion of tags which has emerged from lower levels remain stable, tags emerge

quickly from higher levels, representing the shedding of solid at higher levels. Figure 7.35b again demonstrates the similarity between Tests PFA and PFB.

7.7.5 Analysis of emerged mass from seeded levels

The normalised mass-time curves are shown in Figs 7.36 and 37 for Tests PFA and PFB respectively. The plateaux representing the stable flow funnel shortly after the start of the discharge of Test PFA are clearly seen with a height of about 11% for all levels except Level 1 (Fig. 7.36). The height of the plateau for Level 1 is slightly lower with a value of about 9%. The repeatability of these two tests is again seen.

Whilst the first plateau is clear, it appears that all the levels have a second major plateau which is much higher and lasts longer than the first one. They represent a second stable flow channel after expansion part way through the discharge. This second channel is much larger than the first. Although model tests (e.g. Gale *et al*, 1986; Carson *et al*, 1991; Watson, 1993) have indicated that the formation of the flow channel is a gradual process after the discharge starts, this appears to be the first occasion that two distinct stable funnels have been observed in full scale tests.

In Test PFA, the discharge was first performed with a low discharge rate of 8.35m^3/h for 2 hours and 20 minutes. The outlet was opened only half way during this first discharge (see Chapter 6). The discharge was then stopped and restarted with the outlet fully open. The discharge rate was accordingly increased to 18.0m^3/h in the second discharge. The total volume of solids discharged during the first discharge was found to be 19.5m^3. This represents about 16% of the total 120m^3 of solids in the silo before discharge. The test procedure was similar in Test PFB.

In Figs 7.36, the solid from Levels 3-7 emerge through the outlet to form the lower plateaux at about 2%, 3%, 6%, 9% and 10% respectively of the total mass discharged. Shortly after solids from a particular level begin to pass through the outlet, the lower plateau is formed and no further material emerges through the outlet from this level for an extended period, indicating a stable flow channel. Materials

again appear through the outlet from these levels at about 26%, 19%, 20%, 22% and 22% respectively of the total mass discharged. The differences between these two sets values are respectively 24%, 16%, 14%, 13% and 12% with a mean value of 15.8%. This strongly suggests that the expansion of the flow funnel was at the time when the discharge was stopped and restarted with the outlet fully open. The lowest two levels were excluded from this consideration either because no expansion of flow funnel occurred at these levels or the expansion was not detected due to the sparse placement of the tags). The highest level is also excluded.

The reason for the formation of the second stable funnel is not known yet, but may possibly be due to the change of discharge rate or opening size of the outlet, the change of stress state and the dilation of the solids during flow. It is reasonable to attribute the expansion of the flow funnel to the change of opening of the outlet because the second stable flow funnel was formed at the time when discharge rate was increased. Although model tests (e.g. Giunta, 1969) have indicated that the discharge rate has no effect on the flow channel geometry, it is not certain that it has no effect at a larger scale. Further, in Giunta's experiments (1969) solids were filled into the silo during discharge to maintain a constant height of solids (steady state flow), which differs from the experiments described here (time-dependent flow).

Two sets of plateaux have been identified for each of the two tests. The plan cross-sectional area of the flow channel deduced from the first set of plateaux represents the flow channel in the first discharge and that from the second set represent the one shortly after the start of the second discharge. They are shown in Figs 7.38a and b respectively. The first flow channel (Fig. 7.38a) widens at the lowest two levels and is then quite vertical. It is very small compared with the cross-section of the silo, representing a narrow pipe flow. The second flow channel (Fig. 7.38b) widens quickly at the lowest four levels and is then close to vertical, with a much bigger cross-sectional area than the first.

7.7.6 Estimation of the flow channel development

In the residence time measurement technique, the time at which a marker passes through the outlet is recorded. It is not known from the raw data when the marker starts to move or how it moves. In the general description of flow patterns, it is however not normally interesting to know when some particular material reaches the outlet. The most important question is to know which part of the material is in motion and when they start to move. The major difficulty in interpreting flow patterns from residence times lies in finding good methods for deducing the motion of a marker from its observed residence time and those of adjacent markers.

For a vertical flow channel, if the velocity distribution is uniform within it, it may be expected that all the materials from a given level in the channel reach the outlet at the same time. Let T_0 be the time at which material from the level first reaches the outlet. If the travel time for materials outside the flow funnel at the same level to the outlet is also T_0, the normalised mass-time curve may be shifted left by T_0 so that the curve starts to rise from the origin. In this way, the vertical coordinate on the curve may be made to represent the percentage of the mass at the level which is in motion.

Following this description, the normalised mass-time curves for Test PFA (Fig. 7.36) were shifted so that all the curves began to rise from the origin. The vertical coordinate was also changed to indicate the percentage of mass from the level which is in motion. The results are shown in Fig. 7.39. A flow channel is defined such that the materials inside the channel are in motion while those outside are stationary. In Fig. 7.39, a vertical line at a discharged mass m may intersect the curve for a level at a vertical coordinate μ. From the above, μ% mass at the level is in motion while the rest is stationary. The value of μ therefore also represents the size of the flow channel at the level when m% mass has been discharged. The size of the flow channel at all the levels at any instant is then directly deduced.

The deduced size of the flow channel at different stages of discharge is shown in Fig. 7.40. When 2% mass has been discharged, the flow channel is almost vertical

but the highest level starts to expand. At 10% mass discharged, the flow channel expands slightly down the full height and the materials at the highest level start to slough off to form a repose angle. As the discharge progresses, the flow channel at higher levels expands quickly and materials at the top surface continue to slough off. At 20% mass discharged, all the materials at Level 8 have sloughed off and only the flow channel at the lowest three levels is still stable. This process continues until all the solids at the side opposite the outlet have sloughed off, finally leaving a dead zone when the discharge finishes.

This figure shows that the flow channel found in the previous section for the first discharge is only valid at about 2% of the total mass discharged. The flow channel is indeed very transitory. The results for Test PFB are very similar and not shown.

The results deduced here are indeed rather unrewarding after so many interpretative processes. However, they do show something interesting.

7.7.7 Flow channel boundary

As discussed earlier, two distinct flow channels were identified for the first and the second discharge in the two fully eccentric discharge tests. The contour value of the remaining volume for drawing the flow channel boundary at each level is listed in Table 7.4 for both tests.

Table 7.4 Value of remaining volume at the flow channel boundary V_f (m^3) (Fully eccentric discharge tests)

Discharge	Test	Level 1	Level 2	Level 3	Level 4	Level 5	Level 6	Level 7	Level 8
Early	PFA	71	89	99	102	100	99	97	99
Later	PFA	71	51	60	60	68	73	80	86
Early	PFB	72	71	99	100	100	99	98	99
Later	PFB	72	71	63	58	67	72	85	92

Two same methods which were used in Section 7.6.8 are used again here to draw flow channel boundaries: a) the flow channel is assumed to be circular and b) remaining volume contours are drawn using the above values.

The calculation of the radius of the flow channel from its cross-sectional area is not straightforward here because the channel boundary is only part of a circle (Fig. 7.41) since it intersects the wall. For a given plan cross-sectional area of the flow channel A_f and given coordinates for its centre (x_f, 0), the radius of the flow channel r_f may be found as

$$r_f = \sqrt{\frac{A_f}{\pi}}, \quad \text{for } \sqrt{\frac{A_f}{\pi}} \le R - x_f \tag{7.3}$$

in which R is the radius of the silo. The flow is internal in this case. If the inequality condition for this equation is not satisfied, the flow channel will make contact with the wall. Parameters A_f, r_f, R and ω_f can be found to have the following relationships (Fig. 7.41)

$$r_f^2 = R^2 + x_f^2 - 2x_f R\cos\omega_f \tag{7.4}$$

$$A_f = R^2\omega_f + r_f^2\left(\pi - \sin^{-1}\frac{R\sin\omega_f}{r_f}\right) - Rx_f\sin\omega_f, \quad \text{for } R\cos\omega_f \ge x_f \tag{7.5a}$$

$$A_f = R^2\omega_f + r_f^2\sin^{-1}\frac{R\sin\omega_f}{r_f} - Rx_f\sin\omega_f, \quad \text{for } R\cos\omega_f < x_f \tag{7.5b}$$

in which ω_f is the angle in the plan section at which the flow channel intersects the silo wall at a given level. r_f and ω_f are obtained by iteratively solving Eqs 7.4 and 5.

The flow channels found for the first and the second discharge are separately described as follows. It should perhaps be re-emphasised that the accuracy of the interpretation is limited by the sparse distribution of radio tags.

7.7.7.1 First discharge

By assuming that the flow channel is circular and the locus of its centre is a straight vertical line through the centre of the outlet, the flow channel boundary may be drawn as in Figs 7.42a-c for Test PFA and Figs 7.43a-c for Test PFB. In Fig. 7.42a, the flow channel expands quickly at the two lowest levels and then has almost vertical sides in Test PFA. The radius of the steep-sided flow channel is 0.80m. The flow channel boundary close to the outlet makes an angle of 30.6° from the vertical. The dead zone is found to form a repose angle of 40.3°. The steep-sided part of the flow channel intersects the wall at a horizontal angle $\omega_f=\pm 21°$ (Fig. 7.42b). Figure 7.42c shows the flow channel at each level.

The flow channel boundary drawn from remaining volume contours (Fig. 7.42d) showed that it expands slightly with height in the silo. The areas surrounded by these contours are slightly larger than those in Fig. 7.42c due to the use of different methods. However, the angle where these contours intersect the wall is very close to those in Fig. 7.42c except at Level 3, which is misleading as noted before. This suggests that the flow channel may be quite circular. The 3D view of the flow channel is shown in Fig. 7.42e.

The results for Test PFB (Fig. 7.43a-e) again demonstrate the repeatability of these tests. The radius of the steep-sided section of the flow channel, its angle near the outlet and plan angle intersecting the wall are 0.80m, 32.0° and ±21° respectively. The repose angle of the dead zone is 42.9°.

7.7.7.2 Second discharge

In addition to the assumption that the flow channel boundary is circular in plan, it is assumed here that the centre of the flow channel inclines towards the nearest wall (0°) at 5° from the vertical, but without passing outside the silo. This is necessary because otherwise the plotted flow channel is a poor match with the remaining volume contours. This centre of the flow channel is then found to reach the wall between Levels 4 and 5 and is assumed to be coincident with the wall at the higher levels.

The flow channel boundary in the vertical x-z plane (Section AE) in Test PFA is shown in Fig. 7.44a. It is evident that the flow channel at the higher levels lies between the wall and the centre of the silo with a radius of 2.03m. The flow channel angle close to the outlet on the left side is 28.4° from the vertical. However, the slight decrease of this angle comparing with that in the first discharge (30.6°) is due to the assumption of an inclined flow channel here which would otherwise remain unchanged. The angle in the plan view at which the flow channel intersects the wall in the higher parts is $\omega_f=\pm 57.8°$. The part of the channel which contacts the wall is shown in Fig. 7.44b. The FCB at each horizontal level is shown in Fig. 7.44c. Compared with interpretations drawn from remaining volume contours (Fig. 7.44d), the flow channel at Levels 1 and 4-7 are very similar in the two figures. However, those drawn from remaining volume contours appear to have slightly larger radii. Levels 2, 3 and 8 in Fig. 7.44d is rather anomalous due to the automatic extrapolations in the computer contouring program and the difficulty in determining values of V_f for the contours. Figure 7.44e shows a 3D view of the flow channel.

The results for Test PFB are shown in Figs 7.45a-e. The flow channel boundary drawn from the remaining volume contours (Figs 7.45d and e) matches that found by assuming a circular flow channel (Fig. 7.45a-c) slightly better than for Test PFA. The radius of the steep-sided part of the flow channel and its angle of intersection in plan with the wall are 2.04m and 58.2° respectively.

7.8 Flow patterns under half eccentric discharge

7.8.1 Introduction

The half-eccentric discharge Test PHA was the only one of its kind undertaken. This is because the condition is less severe on the structure than a fully eccentric discharge, and it could not be used as a means of verifying the test procedure as the concentric tests could. Nevertheless, the half eccentric test is important because it should give an important indication of whether the flow channel remains vertical when it is free to move within the solid under systematically unsymmetrical conditions.

As noted earlier, mean velocity contours provide a clearer picture of flow pattern than remaining volume contours, but little further information can be obtained from them. The flow visualisation program was written as a visual aid. Whilst it is most helpful in interpreting the flow pattern, the presentation of still black and white images is not very interesting. For these reasons, the mean velocity contours and computer flow visualisation images are not shown for this test. The remaining volumes at the instant each marker passed through the outlet are shown in full because they are the actual measured data and the basis of all further interpretations.

7.8.2 Residence time observations: remaining volume at marker exit

The remaining volumes at the exit of markers are shown in horizontal sections in Figs 7.46a-h. The contours suggest that the channel is fairly vertical between higher Levels 4-8, but it is drawn towards the wall at the lower levels. It is unfortunate that most of the markers at Level 8 on the flow channel side of the silo centre (Fig. 7.6.3a) were not detected. This hole in the data makes the determination of the flow channel boundary very difficult at this level.

The lowest level (Fig. 7.46h) has so little data to support it that the triangular channel shape should not be taken seriously. Again, the data points with the remaining value of 0 are those which were left in the dead zone after the discharge finished. They are used here to constrain the contours around the outlet.

Two perpendicular vertical sections through the silo are shown in Figs 7.47a and b. The section through the outlet (Section AE) shows the expected funnel flow pattern. It is clearer in this figure that the centre of the flow channel is slightly inclined towards the wall at the lowest three levels but remains roughly vertical at the higher levels. Section CG (Fig. 7.47b) shows that symmetrical conditions about $\theta=0°$ are substantially achieved, with small variations.

7.8.3 Analysis of emerged mass from seeded levels

Figures 7.48a and b show the normalised mass-time curves. The characteristics of funnel flow are clearly seen. Again, the flow channel at the lower levels (Fig. 7.48a) is stable for an extended period whilst it is short lived at the higher levels (Fig. 7.48b). The last parts of the curves for Levels 6, 7 and 8 indicate that a small part of the solid (less than 15% for Level 8 and less than 10% for Levels 6 and 7) has been stationary for a short time. This material may be identified in the remaining volume contours at the opposite side from the outlet for Levels 8 and 7 (Fig. 7.46a and b) and near the wall at Generator C at Level 6 (Fig. 7.46c). This situation is also seen in the vertical Section AE (Fig. 7.47a) at Levels 7 and 8. The few tags close to Generator E at the two highest levels are expected to have larger values of remaining volume than those at Level 6 because they are outside the flow funnel. If semi-mass flow had developed in the higher part of the silo, the effective transition could perhaps be either above or below Level 6. However, this behaviour requires that the solids at the two highest levels were discharged before those at Level 5, which does not match the measured data. The unexpected results in this small area are probably caused by stopping and restarting the discharge with a higher discharge rate, though the marked effects seen in the fully eccentric discharge tests is not observed here.

The heights of the plateaux which represent the size of the flow channel at the level in question can be easily determined at lower levels. The plateau is not clear at the higher Levels 6 and 7. However, for the purposes of the interpreting process being used here, the plateau is taken to lie at the mean value in the zone where this curve moves slowly (between 40% and 50%) for Level 6, and the small step at about 63% at Level 7. The deduced flow channel size is shown in Fig. 7.49. It expands rapidly with height at the two lowest levels and rises steeply through Levels 3 to 5. It expands rapidly again at the higher levels.

The values of remaining volume used to draw the contours of the flow channel boundary are listed in Table 7. 5.

Table 7.5 Value of remaining volume at the flow channel boundary V_f (m^3) (Half eccentric discharge test)

Test	Level 1	Level 2	Level 3	Level 4	Level 5	Level 6	Level 7	Level 8
PHA	51	68	84	95	91	73	62	62

7.8.4 Flow channel boundary

The remaining volume contours (Figs 7.46 and 47) show clearly that the flow channel moves towards the wall. It was next assumed that the flow channel was circular and that the locus of its centre moves towards the wall at a small angle. Several values were considered for this angle. The results with an angle of 5° seem to match the remaining volume contours best. Figure 7.50a shows the outcome in the diametral Section AE through the outlet. The flow channel expands quickly at the two lowest levels and then rises vertically. The slope of the flow channel boundary near the outlet on the left side is 29.7° to the vertical. This angle would have been 33.3° if the flow funnel had been assumed vertical. Close to the top surface, the flow channel is still quite steep with an angle of 16.4° at the highest level. The maximum radius at Levels 2 to 5 is 1.18m. The final dead zone forms a repose angle of 41.0°.

The contact of the flow channel with the wall is shown in Fig. 7.50b. The flow channel boundary on the wall is close to triangular.

A plan view of the flow channel at each level is shown in Fig. 7.50c. These can be compared with those drawn from remaining volume contours (Fig. 7.50d). Overall, they match each other nicely. The flow channel shown in Fig. 7.50d is fairly symmetrical about Section AE except at Levels 6 and 7. It may be noted that the raw data in Figs 7.46b and c do not appear to support the asymmetry indicated by the computer contouring program. This asymmetry is due to two missing data points close the wall at Generator C at Level 7 and one at Generator G at Level 6. The 3D view of the flow channel is shown in Fig. 7.50e.

It may be observed that the flow channel was inclined towards the closest wall in all the eccentric discharge tests (including the half eccentric discharge test here and two fully eccentric discharge tests in the previous section). The reason for this is not clear yet, but it may be due to the minor segregation of solids during concentric filling or related to the non-uniformity of the stress distribution at a level. The segregation of solids during concentric filling results in larger particles near the walls and more fine content at the centre (Rotter *et al*, 1995). The solids with a higher level of fine content at the centre may be expected to develop a higher strength under the filling consolidating stress, leading to a lower flowability.

It is well known that the consolidating stress may affect the shape and size of the flow channel (e.g. Johanson, 1969). In general, the smaller the consolidating stress, the easier the flow would be. Predictions made using finite element method indicate that the vertical stress near the silo bottom is much larger at the centre than at the wall in both deep and squat silos (Ooi and Rotter, 1990b). The vertical stress is approximately the major principal stress in the solid. The higher consolidating stress at the centre would also suggest a lower flow flowability for solids there.

The additive effects of the segregation and the non-uniformity of filling stress may therefore draw the flow channel towards the nearest wall. This may also be used to explain why the flow channel does not behave in a perfectly axisymmetric manner under concentric conditions. In the concentric discharge tests, the flow channel was inclined in a random manner in both magnitude and direction because the factors causing asymmetric are random in character.

7.9 Modelling of flow channel geometry

7.9.1 Characteristics of flow channel geometry

As has been mentioned before, the inferred flow channel in these tests on iron ore pellets is typically like an inverted bell. It may be typically divided into three parts: the lower expansion channel which is close to the outlet, the intermediate steep-sided channel which is sometimes vertical, and the higher expansion channel close to the top surface. Figure 7.51 shows an idealised typical concentric flow channel. Under eccentric discharge, the shape of the flow funnel is similar, but one side may be cut by the silo wall. However, the flow channel is not vertical but often inclined at a small angle towards the nearest wall. The angle of inclination of the flow channel centre may vary with the properties of the stored materials, the silo geometry, the wall friction factor and possibly other factors. It is typically of the order of 5° in the experiments analysed in this chapter. Under concentric discharge, the direction and the magnitude of the angle of inclination of the centre of the flow funnel may vary in a random manner. The value of the angle of inclination has been estimated as of the order of 3° in these experiments.

The lower expansion channel was clearly defined in all the tests. The intermediate steep-sided channel was also well defined in all the tests except Test PCA, in which the filling height was too small. The height of the intermediate steep channel varied from one test to another but was well correlated with the filling height.

The shape of the higher expansion channel is not well defined in these tests for the following reasons:

a) It was difficult to determine the position of the flow funnel from the normalised mass-time curves;
b) In most of the tests some solid was above the highest seeded level, so the flow channel above the highest level was unclear. In many of these tests (typically in fully eccentric discharge tests), the higher expansion channel was not seen at all; and most importantly
c) The flow channel in the higher part of the silo is very short lived, so it is not worthy of extensive investigation.

The storing pressure in the higher parts of the silo is relatively small. Together with the larger size of the flow channel in this zone, this means that the structural consequences of a pressure change due to flow in the higher parts of the silo is far less important than that in the middle and lower parts. The following discussion is therefore focused on modelling only the lower expansion channel and the intermediate steep-sided flow channel.

At a horizontal section, the geometry of the flow channel in all the tests was not exactly circular. The exact shape of the channel cannot be inferred from these tests because the density of tags was not high enough. Until the flow channel shape can be defined more precisely, it is a good approximation to assume that it is circular.

7.9.2 A two parameter model

The flow channel may possibly be described by two parameters as shown in Fig. 7.51: the flow channel angle at the outlet θ_f and the maximum radius of the intermediate steep-sided channel R_f. They have been defined in the previous sections for each test and are summarised in Table 7.6. The flow channel angle defined in the previous sections was the secant angle from the outlet to Level 1. A better and more useful definition would be the tangent angle at the outlet. This may be found from

curve fitting and is listed in Table 7.6. This angle is unique and does not vary with the slight difference of seeding height of Level 1 in different experiments.

Table 7.6 Parameters for describing the flow channel geometry

Test	PCA	PCB	PCC	PHA	PFA	PFB	PFA	PFB
					Early discharge		Later discharge	
Discharge	Con-centric	Con-centric	Con-centric	Half eccentric	Fully eccentric	Fully eccentric	Fully eccentric	Fully eccentric
Mean filling height, m	4.45	6.43	8.395	8.48	8.53	8.33	7.04	7.00
$\bar{\sigma}_v$ at bottom, kPa	81.1	107.2	128.3	129.1	128.7	127.7	114.1	113.8
R_f, m		1.28	1.38	1.18	0.80	0.80	1.72	1.73
Secant angle from outlet to Level 1, ° (to the vertical)	18.2	23.9	31.9	33.3	30.6	32.0	30.6	32.0
Tangent angle at outlet θ_f, ° (to the vertical)	30.8	38.1	41.2	44.5	42.8	43.4	45.6	42.8
Angle of repose of dead zone ϕ_r, °		44.3	47.4	41.0	40.3	42.9	40.3	42.9
Eccentricity of discharge e	0	0	0	0.40	0.81	0.81	0.81	0.81

The mean filling height and the mean vertical stress at the silo bottom are also listed in Table 7.6 for reference. In Tests PFA and PFB, the mean filling height has been estimated in the second discharge by deducting the mass discharged during the first discharge. The mean vertical stress $\bar{\sigma}_v$ at the silo bottom has been estimated assuming the Janssen pressure distribution with k=0.212, deduced from k=1−sinϕ. Here ϕ=52° is the experimental internal friction angle of these iron ore pellets.

The geometry of the flow channel may be approximated by

$$r(z) = (R_f - R_o)\left[1 - e^{-z \tan\theta_f/(R_f-R_o)}\right] + R_o \qquad (7.6)$$

in which r(z) is the radius of the flow channel at a height z above the silo floor, R_o is the radius of the outlet.

Two parameters are required in Eq. 7.6 to estimate the geometry of the flow channel boundary: the maximum radius R_f and the flow channel angle θ_f (tangent at the outlet). The experimental estimates are listed in Table 7.6. For the tests on iron ore pellets, the comparisons between the flow channel calculated from Eq. 7.6 and those inferred from the residence time measurements are shown in Figs 7.52a-c. It is seen that a fairly good agreement is achieved with the form of Eq. 7.6 if the two parameters R_f and θ_f can be estimated well.

Empirical relations for θ_f and R_f are discussed in the following sections.

In design, the flow channel centre may be assumed to incline towards the nearest wall (for eccentric discharge) at a small angle. Under concentric discharge, the direction and magnitude of this angle vary in a random manner. Having determined the radius and the position of its centre, the flow channel can be easily drawn. The plan intersection angle of the flow channel with the wall ω_f at a given height of the silo can then be found from Eq. 7.4.

7.9.3 Comparison with previous descriptions

7.9.3.1 Concentric discharge

A few attempts have been made to predict the shape of flow channels in funnel flow silos. Among them Giunta's study (1969), on which the flow channel prediction method in the ACI-313 code (1990) is based, may be the best known. Giunta (1969) assumed that under concentric conditions, the flow channel consists of an effective converging hopper in the lower section of the silo and a vertical cylindrical channel at higher levels. The radius R_f of the cylindrical flow channel was predicted to be

$$R_f = R_o + \tan\theta_f\left(\frac{H - \alpha R_o}{1 + \alpha\tan\theta_f}\right) \qquad (7.7)$$

in which H is the head of material in the silo, α is a factor for the geometry of the silo bottom and β_f is the half angle of the effective hopper channel. The notation in this equation has been changed so that it is consistent with the rest of this chapter. The values of θ_f and α were proposed by Giunta (1969) to be functions of the effective angle of internal friction of the stored solids.

For the properties of the iron ore pellets used in the experiments here, the coefficients θ_f and α are found to be 2.7° and 1.7 from the curves given in Giunta (1969). Substituting them into Eq. 7.7 gives the radius of the cylindrical flow channel R_f as 0.5m and 0.6m for Tests PCB and PCC respectively (the difference is a result of the different filling level). The results are shown in Fig. 7.52a. Clearly, the flow channel predicted using Giunta's equation (1969) is far smaller than that found in the experiments.

Whilst Giunta's description of the flow channel is simple, the discontinuity of slope of the flow channel boundary at the transition between the lower converging and higher parallel sections is clearly invalid. Instead, the FCB should be a streamline. In this sense, the model proposed here (Eq. 7.6) should describe the FCB better.

7.9.3.2 Eccentric discharge

Previous experimental work on eccentrically discharging silos has suggested that the best approximation of the flow channel might be parabolic (Fitz-Henry, 1986; Fleming, 1985). A more general power law model was proposed by Berry (1988) as

$$r_f(z) = b(z + z_o)^{1/n} \qquad (7.8)$$

in which coefficients b and z_o may be expressed in terms of the outlet radius R_o and flow channel angle θ_f, which leads to

$$b = (nR_o^{n-1} \tan\theta_f)^{1/n} \tag{7.9a}$$

$$z_o = \frac{R_o}{n \tan\theta_f} \tag{7.9b}$$

For typical values of n=1, 2 and 3, Equation 7.8 results in linear, parabolic and cubic flow channels respectively. Figure 7.53a shows the flow channel calculated from Eqs. 7.8 and 7.9 by substituting the flow channel angle inferred in the fully eccentric Test PFA (Table 7.6) into them. The results calculated from Eq. 7.6 are also shown for comparison. Clearly, Equation 7.8 cannot easily represent such a steep flow channel as that found in the experiments analysed here.

If the flow channel angle is ignored and b and z_o are found from best fit, the results cannot represent the observed flow channel either (Fig. 7.53b). Many other values of n have also been explored. None of them produce a better result than Eq. 7.6.

7.9.4 Flow channel angle

The flow channel angle θ_f is clearly correlated to the mean filling height or to the mean vertical stress at the silo bottom (Table 7.6): the larger the filling height or mean vertical stress, the larger the flow channel angle. The relationship between the angle and the vertical stress may be assumed to be linear as a first approximation:

$$\theta_f = \theta_0 + \alpha_\theta \bar{\sigma}_v \tag{7.10}$$

The coefficients in Eq 7.10 may be found from a best fit to the test results as

$$\theta_0 = 10°; \qquad \alpha_\theta = 0.25 \text{ degree/kPa} \tag{7.11}$$

The coefficients of variation of this fit are 30% (standard deviation = 3°) for θ_0 and 11% for α_θ. Because the initial conditions were very different for the second discharge (the end of the first discharge) from those for the first, and the early stages are the most important for structural design, the results in the second discharge for the fully eccentric discharge tests have not been included in this and all the following regression analyses.

If the constant θ_0 is constrained to 0°, the regression results in

$$\theta_0 = 0°; \qquad \alpha_\theta = 0.34 \text{ degree/kPa} \tag{7.12}$$

The coefficient of variation for α_θ is 2% in this fit. However, the decrease of the CoV of α_θ in this fit does not mean that it is better than Eq. 7.11 but instead it is due to an increase in the number of degrees of freedom. Here θ_0 is constrained to 0° because it gives θ_f=0° if $\bar{\sigma}_v \rightarrow 0$. It means that the flow channel would be a vertical pipe with the same size as the outlet when the solids are in a state of no stress. Both inferred results from experiment and calculated from Eqs 7.10-7.12 are shown in Fig. 7.54a.

When $\bar{\sigma}_v$ is very small such as in model silo tests, parameters in Eq. 7.12 results in θ_f very close to 0°. This seems agree with the very steep flow pattern observed in Giunta's model tests (1969). However, it needs to be noted that Eqs 7.10-7.12 should not be used in cases where the mean vertical stress exceeds the ranges listed in Table 7.6 nor for materials with different properties. When the mean vertical stress is very large, Equation 7.10 may result in a large value for θ_f which is clearly untrue because θ_f should not be larger than 90-ϕ_r.

To overcome some of the shortcomings of the linear model, a probability model is proposed here

$$\theta_f = 90 - \phi_r - (90 - \phi_r)e^{-\bar{\sigma}_v^2/\sigma_0^2} \quad (7.13)$$

in which ϕ_r is the angle of repose of the solid and σ_0 is a coefficient to be found. For the five tests listed in Table 7.6 (excluding Test PCA and the second discharge for Tests PFA and PFB), the mean values of ϕ_r and σ_0 may be found as

$$\phi_r = 43.1°;\ \sigma_0 = 81.1\text{kPa} \quad (7.14)$$

The CoVs are 7% for ϕ_r and 10% for σ_0. The results are shown in Fig. 7.54b.

7.9.5 Maximum radius of the flow channel

Table 7.6 indicates that the maximum radius of the flow channel R_f may increase with an increase in $\bar{\sigma}_v$ in the concentric discharge tests. The discharge method seems to have a significant effect on R_f, which contrasts with the insensitivity of θ_f to it. An empirical relationship may be established as

$$R_f = R_o + \alpha_e \alpha_r \sqrt{\bar{\sigma}_v} \quad (7.15)$$

in which α_r is the coefficient associated with the mean vertical stress at the silo bottom and α_e is a coefficient reflecting the influence of the eccentricity of discharge. From the two concentric discharge Tests PCB and PCC (α_e=1), α_r may be found as

$$\alpha_r = 0.1\ \text{m}/\sqrt{\text{kPa}} \quad (7.16)$$

The eccentricity coefficient α_e may be expressed as

$$\alpha_e = \frac{0.60}{0.60 + e^{2.3}} \quad (7.17)$$

in which the eccentricity of discharge e is defined as

$$e = \frac{\sqrt{x_o^2 + y_o^2}}{R} \tag{7.18}$$

where x_o and y_o are the coordinates of the centre of the outlet (with the origin of the coordinate system at the centre of the silo).

Figure 7.55 shows the relationship between R_f and $\bar{\sigma}_v$ for concentric discharge. The relationship between e and α_e is shown in Fig. 7.56.

The good agreement between the experimental value of R_f and that calculated from Eq. 7.15 (Table 7.7) does not mean that Eq. 7.15 is accurate in predicting the size of the flow channel. It arises because the coefficients have been found by regression from a very limited number of experiments. Its value needs to be verified by further experiments. The value of e is also listed in Table 7.7 for the tests used in the regression.

Table 7.7 Maximum radius of flow channel, R_f

Test	PCB	PCC	PHA	PFA (1st discharge)	PFB (1st discharge)
Experiment	1.28	1.38	1.18	0.80	0.80
Eq. 7.15	1.28	1.37	1.18	0.80	0.80
Eccentricity e	0	0	0.40	0.81	0.81

7.10 Conclusions

The results of these tests on iron ore pellets showed steep-sided funnel flow patterns under both concentric and eccentric discharge. The plan cross-sectional shape of the

flow channel was close to but not exactly circular. An accurate determination of the flow channel boundary at every point would need a much higher density of tags to be seeded in the experiments.

Under concentric discharge, the axial symmetry of the flow pattern was strongly correlated with the filling height. If the filling height is small, the flow pattern was found to be close to but not exactly axisymmetrical. However, it may be very unsymmetrical in the higher parts of the silo when the filling height is large. If the asymmetry of the flow pattern is expressed instead of the angle of inclination of the centre of the flow channel, then it is found to be relatively invariant with height. The magnitude and direction of this angle appear to vary in a random manner. The value of this angle may have been less than 5° (and typically 3°) in these tests. It is particularly important to consider such random asymmetries in the design of silos with high aspect ratios because it may result in significant asymmetry in the higher parts of a silo.

Under eccentric (both fully eccentric and half eccentric) discharge, the flow pattern in the same silo is not simply related to the concentric discharge pattern as a horizontal translation of the flow channel. The flow channel was always found to be inclined towards the nearest wall, probably due to the effects of segregation and the non-uniform stress distribution near the bottom of the silo. However, the channel was found to remain highly symmetrical relative to the vertical diametrical plane of symmetry through the outlets.

Under fully eccentric discharge, the flow pattern in the same silo developed as a narrow channel against the silo wall when the discharge rate was low, similar to the pattern proposed by some earlier speculative writings on the subject (e.g. Wood, 1983; Rotter, 1986b). The size of the flow channel appears to have increased dramatically at the beginning of the second discharge and formed a wider stable flow channel. The cause is not yet known, but may possibly be due to the dilation of solids during flow and a change of stress state. The reason remains a challenge for

future studies. Fortunately, the increase in the size of the flow channel does not cause concern for the structural design.

A two parameter model (Eq. 7.6) has been proposed to describe the shape of the flow channel in the first stage of discharge under both concentric discharge and eccentric discharge of iron ore pellets. The flow channel angle θ_f was found to vary approximately either linearly (Eq. 7.10) or as a probability function (Eq. 7.13) of the estimated mean vertical stress at the silo bottom. The parameters in Eq. 7.12 for the linear relationship or in Eq. 7.14 for the probability function may be used for iron ore pellets within the range of mean vertical stress listed in Table 7.6.

The maximum radius of the flow channel R_f was found to be correlated with both the mean vertical stress near the silo bottom and the outlet position. R_f was found to vary approximately linearly with the square root of the estimated mean vertical stress at the silo bottom (Eq. 7.15). The effect of the eccentricity of discharge on R_f was found to be approximately represented by a power law model (Eq. 7.17). However, the validity of these relationships need to be verified by many more experiments because the total number of coefficients in the fits is very close to the number of experiments.

7.11 Notation

A	cross-sectional area of the silo
A_f	cross-sectional area of the flow channel
M	remaining mass
R	radius of the silo
R_f	maximum asymptotic radius of the intermediate steep part of a flow channel
T	Residence time of a marker
T′	transformed residence time of a marker
V	volume

V_f value of a remaining volume contour drawing as flow channel boundary

e eccentricity of discharge (Eq. 7.18)

k lateral pressure ratio

r_f radius of the flow channel

z vertical coordinate/height above silo floor

x_0 x coordinate of the flow channel centre

x_f, y_f coordinates of the centre of flow channel at a given height

x_o, y_o coordinates of the centre of outlet

α coefficient

β_f effective hopper half angle

ϕ angle of internal frictional

ϕ_r angle of repose

γ density of solids

θ_0 flow channel angle when mean vertical stress is zero

θ_f flow channel (tangent) angle at the outlet

ρ discharge rate (volume/time)

σ stress

$\bar{\sigma}_v$ mean vertical stress near silo bottom

ω_f plan intersection angle of flow channel with the wall

Subscripts

e eccentricity of discharge

f flow channel

o outlet

r radius/repose

v vertical

o outlet

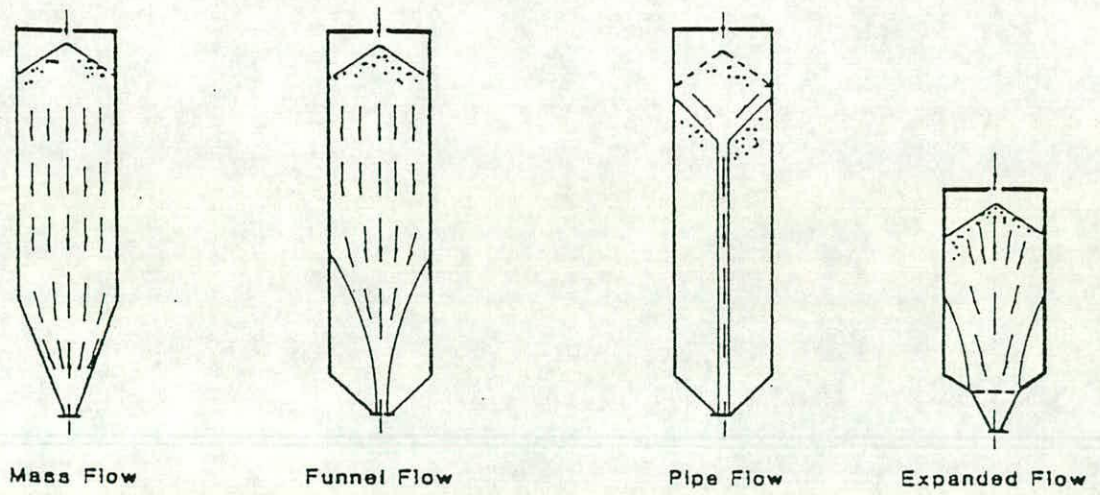

Fig. 7.1a Different forms of axisymmetric flow pattern

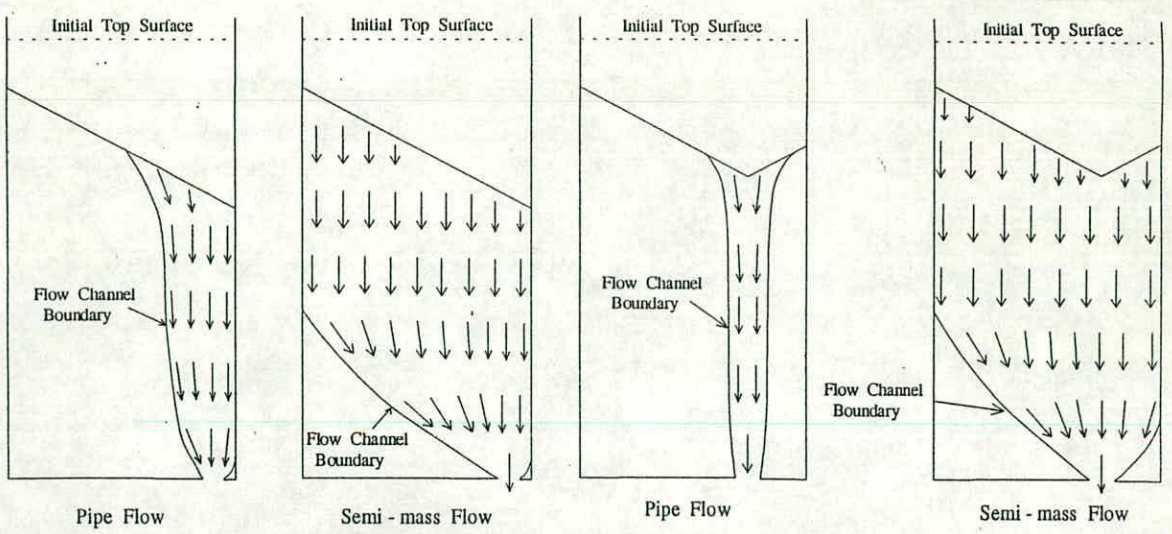

Fully eccentric **Half eccentric**

Fig. 7.1b Different forms of eccentric flow pattern

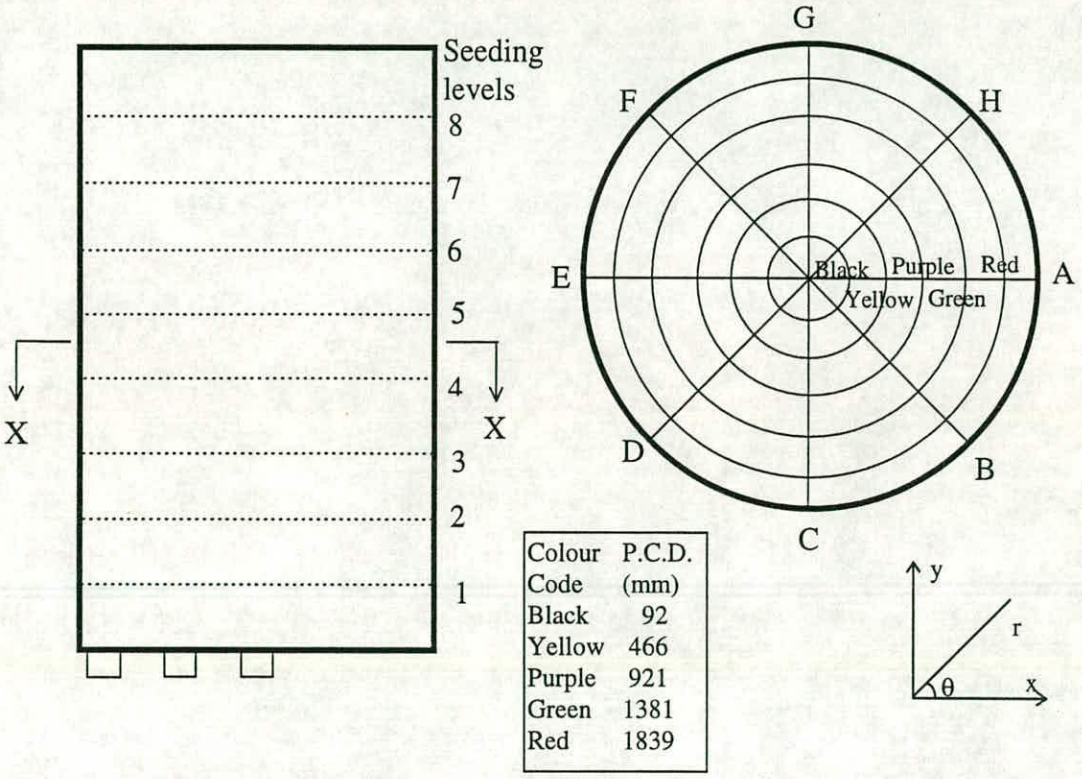

Fig. 7.2 Marker layout and coordinate system

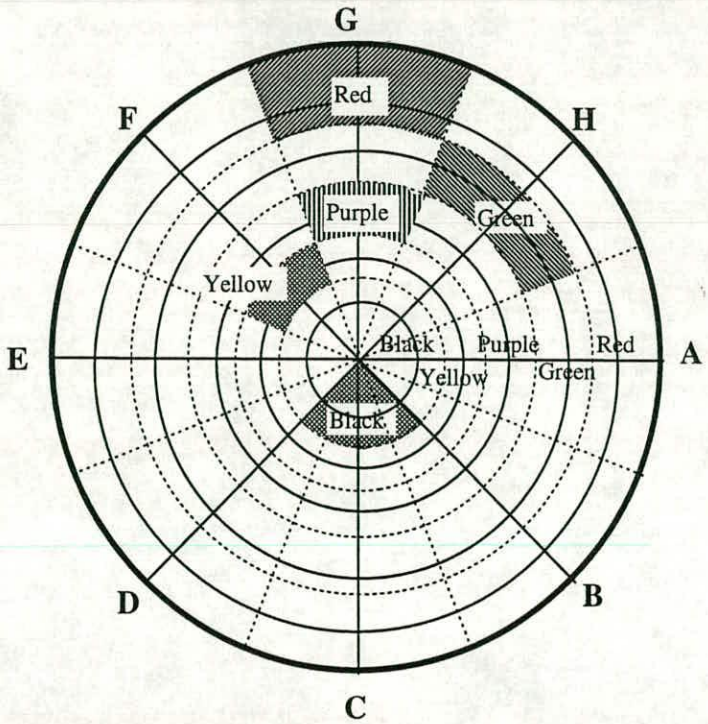

Fig. 7.3 Areas represented by markers at different rings

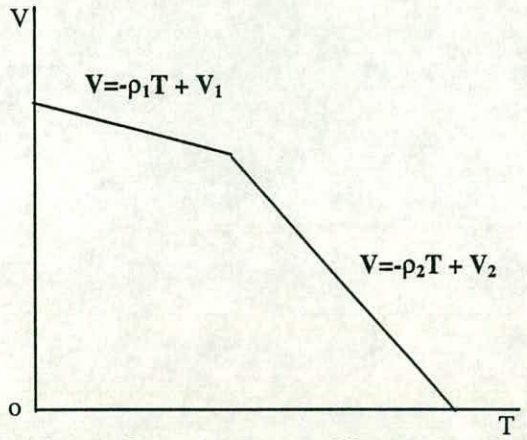

Fig. 7.4 Remaining volume versus residence time in the experiments

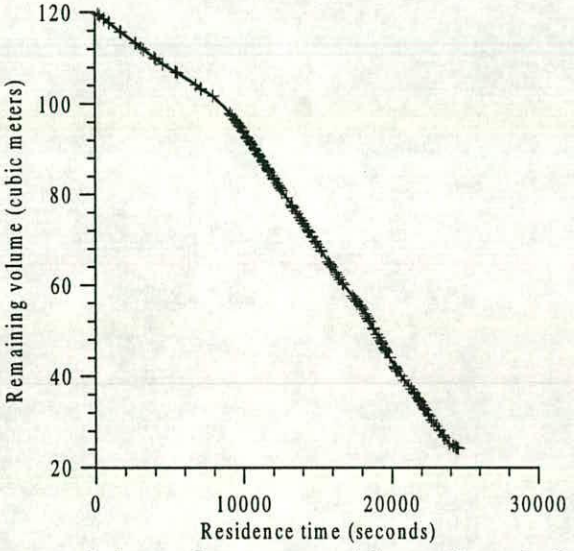

Fig. 7.5a Test PFA: remaining volume vs. residence time: before transformation

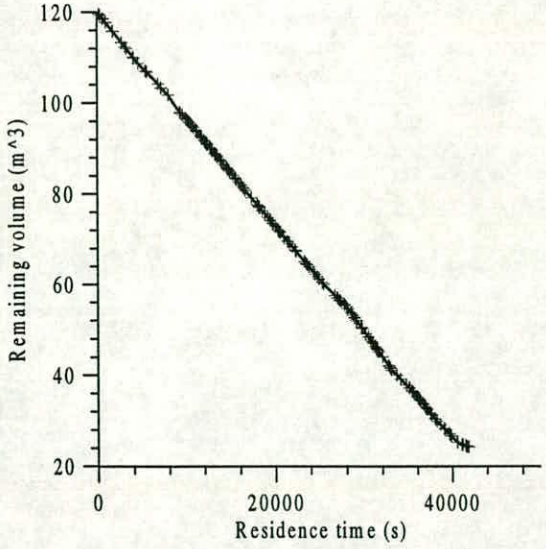

Fig. 7.5b Test PFA: remaining volume vs. residence time: after transformation

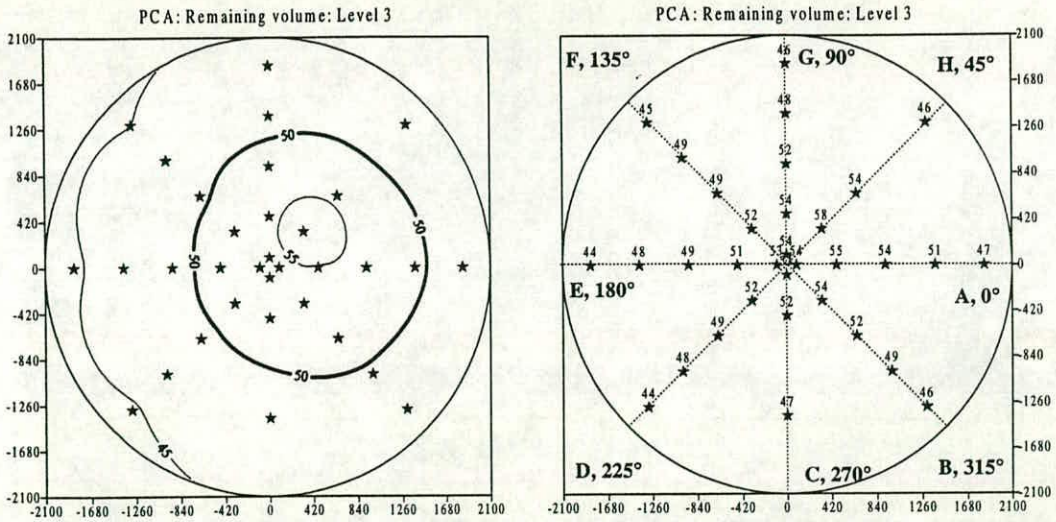

Fig. 7.6a PCA: Remaining mass: Level 3: Contours and spot values

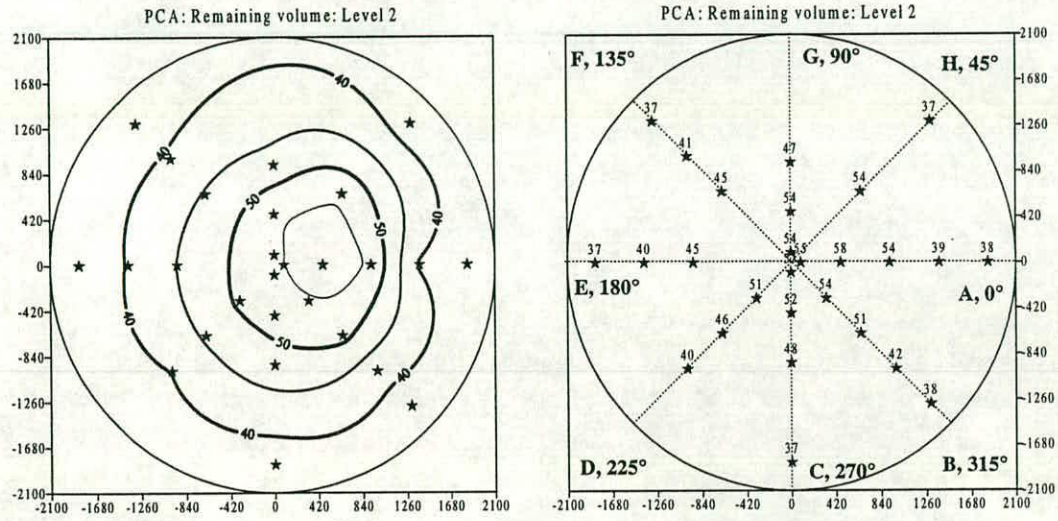

Fig. 7.6b PCA: Remaining mass: Level 2: Contours and spot values

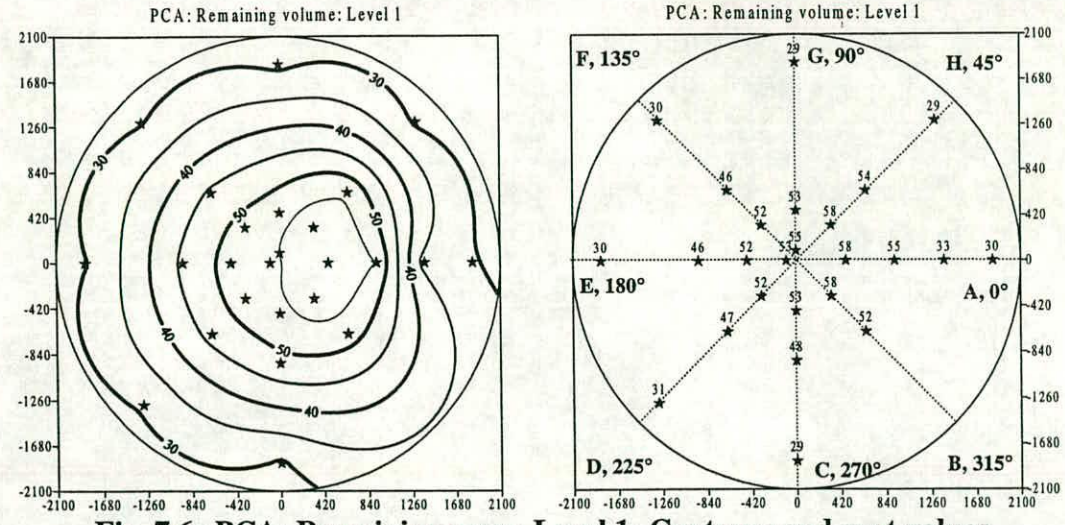

Fig. 7.6c PCA: Remaining mass: Level 1: Contours and spot values

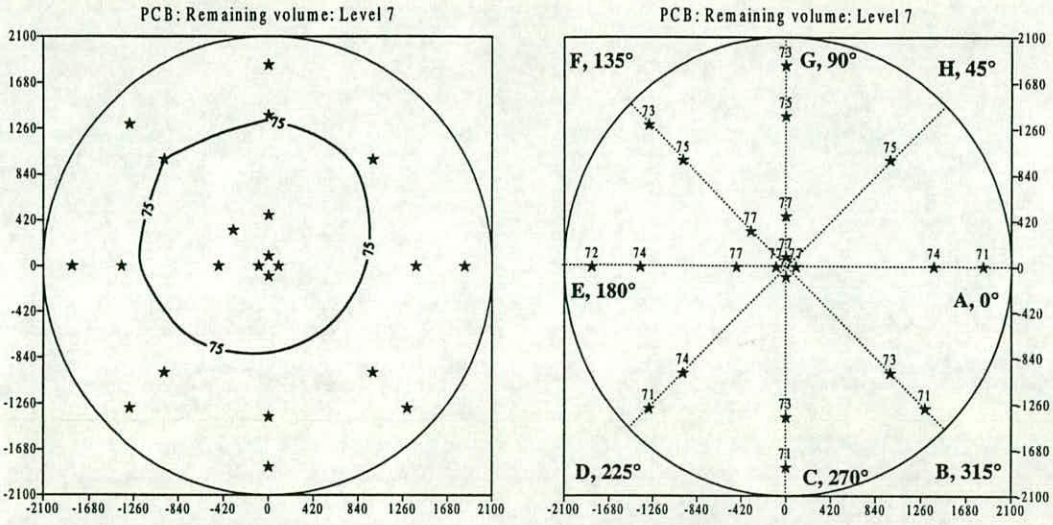

Fig. 7.7a PCB: Remaining mass: Level 7: Contours and spot values

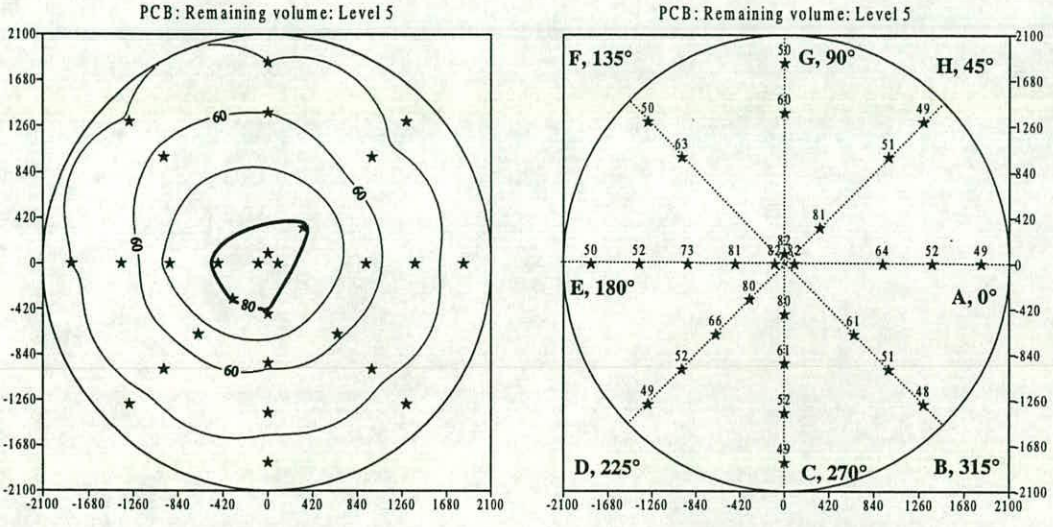

Fig. 7.7b PCB: Remaining mass: Level 5: Contours and spot values

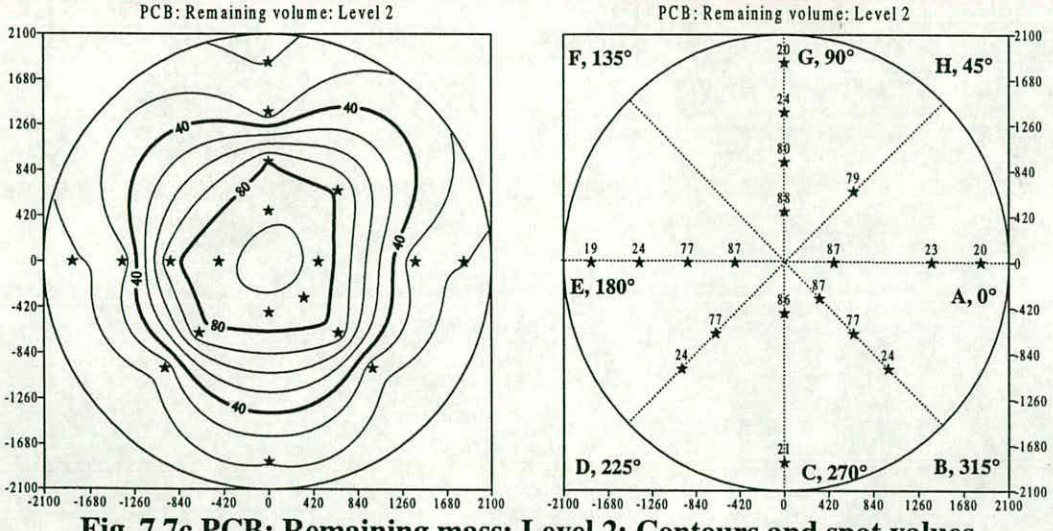

Fig. 7.7c PCB: Remaining mass: Level 2: Contours and spot values

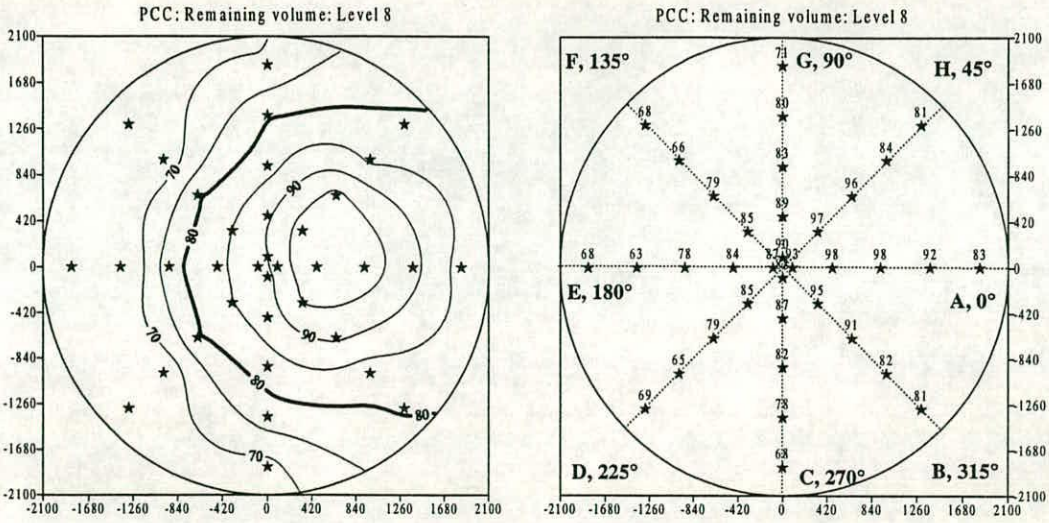

Fig. 7.8a PCC: Remaining volume: Level 8: Contours and spot values

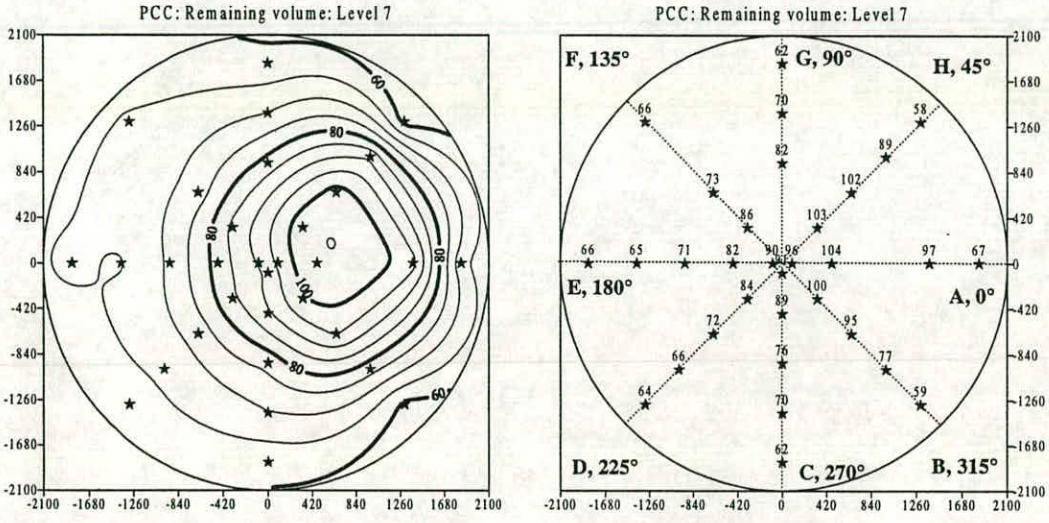

Fig. 7.8b PCC: Remaining volume: Level 7: Contours and spot values

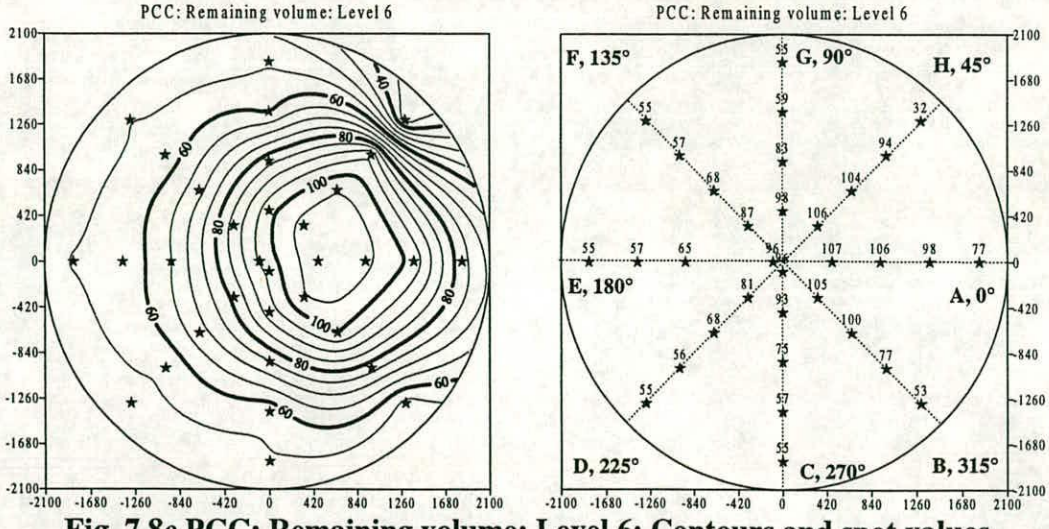

Fig. 7.8c PCC: Remaining volume: Level 6: Contours and spot values

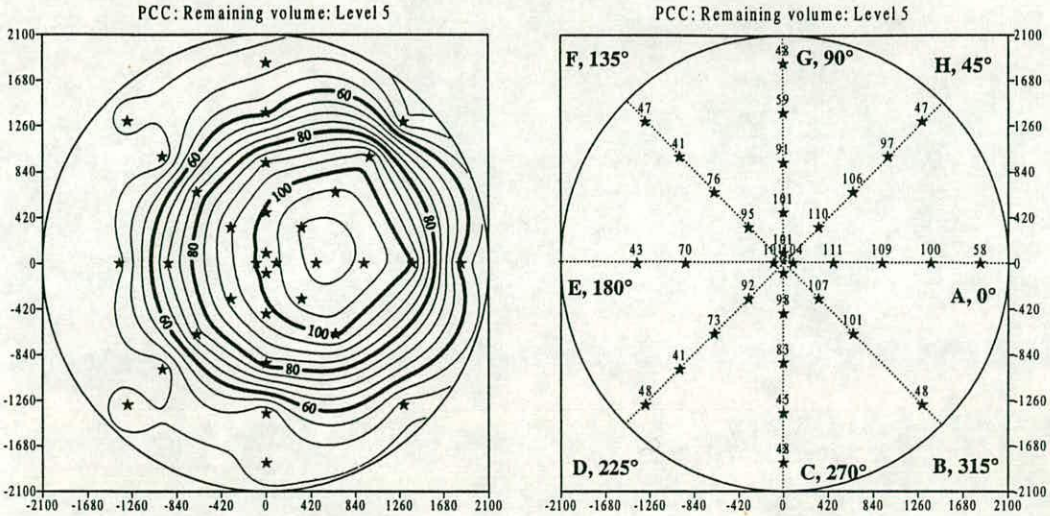

Fig. 7.8d PCC: Remaining volume: Level 5: Contours and spot values

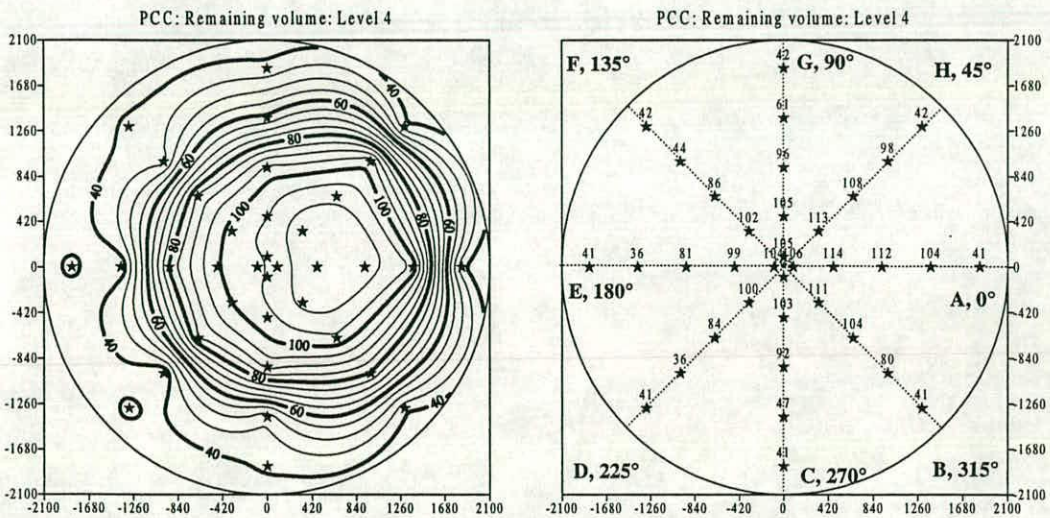

Fig. 7.8e PCC: Remaining volume: Level 4: Contours and spot values

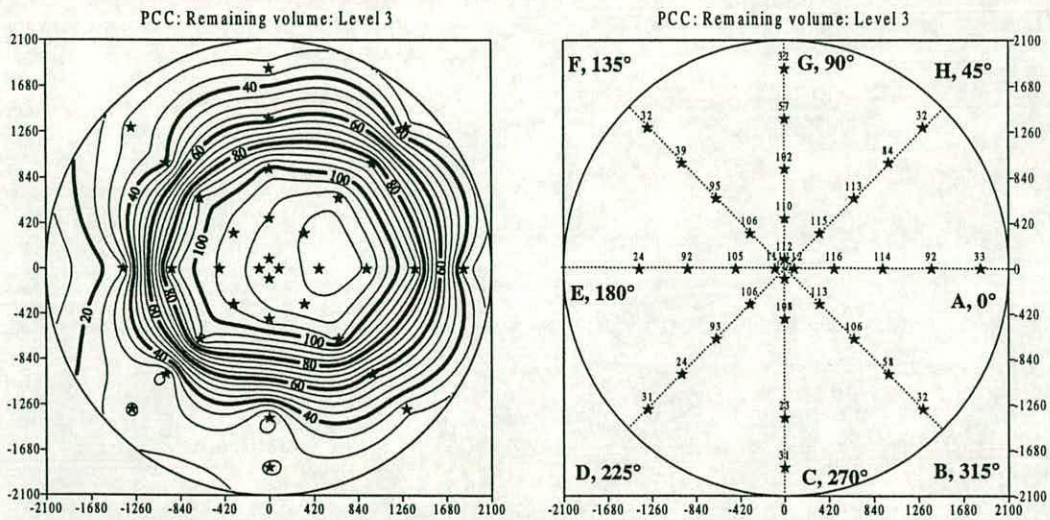

Fig. 7.8f PCC: Remaining volume: Level 3: Contours and spot values

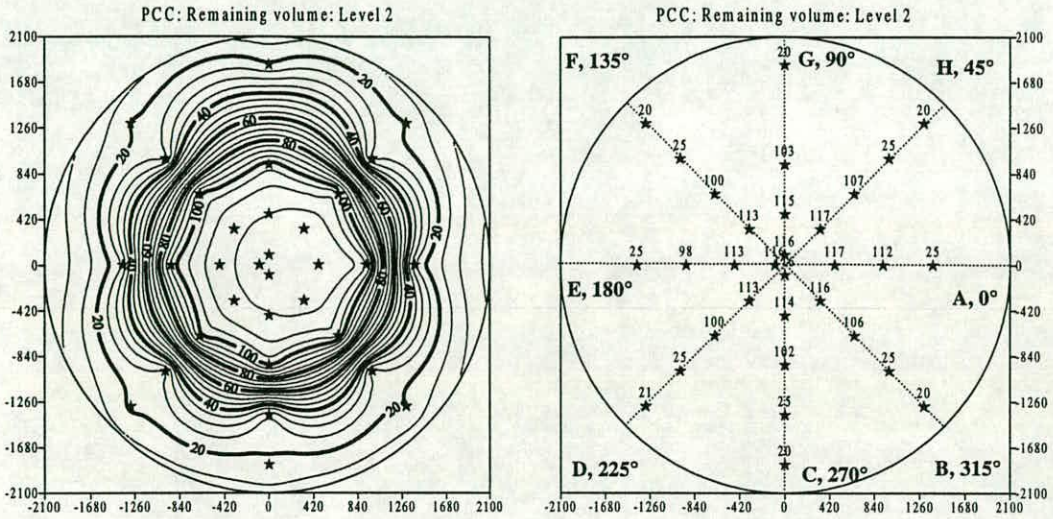

Fig. 7.8g PCC: Remaining volume: Level 2: Contours and spot values

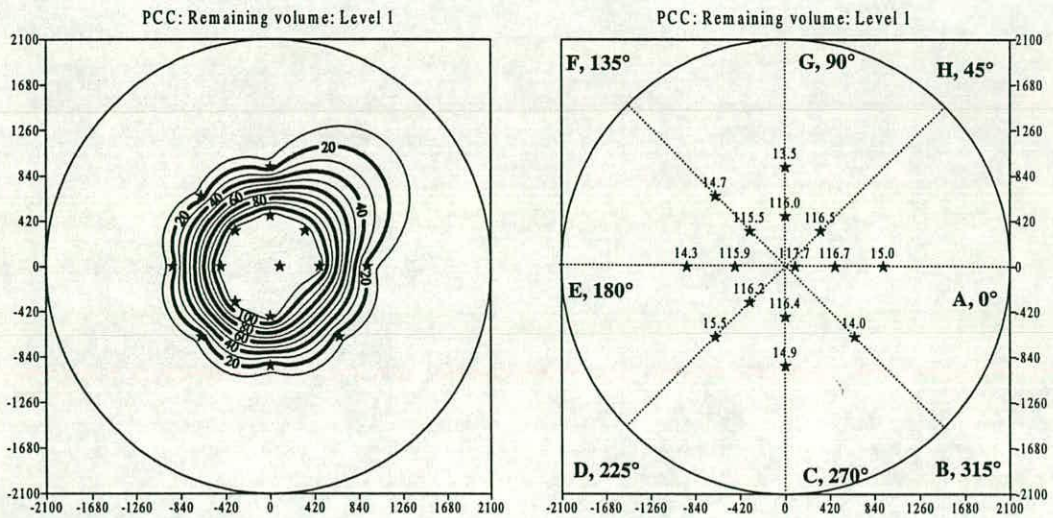

Fig. 7.8h PCC: Remaining volume: Level 1: Contours and spot values

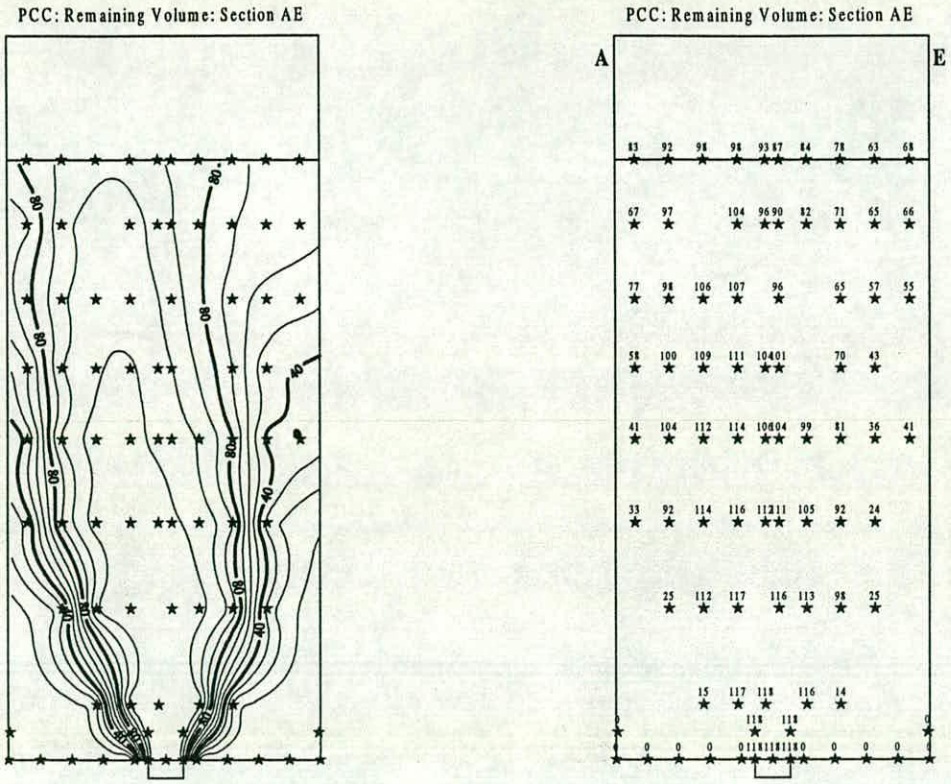

Fig. 7.9a PCC: Remaining volume: Vertical diametral section A-E: Contours and spot values

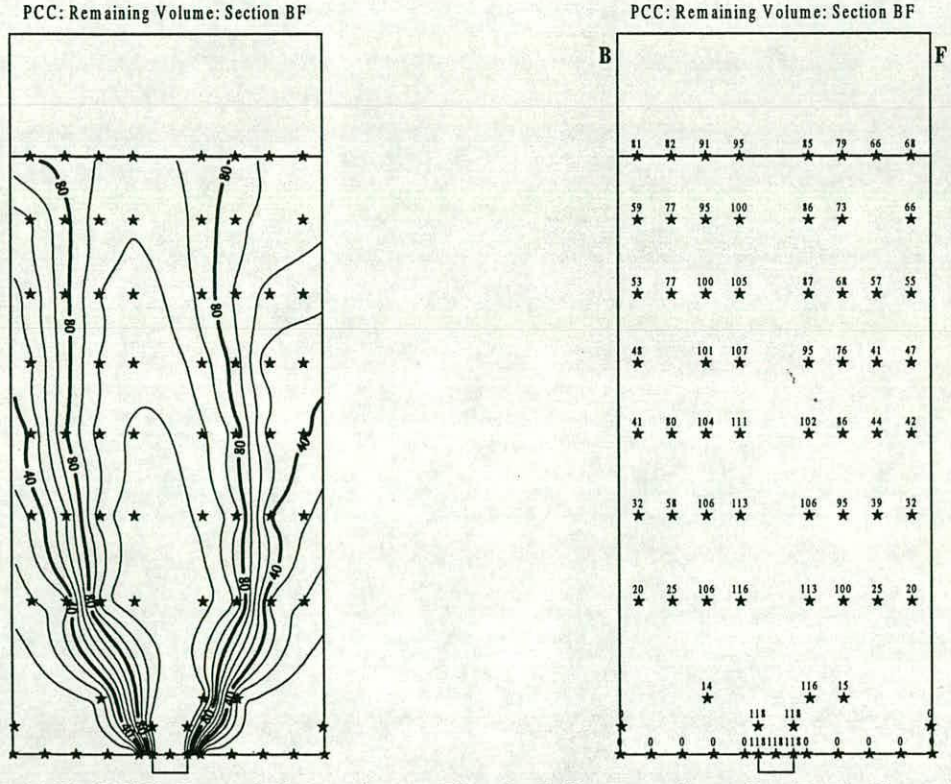

Fig. 7.9b PCC: Remaining volume: Vertical diametral section B-F: Contours and spot values

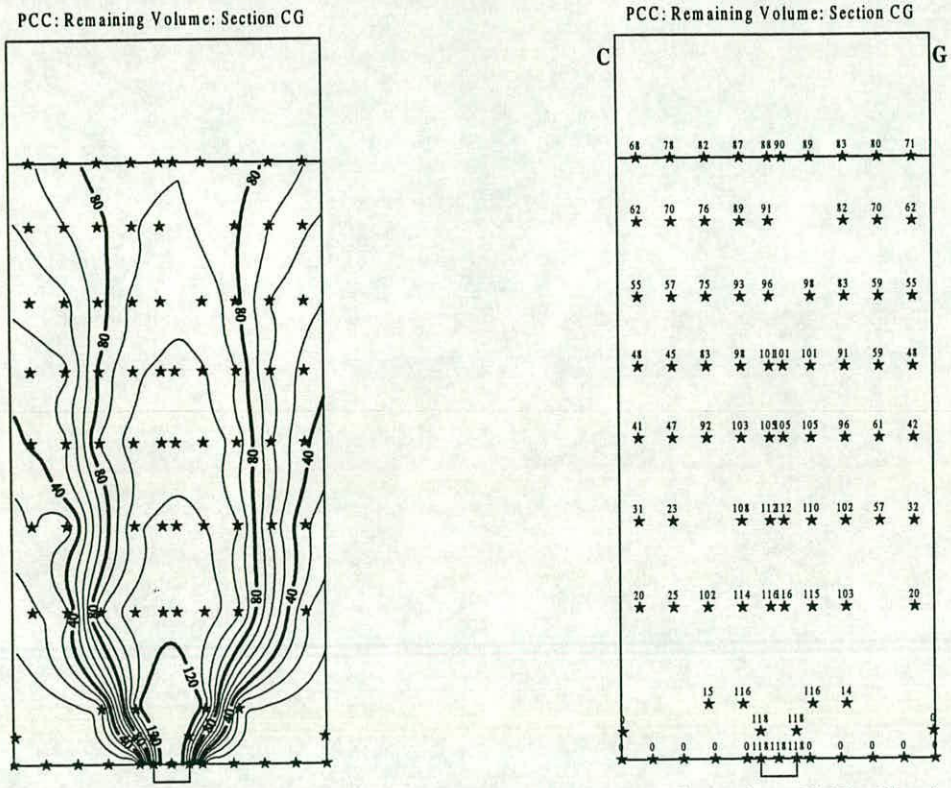

Fig. 7.9c PCC: Remaining volume: Vertical diametral section C-G: Contours and spot values

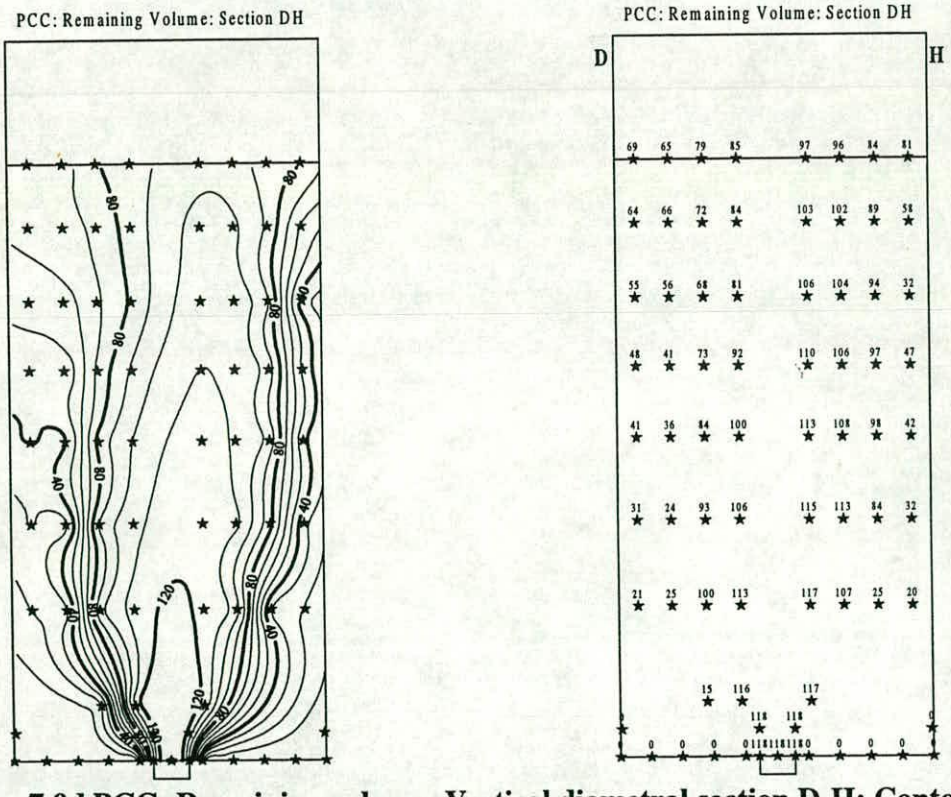

Fig. 7.9d PCC: Remaining volume: Vertical diametral section D-H: Contours and spot values

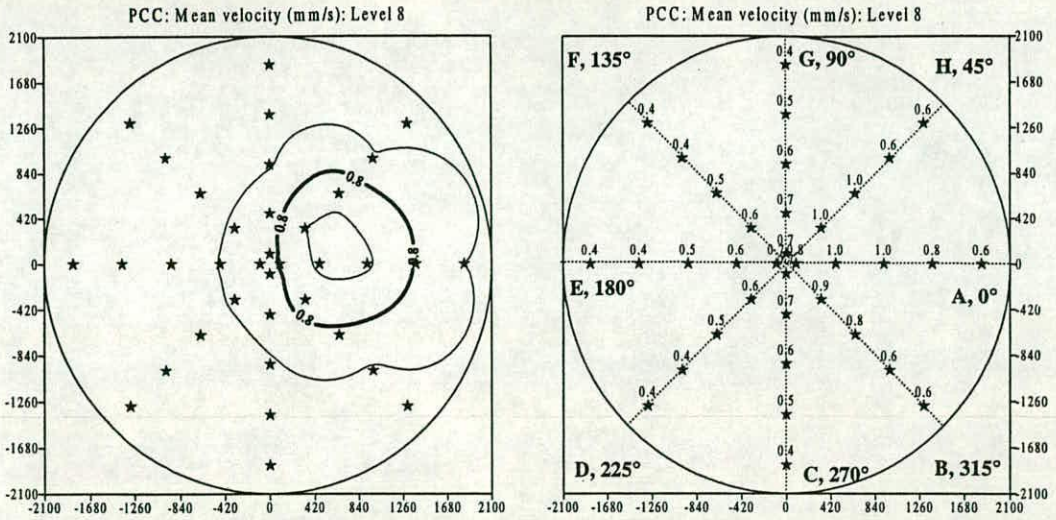

Fig. 7.10a PCC: Mean velocity: Level 8: Contours and spot values

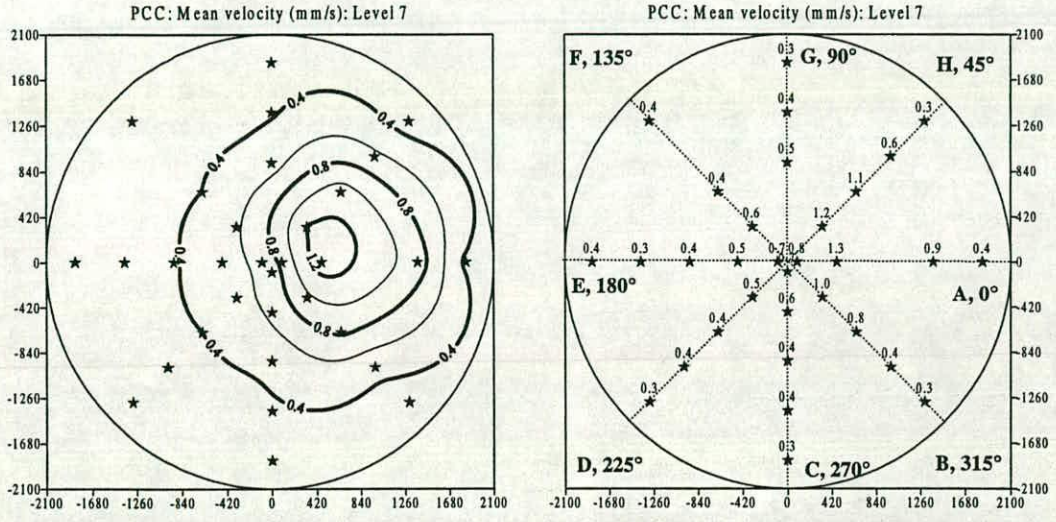

Fig. 7.10b PCC: Mean velocity: Level 7: Contours and spot values

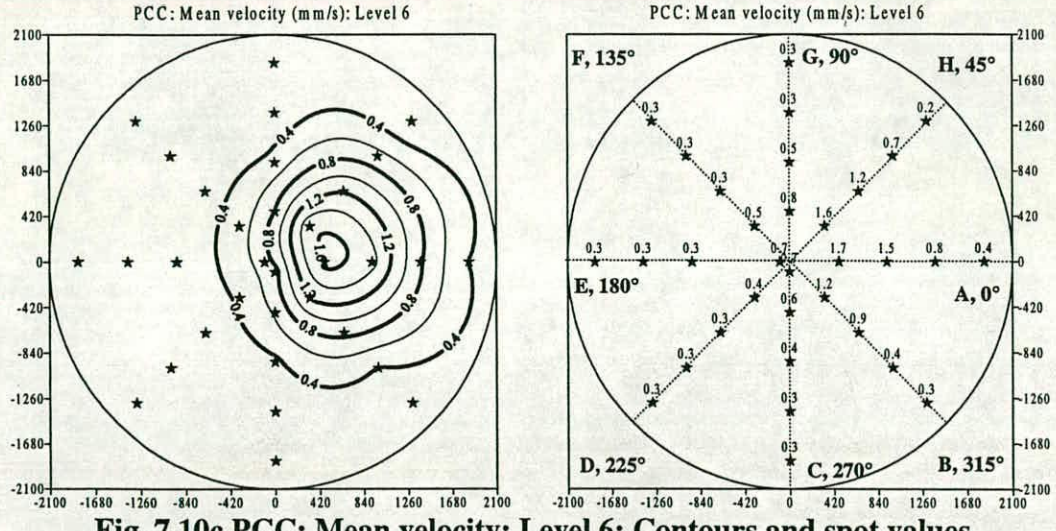

Fig. 7.10c PCC: Mean velocity: Level 6: Contours and spot values

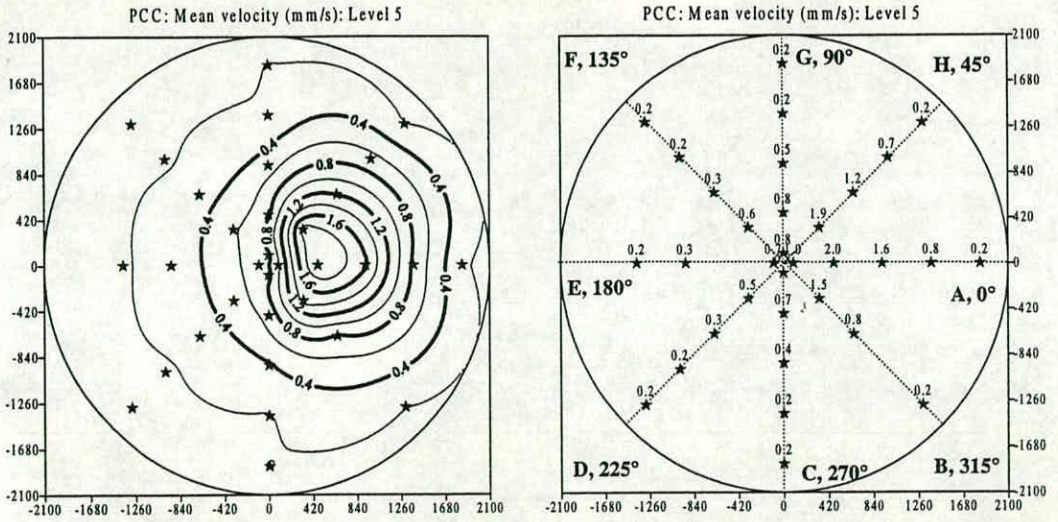

Fig. 7.10d PCC: Mean velocity: Level 5: Contours and spot values

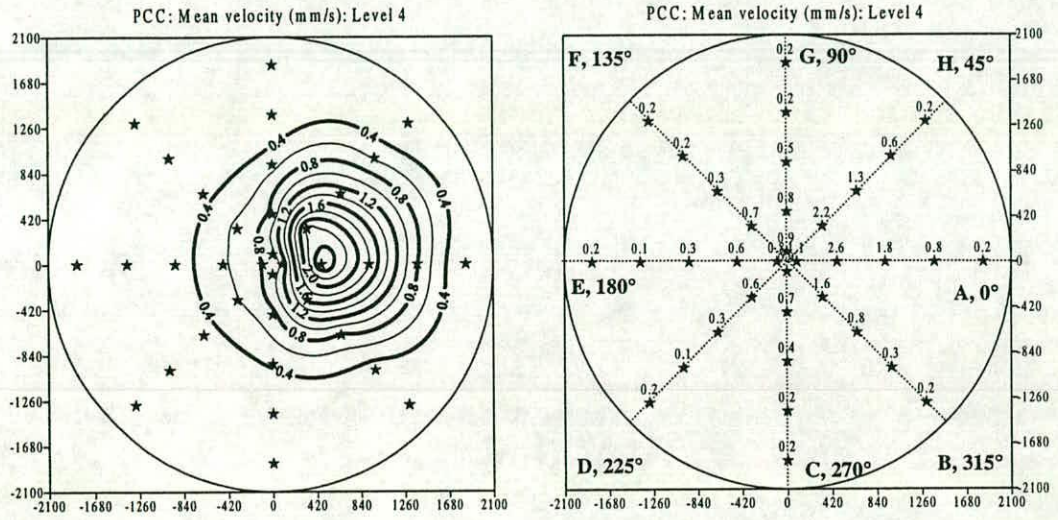

Fig. 7.10e PCC: Mean velocity: Level 4: Contours and spot values

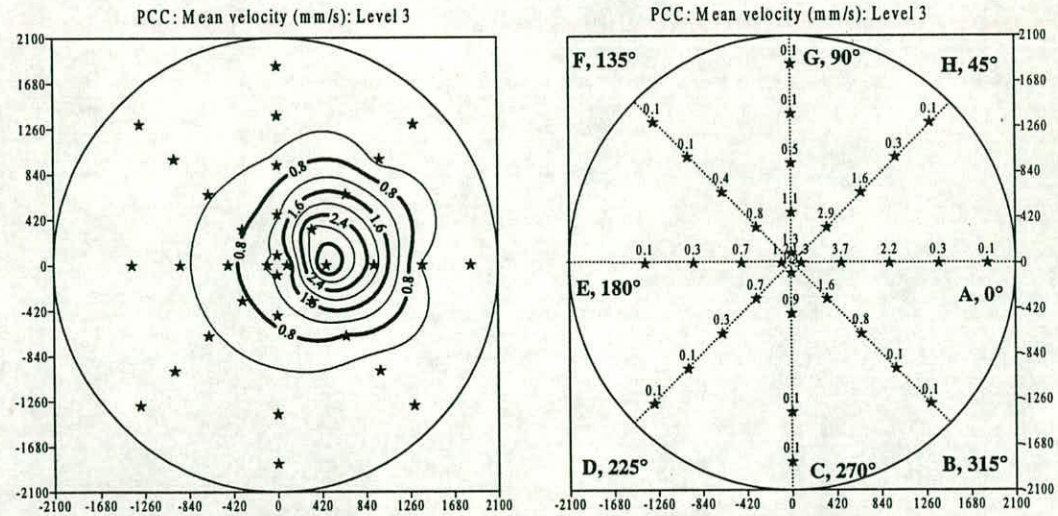

Fig. 7.10f PCC: Mean velocity: Level 3: Contours and spot values

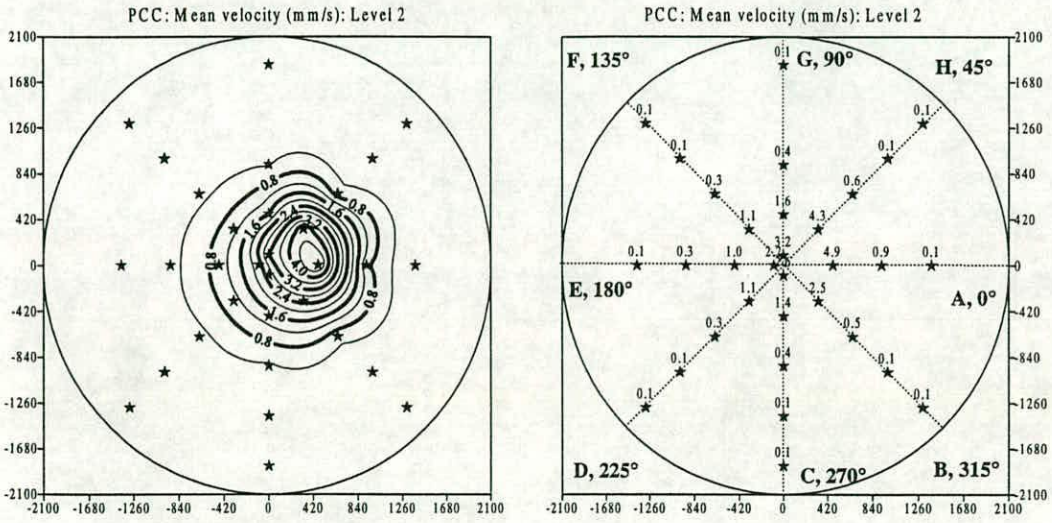

Fig. 7.10g PCC: Mean velocity: Level 2: Contours and spot values

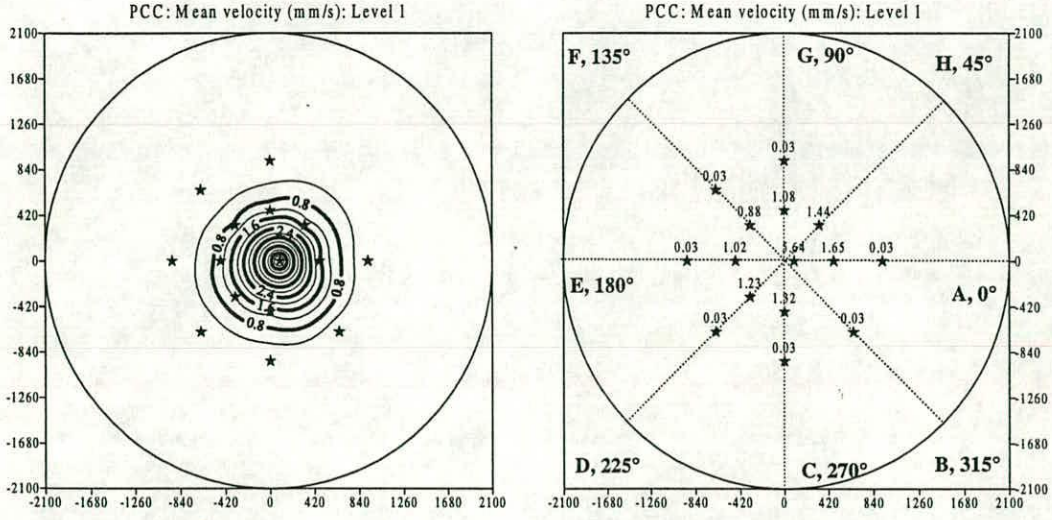

Fig. 7.10h PCC: Mean velocity: Level 1: Contours and spot values

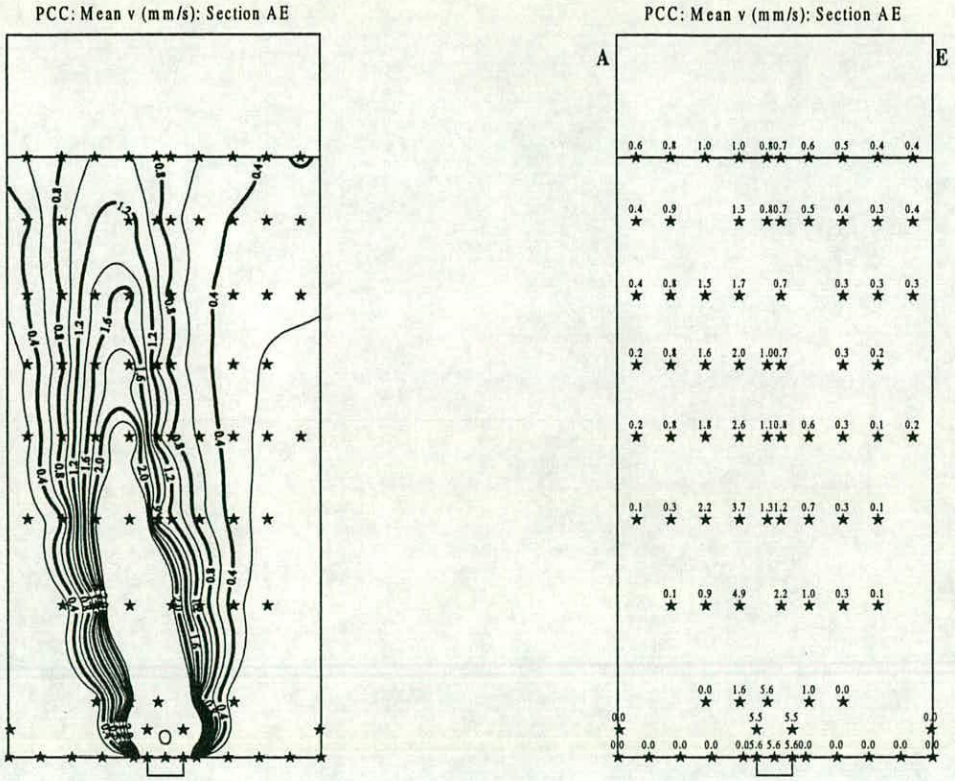

Fig. 7.11a PCC: Mean velocity: Vertical diametral section A-E: Contours and spot values

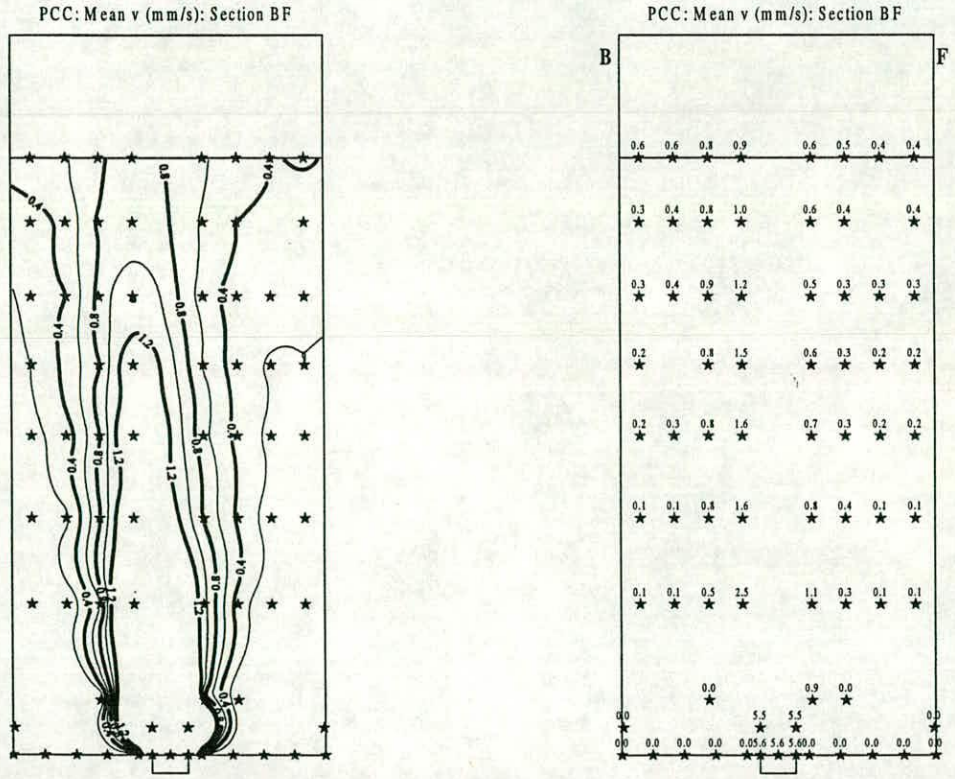

Fig. 7.11b PCC: Mean velocity: Vertical diametral section B-F: Contours and spot values

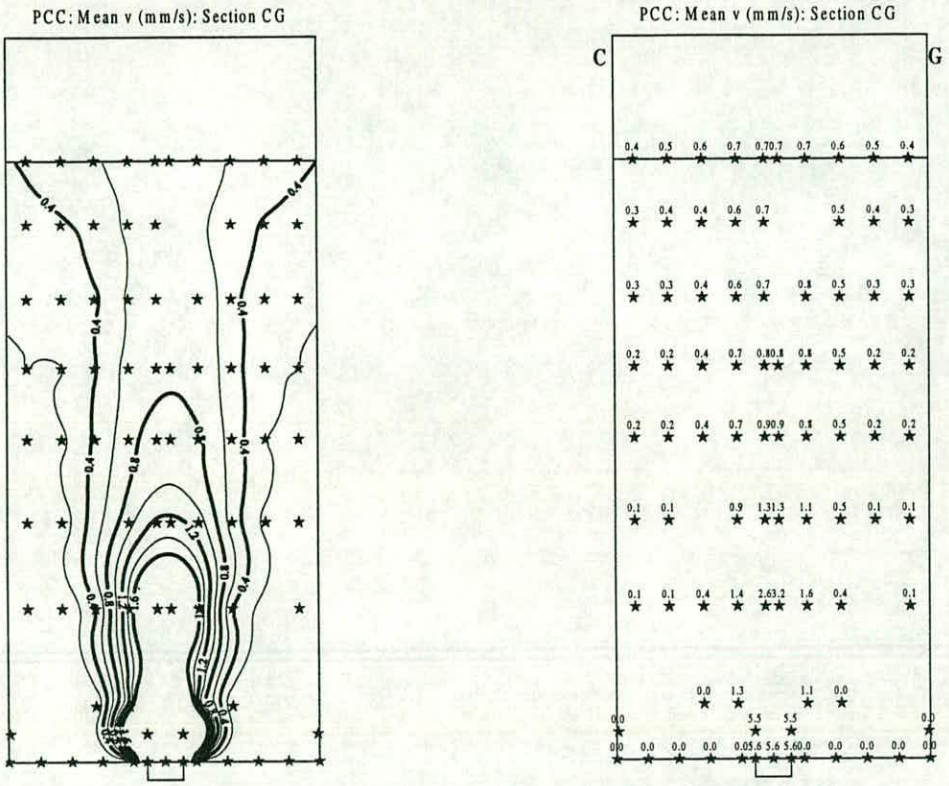

Fig. 7.11c PCC: Mean velocity: Vertical diametral section C-G: Contours and spot values

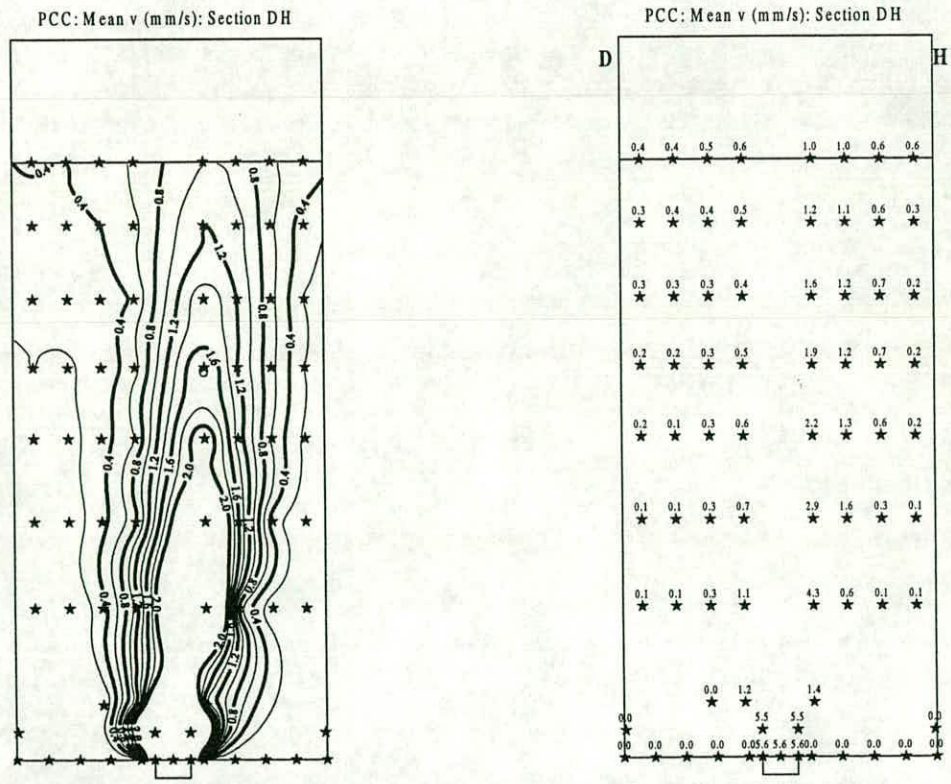

Fig. 7.11d PCC: Mean velocity: Vertical diametral section D-H: Contours and spot values

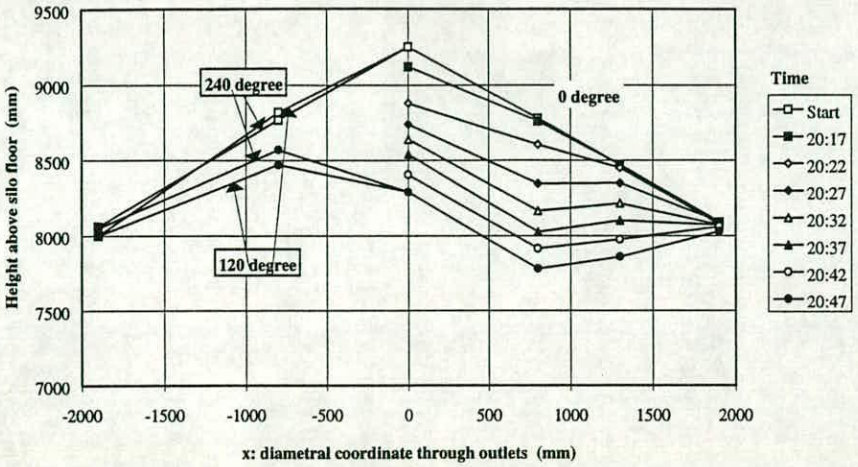

Fig. 7.12a PCC: Top surface profile during discharge (on x-z plane)

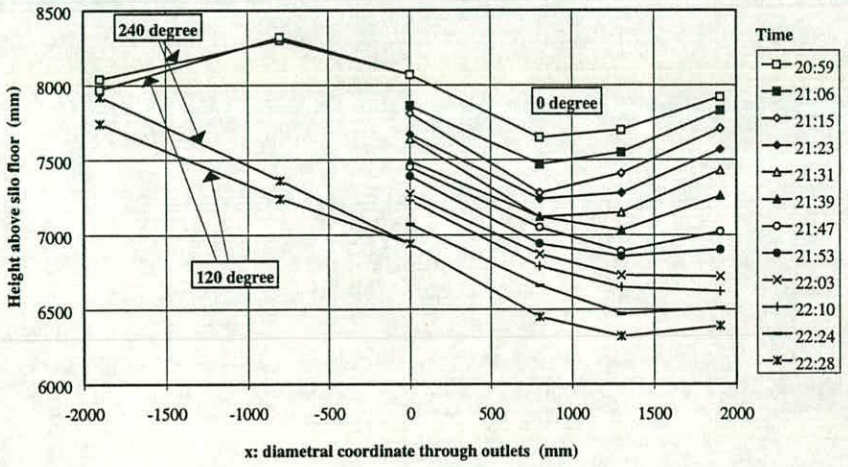

Fig. 7.12b PCC: Top surface profile during discharge (on x-z plane)

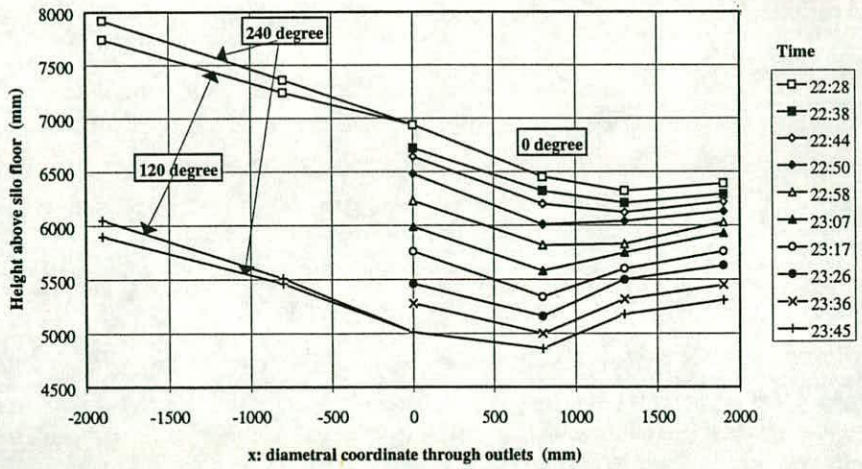

Fig. 7.12c PCC: Top surface profile during discharge (on x-z plane)

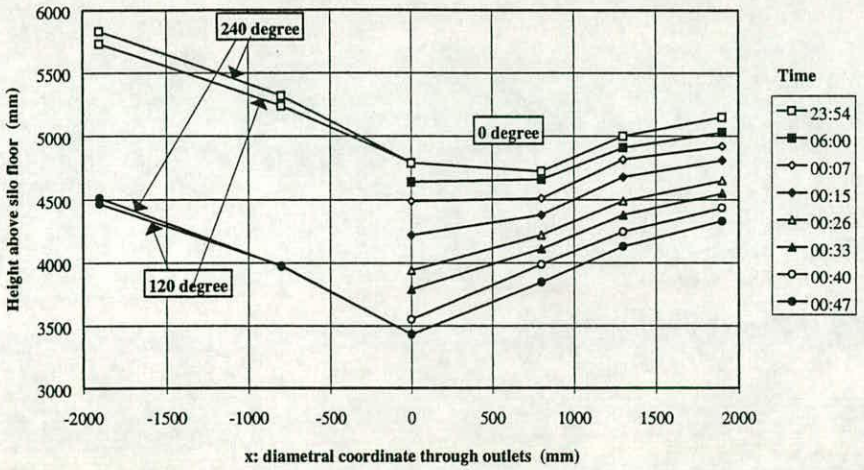

Fig. 7.12d PCC: Top surface profile during discharge (on x-z plane)

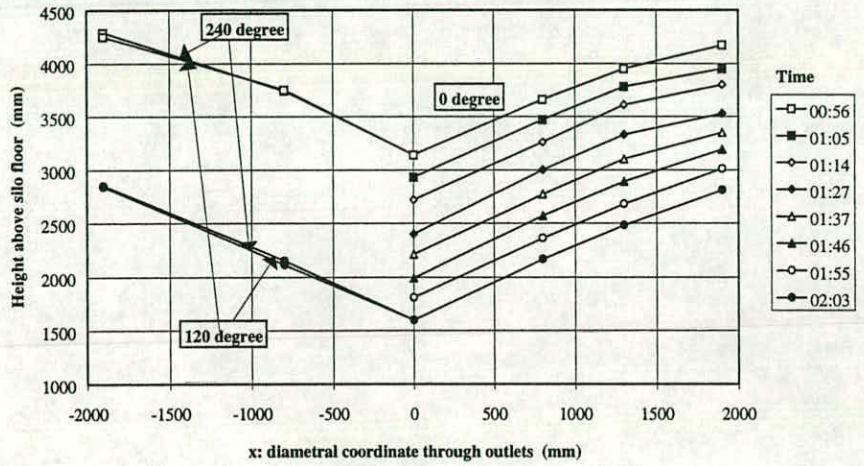

Fig. 7.12e PCC: Top surface profile during discharge (on x-z plane)

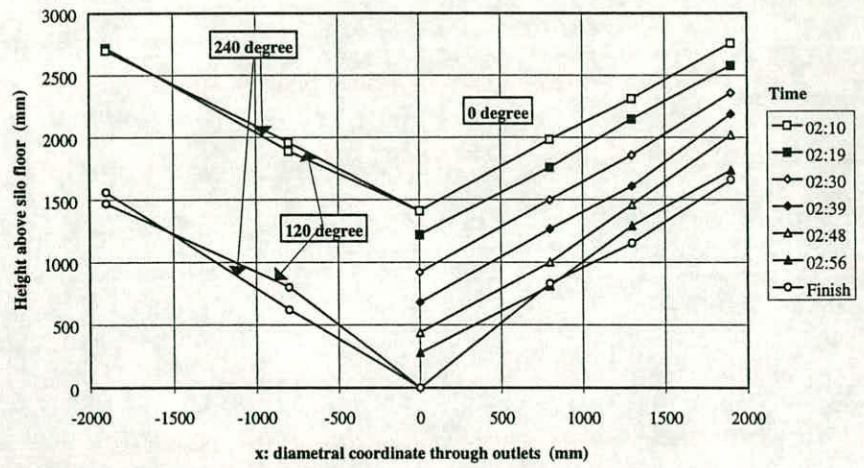

Fig. 7.12f PCC: Top surface profile during discharge (on x-z plane)

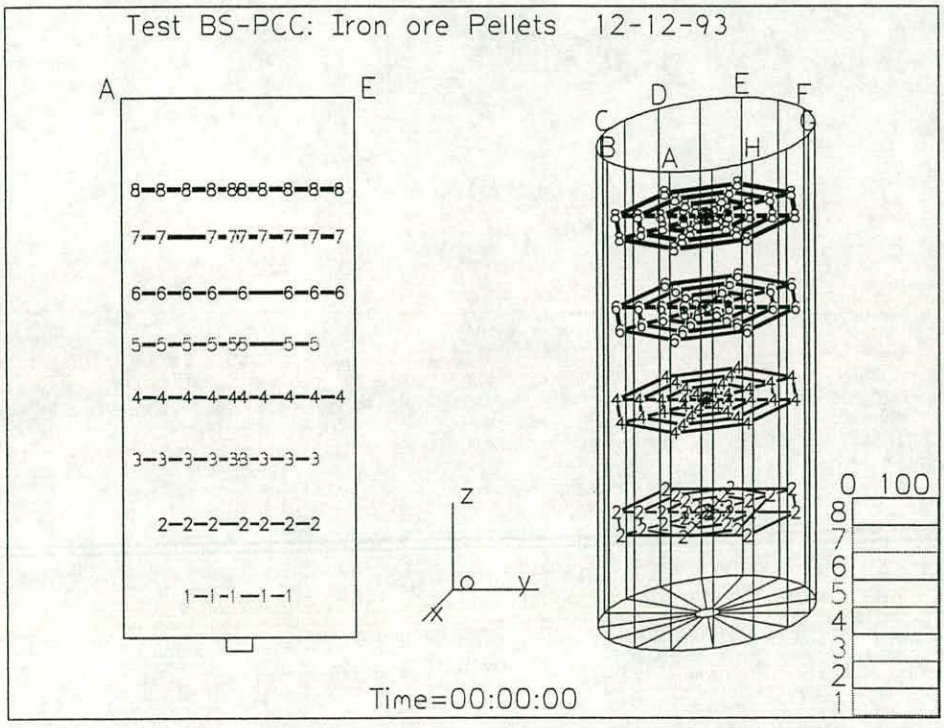

Fig. 7.13a Test PCC: Simple visualization: Diametral section AE

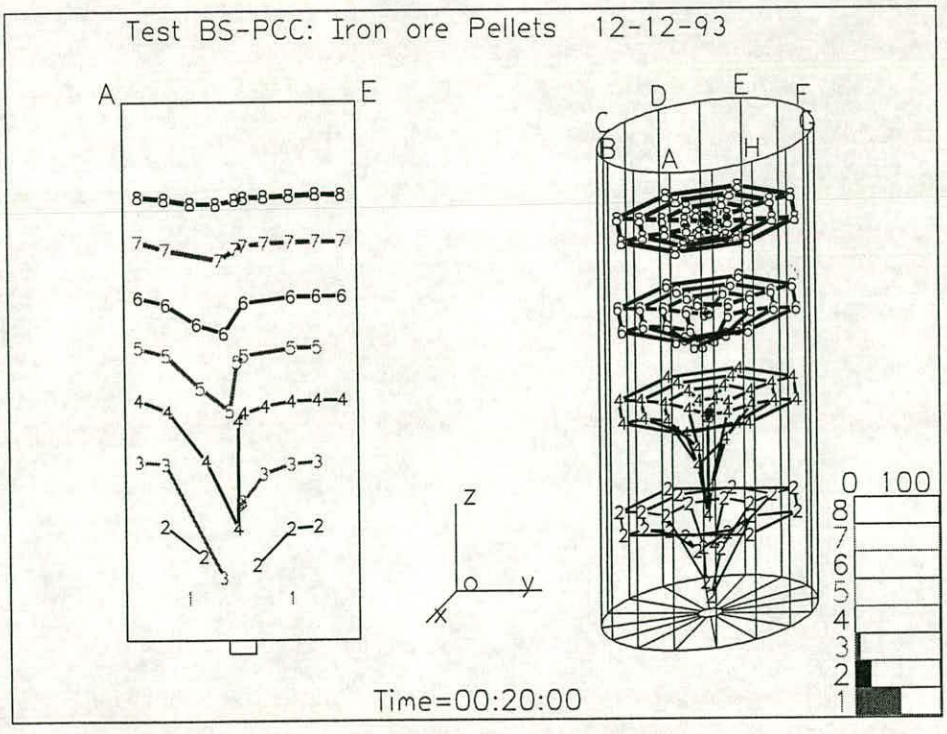

Fig. 7.13b Test PCC: Simple visualization: Diametral section AE

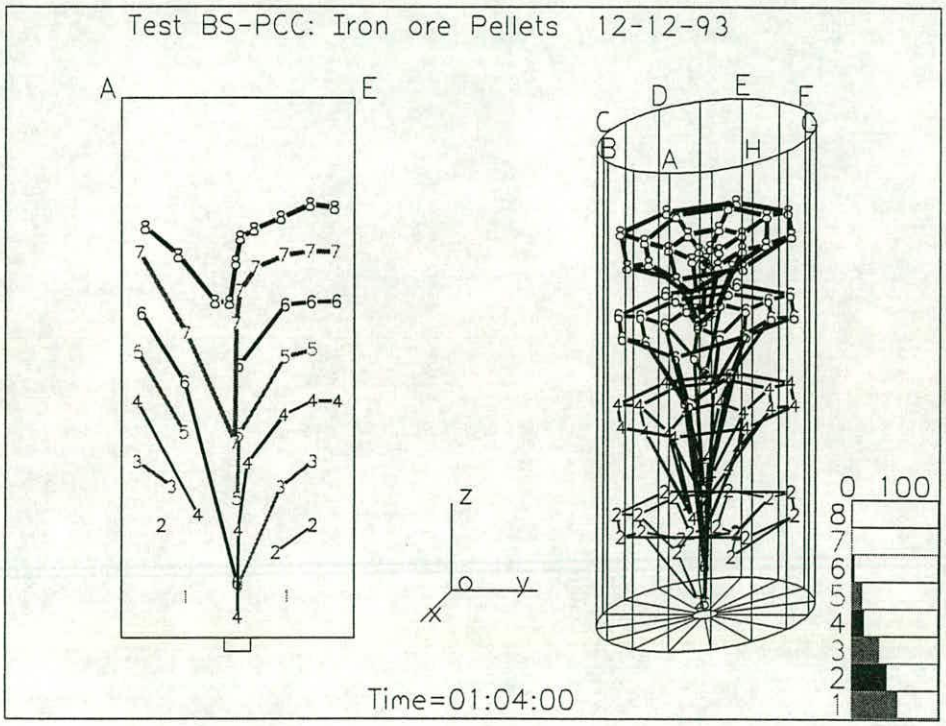

Fig. 7.13c Test PCC: Simple visualization: Diametral section AE

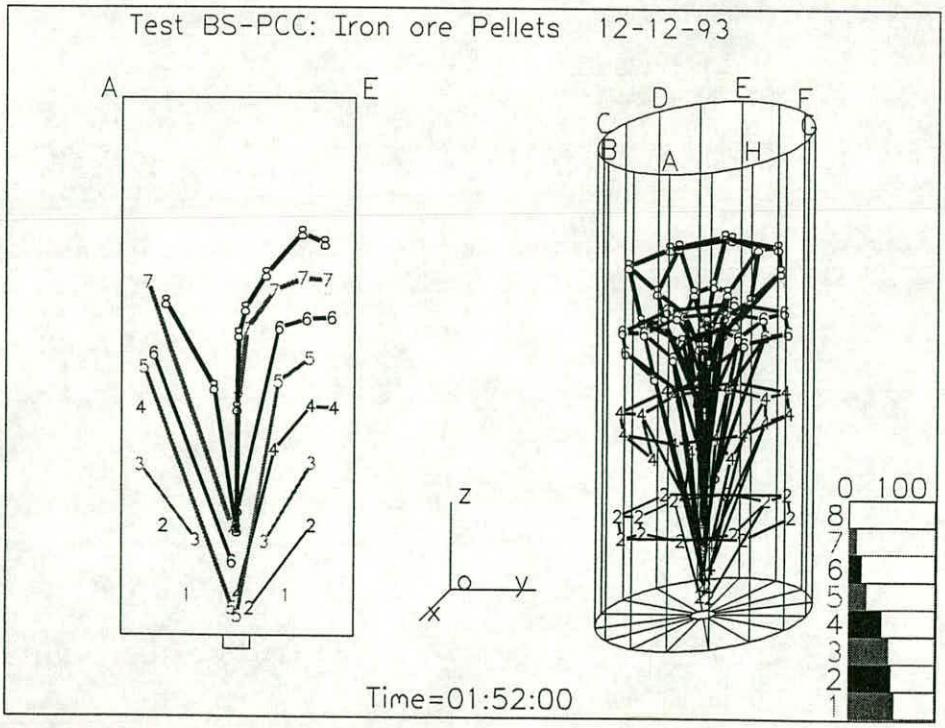

Fig. 7.13d Test PCC: Simple visualization: Diametral section AE

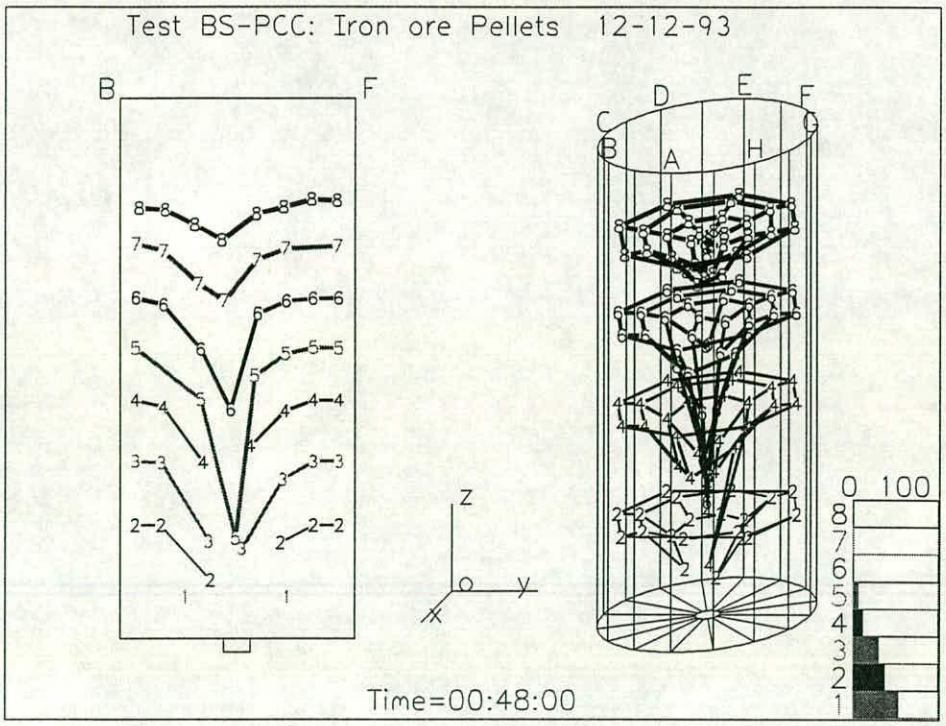

Fig. 7.13e Test PCC: Simple visualization: Diametral section BF

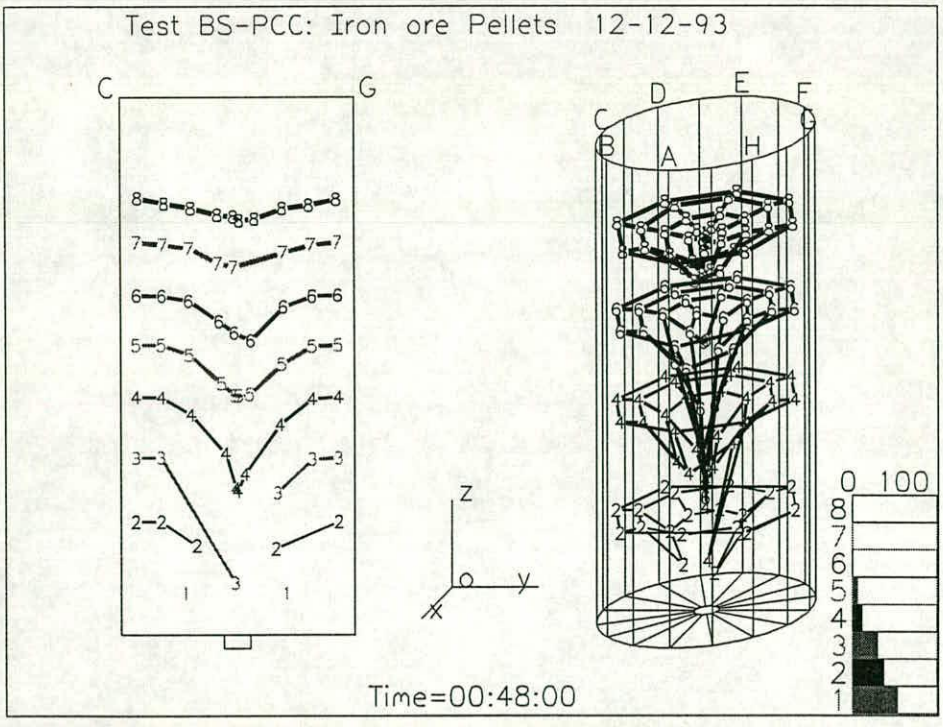

Fig. 7.13f Test PCC: Simple visualization: Diametral section CG

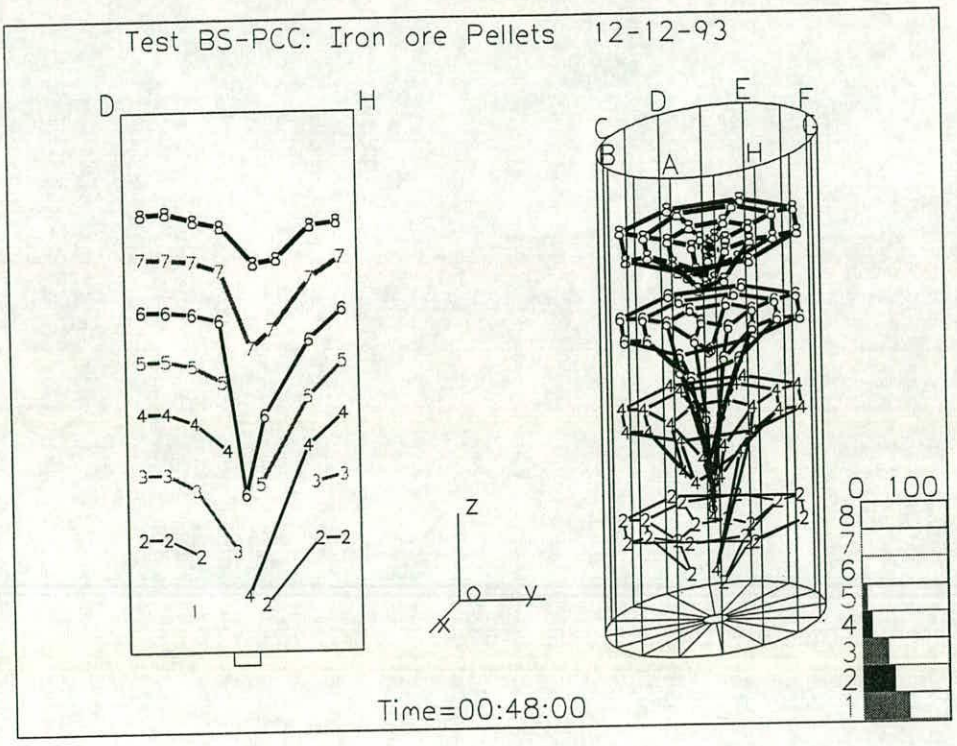

Fig. 7.13g Test PCC: Simple visualization: Diametral section DH

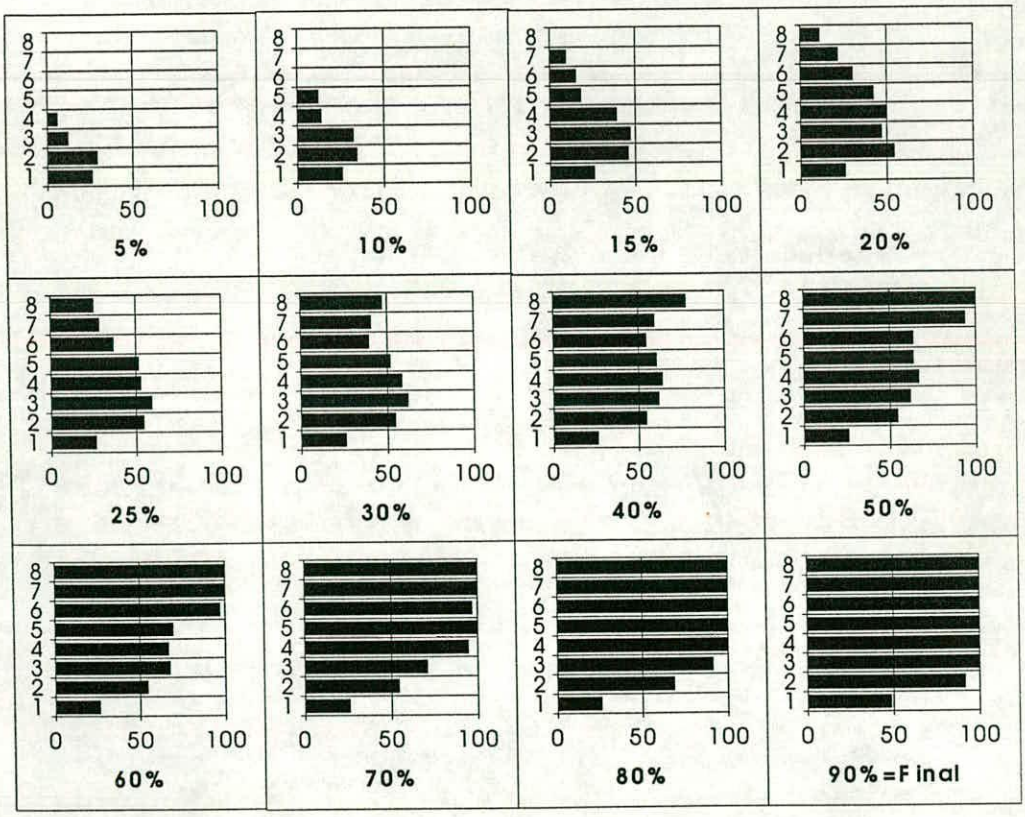

Fig. 7.14 Test PCC: Bars of tags exited from the outlet at different stages

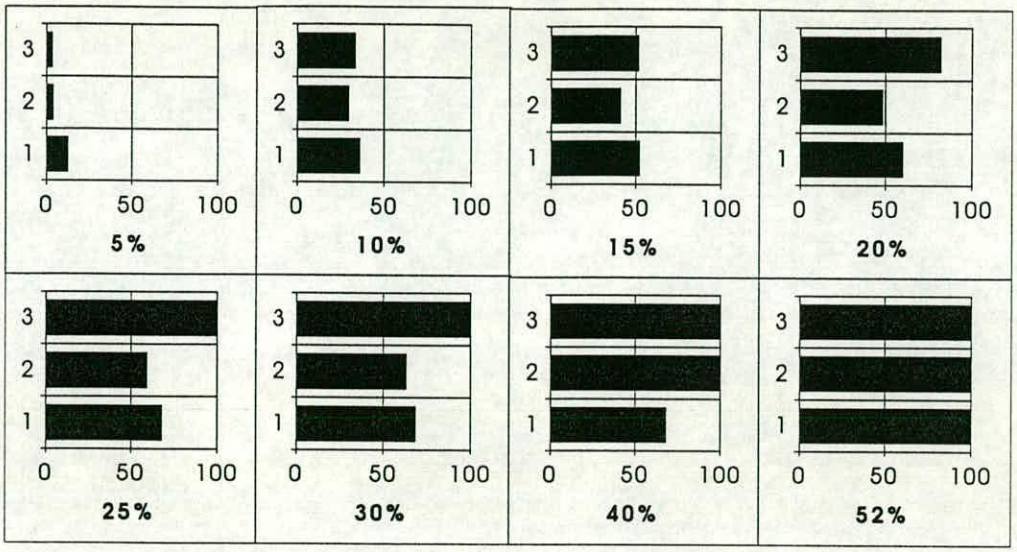

Fig. 7.15 Test PCA: Bars of tags exited from the outlet at different stages

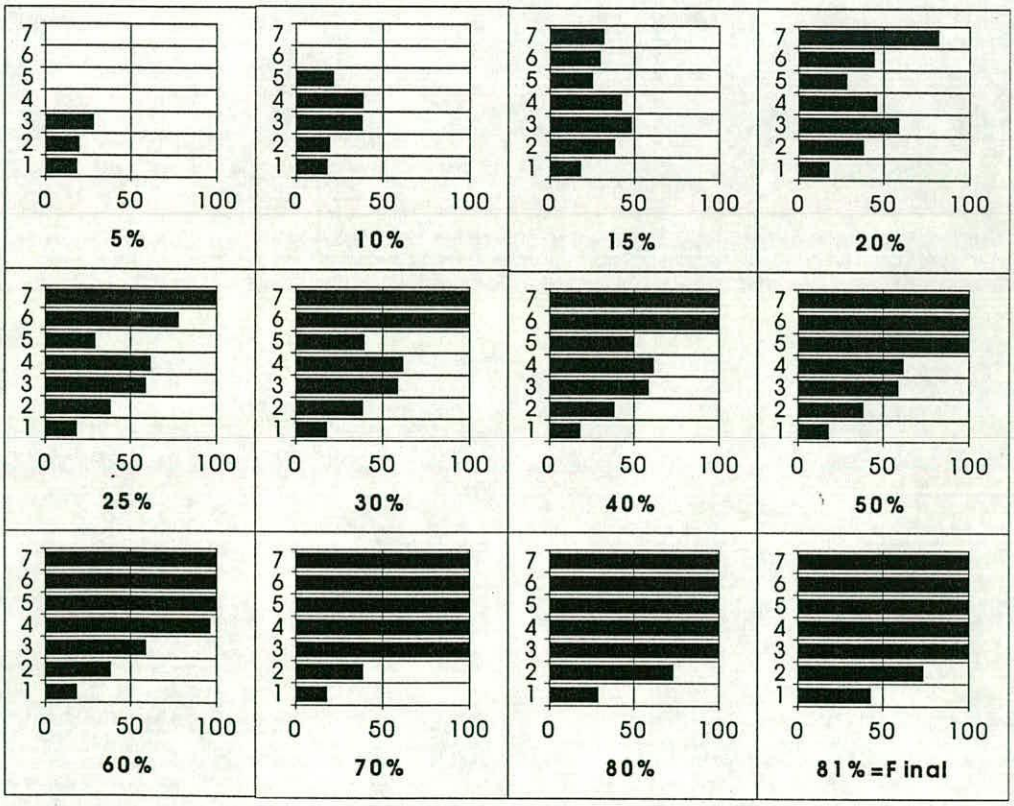

Fig. 7.16 Test PCB: Bars of tags exited from the outlet at different stages

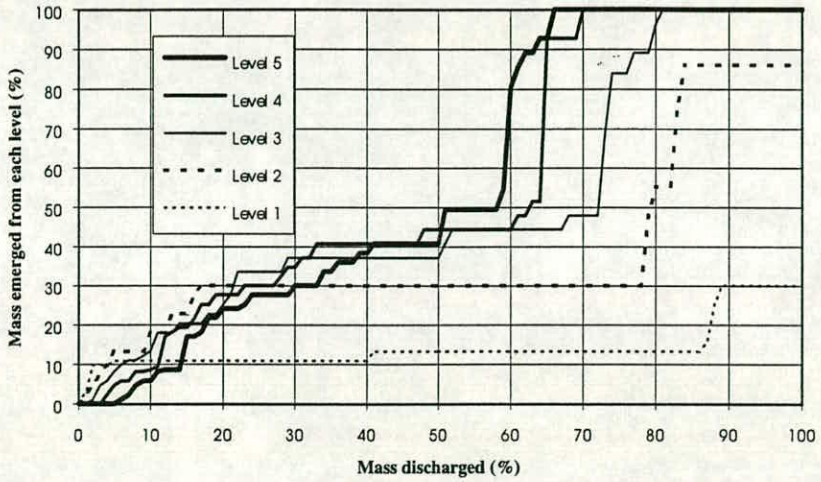

Fig. 7.17a Test PCC: Mass emerged from different levels vs. mass discharged

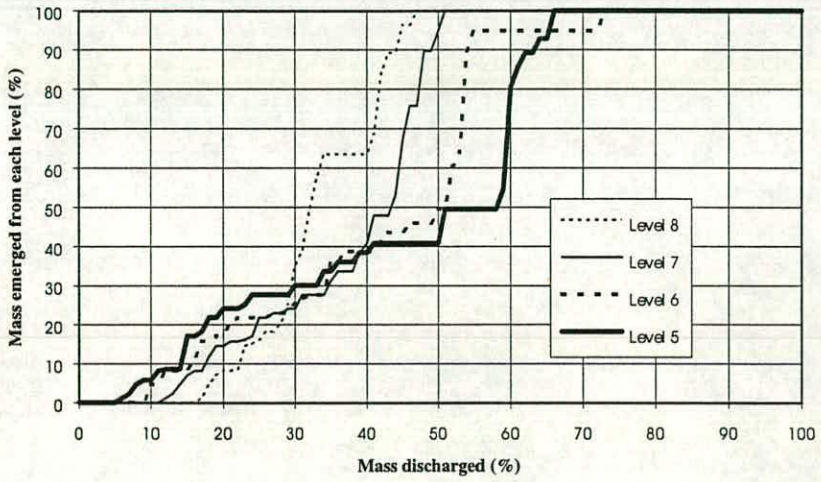

Fig. 7.17b Test PCC: Mass emerged from different levels vs. mass discharged

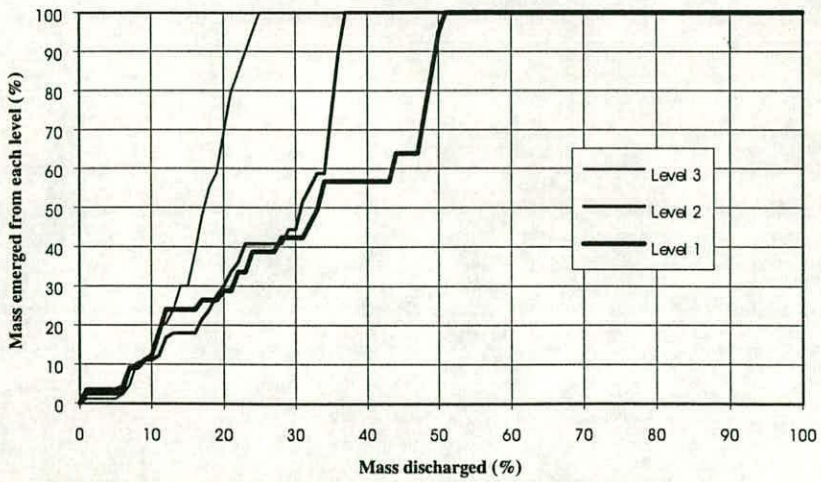

Fig. 7.18 Test PCA: Mass emerged from different levels vs. mass discharged

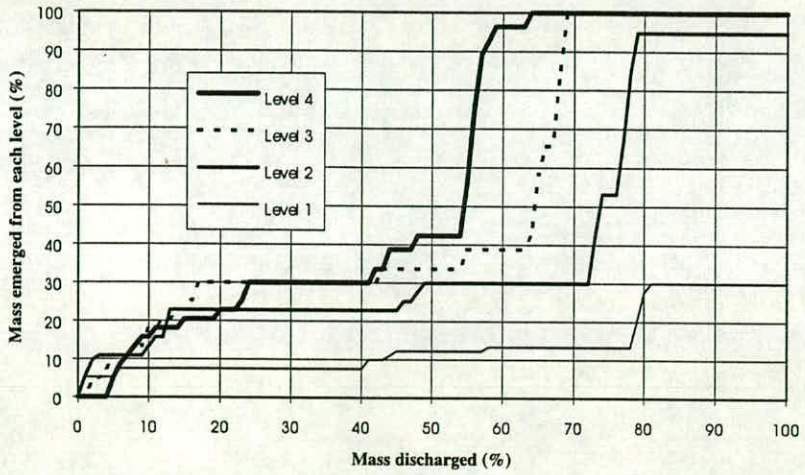

Fig. 7.19a Test PCB: Mass emerged from different levels vs. mass discharged

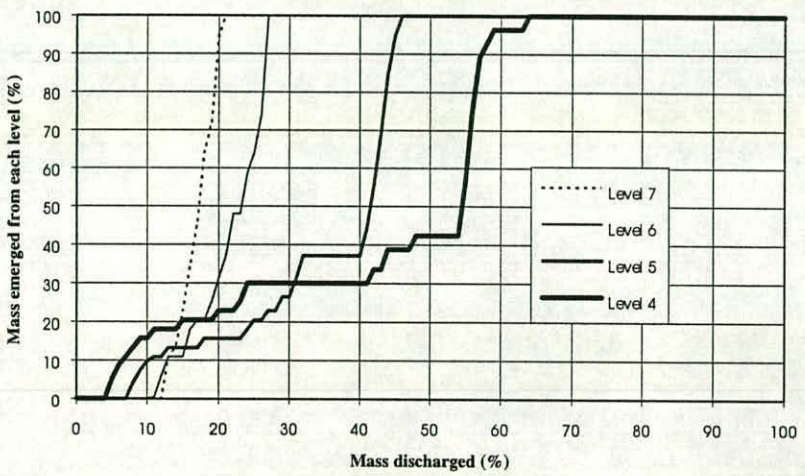

Fig. 7.19b Test PCB: Mass emerged from different levels vs. mass discharged

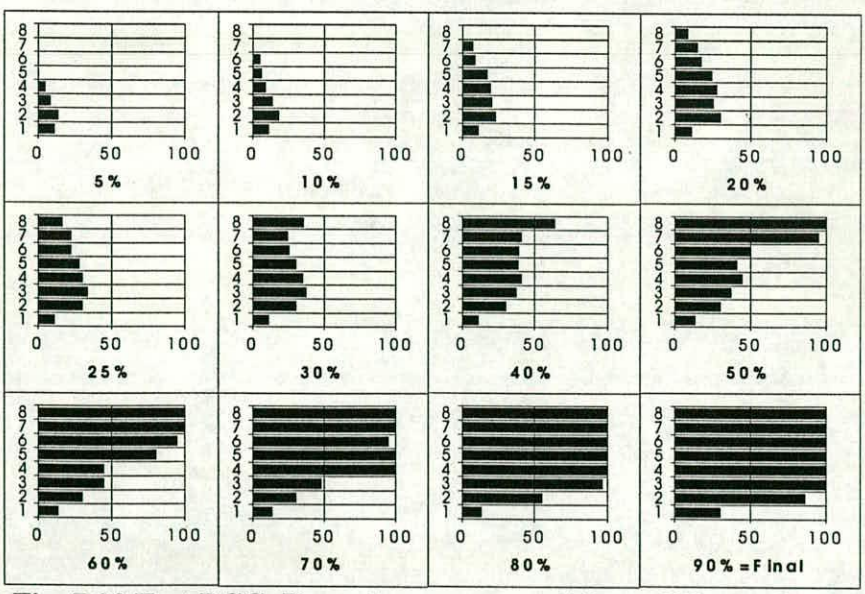

Fig. 7.20 Test PCC: Bars of mass emerged from different levels

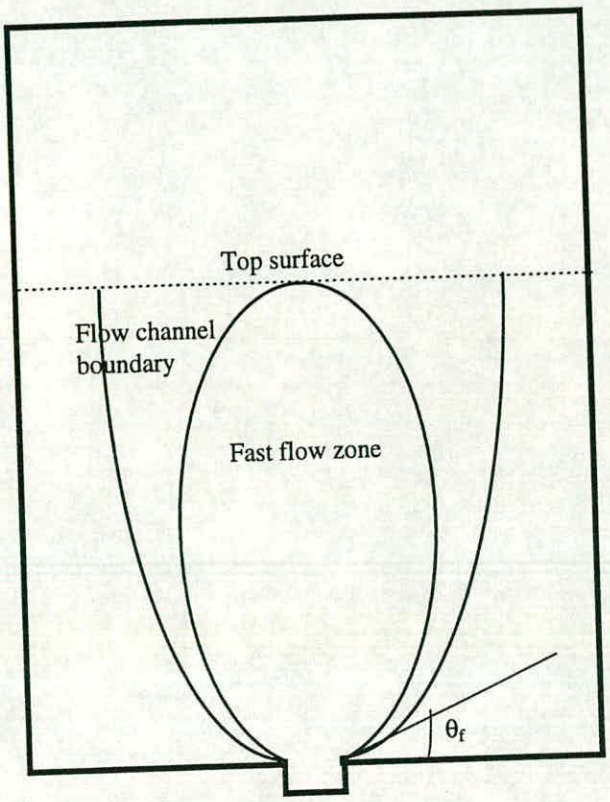

Fig. 7.21 Typical fast flow zone within a flow channel

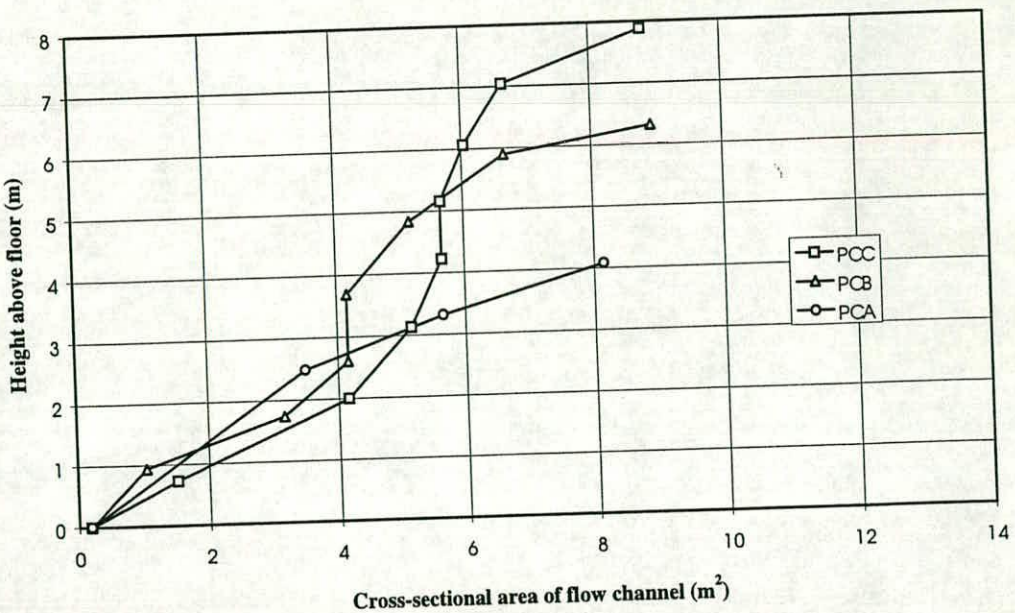

Fig. 7.22 Cross sectional area of flow channel: concentric discharge tests

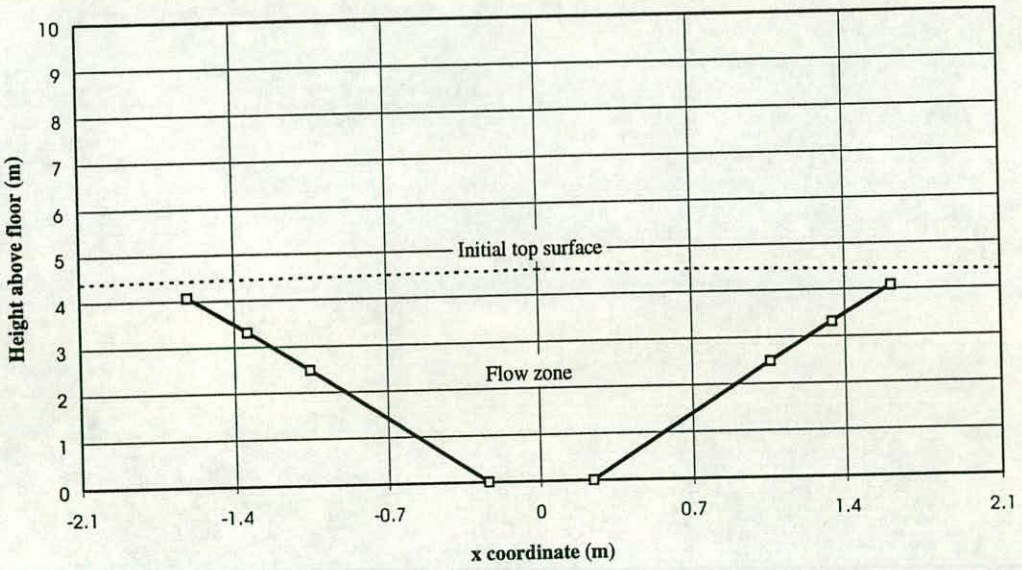

Fig. 7.23a Test PCA: Flow channel boundary: Assumed axisymmetric flow

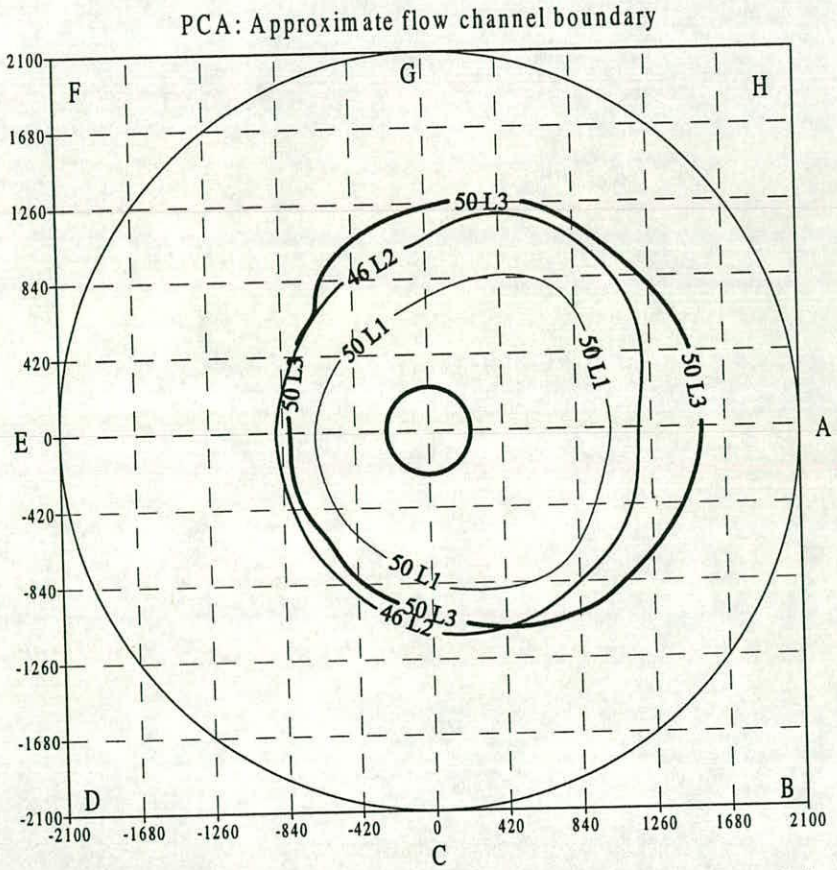

Fig. 7.23b Test PCA: Flow channel boundary: Drawn from remaining volume contour

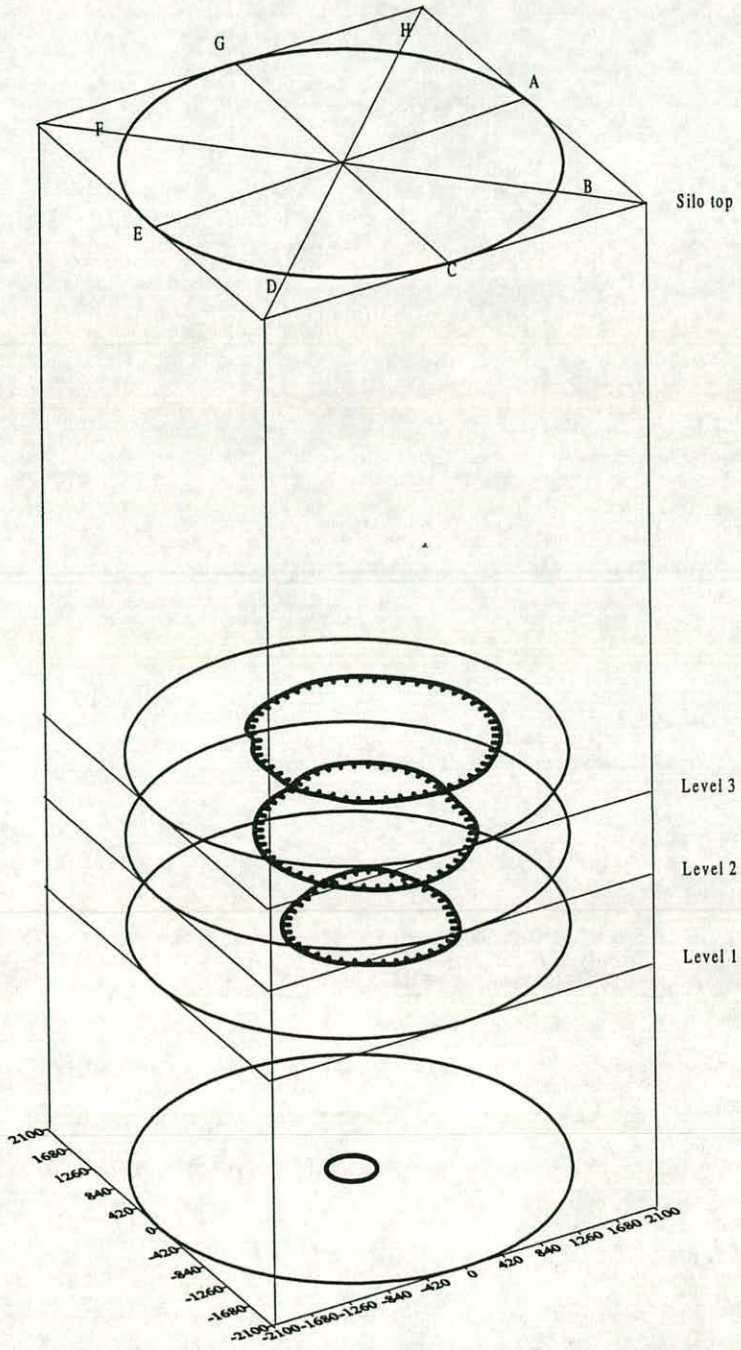

Fig. 7.23c Test PCA: Flow channel boundary: Drawn from remaining volume contour (3D view)

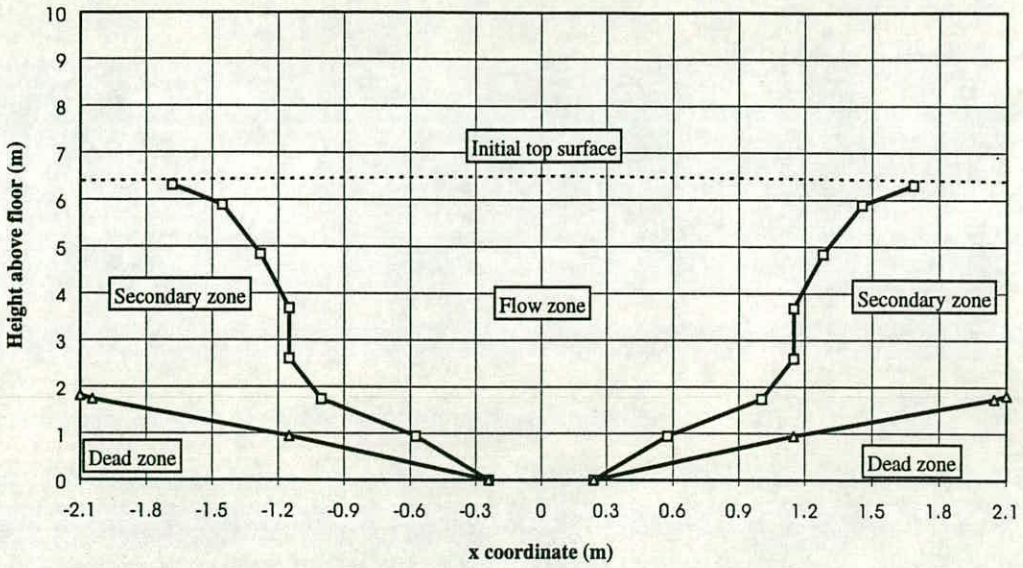

Fig. 7.24a Test PCB: Flow channel boundary: Assumed axisymmetric flow

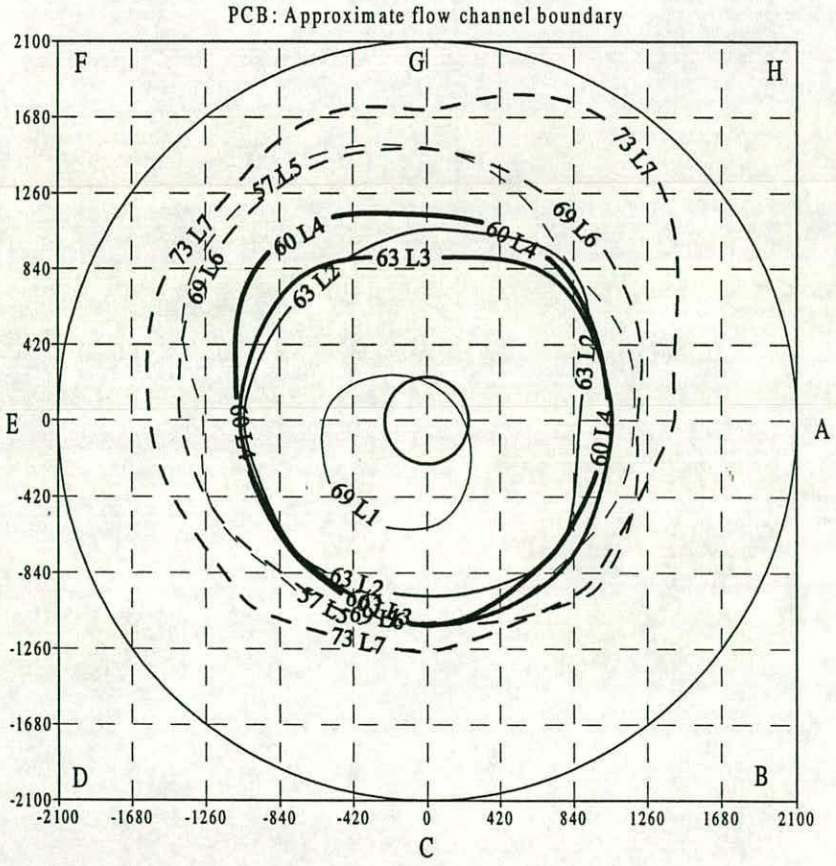

Fig. 7.24b Test PCB: Flow channel boundary: Drawn from remaining volume contour

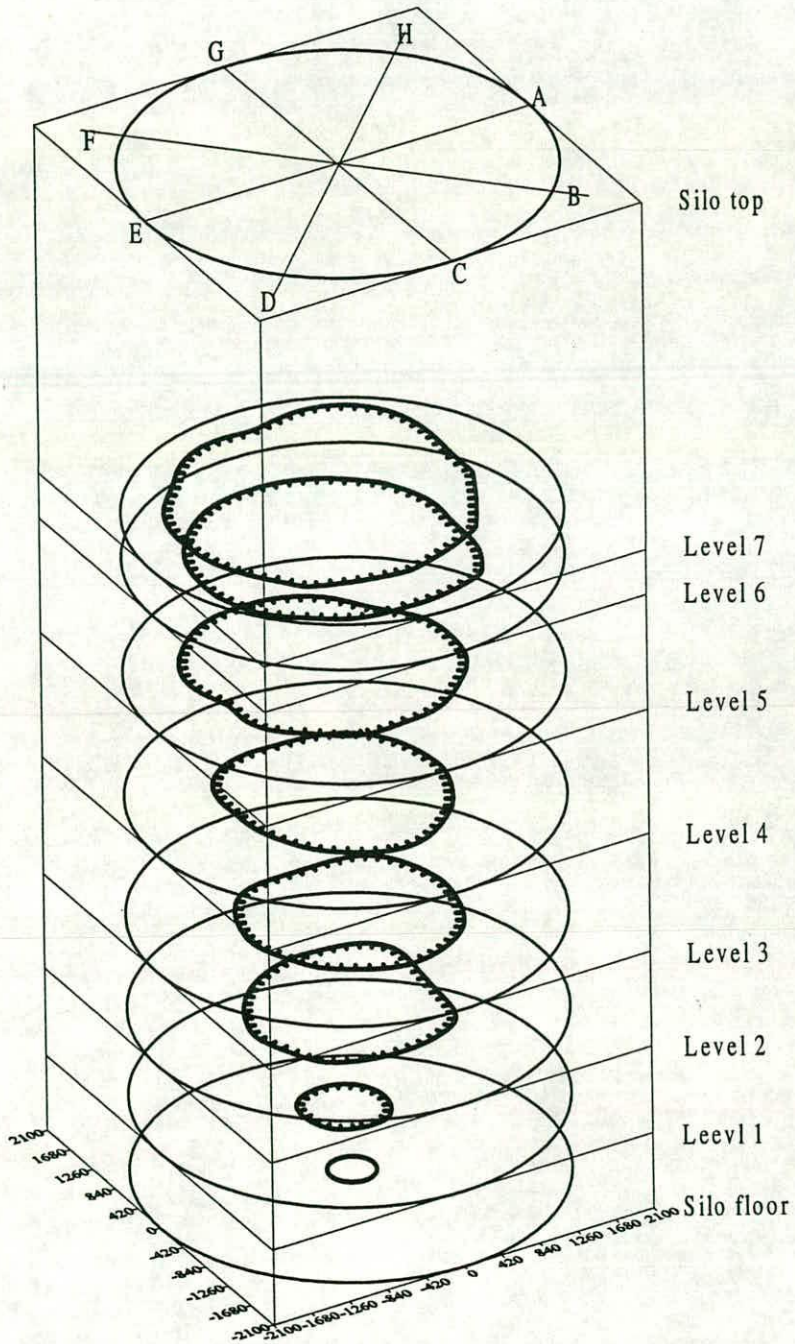

Fig. 7.24c Test PCB: Flow channel boundary: Drawn from remaining volume contour (3D view)

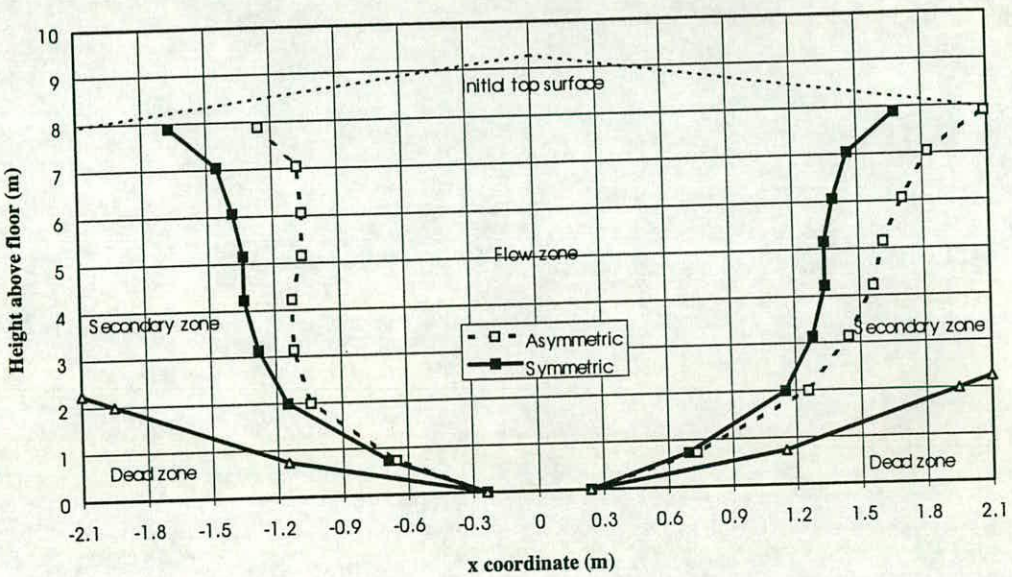

Fig. 7.25a Test PCC: Flow channel boundary: Assumed axisymmetric flow

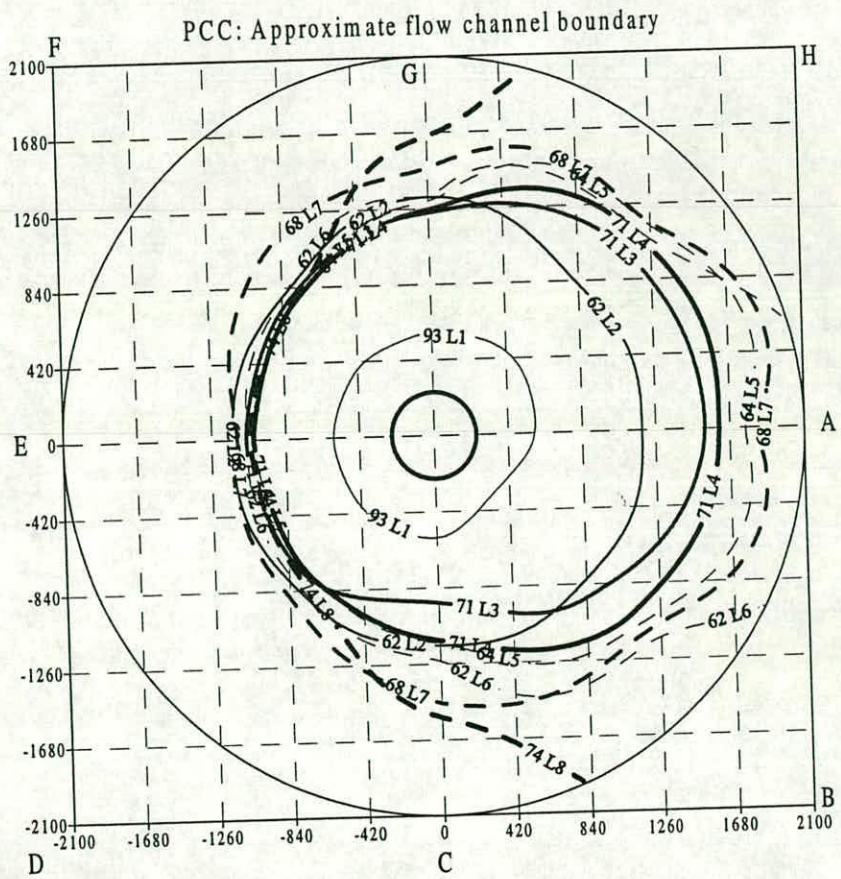

Fig. 7.25b Test PCC: Flow channel boundary: Drawn from remaining volume contour

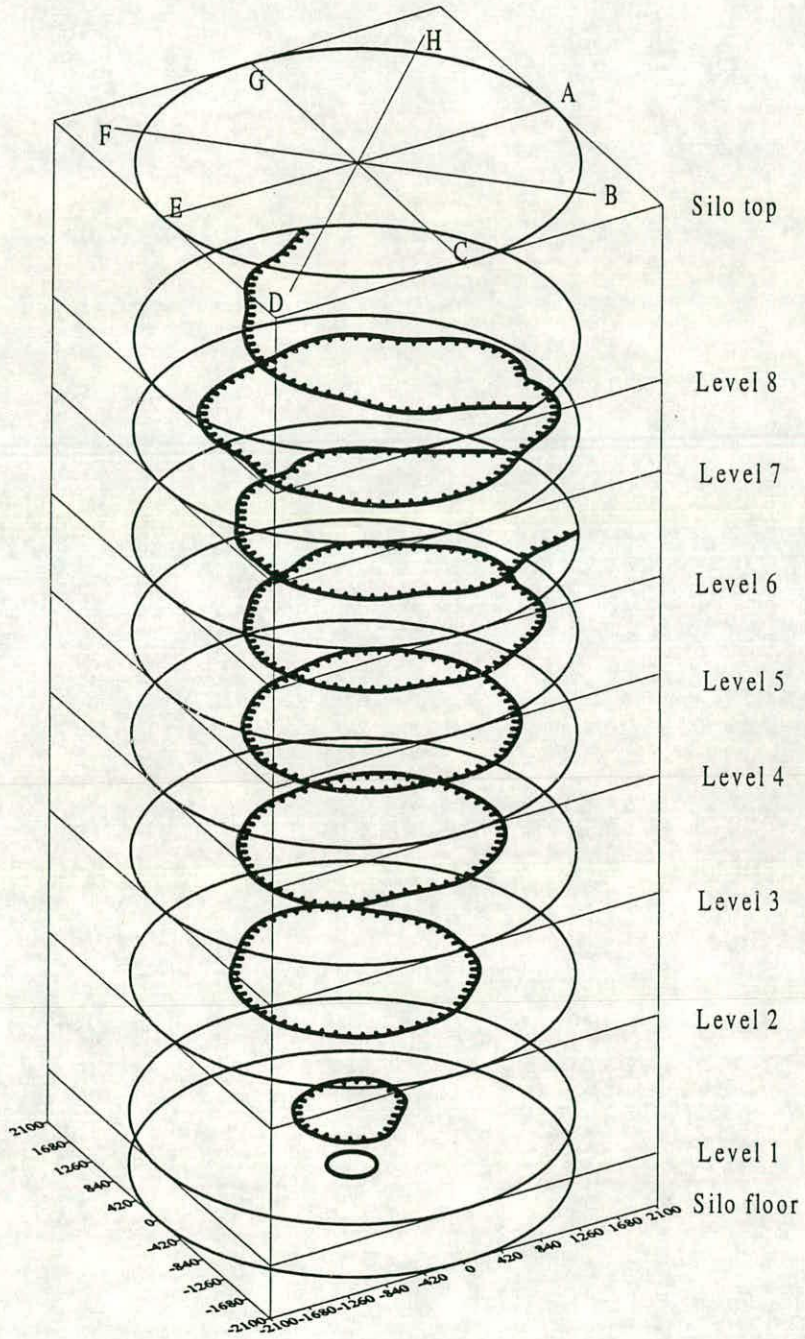

Fig. 7.25c Test PCC: Flow channel boundary: Drawn from remaining volume contour (3D view)

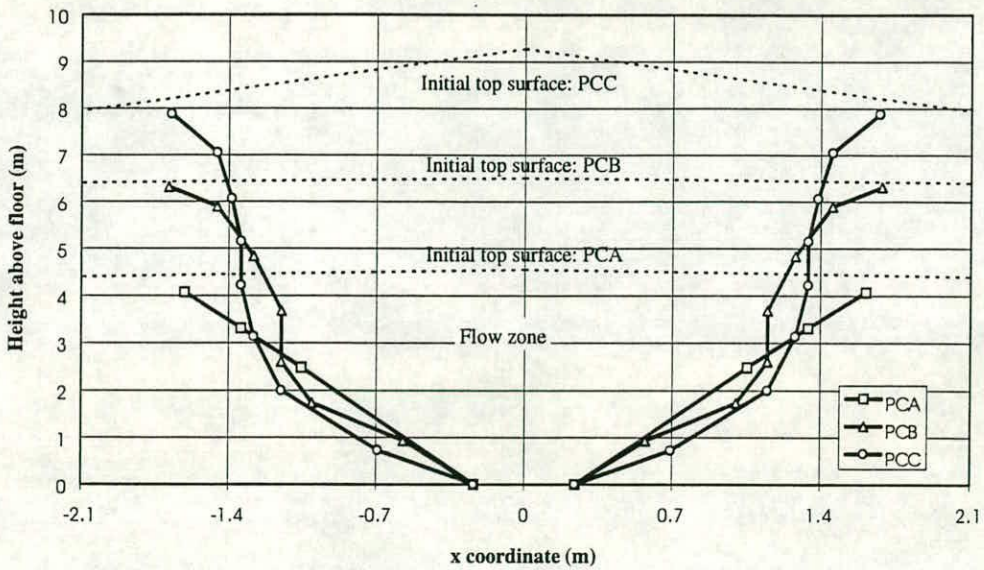

Fig. 7.26 Flow channel boundary on concentric discharge (Assumed axisymmetric flow)

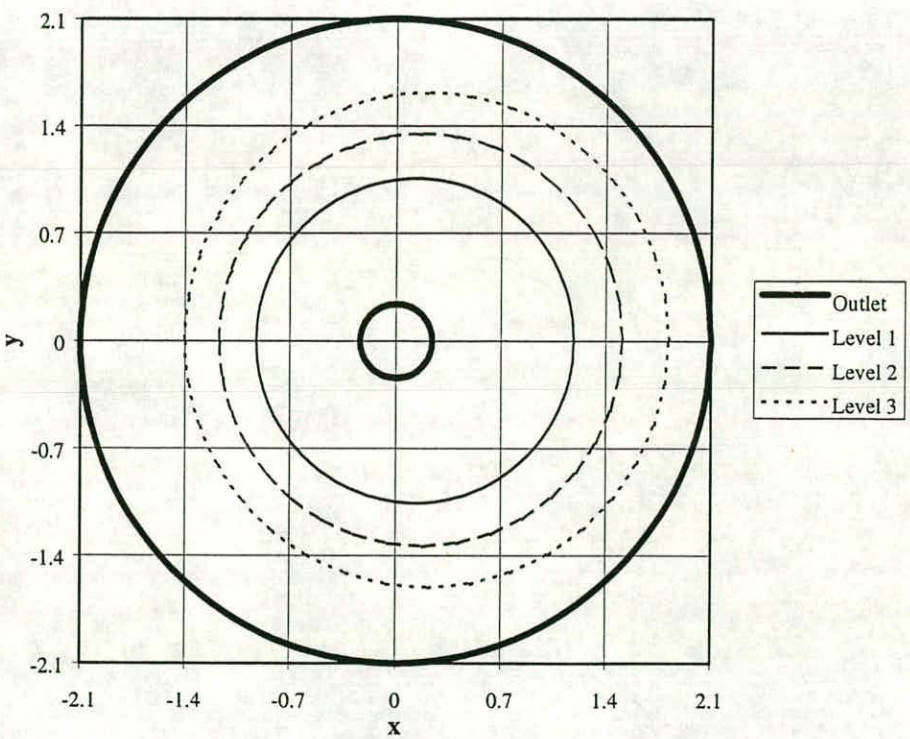

Fig. 7.27a Test PCA: Flow channel boundary at different levels (Assumed cicular flow channel with 3° inclined centre)

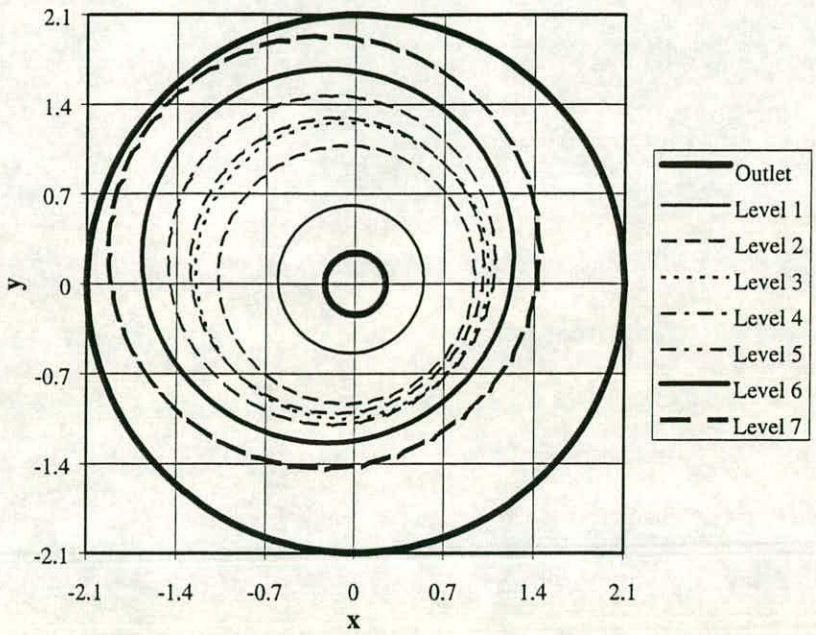

Fig. 7.27b Test PCB: Flow channel boundary at different levels (Assumed circular flow channel with 3° inclined centre)

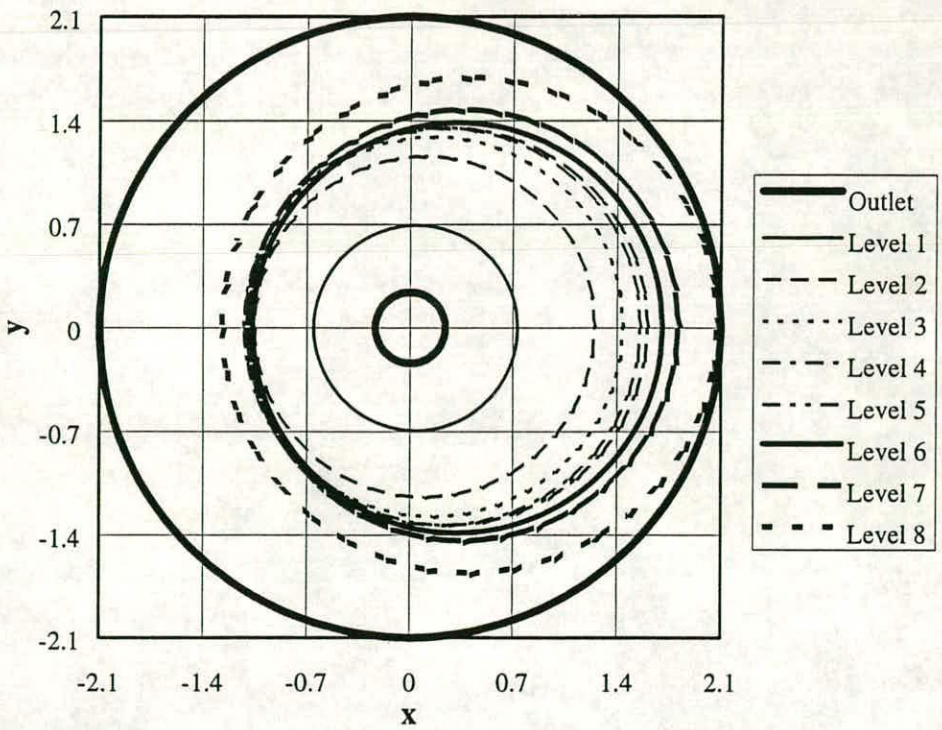

Fig. 7.27c Test PCC: Flow channel boundary at different levels (Assumed circular flow channel with 3° inclined centre)

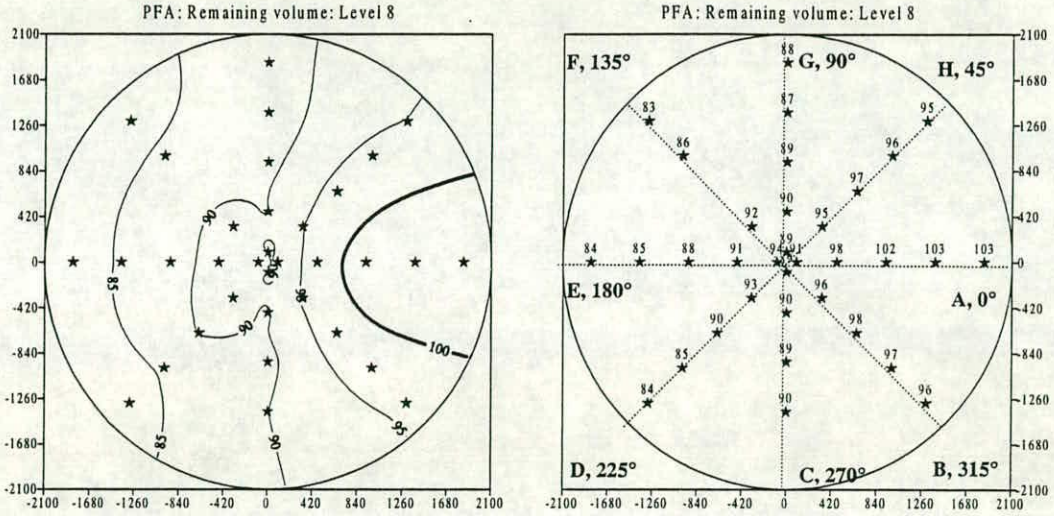

Fig. 7.28a PFA: Remaining volume: Level 8: Contours and spot values

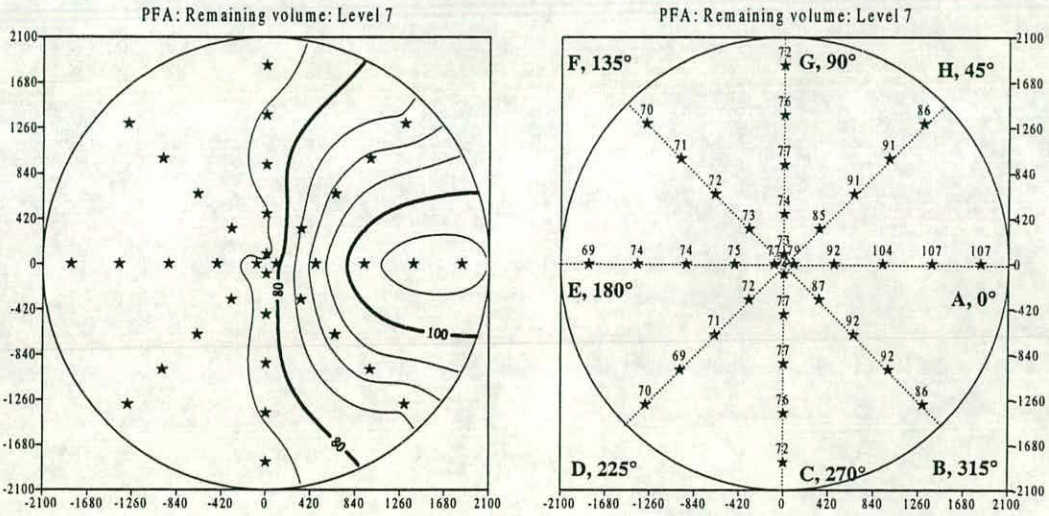

Fig. 7.28b PFA: Remaining volume: Level 7: Contours and spot values

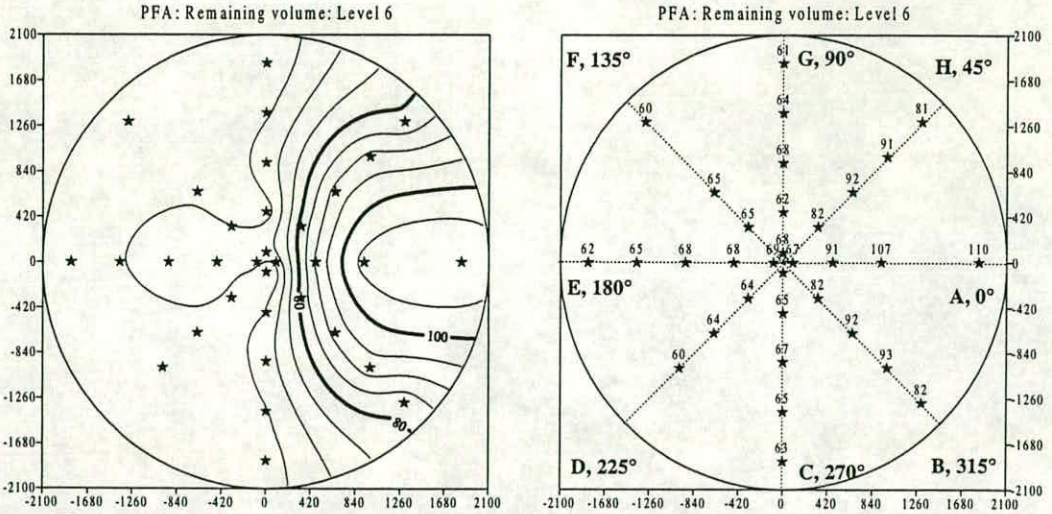

Fig. 7.28c PFA: Remaining volume: Level 6: Contours and spot values

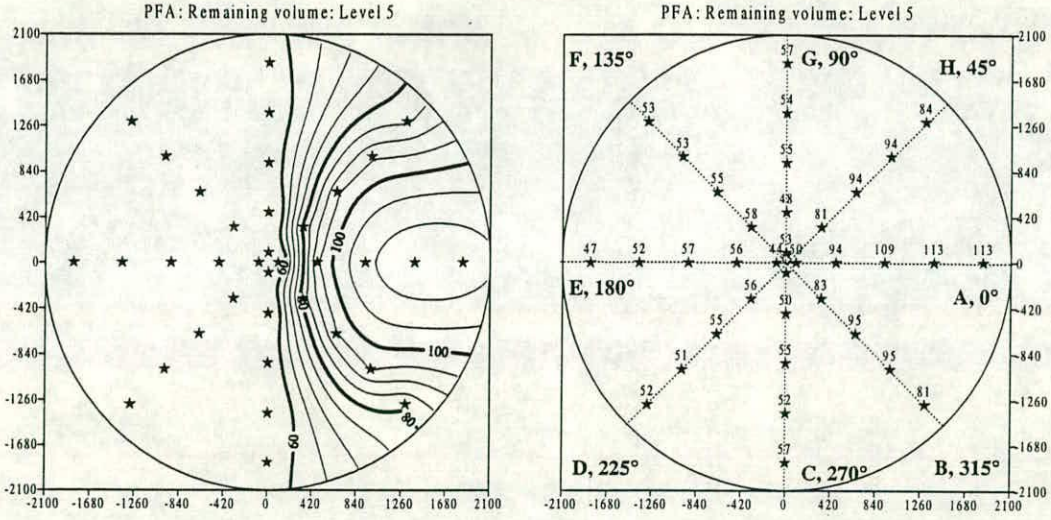

Fig. 7.28d PFA: Remaining volume: Level 5: Contours and spot values

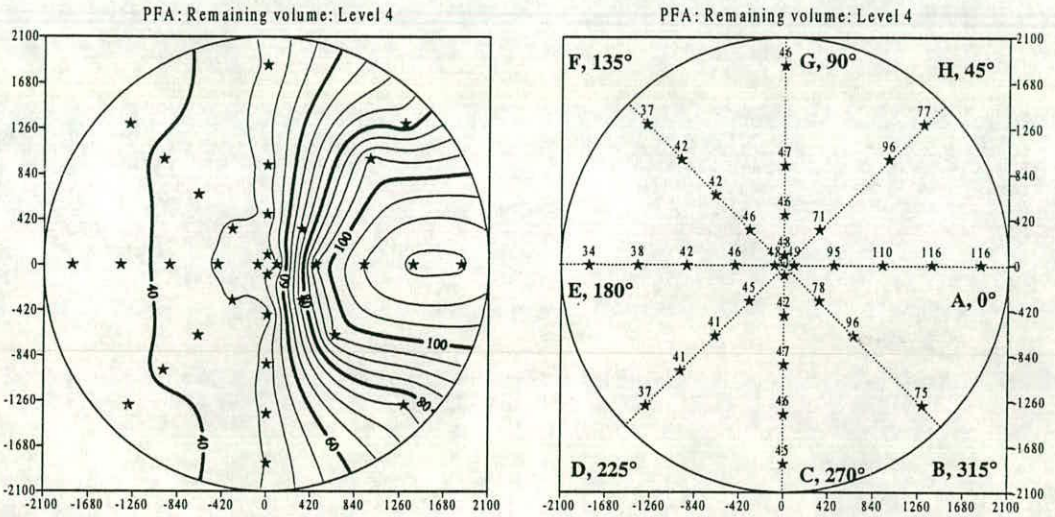

Fig. 7.28e PFA: Remaining volume: Level 4: Contours and spot values

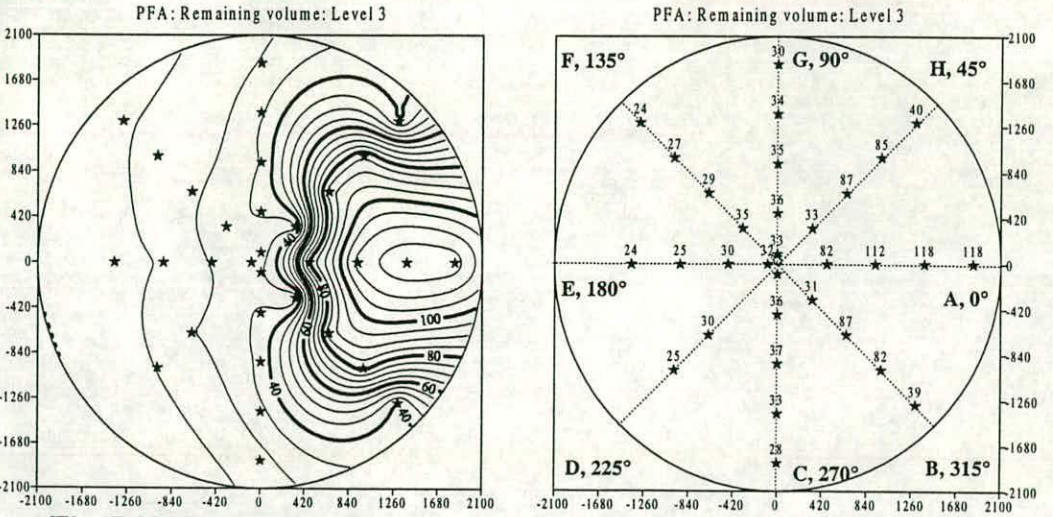

Fig. 7.28f PFA: Remaining volume: Level 3: Contours and spot values

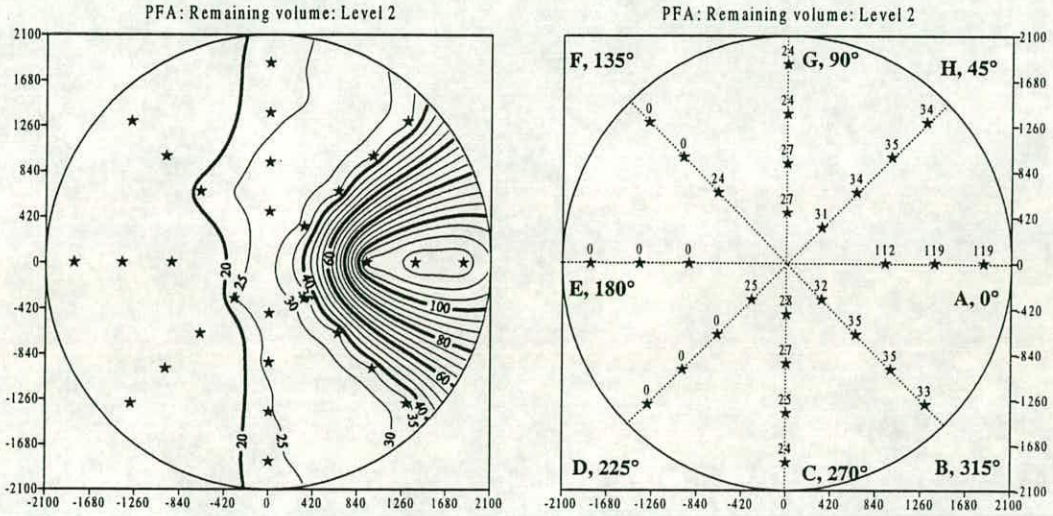

Fig. 7.28g PFA: Remaining volume: Level 2: Contours and spot values

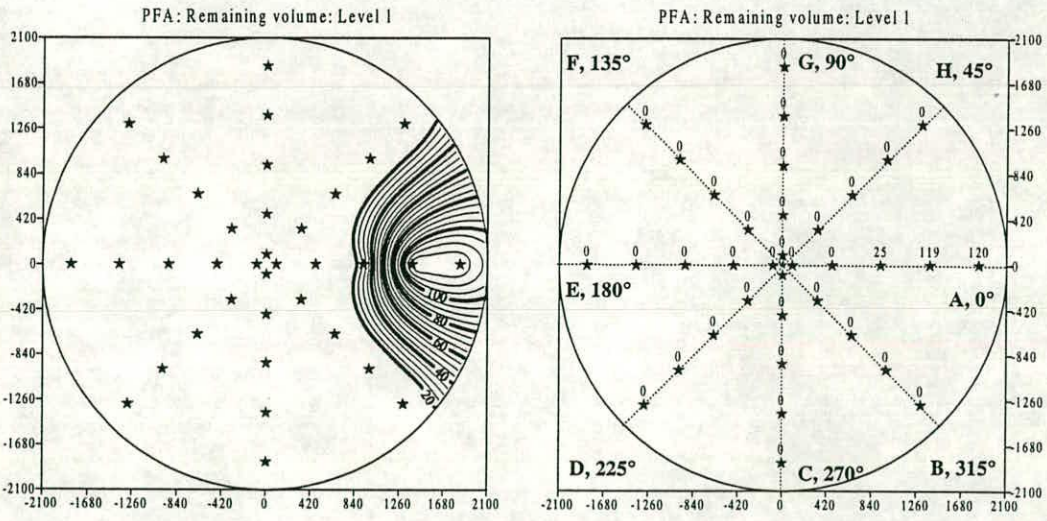

Fig. 7.28h PFA: Remaining volume: Level 1: Contours and spot values

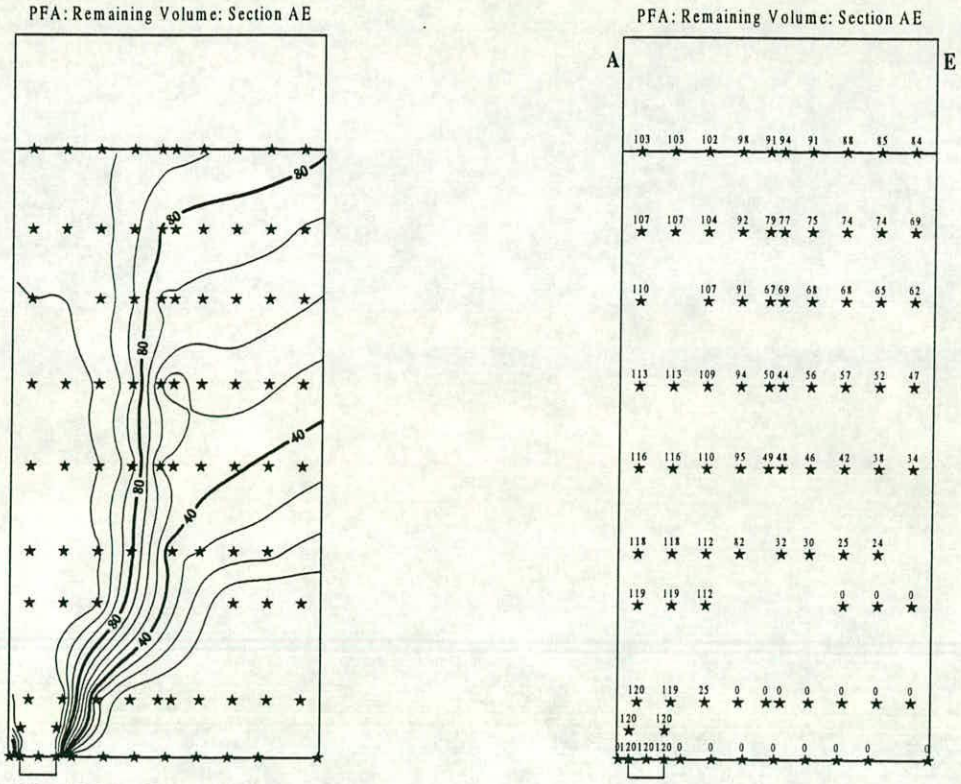

Fig. 7.29a PFA: Remaining volume: Vertical diametral section A-E: Contours and spot values

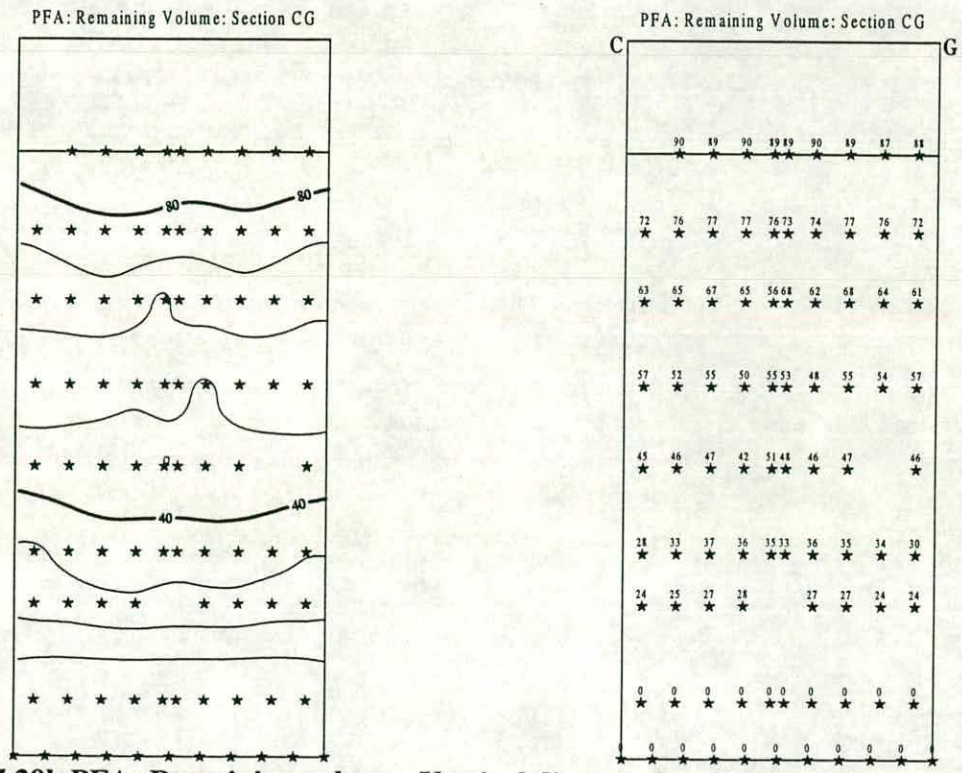

Fig. 7.29b PFA: Remaining volume: Vertical diametral section C-G: Contours and spot values

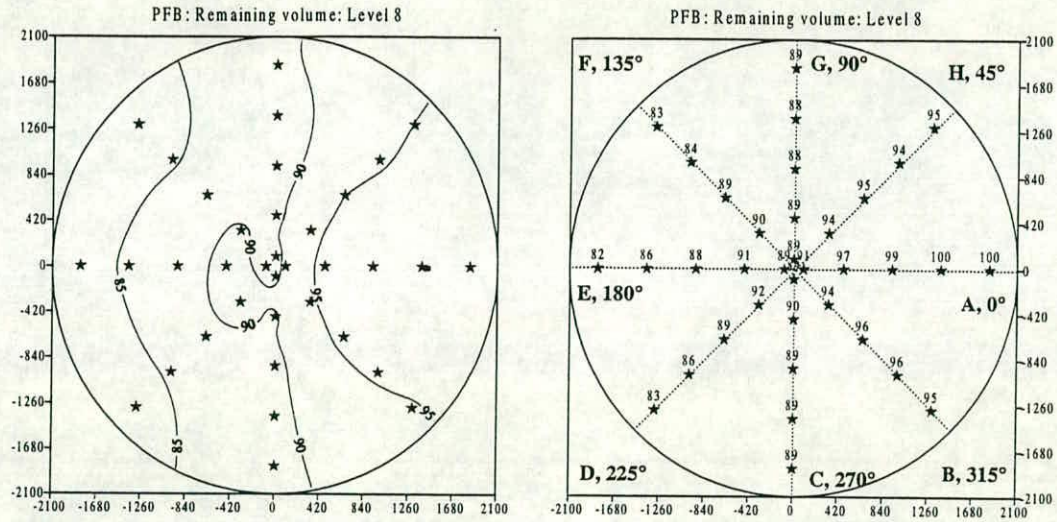

Fig. 7.30a Test PFB: Remaining volume: Level 8: Contours and spot values

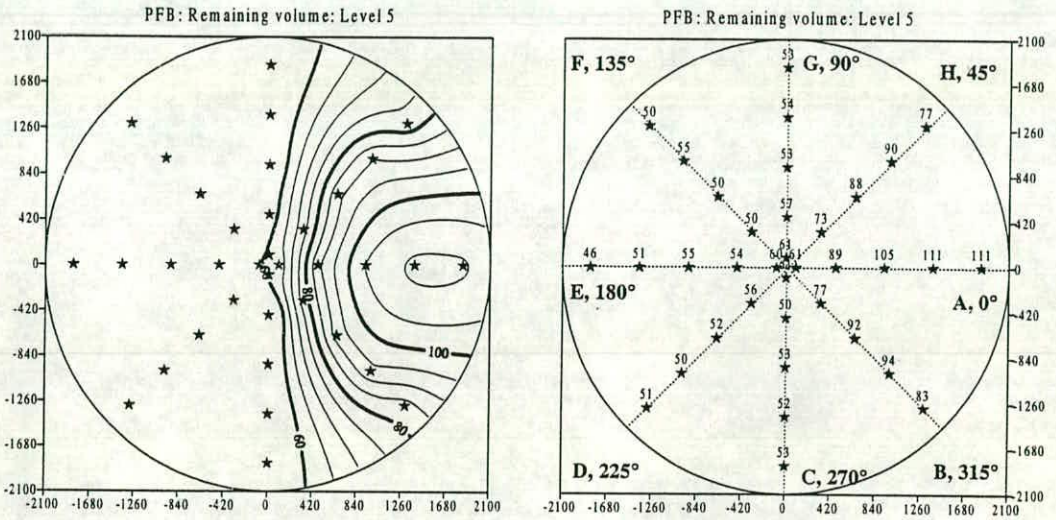

Fig. 7.30b Test PFB: Remaining volume: Level 5: Contours and spot values

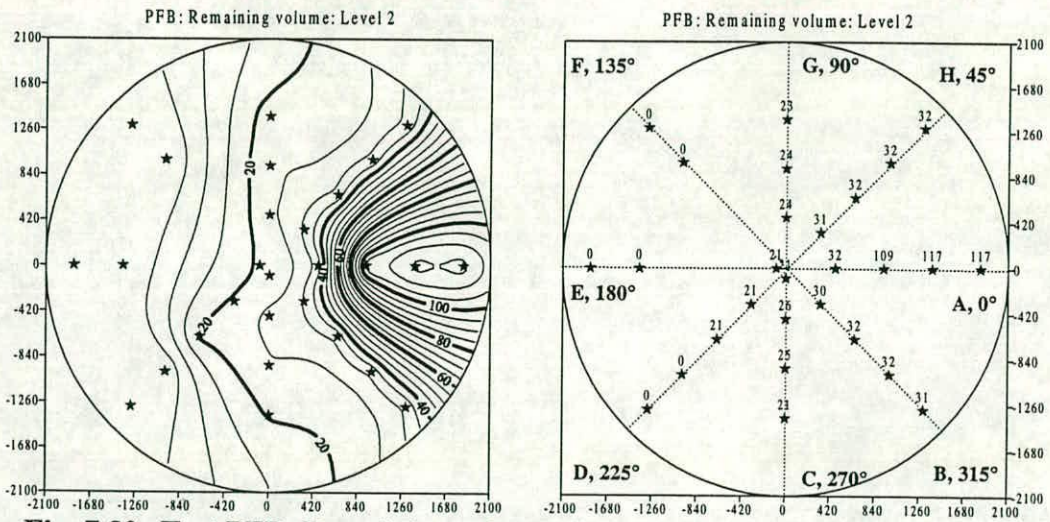

Fig. 7.30c Test PFB: Remaining volume: Level 2: Contours and spot values

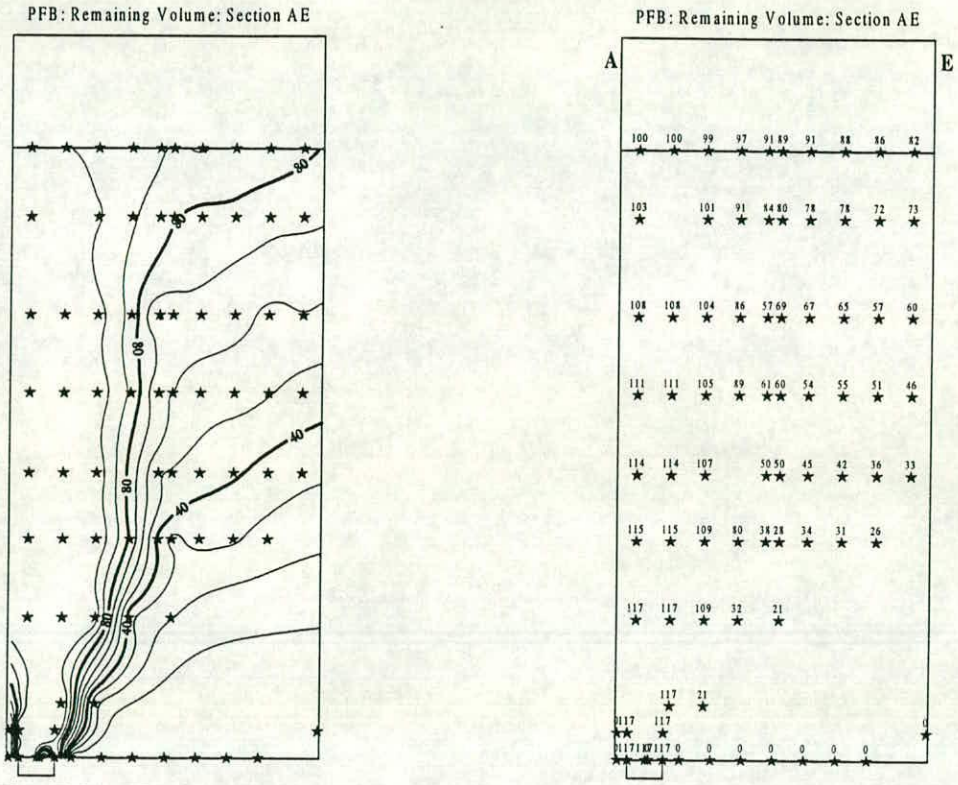

Fig. 7.31a Test PFB: Remaining volume: Vertical diametral section A-E: Contours and spot values

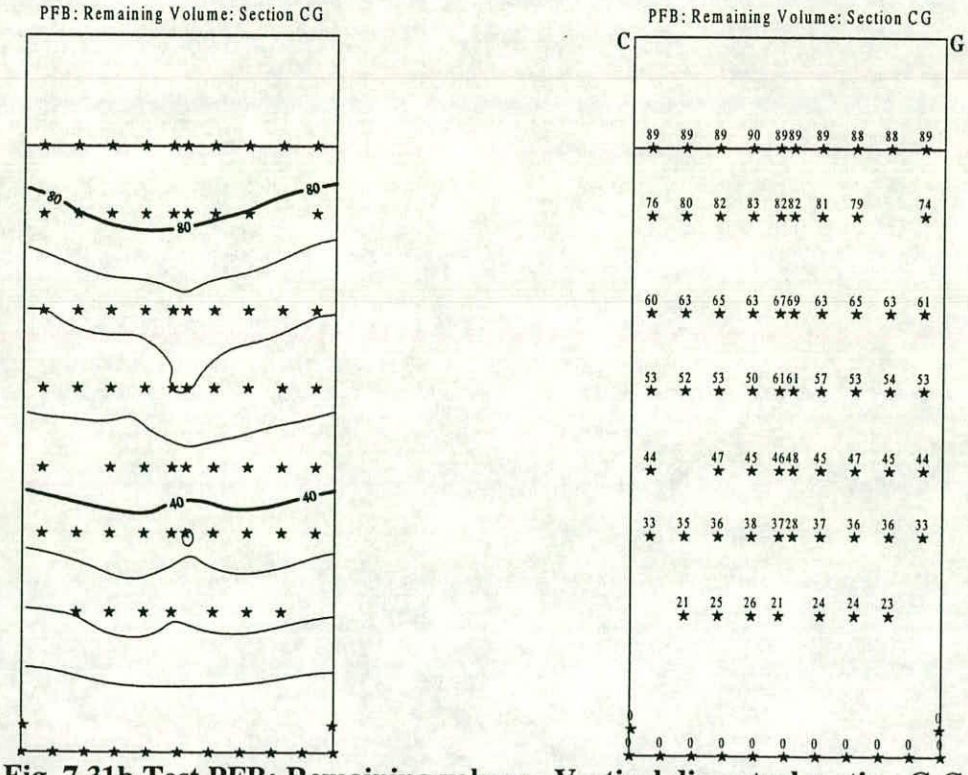

Fig. 7.31b Test PFB: Remaining volume: Vertical diametral section C-G: Contours and spot values

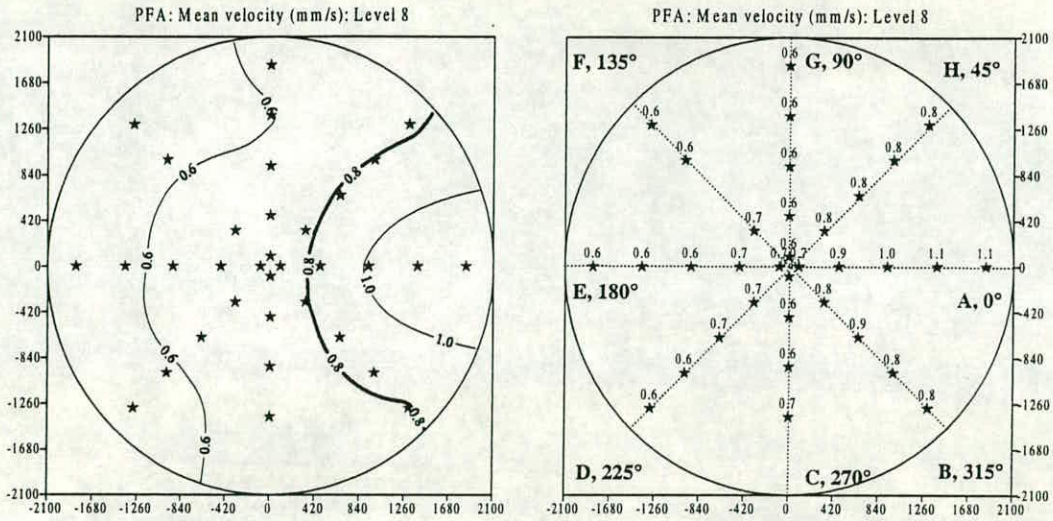

Fig. 7.32a Test PFA: Mean velocity: Level 8: Contours and spot values

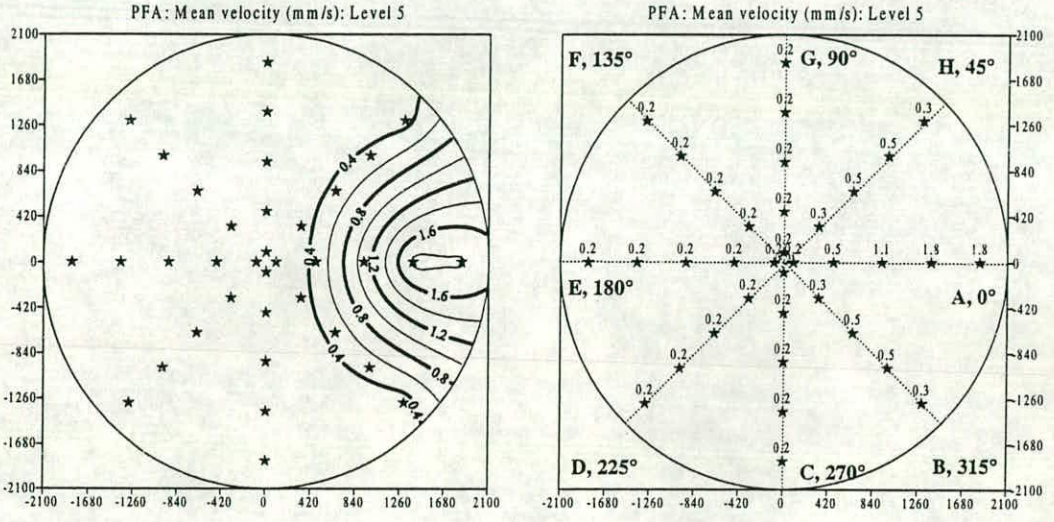

Fig. 7.32b Test PFA: Mean velocity: Level 5: Contours and spot values

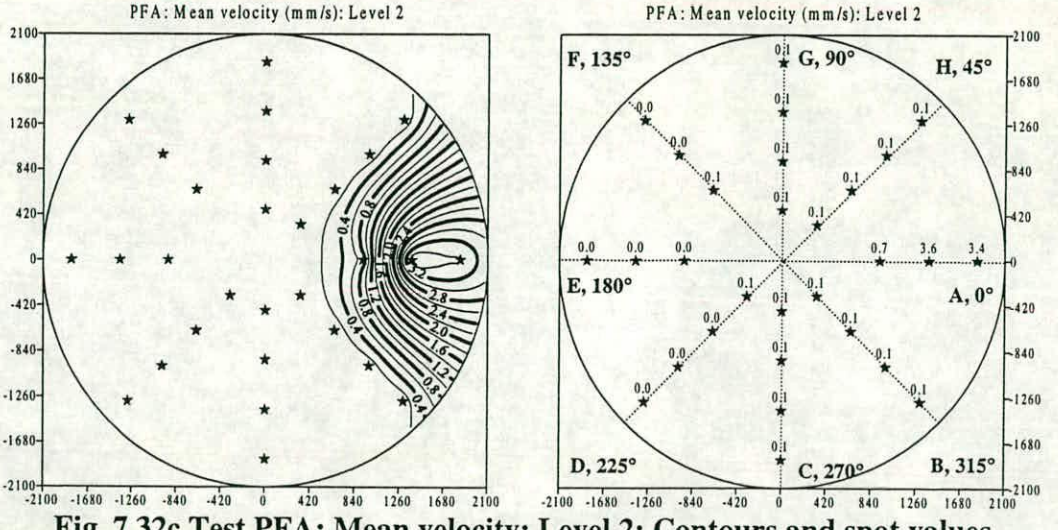

Fig. 7.32c Test PFA: Mean velocity: Level 2: Contours and spot values

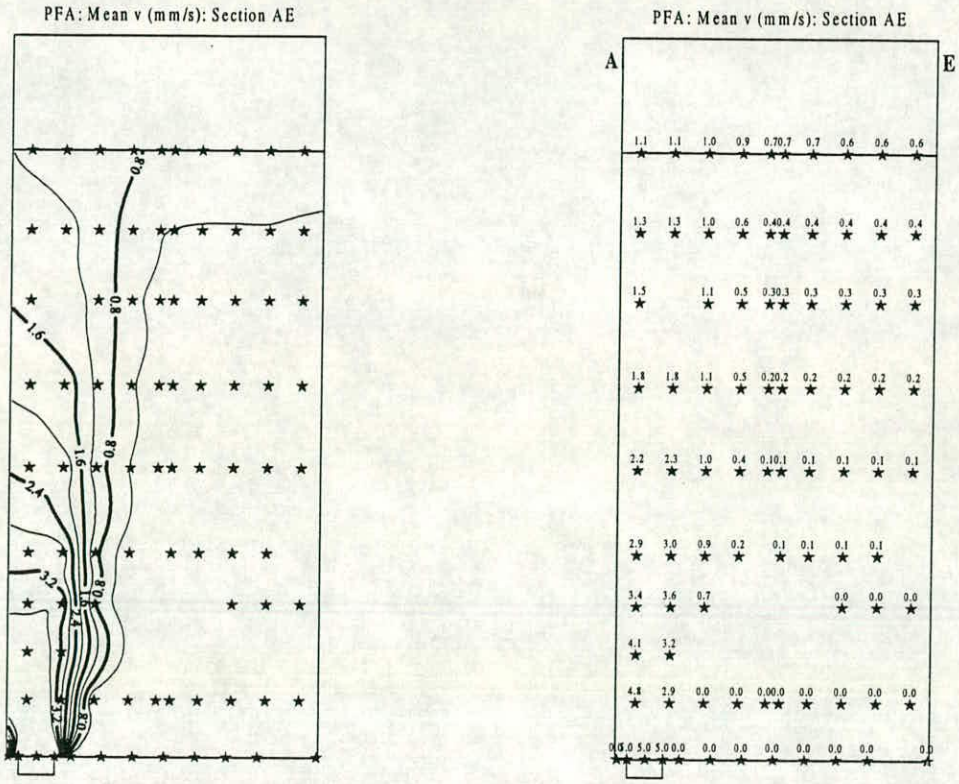

Fig. 7.33a Test PFA: Mean velocity: Vertical diametral section A-E: Contours and spot values

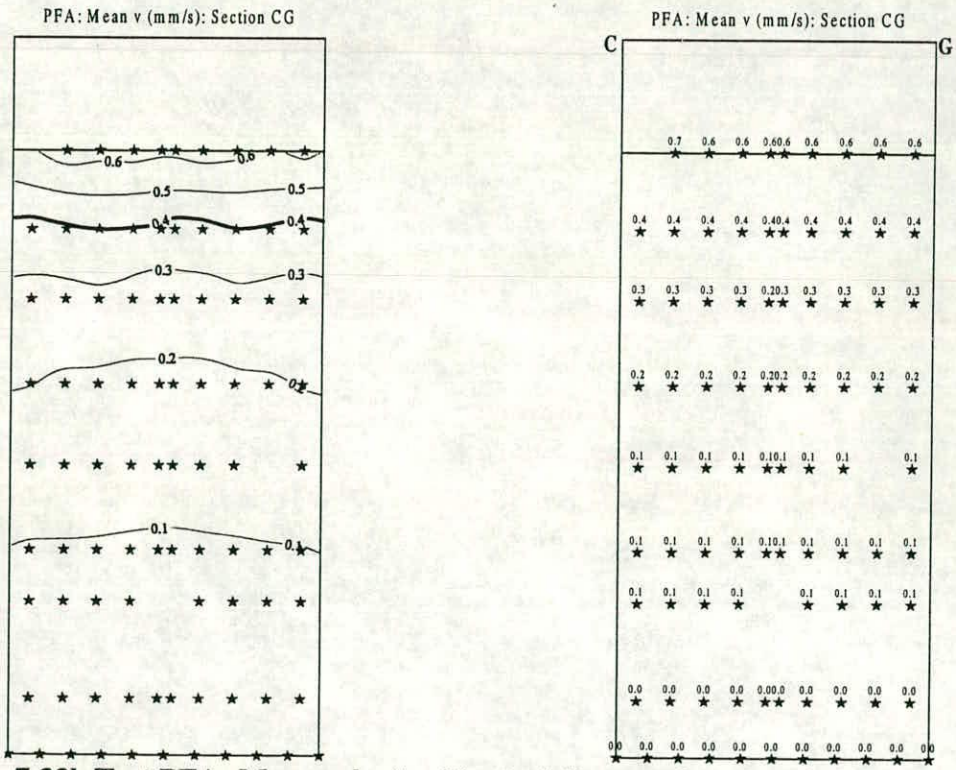

Fig. 7.33b Test PFA: Mean velocity: Vertical diametral section C-G: Contours and spot values

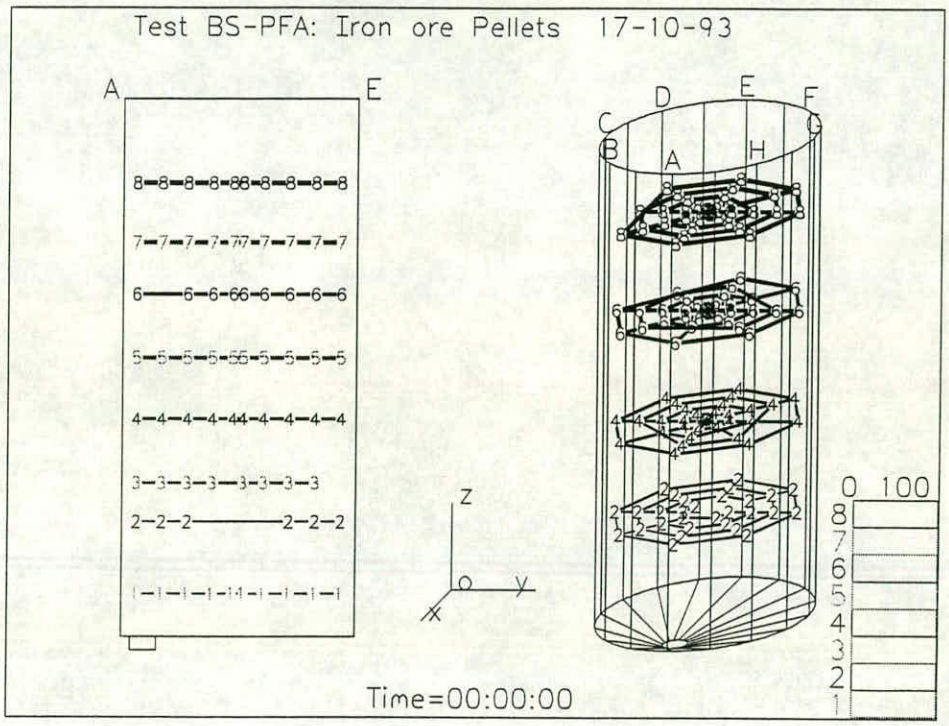

Fig. 7.34a Test PFA: Simple visualisation

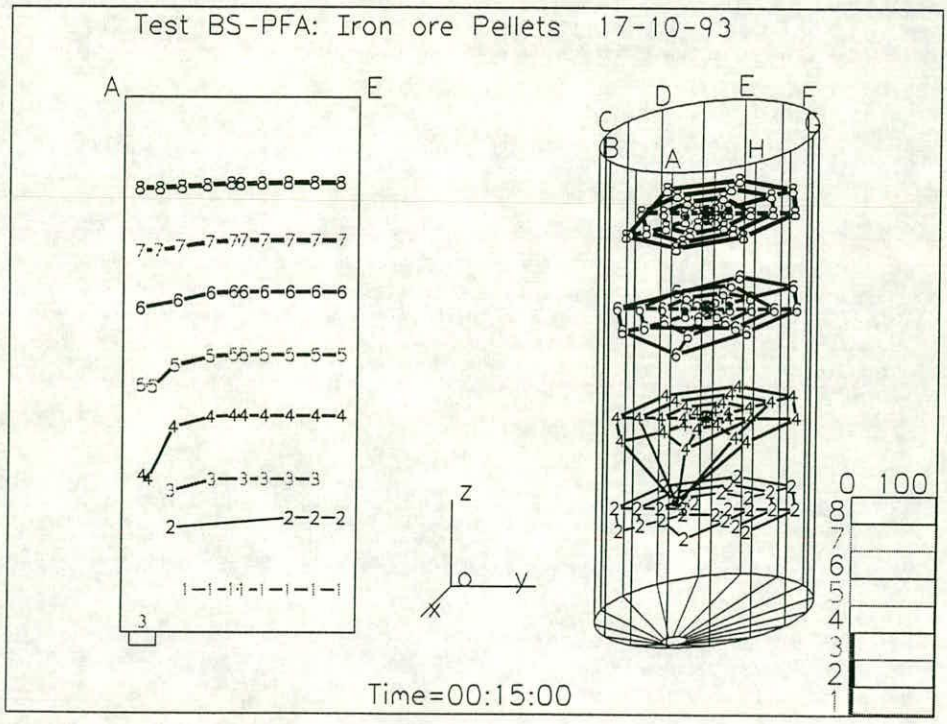

Fig. 7.34b Test PFA: Simple visualisation

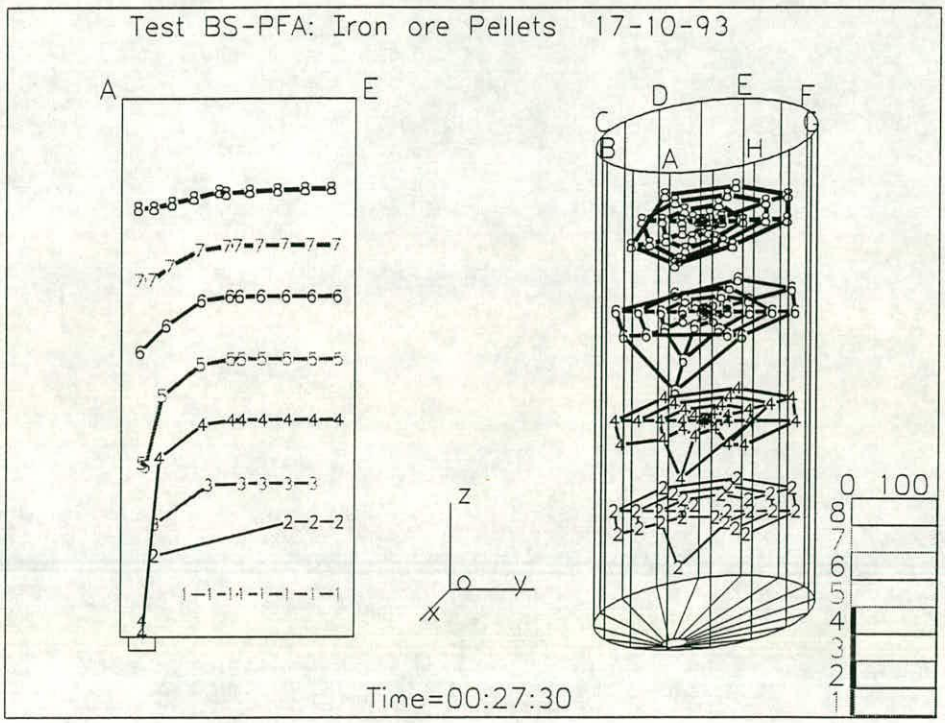

Fig. 7.34c Test PFA: Simple visualisation

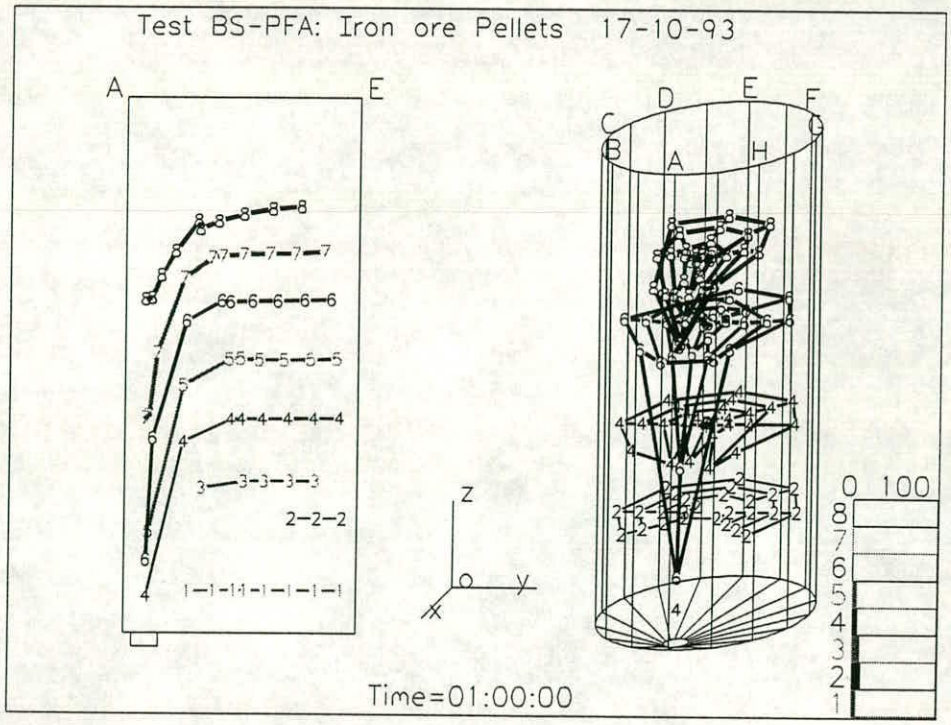

Fig. 7.34d Test PFA: Simple visualisation

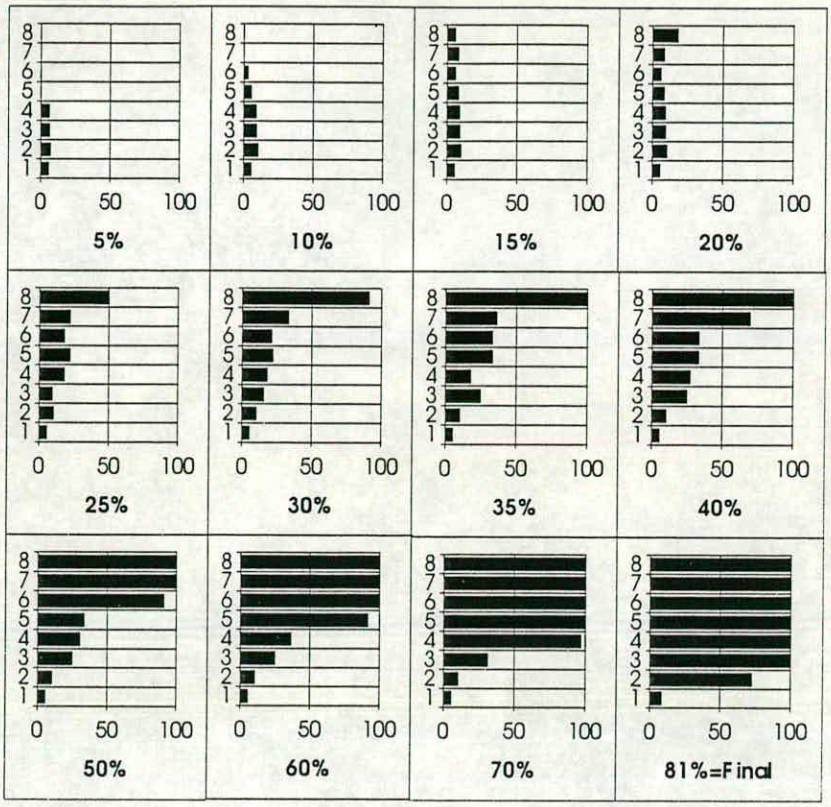

Fig. 7.35a Test PFA: Bars tags exited from the outlet at different stages

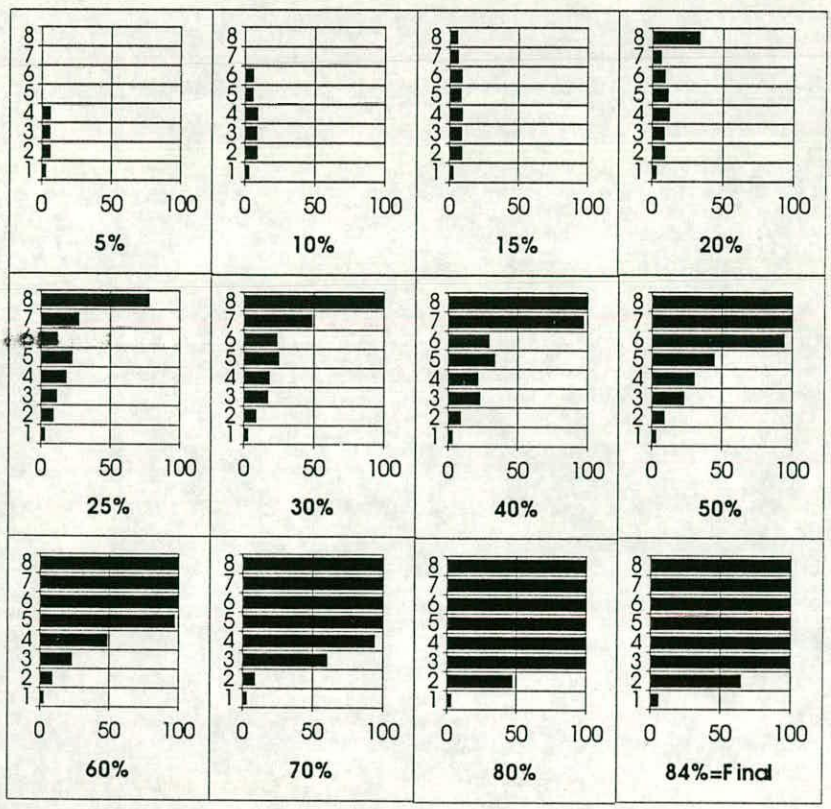

Fig. 7.35b Test PFB: Bars tags exited from the outlet at different stages

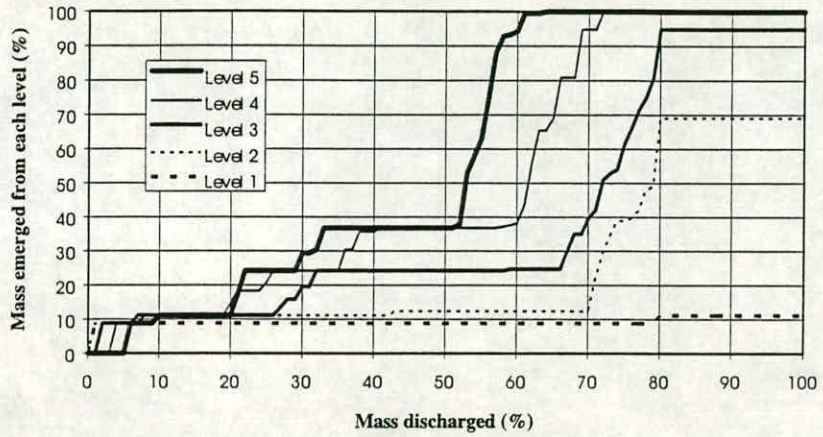

Fig. 7.36a Test PFA: Mass emerged from each level vs. mass discharged

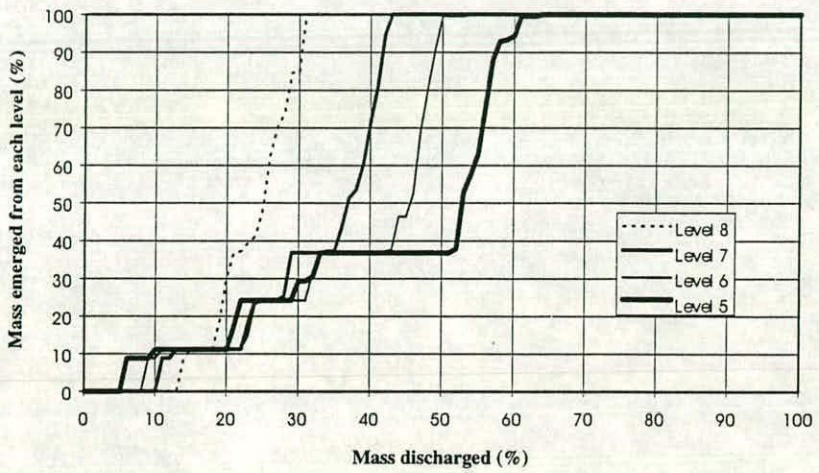

Fig. 7.36b Test PFA: Mass emerged from each level vs. mass discharged

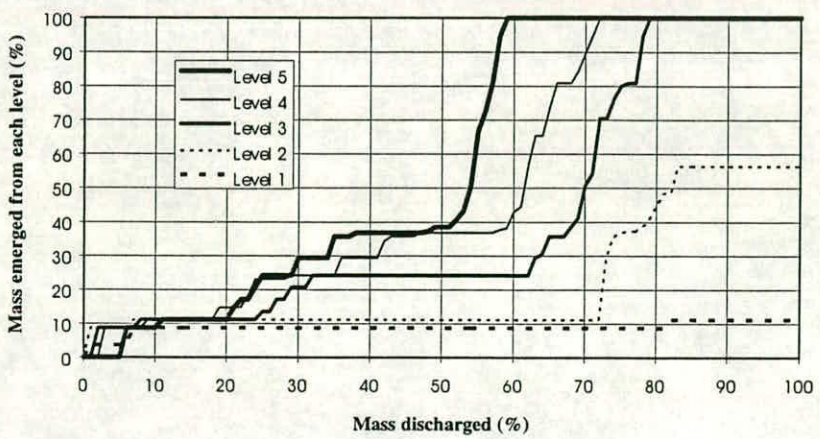

Fig. 7.37a Test PFB: Mass emerged from each level vs. mass discharged

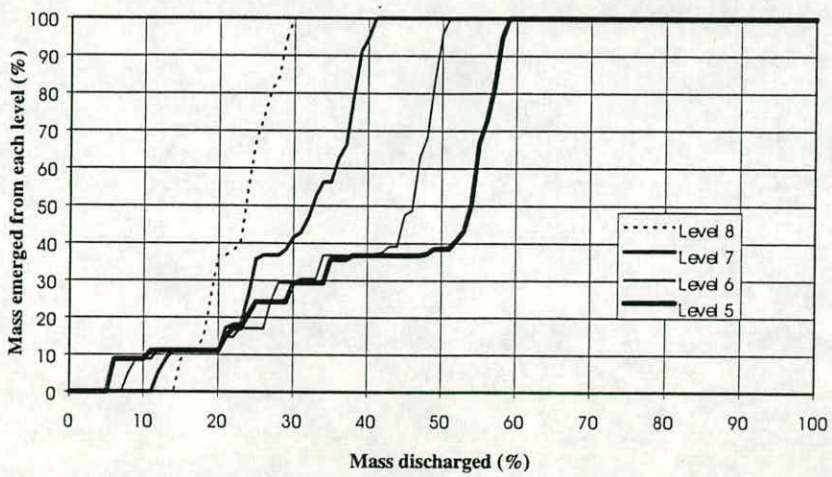

Fig. 7.37b Test PFB: Mass emerged from each level vs. mass discharged

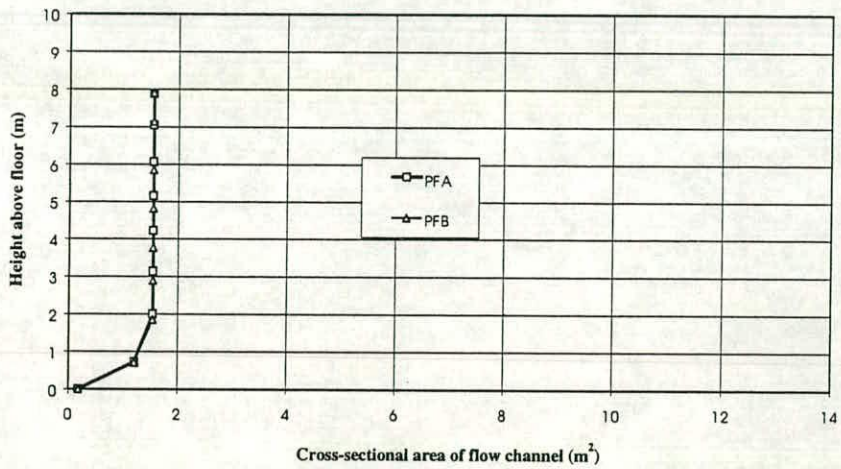

Fig. 7.38a Full eccentric discharge tests: Cross sectional area of flow funnel (First discharge)

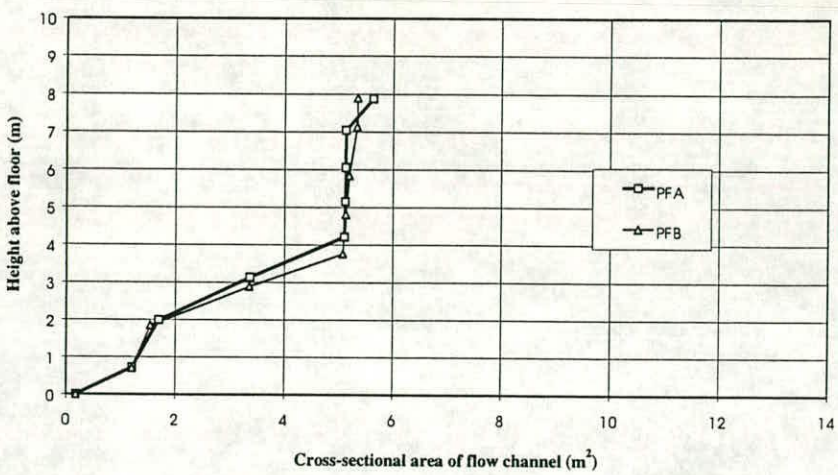

Fig. 7.38b Full eccentric discharge tests: Cross sectional area of flow funnel (Second discharge)

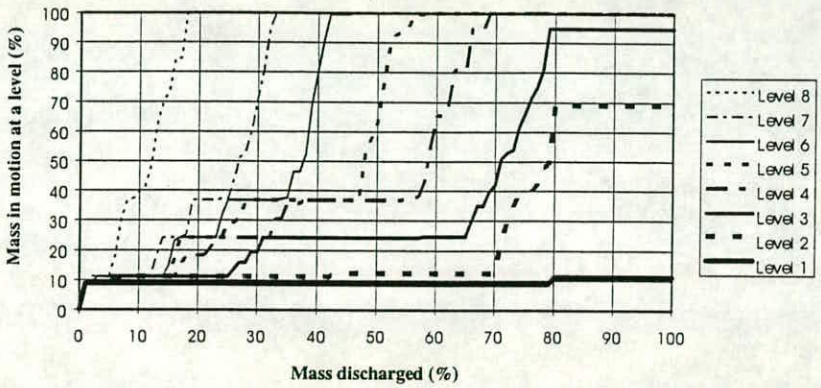

Fig. 7.39 Test PFA: Moving mass at a level vs. mass discharged

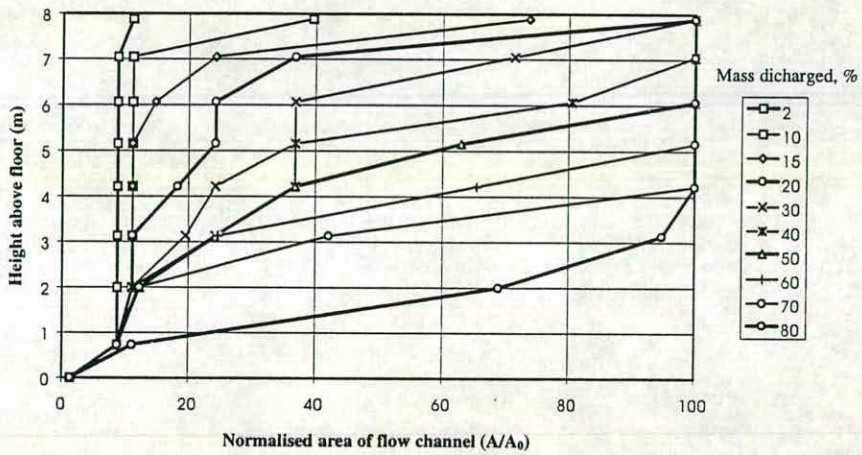

Fig. 7.40 Test PFA: Development of flow channel

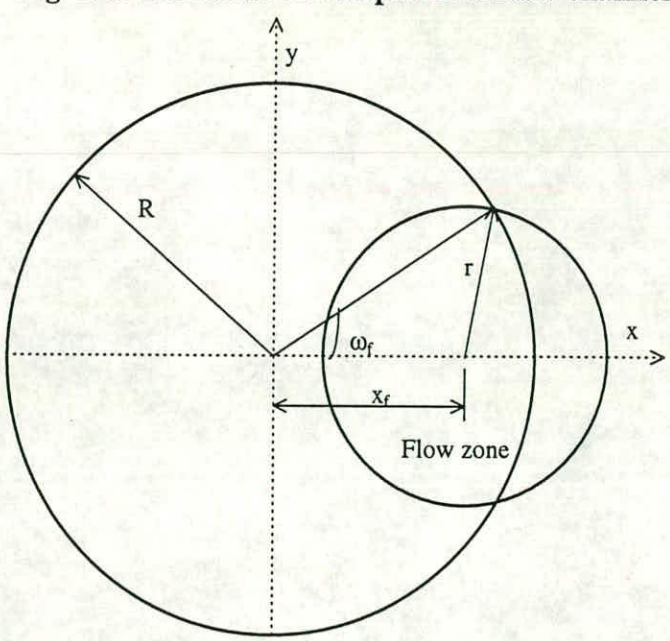

Fig. 7.41 Geometry of flow channel on eccentric discharge (idealised)

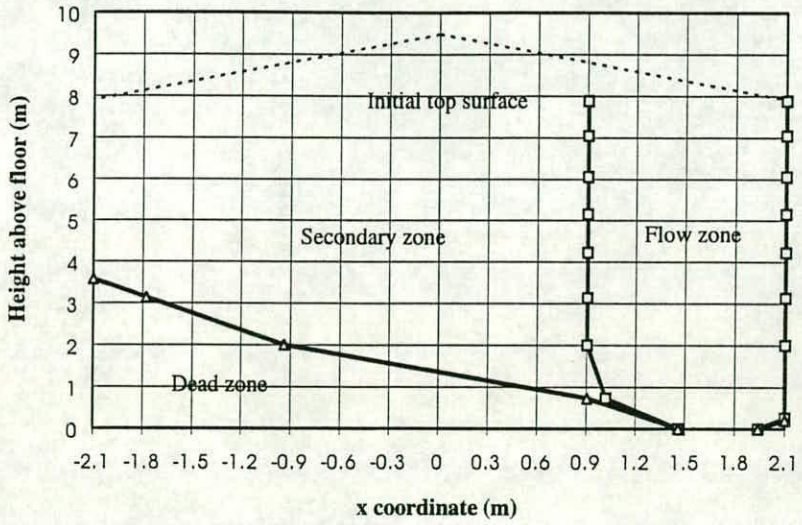

Fig. 7.42a Test PFA: Approximate flow channel boundary on x-z plane (Assumed circular channel: First discharge)

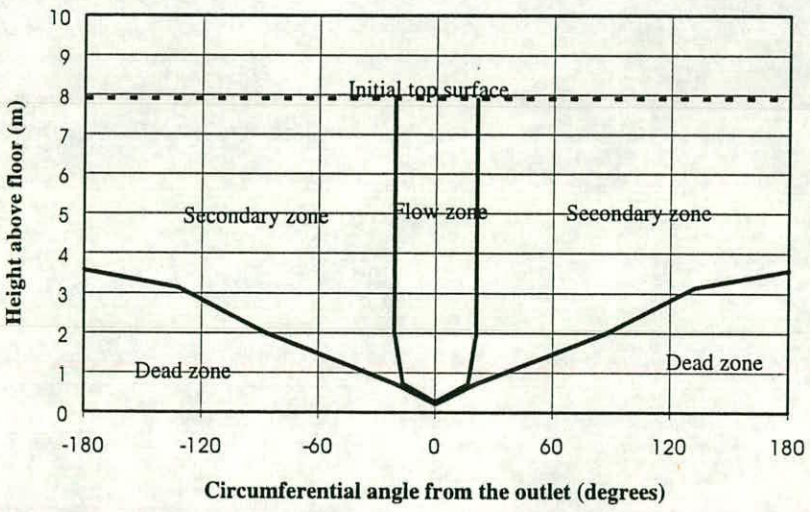

Fig. 7.42b Test PFA: Approximate flow channel boundary on wall (Assumed circular channel: First discharge)

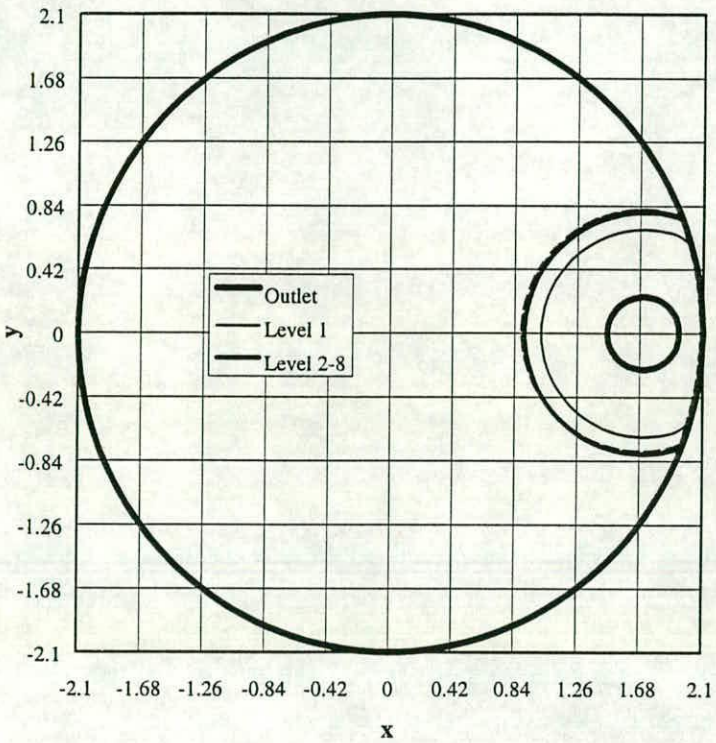

Fig. 7.42c Test PFA: Approximate flow channel boundary: plan (Assumed circular channel: First discharge)

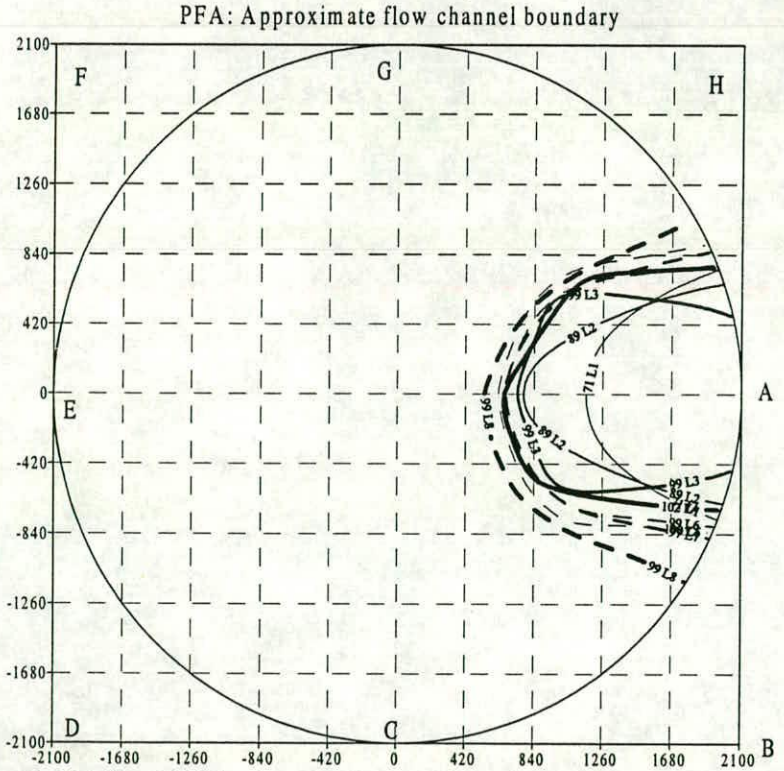

Fig. 7.42d Test PFA: Approximate flow channel boundary: plan (Drawn from remaining volume contours: First discharge)

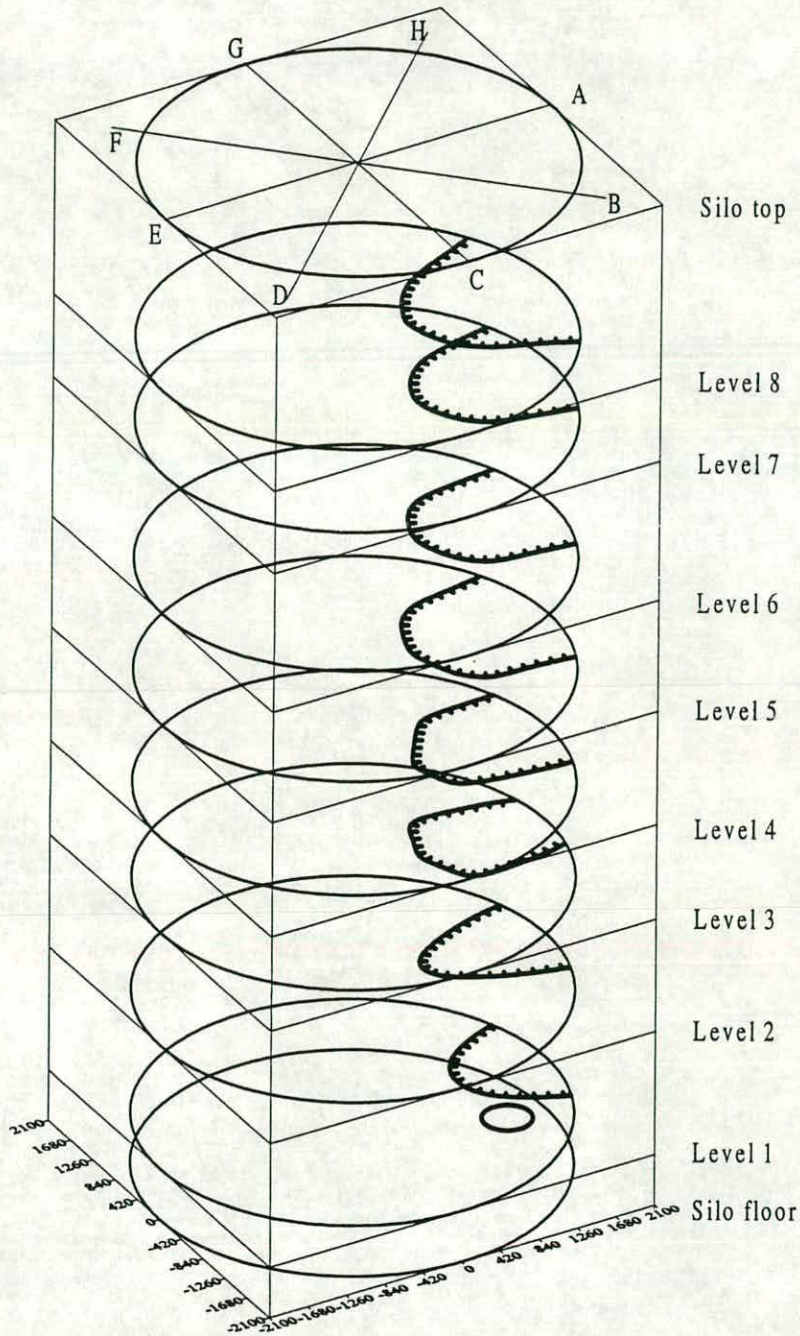

Fig. 7.42e Test PFA: Approximate flow channel boundary: 3D view (Drawn from remaining volume contours: First discharge)

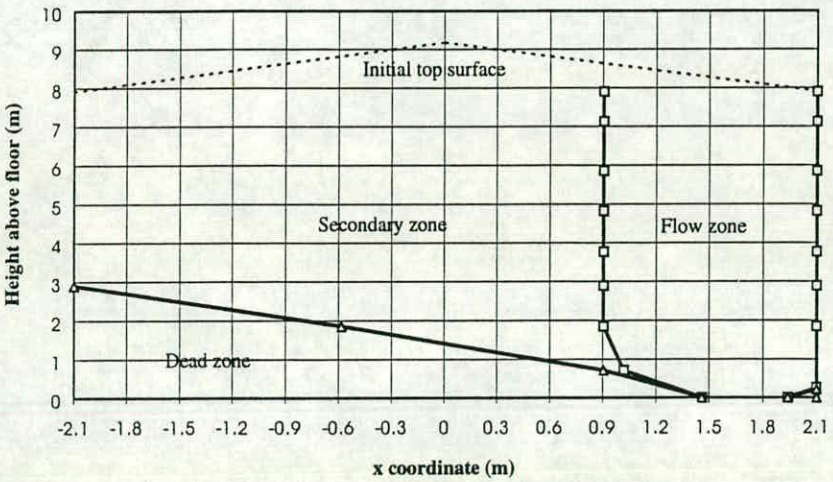

Fig. 7.43a Test PFB: Approximate flow channel boundary on x-z plane (Assumed circular channel: First discharge)

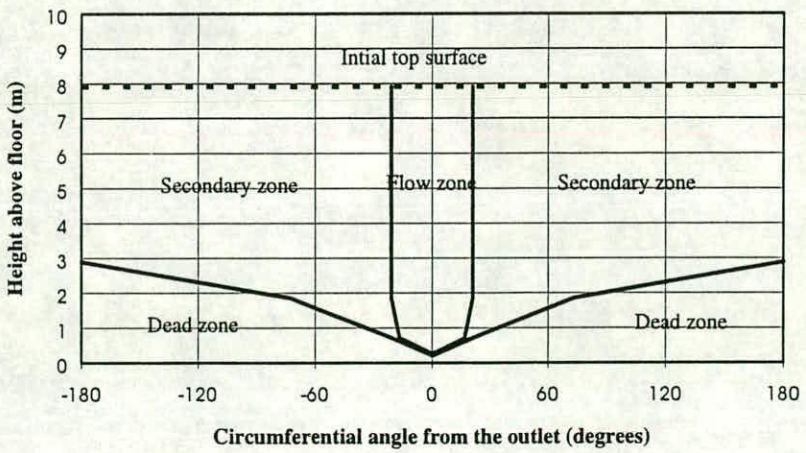

Fig. 7.43b Test PFB: Approximate flow channel boundary on wall (Assumed circular channel: First discharge)

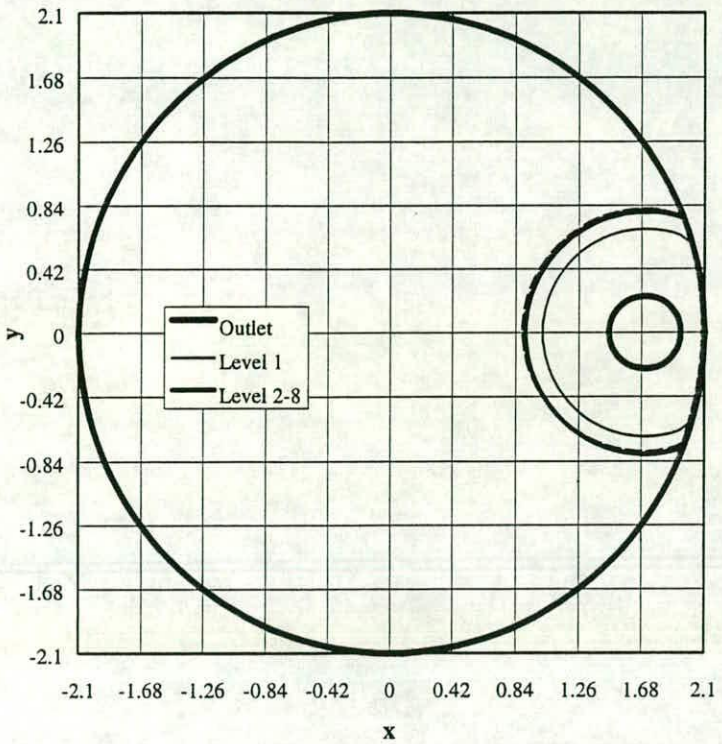

Fig. 7.43c Test PFB: Approximate flow channel boundary: plan (Assumed circular channel: First discharge)

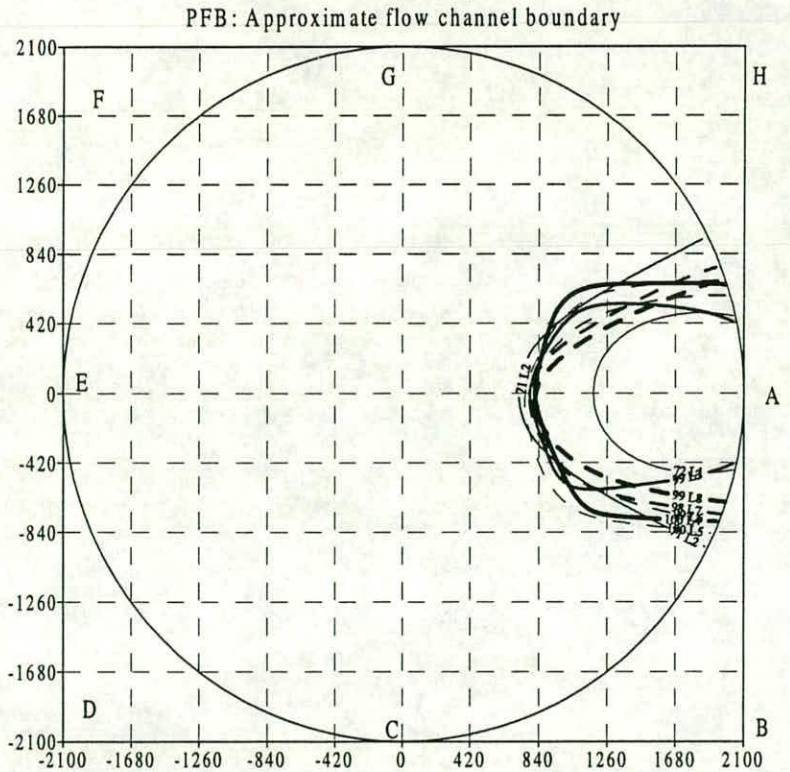

Fig. 7.43d Test PFB: Approximate flow channel boundary: plan (Drawn from remaining volume contours: First discharge)

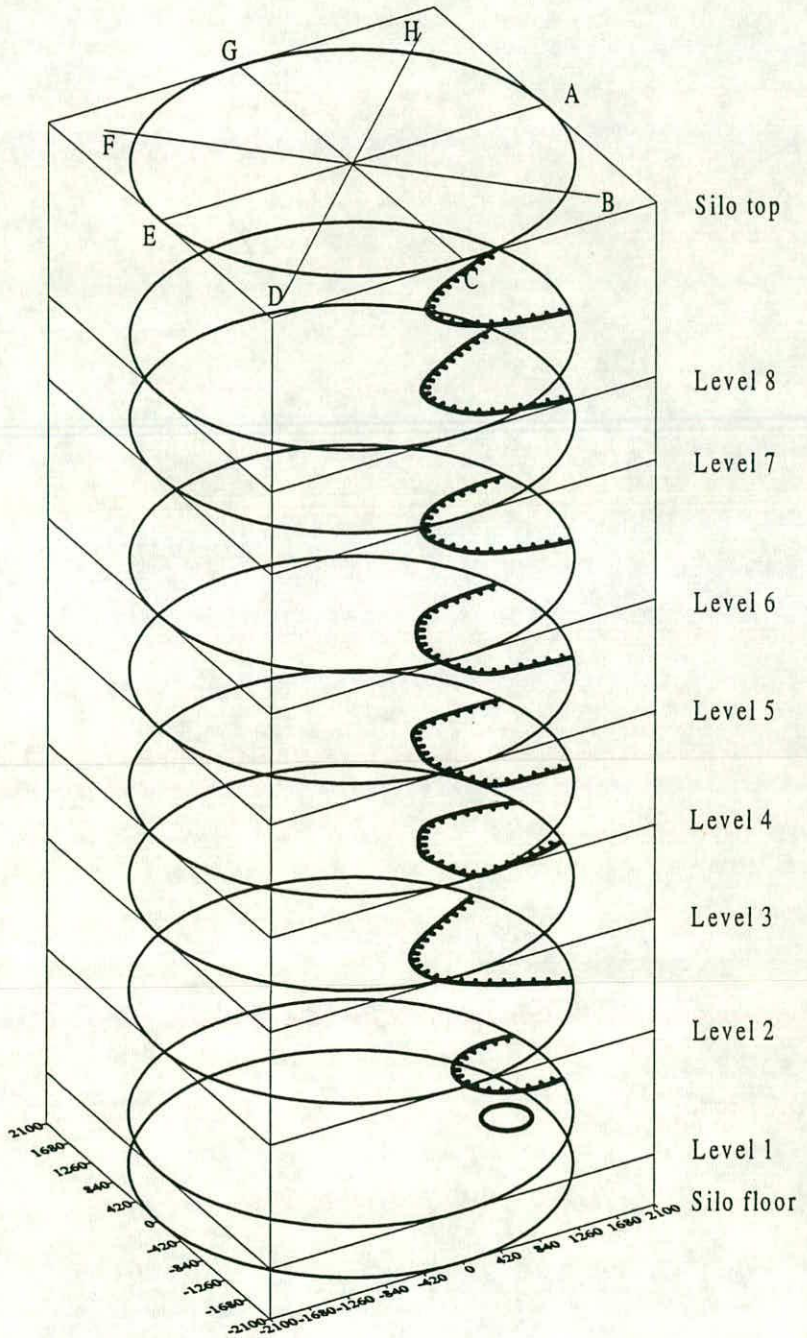

Fig. 7.43e Test PFB: Approximate flow channel boundary: 3D view (Drawn from remaining volume contours: First discharge)

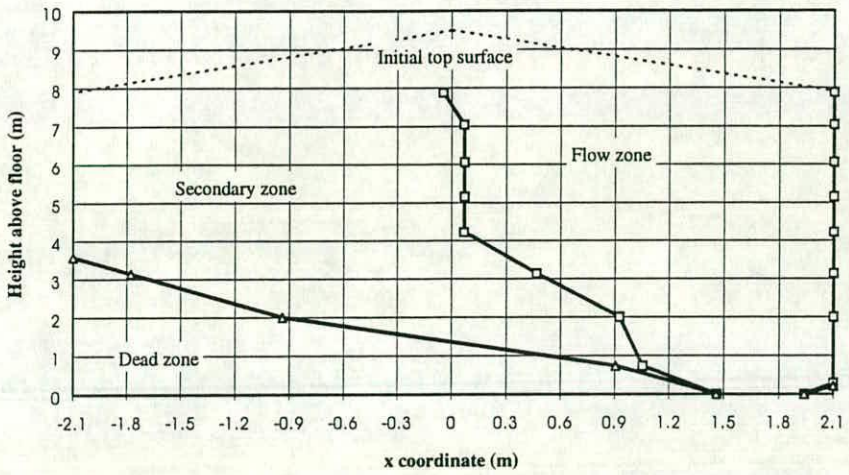

Fig. 7.44a Test PFA: Approximate flow channel boundary on x-z plane (Assumed circular channel: Second discharge)

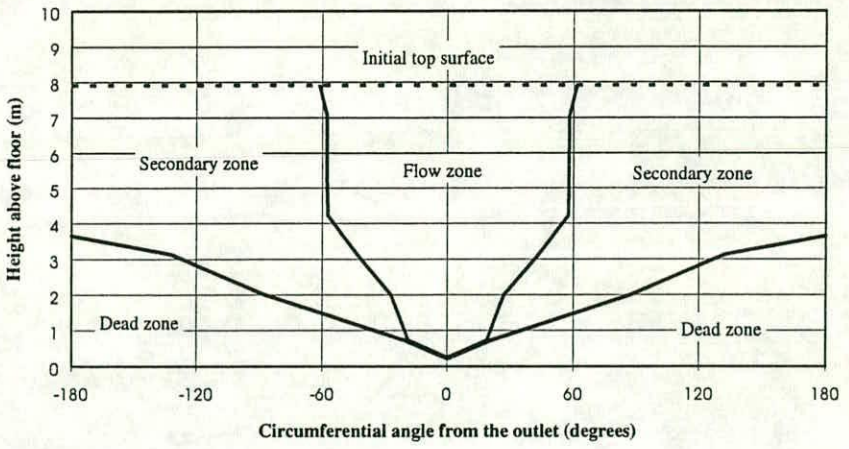

Fig. 7.44b Test PFA: Approximate flow channel boundary on wall (Assumed circular channel: Second discharge)

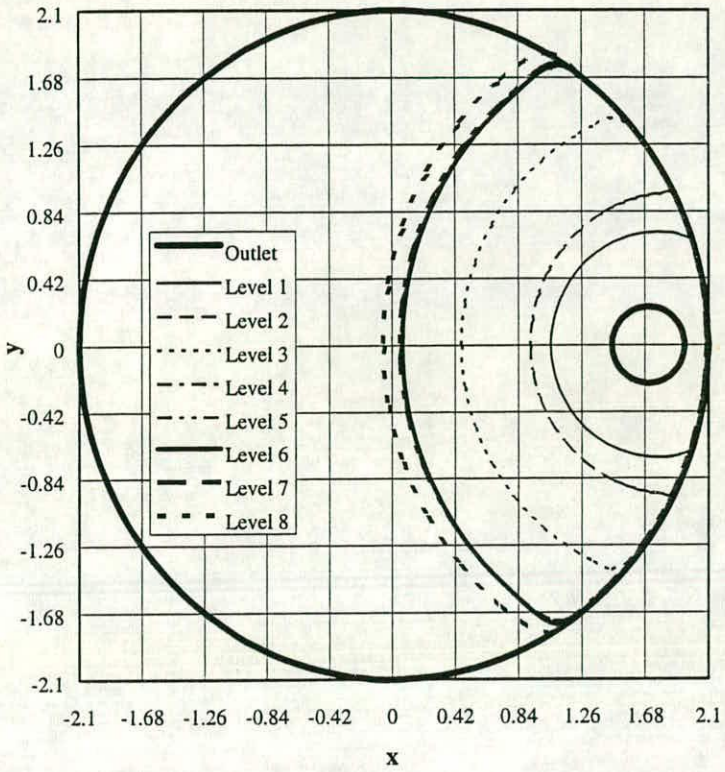

Fig. 7.44c Test PFA: Approximate flow channel boundary: plan (Assumed circular channel: Second discharge)

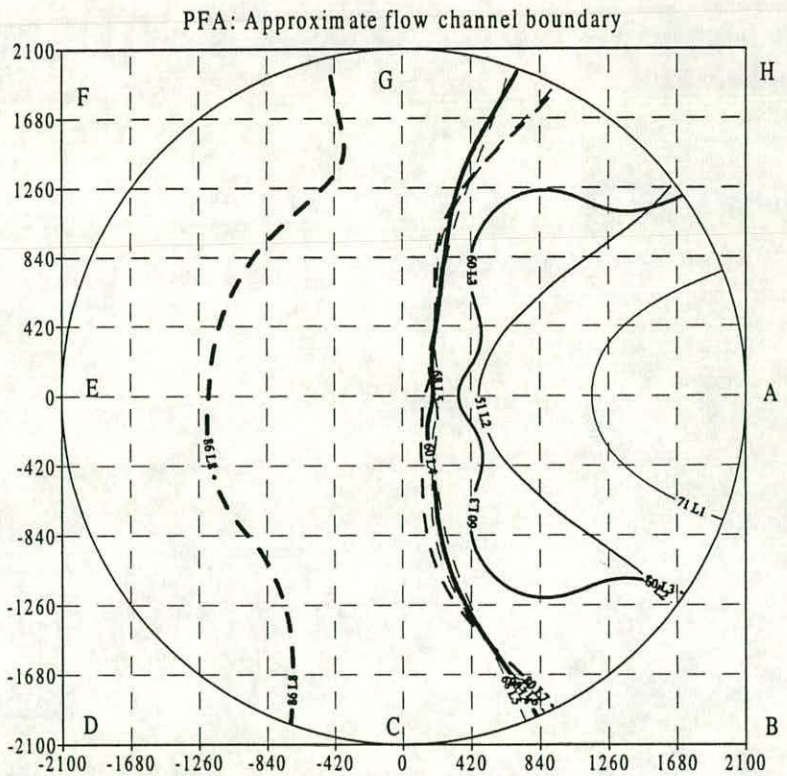

Fig. 7.44d Test PFA: Approximate flow channel boundary: plan (Drawn from remaining volume contours: Second discharge)

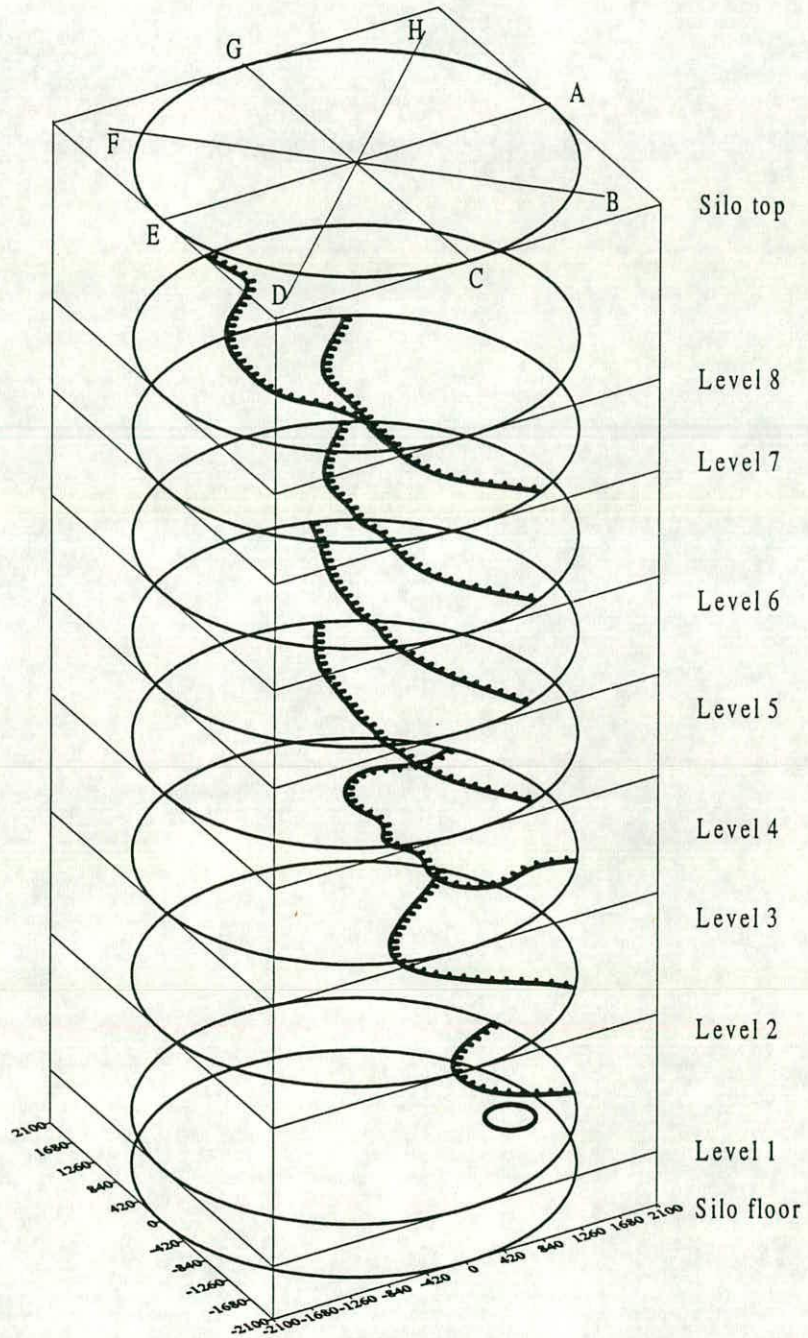

Fig. 7.44e Test PFA: Approximate flow channel boundary: 3D view (Drawn from remaining volume contours: Second discharge)

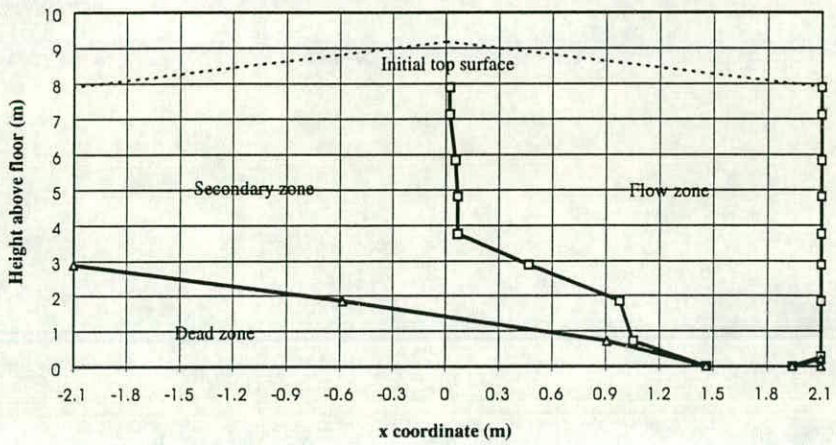

Fig. 7.45a Test PFB: Approximate flow channel boundary on x-z plane (Assumed circular channel: Second discharge)

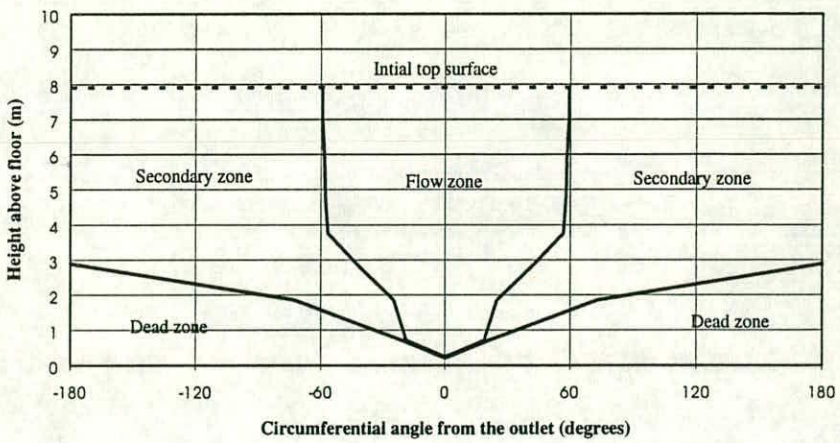

Fig. 7.45b Test PFB: Approximate flow channel boundary on wall (Assumed circular channel: Second discharge)

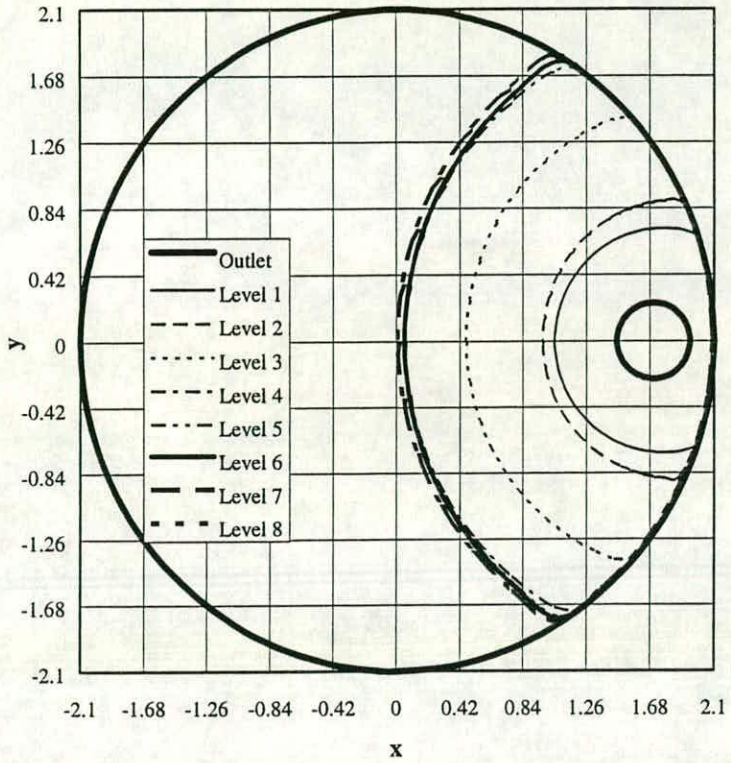

Fig. 7.45c Test PFB: Approximate flow channel boundary: plan (Assumed circular channel: Second discharge)

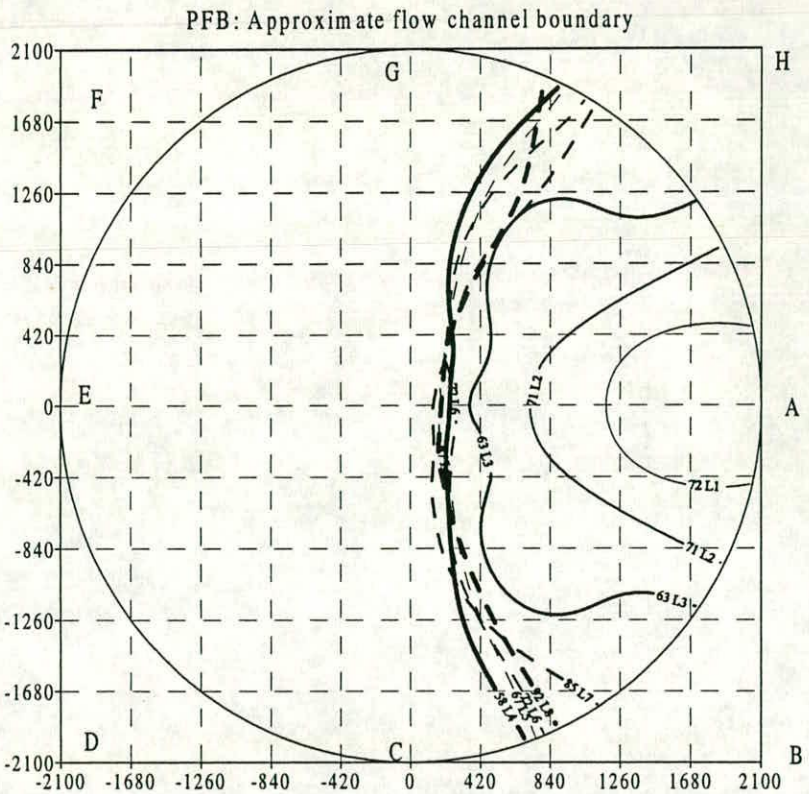

Fig. 7.45d Test PFB: Approximate flow channel boundary: plan (Drawn from remaining volume contours: Second discharge)

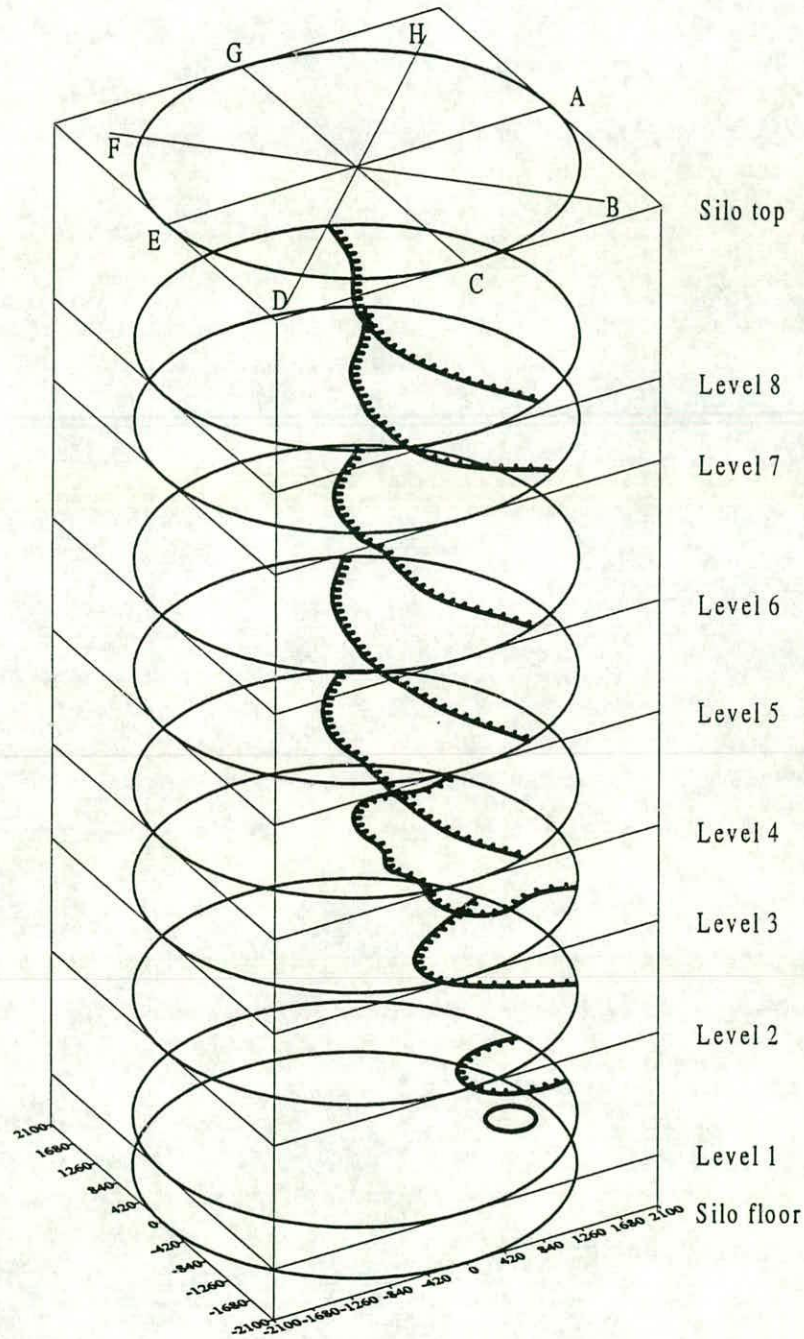

Fig. 7.45e Test PFB: Approximate flow channel boundary: 3D view (Drawn from remaining volume contours: Second discharge)

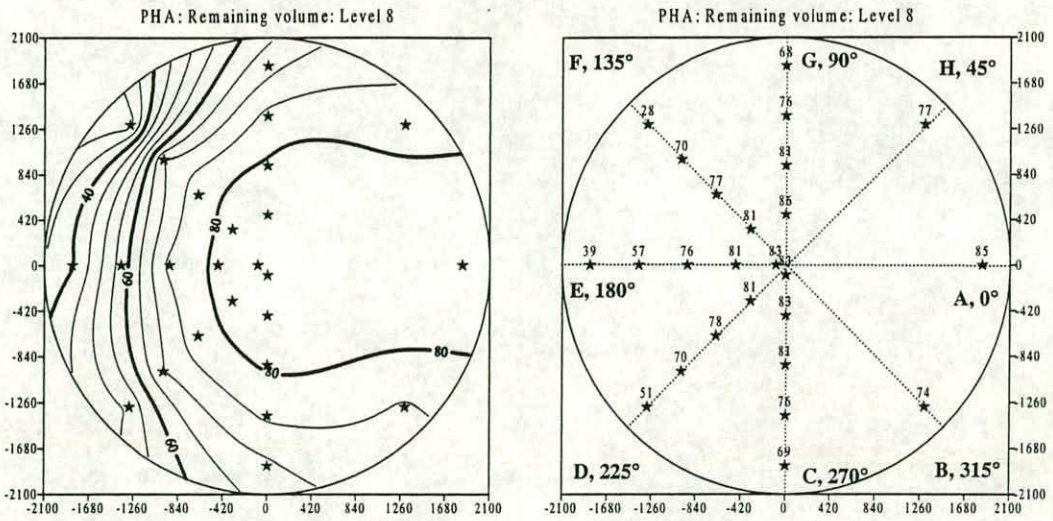

Fig. 7.46a Test PHA: Remaining volume: Level 8: Contours and spot values

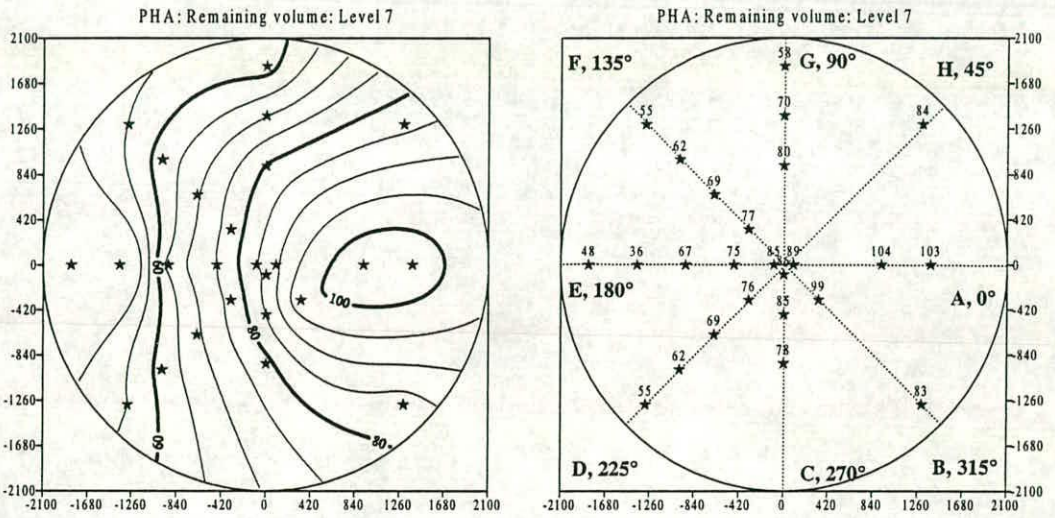

Fig. 7.46b Test PHA: Remaining volume: Level 7: Contours and spot values

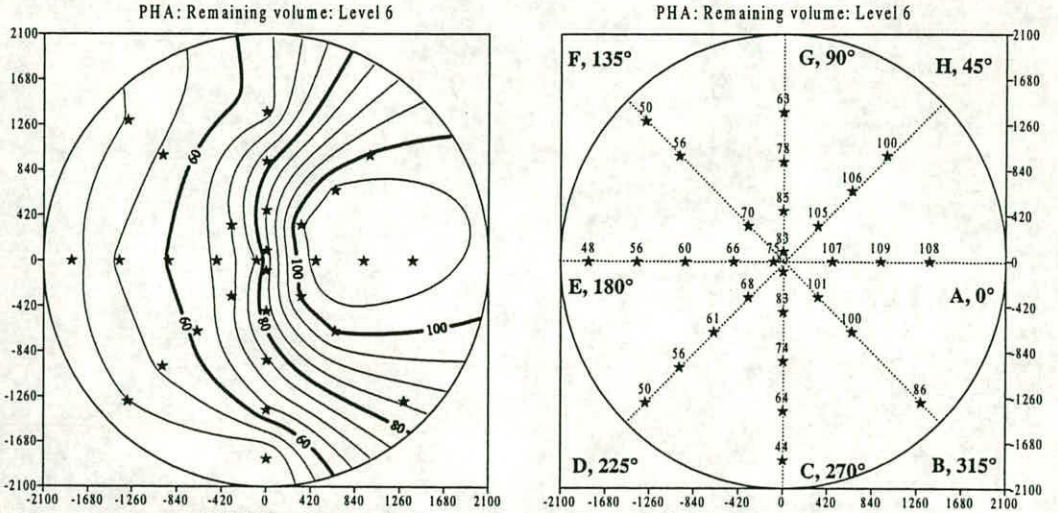

Fig. 7.46c Test PHA: Remaining volume: Level 6: Contours and spot values

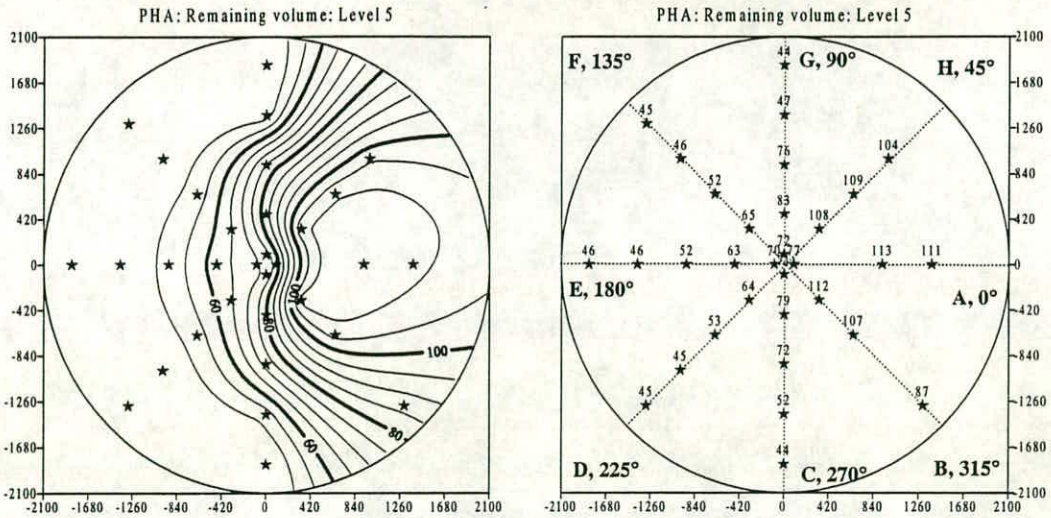

Fig. 7.46d Test PHA: Remaining volume: Level 5: Contours and spot values

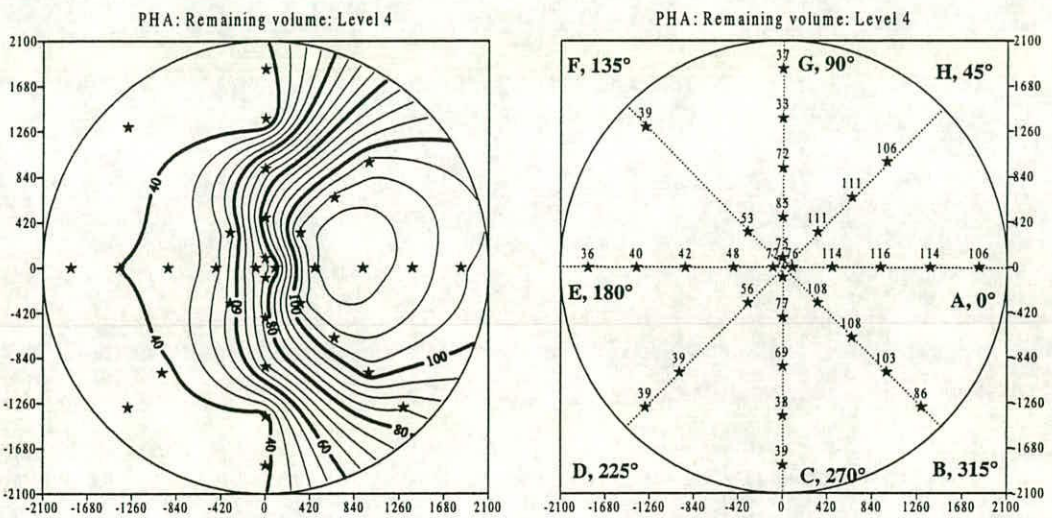

Fig. 7.46e Test PHA: Remaining volume: Level 4: Contours and spot values

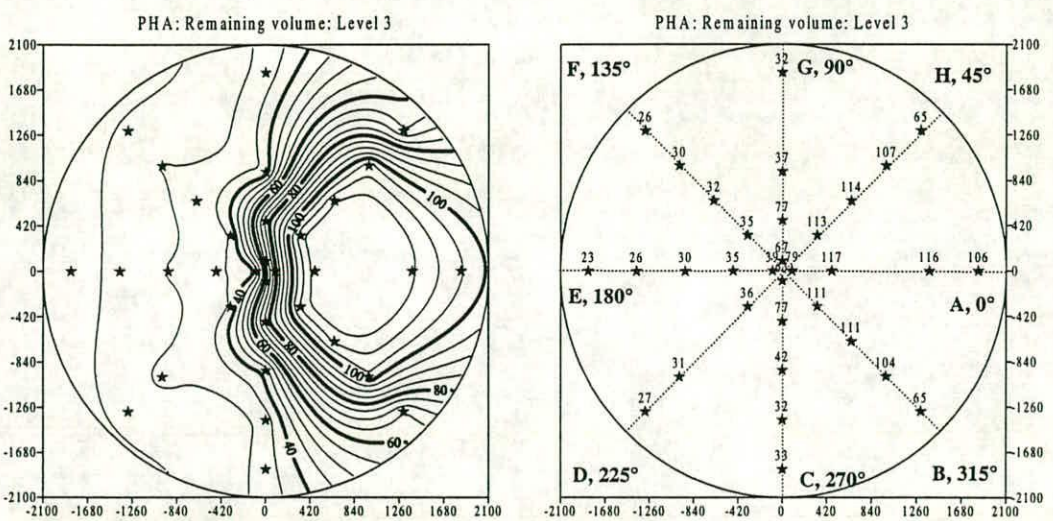

Fig. 7.46f Test PHA: Remaining volume: Level 3: Contours and spot values

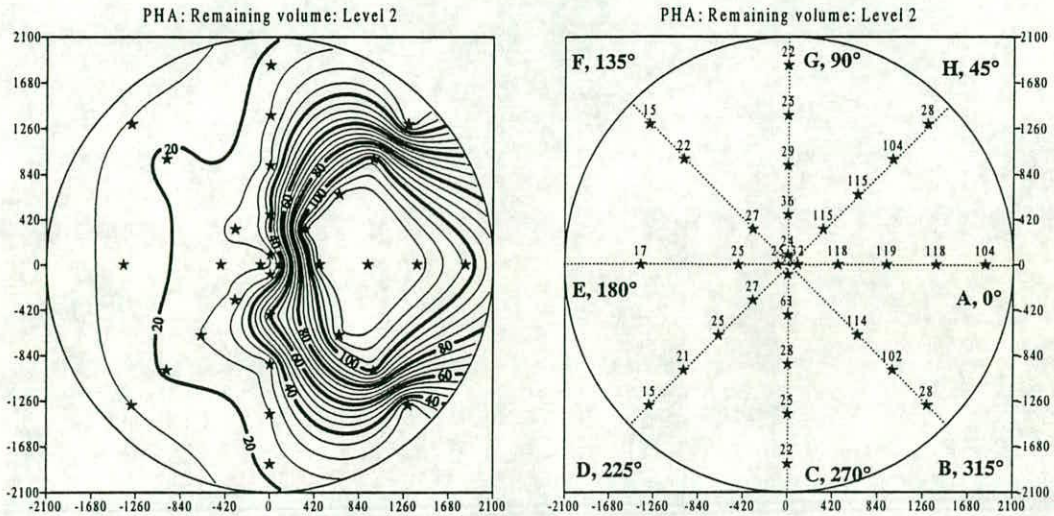

Fig. 7.46g Test PHA: Remaining volume: Level 2: Contours and spot values

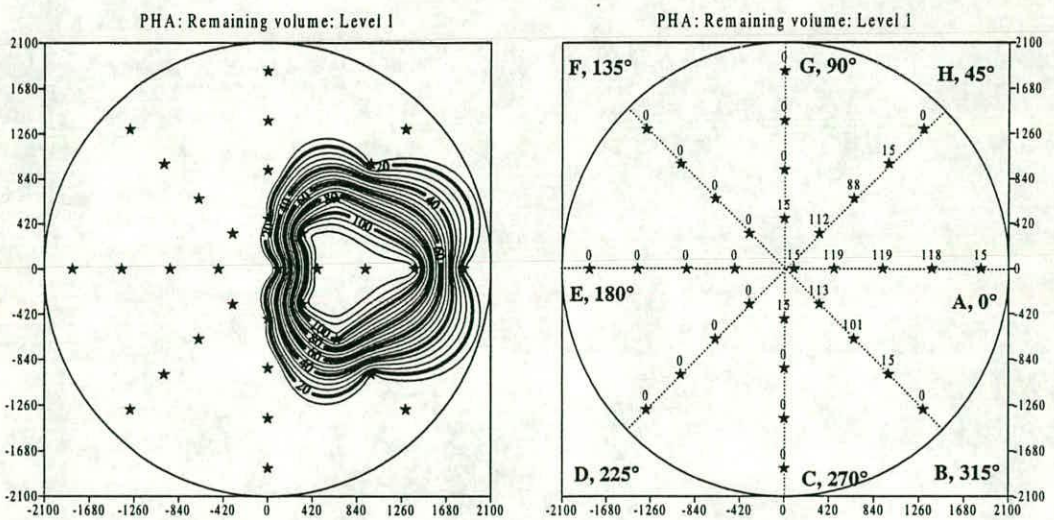

Fig. 7.46h Test PHA: Remaining volume: Level 1: Contours and spot values

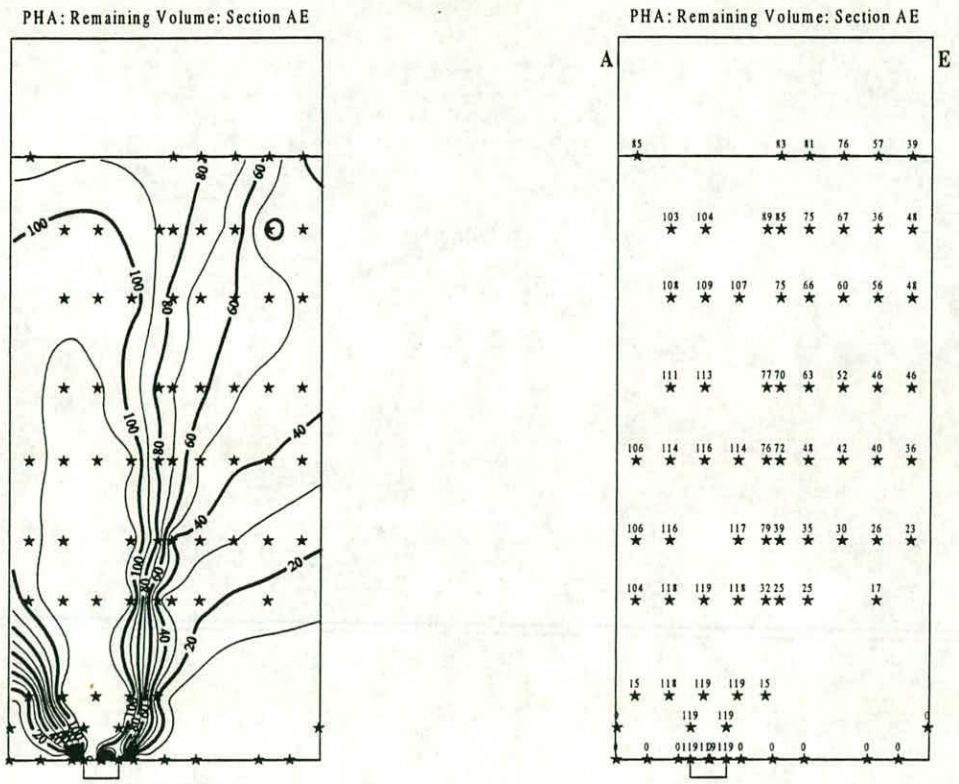

Fig. 7.47a Test PHA: Remaining volume: Vertical diametral section A-E: Contours and spot values

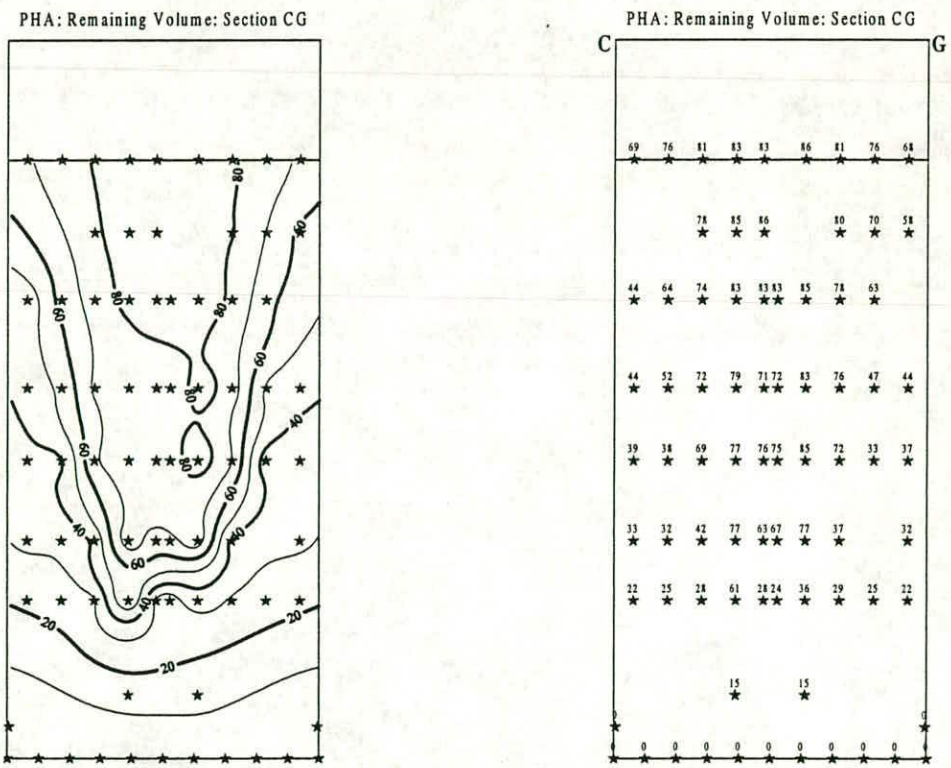

Fig. 7.47b Test PHA: Remaining volume: Vertical diametral section C-G: Contours and spot values

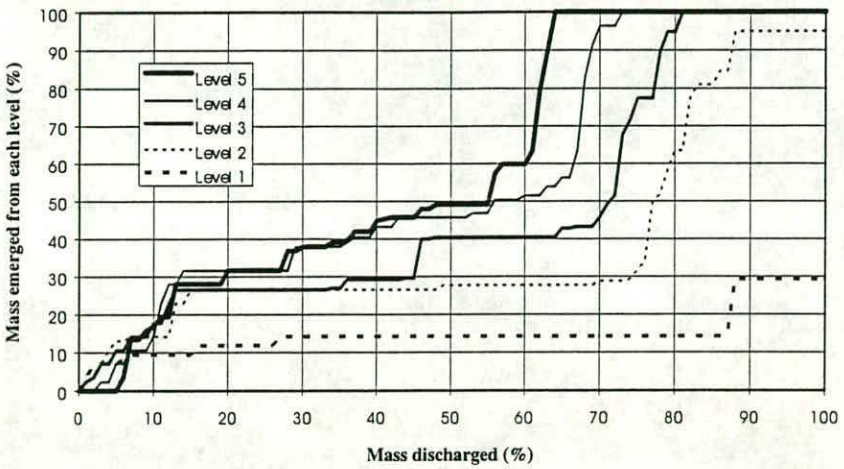

Fig. 7.48a Test PHA: Mass emerged from each level vs. mass discharged

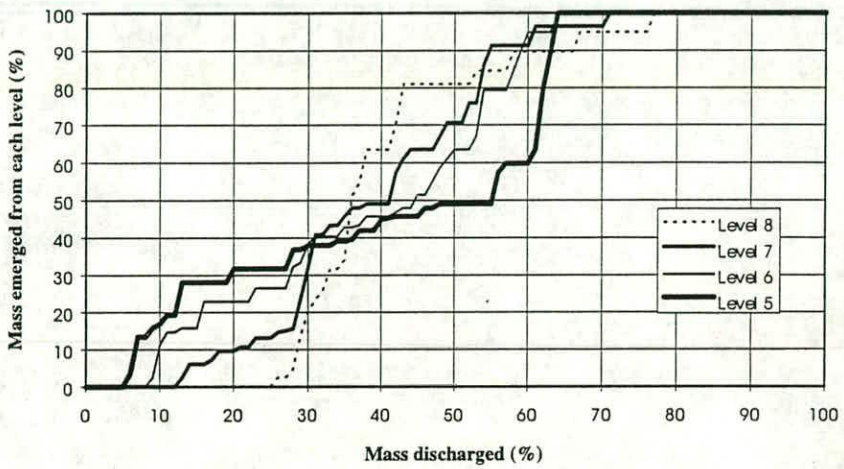

Fig. 7.48b Test PHA: Mass emerged from each level vs. mass discharged

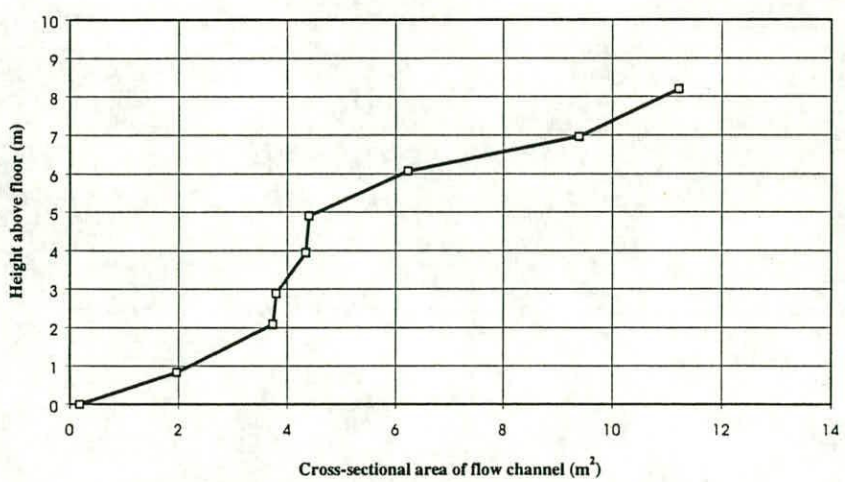

Fig. 7.49 Test PHA: Cross sectional area of flow funnel

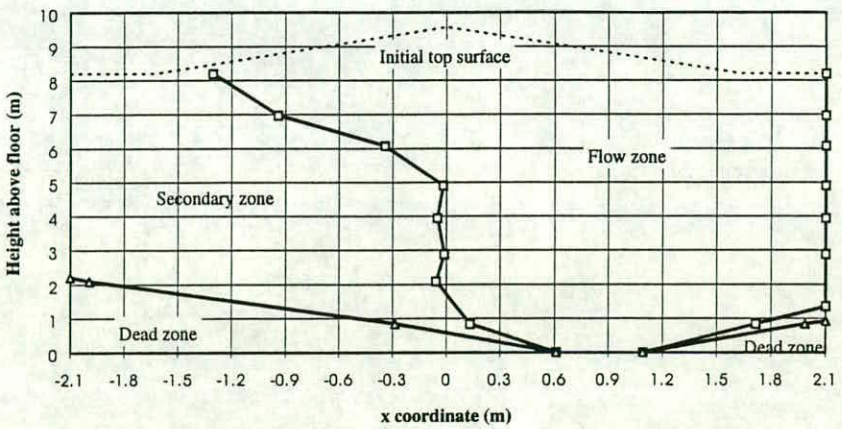

Fig. 7.50a Test PHA: Approximate flow channel boundary on x-z plane (Assumed circular channel)

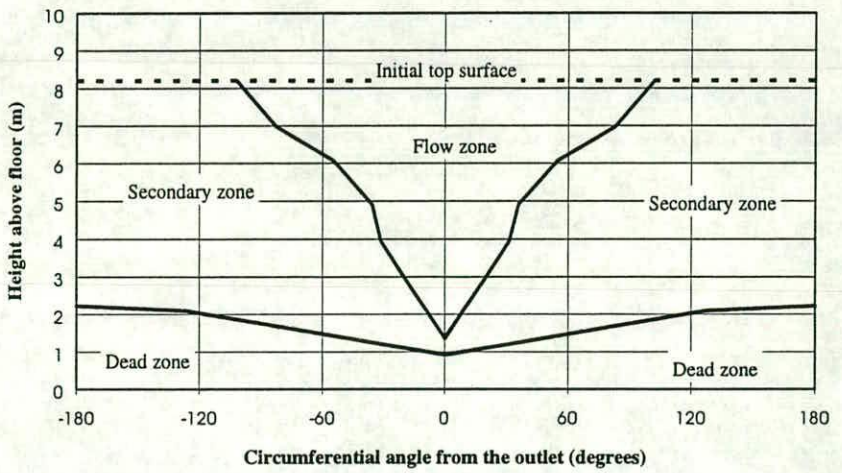

Fig. 7.50b Test PHA: Approximate flow channel boundary on wall (Assumed circular channel)

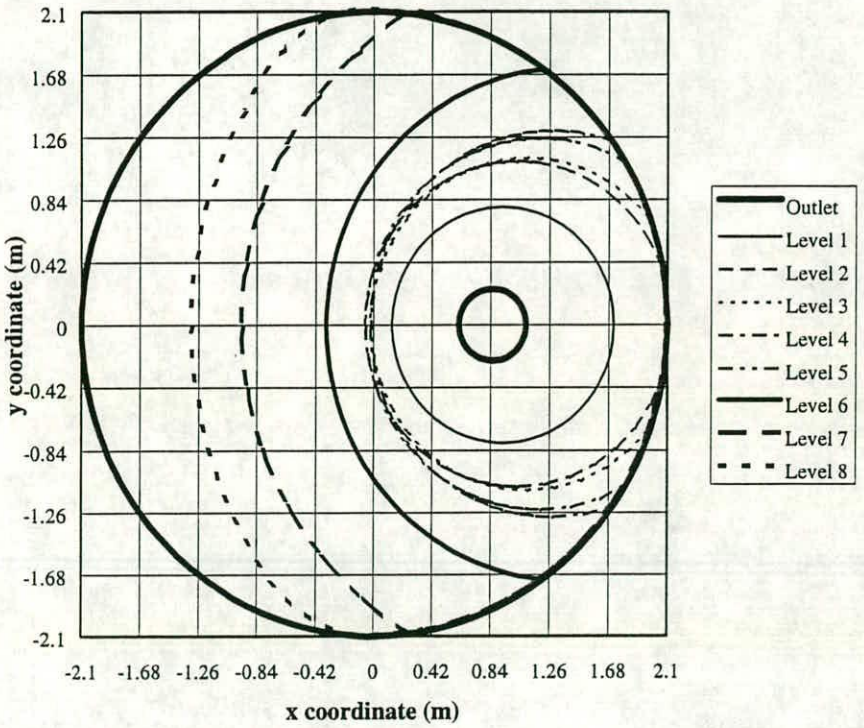

Fig. 7.50c Test PHA: Approximate flow channel boundary: plan (Assumed circular channel)

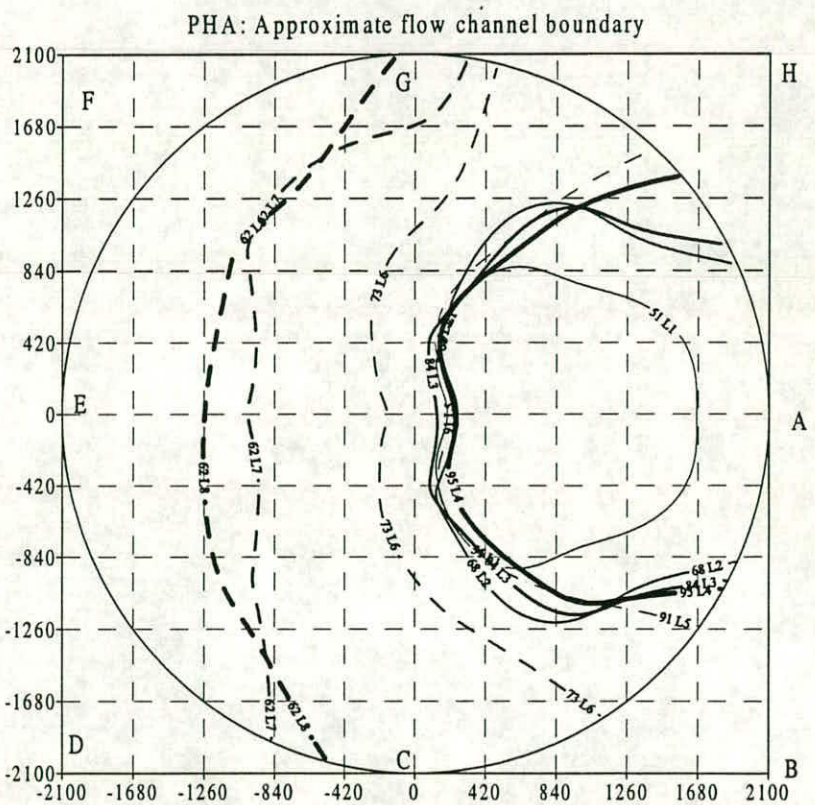

Fig. 7.50d Test PHA: Approximate flow channel boundary: plan (Drawn from remaining volume contours)

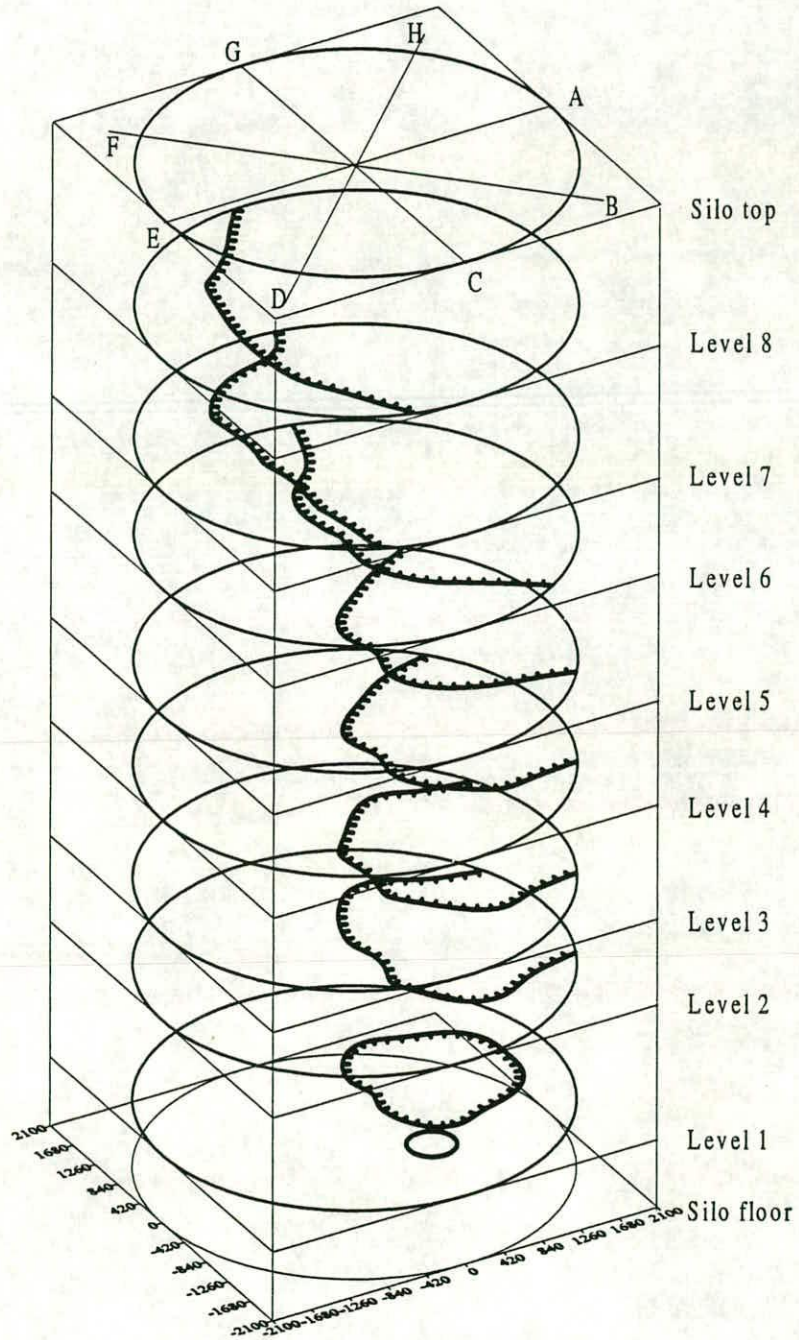

Fig. 7.50e Test PHA: Approximate flow channel boundary: 3D view (Drawn from remaining volume contours)

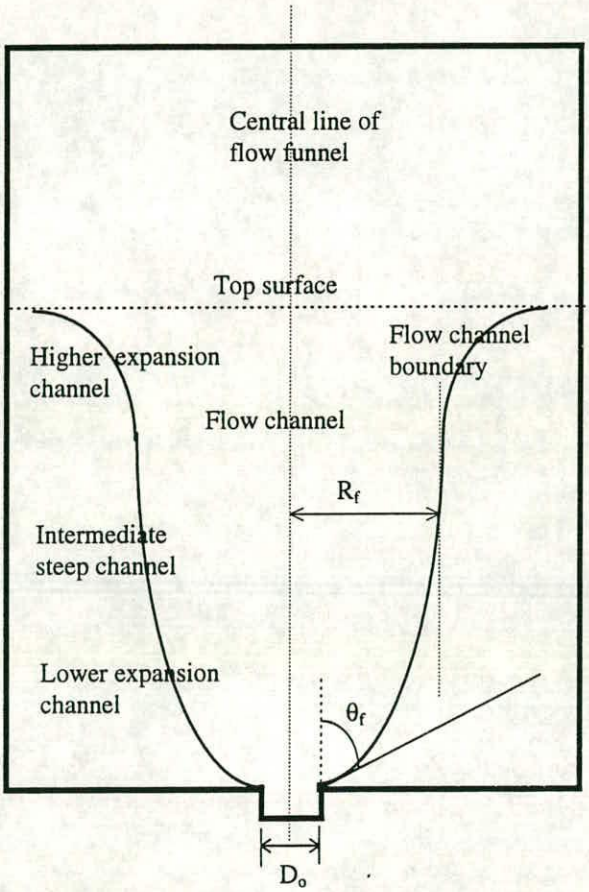

Fig. 7.51 Idealised vertical flow funnel

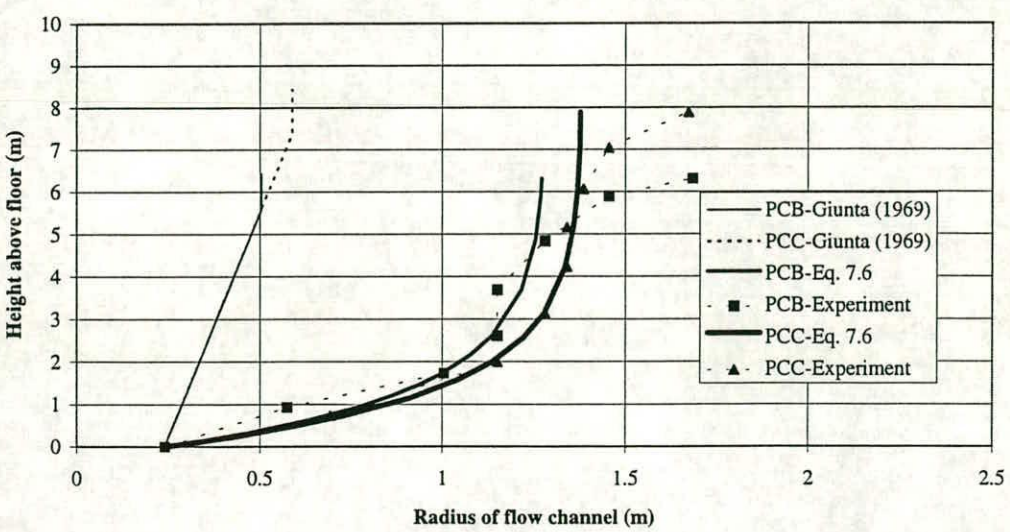

Fig. 7.52a Comparison of inferred flow channel with Eq. 7.6 and Giunta (1969) (Concentric discharge tests)

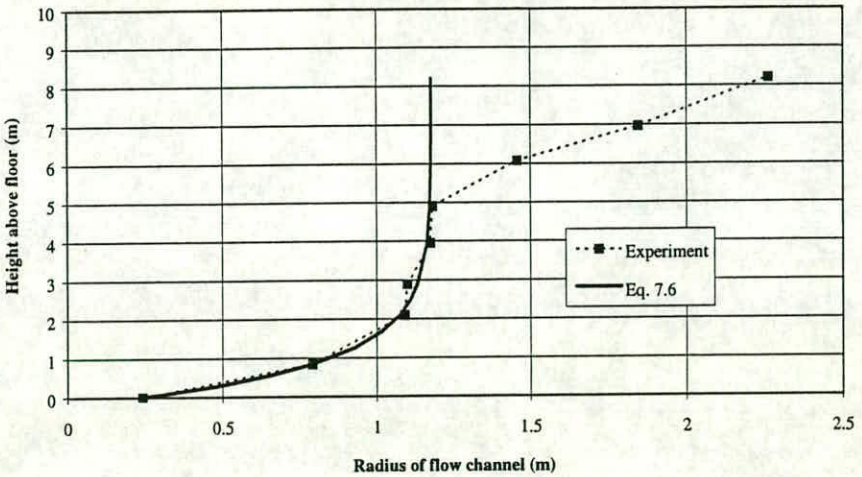

Fig. 7.52b Comparison of inferred flow channel with Eq. 7.6 (Half eccentric discharge test)

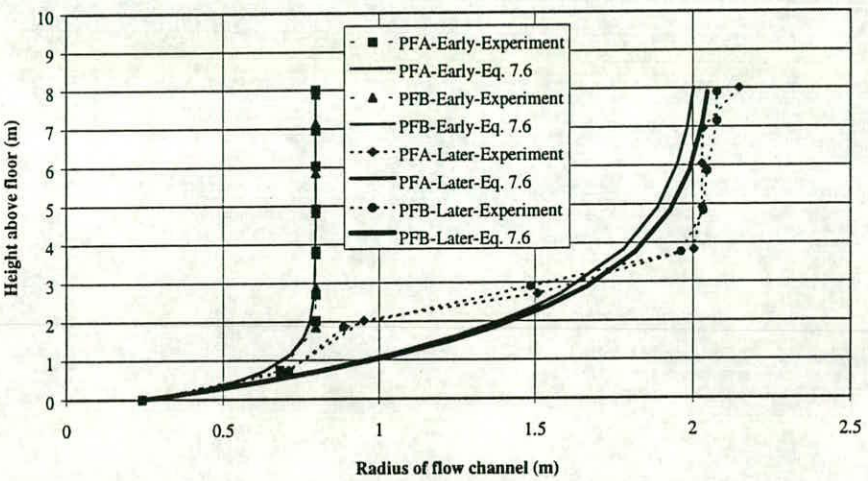

Fig. 7.52c Comparison of inferred flow channel with Eq. 7.6 (Fully eccentric discharge tests)

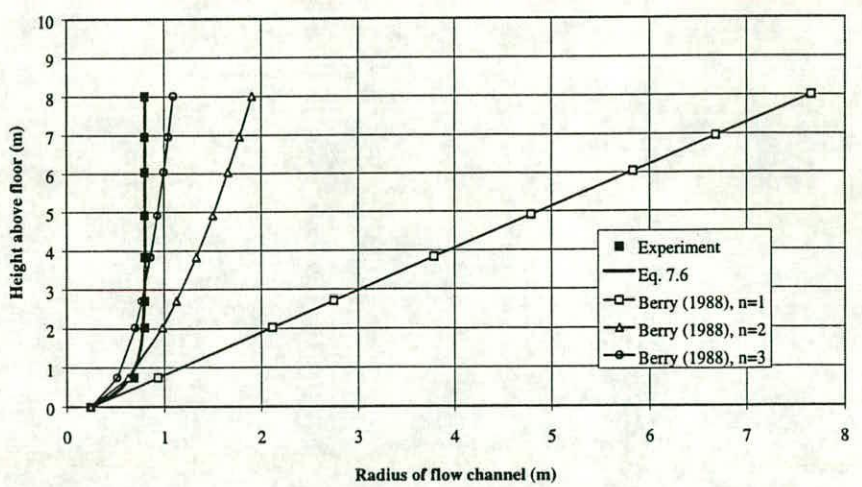

Fig. 7.53a Test PFA: Power model vs. inferred flow channel (flow channel angle preserved)

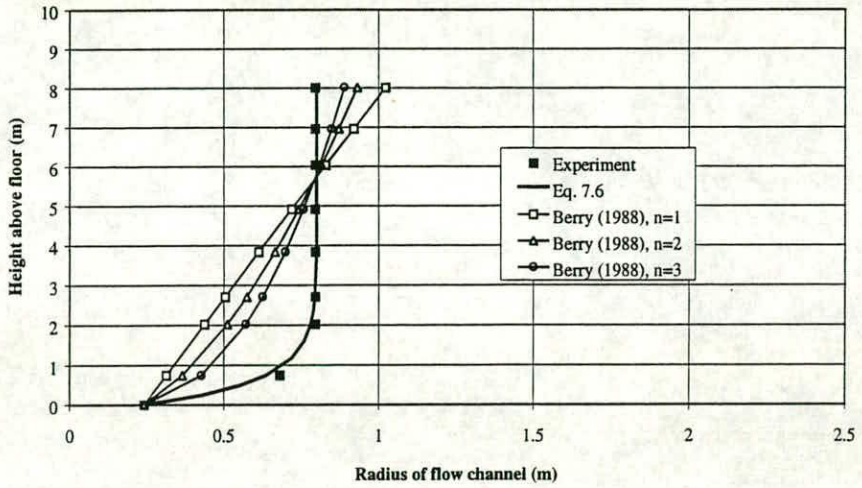

Fig. 7.53b Test PFA: Power model vs. inferred flow channel (flow channel angle not preserved)

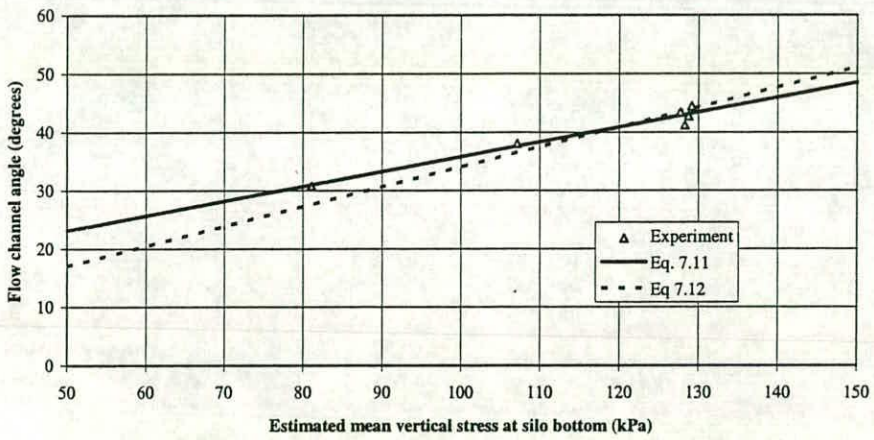

Fig. 7.54a Flow channel angle vs. estimated mean vertical stress at silo bottom (Linear model)

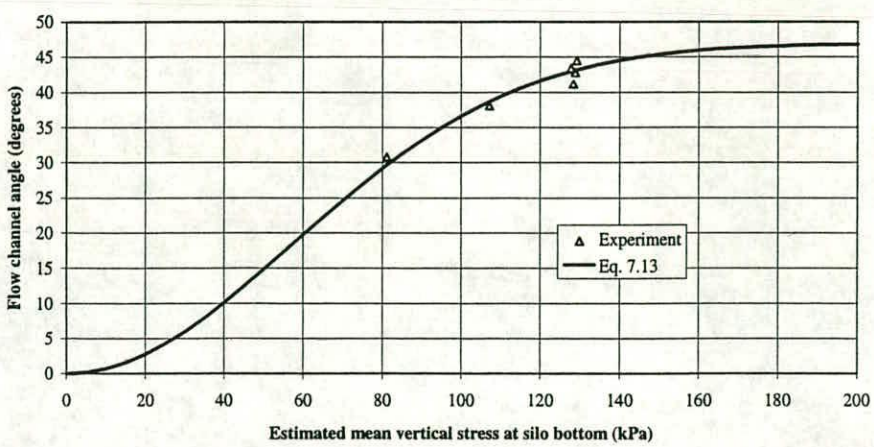

Fig. 7.54b Flow channel angle vs. estimated mean vertical stress at silo bottom (probability model)

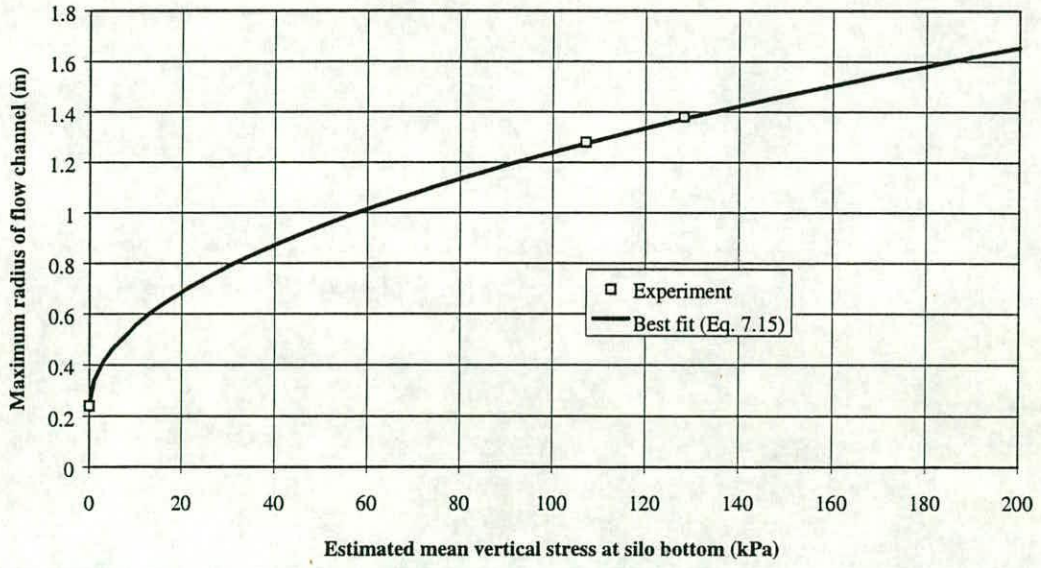

Fig. 7.55 Effect of mean vertical stress at silo bottom on radius of flow channel

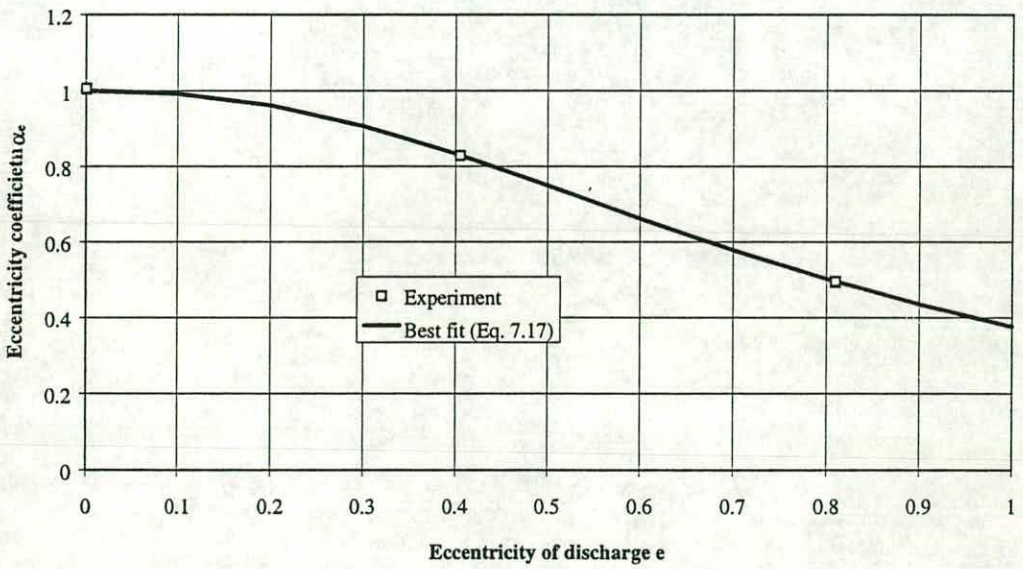

Fig. 7.56 Effect of eccentricity of discharge on the radius of flow channel